

University of Sannio

Department of Science and Technology

PhD Program in Science and Technology for the Environment and Health

XXXVIII CYCLE

Legacy mercury in soils from artisanal and small-scale gold mining (ASGM) landscapes in Jardim do Ouro, Pará (Brazilian Amazon): persistence, risk, and retention controls

PhD Candidate
Marcelo da Silveira Tortolero Araujo Lourenço

PhD Advisor
Prof. Mariano Mercurio

Co-advisor
Prof. Alessio Langella

PhD Course Coordinator
Prof. Marina Paolucci

Co-advisor
Dr. Rosa Maria di Maggio

2026

Acknowledgements

First and foremost, I would like to express my sincere gratitude to the institutions that made my doctoral research possible: the Università degli Studi del Sannio for the opportunity and financial support throughout my PhD, as well as the Brazilian Federal Police, Serabi Gold, the IUGS-Initiative on Forensic Geology, and the University of Naples Federico II for their support.

To my fiancée, Lara — none of this would have been possible without you. Thank you for everything we have lived together over these past ten years, for always being by my side, for constantly wishing the best for me, and for being my rock through it all. I am deeply grateful for the family we are building — you, me, and Uhura. I love you.

To my cousins (and younger brothers in every way that matters), Carlos, Sergio, and Leonardo, who have always been there with thoughtful advice and countless hours of video calls — a special thank you to Carlos for always helping me make sense of my thoughts and for showing me how to see life a little more like a Hobbit.

To my parents, Marcelo and Estela, who have moved heaven and earth since the very beginning so that I could get here — and I did. This achievement is as much yours as it is mine.

To my siblings, Renato and Laura, thank you for always being so caring and understanding with me. I am sorry for having been away from you for so long, I love you guys.

To my aunt Fernanda, thank you so much for always being there for me with so much care and attention, truly like a second mother. You know that to me, you are more than an aunt — you are my second mother.

To my grandparents, Maiza and Osnir, you are a true inspiration to me. Being close to you is one of the things that matters most in my life. Without you helping my parents raise me from such a young age, teaching me so many valuable lessons, and always caring for me with the greatest love, attention, and kindness, I would not have made it this far.

To my parents-in-law, Roger and Cris, who became like parents to me as well — how lucky I am to have your support and care throughout this journey.

I am sincerely grateful to Professor Mariano Mercurio for his support from before my arrival until the completion of my PhD, always present with thoughtful guidance and advice that allowed me to develop my work in the best possible way.

My heartfelt thanks to my co-supervisor, Rosa Maria di Maggio, who connected me with Professor Mariano Mercurio and supported me from the very beginning. Thank you for your kindness and for being such a warm and generous presence throughout this journey.

I would also like to thank Professor Alessio Langella for his co-supervision and valuable feedback, Professor Celestino Grifa for his support from the early stages, and Francesco Izzo for everything he has taught me over these years.

Finally, I am deeply grateful to Professor David Debruyne, who guided me closely throughout these three years and kindly hosted me during my research period abroad at the University of Campinas.

Summary

Abstract 12

1. Introduction 14

References 20

2. Mercury contamination in Brazil related to (historical) artisanal and small-scale gold mining activity: a narrative review with quantitative synthesis 25

2.1. Introduction 27

2.2. Context for the study 29

2.2.1. Mercury 29

2.2.2. A Concise Historical Overview of Gold Mining in Brazil 33

2.3. Methodology 36

2.3.1. Data collection and screening 37

2.3.2. Data analysis 39

2.4. Results 39

2.4.1. Search results 39

2.4.2. Mercury in human tissues 41

2.4.3. Environmental matrices 47

2.4.4. Mercury bioaccumulation in aquatic and terrestrial wildlife fauna 56

2.5. Discussion 64

2.5.1. Regional distribution and research coverage across time 64

2.5.2. Geogenic mercury baselines, Hg mobilization, and policy challenges in contamination attribution 65

2.5.3. Mercury bioaccumulation in human populations 67

2.5.4. Bioaccumulation in flora 70

2.5.5. Mercury retention in environmental compartments 72

2.5.6. Bioaccumulation in fauna 74

2.6. Limitations and future directions 76

2.7. Conclusions 79

References 80

3. Study area and socio-environmental setting 121

3.1. Regional setting, climate and land-use context 121

3.2. Geological and metallogenic context of the Tapajós Mineral Province (TMP) 123

3.3. Soil sampling, description and field observations 128

APPENDIX 1: Complete field soil descriptions 140

References 144

4. Legacy and ongoing mercury contamination in soils from ASGM sites in the Tapajós Gold Province, Pará, Brazil 149
4.1. Introduction 150
4.2. Materials and methods 153
4.2.1. Study area 153
4.2.2. Soil sampling 154
4.2.3. Sample preparation and analysis 155
4.2.4. Data analysis 155
4.2.5. Geostatistical analysis 156
4.2.6. Contamination and ecological risk indices 157
4.3. Results 159
4.3.1. Total mercury (THg) 159
4.3.2. Exploratory and comparative analyses of THg in the different ASGM areas 164
4.3.3. Geoaccumulation index ($Igeo$) 166
4.3.4. Contamination factor (CF) and ecological risk index (Er) 166
4.4. Discussion 167
4.5. Conclusion 172
APPENDIX 2: Total mercury (THg) concentrations. 173
APPENDIX 3: Percentage of fine particles (< 105 µm) for the ~30 years deactivated ASGM. 175
APPENDIX 4: Data — Contamination factor, ecological risk index, and geoaccumulation index. 176
References 178
5. Physicochemical, mineralogical and thermal characterization of the soils 187
5.1. Methodology 189
5.1.1. Mineralogical composition 189
5.1.2. Attenuated Total Reflectance Fourier-Transformed Infrared (ATR-FTIR) characterization of soil functional groups 189
5.1.3. Thermal behavior of soils assessed by Simultaneous Thermal Analysis (STA) 190
5.1.4. Soil physicochemical properties: pH and water holding capacity (WHC) 190
5.2. Results 192
5.2.1. Mineralogical composition 192
5.2.2. Attenuated Total Reflectance Fourier-Transformed Infrared (ATR-FTIR) characterization of soil functional groups 196
5.2.3. Thermal behavior of soils assessed by Simultaneous Thermal Analysis (STA) 199
5.2.4. Soil physicochemical properties: pH and water holding capacity (WHC) 202
5.2.5. Integrated analysis of total mercury concentrations and behavior based on soil physicochemical, mineralogical and thermal properties 204

5.3. Discussion 221
5.4. Conclusion 230
APPENDIX 5: X-ray diffraction patterns of all studied samples. 233
APPENDIX 6: TG/DSC curves of all samples. 255
APPENDIX 7: pH and WHC (%) data. 292
References 294
6. General conclusions 302
Main contributions of this thesis 306

List of figures

Figure 1: ASGM gold ore processing. Adapted from: Yoshimura et al. (2021) 33
Figure 2: A summarized timeline of gold exploration in Brazil from the 16th Century to the present day. Information synthesized from Clearly (1990); Machado and Figuerôa (2001); Cabral et al. (2002); Theije (2020); Abad and Palma (2021); Costa and Rios (2022); Soares and Saes (2023); Diogens et al. (2024). 35
Figure 3: PRISMA flow diagram. Adapted from Page et al. (2021).....40
Figure 4: Number of publications by year. The solid grey line represents the annual number of publications, while the red dashed line represents the moving average of three years. 41
Figure 5: Number of studies that evaluated Hg concentrations in human tissues by state. 21 studies were conducted in the State of Pará, 7 in Amazonas, 5 in Rondônia, 3 in Mato Grosso, 2 in Roraima, and 1 in Amapá. 42
Figure 6: (A) Boxplots of Hg concentrations (ppb) in hair across different regions of Pará. At 10,000 ppb is the threshold that marks where health risks begin, while 1,000 ppb is considered the safe level (WHO, 2021); (B) Map of the State of Pará showing the division of the analyzed regions. The regions were delineated based on the areas approached by the included studies and considering the Au districts, providing context for the comparisons presented in the boxplots of Figure 6A. The numbers displayed on the map correspond to the references associated with each region, as follows: [1] Akagi et al. (1995); [2] Akagi et al. (2000); [3] Barbosa et al. (1995); [4] Basta et al. (2021); [5] Castilhos et al. (2015); [6] Crompton et al. (2002); [7] Dolbec et al. (2000); [8] Dorea et al. (2005); [9] Grandjean et al. (1999); [10] Harada et al. (2001); [11] Kehrig et al. (1997); [12] Leino and Lodenius (1995); [13] Oliveira et al. (2022); [14] Perini et al. (2021); [15] Pinheiro et al. (2008); [16] Pinheiro et al. (2012); [17] Santos et al. (2000); [18] Santos et al. (2002a); and [19] Santos et al. (2002b). 45
Figure 7: Boxplots of Hg concentrations (ppb) in blood and urine from Pará. Thresholds: 5 ppb (urine safe level), 5.8 ppb (blood safe level), 20 ppb (elevated blood level), 30 ppb (urine occupational exposure), and 50 ppb (blood occupational exposure and urine toxic level). Sample sizes (n): 4 (ASGM workers), 6 (blood) and 3 (urine) (general population), 6 (blood) and 1 (urine) (traditional populations). 46

Figure 8: Frequency of analytical techniques applied to different environmental matrices, including CV-AAS, CV-AFS, TD-AAS, and others. Each bar represents the number of studies using a specific technique for each environmental matrix. 49
Figure 9: Boxplots comparing Hg concentrations (ppb) in different plant tissues (log scale). (A) Aggregated data for all species (Leaves = 25, Root = 35, Stem = 8, Stem + Leaves = 27). (B) Data specific to Eichhornia crassipes (Leaves = 1, Root = 5, Shoot = 2, Stem = 1, Whole plant = 1). 50
Figure 10: Boxplot of Hg concentrations in sediments, soils, and SPM (log-transformed, natural log scale). The red dashed line represents the Hg prevention levels for soils in Brazil (CONAMA, 2010). 51
Figure 11: Boxplots showing Hg concentrations in water (ppb) across seven States in Brazil (log-transformed, natural log scale). The red dashed line represents the maximum allowable value for drinking water (CONAMA, 2008). 54
Figure 12: Boxplot of air mercury (Hg) concentrations (ng/m³) in ASGM hubs (left) and in non-ASGM related areas (right). The red dashed line at 20,000 indicates the threshold for above which mild, subclinical signs of central nervous system toxicity may develop in workers who have been chronically exposed to elemental mercury in the air (WHO, 2021). The y-axis shows Hg concentrations in log-transformed, natural log scale. 55
Figure 13: Boxplot of mercury (Hg) concentrations in different alligator tissues from Mato Grosso (Vieira et al., 2011; Lázaro et al., 2015), Mato Grosso do Sul (Vieira et al., 2011), Pará (Akagi et al., 1995), and Rondônia (Oliveira et al., 2021a)..... 60
Figure 14: Boxplot of mercury concentrations (ppb, wet weight), log-transformed using the natural logarithm scale, in muscles of different fish species from Brazil, categorized by feeding habit..... 61
Figure 15: Boxplot of mercury (Hg) concentrations in different invertebrate species in Brazil. The y-axis indicates Hg concentration (log-transformed, natural log scale) in ppb. 63
Figure 16: Location map of the study area, showing Brazil, the Brazilian Legal Amazon, Pará State, and the municipality of Itaituba, providing geographical context for the four studied sites. 122
Figure 17: Geological map of the study area. Adapted from: CPRM (2004). 126
Figure 18: Representative field photos illustrating the physical heterogeneity of soils in the ~30 years deactivated ASGM area. (A) MTBP-18: brownish soil with a noticeable fine fraction, collected in a waterlogged setting; (B) MTBP-23: yellowish, sand-dominated soil with abundant leaf litter at the surface; (C) MTBP-28: white, quartz-rich sediment with

minimal fine material; and (D) MTBP-31: brownish sandy soil collected near a small water body. Together, these images highlight the strong variability in texture, color, moisture conditions and organic inputs that characterize post-mining soils within the study area. 130
Figure 19: Waterlogged soils from low-lying areas of the ~30 years deactivated ASGM site. (A) MTBP-08 and (B) MTBP-17 illustrate saturated conditions controlled by local topography, highlighting moisture-driven heterogeneity within the study area. 131
Figure 20: Representative forest soils from the site without ASGM records (control area). (A) MTBVP-02 and (B) MTBVP-04 illustrate textural and color variability under forest cover, with the presence of roots and litter highlighting organic matter–rich surface conditions. 132
Figure 21: Figure 21: Landscape conditions of the studied active ASGM site. (A) deforestation for 'clearing' the site and (B) open pit for ASGM operations. 133
Figure 22: Field photos highlighting heterogeneity within the active ASGM site , highlighting the coexistence of contrasting microenvironments over short spatial scales. (A) MTPS-05 soil with a greyish color and clear predominance of fine particles (silt–clay), occurring beneath an organic layer, (B) MTPS-09 sediment dominated by coarse sand and gravel, collected near a swampy area, and (C) MTPS-13 greyish soil with high clay content, sampled below the sluice box 135
Figure 23: (A) Flooded abandoned open pit showing stagnant turquoise-colored water, indicative of acidic, metal-rich conditions in the site deactivated in January 2024. (B) Secondary vegetation re-stabilization after cessation of ASGM activities in the site deactivated in January 2024. 136
Figure 24: Representative soil samples from the ASGM site deactivated in January 2024. (A) MTNC-04, rusty-colored, sand-dominated soil with abundant gravel and visible oxide-rich grains, collected at the margin of the flooded open pit, (B) sandy soil with gravel, oxide grains, showing accumulation of organic matter fragments, also sampled at the border of the flooded open pit, and (C) brownish soil with mixed silt/clay and sand fractions and absence of gravel, collected at the distal end of the open-pit drainage pathway. 138
Figure 25: Location map of the study area, generated using WGS84/UTM Zone 21S, EPSG: 32721, with units in meters. 154
Figure 26: Boxplot of total mercury (THg) concentrations in soil from four sites with distinct ASGM activity histories (ng g-1, log scale). The red dashed line represents the soil prevention level established by CONAMA (2009). 160
Figure 27: IDW-interpolated maps showing the spatial distribution of log-transformed THg concentrations in (A) site deactivated for approximately 30 years, (B) active site, and (C) site

deactivated in January 2024. Maps were generated using WGS84/UTM Zone 21S, EPSG: 32721, with units in meters. 163
Figure 28: Relationship between fine material content (<105 μm) and log-transformed THg concentrations in the approximately 30 years deactivated ASGM. The linear trendline represents the fitted regression model. 164
Figure 29: Hierarchical clustering of soil samples based on log-transformed THg concentrations. Vertical red dashed lines indicate cluster boundaries, while the green dotted line represents the THg background assumed in this study. 165
Figure 30: Distribution of Igeo classes by area. Igeo class abbreviations: U (Uncontaminated); U–MC (Uncontaminated to moderately contaminated); MC (Moderately contaminated); M–HC (Moderately to heavily contaminated); HC (Heavily contaminated); H–EC (Heavily to extremely contaminated); EC (Extremely contaminated). 166
Figure 31: XRD diffractograms of the studied sites' representative samples. (A) MTBP-01, ~30 years deactivated ASGM, (B) MTBVP-01, without ASGM records, (C) MTNC-08, ASGM deactivated in January 2024, and (D) MTPS-05, active ASGM. 195
Figure 32: ATR-FTIR spectra of one representative sample from each area: (A) MTBP-01, (B) MTBVP-01, (C) MTNC-07, and (D) MTPS-05. 198
Figure 33: Representative TG, DTG and DSC curves of selected soil samples from the different studied sites: (A) ~30 years deactivated site (MTBP-01); (B) site deactivated in January 2024 (MTNC-07); (C) active ASGM site (MTPS-05); and (D) site without ASGM records (MTBVP-01). 202
Figure 34: Distribution of soil pH and water holding capacity (%) across the studied sites. Boxplots summarize the median, interquartile range and overall variability for each parameter, with colors indicating site classification. Only samples for which pH and WHC were measured are included. 203
Figure 35: Boxplots of mass loss (ΔW, %) for each temperature interval derived from TG analysis, grouped by studied site. Boxes represent the interquartile range, the central line indicates the median, and whiskers extend to 1.5 times the interquartile range. 208
Figure 36: Principal component analysis (PCA) of thermogravimetric mass loss profiles across all temperature intervals. PC1 accounted for 80.5% of the total variance and represents the overall magnitude of mass loss, while PC2 accounted for 10.7% of the variance and contrasts mass losses occurring in the 200–380 °C interval with those occurring above 600 °C. Points represent individual samples and ellipses indicate the 68% confidence region for each site category. 211

Figure 37: Violin plots of distances to group centroids obtained from the PERMDISP analysis, showing differences in multivariate dispersion among site categories. Violin width represents the density of distances, and boxplots summarize median and interquartile range. Larger distances indicate greater heterogeneity in thermogravimetric mass loss profiles within sites. 212
Figure 38: Observed versus predicted log10THg values obtained from the final multiple linear regression model (Model 2: TG + Site). Points represent individual soil samples and are colored by site category. The solid 1:1 line indicates perfect agreement between observed and predicted values; deviations from this line reflect model residuals. 217
Figure 39: Relationship between WHC and THg concentrations in soils from the ~30 years deactivated ASGM site. Points represent individual samples. The solid line corresponds to the robust linear regression fitted using $\log_{10}$-transformed THg concentrations. The y-axis is displayed on a logarithmic scale using original THg units (ng g^{-1}) to facilitate interpretation. 219
Figure 40: Spearman correlation matrix among total mercury concentrations (THg), water holding capacity (WHC), soil pH, and fine particle content (<105 μm) for the ~30 years deactivated ASGM site. Numeric labels represent Spearman's correlation coefficients (ρ). Statistical significance is indicated by asterisks (**p < 0.01; ***p < 0.001). 220

List of tables

Table 1: Criteria for inclusion and exclusion of studies. 38
Table 2. Hg concentrations in human tissues by State. 43
Table 3. Hg concentrations in sediments, soils and SPM by State. 52
Table 4. Hg concentrations and SD (d.w. ppb) in different tissues of mammal species studied by the articles included. 57
Table 5. Hg concentrations and SD (d.w. ppb) in tissues of avian species studied by the articles included. 58
Table 6. Contamination factor (CF) and ecological risk index (Er) across study sites. 167
Table 7. Occurrence frequency (n) of mineral groups identified by qualitative XRD in soils across the studied sites. 192
Table 8. Total mercury (THg) concentrations in soils from ASGM sites at different ASGM stages, highlighting samples with identified Fe–Mn (oxyhydr)oxides. 205
Table 9. Effect of Fe–Mn oxyhydroxide presence on log-transformed THg concentrations by area (robust regression). 206
Table 10. Summary statistics of mass loss (ΔW, %) for each temperature interval and site. 208
Table 11. Pairwise comparisons of mass loss (%) among sites for each temperature interval using Dunn's test with Bonferroni adjustment. 209
Table 12. Spearman correlation between mass loss (ΔW, %) and THg concentrations (ng g-1) by ASGM context. 212
Table 13. Multiple linear regression models linking log10(THg) to thermogravimetric mass loss (ΔW, %) and ASGM site context. 214
Table 14. Nested model and AIC-based comparisons among multiple linear regression models for log10THg. 216
Table 15. Spearman correlation between water holding capacity (WHC) and log10-transformed total mercury (THg) concentrations by ASGM context. 218

Abstract

Mercury (Hg) contamination associated with artisanal and small-scale gold mining (ASGM) is a persistent environmental issue in the Brazilian Amazon. While ASGM is widely recognized as a major source of Hg, elevated concentrations in soils and sediments cannot always be attributed to mining alone. Geogenic enrichment, long-term atmospheric deposition, and landscape processes such as erosion and sediment transport can also contribute substantially to Hg distribution. In highly disturbed Amazonian landscapes, this overlap complicates contamination attribution and can bias risk assessments when regional geochemical baselines are not defined. In this context, this thesis investigates Hg contamination in superficial soils from Jardim do Ouro village (Pará State), comparing three ASGM sites with contrasting activity histories (active, deactivated in January 2024, and deactivated for ~30 years) against a control area without ASGM records used as a regional geogenic baseline. The study integrates total mercury (THg) concentrations and ecological risk indices with particle-size distribution, mineralogical and surface characterization (XRD and ATR-FTIR), thermogravimetric data (TG/DSC), and basic physicochemical properties (WHC and pH). This approach was designed to clarify both the persistence of legacy Hg in post-ASGM landscapes and the soil fractions controlling Hg retention under different disturbance histories. Soils from the ASGM site deactivated for ~30 years still exhibited elevated THg concentrations (27 to 8,862 ng g^{-1}; median = 324 ng g^{-1}) and ecological risk levels above regulatory thresholds, demonstrating that Hg contamination can remain environmentally relevant decades after mining activity has ceased. In contrast, the active and recently deactivated sites generally displayed THg concentrations close to the regional baseline (178 ng g^{-1}), with exceedances largely restricted to localized hotspots directly associated with ASGM operations. These results indicate that current mining activity does not necessarily translate into higher median THg at the site scale, whereas long-term deactivated areas can retain a strong contamination legacy. In the long-term deactivated site, fine particle content explained 73% of the variability in $\log_{10}$-transformed THg, revealing a robust texture control on Hg retention. Mineralogical analyses indicated broadly similar frameworks dominated by quartz and kaolinite-group minerals, consistent with highly weathered tropical soils developed on granitic parent material. However, accessory phases such as gibbsite, mica-type phyllosilicates, smectites, and sporadically occurring feldspars highlighted meaningful sample-scale variability linked to weathering intensity, soil development, and disturbance history. The association between Fe–Mn (oxyhydr)oxides and THg was not uniform across sites, supporting a context-dependent role of reactive phases in Hg retention and redistribution. Thermogravimetric profiles were

dominated by mass loss in the 380–600 °C interval, and the strongest between-site contrasts were expressed in this range, indicating that site-related differences are primarily reflected in major soil fractions controlling thermal behavior. THg was systematically associated with thermogravimetric fractions, particularly in the ~30 years deactivated site, where strong correlations across all temperature intervals linked Hg enrichment to multiple soil components. WHC was positively associated with THg only in the long-term deactivated site, consistent with preferential Hg enrichment in fine-textured soils with higher water retention capacity. Soil pH showed no significant relationship with THg in any site. Overall, this thesis demonstrates that Hg risk in ASGM landscapes is not defined solely by the presence of active mining, but by the interaction between contamination legacy, soil texture, physical properties, reactive mineral phases, and disturbance history. These findings reinforce the need for regional geochemical baselines, long-term monitoring, and soil-informed approaches to Hg risk assessment and management in the Brazilian Amazon.

1. Introduction

Artisanal and small-scale gold mining (ASGM) remains one of the most persistent and complex sources of mercury (Hg) contamination in the Brazilian Amazon **(Crespo-Lopez et al., 2021; Lourenço et al., 2025)**. Despite being widely recognized as an environmental and public health issue, ASGM continues to expand and reconfigure across the region. In Brazil, this activity is often associated with illegal operations, which tend to occur in highly dynamic riverine and forest environments where monitoring is limited and enforcement is intermittent **(Neto et al., 2024)**. Within this context, Hg contamination has become one of the most challenging legacies of ASGM, not only because of its toxicity, but also because of its persistence, mobility, and ability to re-enter ecological cycles long after mining has ceased **(Dhiman, 2023; Uddin et al., 2024)**.

Mercury use in gold extraction is particularly problematic because it involves direct handling and release of elemental Hg, which can contaminate air, water, and soils **(**e.g., **Lourenço et al., 2025)**. Once introduced into the environment, Hg can undergo complex transformations and redistribution processes, including long-range atmospheric transport, sediment burial, re-mobilization, and microbial methylation **(**e.g., **Jackson, 1997; Amos et al., 2014; Helmrich et al., 2022; Peng et al., 2024)**. In Amazonian systems, the conversion of inorganic Hg into methylmercury (MeHg) is of special concern due to its high bioavailability and strong biomagnification in aquatic food webs **(Nyholt et al., 2022; Pierezan et al., 2024)**. As a result, Hg contamination linked to ASGM has been consistently associated with occupational exposure in miners, as well as dietary exposure through fish consumption in riverine and Indigenous communities **(**e.g., **Basta et al., 2021; Lourenço et al., 2025; Lucchini et al., 2025)**. These impacts reinforce that Hg is not only an environmental

contaminant, but also a One Health issue, connecting ecosystem integrity with human and animal health outcomes.

While ASGM is a major driver of Hg release in the Amazon **(Crespo-Lopez et al., 2021; Castilhos & Domingos, 2024)**, the environmental distribution of Hg is not exclusively controlled by mining activity **(**e.g., **Figueiredo et al., 2018; Gerson et al., 2022)**. Naturally enriched soils, long-term atmospheric deposition, and geomorphological processes such as erosion and sediment transport can produce spatially heterogeneous Hg concentrations that may overlap with ASGM-impacted areas. In addition, landscape-scale disturbances such as deforestation, road opening, and dam construction can mobilize both geogenic and legacy Hg **(Diringer et al., 2019; Lourenço et al., 2025)**. This makes Hg attribution particularly challenging in tropical settings, where weathered soils, high rainfall, and intense sediment redistribution create a highly dynamic geochemical environment **(Wasserman et al., 2003; Yuan et al., 2024)**.

In this scenario, soils represent a critical but still underexplored compartment for understanding Hg persistence ASGM landscapes with different history. Soils can act simultaneously as sinks, reservoirs, and secondary sources of Hg, depending on physical disturbance, hydrological connectivity, and geochemical conditions **(**e.g., **Lima et al., 2022; Hou, 2023; Paiva et al., 2024)**. In active ASGM sites, mechanical reworking and the continuous turnover of substrate can redistribute Hg across soil fractions and expose new reactive surfaces **(**e.g., **Blouin et al., 2005)**. In recently deactivated areas, soils may retain a strong imprint of disturbance while beginning to reorganize physically and chemically. In long-term deactivated sites, Hg can remain stored in soil matrices for decades, potentially sustaining environmental risk through gradual release, erosion, or transformation processes **(Wei et al., 2025)**. Importantly, this persistence is not necessarily reflected by visible signs of ASGM

activity, meaning that post-ASGM landscapes may remain environmentally relevant even when they appear "recovered" at first glance.

The behavior of Hg in soils is strongly influenced by the interaction between substrate properties and environmental context **(Singh et al., 2023; Qin et al., 2023)**. In highly weathered tropical soils, mineralogical assemblages are typically dominated by quartz and kaolinite-group minerals, often accompanied by variable proportions of gibbsite, Fe–Mn (oxyhydr)oxides, and phyllosilicates **(Souza et al., 2018; Rocha et al., 2022)**. These phases can influence Hg retention through sorption, complexation, and co-precipitation mechanisms, but their roles are not uniform and can shift depending on redox dynamics, organic matter composition, and physical disturbance **(Blouin et al., 2005; Waychunas et al., 2005; Debure et al., 2020; McLagan et al., 2024)**. In addition, particle-size distribution is a key factor controlling Hg concentrations, since fine fractions generally provide higher surface area and greater sorption capacity **(**e.g., **Wang et al., 2024; Elsaid & Roushdi, 2025)**. Therefore, Hg enrichment in soils cannot be interpreted solely in terms of contamination inputs; it also reflects how soil texture, mineralogy, and physicochemical properties control retention and redistribution over time.

Despite the relevance of these processes, many studies on Hg in ASGM settings focus primarily on water and biota due to its direct impact on human health **(**e.g. **Basta et al., 2021; Lucchini et al., 2025)**, while soil compartments are often treated as secondary or characterized only by bulk concentration measurements. Moreover, even when soil Hg is measured, the interpretation is frequently limited by the absence of regional geochemical baselines, which makes it difficult to distinguish anthropogenic enrichment from naturally elevated background levels. This limitation is especially critical in Amazonian areas developed on geologically diverse terrains, where Hg can be naturally enriched in certain parent materials. Without baseline values defined at the regional scale, there is a risk of misattribution **(Sahoo et al.,**

2023; Lourenço et al., 2025), potentially leading to distorted risk assessments and inappropriate policy or remediation priorities.

Another key gap concerns the long-term evolution of Hg retention mechanisms after ASGM cessation. In many post-ASGM landscapes, the assumption is that environmental relevance decreases once mining stops. However, evidence from different Amazonian settings indicates that Hg can persist for decades in soils and sediments, especially in fine-textured materials and in compartments associated with reactive mineral phases. At the same time, the mechanisms controlling this persistence remain poorly resolved, particularly when considering how disturbance history affects soil structure, hydration, organic matter distribution, and the availability of reactive surfaces. Addressing this gap requires not only quantifying total Hg concentrations, but also integrating different soil data that can clarify why some sites retain Hg more efficiently than others, and how this retention evolves across different ASGM histories.

In this thesis, these questions are addressed through a comparative study design that explicitly incorporates disturbance history as a central interpretative framework. By investigating surface soils from three ASGM sites with contrasting activity histories (*i.e.*, active, recently deactivated, and deactivated for ~30 years) and comparing them with a control area without ASGM records, the study evaluates how legacy Hg persists and how soil properties influence its distribution. This approach recognizes that "ASGM contamination" is not a single state, but a continuum of disturbance stages with different physical and geochemical conditions. It also acknowledges that site-scale patterns can only be interpreted meaningfully when anchored in a regional baseline, particularly in settings where geogenic Hg may be significant.

To strengthen mechanistic interpretation, the study integrates multiple lines of evidence. Total Hg (THg) concentrations and ecological risk indices are combined with particle-size

distribution to test whether Hg enrichment is systematically associated with fine fractions and to quantify the extent to which texture explains variability. Qualitative mineralogical and surface characterization (XRD and ATR-FTIR) provides context for interpreting reactive phases, surface hydration, and organic matter signals. Thermogravimetric analysis (TG/DSC) is used as an additional proxy to explore the contribution of soil fractions linked to moisture-related losses, organic matter decomposition, and mineral dehydroxylation processes, offering a complementary perspective on soil matrix differences across sites. Finally, basic physicochemical properties such as water holding capacity (WHC) and pH are incorporated to evaluate whether physical retention capacity and acidity contribute to THg patterns at the site scale.

By combining these approaches within one of the most critical illegal ASGM settings in Brazil, this thesis aims to clarify not only whether Hg persists after mining, but also how and why it persists in soils with different disturbance histories. Ultimately, this contributes to a more context-sensitive understanding of Hg contamination in Amazonian ASGM landscapes, supporting improved monitoring strategies, more realistic risk assessments, and better-informed decisions for environmental management and remediation.

In this context, this thesis investigates mercury contamination in surface soils across three ASGM sites with contrasting activity histories (active, deactivated in January 2024, and deactivated for ~30 years), using a regional control area without ASGM records as a geogenic baseline in Jardim do Ouro village, Pará State, Brazilian Amazon. By integrating THg measurements and ecological risk indices with particle-size distribution, qualitative mineralogical and surface characterization (XRD and ATR-FTIR), thermogravimetric data (TG/DSC), and basic physicochemical properties (WHC and pH), the study aims to clarify both the persistence of legacy Hg in post-mining landscapes and the context-dependent soil fractions controlling Hg retention. Therefore, the specific objectives of this thesis are:

- To quantify total mercury (THg) concentrations in soils across ASGM sites with contrasting activity histories (active, deactivated in January 2024, ~30 years deactivated) and a control area without ASGM records in Jardim do Ouro, Pará, Brazilian Amazon;
- To evaluate the persistence of legacy mercury contamination and ecological risk in soils decades after ASGM cessation;
- To assess the influence of particle-size distribution on THg retention, testing whether fine fractions systematically concentrate Hg across sites and explaining within-site variability;
- To characterize soil mineralogical and surface-related properties (XRD and ATR-FTIR) and assess their relevance for Hg retention;
- To investigate thermogravimetric signatures (TG/DSC) as indicators of soil fractions linked to THg enrichment, and to determine whether these signatures differ across ASGM contexts;
- To integrate soil physical properties (WHC, pH) with mineralogical and thermal data to develop a context-dependent interpretation of mercury retention mechanisms across ASGM histories.

The thesis is structured as follows: Section 2 presents a systematic review on Hg contamination linked to ASGM (*garimpos*, in Brazilian Portuguese) in Brazil; Section 3 is dedicated to providing regional socio-environmental, geological and metallogenetic context, as well as sampling strategy, and field and soil descriptions; in Section 4 THg data and its distributions are presented, as well as an ecological risk assessment across ASGM contexts; and in Section 5 soil mineralogical, physicochemical and thermogravimetric data are presented and discussed to provide insights on the controls of THg retention and distribution in the studied sites. Together, these Sections provide an integrated interpretation of how disturbance

history from ASGM and soil properties control Hg persistence and retention in the studied soils from one of the most critical illegal ASGM settings in Brazil.

References

Amos, H. M., Jacob, D. J., Kocman, D., Horowitz, H. M., Zhang, Y., Dutkiewicz, S., Horvat, M., Corbitt, E. S., Krabbenhoft, D. P., & Sunderland, E. M., 2014. Global biogeochemical implications of mercury discharges from rivers and sediment burial. Environmental science & technology, 48(16), 9514-9522. https://doi.org/10.1021/es502134t

Basta, P. C., Viana, P. V. D. S., Vasconcellos, A. C. S. D., Périssé, A. R. S., Hofer, C. B., Paiva, N. S., Kempton, J. W., Andrade, D. C., Oliveira, R. A. A., Achatz, R. W., Perini, J. A., Meneses, H. N. M., Hallwass, G., Lima, M. O., Jesus, I. M., Santos., C. C. R., & Hacon, S. D. S. (2021). Mercury exposure in Munduruku indigenous communities from Brazilian Amazon: Methodological background and an overview of the principal results. International journal of environmental research and public health, 18(17), 9222. https://doi.org/10.3390/ijerph18179222

Blouin, V. M., Schmidt, M. G., Bulmer, C. E., & Krzic, M., 2005. Mechanical disturbance impacts on soil properties and lodgepole pine growth in British Columbia's central interior. Canadian Journal of Soil Science, 85(5), 681-691. https://doi.org/10.4141/S04-077

Crespo-Lopez, M. E., Augusto-Oliveira, M., Lopes-Araújo, A., Santos-Sacramento, L., Takeda, P. Y., Macchi, B. M., Nascimento, J. L. M., Maia, C. S. F., Lima, R. R. & Arrifano, G. P., 2021. Mercury: What can we learn from the Amazon?. Environment International, 146, 106223. https://doi.org/10.1016/j.envint.2020.106223

Castilhos, Z. C., & Domingos, L. M. B., 2024. A picture of artisanal and small-scale gold mining (ASGM) in Brazil and its mercury emissions and releases. Environmental Geochemistry and Health, 46(3), 101. https://doi.org/10.1007/s10653-024-01881-z

Debure, M., Grangeon, S., Robinet, J. C., Madé, B., Fernández, A. M., & Lerouge, C., 2020. Influence of soil redox state on mercury sorption and reduction capacity. Science of The Total Environment, 707, 136069. https://doi.org/10.1016/j.scitotenv.2019.136069

Dhiman, V., 2023. Remediation strategies of environmental mercury: An overview of its environmental persistence, associated threats, and health impacts. Mercury toxicity: Challenges and solutions, 235-247. https://doi.org/10.1007/978-981-99-7719-2_9

Diringer, S. E., Berky, A. J., Marani, M., Ortiz, E. J., Karatum, O., Plata, D. L., Pan, W. K. & Hsu-Kim, H., 2019. Deforestation due to artisanal and small-scale gold mining exacerbates soil and mercury mobilization in Madre de Dios, Peru. Environmental science & technology, 54(1), 286-296. https://doi.org/10.1021/acs.est.9b06620

Elsaid, S. M., & Roushdi, M., 2025. Thermodynamic and kinetic parameters of arsenic and mercury adsorption on chromic acid-activated-bentonite in wastewater treatment. Water Science, 39(1), 232-246. https://doi.org/10.1080/23570008.2025.2574783

Figueiredo, B. R., De Campos, A. B., Da Silva, R., & Hoffman, N. C., 2018. Mercury sink in Amazon rainforest: soil geochemical data from the Tapajos National Forest, Brazil. Environmental Earth Sciences, 77(8), 296.. https://doi.org/10.1007/s12665-018-7471-x

Gerson, J. R., Szponar, N., Zambrano, A. A., Bergquist, B., Broadbent, E., Driscoll, C. T., Erkenswick, G., Evers, D. C., Fernandez, L. E., Hsu-Kim, H., Inga, G., Lansdale, K. N., Marchese, M. J., Martinez, A., Moore, C., Pan, W. K., Purizaca, R. P., Sánchez, V., Silman, M., Ury, E. A., Vega, C., Watsa, M., & Bernhardt, E. S. (2022). Amazon forests capture high levels of atmospheric mercury pollution from artisanal gold mining. Nature communications, 13(1), 559. https://doi.org/10.1038/s41467-022-27997-3

Helmrich, S., Vlassopoulos, D., Alpers, C. N., & O'Day, P. A. (2022). Critical review of mercury methylation and methylmercury demethylation rate constants in aquatic sediments for biogeochemical modeling. Critical Reviews in Environmental Science and Technology, 52(24), 4353-4378. https://doi.org/10.1080/10643389.2021.2013073

Hou, X., 2023. Prediction of the Soil–Water Retention Curve of Loess Using the Pore Data from the Mercury Intrusion Technique. Water, 15(18), 3273. https://doi.org/10.3390/w15183273

Jackson, T. A., 1997. Long-range atmospheric transport of mercury to ecosystems, and the importance of anthropogenic emissions A critical review and evaluation of the published evidence. Environmental Reviews, 5(2), 99-120. https://doi.org/10.1139/a97-005

Lima, F. R., Pereira, P., Junior, E. C. S., Vasques, I. C., Oliveira, J. R., Windmöller, C. C., Inda, A. V., Weindorf, D. C., Curi, N., Ribeiro, B. T., Guilherme, L. R. G., Marques, J. J., 2022. Geochemistry signatures of mercury in soils of the Amazon rainforest biome. Environmental Research. 215, 114147. https://doi.org/10.1016/j.envres.2022.114147

Lourenço, M. S. T. A., Debruyne, D., Di Maggio, R. M., Germinario, C., Grifa, C., Izzo, F., Langella, A., de Paula, L. S., Salvador, F. A. S., & Mercurio, M., 2025. Mercury contamination in Brazil related to (historical) artisanal and small-scale gold mining activity: a narrative review with quantitative synthesis. Environmental Geochemistry and Health, 48(1), 45. https://doi.org/10.1007/s10653-025-02929-4

Lucchini, R. G., Basta, P. C., Crespo-Lopez, M. E., del Carmen Gastañaga, M., O'Callaghan-Gordo, C., Olivero-Verbel, J., ... & Deoraj, A. (2025). Mercury Contamination and Co-exposures in the Amazon Basin: At the Center of the Planetary Environmental Crisis. Annals of Global Health, 91(1), 42. https://doi.org/10.5334/aogh.4817

McLagan, D. S., Esser, C., Schwab, L., Wiederhold, J. G., Richard, J. H., & Biester, H., 2024. Organic matters, but inorganic matters too: column examination of elevated mercury sorption on low organic matter aquifer material using concentrations and stable isotope ratios. Soil, 10(1), 77-92. https://doi.org/10.5194/soil-10-77-2024

Neto, L. C. F., Diniz, C. G., Maretto, R. V., Persello, C., Pinheiro, M. L. S., Castro, M. C., Sadeck, L. W. R., Filho, A. F., Cansado, J., Souza, A. A. A., Feitosa, J. P., Santos, D. C., Adami, M., Souza-filho, P. W., Stein, A., Biehl, A., & Klautau, A., 2024. Uncontrolled illegal mining and Garimpo in the Brazilian Amazon. Nature communications, 15(1), 9847. https://doi.org/10.1038/s41467-024-54220-2

Nyholt, K., Jardine, T. D., Villamarín, F., Jacobi, C. M., Hawes, J. E., Campos-Silva, J. V., Srayko, S., & Magnusson, W. E., 2022. High rates of mercury biomagnification in fish from Amazonian floodplain-lake food webs. Science of the Total Environment, 833, 155161. https://doi.org/10.1016/j.scitotenv.2022.155161

Paiva, T. C., Pestana, I. A., de Oliveira, B. C. V., Malm, O., de Rezende, C. E., & Kasper, D., 2024. Temporal variation of mercury levels in fish, soil, and sediments in an Amazon reservoir: insights from 35 years of river impoundment in Pará State, Brazil. Environmental Monitoring and Assessment, 196(11), 1089. https://doi.org/10.1007/s10661-024-13199-5

Peng, X., Yang, Y., Yang, S., Li, L., & Song, L., 2024. Recent advance of microbial mercury methylation in the environment. Applied Microbiology and Biotechnology, 108(1), 235. https://doi.org/10.1007/s00253-023-12967-6

Pierezan, M. D., Hoff, R. B., Marsico, E. T., & Verruck, S., 2024. Total mercury and methylmercury levels in Brazilian Amazon fish: A scope review with meta-analysis and local population health risk assessment. Journal of Trace Elements and Minerals, 10, 100196. https://doi.org/10.1016/j.jtemin.2024.100196

Qin, A., Ran, S., He, T., Yin, D., & Xu, Y., 2023. The effects of different soil component couplings on the methylation and bioavailability of mercury in soil. Toxics, 11(11), 942. https://doi.org/10.3390/toxics11110942

Rocha, D. R., Barber, X., Jordán-Vidal, M. M., Urbano, A., Melquiades, F. L., Thomaz, E. L., & Mataix-Solera, J., 2022. Multivariate analysis with XRD data as a fingerprinting technique to study burned soils. Minerals, 12(11), 1402. https://doi.org/10.3390/min12111402

Sahoo, P. K., Dall'Agnol, R., Salomão, G. N., Guimarães, J. T. F., Angelica, R. S., Ramos, S. J., Costa, M. F., & de Siqueira, J. O. (2023). Mercury in multimedia system of Itacaiúnas Basin, Brazilian Amazon: An integrated approach to understand its distribution, origin, and ecological risk. Environmental Research, 232, 115107. https://doi.org/10.1016/j.envres.2022.115107

Singh, A. D., Khanna, K., Kour, J., Dhiman, S., Bhardwaj, T., Devi, K., Sharma, N., Kumar, P., Kapoor, N., Sharma, P., Arora, P., Sharma, A., & Bhardwaj, R., 2023. Critical review on biogeochemical dynamics of mercury (Hg) and its abatement strategies. Chemosphere, 319, 137917. https://doi.org/10.1016/j.chemosphere.2023.137917

Souza, E. S. D., Fernandes, A. R., De Souza Braz, A. M., Oliveira, F. J. D., Alleoni, L. R. F., & Campos, M. C. C., 2018. Physical, chemical, and mineralogical attributes of a representative group of soils from the eastern Amazon region in Brazil. Soil, 4(3), 195-212. https://doi.org/10.5194/soil-4-195-2018

Uddin, S., Khanom, S., & Islam, M. R., 2024. Source and distribution of mercury in environment—A Review. Mercury toxicity mitigation: Sustainable nexus approach, 3-43. https://doi.org/10.1007/978-3-031-48817-7_1

Wang, P., Shen, X., Qiu, S., Zhang, L., Ma, Y., & Liang, J., 2024. Clay-based materials for heavy metals adsorption: Mechanisms, advancements, and future prospects in environmental remediation. Crystals, 14(12), 1046. https://doi.org/10.3390/cryst14121046

Wasserman, J. C., Hacon, S., & Wasserman, M. A., 2003. Biogeochemistry of mercury in the Amazonian environment. Ambio: A Journal of the Human Environment, 32(5), 336-342.. https://doi.org/10.1579/0044-7447-32.5.336

Waychunas, G. A., Kim, C. S., & Banfield, J. F., 2005. Nanoparticulate iron oxide minerals in soils and sediments: unique properties and contaminant scavenging mechanisms. Journal of nanoparticle research, 7(4), 409-433. https://doi.org/10.1007/s11051-005-6931-x

Wei, X., Zhang, P., Chen, L., Cao, M., Zhang, W., Zhang, X., Zhu, X., Wang, S., & Liang, Y., 2025. Historical artisanal gold mining poses long-term risk of mercury to river ecosystems: A case study in Tongguan area of northwestern China. Environmental Pollution, 127156. https://doi.org/10.1016/j.envpol.2025.127156

Yuan, W., Wang, X., Lin, C. J., Zhang, G., Wu, F., Liu, N., Jia, L., Zhang, H., Lu, H., Dong, J., & Feng, X., 2024. Fate and transport of mercury through waterflows in a tropical rainforest. Environmental Science & Technology, 58(11), 4968-4978. https://doi.org/10.1021/acs.est.3c09265

2. Mercury contamination in Brazil related to (historical) artisanal and small-scale gold mining activity: a narrative review with quantitative synthesis

This chapter reproduces the content of the article published by **Lourenço et al. (2025)** in *Environmental Geochemistry & Health*. The text is included in this thesis with minor editorial adjustments, in order to integrate the published results into the body of the doctoral dissertation.

Artisanal and Small-Scale Gold Mining (ASGM), locally known as *garimpo*, remains one of the most important sources of mercury (Hg) contamination worldwide and continues to pose significant risks to environmental integrity and human health. In Brazil, where ASGM has been practiced for centuries, mercury pollution reflects a complex interaction between natural geological backgrounds and multiple anthropogenic processes associated with gold extraction. Elevated Hg concentrations in affected regions result not only from the intentional release of elemental mercury during gold amalgamation, but also from the large-scale mechanical disturbance of soils and sediments that mobilizes previously stored mercury, including both legacy contamination from historical mining and naturally accumulated Hg derived from geogenic sources and long-term atmospheric deposition.

This chapter synthesizes evidence from peer-reviewed studies addressing mercury contamination associated with ASGM activities in Brazil, covering a wide range of environmental and biological matrices, including soils, sediments, water, air, aquatic and terrestrial biota, and human tissues. Particular emphasis is placed on the Amazon region, which emerges as a global hotspot of mercury contamination due to the convergence of exceptionally high natural Hg backgrounds with intense historical and ongoing artisanal gold mining. In this context, mercury cycling is strongly influenced by regional geological substrates, extensive

weathering profiles, hydrological connectivity, and biogeochemical conditions that favor mercury retention, remobilization, and transformation.

Human exposure to mercury in ASGM-impacted regions occurs primarily through two pathways: occupational inhalation of elemental mercury vapor during amalgamation and burning processes, and dietary intake of methylmercury (MeHg) through fish consumption. The latter pathway disproportionately affects riverine and Indigenous populations whose subsistence relies heavily on aquatic resources. Numerous studies document mercury concentrations in fish and human biomarkers that exceed national and international health guidelines, highlighting the persistence of exposure risks even in areas where active mining has ceased.

Environmental compartments such as soils, river sediments, floodplains, and suspended particulate matter frequently exhibit mercury concentrations above prevention or intervention thresholds, underscoring mercury's long residence time and its capacity for repeated remobilization. In aquatic systems, mercury methylation is enhanced under anoxic and organic-rich conditions typical of Amazonian wetlands, floodplains, and reservoirs, leading to efficient bioaccumulation and biomagnification across food webs. These processes sustain mercury contamination over decadal timescales, independent of current mining intensity.

Although Brazil ratified the Minamata Convention in 2017, the legacy of historical ASGM and the vast reservoirs of mercury stored in soils and sediments imply that environmental recovery will be slow. Reductions in fish methylmercury concentrations may take decades, as previously deposited mercury continues to cycle through terrestrial and aquatic systems. Effective mitigation therefore requires a combination of mercury-free mining technologies, strengthened enforcement of environmental regulations, long-term environmental monitoring,

and culturally appropriate public health strategies tailored to regional geological and biogeochemical variability.

By integrating data across disciplines and environmental compartments, this chapter highlights the multifaceted nature of ASGM-related mercury contamination in Brazil. The synthesis provides a foundation for understanding how geological, geomorphological, and anthropogenic factors jointly control mercury distribution and exposure pathways, offering critical insights to inform research priorities, policy development, and management strategies aimed at protecting both ecosystem health and human well-being.

2.1. Introduction

Mercury (Hg) is widely recognized as a global pollutant due to its persistence, mobility, and high potential for bioaccumulation and biomagnification in aquatic and terrestrial food webs **(Esdaile and Chalker, 2018; Gworek et al., 2020; Wang et al., 2022)**. Among anthropogenic sources, artisanal and small-scale gold mining (ASGM, known as *garimpo* in Brazilian Portuguese) is particularly noteworthy for its extensive reliance on elemental mercury to amalgamate gold, a practice that significantly contributes to global Hg emissions (**Gyamfi et al., 2021; Cheng et al., 2023**). In this manuscript, we use both the term ASGM and the Brazilian Portuguese equivalent, *garimpo*, to refer to artisanal and small-scale gold mining. In 2013, the urgency of controlling mercury releases was highlighted by the enforcement of the Minamata Convention on Mercury—an international treaty endorsed by national governments and coordinated by the United Nations Environment Programme (UNEP), which aims to protect both human health and the environment through measures targeting mercury production, trade, and use **(UNEP, 2013)**. Although Brazil ratified the Convention in 2017,

effectively reducing Hg exposure and achieving sustainable mining practices remain formidable challenges **(Gerson et al., 2022; Crespo-Lopez et al., 2023)**.

Within Brazil, high mercury levels arise not only from active emissions at *garimpos*, but also from the mobilization of legacy and geogenic Hg stocks—long-stored mercury in soils and sediments that can be remobilized through deforestation, dredging, and hydrological disruption **(Fostier et al., 2000; Lechler et al., 2000; Sahoo et al., 2020)**. Historical and ongoing *garimpos* have been extensively documented in the Amazon biome, where gold rushes in the 20th century significantly boosted mercury usage **(Machado and Figuerôa, 2001; Theije, 2020)**. Recent work by **Martoredjo et al. (2024)** provides a key step toward understanding contemporary contamination patterns in that region, demonstrating consistently high mercury levels in both human populations and wildlife as reported in a large number of studies on the Amazon area (2017–2023). Their findings underscore the critical need for rapid intervention in Amazonian *garimpo* sites, although mercury contamination from *garimpos* also extends beyond the Amazon, occurring in longstanding mining districts throughout Minas Gerais, Goiás, and other regions of Brazil **(Pfeiffer et al., 1991; Egler et al., 2006; Bruno et al., 2020)**. Hence, there is an urgent need for a broader national-level appraisal, which encompasses historical and current studies and, at the same time, takes into account more diversified environmental matrices.

In response to this challenge, the present review compiles Hg contamination data from a wide range of matrices—including air, flora, sediments, suspended particulate matter, and soils—in *garimpo*-impacted sites throughout Brazil. By synthesizing these diverse datasets, this work aims to (1) provide a more holistic perspective on the spatial distribution and severity of mercury pollution; (2) identify typical Hg concentration ranges in different environmental compartments; and (3) elucidate implications for environmental management and public health in light of the Minamata Convention's objectives. In conclusion, our analysis builds on and

extends the insights offered by **Martoredjo et al. (2024)** beyond the Amazon region and over a longer time frame, supporting a more comprehensive understanding of *garimpo*-related Hg contamination.

2.2. Context for the study

2.2.1. Mercury

Mercury (Hg) is a naturally occurring toxic heavy metal **(Oz et al., 2012; Lu et al., 2020)** that is persistent and mobile **(Tibau and Grube, 2019; Gworek et al., 2020)**, and it is considered a global pollutant **(Yoshino et al., 2020; Wang et al., 2022)**. This metal poses significant risks to One Health **(Kumari et al., 2020; Gyamfi et al., 2021; Kwasigroch et al., 2021)** due to its high bioaccumulation and persistent biomagnification **(Kozak et al., 2021; Liu et al., 2021; Seco et al., 2021)**. Consequently, Hg contamination and mobilization is highlighted as one of the primary global chemical concerns **(Bank, 2020; Gyamfi et al., 2021)**.

Alongside bromine, mercury composes the group of only two chemical elements that are liquids at ambient conditions **(Gustin et al., 2020)**, being Hg the only metal with this attribute. This element can be classified by its oxidation states, by its forms, or by its physical characteristics **(Al-Sulaiti et al., 2022)**. In the environment, mercury can be found in three different oxidation states: elemental (Hg^0), mercurous/monovalent (Hg_2^{2+}), or mercuric/divalent (Hg^{2+}) **(Edwards et al., 2021; Petry-Podgórska et al., 2021; Lima et al., 2022)**. In addition, there are three forms of Hg that can be found in nature: the elemental mercury itself (Hg^0), organic compounds (such as methylmercury), and inorganic mercury (Hg^+ and Hg^{2+}) **(Oz et al., 2012; Ajsuvakova et al., 2020; Lu et al., 2020; Yang et al., 2020; Emenike et al., 2023; Nava et al., 2023)**. Finally, in terms of physical characteristics, mercury

can be categorized into three groups: dissolved forms (such as complexed ionic mercury, monomethylmercury halides, dialkylmercury), insoluble or suspended mercury compounds (including HgS and HgSe), and volatile mercury (dialkylmercury and elemental mercury) **(Saleh et al., 2020)**.

Elemental mercury (Hg^0) is a toxic liquid silvery metal at room temperature **(Navarro, 2008; Oz et al., 2012; Rodrigues et al., 2019; Güven and Özbek, 2022)**, with a melting point of -38.7 °C, exhibiting a vapour pressure of 0.002 mm Hg at 25 °C, signifying its propensity to release vapours **(Langford and Ferner, 1999; Colás, 2021)**. In its gaseous state, mercury is odourless and tasteless but significantly toxic **(Oz et al., 2012)**, and it can travel through the atmosphere, dispersing over long distances before eventually settling into the soil **(Singh et al., 2023; Pan et al., 2024)**. Once deposited from the atmosphere, it circulates through surface environments such as oceans and soils, and can be re-released into the atmosphere by being reduced back to its elemental form **(Streets et al., 2018; Castilhos and Domingos, 2024)**.

In the environment, Hg^0 can be converted through biological and chemical processes into Hg^{2+} and simple organomercury compounds such as the neurotoxic methylmercury ($MeHg^+$) and ethylmercury ($EtHg^+$) **(Petry-Podgórska et al., 2021)**. Within this scenario, organic compounds are considered the most toxic form of Hg **(Stopford and Goldwater, 1975; Mahaffey, 1999; McElwee and Freedman, 2011; Hong et al., 2012; Azar et al., 2021; Cardoso et al., 2023)**. In addition, $MeHg^+$ is the form that presents the highest bioavailability when compared to the other mercury forms **(**e.g., **Yang et al., 2020)**. However, as the toxicity of Hg greatly depends on its chemical form **(Frossard et al., 2018)**, different forms of mercury carry distinct toxic attributes, with toxicity influenced not only by its chemical composition but also predominantly by specific metabolic and distribution fractions **(Clarkson et al., 2007; Ajsuvakova et al., 2020)**.

Mercury can be released and mobilized into the environment through a variety of natural processes and human activities **(Fostier et al., 2000; Duan et al., 2019; Cooke et al., 2020; Natasha et al., 2020; Qin et al., 2020; Raj and Maiti, 2020; Feinberg et al., 2024)**. Since the 19th century, the rise in mercury production and its widespread use has led to a growing concern over mercury pollution **(Liu et al., 2021)**. Nevertheless, to comprehend the biogeochemical cycle of mercury and develop effective reduction strategies, it is essential to clearly identify and accurately quantify emissions from major atmospheric mercury sources **(Qin et al., 2020)**.

The primary natural sources of mercury emissions include volcanic eruptions **(Grasby et al., 2019; Edwards et al., 2021)** and geothermal activities **(Sun et al., 2020; Pan et al., 2024)**, while the main anthropogenic sources are coal combustion in power plants **(Misztal et al., 2022; Sahu et al., 2024)**, ASGM **(Gyamfi et al., 2021; Cheng et al., 2023; Keane et al., 2023)**, industrial processes such as cement production **(Chen et al., 2020; Kogut et al., 2021)** and waste incineration **(Tao et al., 2017)**. Despite the existence of both natural and anthropogenic sources of mercury emissions into the environment, the Hg contamination is primarily attributed to human activities **(Yang et al., 2020)**.

The primary Hg emission sources also vary geographically. In Europe, the cement industry occupies the second position in the ranking of mercury emissions, behind the coal-based thermal power plants **(Kogut et al., 2021)**, while in China it represents the main mercury emission source **(Chen et al., 2020)**. In the Global South, *garimpos* play the major role in terms of atmospheric mercury emissions **(Gerson et al., 2022)**, with the Amazon region acting as the main source in South America **(Crespo-Lopez et al., 2023)**. Thus, **AMAP/UNEP (2019)** encourages studies on mercury distribution and its species in water, soils, and air from operating *garimpos* due to evidence suggesting that historic emissions from Ag and Au mining were geographically more restricted in comparison to nowadays. The predominance of recent

studies on mercury in *garimpos* **(**e.g., **Bruno et al., 2020; Pestana et al., 2022; Casagrande et al., 2023; Fritz et al., 2023; Castilhos and Domingos, 2024)** suggests that *garimpos* are currently a concerning source of Hg emissions in Brazil.

2.2.1.1. Mercury Use in Gold Mining

Amalgamation is an ancient method for gold extraction and remains widely used due to its simplicity and low cost **(Cesareo et al., 2020; Leiva and Morales, 2013; Colás, 2021; Silva and Guimarães, 2024)**. The process involves mixing mercury with gold ore to form an amalgam, a compound that can be separated from other minerals by panning **(Mozgai et al., 2021; Verbrugge et al., 2021; Donkor et al., 2024; Chen et al., 2024)**. Excess mercury is manually removed by squeezing the amalgam in fabric, leaving a mixture containing 40–50% mercury **(Veiga et al., 2014; Yoshimura et al., 2021)**. The amalgam is then heated, vaporizing the mercury and leaving behind a semi-pure gold doré—a gold-silver alloy bar containing additional impurities **(Smith, 2019; Aquino et al., 2022)**. The steps of the amalgamation process are schematized in **Figure 1**.

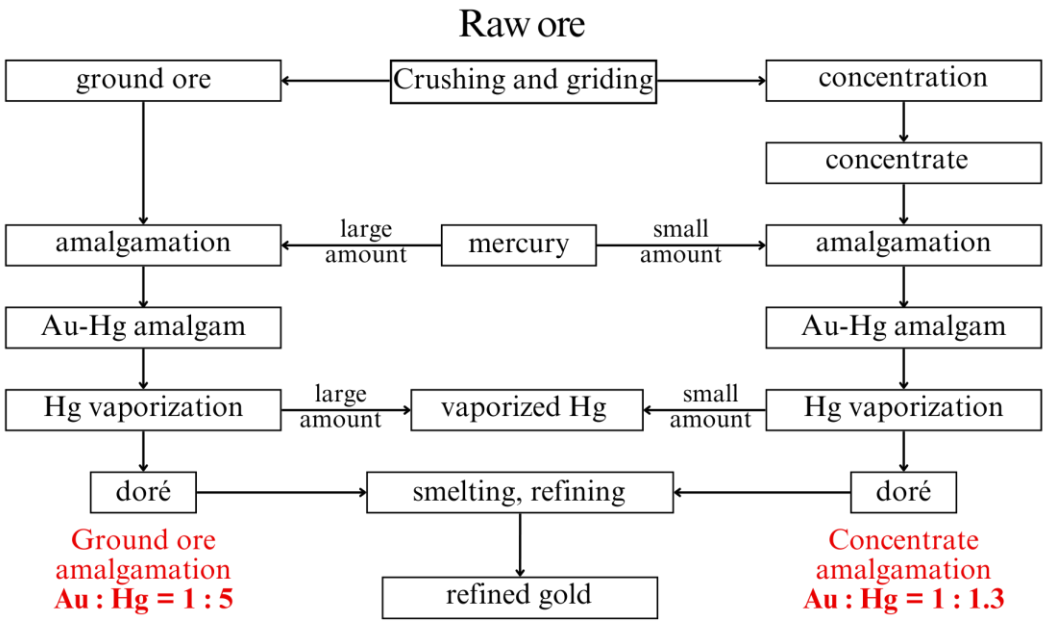


Figure 1: ASGM gold ore processing. Adapted from: Yoshimura et al. (2021)

Despite its historical importance, amalgamation is a highly inefficient technique for recovering gold. Recovery rates are often below 30%, although they may occasionally reach up to 50% **(Veiga and Fadina, 2020)**. This low efficiency, combined with the environmental and health risks posed by mercury vaporization, highlights the need for more effective and sustainable gold recovery methods.

2.2.2. A Concise Historical Overview of Gold Mining in Brazil

The extraction and utilization of Earth materials have played a significant role in human civilization's evolution throughout history, becoming an indispensable industry to contemporary societies **(Viljoen, 1979; Donnelly et al., 2021; Luckeneder et al., 2021; Pešа and Ross, 2021; Nwaila et al., 2022)**. Even for the early civilizations, precious minerals and metals were considered enchanting and valuable materials **(Delaere et al., 2019; Zabyelina and Uhm, 2020; Asare and Afriyie, 2021; Mathioudakis et al., 2023)**. Actually, it might be

considered one of the reasons why, historically, humankind developed its societies and lifestyles based on the intensive utilization of Earth materials. The fact that the Ages of Man are marked by the use of different minerals and metals (e.g., the Stone Age, the Copper Age, the Bronze Age, and the Iron Age) confirms the relevance of geological materials for humankind's evolution **(Gregory, 2021; Pandey et al., 2023)**.

Gold has been a desired metal to humankind for thousands of years **(Fritz et al., 2023; Mathioudakis et al., 2023)**; therefore, its extraction and use in pre-Columbian Spanish America is also widely studied **(Cesareo et al., 2020; Kaal et al., 2020; Socha et al., 2020; Vieri et al., 2020; Vetter and Carcedo, 2022)**. So far, there is no literature data on the pre-colonial exploration of gold by Brazilian civilizations. However, the history of gold exploration in Brazil from the 1500s is well documented **(Figure 2)**.

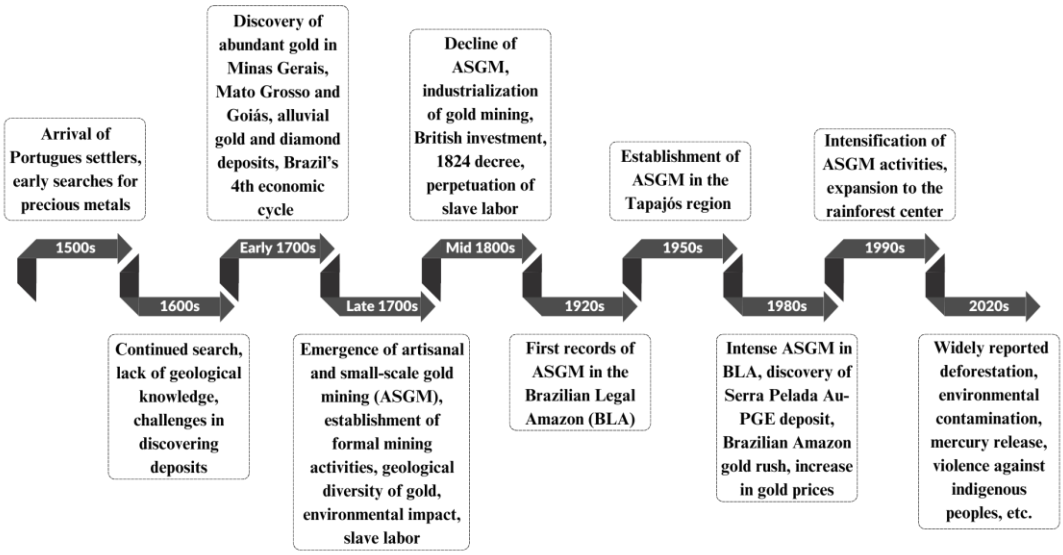


Figure 2: A summarized timeline of gold exploration in Brazil from the 16th Century to the present day. Information synthesized from Clearly (1990); Machado and Figuerôa (2001); Cabral et al. (2002); Theije (2020); Abad and Palma (2021); Costa and Rios (2022); Soares and Saes (2023); Diogens et al. (2024).

It is well known that an intensive search for precious metals took place after the arrival of the Portuguese settlers in the 16th century **(Machado and Figuerôa, 2001; Diogens et al., 2024)**, resulting in discoveries of alluvial gold deposits in the late 17th century in Minas Gerais, Mato Grosso, and Goiás **(Theije, 2020; Abad and Palma, 2021; Costa and Rios, 2022; Diogens et al., 2024)**. In 1731, the royal monopoly on gold was established, when illegal activities related to gold mining in Brazil started **(Ebert, 2011; Le Tourneau, 2021)**.

As a result of the *garimpo* decrease during the late 18th century, the early and mid-19th century was marked by the British investment in industrial gold mining in Brazil **(Clearly, 1990; Costa and Rios, 2022; Soares and Saes, 2023)**. Finally, during the 20th century gold exploration reached the state of Pará, establishing a gold rush within the Brazilian Legal Amazon (BLA) **(Clearly, 1990; Machado and Figuerôa, 2001; Cabral et al., 2002; Kolen et al., 2013; Theije, 2020; Costa and Rios, 2022; Diogens et al., 2024)** that persists to this

day **(Lobo et al., 2016; Calvimontes et al., 2020; Bakker et al., 2021; Fritz et al., 2023; Junior and Carvalho, 2022; Queiroz et al., 2022; Castilhos and Domingos, 2024)**.

Currently, declared *garimpo* gold production accounts for approximately 25% of Brazil's total gold output **(Castilhos and Domingos, 2024)**. On the other hand, *garimpo* leaves a legacy of both environmental and socioeconomic consequences **(Diogens et al., 2024)** such as deforestation **(Fearnside, 2017; Siqueira-Gay and Sánchez, 2021)** and environmental contamination **(Malm, 1998; Souza Neto et al., 2020; Teixeira et al., 2021)**, alongside alcohol and drug abuse, prostitution, poverty, and several types of diseases **(Veiga and Hinton, 2002; Schwartz et al., 2021)**.

Since the gold extracted by *garimpo* in Brazil is predominantly sourced from secondary gold deposits, a persistent use of the amalgamation process involving mercury **(Fritz et al., 2023; Castilhos and Domingos, 2024)**, which is extremely harmful to the environment and human health, is considered one of the main issues of *garimpo* in Brazil **(Balzino et al., 2015; Yoshimura et al., 2021; Fritz et al., 2023; Castilhos and Domingos, 2024**).

2.3. Methodology

A preliminary scoping phase helped define the review's thematic focus by mapping existing literature, identifying research gaps, and refining key questions. These included: (I) What levels and patterns of Hg contamination are reported across matrices in *garimpo*-impacted areas of Brazil? (II) Which regions, pathways, and populations are most affected? (III) How do methods vary across studies, and what are their limitations?

This narrative review with quantitative synthesis was designed to provide a comprehensive overview of empirical evidence on Hg levels related to *garimpo* in Brazil. It covers multiple

environmental and biological matrices—including soil, water, air, suspended particulate matter, vegetation, wildlife, and human biological samples (hair, urine, blood)—to support an integrated understanding of Hg distribution, bioaccumulation, and exposure risks. The review followed the Preferred Reporting Items for Systematic Review and Meta-analysis (PRISMA) statements **(Page et al., 2021)** to ensure methodological transparency and reproducibility, including clear documentation of search strategies, eligibility criteria, and study selection processes.

2.3.1. Data collection and screening

We collected data by searching in the electronic databases Web of Science, Scopus, and PubMed, covering all publication years up to June 4, 2024. The search strategy combined Boolean logic with free-text keywords, to identify relevant publications—regardless of publication date—addressing mercury contamination in Brazil, particularly in relation to gold mining activities: (mercury OR Hg) AND (contamination OR pollution) AND (Brazil OR brazilian) AND (ASGM OR *garimpo* OR gold mining*) AND (environmental impact OR ecosystem OR river water OR sediment OR health effects OR health risks OR indigenous communities OR traditional populations OR wildlife OR biodiversity OR soil OR air OR atmosphere OR atmospheric).

We recorded the number of documents retrieved from each database to assess literature coverage. After removing duplicates, titles and abstracts of the remaining publications were independently screened for relevance by two authors (MSTAL and LSP), based on the established eligibility criteria for this review **(Table 1)**, with any discrepancies resolved by consensus. Eligible studies underwent full-text assessment, and several were excluded due to reasons including absence of original data (e.g., review articles), studies focused exclusively

on Hg analytical techniques without environmental application, studies outside the geographic or thematic scope, and incomplete reporting of relevant results.

Table 1: Criteria for inclusion and exclusion of studies.

Inclusion	Exclusion
Research articles that investigated Hg contamination as a result of *garimpo*	Studies that investigated Hg contamination from other sources (e.g., coal mining, the cement industry, forest fires, etc.)
Studies in Brazil	Studies in other countries
Emphasis on environmental matrices (e.g. water, soil, sediments, suspended particulate matter, and air)	Studies that do not provide clear or extractable quantitative data on Hg
Emphasis on biological matrices (e.g. wildlife fauna and flora, human hair, blood, and urine)	Theses, dissertations, and conference papers
Studies in English	Experimental studies

Quantitative results (*i.e.* Hg concentrations) were extracted from eligible studies using a standardized spreadsheet and grouped by matrix type and geographic region. Descriptive statistics (range, mean, median) were calculated where possible. Matrix-specific trends were synthesized in narrative form, complemented by summary tables and visualizations to highlight spatial patterns and dominant exposure routes. The review does not include a meta-analysis due to the intentional preselection of studies reporting elevated Hg concentrations (*i.e. garimpo*-related areas), as well as the heterogeneity in sampling strategies, matrix types, and analytical methods, but emphasizes comparative synthesis of reported values and methodological consistency across studies.

2.3.2. Data analysis

Data analysis was conducted in R version 4.4.2 **(R Core Team, 2024)**, using the packages *tidyverse* **(Wickham et al., 2019)**, *dplyr* **(Wickham et al., 2023)**, *stringr* **(Wickham, 2023)**, *FSA* **(Ogle et al., 2025)**, *ggplot2* **(Wickham, 2016)**, *gridExtra* **(Auguie, 2017)**, and *grid* **(R Core Team, 2024)**. Code details, mean and standard deviation (SD) estimation, as well dry-to-wet weight conversions, are in the **Supplementary Materials**. Outliers were identified using Tukey's upper inner fence method (1.5 times the interquartile distance), and species represented by fewer than three studies were grouped by taxonomic class.

2.4. Results

2.4.1. Search results

An initial search across Web of Science, Scopus, and PubMed yielded 1,719 publications on *garimpo*-related Hg contamination in Brazil. Following the screening process, 116 studies met the inclusion criteria and were selected for review (**Figure 3**).

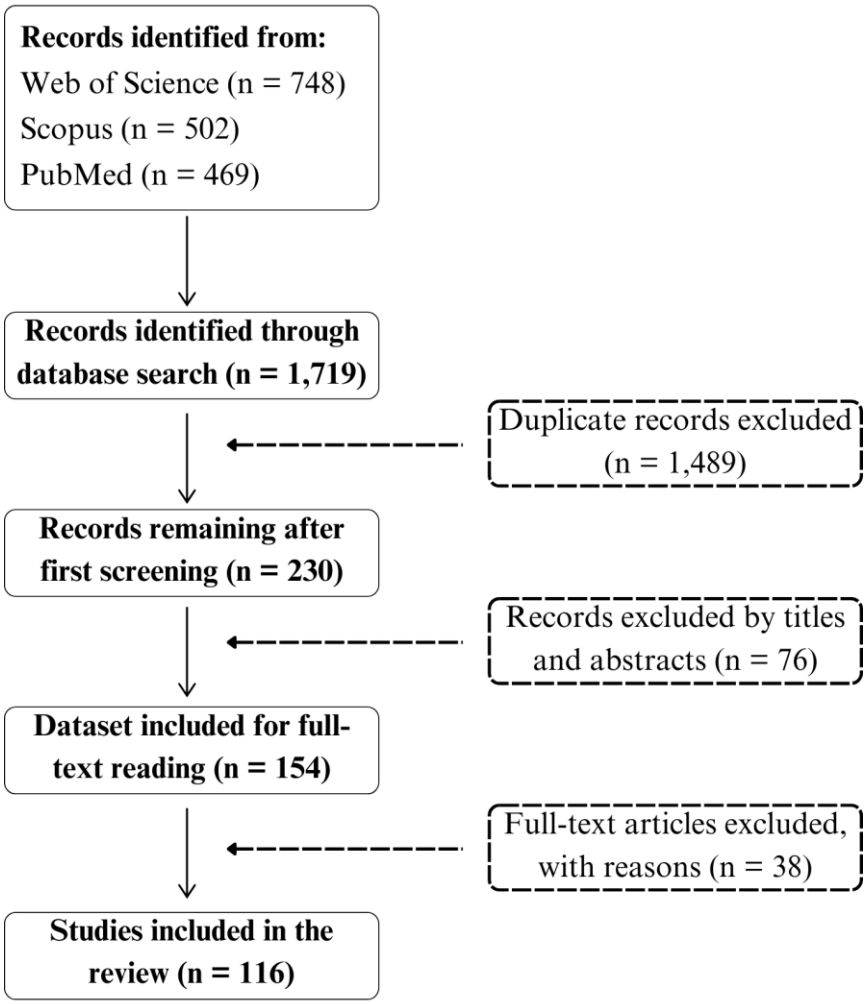


Figure 3: PRISMA flow diagram. Adapted from Page et al. (2021).

Publication trends show a peak in the mid-to-late 1990s, followed by a decline in the 2000s and a subsequent increase in the 2010s **(Figure 4)**.

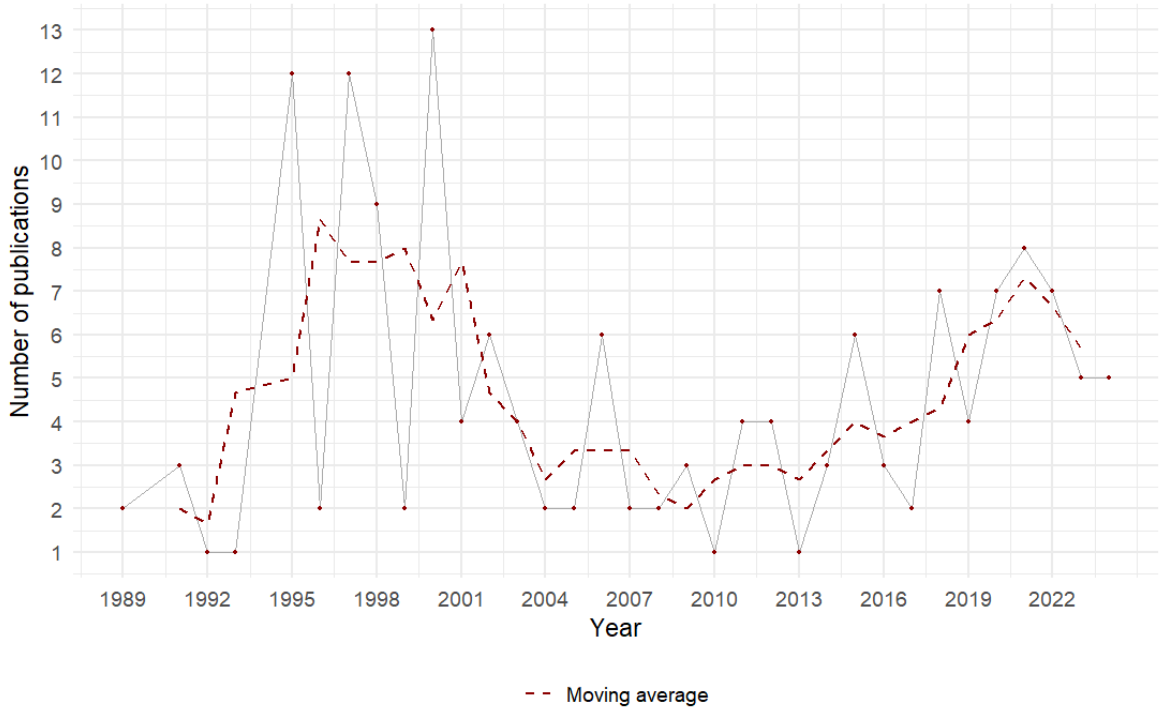


Figure 4: Number of publications by year. The solid grey line represents the annual number of publications, while the red dashed line represents the moving average of three years.

2.4.2. Mercury in human tissues

Most studies on Hg contamination in human tissues were conducted in the Northern region (Amazon biome), with only three outside this area **(Akagi and Naganuma, 2000; Hacon et al., 2000; Dorea et al., 2005)**, all in northern Mato Grosso (Alta Floresta and Kayabi Indigenous Land), which also belongs to the Amazon biome **(Figure 5)**.

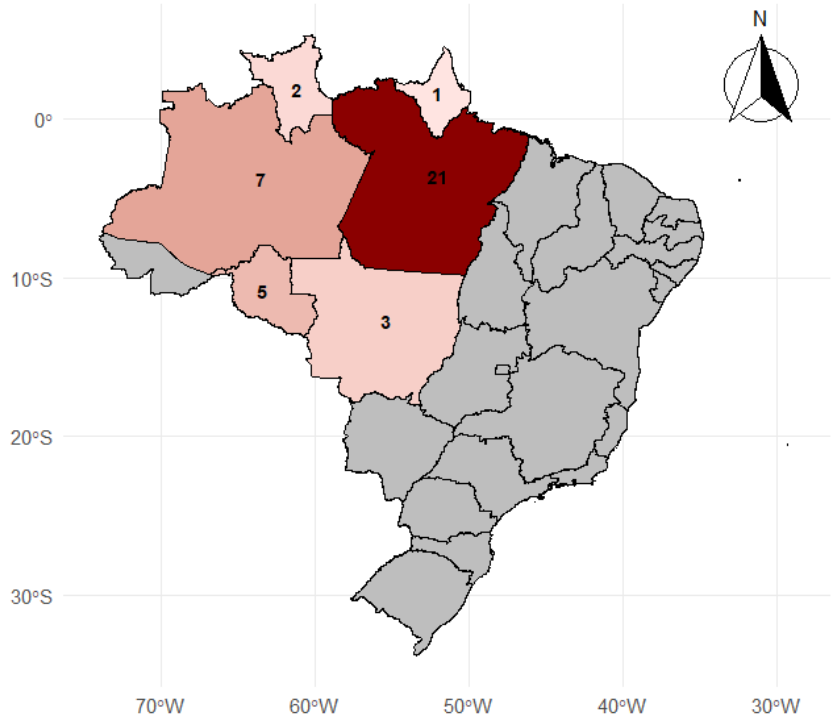


Figure 5: Number of studies that evaluated Hg concentrations in human tissues by state. 21 studies were conducted in the State of Pará, 7 in Amazonas, 5 in Rondônia, 3 in Mato Grosso, 2 in Roraima, and 1 in Amapá.

The State of Pará was the most investigated, with 21 studies **(Branches et al., 1993; Akagi et al., 1995; Barbosa et al., 1995; Leino and Lodenius, 1995; Kehrig et al., 1997; Grandjean et al., 1999; Akagi and Naganuma, 2000; Dolbec et al., 2000; Santos et al., 2000a; Harada et al., 2001; Crompton et al., 2002; Santos et al., 2002a; Santos et al., 2002b; Dorea et al., 2005; Pinheiro et al., 2008; Pinheiro et al., 2012; Castilhos et al., 2015; Basta et al., 2021; Perini et al., 2021; Meneses et al., 2022; Oliveira et al., 2022)**, followed by Amazonas **(Malm et al., 1995b; Eve et al., 1996; Kehrig et al., 1997; Silva-Forsberg et al., 1999; Dorea et al., 2003; Alves et al., 2006; Bastos et al., 2006)** and Rondônia **(Barbosa et al., 1995; Boischio et al., 1995; Kehrig et al., 1997; Bastos et al., 2006; Motts et al., 2014)**, with 7 and 5 studies, respectively. Mato Grosso **(Akagi and Naganuma, 2000; Hacon et al., 2000; Dorea et al., 2005)** accounted for 3 studies, while Roraima **(Malm et al., 1995b; Sing et al., 2003)** and Amapá **(Akagi et al., 1995)** are represented respectively by 2 and 1 study.

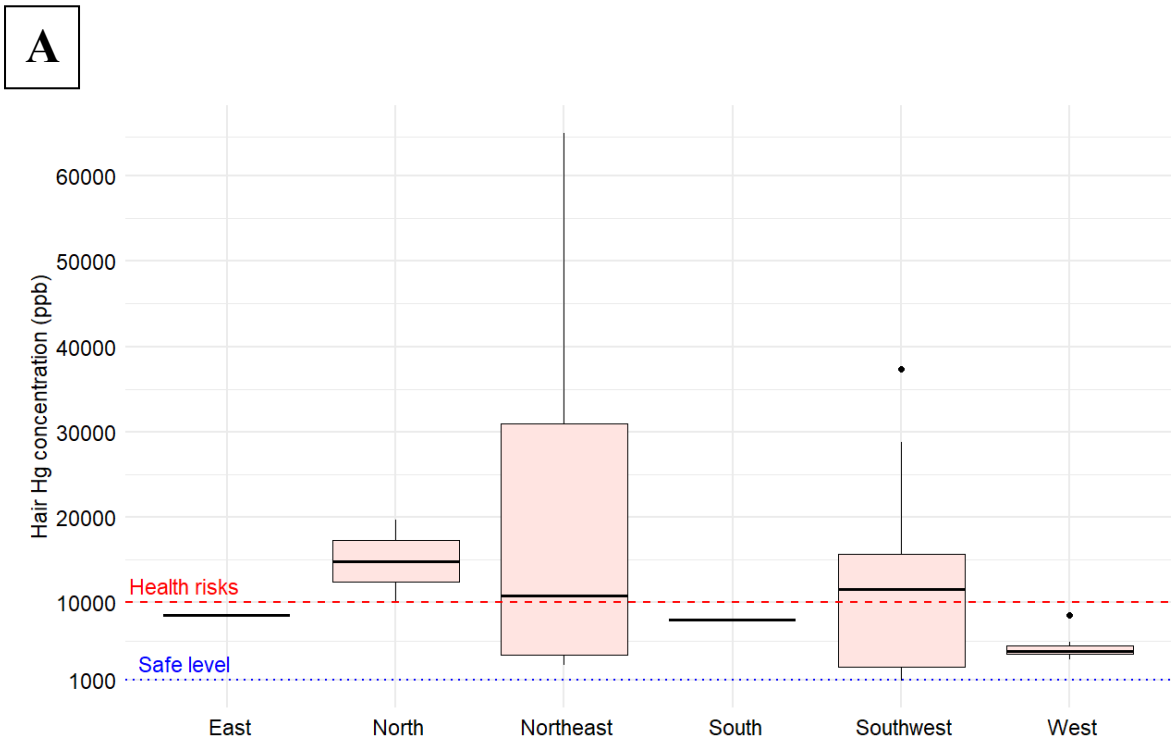
Hair, blood, and urine were the human tissues analyzed, with 27, 7, and 5 studies, respectively. The primary analytical technique for Hg levels in all tissues was cold vapour atomic absorption spectroscopy (CV-AAS), used in 77.78% of hair studies, 57.14% of blood studies, and 60% of urine studies. A complete list of methods is provided in **Table 1 of the Supplementary materials**.

Hair Hg concentrations showed significant variations across States, with Amazonas, Pará and Rondônia presenting medians above the health risk threshold of 10,000 ppb **(WHO, 2021) (Table 2)**. In addition, the relatively broad regional coverage of hair Hg concentration data in Pará allowed us to analyze variations across different regions of the State **(Figure 6 A,B)**.

Table 2. Hg concentrations in human tissues by State.

State	Matrix	Min—max (ppb)	Median (ppb)	Mean (ppb)	Outliers (ppb)
Amazonas	Hair (n = 70)	1,000—97,440	16.420	24,137	76,650; 97,440
Mato Grosso	Hair (n = 3)	1,120—12,800	5,200	6,373	-
	Blood (n = 1)	-	12.2	12.2	-
Pará	Hair (n = 126)	1,500—65,000	11,195	12,149	37,000; 37,400; 65,000
	Blood (n = 16)	16.5—150	31.8	48.4	131; 150
	Urine (n = 8)	3.91—61	13.9	20.1	61
Rondônia	Hair (n = 28)	1,600—28,590	11,155	12,467	28,590
	Urine (n = 1)	-	2.6	2.6	-

Roraima	Hair (n = 1)	-	3,610	3,610	-
	Blood (n = 8)	24.5—48.7	30	33.3	48.7



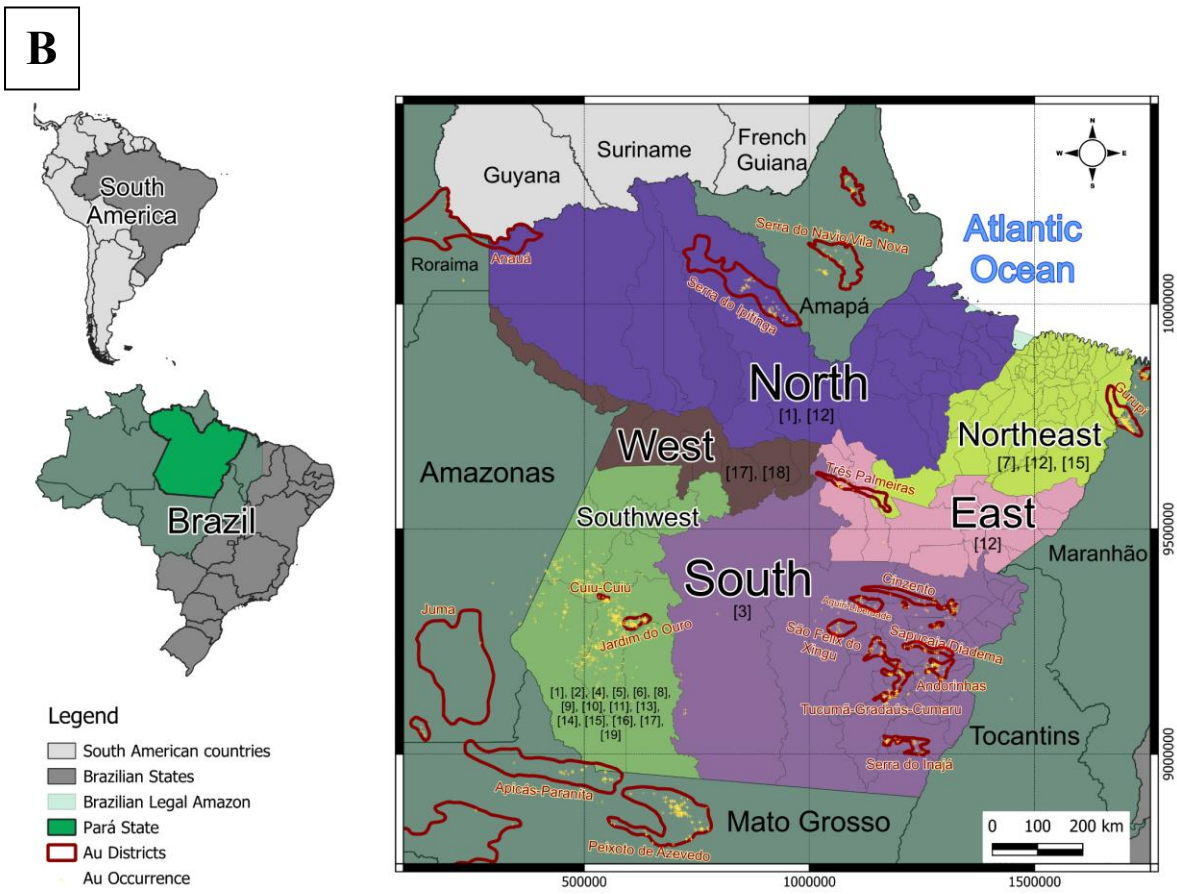


Figure 6: (A) Boxplots of Hg concentrations (ppb) in hair across different regions of Pará. At 10,000 ppb is the threshold that marks where health risks begin, while 1,000 ppb is considered the safe level (WHO, 2021); (B) Map of the State of Pará showing the division of the analyzed regions. The regions were delineated based on the areas approached by the included studies and considering the Au districts, providing context for the comparisons presented in the boxplots of Figure 6A. The numbers displayed on the map correspond to the references associated with each region, as follows: [1] Akagi et al. (1995); [2] Akagi et al. (2000); [3] Barbosa et al. (1995); [4] Basta et al. (2021); [5] Castilhos et al. (2015); [6] Crompton et al. (2002); [7] Dolbec et al. (2000); [8] Dorea et al. (2005); [9] Grandjean et al. (1999); [10] Harada et al. (2001); [11] Kehrig et al. (1997); [12] Leino and Lodenius (1995); [13] Oliveira et al. (2022); [14] Perini et al. (2021); [15] Pinheiro et al. (2008); [16] Pinheiro et al. (2012); [17] Santos et al. (2000); [18] Santos et al. (2002a); and [19] Santos et al. (2002b).

Concentrations in northern Pará ranged from 10,000 ppb to 19,700 ppb, with the value of 14,850 ppb for both the median and the mean (SD = 6,859 ppb). The highest variability was observed in the northeast region, ranging from 2,720 ppb up to 65,000 ppb, with a median of 10,800 ppb and a mean of 19,410 ppb (SD = 21,021 ppb). In southwestern Pará, the range of hair Hg concentrations was 860—37,400 ppb, the median was 11,615 ppb, while the mean was 10,663 ppb (SD = 7,873 ppb). The west, represented by the western portion above the Tapajós region (southwest), showed lower concentrations that ranged from 3,340 ppb to 8,850 ppb, with a median of 4,350 ppb and a mean of 4,577 ppb (SD = 1,184 ppb). Hair Hg concentrations

in both the east and south regions of Pará were reported only by one study each, with concentrations of 8,500 ppb **(Leino and Lodenius, 1995)** and 8,000 ppb **(Barbosa et al., 1995)**, respectively. Two outliers were identified, 37,400 ppb in southwestern Pará and 8,580 ppb in the west portion of the State.

Blood and urine Hg concentrations by State were much lower when compared to hair Hg concentrations **(Table 2)**. Additionally, ASGM-related workers present higher Hg levels in urine when compared to the other two groups analyzed, while traditional populations show higher Hg levels in blood **(Figure 7)**.

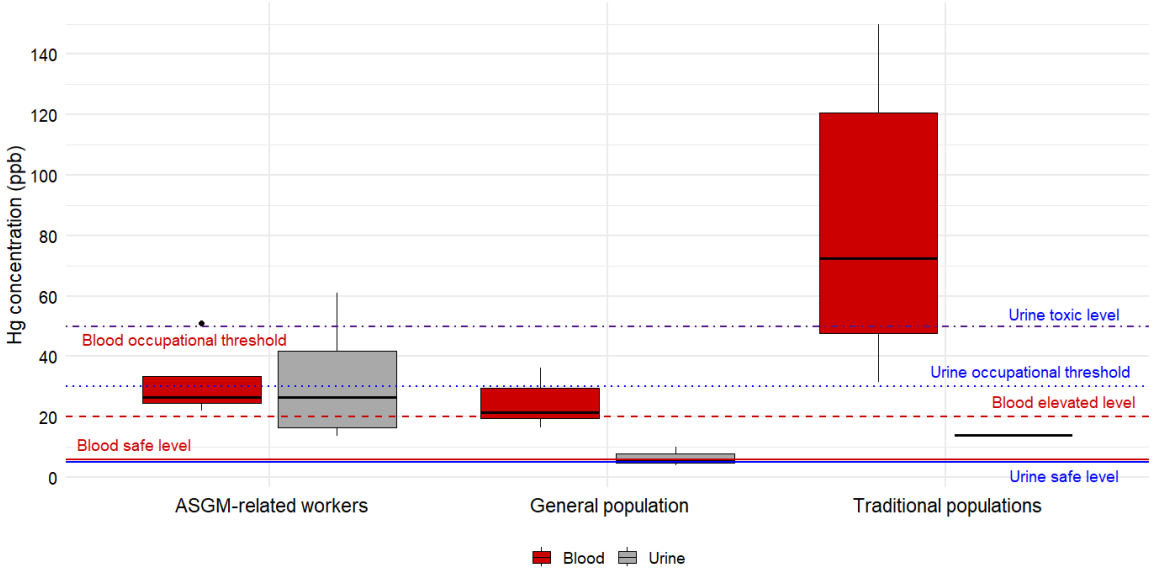


Figure 7: Boxplots of Hg concentrations (ppb) in blood and urine from Pará. Thresholds: 5 ppb (urine safe level), 5.8 ppb (blood safe level), 20 ppb (elevated blood level), 30 ppb (urine occupational exposure), and 50 ppb (blood occupational exposure and urine toxic level). Sample sizes (n): 4 (ASGM workers), 6 (blood) and 3 (urine) (general population), 6 (blood) and 1 (urine) (traditional populations).

Urine Hg concentrations in ASGM-related workers varied between 13.8 ppb and 61 ppb, with a median of 26.4 ppb and a mean of 31.9 ppb (SD = 21.6 ppb). On the other hand, within the general population, Hg levels in urine varied between 3.91—9.9 ppb, with a median and a mean of 5.73 ppb and 6.51 (SD = 3.07 ppb), respectively. Only one study reported urine

Hg levels in traditional populations **(Barbosa et al., 1995)**, with a concentration of 14 ppb. On the other hand, blood Hg concentrations observed within the traditional populations were between 31.50 ppb and 150 ppb, with a median of 72.4 and a mean of 83.7 ppb (SD = 48.3 ppb), while in the ASGM-related worker it varied from 22 ppb to 51 ppb with a median of 26.5 ppb and a mean of 31.5 ppb (SD = 13.2 ppb). Finally, blood Hg levels in the general population were between 16.5 ppb and 36.1 ppb, with the median and mean of 21.4 ppb and 24.4 ppb (SD = 7.8 ppb), respectively.

Additionally, the Kruskal-Wallis test indicated statistically significant differences among at least one group (combining tissue and occupation, **Figure 7**) compared to the others (p = 0.0093). Consequently, Dunn's test revealed a statistical difference between blood Hg concentrations in the traditional populations compared to the general population (Z = -2.286, p = 0.022). The complete Dunn's test results are provided in **Table 2 of the Supplementary Materials**.

2.4.3. Environmental matrices

Sediments were the most frequently investigated environmental matrix, with 28 studies focusing on it **(Pfeiffer et al., 1989; Lacerda et al., 1991a, b; Pfeiffer et al., 1991; Aula et al., 1995; Reuther, 1994; Pestana et al., 1997; Hylander et al., 2000a; Lechler et al., 2000; Leady and Gottgens, 2001; Cordeiro et al., 2002; Pestana and Formoso, 2003; Bastos et al., 2006; Bonotto et al., 2006; Egler et al., 2006; Mulholland et al., 2012; Santolin et al., 2015; Mendes et al., 2016; Azevedo et al., 2017; Rhodes et al., 2018; Siqueira et al., 2018; Lino et al., 2019; Santos et al., 2020; Gomes et al., 2022; Montes et al., 2022; Jacques et al., 2023; Nunes et al., 2024)**. This was followed by soil (14 studies—**Pfeiffer et al., 1991; Malm et al., 1995b; Windmöller et al., 1996; Gonçalves et al., 1998; Gonçalves et al., 2000;**

Lechler et al., 2000; Pestana and Formoso, 2003; Lacerda et al., 2004; Egler et al., 2006; Hinton and Veiga, 2009; Júnior et al., 2009; Cesar et al., 2011; Teixeira et al., 2018; Montoya et al., 2019) and water (12 studies—**Pfeiffer et al., 1989; Lacerda et al., 1991b; Pfeiffer et al., 1991; Nriagu et al., 1992; Palheta and Taylor, 1995; Roulet et al., 1998; Fostier et al., 2000; Bonzongo et al., 2002; Barbosa et al., 2003; Lino et al., 2019; Bastos et al., 2020; Gomes et al., 2022**). Nine studies examined air Hg concentrations **(Pfeiffer et al., 1991; Hacon et al., 1995; Malm et al., 1995b; von Tümpling Jr. et al., 1995; Villas Bôas, 1997; Hachiya et al., 1998; Artaxo et al., 2000; Oliveira et al., 2004; Castilhos and Domingos, 2024)**, eight focused on suspended particulate matter (SPM) **(Martinelli et al., 1989; Nogueira et al., 1997; Roulet et al., 1998; Oliveira et al., 2004; Azevedo et al., 2017; Lino et al., 2019; Bastos et al., 2020; Gomes et al., 2022)**, and seven investigated Hg levels in plants **(Martinelli et al., 1989; Lacerda et al., 1991b; Aula et al., 1995; Leady and Gottgens, 2001; Egler et al., 2006; Gomes et al., 2022; Júnior and Carvalho, 2022)**. Periphyton, plankton, rocks and tailings were each studied once. Cold Vapor Atomic Absorption Spectrometry (CV-AAS) was the most utilized analytical technique to investigate environmental matrices, followed by Cold Vapor Atomic Fluorescence Spectrometry (CV-AFS) and Thermal Desorption Atomic Absorption Spectrometry (TD-AAS) **(Figure 8)**.

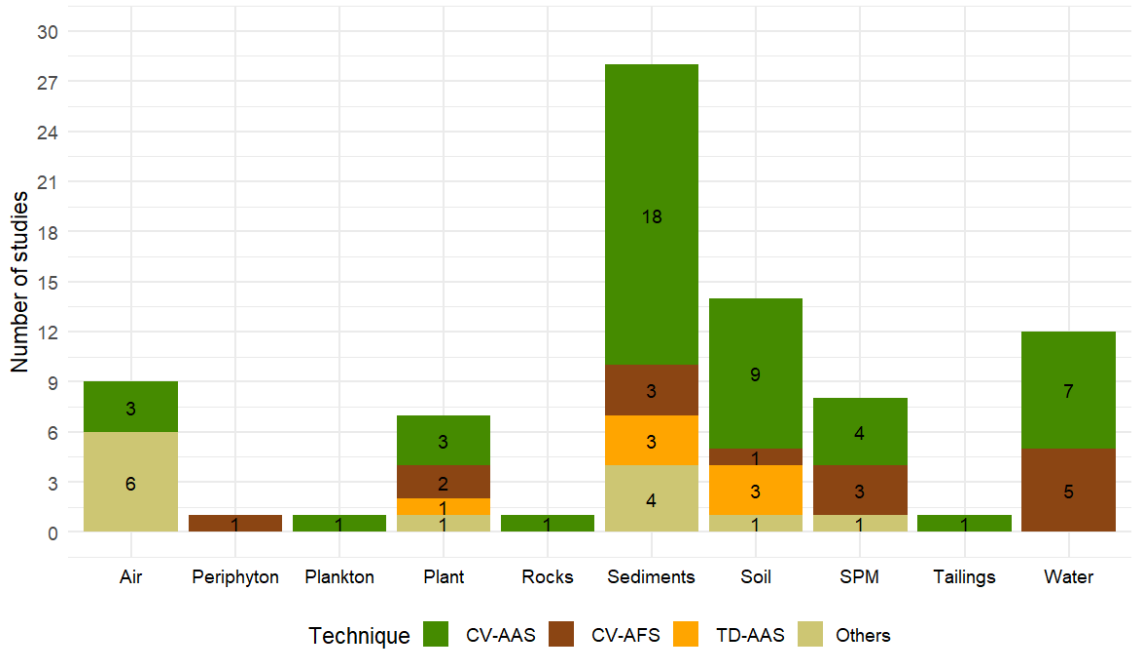


Figure 8: Frequency of analytical techniques applied to different environmental matrices, including CV-AAS, CV-AFS, TD-AAS, and others. Each bar represents the number of studies using a specific technique for each environmental matrix.

As far as the air matrix is concerned, the utilized techniques included CV-AAS (3 studies), along with other atomic spectroscopy methods such as AFS, ZAAS, TV-AAS, and specialized mercury detection techniques like the Gold Film Mercury Vapor Analyzer, Gold Trap-Heating-AFS, and one unspecified technique. For sediments, the most utilized technique was CV-AAS (18 studies), followed by CV-AFS and TD-AAS, each with 3 studies. Additional techniques used to investigate Hg levels in sediments included ICP-OES, HG-AAS, AAS, and one unspecified method. In plants and SPM, Incineration-AAS was used once for each, while RNAA was applied once for soil Hg analysis.

2.4.3.1. Mercury in plant tissues

The four most analyzed plant tissues in the selected papers were roots (35), stem + leaves (27), leaves (25), and stem (8) (**Figure 9A**). Furthermore, *Eichhornia crassipes* was the

only species investigated in more than one study with specific focus on roots **(Aula et al., 1995; Leady and Gottgens, 2001; Júnior and Carvalho, 2022)**, shoots **(Leady and Gottgens, 2001)**, stem, and leaves **(Júnior and Carvalho, 2022)**, and the whole plant (**Martinelli et al. 1989) (Figure 9B)**.

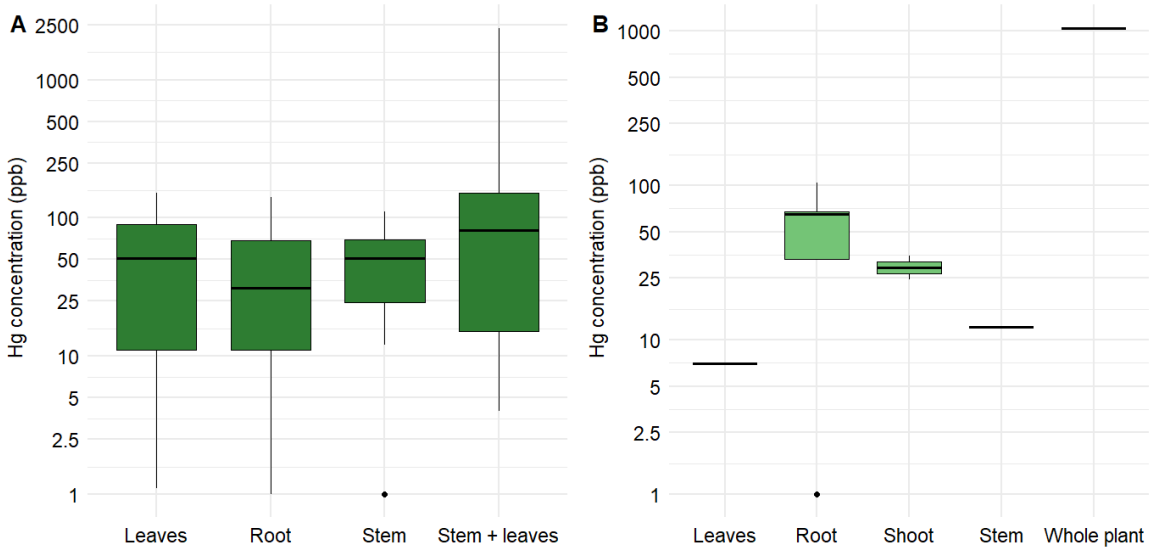


Figure 9: Boxplots comparing Hg concentrations (ppb) in different plant tissues (log scale). (A) Aggregated data for all species (Leaves = 25, Root = 35, Stem = 8, Stem + Leaves = 27). (B) Data specific to Eichhornia crassipes (Leaves = 1, Root = 5, Shoot = 2, Stem = 1, Whole plant = 1).

For the aggregated data, root Hg concentrations ranged from 0 to 140 ppb, with a median of 30 ppb and a mean of 43.20 ppb. The mix of stem and leaves (stem + leaves) had Hg values between 3 ppb and 2,370 ppb, with a median of 80 ppb and a mean of 228.85 ppb, while four values were identified as outliers (370 ppb, 920 ppb, 960 ppb, and 2,370 ppb). In leaves, Hg levels ranged from 0.1 ppb to 150 ppb, with a median of 50 ppb and a mean of 54.05 ppb. Hg levels in stems varied between 0 and 110 ppb, with a median of 50 ppb and a mean of 51.38 ppb.

On the other hand, the highest Hg concentration in *Eichhornia crassipes* was in the whole plant (1,040 ppb). Root concentrations varied from 0 (outlier) ppb to 102 ppb, while shoots had a narrower range (23.5—34 ppb), and stems and leaves presented single concentrations each, 11 ppb and 6 ppb, respectively. Median concentrations were 64.10 ppb (mean of 52.82 ppb) in roots, followed by 28.75 ppb shoots, 11 ppb in stems, and 6 ppb in leaves.

2.4.3.2. Mercury in sediments, soils and suspended particulate matter (SPM)

Data from 28, 14, and 8 studies on sediments, soils, and SPM, respectively, were analyzed to compare Hg concentration differences across matrices **(Figure 10)**, and among States **(Table 3)**.

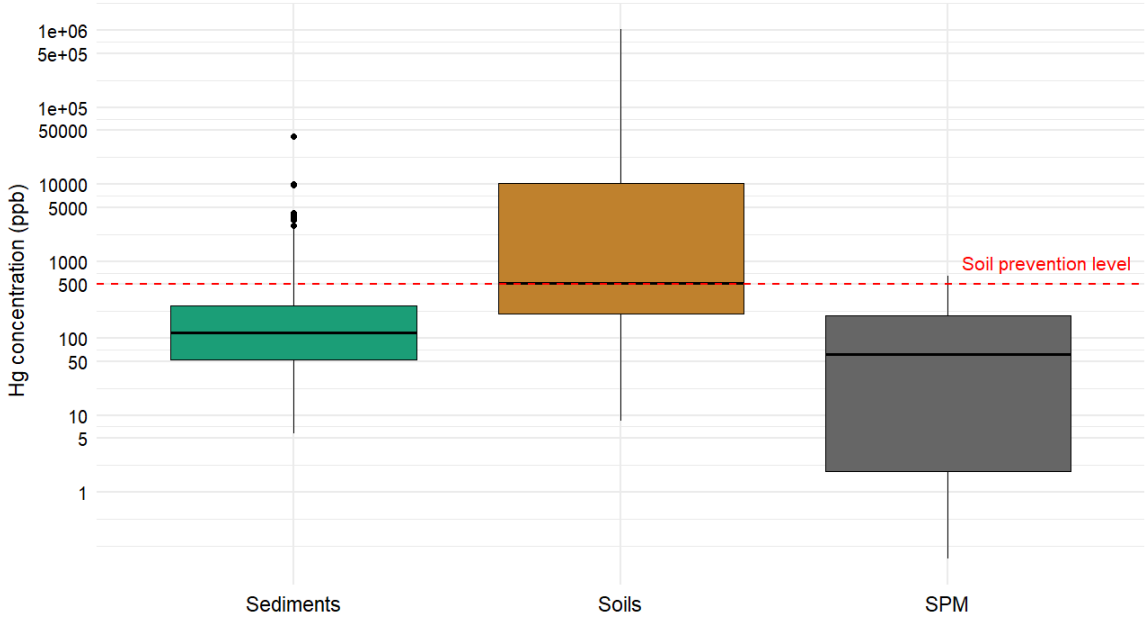


Figure 10: Boxplot of Hg concentrations in sediments, soils, and SPM (log-transformed, natural log scale). The red dashed line represents the Hg prevention levels for soils in Brazil (CONAMA, 2010).

Table 3. Hg concentrations in sediments, soils and SPM by State.

State	Matrix	Min—max (ppb)	Median (ppb)	Mean (ppb)	Outliers (ppb)
Amapá	Soils (n = 33)	22–26,700	230	1,578.39	18,100; 26,700
Amazonas	Sediments (n = 14)	41–339	57.47	113.78	322; 322; 339
	Soils (n = 8)	41–346	322	227	-
	SPM (n = 4)	50–161.10	56.89	81.22	-
Roraima	Sediments (n = 1)	264	264	264	-
	Soils (n = 4)	210–7,450	1,200	2,515	-
Rondônia	Sediments (n = 66)	20–10,015	190	1,059.60	3,450; 3,730; 4,050; 4,290; 9,820; 10,015
	Soils (n = 15)	41–7,450	322	840.40	2,010; 7,450
Pará	Sediments (n = 13)	12–675	77	155.82	490; 675
	Soils (n = 50)	8.4–1,022,000	1,314.89	79,252.77	60,800; 248,000; 248,970; 523,040; 959,870; 1,022,000
	SPM (n = 3)	70–303.36	219.92	197.76	-
Mato Grosso	Sediments (n = 39)	20–348	65	85.63	348
	Soils (n = 7)	33.80–170,400	390	25,793.67	170,400
	SPM (n = 2)	192.5–645.55	419.03	419.03	-
Mato Grosso do Sul	Sediments (n = 13)	7.81–65.08	30.98	35.94	-

Bahia	Sediments (n = 2)	169–312	240.50	240.5	-
Minas Gerais	Sediments (n = 47)	7.81–41,850	183	1,281	650; 1,207; 2,312; 3,581; 3,835; 41,580
	Soils (n = 55)	15.90–590,000	10,000	80,444.08	214,000; 222,000; 383,000; 413,000; 419,000; 483,000; 554,000; 590,000
Rio de Janeiro	Sediments (n = 8)	35–325	46.25	91.44	325
	SPM (n = 7)	0.136–256	1.57	46.88	-
Rio Grande do Sul	Sediments (n = 12)	71–252	139	143.54	-
	Soils (n = 1)	103,151.20	103,151.20	103,151.20	-

Mercury concentrations in soils, sediments, and suspended particulate matter (SPM) across various Brazilian States showed marked variability and numerous high outliers **(Table 3; Figure 10)**. While sediment values generally ranged from single-digit to a few hundred ppb (e.g., 7.81–339 ppb in Amazonas, up to 41,850 ppb in Minas Gerais), soils exhibited some of the most extreme concentrations, particularly in Pará (reaching 1,022,000 ppb) and Minas Gerais (up to 590,000 ppb). In addition, the Kruskal-Wallis test showed statistically significant differences in Hg concentrations between soils and sediments in Mato Grosso ($p = 0.018$), Minas Gerais ($p = 1.991 \times 10^{-9}$), and Pará ($p = 1.087 \times 10^{-5}$). Ranges in SPM were typically narrower (e.g., 50–161.10 ppb in Amazonas, 192.5–645.55 ppb in Mato Grosso), yet notable outliers were also present.

2.4.3.3. Dissolved mercury in water

Dissolved Hg in water was generally lower compared to the other previously mentioned matrices **(Figure 11)** and always, except in one case (Rondônia), above the maximum allowable value for drinking water.

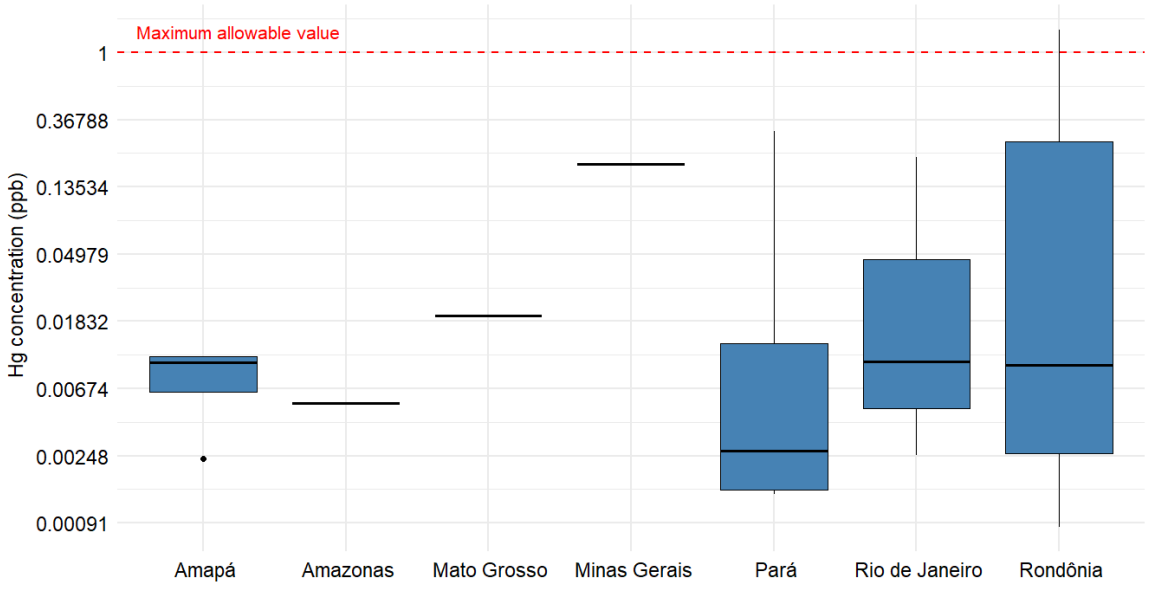


Figure 11: Boxplots showing Hg concentrations in water (ppb) across seven States in Brazil (log-transformed, natural log scale). The red dashed line represents the maximum allowable value for drinking water (CONAMA, 2008).

The levels ranged from 0.00238 to 0.0109 ppb in Amapá **(Fostier et al., 2000)**, 0.0014 to 0.3090 ppb in Pará **(Roulet et al., 1998; Lino et al., 2019)**, 0.0025 to 0.1038 ppb in Rio de Janeiro **(Pfeiffer et al., 1989; Gomes et al., 2022)**, and 0.0009 to 1.4 ppb in Rondônia **(Pfeiffer et al., 1989; Pfeiffer et al., 1991; Nriagu et al., 1992; Bonzongo et al., 2002; Bastos et al., 2020)**. The median and mean concentrations were, respectively, 0.0099 ppb and 0.0083 ppb in Amapá, 0.00308 ppb and 0.0791 ppb in Pará, 0.01 ppb and 0.0742 ppb in Rio de Janeiro, and 0.0095 ppb and 0.2203 ppb in Rondônia. Two outliers were identified: one in Pará (0.309 ppb) and another in Rondônia (1.4 ppb). In Amazonas, Mato Grosso, and Minas Gerais, only single

values were reported, at 0.00542 ppb **(Barbosa et al., 2003)**, 0.02 ppb **(Lacerda et al., 1991b)**, and 0.19 ppb **(Pfeiffer et al., 1991)**, respectively.

2.4.3.4. Mercury concentrations in air

The Hg concentrations (ng/m^3, gaseous Hg^0) in air are presented separately for ASGM hubs and non-ASGM related areas **(Figure 12) (Pfeiffer et al., 1991; Hacon et al., 1995; Malm et al., 1995b; von Tümpling Jr. et al., 1995; Villas Bôas, 1997; Hachiya et al., 1998; Artaxo et al., 2000; Oliveira et al., 2004; Castilhos and Domingos, 2024)**. The term 'ASGM hubs' refers to Hg concentrations measured in both *garimpo* sites and gold shops.

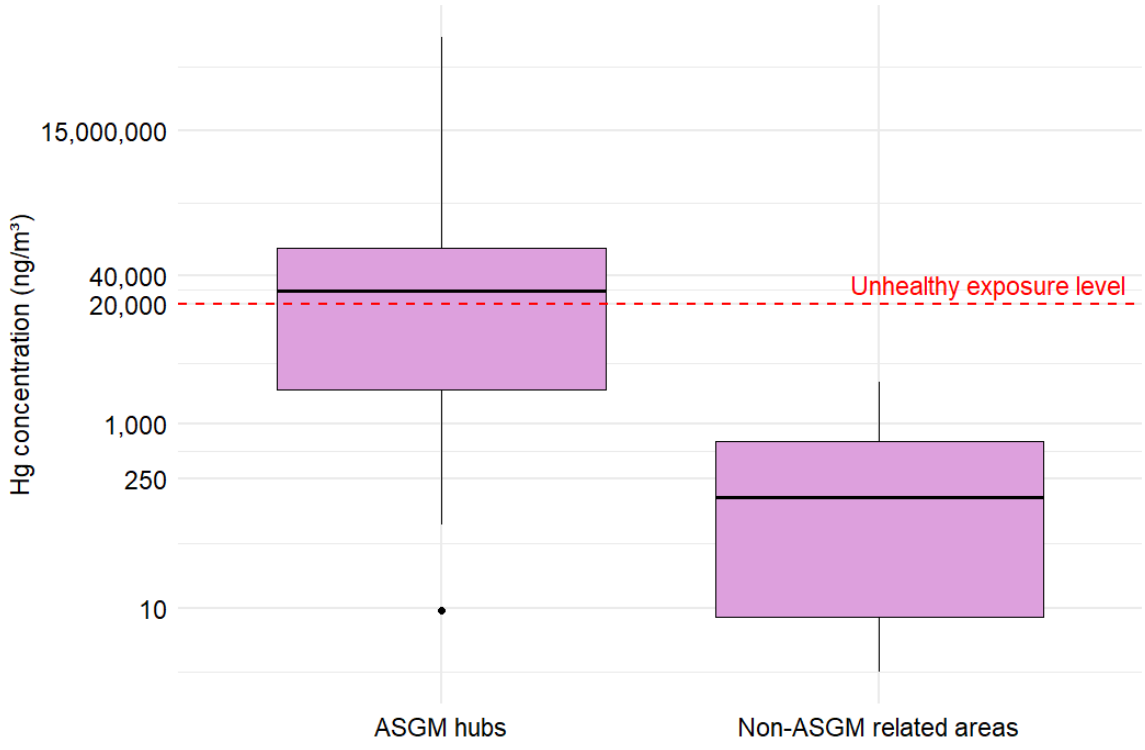


Figure 12: Boxplot of air mercury (Hg) concentrations (ng/m^3) in ASGM hubs (left) and in non-ASGM related areas (right). The red dashed line at 20,000 indicates the threshold for above which mild, subclinical signs of central nervous system toxicity may develop in workers who have been chronically exposed to elemental mercury in the air (WHO, 2021). The y-axis shows Hg concentrations in log-transformed, natural log scale.

Hg levels for non-ASGM related areas ranged from 2 to 2,800 ng/m³, with a median of 158 ng/m³ and a mean of 379.99 ng/m³, and one outlier at 2,800 ng/m³. On the other hand, considerably higher concentrations were observed in the ASGM hubs, ranging from 9.5 ng/m³ to 15,499,000 ng/m³, with a median of 27,966.67 ng/m³ and a mean of 411,477.96 ng/m³. In addition, all values above 201,000 ng/m³ in the ASGM hubs were considered outliers (201,000 ng/m³, 354,000 ng/m³, 374,666.70 ng/m³, 392,666.70 ng/m³, 1,280,000 ng/m³, and 15,499,000 ng/m³). A statistically significant difference between air Hg concentrations in ASGM hubs and non-ASGM areas was confirmed by the Dunn's test ($Z = 6.23$, $p = 4.636 \times 10^{-10}$).

2.4.4. Mercury bioaccumulation in aquatic and terrestrial wildlife fauna

Both aquatic and terrestrial faunas were studied by the articles included in this review, with a predominance of studies on fish (45 studies) **(Martinelli et al., 1989; Pfeiffer et al., 1989; Pfeiffer et al., 1991; Akagi et al., 1995; Boischio et al., 1995; Malm et al., 1995b; Palheta and Taylor, 1995; Porvari, 1995; Reuther, 1994; Bidone et al., 1997a; Bidone et al., 1997b; Hacon et al., 1997; Castilhos et al., 1998; Akagi and Naganuma, 2000; Brabo et al., 2000; Hylander et al., 2000b; Santos et al., 2000b; Leady and Gottgens, 2001; Uryu et al., 2001; Santos et al., 2002a; Santos et al., 2002b; Barbosa et al., 2003; Dorea et al., 2003; Farias et al., 2005; Bastos et al., 2006; Bastos et al., 2007; Dorea and Barbosa, 2007; Rabitto et al., 2011; Windom et al., 2012; Hacon et al., 2013; Martín-Doimeadios et al., 2014; Bastos et al., 2015; Castilhos et al., 2015; Azevedo et al., 2017; Ferreira et al., 2017; Lino et al., 2019; Silva et al., 2019; Hacon et al., 2020; Oliveira et al., 2021a; Vasconcellos et al., 2021; Oliveira et al., 2022; Vasconcellos et al., 2022; Basta et al., 2023; Neto et al., 2024)**. Among the included studies Hg concentrations in tissues of mammals, avian species, reptiles, and invertebrates were also investigated.

2.4.4.1. Mercury bioaccumulation in mammals

Mercury concentrations in mammals varied according to the tissue and species analyzed **(Table 4)**.

Table 4. Hg concentrations and SD (d.w. ppb) in different tissues of mammal species studied by the articles included.

Mammals				
Species	**n**	**Tissue**	**Mean ± SD (d.w. ppb)**	**Reference**
Trichechus inunguis	20	Muscle	59.30 ± 104.40	Júnior and Carvalho (2022)
	10	Liver	48.60 ± 54.30	
	7	Kidney	23.70 ± 33.60	
	7	Lung	1.30 ± 3.20	
	3	Brain	51.70 ± 46.70	
	2	Skin	154 ± 133.20	
	29	Vibrissae	< 0.001	
Tayassu tajacu	6	Muscle	11 ± 10	Oliveira et al. (2021b)
Tayassu pecari	7	Muscle	5 ± 18	
Hydrochoerus hydrochaeris	3	Muscle	26 ± 8	
Cebus apella	2	Muscle	19	

Tapirus terrestris	5	Muscle	18 ± 10	
Cuniculus paca	7	Muscle	7 ± 22	
Dasyprocta aguti	3	Muscle	5 ± 2	
Dasypus novemcinctus	2	Muscle	4 ± 3	
Mazama americana	2	Muscle	4 ± 16	
Ozotoceros bezoarticus	1	Muscle	4	
Pteronura brasiliensis	19	Fur	7,149.47 ± 2,907.37	Soresini et al. (2021)

The minimum value observed (< 0.001 ppb) was in vibrissae of *Trichechus inunguis* **(Júnior and Carvalho, 2022)**, while the highest values were found in fur of *Pteronura brasiliensis* **(Soresini et al., 2021)**.

2.4.4.2. Mercury bioaccumulation in avian species

Only three avian species were analyzed in the articles included in this study **(Table 5)**.

Table 5. Hg concentrations and SD (d.w. ppb) in tissues of avian species studied by the articles included.

			Avian	
Species	**n**	**Tissue**	**Mean ± SD (d.w. ppb)**	**Reference**

Ara macao	2	Muscle	35 ± 19	Oliveira et al. (2021b)
Crypturellus parvirostris	1	Muscle	11	
Mycteria americana	124	Nestling feathers	557 ± 627	Lama et al. (2011)

Hg concentrations in the nestling feathers of *Mycteria americana* from different regions of Mato Grosso do Sul were studied by **Lama et al. (2011)**, whereas Hg concentrations in the muscles of *Ara macao* and *Crypturellus parvirostris* from Rio Branco Indigenous Reserve (Rondônia) were investigated by **Oliveira et al. (2021b)**.

2.4.4.3. Mercury bioaccumulation in reptiles

Two species of freshwater turtles were investigated: *Podocnemis unifilis* **(Oliveira et al., 2021a)** and *Podocnemis expansa* **(Targino et al., 2023; Oliveira et al., 2021a)**. In the muscles of *P. unifilis* (n = 3) and *P. expansa* (n = 8) from Rio Branco Indigenous Reserve in Rondônia, mean concentrations were, respectively, 12 ± 2 ppb (d.w.) and 9 ± 16 ppb (d.w.) **(Oliveira et al., 2021a)**. However, in Amazonas Hg concentrations in muscles (n = 19) of *P. expansa* were considerably higher, with a mean of 109.1 ± 122 ppb (d.w.). Additionally, mean concentrations of 104.4 ± 106.9 ppb (d.w.) in skin (n = 28), and 60 ± 0.9 ppb (d.w.) in brain tissue of *P. expansa* were reported **(Targino et al., 2023)**.

Hg concentrations in claws, scutes **(Lázaro et al., 2015)**, and muscles **(Akagi et al., 1995; Vieira et al., 2011; Oliveira et al., 2021a)** of different alligator species—*Caiman crocodilus yacare* **(Vieira et al., 2011; Lázaro et al., 2015)**, *Caiman crocodilus crocodilus* and *Melanosuchus niger* **(Oliveira et al., 2021a)**, and an unidentified species **(Akagi et al., 1995)**—were also investigated **(Figure 13)**.

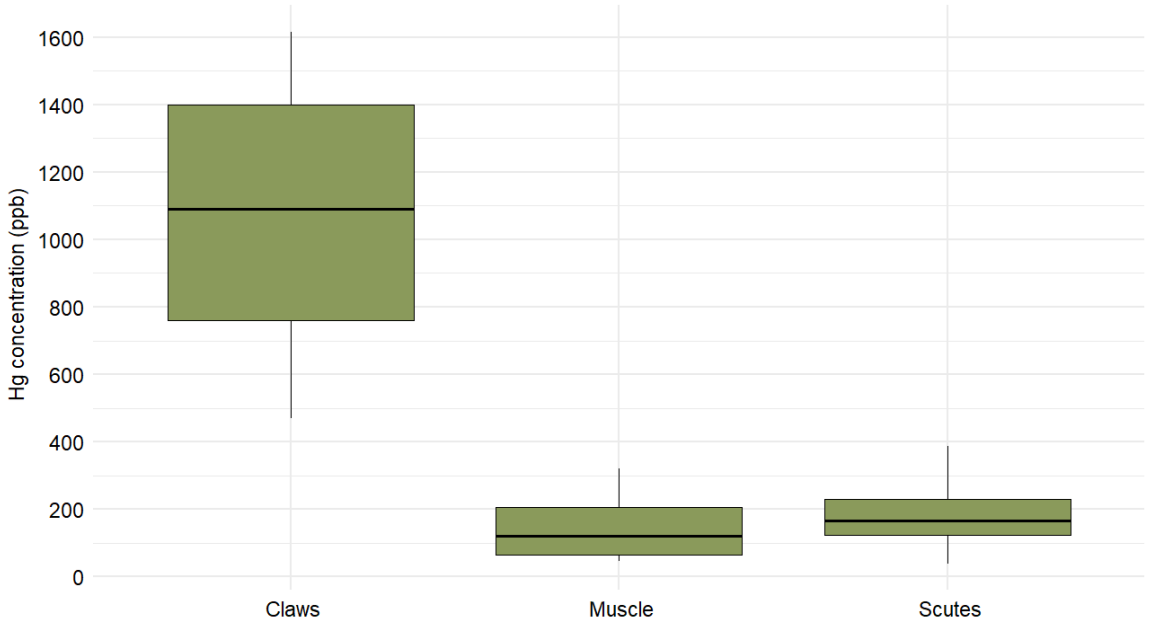


Figure 13: Boxplot of mercury (Hg) concentrations in different alligator tissues from Mato Grosso (Vieira et al., 2011; Lázaro et al., 2015), Mato Grosso do Sul (Vieira et al., 2011), Pará (Akagi et al., 1995), and Rondônia (Oliveira et al., 2021a).

Among the studied tissues, claws exhibited the highest Hg concentrations (see **Figure 13**), ranging from 468.24 to 1,616.40 ppb, with a median of 1,091 ppb and a mean of 1,066 ppb. In contrast, scutes and muscles displayed similar Hg concentrations, although values were slightly higher in scutes. Hg concentrations in scutes ranged from 38.14 to 387.40 ppb, with a median of 164.90 ppb and a mean of 188.84 ppb. In muscles, concentrations varied between 45.92 and 320 ppb, with a median of 120 ppb and a mean of 146.17 ppb. Statistically significant differences were observed through Dunn's post-hoc test, confirming that Hg concentrations in claws are higher than both muscles ($p = 0.0047$) and scutes ($p = 0.0328$).

2.4.4.4. Mercury bioaccumulation in fish

Muscle was the most examined tissue in fish (n = 833), followed by liver and gills (n = 10 each), while eggs were analyzed in only two cases. Hg concentrations in muscles of different fish species by feeding habit are presented in **Figure 14**.

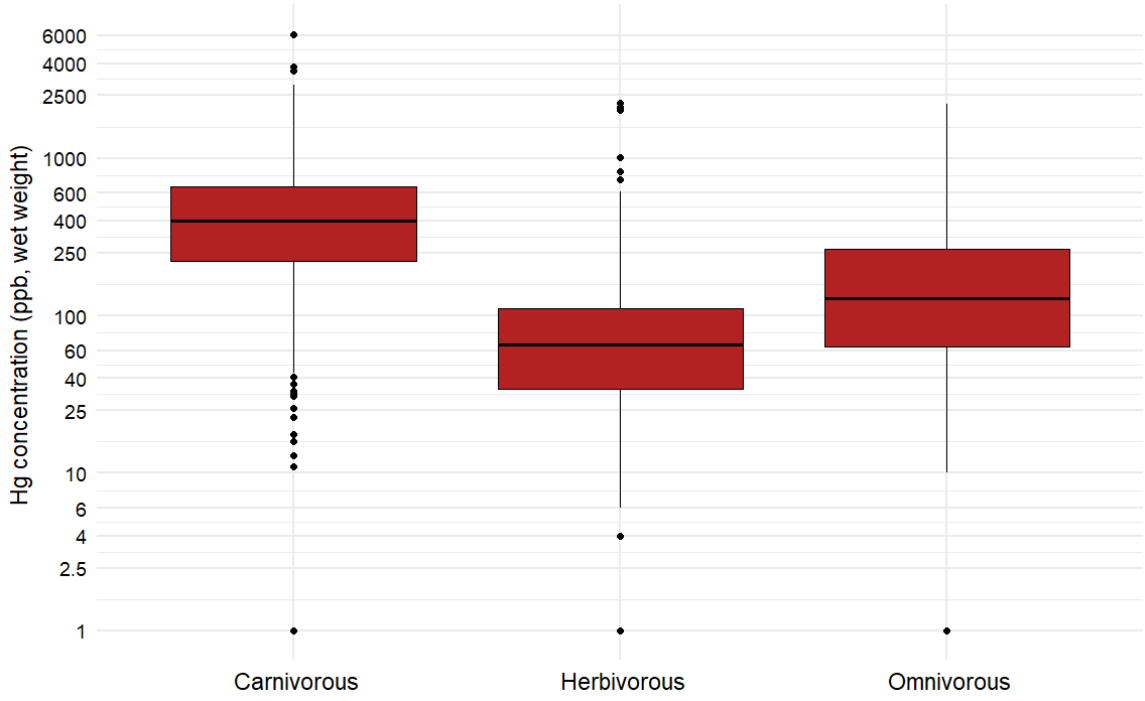


Figure 14: Boxplot of mercury concentrations (ppb, wet weight), log-transformed using the natural logarithm scale, in muscles of different fish species from Brazil, categorized by feeding habit.

Carnivorous species exhibited the highest Hg concentrations, followed by omnivorous and herbivorous species. Hg concentrations ranged from 0 to 6,110 ppb in carnivorous species, from 0 to 2,210 ppb in omnivorous species, and from 0 to 2,240 ppb in herbivorous species. Median concentrations were 400 ppb in carnivorous, 127 ppb in omnivorous, and 64.10 ppb in herbivorous species, while the means were 550.07 ppb in carnivorous, 230.65 ppb in omnivorous, and 145.07 ppb in herbivorous. Outliers were identified in all three categories:

values above 1,320.63 ppb in carnivorous, 560.46 ppb in omnivorous, and 225.50 ppb in herbivorous were considered outliers.

2.4.4.5. Mercury bioaccumulation in invertebrates

Five of the selected studies investigated Hg concentrations in invertebrates, covering the following species: *Ampullaris sp.* **(Lacerda et al., 1991b)**, *Eisenia fetida* **(Hinton and Veiga, 2009)**, *Hydrophilidae* and *Pomacea bridgesii* **(Leady and Gottgens, 2001)**, *Macrobrachium amazonicum* **(Albuquerque et al., 2020a)**, *Marisa planogyra*, *Pomacea lineata* and *Pomacea scalaris* **(Callil and Junk, 2001)**. The selected studies covered the States of Mato Grosso **(Lacerda et al., 1991b; Callil and Junk, 2001; Leady and Gottgens, 2001)**, Mato Grosso do Sul **(Leady and Gottgens, 2001)**, and Pará **(Hinton and Veiga, 2009; Albuquerque et al., 2020a)**. The Hg concentrations in invertebrates are presented in **Figure 15**.

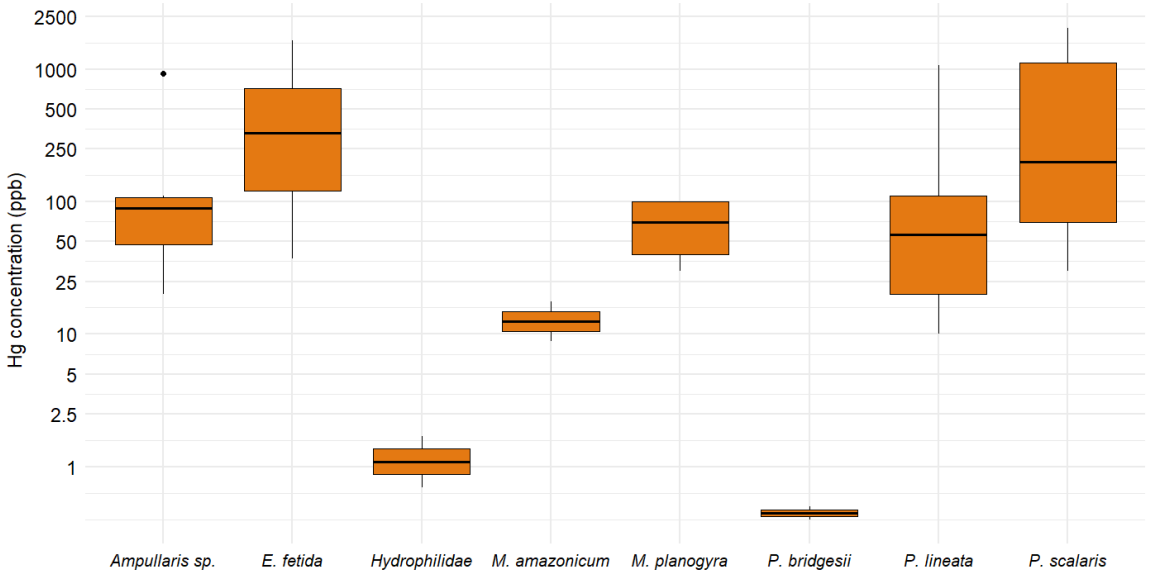


Figure 15: Boxplot of mercury (Hg) concentrations in different invertebrate species in Brazil. The y-axis indicates Hg concentration (log-transformed, natural log scale) in ppb.

In *Macrobrachium amazonicum*, concentrations ranged between 8.78 ppb to 17.57 ppb, with both the median and mean at 13.175 ppb. A higher variability was observed in *Ampullaris* sp., with concentrations ranging from 20 ppb to 930 ppb (outlier), a median of 90 ppb and a mean of 213.33 ppb. For *Eisenia fetida*, values ranged between 37 and 1,630 ppb, with a median of 330 ppb and a mean of 536.92 ppb. *Hydrophilidae* and *Pomacea bridgesii* showed lower concentrations, ranging from 0.70 to 1.70 ppb and 0.40 to 0.50 ppb, respectively. The median and mean values for these species were 1.20 ppb and 0.45 ppb. Concentrations in *Marisa planogyra* varied between 30 ppb and 100 ppb, with a median of 70 ppb and a mean of 68 ppb. In *Pomacea lineata*, levels ranged from 10 ppb to 1,060 ppb, with a median of 56 ppb and a mean of 195.11 ppb. Two outliers were identified for this species (350 ppb and 1,060 ppb). *Pomacea scalaris* exhibited concentrations between 30 ppb and 2,040 ppb, with a median of 200 ppb and a mean of 682.22 ppb.

2.5. Discussion

2.5.1. Regional distribution and research coverage across time

Our findings indicate a geographic focus on the northern region of Brazil, specifically in the Amazon biome. It likely reflects the historical and ongoing intensity of *garimpos* in the Amazon (**Pfeiffer et al., 1989; Machado and Figuerôa, 2001; Lobo et al., 2016; Castilhos and Domingos, 2024)**, where extensive gold mining has led to some of the highest reported Hg concentrations in both human (**Leino and Lodenius, 1995; Eve et al., 1996; Silva-Forsberg et al., 1999; Lopes-Araújo et al., 2023**) and environmental matrices (**Pfeiffer et al., 1991; Egler et al., 2006; Hinton and Veiga, 2009**). States outside the Amazon—such as Rio de Janeiro, Rio Grande do Sul, and Minas Gerais—have fewer studies, even though elevated sediment Hg levels were occasionally reported (*e.g.* **Pfeiffer et al., 1989; Pestana and Formoso, 2003; Júnior et al., 2009; Mendes et al., 2016**), suggesting that impacts of both historical and contemporary gold mining activities can extend beyond the Amazon region.

The historical evolution of research **(Figure 4)** indicates an initial surge in Hg-related investigations in the late 1980s and early 1990s, likely driven by greater awareness of *garimpo*'s negative impacts **(Malm et al., 1995b; Lacerda, 1997)**. However, the moving average indicates fluctuations in research intensity over the years. The establishment of international collaborations on mercury research in the 1990s **(Hacon et al., 2008)** may help explain the higher peaks in the mid—late 1990s in the moving average of **Figure 4**. Furthermore, the growth of publications in the last decade may be related to different factors, for example: (I) international agreements like the Minamata Convention **(UNEP, 2013)**, and (II) increased concern on mercury contamination and health risks in Brazil **(Crespo-Lopez et al., 2024)** due to the weakening of environmental policies and inspection over the last decade **(Agapito et al., 2022; Seifert Jr. et al., 2023)**.

Regarding analytical techniques, CV-AAS remains the most widely used analytical technique in both human and environmental samples (**Figure 8; supplementary materials**) due to its relative simplicity and effectiveness. To enhance specificity and sensitivity, more recent studies have incorporated alternative methods, such as TD-AAS (e.g. **Meneses et al., 2022; Oliveira et al., 2022**), and CV-AFS (e.g. **Hacon et al., 2020; Gomes et al., 2022**).

2.5.2. Geogenic mercury baselines, Hg mobilization, and policy challenges in contamination attribution

Understanding Hg levels requires acknowledging that some regions have never been "zero-mercury" environments, such as the Amazon. Across Brazil, naturally elevated Hg levels can occur due to the country's diverse geology, particularly in mineral-rich provinces like Carajás (Pará State). Soils from this region often exceed global crustal averages, prompting calls for locally defined geochemical baselines. For example, **Sahoo et al. (2020)** recommend a baseline of approximately 320 ppb in the Carajás–Itacaiúnas region, while historical sediment cores from the same area show even higher values in older layers (~574 ppb), confirming that natural Hg baselines vary across time and space **(Sahoo et al., 2024)**. Similar spatial variability is observed in other Amazonian subregions, with background soil levels ranging from 117 ± 70 ppb in the Itacaiúnas Basin **(Sahoo et al., 2023)** to 172 ppb in the Rio Negro Basin **(Fadini & Jardim, 2001)** and 149 ± 13 ppb near Santarém **(Lima et al., 2022)**. In the Tapajós Valley, **Roulet et al. (1998)** reported soil background values between 90 and 120 ppb, in which approximately 97% of surface soil mercury in an oxisol–spodosol system was of natural origin. Natural processes such as erosion, sediment transport, and deposition further contribute to mercury redistribution across the landscape. In particular, the Negro and Tapajós rivers function as major pathways for geogenic mercury entering aquatic systems, even in areas with

minimal *garimpo* activity (**Lechler et al., 2000; Siqueira et al., 2018**). Overall, this demonstrates that a single low baseline value cannot be assumed for the entire Amazon.

This heterogeneity reflects both the region's complex geology and the long-term accumulation of atmospheric deposition. Deeply weathered tropical soils, particularly lateritic oxisols and podzols, have high binding capacity for mercury due to their abundance of iron and aluminum oxyhydroxides **(Roulet & Lucotte, 1995; Roulet et al., 1998; Carvalho et al., 2019; Lima et al., 2022)**, while dense forest canopies actively scavenge atmospheric Hg and transfer it to soils via litterfall and throughfall **(Lechler et al., 2000; Fostier et al., 2000)**, a mechanism shown globally to account for 60–90% of terrestrial Hg deposition **(Zhou et al., 2018)**. For instance, **Fostier et al. (2000)** measured throughfall Hg deposition of approximately 72 $\mu g\ m^{-2} \cdot yr^{-1}$ in a pristine catchment in Amapá State (nearly four times greater than rainfall inputs) and found that most of this Hg accumulated in surface soils (~36,480 $\mu g\ m^{-2}$ in the top 10 cm), with minimal export to streams. These data highlight the Amazon forest's role as a long-term Hg sink and internal recycler, not merely a passive recipient of contamination.

However, natural mercury reservoirs can also be remobilized by anthropogenic disturbance. Deforestation, gold dredging, and hydrological interventions such as dam construction destabilize Hg-rich soils and sediments, increasing erosion and the likelihood of methylation. In the same Amapá catchment, **Fostier et al. (2000)** found that vegetation removal more than tripled the export of mercury into waterways. Model projections further indicate that continued deforestation in the Amazon could increase regional Hg emissions by approximately 150 Mg $year^{-1}$ by 2050 **(Feinberg et al., 2024)**. Seasonally flooded forests and floodplains, already enriched in organic matter and total Hg, become biogeochemical hotspots under anoxic conditions, where microbial activity facilitates the conversion of inorganic Hg to methylmercury (MeHg) **(e.g., Pestana et al., 2019)**, a process that can be intensified by *garimpo*-related disturbance and organic carbon loading.

These dynamics carry important policy implications. In the absence of regionally defined baselines, naturally elevated Hg levels may be erroneously attributed to contemporary *garimpo* activity, leading to misinterpretation of contamination patterns and misdirected enforcement efforts. Legacy and geogenic Hg stocks, remobilized through mining, deforestation, or hydrological change, can sustain MeHg production and bioaccumulation long after direct emissions decline. Effective mitigation therefore depends on distinguishing between new anthropogenic inputs and the reactivation of natural or legacy sources, as each presents distinct management challenges.

From a health perspective, this geogenic context reframes exposure risk. High mercury levels in fish and wildlife may stem not only from active emissions but also from the methylation of long-stored Hg already present in soils and sediments. Thus, environmental monitoring and risk assessment must integrate ecological characteristics and locally relevant baselines to correctly attribute sources and guide interventions. The next section addresses how these processes intersect to shape human exposure, particularly among Indigenous and riverine communities whose reliance on fish-based diets places them at heightened risk.

2.5.3. Mercury bioaccumulation in human populations

Significant findings from this study include the high Hg levels detected in hair **(Table 2)** and valuable insights into the nature of exposure obtained from the analysis of Hg concentrations in blood and urine **(Figure 7)**.

Hair was the primary human biomarker within the studies included, likely due to its non-invasive nature and its ability to reflect long-term mercury exposure, particularly to methylmercury (**Ruggieri et al., 2017; Calao-Ramos et al., 2021**). The Hg levels exceeded safety threshold **(WHO, 2021)** in all analyzed States and were above the health risk threshold

in the northern region States of Amazonas, Pará and Rondônia **(Table 2)**, indicating chronic exposure primarily through the consumption of contaminated fish, a fundamental resource for riverine and indigenous communities **(Barbosa et al., 1995; Mendes et al., 2021; Vasconcellos et al., 2022; Basta et al., 2023; Canela et al., 2024)**. This aligns with **Queipo-Abad et al. (2019)**, who emphasize that lifestyle factors, such as fish consumption, strongly influence hair Hg concentrations, whereas acute exposure to elemental mercury plays a lesser role.

Furthermore, the combined data show a clear geographical relationship between *garimpo* activities and hair mercury concentrations. Regions historically associated with *garimpo*, such as the Madeira River basin in Amazonas and Rondônia **(Bastos et al., 2006; Pestana et al., 2022; Quintarelli et al., 2024)** and the Tapajós River basin in southwestern Pará (**Figure 6**) **(Lobo et al., 2016; Bruno et al., 2020)**, exhibited some of the highest median Hg concentrations in hair **(Barbosa et al., 1995; Boischio et al., 1995; Kehrig et al., 1997; Grandjean et al., 1999; Akagi and Naganuma, 2000; Dolbec et al., 2000; Harada et al., 2001; Pinheiro et al., 2008; Pinheiro et al., 2012)**. The high median Hg concentrations in hair observed in northern and northeastern Pará **(Figure 6)** can be associated with: (I) fish consumption from upstream *garimpo*-impacted areas, where mercury is bioaccumulated in the food web (e.g. Ponta de Pedras, downstream Tapajós River basin) **(Akagi et al., 1995)**, or (II) more complex environmental dynamics, where the main Hg source is unclear, such as contamination associated with reservoirs, which can enhance Hg methylation due to long water-residence times and redox stratification, as observed in the Tucuruí area **(Leino and Lodenius, 1995)**. Therefore, these findings highlight the role of *garimpo* in both the emission and (re) mobilization of Hg in these regions, contributing to Hg persistence in the environment.

In **Table 2**, Pará was the State with the largest sample size for both urine and blood Hg levels, which strengthens the reliability of our findings in this region. Urine Hg levels are

mainly associated with chronic exposure, especially to inorganic and elemental Hg **(Ruggieri et al., 2017; Calao-Ramos et al., 2021)**. Although not statistically demonstrated through our results from the Dunn's test, **Figure 7** indicates that acute exposure can also temporarily elevate urinary Hg concentrations, reinforcing its reliability as a biomarker for inorganic Hg exposure compared to hair or blood **(Bose-O'Reilly et al., 2010)**. This is particularly relevant in *garimpo* settings, where exposure to elemental Hg vapour is intense, as observed in the airborne Hg concentrations measured in ASGM hubs **(Figure 12)**. The median Hg concentration in these areas exceeded the WHO's threshold of 20,000 ng/m³, with a maximum value reaching 15,499,000 ng/m³, suggesting extremely high exposure levels, especially during amalgamation and gold burning processes. These values significantly contrast with the air Hg concentrations recorded in non-ASGM-related areas **(Figure 12)**, reinforcing the occupational nature of Hg exposure in *garimpo* environments.

Given these high levels of Hg in the air, it is not surprising that elevated urine Hg concentrations were predominantly linked to occupational exposure **(Barbosa et al., 1995; Akagi and Naganuma, 2000; Calao-Ramos et al., 2021; He et al., 2021)**, with the highest levels observed in *garimpo*-related workers, who are directly exposed to metallic Hg and elemental mercury vapour on a daily basis. Since inhalation is the primary route of elemental Hg absorption, the high Hg levels in ASGM air help explain the urinary Hg concentrations observed among workers **(Figure 7)**, reinforcing urine as a robust biomarker for exposure to Hg vapour.

This pattern is particularly evident in Pará, which exhibited some of the highest urinary Hg concentrations **(Table 2)**, likely reflecting intensified *garimpo* activity **(Coelho et al., 2016; Lobo et al., 2016; Fritz et al., 2023)** and increased occupational exposure within this State. Although the median urinary Hg concentration among ASGM-related workers did not exceed

the occupational threshold set by the **WHO (2021)**, some individuals presented levels above the toxic threshold of 50 ppb, indicating potential health risks in these cases.

The two most studied States regarding Hg concentrations in blood were Pará and Roraima **(Table 2)**, both of which had elevated median concentrations. This is particularly concerning given that these States have significant indigenous populations who rely heavily on fish as an essential part of their diet—Roraima has the highest proportion of indigenous inhabitants in Brazil (15.29% of the state population), while Pará ranks sixth in absolute numbers, with 80,974 individuals **(IBGE, 2023)**. Blood Hg levels primarily reflect recent exposure (**Calao-Ramos et al., 2021**), mostly to methylmercury from fish consumption **(Akagi and Naganuma, 2000; Ruggieri et al., 2017; Wiseman et al., 2019; Packull-McCormick et al., 2022)**, which is consistent with our finding that blood Hg concentrations were significantly higher in traditional populations compared to the general population ($Z = -2.286$, p-value = 0.022), likely due to differences in dietary habits. Accordingly, as shown in **Figure 7**, minimum blood Hg levels in indigenous and riverine communities exceeded the threshold for elevated Hg in blood **(WHO, 2021)**, likely due to their daily fish-based diet **(Basta et al., 2021; Mendes et al., 2021)**.

Collectively, these findings highlight two key pathways of Hg exposure in *garimpo*-impacted areas: elemental mercury inhalation among *garimpo*-related workers and dietary methylmercury intake in traditional communities.

2.5.4. Bioaccumulation in flora

In the aggregated data across multiple plant species, we observed that leaves and stems seem to accumulate higher Hg levels than roots **(Figure 9A),** likely due to their exposure to atmospheric inorganic Hg **(Tomiyasu et al., 2005; Wang et al., 2021)**. This observed pattern

is consistent with findings by **Córdoba-Tovar et al. (2025)** in Colombia. However, Hg uptake and partitioning in plant tissues may vary depending on environmental conditions such as soil moisture, organic matter content and pH, atmospheric Hg levels **(Ericksen et al., 2003; Yang et al., 2007; Ordak et al., 2016; Aslam et al., 2022)**, and species-specific traits **(Peng et al., 2023; Baustein et al., 2024)**.

A notable exception to this trend is *Eichhornia crassipes* (water hyacinth), a species widely recognized for its strong capacity to bioaccumulate contaminants **(Koley et al., 2022; Mohanty, 2023)**. In our analysis (**Figure 9B**), water hyacinth exhibited higher THg concentrations in roots compared to leaves and stems—a pattern in line with previous studies **(Giri and Patel, 2011; Chattopadhyay et al., 2012; Monroy-Licht et al., 2022)**. This suggests that ionic mercury (Hg^{2+}) is the dominant form taken up, while elemental mercury (Hg^0) demonstrates limited translocation from roots to shoots. Consistent with this, the single concentration reported in stems also exceeded that in leaves **(Júnior and Carvalho, 2022)**, underscoring the limited upward mobility of Hg^0 within this species and reinforcing the predominance of Hg^{2+} in water hyacinth tissues **(Giri and Patel, 2011)**.

Once sequestered in plant tissues, mercury can induce various toxic effects, including reduced growth parameters, lower germination rates, and diminished carbohydrate and protein content **(Mani et al., 2024; Mani et al., 2025)**. These detrimental impacts on flora can also propagate through food webs, given that herbivores may feed on contaminated plants. For instance, **Júnior and Carvalho (2022)** suggested that Amazonian manatees in certain regions might be exposed to mercury partly through water hyacinths grown in contaminated water. By highlighting water hyacinth's capacity to bioaccumulate metals **(Koley et al., 2022; Mohanty, 2023)**, these findings emphasize the potential for trophic transfer of mercury to herbivorous fauna and underscore the broader ecological implications of *garimpo*-related Hg pollution.

2.5.5. Mercury retention in environmental compartments

Sediments and soils were the primary environmental compartments studied **(Figure 8)**, likely reflecting their key role in understanding Hg speciation, mobility, and bioavailability **(Acquavita et al., 2021; Acquavita et al., 2022; Anselm et al., 2021; Jiang et al., 2021; Hussain et al., 2022; Li et al., 2022)**, as well as their typically higher concentrations compared to the other abiotic matrices **(Table 3)** and implications for One Health. The elevated Hg concentrations in sediments from Minas Gerais **(Table 3)** reflect the lasting impact of historical *garimpo* **(Júnior et al., 2009; Cesar et al., 2011; Mendes et al., 2016)**. It is worth mentioning that the median Hg concentration in this region is comparable to levels reported in sediments from historical gold mines in Canada **(Cheney et al., 2024)**, while the presence of outliers suggests localized contamination hotspots.

Even higher Hg contents were observed in soils, with median values above the prevention level of 500 ppb **(CONAMA, 2010)** in Minas Gerais, Pará, Rio Grande do Sul and Roraima **(Table 3)**. The higher Hg concentrations in soils, compared to sediments **(Table 3)**, specifically in Mato Grosso, Minas Gerais, and Pará, can be attributed to specific retention-enhancing properties such as: (I) higher proportion of fine particles, particularly clay **(Egert et al., 2006; Cesar et al., 2011; Elkhabit et al., 2017; Ding et al., 2017; Gomes et al., 2022)**, commonly associated with (II) the presence of oxides (e.g. Al_2O_3, Fe_2O_3, and TiO_2) **(Carvalho et al., 2019; Lima et al., 2022)**, and (III) organic matter content **(Soares et al., 2015; Ramírez et al., 2021; Méndez-López et al., 2023)**.

Suspended particulate matter (SPM) plays a key role in the transport and distribution of Hg in river systems. **Liu et al. (2024)** demonstrated that SPM dynamics control THg and particulate Hg (PHg) concentrations in river water, with seasonal variations influencing re-

suspension and deposition processes. Consistently, **Liu et al. (2023)** reported that in the lower Yellow River (China), more than 99% of THg and 86.3% of MeHg were associated with particles, reinforcing the importance of SPM in Hg retention and transport. These results align with Hg strongly binding to organic matter and OM-coated minerals, which retain and immobilize it, promoting its accumulation in suspended particles rather than in solution **(Du et al., 2023)**.

This pattern is also reflected in our study, where relatively high Hg levels in SPM were observed in areas with significant active or historical *garimpo* in Pará and Mato Grosso **(Table 2)**, while considerably lower dissolved Hg concentrations were observed in water **(Figure 11)**. This suggests that, in these regions, most of the Hg is likely bound to particulate matter, increasing its potential for downstream transport and influencing its bioavailability.

In contrast, despite historical mercury input into the Paraíba do Sul River basin (Rio de Janeiro) due to the use of organomercury fungicides and *garimpo* in the 1980s **(Azevedo et al., 2017; Gomes et al., 2022; Gomes et al., 2023)**, a relatively low median of Hg concentrations in SPM was observed in this region (1.57 ppb), possibly reflecting shifts in land use and strengthened environmental regulations over the years **(Gomes et al., 2023)**.

Further supporting this pattern, only one sample from Madeira River **(Pfeiffer et al., 1989)** exceeded the threshold of 1 ppb. This is consistent with recent data by **Quintarelli et al. (2024)**, who reported Hg concentrations in all water samples from *garimpo* areas in Madeira River below the limit of detection.

Overall, these findings suggest that most of the Hg in the aquatic environments analyzed in this study is associated with particulate matter, which plays a crucial role in controlling its transport and bioavailability. Despite low concentrations of dissolved Hg in water, concerns remain as these values may not fully reflect water quality and could

underestimate the risks associated with microbial methylation and bioaccumulation in aquatic food webs.

2.5.6. Bioaccumulation in fauna

Although fewer studies have reported Hg concentrations in wildlife fauna compared to human populations or abiotic matrices, available data consistently highlight the role of biomagnification and bioaccumulation across a diverse range of species. These processes are influenced by local environmental factors (e.g., flooded conditions, mining history), deposition patterns in specific tissues, and organismal traits such as trophic position and feeding habits.

Environmental conditions—such as flooded areas, hydroelectric reservoirs, and historical mining—strongly govern mercury availability and methylation. Flooded habitats often create anoxic conditions that favour sulfate-reducing bacteria, thereby elevating Hg methylation and bioavailability **(Frohne et al., 2012; Howie et al., 2018)**. This process is evident in the Poconé Region of the Pantanal and near hydroelectric reservoirs (e.g., Balbina), where historical *garimpo*, cassiterite mining, and atmospheric deposition have cumulatively increased mercury loads **(Lama et al., 2011; Oliveira et al., 2021b; Júnior and Carvalho, 2022; Targino et al., 2023)**. As a result, wildlife in these areas—such as *M. americana* in flooded zones **(Lama et al., 2011)**—often exhibit higher Hg concentrations compared to non-flooded regions. Similar patterns in the northern Pantanal (Bento Gomes River) highlight that historical mining activities can drive long-standing contamination **(Lázaro et al., 2015; Vieira et al., 2011)**.

The extent of mercury accumulation varies among tissues, influenced by mercury speciation (MeHg vs. inorganic Hg) and the duration of exposure within an organism. In avian species, although data are limited, feathers generally contain higher Hg levels than muscle,

partly because they sequester mercury during growth and thus offer a non-invasive biomonitoring tool **(Lama et al., 2011; Santos et al., 2021; Tian et al., 2024)**. In alligators, tissue-specific discrepancies reflect greater Hg accumulation in claws and scutes compared to muscle or blood **(Figure 13)**; since these keratinized tissues indicate prolonged exposure, their mercury levels often correlate with those in internal organs **(Lemaire et al., 2021; Moore et al., 2022)**. Claws, in particular, provide a reliable, non-lethal sampling method for assessing contamination across diverse habitats **(Lázaro et al., 2015)**. Elevated Hg in the muscle tissue of *H. hydrochaeris* and *T. inunguis* suggests strong exposure in species in contact with contaminated abiotic environments or feeding on aquatic vegetation such as *E. crassipes* **(Oliveira et al., 2021a; Júnior and Carvalho, 2022)**. Regional discrepancies in sediment and water quality—e.g., northern Amazonas vs. Rondônia—further explain variation in chelonians like *P. unifilis* and *P. expansa* **(Oliveira et al., 2021a; Targino et al., 2023)**. Another tissue type, fur, remains understudied according to our search **(Table 4)**; only one study on *P. brasiliensis* reported relatively high Hg levels in riverine habitats **(Soresini et al., 2021)**, highlighting the potential for further research into non-invasive tissues of mammals as indicators of mercury exposure.

Dietary ecology also determines the entry and increase of Hg in food webs. Higher trophic-level fish often exhibit elevated Hg concentrations **(Figure 14)**, aligning with established biomagnification patterns, in which this metal accumulates and intensifies along successive trophic levels **(Barbosa et al., 1995; Mendes et al., 2021; Vasconcellos et al., 2022; Martoredjo et al., 2024)**. Muscle tissue remains the focus for these assessments because it typically accumulates methylmercury and is widely consumed by humans. Large aquatic herbivores, including *H. hydrochaeris* and *T. inunguis*, ingest mercury through both contaminated sediments and vegetation, reinforcing the connection between flooded environments and high tissue concentrations **(Oliveira et al., 2021a; Júnior and Carvalho,**

2022). Meanwhile, invertebrates such as *Pomacea spp.* **(Callil and Junk, 2001)** and *Eisenia fetida* **(Hinton and Veiga, 2009)** can retain variable Hg levels, with outliers exceeding 1,000 ppb **(Figure 15)**. This variability likely stems from direct contact with contaminated substrates and detritus, positioning these snails and earthworms as potential vectors for further Hg transfer to higher trophic levels, including birds, fish and reptile predators.

Collectively, these observations highlight the interactive roles of local environment, tissue-specific deposition, and organismal traits in driving mercury bioaccumulation. Flooded or reservoir-impacted habitats with a history of mining pose increased risks to wildlife and human populations. Predatory species—whether carnivorous fish or apex mammals—tend to retain especially high Hg loads, raising concerns for food security and public health in communities that depend on bushmeat and fish **(Basta et al., 2023; Canela et al., 2024)**. Addressing these risks necessitates targeted research on underexplored tissues, in addition to ecological studies that clarify mercury's multiple pathways in *garimpo*-influenced ecosystems. This knowledge is essential for developing effective mitigation, monitoring and management strategies to safeguard vulnerable habitats and populations.

2.6. Limitations and future directions

While this study provides an overview of Hg contamination linked to *garimpo* in Brazil, several important limitations must be acknowledged as hereafter listed and shortly discussed:

i) the geographical scope of available studies is heavily skewed toward the Amazon region. Other States with known *garimpo* activity such as Minas Gerais, Bahia, Pernambuco, Tocantins, and Goiás remain underrepresented **(Bruno et al., 2020; Castilhos & Domingos, 2024)**. To obtain a more complete national perspective, future studies should expand spatial

coverage to include the above mentioned underrepresented regions, considering local variability in mining practices, environmental characteristics, and regulatory enforcement.

ii) the limited number of available urine and blood samples prevents a robust evaluation of these biological matrices as indicators of human exposure. Increasing sample sizes, especially from vulnerable populations such as riverine and Indigenous communities, and controlling for other influencing variables (e.g., dietary habits, occupational history, proximity to geogenic Hg sources) would greatly improve exposure assessment and enable more accurate interpretation of health risks.

iii) the interpretation of contamination levels remains complicated in regions with naturally high and geochemically variable mercury background, such as the Amazon. Baseline Hg levels can vary widely depending on soil type, organic matter content, and underlying lithology (e.g., lateritic oxisols, sulfide-rich formations), as shown by **Lechler et al. (2000)**, **Fostier et al. (2000)**, and **Sahoo et al. (2020)**. Without clearly defined regional geochemical baseline values, there is a risk of over-attributing observed Hg concentrations solely to recent *garimpo* activity. Future research should prioritize establishing geochemical background threshold values (GBTVs) and employ source-tracing tools such as Hg stable isotopes to distinguish natural, legacy, and recent anthropogenic inputs. While this study did not incorporate regional geochemical mapping, publicly available datasets, such as those developed by the Geological Survey of Brazil (SGB), offer valuable tools for identifying geogenic mercury baselines. Using these resources could help clarify background variability, strengthen source attribution, and support more targeted monitoring and remediation strategies.

iv) the dataset may also be affected by publication bias, particularly toward studies reporting higher Hg concentrations. This could lead to overestimation of contamination in certain matrices or regions. This issue is compounded by methodological heterogeneity

involving differences in instrumentation, detection limits, and quality control protocols, which limits comparability across studies. Adopting standardized and validated protocols for mercury quantification and speciation would increase reproducibility and facilitate more reliable meta-analyses.

v) temporal interpretation is constrained. Most studies present single-timepoint data, and few include long-term monitoring. This makes it difficult to evaluate temporal trends in mercury use, transport, and methylation—particularly given recent increases in illegal mining and environmental changes (e.g., dam construction, deforestation). Establishing long-term, spatially distributed monitoring frameworks would be key to understanding evolving contamination patterns.

vi) inconsistencies in the types of matrices analyzed (e.g., sediment vs. water vs. biota) often prevent clear assessment of mercury transfer and bioaccumulation. Few studies sample multiple compartments simultaneously at the same location, limiting our understanding of exposure pathways and ecological dynamics. Future research should emphasize integrated, multi-matrix designs to better trace Hg movement through aquatic and terrestrial systems and its conversion to methylmercury in biologically relevant compartments.

Finally, while on-the-ground initiatives led by Non-Governmental Organizations (NGOs) and researchers have shown promise in guiding *garimpo* operations toward safer and more compliant practices (e.g., **Monteiro et al., 2024**), these efforts are often fragmented and under-evaluated. Future work should assess the effectiveness and scalability of such interventions and support collaboration with affected communities. This should be complemented by strengthening the operational capacity of regulatory agencies (e.g., IBAMA, ANM) and enforcement bodies such as the Federal Police to curb illegal activity and ensure sustained policy implementation in high-risk areas.

2.7. Conclusions

This review confirms that mercury (Hg) contamination linked to *garimpos* is persistent and widespread in Brazil, especially in the Amazon. By consolidating evidence across environmental and biological matrices, the study highlights key pathways of exposure—occupational inhalation of elemental Hg vapor and dietary intake of methylmercury (MeHg) through fish consumption in riverine and Indigenous communities.

However, elevated Hg levels in many regions cannot be attributed solely to *garimpos*. Naturally enriched soils, long-term atmospheric deposition, and dynamic processes such as erosion and sediment transport contribute significantly to Hg distribution. Human disturbances—including mining, deforestation, and damming—can further mobilize legacy or geogenic Hg, sustaining MeHg production and ecological risk. Without regionally defined geochemical baselines, there is a risk of misattribution that could distort policy responses and health advisories.

A One Health approach—integrating environmental, human, and animal health—is needed to guide risk assessment and intervention strategies. Effective action requires better attribution of contamination sources, long-term monitoring, and inclusive governance.

We recommend that future efforts:

I. Expand environmental and biological monitoring to underrepresented *garimpo* regions (e.g., Minas Gerais, Tocantins, Goiás), using consistent, validated protocols and including Hg speciation;

II. Prioritize the development of geochemical background threshold values (GBTVs) and apply source-tracing methods such as Hg stable isotopes to disentangle natural, legacy, and recent anthropogenic sources;

III. Implement integrated, multi-matrix sampling strategies to clarify mercury transfer and bioaccumulation pathways across abiotic and biotic compartments;

IV. Control for confounding factors such as dietary patterns, occupational exposure, and proximity to geogenic Hg when interpreting human biomonitoring data;

V. Establish long-term, spatially distributed monitoring frameworks to evaluate policy effectiveness and track evolving trends in mercury dynamics;

VI. Support the transition to mercury-free extraction technologies via technical assistance, financial incentives, and regulatory enforcement;

VII. Strengthen the operational capacity of enforcement agencies (e.g., IBAMA, ANM, Federal Police) to curb illegal *garimpo* activity;

Foster and evaluate collaborative, community-based interventions—especially those led by NGOs and researchers—to scale culturally appropriate education, outreach, and risk-reduction strategies.

References

Abad, L.A., Palma, N., 2021. The Fruits of El Dorado: The Global Impact of American Precious Metals, in: Dobado-González, R., García-Hiernaux, A. (Eds.), The Fruits of the Early Globalization. Palgrave Studies in Comparative Global History. Palgrave Macmillan, Cham. https://doi.org/10.1007/978-3-030-69666-5_4

Acquavita, A., Floreani, F., Covelli, S., 2021. Occurrence and speciation of arsenic and mercury in alluvial and coastal sediments. Current Opinion in Environmental Science & Health. 22, 100272. https://doi.org/10.1016/j.coesh.2021.100272

Acquavita, A., Brandolin, D., Cattaruzza, C., Felluga, A., Maddaleni, P., Meloni, C., Pasquon, M., Predonzani, S., Poli, L., Skert, N., Zanello, A., 2022. Mercury distribution and speciation in historically contaminated soils of the Isonzo River Plain (NE Italy). Journal of Soils and Sediments. 22(1), 79-92. https://doi.org/10.1007/s11368-021-03038-2

Agapito, L. S., Miranda, M. A., Januário, T. F. X., 2022. A political agenda in conflict with environmental protection: a critical policy essay from Brazil. International Criminology. 2(2), 206. https://doi.org/10.1007/s43576-021-00041-y

Ajsuvakova, O. P., Tinkov, A. A., Aschner, M., Rocha, J. B., Michalke, B., Skalnaya, M. G., Skalny, A. V., Butnariu, M., Dadar, M., Sarac, I., Aaseth, J., Bjørklund, G., 2020. Sulfhydryl groups as targets of mercury toxicity. Coordination chemistry reviews. 417, 213343. https://doi.org/10.1016/j.ccr.2020.213343

Akagi, H., Malm, O., Kinjo, Y., Harada, M., Branches, F. J., Pfeiffer, W. C., Kato, H., 1995. Methylmercury pollution in the Amazon, Brazil. Science of the Total Environment. 175(2), 85-95. https://doi.org/10.1016/0048-9697(95)04905-3

Akagi, H., Naganuma, A., 2000. Human exposure to mercury and the accumulation of methylmercury that is associated with gold mining in the Amazon Basin, Brazil. Journal of Health Science. 46(5), 323-328. https://doi.org/10.1248/jhs.46.323

Albuquerque, F. E. A., Minervino, A. H. H., Miranda, M., Herrero-Latorre, C., Júnior, R. A. B., Oliveira, F. L. C., Dias, S. R., Ortolani, E. L., Lopez-Alonso, M., 2020a. Toxic and essential trace element concentrations in the freshwater shrimp Macrobrachium amazonicum in the Lower Amazon, Brazil. Journal of Food Composition and Analysis. 86, 103361. https://doi.org/10.1016/j.jfca.2019.103361

Alves, M. F. A., Fraiji, N. A., Barbosa, A. C., De Lima, D. S., Souza, J. R., Dórea, J. G., Cordeiro, G. W., 2006. Fish consumption, mercury exposure and serum antinuclear antibody in Amazonians. International Journal of Environmental Health Research. 16(4), 255-262. https://doi.org/10.1080/09603120600734147

Al-Sulaiti, M. M., Soubra, L., Al-Ghouti, M. A., 2022. The causes and effects of mercury and methylmercury contamination in the marine environment: A review. Current Pollution Reports. 8(3), 249-272. https://doi.org/10.1007/s40726-022-00226-7

AMAP/UNEP, 2019. Technical Background Report to the Global Mercury Assessment 2018. https://www.amap.no/documents/doc/technical-background-report-for-the-global-mercury-assessment-2018/1815 (accessed 20 March 2025)

Anselm, O. H., Cavoura, O., Davidson, C. M., Oluseyi, T. O., Oyeyiola, A. O., Togias, K., 2021. Mobility, spatial variation and human health risk assessment of mercury in soil from an informal e-waste recycling site, Lagos, Nigeria. Environmental Monitoring and Assessment. 193(7), 416. https://doi.org/10.1007/s10661-021-09165-0

Aquino, R. Q., Malone, A., Smith, N. M., Zúñiga, F. F. G., 2022. Perceptions and realities of mercury contamination in a Peruvian artisanal and small-scale gold mining (ASGM) community. Environmental Research. 214, 114092. https://doi.org/10.1016/j.envres.2022.114092

Artaxo, P., Campos, R. C., Fernandes, E. T., Martins, J. V., Xiao, Z., Lindqvist, O., Fernández-Jiménez, M. T., Maenhaut, W., 2000. Large scale mercury and trace element measurements in the Amazon basin. Atmospheric Environment. 34(24), 4085-4096. https://doi.org/10.1016/S1352-2310(00)00106-0

Asare, M. O., Afriyie, J. O., 2021. Ancient mining and metallurgy as the origin of Cu, Ag, Pb, Hg, and Zn contamination in soils: A review. Water, Air, & Soil Pollution. 232(6), 240. https://doi.org/10.1007/s11270-021-05166-4

Aslam, M. W., Meng, B., Abdelhafiz, M. A., Liu, J., Feng, X., 2022. Unravelling the interactive effect of soil and atmospheric mercury influencing mercury distribution and accumulation in the soil-rice system. Science of the Total Environment. 803, 149967. https://doi.org/10.1016/j.scitotenv.2021.149967

Auguie, B., 2017. gridExtra: Miscellaneous Functions for "Grid" Graphics. R package version 2.3. https://CRAN.R-project.org/package=gridExtra (accessed 25 March 2025).

Aula, I., Braunschweiler, H., & Malin, I., 1995. The watershed flux of mercury examined with indicators in the Tucurui reservoir in Para, Brazil. Science of the total environment. 175(2), 97-107. https://doi.org/10.1016/0048-9697(95)04906-1

Azar, J., Yousef, M. H., El-Fawal, H. A., & Abdelnaser, A., 2021. Mercury and Alzheimer's disease: a look at the links and evidence. Metabolic Brain Disease. 36, 361-374. https://doi.org/10.1007/s11011-020-00649-5

Azevedo, L. S., Almeida, M. G., Bastos, W. R., Suzuki, M. S., Recktenvald, M. C. N. N., Bastos, M. T. S., Vergílio, C. S., Souza, C. M. M., 2017. Organotropism of methylmercury in fish of the southeastern of Brazil. Chemosphere. 185, 746-753. https://doi.org/10.1016/j.chemosphere.2017.07.081

Bakker, L. B., Gasparinetti, P., de Queiroz, J. M., Vasconcellos, A. C. S., 2021. Economic impacts on human health resulting from the use of mercury in the illegal gold mining in the brazilian amazon: a methodological assessment. International journal of environmental research and public health. 18(22), 11869. https://doi.org/10.3390/ijerph182211869

Balzino, M., Seccatore, J., Marin, T., De Tomi, G., Veiga, M. M., 2015. Gold losses and mercury recovery in artisanal gold mining on the Madeira River, Brazil. Journal of Cleaner Production. 102, 370-377. https://doi.org/10.1016/j.jclepro.2015.05.012

Bank, M. S., 2020. The mercury science-policy interface: History, evolution and progress of the Minamata Convention. Science of the Total Environment. 722, 137832. https://doi.org/10.1016/j.scitotenv.2020.137832

Barbosa, A. C., Boischio, A. A., East, G. A., Ferrari, I., Gonçalves, A., Silva, P. R. M., Cruz, T. M. E., 1995. Mercury contamination in the Brazilian Amazon. Environmental and occupational aspects. Water, Air, and Soil Pollution. 80, 109-121. https://doi.org/10.1007/BF01189660

Barbosa, A. C., Souza, J. D., Dórea, J. G., Jardim, W. F., Fadini, P. S., 2003. Mercury biomagnification in a tropical black water, Rio Negro, Brazil. Archives of Environmental Contamination and Toxicology. 45, 235-246. https://doi.org/10.1007/s00244-003-0207-1

Basri, Sakakibara, M., Sera, K., 2020. Mercury in soil and forage plants from artisanal and small-scale gold mining in the bombana area, Indonesia. Toxics. 8(1), 15. https://doi.org/10.3390/toxics8010015

Basta, P. C., Viana, P. V. S., Vasconcellos, A. C. S., Périssé, A. R. S., Hofer, C. B., Paiva, N. S., Kempton, J. W., Andrade, D. C., Oliveira, R. A. A., Achatz, R. W., Perini, J. A., Meneses, H. N. M., Hallwass, G., Lima, M. O., Jesus, I. M., Santos, C. C.R., Hacon, S. S., 2021. Mercury exposure in Munduruku indigenous communities from Brazilian Amazon: Methodological background and an overview of the principal results. International journal of environmental research and public health. 18(17), 9222. https://doi.org/10.3390/ijerph18179222

Basta, P. C., Vasconcellos, A. C. S., Hallwass, G., Yokota, D., d`El Rei Pinto, D. O., Aguiar, D. S., Souza, C. C., Oliveira-da-Costa, M., 2023. Risk assessment of mercury-contaminated fish consumption in the Brazilian Amazon: an ecological study. Toxics. 11(9), 800. https://doi.org/10.3390/toxics11090800

Bastos, W. R., Gomes, J. P. O., Oliveira, R. C., Almeida, R., Nascimento, E. L., Bernardi, J. V. E., Lacerda, L. D., Silveira, E. G., Pfeiffer, W. C., 2006. Mercury in the environment and riverside population in the Madeira River Basin, Amazon, Brazil. Science of the Total environment. 368(1), 344-351. https://doi.org/10.1016/j.scitotenv.2005.09.048

Bastos, W. R., de Almeida, R., Dórea, J. G., Barbosa, A. C., 2007. Annual flooding and fish-mercury bioaccumulation in the environmentally impacted Rio Madeira (Amazon). Ecotoxicology. 16, 341-346. https://doi.org/10.1007/s10646-007-0138-0

Bastos, W. R., Dórea, J. G., Bernardi, J. V. E., Lauthartte, L. C., Mussy, M. H., Lacerda, L. D., Malm, O., 2015. Mercury in fish of the Madeira river (temporal and spatial assessment), Brazilian Amazon. Environmental research. 140, 191-197. https://doi.org/10.1016/j.envres.2015.03.029

Bastos, W. R., Dórea, J. G., Lacerda, L. D., Almeida, R., Costa-Junior, W. A., Baía, C. C., Sousa-Filho, I. F., Sousa, E. A., Oliveira, I. A. S., Cabral, C. S., Manzatto, A. G., Carvalho, D. P., Ribeiro, K. A. N., Malm, O., 2020. Dynamics of Hg and MeHg in the Madeira River basin (Western Amazon) before and after impoundment of a run-of-river hydroelectric dam. Environmental Research. 189, 109896. https://doi.org/10.1016/j.envres.2020.109896

Bauštein, M., Száková, J., Stefanović, L., Najmanová, J., Sysalová, J., Tlustoš, P., 2024. Assessment of Mercury Uptake by Plants in Former Cinnabar Mining Areas. Minerals. 14(12), 1211. https://doi.org/10.3390/min14121211

Bidone, E. D., Castilhos, Z. C., Santos, T. J. S., Souza, T. D., Lacerda, L. D., 1997a. Fish contamination and human exposure to mercury in Tartarugalzinho River, Amapá State, Northern Amazon, Brazil. A screening approach. Water, Air, and Soil Pollution. 97, 9-15. https://doi.org/10.1007/BF02409640

Bidone, E. D., Castilhos, Z. C., Cid de Souza, T. M., Lacerda, L. D., 1997b. Fish contamination and human exposure to mercury in the Tapajós River Basin, Pará State, Amazon, Brazil: a screening approach. Bulletin of Environmental Contamination and Toxicology. 59, 194-201.

Boischio, A. A. P., Henshel, D., Barbosa, A. C., 1995. Mercury exposure through fish consumption by the Upper Madeira River population, Brazil - 1991. Ecosystem Health. 1(3), 177-192.

Bonotto, D. M., Vergotti, M., Silveira, E. G., 2006. The role of organic matter on the adsorption of mercury in sediments from Amazon lakes, Brazil. Sediment Dynamics and the Hydromorphology of Fluvial Systems. (306), 355.

Bonzongo, J. C., Lyons, W. B., Hines, M. E., Warwick, J. J., Faganeli, J., Horvat, M., Lechler, P. J., Miller, J. R., 2002. Mercury in surface waters of three mine-dominated river systems: Idrija River, Slovenia; Carson River, Nevada; and Madeira River, Brazilian Amazon. Geochemistry: Exploration, Environment, Analysis. 2(2), 111-119. https://doi.org/10.1144/1467-787302-014

Bose-O'Reilly, S., McCarty, K. M., Steckling, N., Lettmeier, B., 2010. Mercury exposure and children's health. Current problems in pediatric and adolescent health care. 40(8), 186-215. https://doi.org/10.1016/j.cppeds.2010.07.002

Brabo, E. S., Santos, E. D., Jesus, I. M., Mascarenhas, A. F. S., Faial, K. D., 2000. Mercury contamination of fish and exposures of an indigenous community in Pará State, Brazil. Environmental Research. 84(3), 197-203. https://doi.org/10.1006/enrs.2000.4114

Branches, F. J., Erickson, T. B., Aks, S. E., Hryhorczuk, D. O., 1993. The price of gold: mercury exposure in the Amazonian rain forest. Journal of Toxicology: Clinical Toxicology. 31(2), 295-306. https://doi.org/10.3109/15563659309000396

Bruno, D. E., Ruban, D. A., Tiess, G., Pirrone, N., Perrotta, P., Mikhailenko, A. V., Ermolaev, V. A., Yashalova, N. N., 2020. Artisanal and small-scale gold mining, meandering tropical rivers, and geological heritage: Evidence from Brazil and Indonesia. Science of the Total Environment. 715, 136907. https://doi.org/10.1016/j.scitotenv.2020.136907

Cabral, A. R., Lehmann, B., Kwitko, R., Costa, C. C., 2002. The Serra Pelada Au-Pd-Pt deposit, Carajás mineral province, northern Brazil: reconnaissance mineralogy and chemistry of very high grade palladian gold mineralization. Economic geology. 97(5), 1127-1138. https://doi.org/10.2113/gsecongeo.97.5.1127

Calao-Ramos, C., Bravo, A. G., Paternina-Uribe, R., Marrugo-Negrete, J. Díez, S., 2021. Occupational human exposure to mercury in artisanal small-scale gold mining communities of Colombia. Environment International. 146, 106216. https://doi.org/10.1016/j.envint.2020.106216

Callil, C. T., and Junk, W. J., 2001. Aquatic Gastropods as Mercury Indicators in the Pantanal of Poconé Region (Mato Grosso, Brasil). Water, Air, and Soil Pollution. 125, 319-330. https://doi.org/10.1023/A:1005230716898

Calvimontes, J., Massaro, L., Araujo, C. H. X., Moraes, R. R., Mello, J., Ferreira, L. C., de Theije, M., 2020. Small-scale gold mining and the COVID-19 pandemic: conflict and cooperation in the Brazilian Amazon. The extractive industries and society. 7(4), 1347-1350. https://doi.org/10.1016/j.exis.2020.08.013

Canela, T. A., Monteiro, L. C., Cabral, C. S., Ximenes, F. S., Oliveira, I. A. S., Bernardi, J. V. E., Almeida, R., Bastos, W. R., 2024. Mercury in fish and human hair and estimated dietary intake in a riverside community of the Madeira River Basin in the Brazilian Amazon. Toxics. 12(3), 208. https://doi.org/10.3390/toxics12030208

Cardoso, P. G., Morais, H., Crespo, D., Tavares, D., Pereira, E., Pardal, M. Â., 2023. Seasonal characterization of mercury contamination along the Portuguese coast: human health and environmental risk assessment. Environmental Science and Pollution Research. 30(45), 101121-101132. https://doi.org/10.1007/s11356-023-29495-5

Carvalho, G. S., Oliveira, J. R., Curi, N., Schulze, D. G., Marques, J. J., 2019. Selenium and mercury in Brazilian Cerrado soils and their relationships with physical and chemical soil characteristics. Chemosphere. 218, 412-415. https://doi.org/10.1016/j.chemosphere.2018.11.099

Casagrande, G. C. R., Dambros, J., De Andrade, E. A., Martello, F., Sobral-Souza, T., Moreno, M. I. C., Battirola, L. D., Andrade, R. L. T., 2023. Atmospheric mercury in forests: accumulation analysis in a gold mining area in the southern Amazon, Brazil. Environmental Monitoring and Assessment. 195(4), 477. https://doi.org/10.1007/s10661-023-11063-6

Castilhos, Z. C., Bidone, E. D., Lacerda, L. D., 1998. Increase of the background human exposure to mercury through fish consumption due to gold mining at the Tapajós River region, Pará State, Amazon. Bulletin of Environmental Contamination and Toxicology. 61, 202-209. https://doi.org/10.1007/s001289900749

Castilhos, Z., Rodrigues-Filho, S., Cesar, R., Rodrigues, A. P., Villas-Bôas, R., Jesus, I., Lima, M., Faial, K., Miranda, A., Brabo, E., Beinhoff, C., Santos, E., 2015. Human exposure and risk assessment associated with mercury contamination in artisanal gold mining areas in the Brazilian Amazon. Environmental Science and Pollution Research. 22, 11255-11264. https://doi.org/10.1007/s11356-015-4340-y

Castilhos, Z. C., Domingos, L. M. B., 2024. A picture of artisanal and small-scale gold mining (ASGM) in Brazil and its mercury emissions and releases. Environmental Geochemistry and Health. 46(3), 101. https://doi.org/10.1007/s10653-024-01881-z

Cesar, R., Egler, S., Polivanov, H., Castilhos, Z., Rodrigues, A. P., 2011. Mercury, copper and zinc contamination in soils and fluvial sediments from an abandoned gold mining area in southern Minas Gerais State, Brazil. Environmental Earth Sciences. 64, 211-222. https://doi.org/10.1007/s12665-010-0840-8

Cesareo, R., Bustamante, A., Azeredo, S., Lopes, R. T., Franco, R. J., Fernandez, A., 2020. Analytical studies on pre-Columbian gold and silver from the North of Peru. Rendiconti Lincei. Scienze Fisiche e Naturali. 31, 473-484. https://doi.org/10.1007/s12210-020-00891-0

Chattopadhyay, S., Fimmen, R. L., Yates, B. J., Lal, V., Randall, P., 2012. Phytoremediation of mercury-and methyl mercury-contaminated sediments by water hyacinth (Eichhornia crassipes). International journal of phytoremediation. 14(2), 142-161. https://doi.org/10.1080/15226514.2010.525557

Chen, L., Liang, S., Zhang, H., Cai, X., Chen, Y., Liu, M., Lin, H., Qi, J., Tong, Y., Zhang, W., Wang, X., Shu, J., 2020. Rapid increase in cement-related mercury emissions and deposition in China during 2005–2015. Environmental Science & Technology. 54(22), 14204-14214. https://doi.org/10.1021/acs.est.0c03512

Chen, D., Zeng, Q., Li, C., Qiao, B., Luo, W., 2024. Exotic treasures or local innovation: gold and silver beads of Han dynasty excavated from Nanyang City, Henan Province, central China. Journal of Archaeological Science. 161, 105903. https://doi.org/10.1016/j.jas.2023.105903

Cheney, C. L., Eccles, K. M., Kimpe, L. E., Lehnherr, I., Blais, J. M., 2024. Mercury deposition to lake sediments near historic gold mines in northern Canada. Environmental Pollution. 342, 123038. https://doi.org/10.1016/j.envpol.2023.123038

Cheng, Y., Watari, T., Seccatore, J., Nakajima, K., Nansai, K., Takaoka, M., 2023. A review of gold production, mercury consumption, and emission in artisanal and small-scale gold mining (ASGM). Resources Policy. 81, 103370. https://doi.org/10.1016/j.resourpol.2023.103370

Clarkson, T. W., Vyas, J. B., Ballatori, N., 2007. Mechanisms of mercury disposition in the body. American journal of industrial medicine. 50(10), 757-764. https://doi.org/10.1002/ajim.20476

Cleary, D., 1990. Fofoca: The Formation of Garimpos, in: Cleary, D. (Eds.), Anatomy of the Amazon Gold Rush. St Antony's/Macmillan Series. Palgrave Macmillan, London. https://doi.org/10.1007/978-1-349-11247-0_3

Coelho, M. C. N., Wanderley, L. J., Costa, R. C., 2016. Small scale gold mining in the XXI century: Examples in the south-west Brazilian Amazon. Anuário do Instituto de Geociências. 39(3), 5-14. http://dx.doi.org/10.11137/2016_3_05_14

Colás, R., 2021. Ancient lead, mercury, and tin, in: Carrizo, P.S. (Eds.), Reverse Engineering of Ancient Metals, Springer Cham, Switzerland, pp. 29-40. https://doi.org/10.1007/978-3-030-72842-7_3

CONAMA (National Environment Council), 2008. Resolução nº 396, de 3 de abril de 2008. Dispõe sobre a classificação e diretrizes ambientais para o enquadramento das águas subterrâneas. Diário Oficial da União. https://cetesb.sp.gov.br/aguas-subterraneas/wp-content/uploads/sites/13/2013/11/res39608.pdf (accessed 07 April 2025).

CONAMA (National Environment Council), 2010. 4º Grupo de Trabalho de Lâmpadas Mercuriais da Câmara Técnica de Sáude, Saneamento Ambiental e Gestão de Resíduos do Conselho Nacional do Meio Ambiente. https://conama.mma.gov.br/index.php?option=com_sisconama&task=documento.download&id=18041#:~:text=Valores%20M%C3%A1ximos%20Permitidos%20(VMPs)%20para,mg%2FL (accessed 07 April 2025).

Cooke, C. A., Martínez-Cortizas, A., Bindler, R., Gustin, M. S., 2020. Environmental archives of atmospheric Hg deposition–a review. Science of the Total Environment. 709, 134800. https://doi.org/10.1016/j.scitotenv.2019.134800

Cordeiro, R. C., Turcq, B., Ribeiro, M. G., Lacerda, L. D., Capitaneo, J., Silva, A. O., Sifeddine, A., Turcq, P. M., 2002. Forest fire indicators and mercury deposition in an intense land use change region in the Brazilian Amazon (Alta Floresta, MT). Science of the total environment. 293(1-3), 247-256. https://doi.org/10.1016/S0048-9697(02)00045-1

Córdoba-Tovar, L., Marrugo-Madrid, S., Castro, L. P., Tapia-Contreras, E. E., Marrugo-Negrete, J., Díez, S., 2025. Exploring the phytoremediation potential of plant species in soils impacted by gold mining in Northern Colombia. Environmental Science and Pollution Research. 32, 3795-3808. https://doi.org/10.1007/s11356-024-35853-8

Costa, M. A., Rios, F. J., 2022. The gold mining industry in Brazil: A historical overview. Ore Geology Reviews. 148, 105005. https://doi.org/10.1016/j.oregeorev.2022.105005

Crespo-Lopez, M. E., Arrifano, G. P., Augusto-Oliveira, M., Macchi, B. M., Lima, R. R., do Nascimento, J. L. M., Souza, C. B., 2023. Mercury in the Amazon: The danger of a single story. Ecotoxicology and Environmental Safety. 256, 114895. https://doi.org/10.1016/j.ecoenv.2023.114895

Crespo-Lopez, M. E., Lopes-Araújo, A., Basta, P. C., Soares-Silva, I., de Souza, C. B., Leal-Nazaré, C. G., Santos-Sacramento, L., Barthelemy, J. L., Arrifano, G. P., Augusto-Oliveira, M., 2024. Environmental pollution challenges public health surveillance: the case of mercury exposure and intoxication in Brazil. The Lancet Regional Health–Americas. 39. https://doi.org/10.1016/j.lana.2024.100880

Crompton, P., Ventura, A. M., De Souza, J. M., Santos, E., Strickland, G. T., Silbergeld, E., 2002. Assessment of mercury exposure and malaria in a Brazilian Amazon riverine community. Environmental Research. 90(2), 69-75. https://doi.org/10.1006/enrs.2002.4358

Delaere, C., Capriles, J. M., Stanish, C., 2019. Underwater ritual offerings in the Island of the Sun and the formation of the Tiwanaku state. Proceedings of the National Academy of Sciences. 116(17), 8233-8238. https://doi.org/10.1073/pnas.1820749116

Ding, X., Wang, R., Li, Y., Gan, Y., Liu, S., Dai, J., 2017. Insights into the mercury (II) adsorption and binding mechanism onto several typical soils in China. Environmental Science and Pollution Research. 24, 23607-23619. https://doi.org/10.1007/s11356-017-9835-2

Diogens, C. J., de Alencar Nääs, I., Benvenga, M. A. C., 2024. The impact of gold mining on regional development in Brazil. European Journal of Sustainable Development Research. 8(2). https://doi.org/10.29333/ejosdr/14471

Dolbec, J., Mergler, D., Sousa Passos, C. J., Sousa de Morais, S., Lebel, J., 2000. Methylmercury exposure affects motor performance of a riverine population of the Tapajos river, Brazilian Amazon. International Archives of Occupational and Environmental Health. 73, 195-203. https://doi.org/10.1007/s004200050027

Donkor, A. K., Ghoveisi, H., Bonzongo, J. C. J., 2024. Use of metallic mercury in artisanal gold mining by amalgamation: a review of temporal and spatial trends and environmental pollution. Minerals. 14(6), 555. https://doi.org/10.3390/min14060555

Donnelly, L. J., Pirrie, D., Harrison, M., Ruffell, A., Dawson, L. A., 2021. A guide to forensic geology. Geological Society of London. London, UK.

Dorea, J., Barbosa, A., Ferrari, Í., Souza, J., 2003. Mercury in hair and in fish consumed by Riparian women of the Rio Negro, Amazon, Brazil. International Journal of Environmental Health Research. 13(3), 239-248. https://doi.org/10.1080/0960312031000122398

Dorea, J. G., Souza, J. R., Rodrigues, P., Ferrari, Í., Barbosa, A. C., 2005. Hair mercury (signature of fish consumption) and cardiovascular risk in Munduruku and Kayabi Indians of Amazonia. Environmental Research. 97(2), 209-219. https://doi.org/10.1016/j.envres.2004.04.007

Dorea, J. G., Barbosa, A. C., 2007. Anthropogenic impact of mercury accumulation in fish from the Rio Madeira and Rio Negro rivers (Amazonia). Biological Trace Element Research. 115, 243-254. https://doi.org/10.1007/BF02685999

Du, H., Yin, X., Gu, X., Wang, D., Pierce, E. M., Gu, B., 2023. Dissolved elemental mercury [Hg (0) aq] reactions and purgeability in the presence of organic and inorganic particulates. Environmental Science & Technology Letters. 10(8), 691-697. https://doi.org/10.1021/acs.estlett.3c00275

Duan, X. L., Yuan, C. G., Jing, T. T., Yuan, X. D., 2019. Removal of elemental mercury using large surface area micro-porous corn cob activated carbon by zinc chloride activation. Fuel. 239, 830-840. https://doi.org/10.1016/j.fuel.2018.11.017

Ebert, C., 2011. From Gold to Manioc: Contraband Trade in Brazil during the Golden Age, 1700–1750. Colonial Latin American Review. 20(1), 109-130. https://doi.org/10.1080/10609164.2011.552551

Edwards, B. A., Kushner, D. S., Outridge, P. M., Wang, F., 2021. Fifty years of volcanic mercury emission research: Knowledge gaps and future directions. Science of the Total Environment. 757, 143800. https://doi.org/10.1016/j.scitotenv.2020.143800

Egler, S. G., Rodrigues-Filho, S., Villas-Bôas, R. C., Beinhoff, C., 2006. Evaluation of mercury pollution in cultivated and wild plants from two small communities of the Tapajós gold mining reserve, Pará State, Brazil. Science of the total environment. 368(1), 424-433. https://doi.org/10.1016/j.scitotenv.2005.09.037

Elkhatib, E., Moharem, M., Mahdy, A., Mesalem, M., 2017. Sorption, release and forms of mercury in contaminated soils stabilized with water treatment residual nanoparticles. Land Degradation & Development. 28(2), 752-761. https://doi.org/10.1002/ldr.2559

Emenike, E. C., Adeniyi, A. G., Iwuozor, K. O., Okorie, C. J., Egbemhenghe, A. U., Omuku, P. E., Okwu, K. C., Saliu, O. D., 2023. A critical review on the removal of mercury (Hg^{2+}) from aqueous solution using nanoadsorbents. Environmental Nanotechnology, Monitoring & Management. 20, 100816. https://doi.org/10.1016/j.enmm.2023.100816

Ericksen, J. A., Gustin, M. S., Schorran, D. E., Johnson, D. W., Lindberg, S. E., & Coleman, J. S., 2003. Accumulation of atmospheric mercury in forest foliage. Atmospheric Environment. 37(12), 1613-1622. https://doi.org/10.1016/S1352-2310(03)00008-6

Esdaile, L. J., Chalker, J. M., 2018. The mercury problem in artisanal and small-scale gold mining. Chemistry–A European Journal. 24(27), 6905-6916. https://doi.org/10.1002/chem.201704840

Eve, E., Oliveira, E. F., Eve, C., 1996. The mercury problem and diets in the Brazilian Amazon: planning a solution. Environmental Conservation. 23(2), 133-139. https://doi.org/10.1017/S0376892900038510

Farias, R. A., Hacon, S., Campos, R. C., Argento, R., 2005. Mercury contamination in farmed fish setup on former garimpo mining areas in the Northern Mato Grosso State, Amazonian region, Brazil. Science of the total environment. 348(1-3), 128-134. https://doi.org/10.1016/j.scitotenv.2004.12.038

Fearnside, P., 2017. Deforestation of the Brazilian Amazon. Oxford Research Encyclopedia of Environmental Science. https://oxfordre.com/environmentalscience/view/10.1093/acrefore/9780199389414.001.0001/acrefore-9780199389414-e-102 (accessed 25 March 2025).

Ferreira, C. M. A., Egler, S. G., Yallouz, A. V., Ignácio, Á. R. A., 2017. Semiquantitative determination of total mercury in Pygocentrus nattereri Kner, 1858 and sediment at the plateau of Upper Paraguai River, Brazil. Chemosphere. 174, 604-612. https://doi.org/10.1016/j.chemosphere.2017.01.059

Fostier, A. H., Forti, M. C., Guimaraes, J. R. D., Melfi, A. J., Boulet, R., Santo, C. E., Krug, F. J., 2000. Mercury fluxes in a natural forested Amazonian catchment (Serra do Navio, Amapá State, Brazil). Science of the Total Environment. 260(1-3), 201-211. https://doi.org/10.1016/S0048-9697(00)00564-7

Fritz, B., Peregovich, B., da Silva Tenório, L., da Silva Alves, A. C., Schmidt, M., 2023. Mercury and CO2 emissions from artisanal gold mining in Brazilian Amazon rainforest. Nature Sustainability. 7(1), 15-22. https://doi.org/10.1038/s41893-023-01242-1

Frohne, T., Rinklebe, J., Langer, U., Du Laing, G., Mothes, S., Wennrich, R., 2012. Biogeochemical factors affecting mercury methylation rate in two contaminated floodplain soils. Biogeosciences. 9(1), 493-507. https://doi.org/10.5194/bg-9-493-2012

Frossard, A., Donhauser, J., Mestrot, A., Gygax, S., Bååth, E., Frey, B., 2018. Long-and short-term effects of mercury pollution on the soil microbiome. Soil Biology and Biochemistry. 120, 191-199. https://doi.org/10.1016/j.soilbio.2018.01.028

Gerson, J. R., Topp, S. N., Vega, C. M., Gardner, J. R., Yang, X., Fernandez, L. E., Bernhardt, E. S., Pavelsky, T. M., 2020. Artificial lake expansion amplifies mercury pollution from gold mining. Science advances. 6(48), eabd4953. https://doi.org/10.1126/sciadv.abd4953

Gerson, J. R., Szponar, N., Zambrano, A. A., Bergquist, B., Broadbent, E., Driscoll, C. T., Erkenswick, G., Evers, D. C., Fernandez, L. E., Hsu-Kim, H., Inga, G., Lansdale, K. N., Marchese, M. J., Martinez, A., Moore, C., Pan, W. K., Purizaca, R. P., Sanchez, V., Silman, M., Ury, E. A., Vega, C., Watsa, M., Bernhardt, E. S., 2022. Amazon forests capture high levels of atmospheric mercury pollution from artisanal gold mining. Nature communications. 13(1), 559. https://doi.org/10.1038/s41467-022-27997-3

Giri, A. K., Patel, R. K., 2011. Toxicity and bioaccumulation potential of Cr (VI) and Hg (II) on differential concentration by Eichhornia crassipes in hydroponic culture. Water Science and Technology. 63(5), 899-907. https://doi.org/10.2166/wst.2011.268

Gomes, P. R., Pestana, I. A., Almeida, M. G., de Oliveira, B. C. V., Rezende, C. E., 2022. Effects of illegal gold mining on Hg concentrations in water, Pistia stratiotes, suspended particulate matter, and bottom sediments of two impacted rivers (Paraíba do Sul River and Muriaé River), Southeastern, Brazil. Environmental monitoring and assessment. 194(11), 797. https://doi.org/10.1007/s10661-022-10477-y

Gomes, P. R., Pestana, I. A., de Almeida, M. G., Rezende, C. E., 2023. The Paraíba do Sul River Basin and its coastal area as a study model of the mercury cycle: A meta-analytical review of three decades of research. Journal of Hazardous Materials. 460, 132442. https://doi.org/10.1016/j.jhazmat.2023.132442

Gonçalves, C., Fávaro, D., De Oliveira, S., Boulet, R., Vasconcellos, M., Saiki, M., 1998. Preliminary study on mercury distribution in soil profiles from Serra do Navio, Amapa, using radiochemical neutron activation analysis. Journal of Radioanalytical and Nuclear Chemistry. 235(1-2), 267-272. https://doi.org/10.1007/bf02385973

Gonçalves, C., Fávaro, D. I. T., Melfi, A. J., De Oliveira, S. M. B., Vasconcellos, M. B. A., Fostier, A. H., Guimaraes, J. R. D., Forti, M. C., 2000. Evaluation of mercury levels in sediment and soil samples from Vila Nova river basin, in Amapá State, Brazil, using radiochemical neutron activation analysis. Journal of Radioanalytical and Nuclear Chemistry. 243, 789-796. https://doi.org/10.1023/A:1010611528825

Grandjean, P., White, R. F., Nielsen, A., Cleary, D., Santos, E. C. O., 1999. Methylmercury neurotoxicity in Amazonian children downstream from gold mining. Environmental health perspectives. 107(7), 587-591. https://doi.org/10.1289/ehp.99107587

Grasby, S. E., Them II, T. R., Chen, Z., Yin, R., Ardakani, O. H., 2019. Mercury as a proxy for volcanic emissions in the geologic record. Earth-Science Reviews. 196, 102880. https://doi.org/10.1016/j.earscirev.2019.102880

Gregory, C. E., 2021. A concise history of mining, 1st ed. CRC Press, London.

Gustin, M. S., Bank, M. S., Bishop, K., Bowman, K., Branfireun, B., Chételat, J., Eckley, C. S., Hammerschmidt, C. R., Lamborg, C., Lyman, S., Martínez-Cortizas, A., Sommar, J., Tsui, M. T., Zhang, T., 2020. Mercury biogeochemical cycling: A synthesis of recent scientific advances. Science of the Total Environment. 737, 139619. https://doi.org/10.1016/j.scitotenv.2020.139619

Güven, D., Özbek, İ., 2022. Characteristics, Treatment, and Prognosis of Elemental Mercury Intoxication in Children: A Single-Center Retrospective Study. Pediatric Emergency Care. 38(10), 481-488. https://doi.org/10.1097/PEC.0000000000002834

Gworek, B., Dmuchowski, W., Baczewska-Dąbrowska, A. H., 2020. Mercury in the terrestrial environment: a review. Environmental Sciences Europe. 32(1), 128. https://doi.org/10.1186/s12302-020-00401-x

Gyamfi, O., Sørensen, P. B., Darko, G., Ansah, E., Vorkamp, K., Bak, J. L., 2021. Contamination, exposure and risk assessment of mercury in the soils of an artisanal gold mining community in Ghana. Chemosphere. 267, 128910. https://doi.org/10.1016/j.chemosphere.2020.128910

Hachiya, N., Takizawa, Y., Hisamatsu, S. I., Abe, T., Abe, Y., Motohashi, Y., 1998. Atmospheric mercury concentrations in the basin of the Amazon, Brazil. Environmental health and preventive medicine. 2, 183-187. https://doi.org/10.1007/BF02931699

Hacon, S., Artaxo, P., Gerab, F., Yamasoe, M. A., Campos, R. C., Conti, L. F., Lacerda, L. D., 1995. Atmospheric mercury and trace elements in the region of Alta Floresta in the Amazon basin. Water, Air, and Soil Pollution. 80, 273-283. https://doi.org/10.1007/BF01189677

Hacon, S., Rochedo, E. R., Campos, R. R., Lacerda, L. D., 1997. Mercury exposure through fish consumption in the urban area of Alta Floresta in the Amazon Basin. Journal of Geochemical Exploration. 58(2-3), 209-216. https://doi.org/10.1016/S0375-6742(96)00066-0

Hacon, S., Yokoo, E., Valente, J., Campos, R. C., Silva, V. A., Menezes, A. C. C., Moraes, L. P., Ignotti, E., 2000. Exposure to mercury in pregnant women from Alta Floresta—Amazon Basin, Brazil. Environmental research. 84(3), 204-210. https://doi.org/10.1006/enrs.2000.4115

Hacon, S., Barrocas, P. R., Vasconcellos, A. C. S. D., Barcellos, C., Wasserman, J. C., Campos, R. C., Ribeiro, C., Azevedo-Carloni, F. B., 2008. An overview of mercury contamination research in the Amazon basin with an emphasis on Brazil. Cadernos de Saúde Pública. 24, 1479-1492.

Hacon, S. S., Mourão, D. S., Oliveira, B., Silva, G. P., Freitas, M. F., Vega, C., Gonçalves, R., Mariani, C. F., Gomes, N., Souza, A. N., Bastos, W., 2013. Intake of predatory fish in Amazonia is a driver of toxicological risk for susceptible exposure groups. E3S Web of Conferences. 1, 41009. https://doi.org/10.1051/e3sconf/20130141009

Hacon, S. S., Oliveira-da-Costa, M., Gama, C. S., Ferreira, R., Basta, P. C., Schramm, A., Yokota, D., 2020. Mercury exposure through fish consumption in traditional communities in the Brazilian Northern Amazon. International Journal of Environmental Research and Public Health. 17(15), 5269. https://doi.org/10.3390/ijerph17155269

Harada, M., Nakanishi, J., Yasoda, E., Pinheiro, M. D. C. N., Oikawa, T., Guimarâes, G. A., Cardoso, B. S., Kizaki, T., Ohno, H., 2001. Mercury pollution in the Tapajos River basin, Amazon: mercury level of head hair and health effects. Environment international. 27(4), 285-290. https://doi.org/10.1016/S0160-4120(01)00059-9

He, L., Liu, F., Zhao, J., Liu, Q., Cui, L., Yu, Y. L., Fan, Y., Li, B., Li, Y. F., 2021. Temporal trends of urinary mercury in Chinese people from 1970s to 2010s: a review. Ecotoxicology and Environmental Safety. 208, 111460. https://doi.org/10.1016/j.ecoenv.2020.111460

Hinton, J. J., Veiga, M. M., 2009. Using earthworms to assess Hg distribution and bioavailability in gold mining soils. Soil and Sediment Contamination. 18(4), 512-524. https://doi.org/10.1080/15320380902978847

Hong, Y. S., Kim, Y. M., Lee, K. E., 2012. Methylmercury exposure and health effects. Journal of preventive medicine and public health. 45(6), 353. https://doi.org/10.3961/jpmph.2012.45.6.353

Howie, M. G., Jackson, A. K., Cristol, D. A., 2018. Spatial extent of mercury contamination in birds and their prey on the floodplain of a contaminated river. Science of the Total Environment. 630, 1446-1452. https://doi.org/10.1016/j.scitotenv.2018.02.272

Hussain, S., Yang, J., Hussain, J., Sattar, A., Ullah, S., Hussain, I., Rahman, S. U., Zandi, P., Xia, X., Zhang, L., 2022. Mercury fractionation, bioavailability, and the major factors predicting its transfer and accumulation in soil–wheat systems. Science of the Total Environment. 847, 157432. https://doi.org/10.1016/j.scitotenv.2022.157432

Hylander, L. D., Meili, M., Oliveira, L. J., e Silva, E. D. C., Guimarães, J. R., Araujo, D. M., Neves, R. P., Stachiw, R., Barros, A. J. P., Silva, G. D., 2000a. Relationship of mercury with aluminum, iron and manganese oxy-hydroxides in sediments from the Alto Pantanal, Brazil. Science of the Total Environment. 260(1-3), 97-107. https://doi.org/10.1016/S0048-9697(00)00544-1

Hylander, L. D., Pinto, F. N., Guimaraes, J. R., Meili, M., Oliveira, L. J., Silva, E. D. C., 2000b. Fish mercury concentration in the Alto Pantanal, Brazil: influence of season and water parameters. Science of the Total Environment. 261(1-3), 9-20. https://doi.org/10.1016/S0048-9697(00)00591-X

IBGE (Brazilian Institute of Geography and Statistics), 2023. Brasil tem 1,7 milhão de indígenas e mais da metade deles vive na Amazônia Legal. https://agenciadenoticias.ibge.gov.br/agencia-noticias/2012-agencia-de-noticias/noticias/37565-brasil-tem-1-7-milhao-de-indigenas-e-mais-da-metade-deles-vive-na-amazonia-legal (accessed 03 April 2025).

Jacques, P. D., Viglio, E. P., & d'El Rei Pinto, D. O., 2023. Environmental Geochemical Analysis in the Yanomami Indigenous Land, Mucajaí River Basin, State of Roraima, Brazil. Toxics. 11(10), 861. https://doi.org/10.3390/toxics11100861

Jiang, L., Zhang, R., Zhang, L., Zheng, R., Zhong, M., 2021. Improving the regulatory health risk assessment of mercury-contaminated sites. Journal of Hazardous Materials. 402, 123493. https://doi.org/10.1016/j.jhazmat.2020.123493

Júnior, W. A. D., Palmieri, H. E. L., Trindade, M. C., Aquino Branco, O. E., Carvalho Filho, C. A., Fleming, P. M., Silva, J. B. B., Windmöller, C. C., 2009. Speciation, distribution, and transport of mercury in contaminated soils from Descoberto, Minas Gerais, Brazil. Journal of Environmental Monitoring. 11(5), 1056-1063. https://doi.org/10.1039/B813997K

Júnior, C. D. M. B., Carvalho, L. G., 2022. Transformations in artisanal and small-scale gold mining work and production structures in the Tapajós region of Brazil's amazon. Resources Policy. 83, 103597. https://doi.org/10.1016/j.resourpol.2023.103597

Kaal, J., Seijo, M. M., Oliveira, C., Wagner-Wysiecka, E., McCoy, V. E., Kraemer, M. M. S., Kerner, A., Wenig, P., Mayo, C., Mayo, J., 2020. Golden artefacts, resin figurines, body adhesives and tomb sediments from the pre-Columbian burial site El Caño (Gran Coclé, Panamá): Tracing organic contents using molecular archaeometry. Journal of Archaeological Science. 113, 105045. https://doi.org/10.1016/j.jas.2019.105045

Keane, S., Bernaudat, L., Davis, K. J., Stylo, M., Mutemeri, N., Singo, P., Twala, P., Mutemeri, I., Nakafeero, A., Etui, I. D., 2023. Mercury and artisanal and small-scale gold mining: Review of global use estimates and considerations for promoting mercury-free alternatives. Ambio. 52(5), 833-852. https://doi.org/10.1007/s13280-023-01843-2

Kehrig, H. A., Malm, O., Akagi, H., 1997. Methylmercury in hair samples from different riverine groups, Amazon, Brazil. Water, Air, and Soil Pollution. 97, 17-29. https://doi.org/10.1007/BF02409641

Kogut, K., Gorecki, J., Burmistrz, P., 2021. Opportunities for reducing mercury emissions in the cement industry. Journal of Cleaner Production. 293, 126053. https://doi.org/10.1016/j.jclepro.2021.126053

Kolen, J., de Theije, M. E. M., Mathis, A., 2013. Formalized small-scale gold mining in the Brazilian Amazon: an activity surrounded by informality, in: Cremers, L., Kolen, J., de Theije, M. (Eds.), Small-scale Gold Mining in the Amazon. The cases of Bolivia, Brazil, Colombia, Peru and Suriname. CEDLA, Amsterdam, pp. 31-45.

Koley, A., Bray, D., Banerjee, S., Sarhar, S., Thahur, R. G., Hazra, A. K., Mandal, N. C., Chaudhury, S., Ross, A. B., Camargo-Valero, A., Balachandran, S., 2022. Water hyacinth (Eichhornia crassipes) a sustainable strategy for heavy metals removal from contaminated waterbodies, in: Garg, V. K., Malik, A., Kidwai, K. (Eds.), Bioremediation of Toxic Metal (loid)s. CRC Press, Boca Raton, pp. 95-114.

Kozak, N., Ahonen, S. A., Keva, O., Østbye, K., Taipale, S. J., Hayden, B., Kahilainen, K. K., 2021. Environmental and biological factors are joint drivers of mercury biomagnification in subarctic lake food webs along a climate and productivity gradient. Science of the Total Environment. 779, 146261. https://doi.org/10.1016/j.scitotenv.2021.146261

Kumari, S., Jamwal, R., Mishra, N., Singh, D. K., 2020. Recent developments in environmental mercury bioremediation and its toxicity: A review. Environmental Nanotechnology, Monitoring & Management. 13, 100283. https://doi.org/10.1016/j.enmm.2020.100283

Kwasigroch, U., Bełdowska, M., Jędruch, A., Łukawska-Matuszewska, K., 2021. Distribution and bioavailability of mercury in the surface sediments of the Baltic Sea. Environmental Science and Pollution Research. 28(27), 35690-35708. https://doi.org/10.1007/s11356-021-13023-4

Lacerda, L. D., Salomons, W., Pfeiffer, W. C., Bastos, W. R., 1991a. Mercury distribution in sediment profiles from lakes of the high Pantanal, Mato Grosso State, Brazil. Biogeochemistry. 14, 91-97. https://doi.org/10.1007/BF00002899

Lacerda, L. D. D., Pfeiffer, W. C., Marins, R. V., Rodrigues, S., Souza, C. M. M., Bastos, W. R., 1991b. Mercury dispersal in water, sediments and aquatic biota of a gold mining tailing deposit drainage in Pocone, Brazil. Water, Air, and Soil Pollution. 55, 283-294. https://doi.org/10.1007/BF00211194

Lacerda, L. D. D., 1997. Evolution of mercury contamination in Brazil. Water, Air, and Soil Pollution. 97, 247-255. https://doi.org/10.1007/BF02407463

Lacerda, L. D., Souza, M., Ribeiro, M. G., 2004. The effects of land use change on mercury distribution in soils of Alta Floresta, Southern Amazon. Environmental pollution. 129(2), 247-255. https://doi.org/10.1016/j.envpol.2003.10.013

Lama, S. N., Rocha, C. D., Jardim, W. F., Tsai, J. S., Frederick, P. C., 2011. Sedentary nestlings of Wood Stork as monitors of mercury contamination in the gold mining region of the Brazilian Pantanal. Environmental Research. 111(8), 1091-1095. https://doi.org/10.1016/j.envres.2011.07.007

Langford, N. J., Ferner, R. E., 1999. Toxicity of mercury. Journal of human hypertension. 13(10), 651-656. https://doi.org/10.1038/sj.jhh.1000896

Lázaro, W. L., de Oliveira, R. F., dos Santos-Filho, M., da Silva, C. J., Malm, O., Ignácio, Á. R., Díez, S., 2015. Non-lethal sampling for mercury evaluation in crocodilians. Chemosphere. 138, 25-32. https://doi.org/10.1016/j.chemosphere.2015.05.007

Le Tourneau, F. M., 2021. Brazilian illegal gold miners resilience in French Guiana. European Review of Latin American and Caribbean Studies/Revista Europea de Estudios Latinoamericanos y del Caribe. (112), 1-27. http://doi.org/10.32992/erlacs.10767

Leady, B. S., Gottgens, J. F., 2001. Mercury accumulation in sediment cores and along food chains in two regions of the Brazilian Pantanal. Wetlands Ecology and Management. 9, 349-361. https://doi.org/10.1023/A:1011856517552

Lechler, P. J., Miller, J. R., Lacerda, L. D. D., Vinson, D., Bonzongo, J. C., Lyons, W. B., Warwick, J. J., 2000. Elevated mercury concentrations in soils, sediments, water, and fish of the Madeira River basin, Brazilian Amazon: a function of natural enrichments?. Science of the Total Environment. 260(1-3), 87-96. https://doi.org/10.1016/S0048-9697(00)00543-X

Leino, T., Lodenius, M., 1995. Human hair mercury levels in Tucuruí area, state of Pará, Brazil. Science of the Total Environment. 175(2), 119-125. https://doi.org/10.1016/0048-9697(95)04908-J

Leiva, M. A. G., Morales, S., 2013. Environmental assessment of mercury pollution in urban tailings from gold mining. Ecotoxicology and Environmental Safety. 90, 167-173. https://doi.org/10.1016/j.ecoenv.2012.12.026

Lemaire, J., Brischoux, F., Marquis, O., Mangione, R., Bustamante, P., 2021. Variation of total mercury concentrations in different tissues of three neotropical caimans: implications for minimally invasive biomonitoring. Archives of Environmental Contamination and Toxicology. 81, 15-24. https://doi.org/10.1007/s00244-021-00846-y

Li, H., Li, Y., Tang, W., Liu, Y., Zheng, L., Xu, N., Gao, Y., Zhao, J., 2022. Bioavailability and methylation of bulk mercury sulfide in paddy soils: New insights into mercury risks in rice paddies. Journal of Hazardous Materials. 424, 127394. https://doi.org/10.1016/j.jhazmat.2021.127394

Lima, F. R., Pereira, P., Junior, E. C. S., Vasques, I. C., Oliveira, J. R., Windmöller, C. C., Inda, A. V., Weindorf, D. C., Curi, N., Ribeiro, B. T., Guilherme, L. R. G., Marques, J. J., 2022. Geochemistry signatures of mercury in soils of the Amazon rainforest biome. Environmental Research. 215, 114147. https://doi.org/10.1016/j.envres.2022.114147

Lino, A. S., Kasper, D., Guida, Y. S., Thomaz, J. R., & Malm, O., 2019. Total and methyl mercury distribution in water, sediment, plankton and fish along the Tapajós River basin in the Brazilian Amazon. Chemosphere. 235, 690-700. https://doi.org/10.1016/j.chemosphere.2019.06.212

Liu, M., Zhang, Q., Maavara, T., Liu, S., Wang, X., Raymond, P. A., 2021. Rivers as the largest source of mercury to coastal oceans worldwide. Nature Geoscience. 14(9), 672-677. https://doi.org/10.1038/s41561-021-00793-2

Liu, X., Wang, Y., Li, Z., Song, Y., Li, Y., Yin, Y., Cai, Y., 2023. Riverine input of suspended particulate matter controls distribution, partitioning and transport of mercury and methylmercury in the Yellow River Estuary. Journal of Hazardous Materials. 455, 131597. https://doi.org/10.1016/j.jhazmat.2023.131597

Liu, X., Wang, Y., Zhang, Q., Liu, C., Song, Y., Li, Y., Yin, Y., Cai, Y., 2024. Confounding effects of seasonality and anthropogenic river regulation on suspended particulate matter-driven mercury transport to coastal seas. Journal of Hazardous Materials. 469, 133979. https://doi.org/10.1016/j.jhazmat.2024.133979

Lobo, F. D. L., Costa, M., Novo, E. M. L. D. M., Telmer, K., 2016. Distribution of artisanal and small-scale gold mining in the Tapajós River Basin (Brazilian Amazon) over the past 40 years and relationship with water siltation. Remote Sensing. 8(7), 579. https://doi.org/10.3390/rs8070579

Lopes-Araújo, A., Arrifano, G. P., Macchi, B. M., Augusto-Oliveira, M., Santos-Sacramento, L., Martín-Doimeadios, R. C. R., Jiménez-Moreno, M., Filho, A. J. M., Alvarez-Leite, J. I., Oriá, R. B., Nascimento, J. L. M., Crespo-Lopez, M. E., 2023. Hair mercury is associated with dyslipidemia and cardiovascular risk: An anthropometric, biochemical and genetic cross-sectional study of Amazonian vulnerable populations. Environmental Research. 229, 115971. https://doi.org/10.1016/j.envres.2023.115971

Lu, Y. T., Qi, W. Z., Wang, S., Song, X. N., Yang, D. Y., Song, M., Hang, T. J., 2020. Toxicity and risk assessment of mercury exposures from cinnabar and Baizi Yangxin Pills based on pharmacokinetic and tissue distribution studies. Journal of Ethnopharmacology. 250, 112489. https://doi.org/10.1016/j.jep.2019.112489

Luckeneder, S., Giljum, S., Schaffartzik, A., Maus, V., Tost, M., 2021. Surge in global metal mining threatens vulnerable ecosystems. Global Environmental Change. 69, 102303. https://doi.org/10.1016/j.gloenvcha.2021.102303

Machado, I. F., Figueirôa, S. F. D. M., 2001. 500 years of mining in Brazil: a brief review. Resources Policy. 27(1), 9-24. https://doi.org/10.1016/S0301-4207(01)00004-6

Mahaffey, K. R., 1999. Methylmercury: a new look at the risks. Public health reports. 114(5), 396.

Makaure, J., Dube, T., Stewart, D., Razavi, N. R., 2023. Mercury exposure in two fish trophic guilds from protected and ASGM-impacted reservoirs in Zimbabwe and possible risks to human health. Archives of environmental contamination and toxicology. 84(2), 199-213. https://doi.org/10.1007/s00244-023-00977-4

Malm, O., Castro, M. B., Bastos, W. R., Branches, F. J., Guimarães, J. R., Zuffo, C. E., Pfeiffer, W. C., 1995b. An assessment of Hg pollution in different gold mining areas, Amazon Brazil. Science of the Total Environment. 175(2), 127-140. https://doi.org/10.1016/0048-9697(95)04909-6

Malm, O., 1998. Gold mining as a source of mercury exposure in the Brazilian Amazon. Environmental research. 77(2), 73-78. https://doi.org/10.1006/enrs.1998.3828

Mani, V., George, B., Saravanan, K., 2024. Toxicological impacts of mercury on the growth and biochemical profiles of pumpkin (Curcurbita moschata duchesne). World Journal of Advanced Research and Reviews. 24(01), 2596-2605. https://doi.org/10.30574/wjarr.2024.24.1.3300

Mani, V., Gurusamy, A. K., Perumal, V., 2025. Toxicological effects of Mercury in Radish (Raphanus Sativus) plants–Biochemical Analysis. Scholars Academic Journal of Pharmacy. 1, 1-8. https://doi.org/10.36347/sajp.2025.v14i01.001

Martín-Doimeadios, R. C. R., Nevado, J. J. B., Bernardo, F. J. G., Moreno, M. J., Arrifano, G. P. F., Herculano, A. M., Nascimento, J. L. M., Crespo-López, M. E., 2014. Comparative study of mercury speciation in commercial fishes of the Brazilian Amazon. Environmental Science and Pollution Research. 21, 7466-7479. https://doi.org/10.1007/s11356-014-2680-7

Martinelli, L. A., Ferreira, J. R., Forsberg, B. R., Victoria, R. L., 1989. Gold rush produces mercury contamination in Amazon. Cultural Survival Quarterly. 13(1), 32-4.

Martoredjo, I., Calvão Santos, L. B., Vilhena, J. C. E., Rodrigues, A. B. L., de Almeida, A., Sousa Passos, C. J., Florentino, A. C., 2024. Trends in mercury contamination distribution among human and animal populations in the Amazon region. Toxics. 12(3), 204. https://doi.org/10.3390/toxics12030204

Mathioudakis, S., Xiroudakis, G., Petrakis, E., Manoutsoglou, E., 2023. Alluvial gold mining technologies from ancient times to the present. Mining. 3(4), 618-644. https://doi.org/10.3390/mining3040034

McElwee, M. K., Freedman, J. H., 2011. Comparative toxicology of mercurials in Caenorhabditis elegans. Environmental toxicology and chemistry. 30(9), 2135-2141. https://doi.org/10.1002/etc.603

Mendes, L. A., de Lena, J. C., do Valle, C. M., Fleming, P. M., Windmöller, C. C., 2016. Quantification of methylmercury and geochemistry of mercury in sediments from a contaminated area of Descoberto (MG), Brazil. Applied Geochemistry. 75, 32-43. https://doi.org/10.1016/j.apgeochem.2016.10.011

Mendes, V. A., de Carvalho, D. P., de Almeida, R., Recktenvald, M. C. N. D. N., Pedrosa, O. P., de Sousa-Filho, I. F., Dorea, J. G., Bastos, W. R., 2021. Mercury in blood, hair, and feces from subsistence fish-eating riverines of the Madeira River Basin (Western Amazon). Journal of Trace Elements in Medicine and Biology. 67, 126773. https://doi.org/10.1016/j.jtemb.2021.126773

Méndez-López, M., Jiménez-Morillo, N. T., Fonseca, F., de Figueiredo, T., Parente-Sendín, A., Alonso-Vega, F., Arias-Estévez, M., Nóvoa-Muñoz, J. C., 2023. Mercury mobilization in shrubland after a prescribed fire in NE Portugal: Insight on soil organic matter composition and different aggregate size. Science of the Total Environment. 904, 167532. https://doi.org/10.1016/j.scitotenv.2023.167532

Meneses, H. N. M., Costa, M. O., Basta, P. C., Morais, C. G., Pereira, R. J. B., Souza, S. M. S., Hacon, S. S., 2022. Mercury contamination: A growing threat to riverine and urban communities in the Brazilian Amazon. International Journal of Environmental Research and Public Health. 19(5), 2816. https://doi.org/10.3390/ijerph19052816

Misztal, E., Chmielniak, T., Mazur, I., Sajdak, M., 2022. The release and reduction of mercury from solid fuels through thermal treatment prior to combustion. Energies. 15(21), 7987. https://doi.org/10.3390/en15217987

Mohanty, M., 2023. Remediation of Heavy Metals by Different Aquatic Macrophytes, in: Kumar, S., Bauddh, K., Singh, R., Kumar, N., Kumar, R. (Eds.), Aquatic Macrophytes: Ecology, Functions and Services. Springer, Singapore, pp. 207-211. https://doi.org/10.1007/978-981-99-3822-3_10

Monroy-Licht, A., Méndez-Cuadro, D., Olivero-Verbel, J., 2023. Elemental mercury accumulation in Eichhornia crassipes (Mart.) Solms-Laubach. Environmental Science and Pollution Research. 30(4), 9898-9913. https://doi.org/10.1007/s11356-022-22521-y

Montes, C. S., Ferreira, M. A. P., Giarrizzo, T., Amado, L. L., & Rocha, R. M., 2022. The legacy of artisanal gold mining and its impact on fish health from Tapajós Amazonian region: A multi-biomarker approach. Chemosphere. 287, 132263. https://doi.org/10.1016/j.chemosphere.2021.132263

Montoya, A. J., Lena, J. C., Windmöller, C. C., 2019. Adsorption of gaseous elemental mercury on soils: Influence of chemical and/or mineralogical characteristics. Ecotoxicology and Environmental Safety. 170, 98-106. https://doi.org/10.1016/j.ecoenv.2018.11.054

Moore, L. A., Finger Jr, J. W., Haskins, D. L., Elsey, R. M., Castleberry, S. B., Glenn, T. C., Jagoe, C. H., Brisbin Jr, I. L., 2022. Tissue distribution of mercury in the bodies of wild American alligators (Alligator mississippiensis) from a coastal marsh in Louisiana (USA). Archives of Environmental Contamination and Toxicology. 83(1), 13-20. https://doi.org/10.1007/s00244-022-00938-3

Motts, J. A., Shirley, D. L., Silbergeld, E. K., Nyland, J. F., 2014. Novel biomarkers of mercury-induced autoimmune dysfunction: A cross-sectional study in Amazonian Brazil. Environmental research. 132, 12-18. https://doi.org/10.1016/j.envres.2014.03.024

Mozgai, V., Bajnóczi, B., May, Z., Mráv, Z., 2021. Non-destructive handheld XRF study of archaeological composite silver objects—the case study of the late Roman Seuso Treasure. Archaeological and Anthropological Sciences. 13(5), 83. https://doi.org/10.1007/s12520-021-01321-4

Mulholland, D. S., Boaventura, G. R., Araújo, D. F., 2012. Geological and anthropogenic influences on sediment metal composition in the upper Paracatu River Basin, Brazil. Environmental earth sciences. 67, 1307-1317. https://doi.org/10.1007/s12665-012-1574-6

Natasha, M. S., Khalid, S., Bibi, I., Bundschuh, J., Niazi, N. K., Dumat, C., 2020. A critical review of mercury speciation, bioavailability, toxicity and detoxification in soil-plant environment: Ecotoxicology and health risk assessment. Science of the total environment. 711, 134749. https://doi.org/10.1016/j.scitotenv.2019.134749

Nava, V., Di Bella, G., Fazio, F., Potortì, A. G., Lo Turco, V., Licata, P., 2023. Hg content in EU and non-EU processed meat and fish foods. Applied Sciences. 13(2), 793. https://doi.org/10.3390/app13020793

Navarro, A., 2008. Review of characteristics of mercury speciation and mobility from areas of mercury mining in semi-arid environments. Reviews in Environmental Science and Bio/Technology. 7, 287-306. https://doi.org/10.1007/s11157-008-9139-6

Neto, O. G. N., Dias, S. R., Albuquerque, F. E. A., Miranda, M., Lopez-Alonso, M., Oliveira, R. B., Pinto, D., Minervino, A. H. H., 2024. Comparative analysis between mercury levels in fish tissues evaluated using direct mercury analyzer and inductively plasma-coupled mass spectrometer. Chemosphere. 351, 141146. https://doi.org/10.1016/j.chemosphere.2024.141146

Nogueira, F., Silva, E. C. E., Junk, W., 1997. Mercury from gold minings in the Pantanal of Pocone (Mato Grosso, Brazil). International Journal of Environmental Health Research. 7(3), 181-192. https://doi.org/10.1080/09603129773823

Nriagu, J. O., Pfeiffer, W. C., Malm, O., Souza, C. M. M., Mierle, G., 1992. Mercury pollution in Brazil. Nature. 356(6368), 389-389. https://doi.org/10.1038/356389a0

Nunes, G. A., Ramos, D. D., Forti, J. C., Ramos, D. D., Oliveira, L., Junior, D. S., Santo, G. E., Santos, F. A., 2024. Relationship of the “Dequada” Phenomenon with Mercury Methylation in Pantanal, Brazil. Water. 16(9), 1204. https://doi.org/10.3390/w16091204

Nwaila, G. T., Frimmel, H. E., Zhang, S. E., Bourdeau, J. E., Tolmay, L. C., Durrheim, R. J., Ghorbani, Y., 2022. The minerals industry in the era of digital transition: An energy-efficient and environmentally conscious approach. Resources Policy. 78, 102851. https://doi.org/10.1016/j.resourpol.2022.102851

Nyanza, E. C., Dewey, D., Manyama, M., Martin, J. W., Hatfield, J., Bernier, F. P., 2020. Maternal exposure to arsenic and mercury and associated risk of adverse birth outcomes in small-scale gold mining communities in Northern Tanzania. Environment International, 137, 105450. https://doi.org/10.1016/j.envint.2019.105450

Ogle, D. H., Doll, J. C., Wheeler, A. P., Dinno, A., 2025. FSA: Simple Fisheries Stock Assessment Methods. R package version 0.9.6. https://CRAN.R-project.org/package=FSA (accessed 25 March 2025).

Oliveira, L. J., Hylander, L. D., Silva, E. D. C., 2004. Mercury behavior in a tropical environment: the case of small-scale gold mining in Poconé, Brazil. Environmental Practice. 6(2), 121-134. https://doi.org/10.1017/S1466046604000237

Oliveira, D. F., Castro, B. S., Recktenvald, M. C. N. N., Júnior, W. A. C., Silva, F. X., Alves, C. L. M., Bastos, W. R., Ott, A. M. T., 2021a. Mercury in wild animals and fish and health risk for indigenous Amazonians. Food Additives & Contaminants: Part B. 14(3), 161-169. https://doi.org/10.1080/19393210.2020.1849410

Oliveira, C. A., Kasper, D., Junior, E. S., Bolson, M. A., Torrezani, L., Zara, L. F., 2021b. Influence of environmental conditions on the mercury levels of the sediment along the Balbina Reservoir, Brazilian Amazon. Environmental Monitoring and Assessment. 193(1), 50. https://doi.org/10.1007/s10661-020-08837-7

Oliveira, R. B., Silva, D. M., Franco, T. S. B. S., Vasconcelos, C. R. S., Sousa, D. J. A., Sarrazin, S. L. F., Sakamoto, M., Bourdineaud, J. P., 2022. Fish consumption habits of pregnant women in Itaituba, Tapajós River basin, Brazil: risks of mercury contamination as assessed by measuring total mercury in highly consumed piscivore fish species and in hair of pregnant women. Archives of Industrial Hygiene and Toxicology. 73(2), 131-142. https://doi.org/10.2478/aiht-2022-73-3611

Ordak, M., Wesolowski, M., Radecka, I., Muszynska, E., Bujalska-Zazdrozny, M., 2016. Seasonal variations of mercury levels in selected medicinal plants originating from Poland. Biological trace element research. 173, 514-524. https://doi.org/10.1007/s12011-016-0645-z

Oz, S. G., Tozlu, M., Yalcin, S. S., Sozen, T., Guven, G. S., 2012. Mercury vapor inhalation and poisoning of a family. Inhalation toxicology. 24(10), 652-658. https://doi.org/10.3109/08958378.2012.708677

Packull-McCormick, S., Ratelle, M., Lam, C., Napenas, J., Bouchard, M., Swanson, H., Laird, B. D., 2022. Hair to blood mercury concentration ratios and a retrospective hair segmental mercury analysis in the Northwest Territories, Canada. Environmental Research. 203, 111800. https://doi.org/10.1016/j.envres.2021.111800

Page, M. J., McKenzie, J. E., Bossuyt, P. M., Boutron, I., Hoffmann, T. C., Mulrow, C. D., Shamseer, L., Tetzlaff, J. M., Akl, E. A., Brennan, S. E., Chou, R., Glanville, J., Grimshaw, J. M., Hróbjartsson, A., Lalu, M. M., Li, T., Loder, E. W., Mayo-Wilson, E., McDonald, S., McGuinness, L. A., Stewart, L. A., Thomas, J., Tricco, A. C., Welch, V. A., Whiting, P., Moher, D., 2021. The PRISMA 2020 statement: an updated guideline for reporting systematic reviews. BMJ. 372. https://doi.org/10.1136/bmj.n71

Palheta, D., Taylor, A., 1995. Mercury in environmental and biological samples from a gold mining area in the Amazon region of Brazil. Science of the Total Environment. 168(1), 63-69. https://doi.org/10.1016/0048-9697(95)04533-7

Pan, F., Huang, J. H., & Feng, X., 2024. Sources, fates, and geochemical cycling of mercury in geothermal fields: Insights from mercury isotopes. Geophysical Research Letters. 51(9), e2023GL107384. https://doi.org/10.1029/2023GL107384

Pandey, R., Wang, N., Sahu, B. B., Moharana, S., Tiwari, S. K., 2023. Metal and Materials Engineering: Historical Prospect, in: Twari, S. K., Kumar, V., Thomas, S., (Eds.), Nanoparticles Reinforced Metal Nanocomposites: Mechanical Performance and Durability. Singapore: Springer Nature Singapore, pp. 1-21.

Peng, D., Chen, M., Su, X., Liu, C., Zhang, Z., Middleton, B. A., Lei, T., 2023. Mercury accumulation potential of aquatic plant species in West Dongting Lake, China. Environmental Pollution. 324, 121313. https://doi.org/10.1016/j.envpol.2023.121313

Perini, J. A., Silva, M. C., Vasconcellos, A. C. S., Viana, P. V. S., Lima, M. O., Jesus, I. M., Kempton, J. W., Oliveira, R. A. A., Hacon, S. S., Basta, P. C., 2021. Genetic Polymorphism of Delta Aminolevulinic Acid Dehydratase (ALAD) Gene and Symptoms of Chronic Mercury Exposure in Munduruku Indigenous Children within the Brazilian Amazon. International Journal of Environmental Research and Public Health. 18(16), 8746. https://doi.org/10.3390/ijerph18168746

Peša, I., Ross, C., 2021. Extractive industries and the environment: Production, pollution, and protest in global history. The Extractive Industries and Society. 8(4), 100933. https://doi.org/10.1016/j.exis.2021.100933

Pestana, M. H. D., Formoso, M. L., Teixeira, E. C., 1997. Heavy metals in stream sediments from copper and gold mining areas in southern Brazil. Journal of Geochemical Exploration. 58(2-3), 133-143. https://doi.org/10.1016/S0375-6742(96)00074-X

Pestana, M. H. D., Formoso, M. L. L., 2003. Mercury contamination in Lavras do Sul, south Brazil: a legacy from past and recent gold mining. Science of the total environment. 307(1-3), 125-140. https://doi.org/10.1016/S0048-9697(02)00535-1

Pestana, I. A., de Rezende, C. E., Almeida, R., de Lacerda, L. D., Bastos, W. R., 2022. Let's talk about mercury contamination in the Amazon (again): the case of the floating gold miners' village on the Madeira River. The Extractive Industries and Society. 11, 101122. https://doi.org/10.1016/j.exis.2022.101122

Petry-Podgórska, I., Schrenková, V., Migašová, M., Matoušek, T., Kratzer, J., 2021. Speciation analysis of mercury employing volatile species generation: Approaches to reliable determination in blood and hair. Microchemical Journal. 170, 106606. https://doi.org/10.1016/j.microc.2021.106606

Pfeiffer, W. C., de Lacerda, L. D., Malm, O., Souza, C. M. M., da Silveira, E. G., Bastos, W. R., 1989. Mercury concentrations in inland waters of gold-mining areas in Rondônia, Brazil. Science of the Total Environment. 87, 233-240. https://doi.org/10.1016/0048-9697(89)90238-6

Pfeiffer, W. C., Malm, O., Souza, C. M. M., De Lacerda, L. D., Silveira, E. G., Bastos, W. R., 1991. Mercury in the Madeira river ecosystem, Rondônia, Brazil. Forest Ecology and Management. 38(3-4), 239-245. https://doi.org/10.1016/0378-1127(91)90145-L

Pinheiro, M. C. N., Macchi, B. M., Vieira, J. L. F., Oikawa, T., Amoras, W. W., Guimarães, G. A., Costa, C. A., Crespo-López, M. E., Herculano, A. M., Silveira, L. C. L., Nascimento, J. L. M., 2008. Mercury exposure and antioxidant defenses in women: a comparative study in the Amazon. Environmental Research. 107(1), 53-59. https://doi.org/10.1016/j.envres.2007.08.007

Pinheiro, M. C. N., Farripas, S. S. M., Oikawa, T., Costa, C. A., Amoras, W. W., Vieira, J. L. F., Silveira, A. J. A., Lima, A. C. M., Souza, G. S., Silveira, L. C. L., 2012. Temporal Evolution of exposure to mercury in riverside communities in the Tapajós Basin, from 1994 to 2010. Bulletin of environmental contamination and toxicology. 89, 119-124. https://doi.org/10.1007/s00128-012-0652-5

Pisconte, J. N., Vega, C. M., Sayers, C. J., Sevillano-Ríos, C. S., Pillaca, M., Quispe, E., Tejeda, V., Ascorra, C., Silman, M. R., Fernandez, L. E., 2024. Elevated mercury exposure in bird communities inhabiting Artisanal and Small-Scale Gold Mining landscapes of the southeastern Peruvian Amazon. Ecotoxicology. 33(4), 472-483. https://doi.org/10.1007/s10646-024-02740-4

Portillo, A., Vega, C. M., Mena, J. L., Bonifaz, E., Ascorra, C., Silman, M. R., Fernandez, L. E., 2024. Mercury bioaccumulation in bats in Madre de Dios, Peru: implications for Hg bioindicators for tropical ecosystems impacted by artisanal and small-scale gold mining. Ecotoxicology. 33(4), 457-469. https://doi.org/10.1007/s10646-023-02719-7

Porvari, P., 1995. Mercury levels of fish in Tucurui hydroelectric reservoir and in River Moju in Amazonia, in the state of Para, Brazil. Science of the Total Environment. 175(2), 109-117. https://doi.org/10.1016/0048-9697(95)04907-X

Qin, C., Du, B., Yin, R., Meng, B., Fu, X., Li, P., Zhang, L., Feng, X., 2020. Isotopic fractionation and source appointment of methylmercury and inorganic mercury in a paddy ecosystem. Environmental Science & Technology. 54(22), 14334-14342. https://doi.org/10.1021/acs.est.0c03341

Queipo-Abad, S., González, P. R., Martínez-Morillo, E., Davis, W. C., Alonso, J. I. G., 2019. Concentration of mercury species in hair, blood and urine of individuals occupationally exposed to gaseous elemental mercury in Asturias (Spain) and its comparison with individuals from a control group formed by close relatives. Science of The Total Environment. 672, 314-323. https://doi.org/10.1016/j.scitotenv.2019.03.367

Queiroz, J., Gasparinetti, P., Bakker, L. B., Lobo, F., Nagel, G., 2022. Socioeconomic cost of dredge boat gold mining in the Tapajós basin, eastern Amazon. Resources Policy. 79, 103102. https://doi.org/10.1016/j.resourpol.2022.103102

Quintarelli, J. M., Garnier, J., de Souza, J. P. R., de Sousa Tonhá, M., Barral, U. M., Roig, H. L., Martinez, J. M., Santini, W., Puita, O., Seyler, P., Kutter, V., Souza, J. R., 2024. Mercury in river samples with artisanal and small-scale gold mining influence: The case of the upper Madeira River Basin (Brazil/Bolivia). Journal of South American Earth Sciences. 145, 105070. https://doi.org/10.1016/j.jsames.2024.105070

R Core Team, 2024. R: A Language and Environment for Statistical Computing. R Foundation for Statistical Computing, Vienna, Austria. https://www.R-project.org/ (accessed 25 March 2025).

Rabitto, I. S., Bastos, W. R., Almeida, R., Anjos, A., de Holanda, Í. B. B., Galvão, R. C. F., Neto, F. F., Menezes, M. L., Santos, C. A. M., de Oliveira Ribeiro, C. A., 2011. Mercury and DDT exposure risk to fish-eating human populations in Amazon. Environment International. 37(1), 56-65. https://doi.org/10.1016/j.envint.2010.07.001

Raj, D., Maiti, S. K., 2020. Sources, bioaccumulation, health risks and remediation of potentially toxic metal (loid)s (As, Cd, Cr, Pb and Hg): an epitomised review. Environmental monitoring and assessment. 192(2), 108. https://doi.org/10.1007/s10661-019-8060-5

Ramírez, M. G. V., Ruiz, C. M. V., Gomringer, R. C., Pillaca, M., Thomas, E., Stewart, P. M., Miranda, L. A. G., Dañobeytia, F. R., Barrantes, J. A. G., Gushiken, M. C., Bardales, J. V., Silman, M., Fernandez, L., Ascorra, C.,

Torres, D. C., 2021. Mercury in soils impacted by alluvial gold mining in the Peruvian Amazon. Journal of Environmental Management. 288, 112364. https://doi.org/10.1016/j.jenvman.2021.112364

Reuther, R., 1994. Mercury accumulation in sediment and fish from rivers affected by alluvial gold mining in the brazilian Madeira river basin, Amazon. Environmental monitoring and assessment. 32, 239-258. https://doi.org/10.1007/BF00546279

Rhodes, V. P., de Lena, J. C., Santolin, C. V. A., da Silva Pinto, T., Mendes, L. A., Windmöller, C. C., 2018. Speciation and quantification of Hg in sediments contaminated by artisanal gold mining in the Gualaxo do Norte River, Minas Gerais, SE, Brazil. Environmental monitoring and assessment. 190, 1-11. https://doi.org/10.1007/s10661-017-6394-4

Rodrigues, P. A., Ferrari, R. G., Dos Santos, L. N., Junior, C. A. C., 2019. Mercury in aquatic fauna contamination: a systematic review on its dynamics and potential health risks. Journal of Environmental Sciences. 84, 205-218. https://doi.org/10.1016/j.jes.2019.02.018

Roulet, M., Lucotte, M., Canuel, R., Rheault, I., Tran, S., Gog, Y. D. F., Farella, N., Vale, R. S., Passos, C. J. S., Silva, E. J., Mergler, D., Amorim, M., 1998. Distribution and partition of total mercury in waters of the Tapajós River Basin, Brazilian Amazon. Science of the Total Environment. 213(1-3), 203-211. https://doi.org/10.1016/S0048-9697(98)00093-X

Ruggieri, F., Majorani, C., Domanico, F., & Alimonti, A., 2017. Mercury in children: current state on exposure through human biomonitoring studies. International journal of environmental research and public health. 14(5), 519. https://doi.org/10.3390/ijerph14050519

Saim, A. K., 2021. Mercury (Hg) use and pollution assessment of ASGM in Ghana: Challenges and strategies towards Hg reduction. Environmental Science and Pollution Research. 28, 61919–61928. https://doi.org/10.1007/s11356-021-16532-4

Sahu, S. K., Mishra, M., Mishra, A., Mangaraj, P., Beig, G., 2024. Quantification and assessment of hazardous mercury emission from industrial process and other unattended sectors in India: A step towards mitigation. Journal of Hazardous Materials. 470, 134103. https://doi.org/10.1016/j.jhazmat.2024.134103

Saleh, T. A., Fadillah, G., Ciptawati, E., & Khaled, M., 2020. Analytical methods for mercury speciation, detection, and measurement in water, oil, and gas. TrAC Trends in Analytical Chemistry, 132, 116016. https://doi.org/10.1016/j.trac.2020.116016

Santolin, C. V., Ciminelli, V. S., Nascentes, C. C., Windmöller, C. C., 2015. Distribution and environmental impact evaluation of metals in sediments from the Doce River Basin, Brazil. Environmental Earth Sciences. 74, 1235-1248. https://doi.org/10.1007/s12665-015-4115-2

Santos, E. C. O., de Jesus, I. M., da Silva Brabo, E., Loureiro, E. C. B., da Silva Mascarenhas, A. F., Weirich, J., Câmara, V. M., Cleary, D., 2000a. Mercury exposures in riverside Amazon communities in Para, Brazil. Environmental Research. 84(2), 100-107. https://doi.org/10.1006/enrs.2000.4088

Santos, L. D. S., Müller, R. C., Sarkis, J. E. S., Alves, C. N., Brabo, E. S., Santos, E. O., Bentes, M. H. S., 2000b. Evaluation of total mercury concentrations in fish consumed in the municipality of Itaituba, Tapajós River Basin, Pará, Brazil. Science of the total environment. 261(1-3), 1-8. https://doi.org/10.1016/S0048-9697(00)00590-8

Santos, E. C. O., Câmara, V. M., Jesus, I. M., Brabo, E. S., Loureiro, E. C. B., Mascarenhas, A. F. S., Fayal, K. F., Sá Filho, G. C., Sagica, F. E. S., Lima, M. O., Higuchi, H., Silveira, I. M., 2002a. A contribution to the establishment of reference values for total mercury levels in hair and fish in Amazonia. Environmental Research. 90(1), 6-11. https://doi.org/10.1006/enrs.2002.4366

Santos, E. C., Jesus, I. M., Câmara, V. M., Brabo, E., Loureiro, E. C. B., Mascarenhas, A., Weirich, J., Luiz, R. R., Cleary, D. 2002b. Mercury exposure in Munduruku Indians from the community of Sai Cinza, State of Pará, Brazil. Environmental Research. 90(2), 98-103. https://doi.org/10.1006/enrs.2002.4389

Santos, M. V. S., Júnior, J. B. S., Carvalho, C. E. V., Vergílio, C. S., Hadlich, G. M., de Santana, C. O., Jesus, T. B., 2020. Geochemical evaluation of potentially toxic elements determined in surface sediment collected in an area under the influence of gold mining. Marine pollution bulletin. 158, 111384. https://doi.org/10.1016/j.marpolbul.2020.111384

Santos, A. N. D., Recktenvald, M. C. N. N., Carvalho, D. P., Puerta, E. L. B., Sousa-Filho, I. F., Dórea, J. G., Bastos, W. R., 2021. Mercury in birds (aquatic and scavenger) from the Western Amazon. Environmental Research. 201, 111574. https://doi.org/10.1016/j.envres.2021.111574

Sayers II, C. J., Evers, D. C., Ruiz-Gutierrez, V., Adams, E., Vega, C. M., Pisconte, J. N., Tejeda, V., Regan, K., Lane, O. P., Ash, A. A., Cal, R., Reneau, S., Martínez, W., Welch, G., Hartwell, K., Teul, M., Tzul, D., Arendt, W. J., Tórrez, M. A., Watsa, M., Erkenswick, G., Moore, C. E., Gerson, J., Sánches, V., Purizaca, R. P., Yurek, H., Burton, M. E. H., Shrum, P. L., Tabares-Segovia, S., Vargas, K., Fogarty, F. F., Charette, M. R., Martínez, A. E., Bernhardt, E. S., Taylor, R. J., Tear, T. H., Fernandez, L. E., 2023. Mercury in Neotropical birds: a synthesis and prospectus on 13 years of exposure data. Ecotoxicology. 32(8), 1096-1123. https://doi.org/10.1007/s10646-023-02706-y

Seifert Jr., C. A., Queiroz-Stein, G., Gugliano, A. A., 2023. Bolsonaro's government and the dismantling of the participative institutions in environmental policy. Latin American Policy. 14(2), 298-315. https://doi.org/10.1111/lamp.12296

Silva, S. F., Oliveira, D. C., Pereira, J. P. G., Castro, S. P., Costa, B. N. S., Oliveira Lima, M., 2019. Seasonal variation of mercury in commercial fishes of the Amazon Triple Frontier, Western Amazon Basin. Ecological Indicators. 106, 105549. https://doi.org/10.1016/j.ecolind.2019.105549

Siqueira, G. W., Aprile, F., Irion, G., Braga, E. S., 2018. Mercury in the Amazon basin: human influence or natural geological pattern?. Journal of South American Earth Sciences. 86, 193-199. https://doi.org/10.1016/j.jsames.2018.06.017

Schwartz, M., Smits, K., Smith, N., Phelan, T., 2021. How lessons from an evolving comprehensive approach for water and sanitation can improve artisanal and small-scale mining environmental initiatives. Journal of Cleaner Production. 282, 124457. https://doi.org/10.1016/j.jclepro.2020.124457

Seco, J., Freitas, R., Xavier, J. C., Bustamante, P., Coelho, J. P., Coppola, F., Saunders, R. A., Almeida, A., Fielding, S., Pardal, M. A., Stowasser, G., Pompeo, G., Tarling, G. A., Brierley, A. S., Pereira, E., 2021. Oxidative stress, metabolic activity and mercury concentrations in Antarctic krill Euphausia superba and myctophid fish of the Southern Ocean. Marine Pollution Bulletin. 166, 112178. https://doi.org/10.1016/j.marpolbul.2021.112178

Silva, H. A. M., Guimarães, J. R. D., 2024. Mercury cyanide complexes and their relevance as environmental contaminants. Chemosphere. 350, 141054. https://doi.org/10.1016/j.chemosphere.2023.141054

Silva-Forsberg, M. C., Forsberg, B. R., Zeidemann, V. K., 1999. Mercury contamination in humans linked to river chemistry in the Amazon Basin. Ambio. 519-521.

Sing, K. A., Hryhorczuk, D., Saffirio, G., Sinks, T., Paschal, D. C., Sorensen, J., Chen, E. H., 2003. Organic mercury levels among the Yanomami of the Brazilian Amazon Basin. AMBIO: a Journal of the Human Environment. 32(7), 434-439. https://doi.org/10.1579/0044-7447-32.7.434

Singh, K., Blechinger, S., Pelletier, L., Karthikeyan, S., St-Amand, A., Liberda, E. N., & Chan, H. M., 2023. Characterizing variability in total mercury hair: blood ratio in the general Canadian population. Environmental Research. 224, 115491. https://doi.org/10.1016/j.envres.2023.115491

Siqueira-Gay, J., Sánchez, L. E., 2021. The outbreak of illegal gold mining in the Brazilian Amazon boosts deforestation. Regional Environmental Change. 21, 1-5. https://doi.org/10.1007/s10113-021-01761-7

Smith, N. M., 2019. “Our gold is dirty, but we want to improve”: challenges to addressing mercury use in artisanal and small-scale gold mining in Peru. Journal of Cleaner Production. 222, 646-654. https://doi.org/10.1016/j.jclepro.2019.03.076

Soares, L. C., Egreja Filho, F. B., Linhares, L. A., Windmoller, C. C., Yoshida, M. I., 2015. Accumulation and oxidation of elemental mercury in tropical soils. Chemosphere. 134, 181-191. https://doi.org/10.1016/j.chemosphere.2015.04.020

Soares, J. A. R., Saes, A. M., 2023. Imperial Brazilian Mining Association (IBMA): a cidade de Londres na economia escravista brasileira no início do século XIX. América Latina en la historia económica. 30(3). https://doi.org/10.18232/20073496.1358

Socha, D. M., Reinhard, J., Perea, R. C., 2021. Inca human sacrifices on Misti volcano (Peru). Latin American Antiquity. 32(1), 138-153. https://doi.org/10.1017/laq.2020.78

Soe, P. S., Kyaw, W. T., Arizono, K., Ishibashi, Y., Agusa, T., 2022. Mercury pollution from artisanal and small-scale gold mining in Myanmar and other southeast asian countries. International Journal of Environmental Research and Public Health. 19(10), 6290. https://doi.org/10.3390/ijerph19106290

Soresini, G., Silva, F. A., Leuchtenberger, C., Mourão, G., 2021. Total mercury concentration in the fur of free-ranging giant otters in a large Neotropical floodplain. Environmental Research. 198, 110483. https://doi.org/10.1016/j.envres.2020.110483

Souza Neto, H. F., da Silveira Pereira, W. V., Dias, Y. N., de Souza, E. S., Teixeira, R. A., Lima, M. W., Ramos, S. J., Amarante, C. B., Fernandes, A. R., 2020. Environmental and human health risks of arsenic in gold mining areas in the eastern Amazon. Environmental Pollution. 265, 114969. https://doi.org/10.1016/j.envpol.2020.114969

Ssenku, J. E., Naziriwo, B., Kutesakwe, J., Mustafa, A. S., Kayeera, D., Tebandeke, E., 2023. Mercury accumulation in food crops and phytoremediation potential of wild plants thriving in artisanal and small-scale gold mining areas in Uganda. Pollutants. 3(2), 181-196. https://doi.org/10.3390/pollutants3020014

Stopford, W., Goldwater, L. J., 1975. Methylmercury in the environment: a review of current understanding. Environmental Health Perspectives. 12, 115-118. https://doi.org/10.1289/ehp.7512115

Streets, D. G., Lu, Z., Levin, L., Ter Schure, A. F., Sunderland, E. M., 2018. Historical releases of mercury to air, land, and water from coal combustion. Science of The Total Environment. 615, 131-140. https://doi.org/10.1016/j.scitotenv.2017.09.207

Sun, Y., Guo, Z., Du, J., Zhao, W., 2020. Diffuse emission and transport of gaseous elemental mercury (GEM) in the Mapamyum geothermal system, Western Tibet (China). Journal of Volcanology and Geothermal Research. 397, 106825. https://doi.org/10.1016/j.jvolgeores.2020.106825

Tao, Z., Dai, S., Chai, X., 2017. Mercury emission to the atmosphere from municipal solid waste landfills: A brief review. Atmospheric Environment. 170, 303-311. https://doi.org/10.1016/j.atmosenv.2017.09.046

Targino, F. J., Ribeiro, J. D. N., Simões, J. S., Carneiro, C. S., Lazzarini, S. M., Souza, A. R., Ferreira, M. S., Mano, S. B., Mársico, E. T., 2023. Total mercury content in the tissues of freshwater chelonium (Podocnemis expansa) and a human health risk assessment for the Amazon population in Brazil. International Journal of Environmental Research and Public Health. 20(15), 6489. https://doi.org/10.3390/ijerph20156489

Taufiq, A., Riniarti, M., Widiastuti, E. L., Prasetia, H., Yuwono, S. B., Asmarahman, C., Rendra, T., 2022. Atmospheric Hg levels in tree barks Due to artisanal small-scale gold mining activity in Bunut Seberang Village in Indonesia. Atmosphere. 13(4), 633. https://doi.org/10.3390/atmos13040633

Teixeira, R. A., Fernandes, A. R., Ferreira, J. R., Vasconcelos, S. S., Braz, A. M. D. S., 2018. Contamination and soil biological properties in the Serra Pelada Mine-Amazonia, Brazil. Revista Brasileira de Ciência do Solo. 42, e0160354. https://doi.org/10.1590/18069657rbcs20160354

Teixeira, R. A., Pereira, W. V. S., Souza, E. S., Ramos, S. J., Dias, Y. N., Lima, M. W., Neto, H. F. S., Oliveira, E. S., Fernandes, A. R., 2021. Artisanal gold mining in the eastern Amazon: Environmental and human health risks of mercury from different mining methods. Chemosphere. 284, 131220. https://doi.org/10.1016/j.chemosphere.2021.131220

Theije, M., 2020. Brazil: forever informal. In: Verbrugge, B., Geenen, S. (Eds.), Global Gold Production Touching Ground. Palgrave Macmillan, Cham., London, pp. 117-134. https://doi.org/10.1007/978-3-030-38486-9_6

Tian, L., Zhu, Y., Yu, R., Zheng, X., 2024. A Pilot Study on Bioaccumulation and Tissue Distribution of Mercury in Barn Swallow (Hirundo rustica). Toxics. 12(3), 206. https://doi.org/10.3390/toxics12030206

Tibau, A. V., Grube, B. D., 2019. Mercury contamination from dental amalgam. Journal of Health and Pollution. 9(22), 190612. https://doi.org/10.5696/2156-9614-9.22.190612

Tomiyasu, T., Matsuo, T., Miyamoto, J., Imura, R., Anazawa, K., & Sakamoto, H., 2005. Low level mercury uptake by plants from natural environments-mercury distribution in Solidago altissima L. Environmental Sciences, 12(4), 231-238.

Tomiyasu, T., Baransano, C., Hamada, Y. K., Kodamatani, H., Kanzaki, R., Hidayati, N., & Rahajoe, J. S., 2020. Distribution of total and organic mercury in soils around an artisanal and small-scale gold mining area in West Java, Indonesia. SN Applied Sciences. 2, 1-11. https://doi.org/10.1007/s42452-020-3008-5

United Nations Environment Programme (UNEP), 2013. Minamata Convention on Mercury. https://www.unep.org/resources/report/minamata-convention-mercury (accessed 05 March 2025).

Uryu, Y., Malm, O., Thornton, I., Payne, I., & Cleary, D., 2001. Mercury contamination of fish and its implications for other wildlife of the Tapajós Basin, Brazilian Amazon. Conservation Biology. 15(2), 438-446. https://doi.org/10.1046/j.1523-1739.2001.015002438.x

Vasconcellos, A. C. S., Hallwass, G., Bezerra, J. G., Aciole, A. N. S., Meneses, H. N. M., Lima, M. O., Jesus, I. M., Hacon, S. S., Basta, P. C., 2021. Health risk assessment of mercury exposure from fish consumption in Munduruku indigenous communities in the Brazilian Amazon. International Journal of Environmental Research and Public Health. 18(15), 7940. https://doi.org/10.3390/ijerph18157940

Vasconcellos, A. C. S., Ferreira, S. R. B., Sousa, C. C., Oliveira, M. W., Lima, M. O., Basta, P. C., 2022. Health risk assessment attributed to consumption of fish contaminated with mercury in the Rio Branco Basin, Roraima, Amazon, Brazil. Toxics. 10(9), 516. https://doi.org/10.3390/toxics10090516

Veiga, M. M., Hinton, J. J., 2002. Abandoned artisanal gold mines in the Brazilian Amazon: a legacy of mercury pollution, in: Natural Resources Forum, in: Blackwell Publishing Ltd. (Eds.), Oxford, UK, and Boston, USA, pp. 15–26. https://doi.org/10.1111/1477-8947.00003

Veiga, M. M., Angeloci-Santos, G., Meech, J. A., 2014. Review of barriers to reduce mercury use in artisanal gold mining. The Extractive Industries and Society. 1(2), 351-361. https://doi.org/10.1016/j.exis.2014.03.004

Veiga, M. M., Fadina, O., 2020. A review of the failed attempts to curb mercury use at artisanal gold mines and a proposed solution. The Extractive Industries and Society. 7(3), 1135-1146. https://doi.org/10.1016/j.exis.2020.06.023

Verbrugge, B., Lanzano, C., Libassi, M., 2021. The cyanide revolution: Efficiency gains and exclusion in artisanal- and small-scale gold mining. Geoforum. 126, 267-276. https://doi.org/10.1016/j.geoforum.2021.07.030

Vetter, L., Carcedo, P., 2022. The use and meaning of Gold in Ancient Peru. Reverse Engineering of Ancient Metals. 41-79. https://doi.org/10.1007/978-3-030-72842-7_4

Vieira, L. M., Nunes, V. D. S., Amaral, M. D. A., Oliveira, A. C., Hauser-Davis, R. A., Campos, R. C. (2011). Mercury and methyl mercury ratios in caimans (Caiman crocodilus yacare) from the Pantanal area, Brazil. Journal of Environmental Monitoring. 13(2), 280-287. https://doi.org/10.1039/C0EM00561D

Vieri, J., Uribe-Villegas, M. A., Martinón-Torres, M., 2020. Of forming, gilding and intentionality in pre-Columbian goldwork: Analytical characterisation of artefacts from the Museo del Oro, Bogotá. Journal of Archaeological Science: Reports. 34, 102626. https://doi.org/10.1016/j.jasrep.2020.102626

Viljoen, D. A., 1979. Minerals from the dawn of mankind to the twenty-first century: presidential address. Journal of the Southern African Institute of Mining and Metallurgy. 79(14), 410-420.

Villas Bôas, R. C., 1997. The mercury problem in the Amazon due to gold extraction. Journal of Geochemical Exploration. 58(2-3), 217-222. https://doi.org/10.1016/S0375-6742(96)00075-1

von Tümpling Jr, W., Wilken, R. D., & Einax, J., 1995. Mercury contamination in the northern Pantanal region Mato Grosso, Brazil. Journal of Geochemical Exploration. 52(1-2), 127-134. https://doi.org/10.1016/0375-6742(94)00040-I

Wang, Q., Li, Z., Feng, X., Wang, A., Li, X., Wang, D., & Fan, L., 2021. Mercury accumulation in vegetable *Houttuynia cordata* Thunb. from two different geological areas in southwest China and implications for human consumption. Scientific reports, 11(1), 52.

Wang, J., Ma, L. Q., Letcher, R., Bradford, S. A., Feng, X., Rinklebe, J., 2022. Biogeochemical cycle of mercury and controlling technologies: Publications in critical reviews in environmental science & technology in the period of 2017–2021. Critical Reviews in Environmental Science and Technology. 52(24), 4325-4330. https://doi.org/10.1080/10643389.2022.2071210

WHO (World Health Organization), 2021. Mercury and human health: educational course. World Health Organization, Regional Office for Europe. https://www.who.int/europe/publications/i/item/9789289055888

Wickham, H., 2016. ggplot2: Elegant Graphics for Data Analysis, second ed. Springer-Verlag, New York.

Wickham, H., Averick, M., Bryan, J., Chang, W., McGowan, L. D. A., François, R., Grolemund, G., Hayes, A., Henry, L., Hester, J., Kuhn, M., Pedersen, T. L., Miller, E., Bache, S. M., Müller, K., Ooms, J., Robinson, D., Seidel, D. P., Spinu, V., Takahashi, K., Vaughan, D., Wilke, C., Woo, K., Yutani, H., 2019. Welcome to the Tidyverse. Journal of open source software. 4(43), 1686. https://doi.org/10.21105/joss.01686

Wickham, H. 2023. stringr: Simple, Consistent Wrappers for Common String Operations. R package version 1.5.1. https://CRAN.R-project.org/package=stringr (accessed 25 March 2025).

Wickham, H., François, R., Henry, L., Müller, K., Vaughan, D., 2023. dplyr: A Grammar of Data Manipulation. R package version 1.1.4. https://CRAN.R-project.org/package=dplyr (accessed 25 March 2025).

Windmöller, C. C., Wilken, R. D., Jardim, W. D. F., 1996. Mercury speciation in contaminated soils by thermal release analysis. Water, air, and soil pollution. 89, 399-416. https://doi.org/10.1007/BF00171644

Windom, H. L., Niencheski, L. F., Wells, D., Brandes, J., 2012. The use of oxygen isotopic ratios to identify natural and anthropogenic mercury concentrations in the Lower Brazilian Pantanal. Environmental earth sciences. 65, 547-553. https://doi.org/10.1007/s12665-011-1369-1

Wiseman, C. L. S., Parnia, A., Chakravartty, D., Archbold, J., Copes, R., Cole, D., 2019. Total, methyl and inorganic mercury concentrations in blood and environmental exposure sources in newcomer women in Toronto, Canada. Environmental Research. 169, 261-271. https://doi.org/10.1016/j.envres.2018.11.011

Xiao, R., Wang, S., Li, R., Wang, J. J., Zhang, Z., 2017. Soil heavy metal contamination and health risks associated with artisanal gold mining in Tongguan, Shaanxi, China. Ecotoxicology and environmental safety. 141, 17-24. https://doi.org/10.1016/j.ecoenv.2017.03.002

Yang, Y. K., Zhang, C., Shi, X. J., Lin, T., Wang, D. Y., 2007. Effect of organic matter and pH on mercury release from soils. Journal of Environmental Sciences. 19(11), 1349-1354. https://doi.org/10.1016/S1001-0742(07)60220-4

Yang, L., Zhang, Y., Wang, F., Luo, Z., Guo, S., Strähle, U., 2020. Toxicity of mercury: Molecular evidence. Chemosphere. 245, 125586. https://doi.org/10.1016/j.chemosphere.2019.125586

Yoshimura, A., Suemasu, K., Veiga, M. M., 2021. Estimation of mercury losses and gold production by artisanal and small-scale gold mining (ASGM). Journal of Sustainable Metallurgy. 7, 1045-1059. https://doi.org/10.1007/s40831-021-00394-8

Yoshino, K., Mori, K., Kanaya, G., Kojima, S., Henmi, Y., Matsuyama, A., Yamamoto, M., 2020. Food sources are more important than biomagnification on mercury bioaccumulation in marine fishes. Environmental pollution. 262, 113982. https://doi.org/10.1016/j.envpol.2020.113982

Zabyelina, Y., van Uhm, D., 2020. The New Eldorado: Organized Crime, Informal Mining, and the Global Scarcity of Metals and Minerals, in: Zabyelina, Y., van Uhm, D. (Eds.), Illegal Mining. Palgrave Macmillan, Cham. pp. 3-30. https://doi.org/10.1007/978-3-030-46327-4_1

3. Study area and socio-environmental setting

3.1. Regional setting, climate and land-use context

Itaituba is a municipality located in the southwestern portion of Pará State, Northern Brazil, with an estimated population of 135,369 inhabitants and a large territorial area of approximately 62,042 km², ranking 13th among Brazilian municipalities in terms of land area **(IBGE, n.d.)**. Mineral exploration in Itaituba was strongly driven during Brazil's military dictatorship (1964–1985), following the discovery of gold in the Tapajós Basin in 1958, as part of a broader strategy to promote territorial occupation and state control over the Amazon region (**Fórum Brasileiro de Segurança Pública, 2024)**.

Currently, Itaituba hosts the largest extension of artisanal and small-scale gold mining (ASGM) activities in Brazil, covering approximately 710 km², and has long been recognized as a hotspot of intense and largely illegal gold mining operations in the Amazon **(Queiroz et al., 2022; Fórum Brasileiro de Segurança Pública, 2024; Neto et al., 2024)**. At present, ASGM activities within the municipality are predominantly located outside the urban center, occurring mainly in mining districts such as Moraes de Almeida, Creporizão, and Creporizinho (**Fórum Brasileiro de Segurança Pública, 2024)**. As a consequence of the intense and largely illegal ASGM activities, Itaituba shows considerable socio-environmental vulnerability, marked by elevated levels of violence, social exploitation, and institutional fragility, which are widely recognized as structural features of ASGM-dominated areas in the Amazon region **(Potter, 2023; Carrança & Schreiber, 2024; Fórum Brasileiro de Segurança Pública, 2024, 2025)**.

The study area is located in the vicinity of the Jardim do Ouro village (6°15′17.58″S, 55°46′8.90″W), in the Moraes de Almeida district, one of the main ASGM hubs within the

municipality of Itaituba (Figure 16). The region lies within the Amazon biome and is predominantly covered by dense tropical rainforest. However, extensive areas have been modified by long-standing ASGM activities, resulting in a highly heterogeneous landscape composed of active ASGM sites, abandoned open pits, secondary vegetation, and relatively preserved forest zones. Observed deforestation and ASGM-driven physical reworking represent the main contemporary drivers of landscape transformation in the region, with direct implications for anthropogenic impacts on soil structure, organic matter inputs, and surface stability. In particular, ASGM has reshaped local hydrology through the formation of water-filled open pits, artificial drainage pathways, and low-lying waterlogged zones, enhancing spatial contrasts in soil moisture and redox conditions.

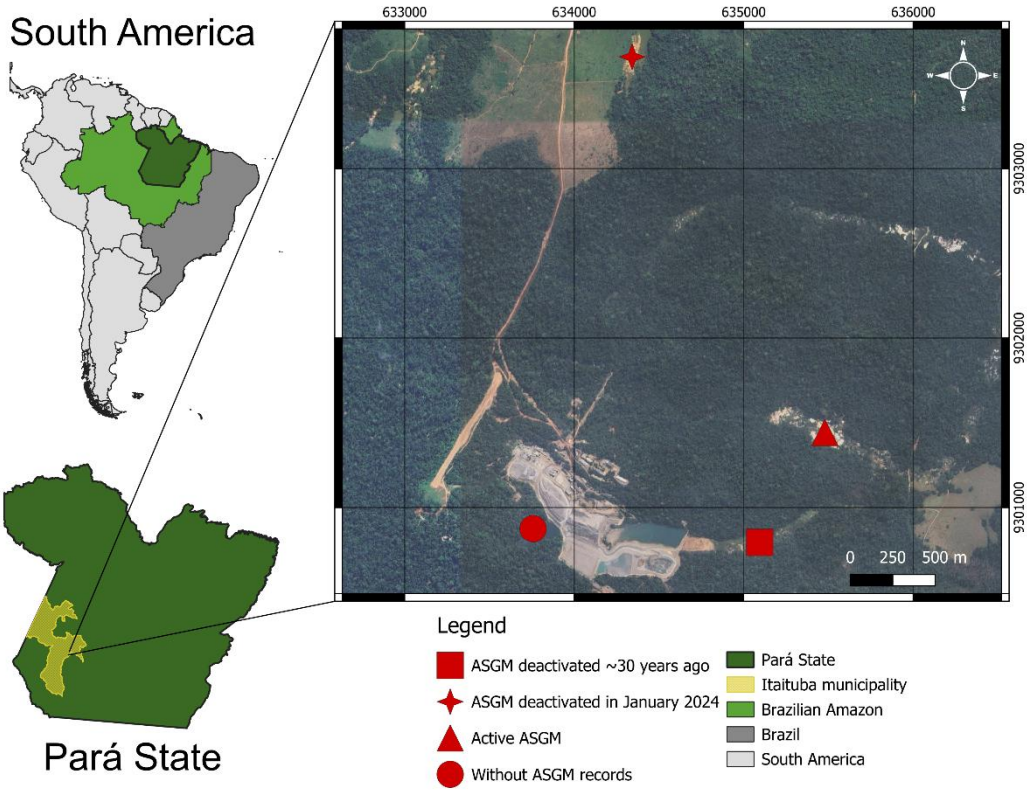


Figure 16: Location map of the study area, showing Brazil, the Brazilian Legal Amazon, Pará State, and the municipality of Itaituba, providing geographical context for the four studied sites.

In terms of climate, the area is classified as warm and humid tropical, with mean monthly temperatures consistently above 18 °C throughout the year **(IBGE, 2002)**. Long-term climate records (1991–2020) indicate an annual mean temperature of 27.6 °C, with a marked seasonal rainfall regime **(INMET, 2022)**. The rainy season extends predominantly from November to May, during which extreme precipitation events (>50 mm day^{-1}) are frequent, whereas the dry season typically spans from June to September, characterized by prolonged periods with minimal rainfall (<10 mm day^{-1}). In 2024, the year of sampling, maximum temperatures reached 36.34 °C during the dry season **(INMET, n.d.)**, intensifying evaporative demand and promoting strong temporal variability in soil moisture conditions. These climatic conditions can also contribute to enhancing erosion, sediment redistribution, and redox variability, particularly in physically disturbed ASGM landscapes.

3.2. Geological and metallogenic context of the Tapajós Mineral Province (TMP)

Located in the central portion of the Amazonian Craton, the Tapajós Mineral Province (TMP) is one of the main gold-producing regions in Brazil **(Guimarães et al., 2021)**. Gold in the TMP occurs in a variety of geological settings, including intrusion-related deposits **(Lobato et al., 2016)**, as well as fault-controlled granite-hosted veins, and, less frequently, in volcanic and sedimentary rocks **(Juliani et al., 2021)**. These geological conditions explain why the Tapajós region has become one of the most important metallogenic provinces in South America.

The geological potential of the province has long supported ASGM. Although gold was first reported in the Tapajós region in the eighteenth century **(Trindade & Barbosa Filho, 2002)**, the ASGM activities expanded significantly during the twentieth century, especially in

alluvial and eluvial deposits that were easily mined **(Pessoa et al., 1977; Juliani et al., 2021)**. Between 1965 and 1996 alone, official records indicate more than 110 tonnes of gold extracted from river deposits in the Tapajós **(Trindade & Barbosa Filho, 2002)**.

Considered the largest artisanal gold mining area in Brazil, the Tapajós region covers about 100,000 km² **(Trindade & Barbosa Filho, 2002)**. The expansion of mining areas has been documented over recent decades, from about 15 km² in 1973 to more than 260 km² in 2012, with major activities in the Crepori, Novo, and Jamanxim sub-basins **(Lobo et al., 2016)**. This expansion reflects how the geological endowment of the Tapajós has directly influenced the growth of ASGM.

This chapter does not aim to provide a detailed geological review, but to explain why gold deposits are present in the Tapajós and how this has supported the development of widespread ASGM. This context is necessary to understand the following chapters, which focus on mercury contamination resulting from artisanal gold extraction.

The Amazonian Craton, one of the largest cratonic areas in South America, hosts significant mineral resources, including iron, gold, tin, copper, and rare earth elements **(Teixeira et al., 1989)**. It is composed of the Guiana and Guaporé shields, separated by the Amazon Basin, and divided into six geochronological provinces—Central Amazonian (> 2.3 Ga); Maroni-Itacaiúnas (2.2–1.95 Ga); Ventuari-Tapajós (1.95–1.80 Ga); Rio Negro-Juruena (1.8–1.55 Ga); Rondonian-San Ignácio (1.55–1.3 Ga), and Sunsás (1.3–1.0 Ga) **(Tassinari & Macambira, 1999; Sial et al., 1999)**. The TMP is part of the Ventuari–Tapajós Province (1.95–1.80 Ga), a Paleoproterozoic tectonic domain characterized by extensive volcano-plutonic sequences and coeval granitoids **(Klein et al., 2016)**.

Within this framework, the Tapajós–Parima orogenic belt developed between 2.03 and 1.87 Ga, with calc-alkaline magmatic arc rocks that host widespread gold mineralization **(Santos et**

al., 2001). The youngest magmatic event of this belt is represented by the Parauari Suite (~1.88 Ga), composed mainly of granites and granodiorites, which is directly associated with the most important gold deposits of the region, such as Tocantinzinho, Cuiú-Cuiú, São Jorge, Palito, and São Chico **(Santos et al., 2001; Serabi Gold plc, 2025)**.

Mineralization in these systems is typically intrusion-related, occurring as quartz–sulfide veins and disseminations within brittle-ductile fault zones, and weathering of these primary deposits has generated secondary alluvial and eluvial concentrations, which became the main target of artisanal miners throughout the twentieth century **(Juliani et al., 2021; Serabi Gold plc, 2025)**. This geological setting helps to explain both the historical and current distribution of ASGM in the Tapajós and provides the necessary background to understand the mercury contamination discussed in subsequent chapters.

The study area is located within the Parauari Suite, specifically within the Palito Granite unit. Although the area itself belongs to a single geologic unit, it is surrounded by several distinct lithostratigraphic units (Figure 17).

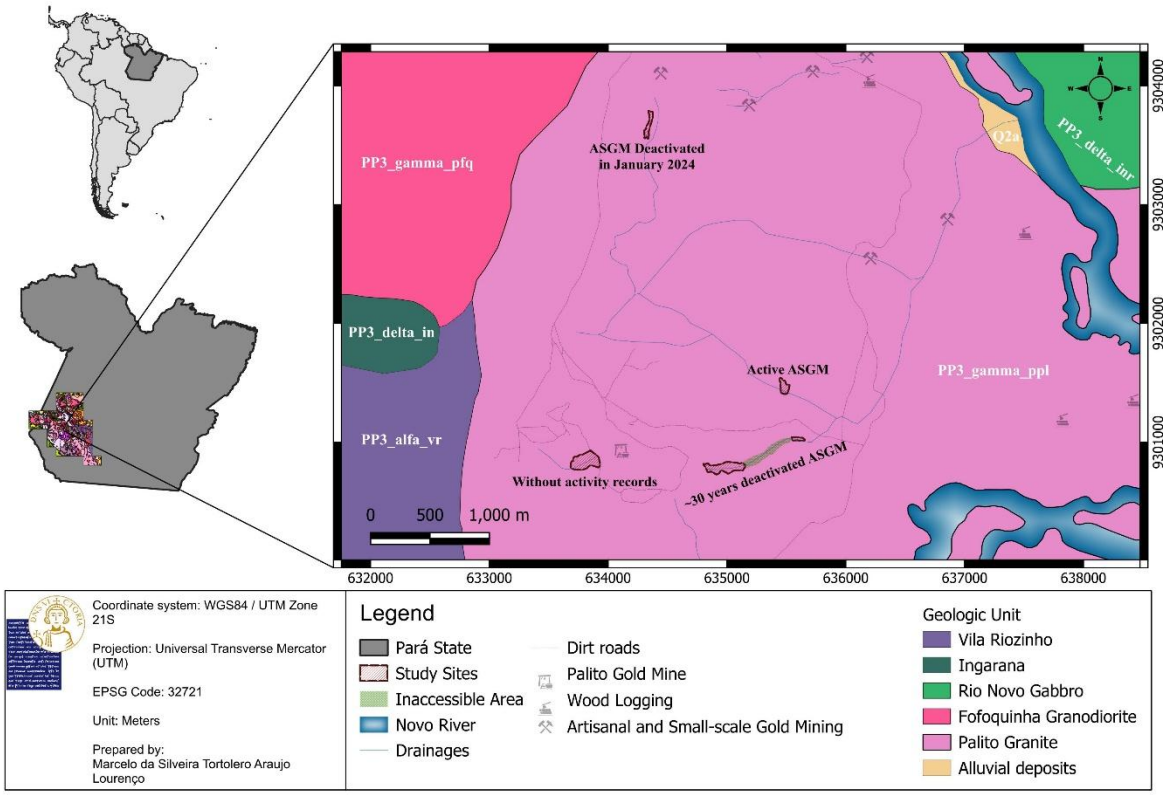


Figure 17: Geological map of the study area. Adapted from: CPRM (2004).

The Palito Granite is predominantly composed of monzogranite. The nearby Fofoquinha Granodiorite unit comprises a variety of lithologies, including monzogranite, quartz diorite, quartz monzodiorite, granodiorite, and tonalite. The Vila Riozinho unit is characterized by volcanic and subvolcanic rocks such as rhyolite, trachyte, dacite, andesite, microdiorite, microgranite, and ignimbrite. The Ingarana unit includes mainly monzogabbro, monzodiorite, gabbronorite, gabbro, quartz monzodiorite, diabase, quartz monzogabbro, and tonalite. Finally, the Rio Novo Gabbro unit is composed by quartz monzodiorite, quartz monzogabbro, and gabbro.

Intrusion-related and structurally controlled gold deposits are frequently targeted by artisanal and small-scale miners because they commonly host gold at shallow depths, either in vein systems or in weathered profiles, where it can be visually identified and extracted using

low-technology methods. In these settings, gold may occur as free or weakly refractory particles **(Vaughan, 2004; Zhou et al., 2004)** associated with quartz–sulfide veins or stockwork zones linked to intrusive bodies **(Sillitoe & Thompson, 2008; Lopes & Moura, 2019)**, or concentrated along faults and shear zones that localize mineralization **(Hodgson, 1989; Santos et al., 2001)**. The geometry, depth, and mineralogical characteristics of these deposits are key factors influencing their suitability for exploitation, favoring systems in which gold is accessible, discontinuous, and amenable to selective, low-technology mining **(Hodgson, 1989; Vishiti et al., 2019)**.

Under tropical conditions such as those predominant in the Tapajós region, prolonged chemical weathering further enhances the attractiveness of these deposits to ASGM. Deep weathering profiles promote the breakdown of sulfide minerals and the residual enrichment of gold in saprolitic, lateritic, eluvial, and alluvial settings **(Valeton, 1994; Anand et al., 2025)**. These secondary concentrations are typically shallow, unconsolidated, and spatially extensive, allowing gold to be recovered by manual excavation and simple gravity-based techniques. As a result, primary intrusion-related and structurally controlled deposits commonly act as sources for secondary gold accumulations that have historically supported widespread ASGM **(Hodgson, 1989; Vishiti et al., 2019; Anand et al., 2025)**.

Given that the feasibility of artisanal extraction in these environments is largely controlled by the physical and mineralogical form of gold, as well as by the continuity and depth of mineralized zones, coarse or visible gold hosted in oxidized, near-surface veins or secondary deposits can be efficiently recovered using panning, sluicing, or rudimentary crushing and concentration, which are the gravity-based techniques most commonly employed in artisanal and small-scale gold mining worldwide **(Vaughan, 2004; Veiga & Gunson, 2020)**. In contrast, fine-grained gold disseminated in unweathered host rocks or encapsulated within refractory sulfide minerals (e.g., pyrite) typically exhibits low recovery when processed by amalgamation

or rudimentary cyanidation and generally requires industrial-scale processing, making it poorly suited to artisanal operations **(Vaughan, 2004; Alfonso et al., 2019)**. Consequently, ASGM activities tend to focus on shallow, structurally controlled or weathered systems where selective extraction of high-grade material is possible.

Because gold in secondary and weathered deposits is commonly fine-grained and dispersed, artisanal miners have historically relied on mercury amalgamation as an accessible method to enhance gold recovery **(**e.g., **Veiga et al., 2014; Ilyas & Lee, 2018)**. Although amalgamation is inefficient for refractory ores, its widespread use in near-surface and alluvial contexts has resulted in repeated and diffuse inputs of mercury into ASGM landscapes/environments (e.g., **Esdaile & Chalker, 2018; Crespo-Lopez et al., 2021; Fritz et al., 2024; Nitschke et al., 2024**). Thus, the same geological, geomorphological, and hydrological conditions that favored gold accumulation and artisanal exploitation also indirectly controlled the spatial distribution and long-term persistence of mercury contamination, a topic approached in the following chapters.

3.3. Soil sampling, description and field observations

For this study, 73 surface soil samples (0–10 cm) were collected across four distinct contexts related to artisanal and small-scale gold mining (ASGM). These included an area where ASGM activities ceased approximately 30 years ago (n = 37), a recently deactivated area (January 2024; n = 15), an active ASGM area (n = 15), and an internal forest control area with no recorded ASGM activity (n = 6), selected for establishing a geogenic regional baseline for mercury in the study area (see Section 2.5.2).

In the field, marked spatial heterogeneity in soil physical properties, texture, color and moisture conditions across the sampled sites were observed, reflecting differences in ASGM history, hydrological setting and post-disturbance recovery.

In the area deactivated for approximately 30 years, soils ranged from fine-fraction–rich, brownish to reddish materials to coarse, sand-dominated substrates with abundant gravel and quartz-rich sediments. Several sampling points were located in humid or waterlogged microenvironments, particularly in topographic depressions and near small water bodies, where soils exhibited darker colors and locally elevated organic matter content. In contrast, better-drained areas were characterized by yellowish to rusty-colored sandy soils, often with gravel accumulation at the surface, indicative of mechanical reworking and sediment sorting during past mining operations. Such heterogeneity is exemplified in Figure 18.





Figure 18: Representative field photos illustrating the physical heterogeneity of soils in the ~30 years deactivated ASGM area. (A) MTBP-18: brownish soil with a noticeable fine fraction, collected in a waterlogged setting; (B) MTBP-23: yellowish, sand-dominated soil with abundant leaf litter at the surface; (C) MTBP-28: white, quartz-rich sediment with minimal fine material; and (D) MTBP-31: brownish sandy soil collected near a small water body. Together, these images highlight the strong variability in texture, color, moisture conditions and organic inputs that characterize post-mining soils within the study area.

Within this long-term deactivated area, secondary vegetation was variably developed and exerted a clear influence on surface soil characteristics. Sampling points located close to vegetation showed higher surface litter input, root presence and, in some cases, visibly finer textures, whereas more exposed zones remained dominated by coarse sandy materials with limited organic inputs. Locally, water-saturated conditions persisted despite the long deactivation period, highlighting the persistence of altered hydrological pathways and microtopography generated during ASGM activities (Figure 19).

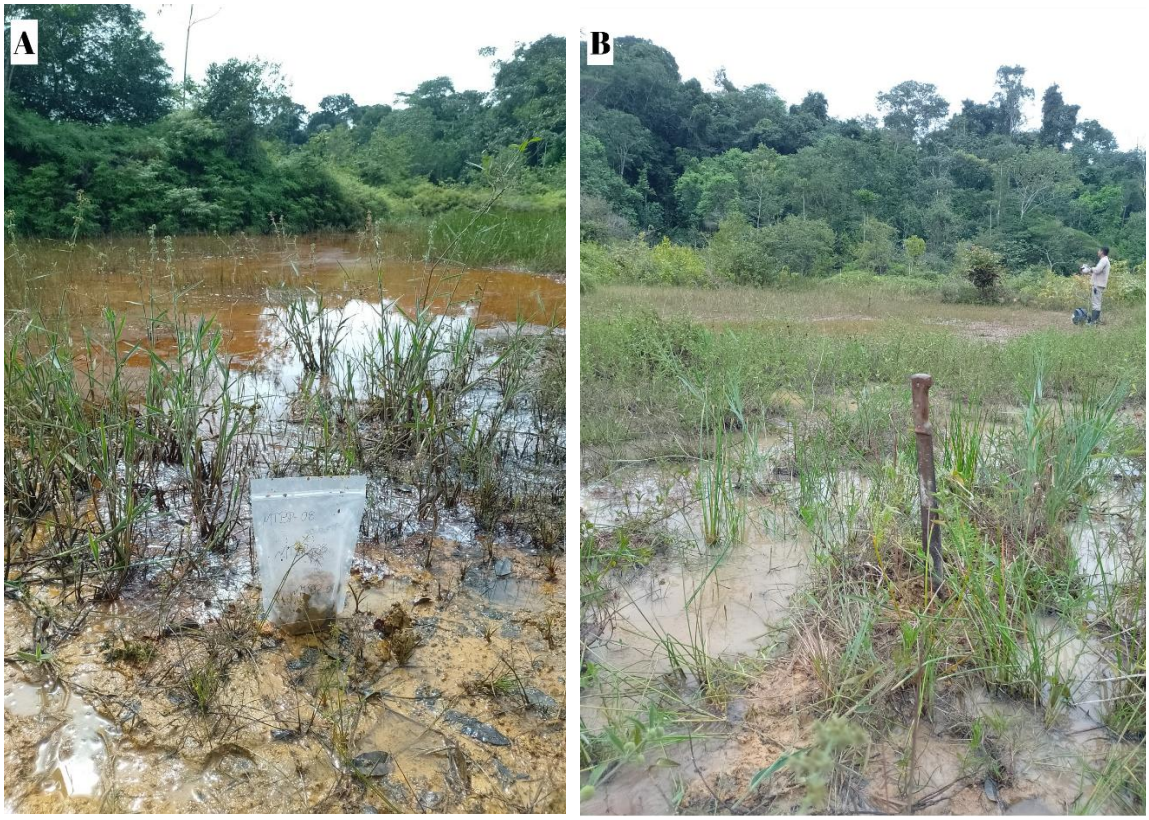


Figure 19: Waterlogged soils from low-lying areas of the ~30 years deactivated ASGM site. (A) MTBP-08 and (B) MTBP-17 illustrate saturated conditions controlled by local topography, highlighting moisture-driven heterogeneity within the study area.

Soils collected from sites without records of mining activity, located inside intact forest, displayed comparatively more homogeneous characteristics. These soils were predominantly brownish to rusty-colored, with clear evidence of organic horizons, abundant roots and surface litter, general dominance of sand fractions relative to the mined areas, as well as the absence of gravel. The more consistent presence of well-developed organic layers and stable forest structure contrasts with the physically disturbed profiles observed in ASGM-affected sites (Figure 20).



Figure 20: Representative forest soils from the site without ASGM records (control area). (A) MTBVP-02 and (B) MTBVP-04 illustrate textural and color variability under forest cover, with the presence of roots and litter highlighting organic matter–rich surface conditions.

The active ASGM site exhibited the highest degree of physical disturbance (Figure 21).





Figure 21: Figure 21: Landscape conditions of the studied active ASGM site. (A) deforestation for 'clearing' the site and (B) open pit for ASGM operations.

Soils were predominantly sandy to sand–gravel mixtures, often light beige to greyish in color, and strongly influenced by ongoing hydraulic processes. Some samples were collected along sluice box outflows, flooded pit margins and swamp-adjacent areas, where water saturation, rapid sediment redistribution and localized accumulation of fine materials were common. In these settings, organic matter was either largely absent due to erosion or, locally, concentrated in low-energy zones where fine sediments accumulated beneath plant debris and roots (Figure 22).


A
B



Figure 22: Field photos highlighting heterogeneity within the active ASGM site , highlighting the coexistence of contrasting microenvironments over short spatial scales. (A) MTPS-05 soil with a greyish color and clear predominance of fine particles (silt–clay), occurring beneath an organic layer, (B) MTPS-09 sediment dominated by coarse sand and gravel, collected near a swampy area, and (C) MTPS-13 greyish soil with high clay content, sampled below the sluice box.

Stagnant water was observed in the abandoned open pit within the site deactivated in January 2024, exhibiting a characteristic turquoise-blue coloration, suggesting low water pH and high dissolved metal loads associated with sulfide oxidation in mining environments (Figure 23A). Growth of secondary vegetation was also observed in some locations, particularly along stabilized surfaces (Figure 23B).



Figure 23: (A) Flooded abandoned open pit showing stagnant turquoise-colored water, indicative of acidic, metal-rich conditions in the site deactivated in January 2024. (B) Secondary vegetation re-stabilization after cessation of ASGM activities in the site deactivated in January 2024.

On the other hand, soils from this area showed intermediate soil characteristics between active and long-term deactivated areas. Particularly, these soils displayed brown to reddish colors, mixed sand and silt/clay textures, and frequent presence of gravel and oxide-rich grains (Figure 24). In addition, a clear spatial gradient was observed along drainage

pathways from flooded open pits, with coarser, gravel-rich materials near pit margins transitioning to finer-textured deposits downstream.





Figure 24: Representative soil samples from the ASGM site deactivated in January 2024. (A) MTNC-04, rusty-colored, sand-dominated soil with abundant gravel and visible oxide-rich grains, collected at the margin of the

flooded open pit, (B) sandy soil with gravel, oxide grains, showing accumulation of organic matter fragments, also sampled at the border of the flooded open pit, and (C) brownish soil with mixed silt/clay and sand fractions and absence of gravel, collected at the distal end of the open-pit drainage pathway.

For more details, see the complete field soil descriptions in Appendix 1. Overall, field observations indicate that ASGM activity produces long-lasting physical heterogeneity in tropical soils, expressed through contrasts in texture, moisture regime, organic matter distribution and surface morphology. Such heterogeneity is expected to generate microenvironments with distinct geochemical conditions, potentially exerting strong controls on mercury retention, mobility and post-depositional transformation processes.

APPENDIX 1: Complete field soil descriptions

ID	Area	Description	Observations
MTBP-01	~30 years deactivated	Brownish soil with a noticeable amount of fine fraction	High humidity, and close to the vegetation
MTBP-02	~30 years deactivated	Brownish soil with a noticeable amount of fine fraction	High humidity, and close to the vegetation
MTBP-03	~30 years deactivated	Brown/redish soil with a noticeable amount of fine fraction	High humidity, and close to the vegetation
MTBP-04	~30 years deactivated	Yellowish soil with a clear predominance of sandy fraction	Close to the vegetation
MTBP-05	~30 years deactivated	Sandy soil, with a light grey/yellowish color	Growth of secondary vegetation
MTBP-06	~30 years deactivated	Rusty-colored soil, humid, with noticeable presence of the fine fraction	Growth of secondary vegetation
MTBP-07	~30 years deactivated	Sandy yellowish soil, with presence of gravel	Water-saturated in the field, close to secondary vegetation
MTBP-08	~30 years deactivated	Yellowish soil with a noticeable amount of fine fraction	Waterlogged area, secondary vegetation
MTBP-09	~30 years deactivated	Reddish soil, with noticeable predominance of the sandy fraction and presence of gravel	Secondary vegetation in the surroundings
MTBP-10	~30 years deactivated	Rusty-colored soil with a clear predominance of sandy fraction, with presence of gravel on the soil surface	-
MTBP-11	~30 years deactivated	Rusty-colored soil with a clear predominance of sandy fraction, with presence of gravel on the soil surface	-
MTBP-12	~30 years deactivated	Rusty-colored soil with a clear predominance of sandy fraction, with presence of gravel on the soil surface	Close to the vegetation
MTBP-13	~30 years deactivated	Rusty-colored soil with a clear predominance of sandy fraction, with presence of gravel on the soil surface	Close to the vegetation
MTBP-14	~30 years deactivated	Brownish soil, with a clear predominance of sandy fraction, and gravel on the surface	Close to the vegetation
MTBP-15	~30 years deactivated	Rusty-colored soil, with a clear predominance of sandy fraction, and gravel on the surface	Close to the vegetation
MTBP-17	~30 years deactivated	Brownish soil with a noticeable amount of fine fraction	Waterlogged area, secondary vegetation
MTBP-18	~30 years deactivated	Brownish soil with a noticeable amount of fine fraction	Waterlogged area
MTBP-19	~30 years deactivated	Brownish soil with a noticeable amount of fine fraction	Waterlogged area
MTBP-20	~30 years deactivated	Reddish soil with a noticeable amount of fine fraction	Waterlogged area, close to the vegetation
MTBP-21	~30 years deactivated	Reddish soil with a noticeable amount of fine fraction	Close to the vegetation
MTBP-22	~30 years deactivated	Reddish soil with a noticeable amount of fine fraction	Close to the vegetation
MTBP-23	~30 years deactivated	Yellowish soil with a clear predominance of sandy fraction	High presence of leaves on the surface

MTBP-24	~30 years deactivated	Yellowish soil with a clear predominance of sandy fraction	High presence of leaves on the surface
MTBP-25	~30 years deactivated	Brownish soil with a noticeable amount of fine fraction	Secondary vegetation
MTBP-26	~30 years deactivated	Rusty-colored soil with a noticeable amount of fine fraction	Secondary vegetation
MTBP-27	~30 years deactivated	White quartz-rich sediment	Close to the vegetation
MTBP-28	~30 years deactivated	White quartz-rich sediment	Close to the vegetation
MTBP-29	~30 years deactivated	Brownish soil with a noticeable predominance of the sandy fraction	Close to the vegetation
MTBP-30	~30 years deactivated	Brownish soil with a noticeable amount of fine fraction	Close to the vegetation
MTBP-31	~30 years deactivated	Brownish sandy soil	Close to a small water body
MTBP-32	~30 years deactivated	Brownish sandy soil with a noticeable amount of fine fraction	Close to a small water body
MTBP-33	~30 years deactivated	Brownish sandy soil	-
MTBP-34	~30 years deactivated	Brownish soil with a noticeable amount of fine fraction	Close to the vegetation
MTBP-35	~30 years deactivated	Brownish soil with a noticeable amount of fine fraction	Waterlogged area, with high OM content, close to the vegetation
MTBP-36	~30 years deactivated	Brownish sandy soil	Close to the vegetation
MTBP-37	~30 years deactivated	Brownish soil with a noticeable amount of fine fraction	Close to a small water body, with high OM content, close to the vegetation
MTBP-38	~30 years deactivated	Brownish soil with a noticeable amount of fine fraction	Close to the vegetation
MTBVP-01	Without records	Rusty-colored soil, with predominance of coarser minerals (quartz)	Inside the forest, presence of roots and litter
MTBVP-02	Without records	Brownish soil	Inside the forest, presence of roots and litter
MTBVP-03	Without records	Brown to redish soil	Inside the forest, presence of roots and litter
MTBVP-04	Without records	Rusty-colored soil, with predominance of coarser minerals (quartz)	Inside the forest, presence of roots and litter
MTBVP-05	Without records	Rusty-colored soil, with noticeable O horizon	Inside the forest, presence of roots and litter
MTBVP-06	Without records	Rusty-colored soil, with noticeable O horizon	Inside the forest, presence of roots and litter
MTPS-01	Active	Dark beige-colored, predominantly sand	In the boarders of a flooded area, with presence of OM
MTPS-02	Active	Dark beige-colored, predominantly sand	In the boarders of a flooded area, with presence of OM
MTPS-03	Active	Beige-colored, predominantly sand	In the boarders of a flooded area, with presence of OM and occurence of gravel
MTPS-04	Active	Brownish soil with a present O horizon	Within the forest, and nearby a flooded area, strong presence of roots

MTPS-05	Active	Grey soil, with predominance of finer fraction (silt/clay)	Below considerable organic matter content, with strong presence of roots, litter, etc.
MTPS-06	Active	-	-
MTPS-07	Active	Beige-colored, predominantly sand	Located where the water from the sluice box flows, presence of gravel
MTPS-08	Active	Beige-colored, predominantly sand	Located where the water from the sluice box flows, presence of gravel, close to the forest
MTPS-09	Active	Sand/gravel predominant	Close to a swamp
MTPS-10	Active	White quartz-rich sediment	In the boarders of the ASGM, close to the vegetation
MTPS-11	Active	White quartz-rich sediment with presence of gravel	In the boarders of the ASGM, close to the vegetation
MTPS-12	Active	Greyish soil	-
MTPS-13	Active	Greyish soil, high presence of clay	Below the sluice box
MTPS-14	Active	Greyish soil	-
MTPS-15	Active	Greyish soil	Close to the boarders of the open pit
MTNC-01	Deactivated in January 2024	Brownish soil, presence of clay, and with noticeable presence of quartz	Secondary vegetation growing
MTNC-02	Deactivated in January 2024	Brownish soil, presence of clay, and with noticeable presence of quartz	Secondary vegetation growing
MTNC-03	Deactivated in January 2024	Brownish soil, presence of clay, and with noticeable presence of quartz	Close to the river, lower height
MTNC-04	Deactivated in January 2024	Rusty-colored soil, predominance of sand fraction, presence of gravel, and presence of oxide grains	Boarder of the flooded open pit
MTNC-05	Deactivated in January 2024	Brown-to-redish-colored soil, predominance of sand fraction, presence of gravel, and presence of oxide grains	Boarder of the flooded open pit
MTNC-06	Deactivated in January 2024	Rusty-colored soil, predominance of sand fraction, presence of gravel, and presence of oxide grains	Boarder of the flooded open pit
MTNC-07	Deactivated in January 2024	Brown-to-redish-colored soil, presence of gravel, and presence of oxide grains, high heterogeinity in terms of grain size	Starting point of the drainage from the open pit
MTNC-08	Deactivated in January 2024	Brown-to-redish-colored soil, presence of gravel, and presence of oxide grains, high heterogeinity in terms of grain size	Drainage from the open pit
MTNC-09	Deactivated in January 2024	Brownish-colored soil, silt/clay and sand predominance (absence of gravel)	Ending point of the drainage from the open pit
MTNC-10	Deactivated in January 2024	Brownish-colored soil, silt/clay and sand predominance (absence of gravel)	Ending point of the drainage from the open pit

MTNC-11	Deactivated in January 2024	Brown sand	Close to the river
MTNC-12	Deactivated in January 2024	Brown sand	Close to the vegetation, presence of litter, roots, etc.
MTNC-13	Deactivated in January 2024	Redish-colored soil, silt/clay and sand predominance (absence of gravel)	-
MTNC-14	Deactivated in January 2024	Brownish-colored soil, silt/clay and sand predominance, presence of gravel	-
MTNC-15	Deactivated in January 2024	Rusty-colored soil, predominance of sand fraction, presence of gravel, and presence of oxide grains	Boarder of the flooded open pit

References

Anand, R.R., Butt, C.R.M., Salama, W.S., Porto, C.G., 2025. Supergene Gold Deposits in Intensely Weathered Regolith. In: Bowell, R.J., Butt, C.R.M. (eds) Geology, Geochemistry and Formation of Supergene Mineral Deposits in Deeply Weathered Terrain. Mineral Resource Reviews. Springer, Cham. https://doi.org/10.1007/978-3-031-75733-4_6

Alfonso, P., Anticoi, H., Yubero, T., Bascompta, M., Henao, L., Garcia-Valles, M., Palacios, S., & Yáñez, J., 2019. The importance of mineralogical knowledge in the sustainability of artisanal gold mining: A mid-south Peru case. Minerals, 9(6), 345. https://doi.org/10.3390/min9060345

Carrança, T. & Schreiber, M., 2024. A vida das mulheres que trocam sexo por ouro na Amazônia. BBC News Brasil, 05 Dec 2024. Available at: https://www1.folha.uol.com.br/cotidiano/2024/12/a-vida-das-mulheres-que-trocam-sexo-por-ouro-na-amazonia.shtml. Accessed: 6 Feb 2026.

CPRM – Serviço Geológico do Brasil, 2004. Carta Geológica do Brasil ao Milionésimo: Tapajós: folha SB.21 [Geological map, GIS]. CPRM, Brasília. Scale 1:1,000,000. Programa Geologia do Brasil. Available at: https://rigeo.sgb.gov.br/handle/doc/4975. Accessed: 6 Feb 2026.

Crespo-Lopez, M. E., Augusto-Oliveira, M., Lopes-Araújo, A., Santos-Sacramento, L., Takeda, P. Y., de Matos Macchi, B., Nascimento, J. L. M., Maia, C. S. F., Lima, R. R., & Arrifano, G. P. (2021). Mercury: What can we learn from the Amazon?. Environment International, 146, 106223. https://doi.org/10.1016/j.envint.2020.106223.

Esdaile, L. J., & Chalker, J. M., 2018. The mercury problem in artisanal and small-scale gold mining. Chemistry–A European Journal, 24(27), 6905-6916. https://doi.org/10.1002/chem.201704840.

Fórum Brasileiro de Segurança Pública, 2024. A nova corrida do ouro na Amazônia: garimpo ilegal e violência na floresta. Fórum Brasileiro de Segurança Pública, São Paulo. Available at: https://publicacoes.forumseguranca.org.br/handle/123456789/248. Accessed: 6 Feb 2026.

Fórum Brasileiro de Segurança Pública, 2025. 19º Anuário Brasileiro de Segurança Pública. Fórum Brasileiro de Segurança Pública, São Paulo. Available at: https://publicacoes.forumseguranca.org.br/handle/123456789/279. Accessed: 6 Feb 2026.

Guimaraes, S. B., Klein, E. L., Harris, C., Costa, I. S. L., 2021. Metallogenesis of the orosirian epithermal coringa gold-silver (Cu-Pb-Zn) deposit, southeastern Tapajós mineral Province, Amazonian craton, Brazil. Ore Geology Reviews, 128, 103908. https://doi.org/10.1016/j.oregeorev.2020.103908.

Hodgson, C. J., 1989. The structure of shear-related, vein-type gold deposits: a review. Ore Geology Reviews, 4(3), 231-273. https://doi.org/10.1016/0169-1368(89)90019-X.

IBGE, n.d. Itaituba (PA) — Overview. Brazilian Institute of Geography and Statistics (Instituto Brasileiro de Geografia e Estatística). Available at: https://cidades.ibge.gov.br/brasil/pa/itaituba/panorama. Accessed: 6 Feb 2026.

IBGE, 2002. Climate map of Brazil [Map]. Scale 1:5,000,000. Brazilian Institute of Geography and Statistics. Available at: https://www.ibge.gov.br/geociencias/cartas-e-mapas/informacoes-ambientais/15817-clima.html?edicao=15887&t=acesso-ao-produto. Accessed: 6 Feb 2026.

Ilyas, S., & Lee, J. C., 2018. Artisanal Gold Mining and Amalgamation. In Gold Metallurgy and the Environment (pp. 29-50). CRC Press.

INMET, n.d. Gráfico anual da estação convencional Itaituba (A231). National Institute of Meteorology. Available at: https://tempo.inmet.gov.br/GraficosAnuais/A231. Accessed: 6 Feb 2026.

INMET, 2022. Normais climatológicas do Brasil: 1991–2020. National Institute of Meteorology. Available at: https://portal.inmet.gov.br/normais#. Accessed: 6 Feb 2026.

Juliani, C., Assis, R. R., Monteiro, L. V. S., Fernandes, C. M. D., Martins, J. E. Z. S., & Costa, J. R. C., 2021. Gold in paleoproterozoic (2.1 to 1.77 Ga) continental magmatic arcs at the Tapajós and Juruena mineral provinces (amazonian craton, Brazil): a new frontier for the exploration of epithermal–porphyry and Related deposits. Minerals, 11(7), 714. https://doi.org/10.3390/min11070714.

Klein, E. L., Rodrigues, J. B., Queiroz, J. D., Oliveira, R. G., Guimarães, S. B., & Chaves, C. L., 2016. Deposition and tectonic setting of the Palaeoproterozoic Castelo dos Sonhos metasedimentary formation, Tapajós Gold Province, Amazonian Craton, Brazil: age and isotopic constraints. International Geology Review, 59(7), 864-883. https://doi.org/10.1080/00206814.2016.1237311.

Lobato, L. M., Costa, M. A., Hagemann, S. G., Martins, R., 2016. Ouro no Brasil: principais depósitos, produção e perspectivas. Recursos minerais no Brasil: problemas e desafios. Rio de Janeiro, Academia Brasileira de Ciências, 46-59. Available at: https://www.researchgate.net/profile/Maisa-Abram/publication/328839006_Fosfato_no_Brasil/links/5be5b5324585150b2baa6e63/Fosfato-no-Brasil.pdf#page=47.

Lobo, F. D. L., Costa, M., Novo, E. M. L. D. M., & Telmer, K., 2016. Distribution of artisanal and small-scale gold mining in the Tapajós River Basin (Brazilian Amazon) over the past 40 years and relationship with water siltation. Remote Sensing, 8(7), 579. https://doi.org/10.3390/rs8070579.

Lopes, A. A. C., & Moura, M. A., 2019. The Tocantinzinho Paleoproterozoic porphyry-style gold deposit, Tapajós Mineral Province (Brazil): Geology, petrology and fluid inclusion evidence for ore-forming processes. Minerals, 9(1), 29. https://doi.org/10.3390/min9010029.

Nitschke, N., Guédron, S., Tessier, E., Tisserand, D., Campillo, S., & Amouroux, D. (2024). Evaluation of the Hg Contamination from Gold Mining in French Guiana at the Watershed Scale Using Hg Isotopic Composition in River Sediments. ACS ES&T Water, 4(8), 3443-3452. https://doi.org/10.1021/acsestwater.4c00270.

Pessoa, M. R., Santiago, A. F., Andrade, A. F. D., Nascimento, J. O. D., Santos, J. O. S., Oliveira, J. R. D., Lopes, R. C., & PRAZERES, W. V., 1977. Projeto Jamanxim: relatório final. CPRM.

Potter, H., 2023. Tráfico e garimpo ilegal compartilham aviões e pilotos para lavar dinheiro na Amazônia. Repórter Brasil, 18 Sep 2023. Available at: https://reporterbrasil.org.br/2023/09/trafico-e-garimpo-ilegal-compartilham-avioes-e-pilotos-para-lavar-dinheiro-na-amazonia/. Accessed: 6 Feb 2026.

Santos, J. O. S., Groves, D. I., Hartmann, L. A., Moura, M. A., & McNaughton, N. J., 2001. Gold deposits of the Tapajós and Alta Floresta Domains, Tapajós–Parima orogenic belt, Amazon Craton, Brazil. Mineralium deposita, 36(3), 278-299. https://doi.org/10.1007/s001260100172.

Serabi Gold plc, 2025. Palito Mining Complex: NI 43-101 Technical Report, Pará State, Brazil. Report date: 10 Sep 2025. Available at: https://wp-serabi-2023.s3.eu-west-2.amazonaws.com/media/2025/09/NI-43-101_Palito-Complex_20250910.pdf. Accessed: 6 Feb 2026.

Sial, A. N., Dall'Agnol, R., Ferreira, V. P., Nardi, L. V., Pimentel, M. M., & Wiedemann, C. M., 1999. Precambrian granitic magmatism in Brazil. Episodes Journal of International Geoscience, 22(3), 191-198. https://doi.org/10.18814/epiiugs/1999/v22i3/006.

Sillitoe, R. H., & Thompson, J. F., 2008. Intrusion–related vein gold deposits: types, tectono-magmatic settings and difficulties of distinction from orogenic gold deposits. Resource Geology, 48(4), 237-250. https://doi.org/10.1111/j.1751-3928.1998.tb00021.x.

Tassinari, C. C., & Macambira, M. J., 1999. Geochronological provinces of the Amazonian Craton. Episodes Journal of International Geoscience, 22(3), 174-182. https://doi.org/10.18814/epiiugs/1999/v22i3/004.

Teixeira, W., Tassinari, C. C. G., Cordani, U. G., & Kawashita, K., 1989. A review of the geochronology of the Amazonian Craton: tectonic implications. Precambrian Research, 42(3-4), 213-227. https://doi.org/10.1016/0301-9268(89)90012-0.

Trindade, A. R., & Barbosa Filho, A. M., 2002. Extração de ouro: princípios, tecnologia e meio ambiente. Departamento Nacional de Produção Mineral / CETEM. Available at: http://mineralis.cetem.gov.br/bitstream/cetem/687/1/extracao-ouro.pdf. Accessed: 6 Feb 2026.

Valeton, I., 1994. Element concentration and formation of ore deposits by weathering. Catena, 21(2-3), 99-129. https://doi.org/10.1016/0341-8162(94)90006-X.

Vaughan, J.P., 2004. The process mineralogy of gold: The classification of ore types. JOM 56, 46–48. https://doi.org/10.1007/s11837-004-0092-8.

Veiga, M. M., Angeloci-Santos, G., & Meech, J. A., 2014. Review of barriers to reduce mercury use in artisanal gold mining. The Extractive Industries and Society, 1(2), 351-361. https://doi.org/10.1016/j.exis.2014.03.004.

Veiga, M. M., & Gunson, A. J., 2020. Gravity concentration in artisanal gold mining. Minerals, 10(11), 1026. https://doi.org/10.3390/min10111026.

Vishiti, A., Etame, J., & Suh, C. E., 2019. Features of gold-bearing quartz veins in an artisanal mining-dominated terrain, Batouri gold district, Eastern region of Cameroon. Episodes Journal of International Geoscience, 42(3), 199-212. https://doi.org/10.18814/epiiugs/2019/019016.

Zhou, J., Jago, B., Martin, C., & Lakefield, S. G. S., 2004. Establishing the process mineralogy of gold ores. Technical bulletin, 3. Available at: https://www.sgs.fi/~/media/Global/Documents/Technical%20Documents/SGS%20Technical%20Papers/SGS%20MIN%20TP2004%2003%20Process%20Mineralogy%20of%20Gold%20Ores.pdf. Accessed: 6 Feb 2026.

4. Legacy and ongoing mercury contamination in soils from ASGM sites in the Tapajós Gold Province, Pará, Brazil

Artisanal and small-scale gold mining (ASGM) has resulted in long-term mercury (Hg) contamination in soils throughout the Brazilian Amazon. Although the environmental impacts of active ASGM sites have been widely investigated, less attention has been given to the persistence, redistribution, and controlling factors of mercury in areas where mining activities have been discontinued. Assessing mercury behavior in post-ASGM landscapes is essential for understanding long-term ecological risks and for guiding environmental management in historically mined regions.

This chapter corresponds to a manuscript submitted to the journal *Soil and Sediment Contamination*. With the exception of the present introductory section, the text is incorporated into this thesis with minor editorial adjustments made exclusively to ensure coherence with the structure and formatting of the doctoral dissertation. In this section, total mercury (THg) concentrations in surface soils are reported for three ASGM sites in the Tapajós region, Brazilian Amazon: (i) an active mining site, (ii) a recently deactivated site (2024), and (iii) an area deactivated for approximately 30 years.

The manuscript applies contamination and ecological risk indices to characterize mercury enrichment and evaluates the influence of soil physical properties, particularly fine particle content, on mercury distribution. By comparing sites with contrasting mining histories, the study directly addresses a critical knowledge gap concerning the long-term persistence of mercury in tropical soils after the cessation of ASGM activities. The results

demonstrate that historically mined areas may retain substantial mercury concentrations decades after abandonment, highlighting the role of soil texture and other matrix-related characteristics in controlling mercury retention and potential remobilization.

The findings of this chapter extend current understanding of mercury dynamics beyond active ASGM sites by demonstrating the long-term persistence of contamination in deactivated areas. They emphasize the role of substrate characteristics in controlling contamination patterns and ecological risk, and point to the need for further investigation of the mineralogical, geochemical, and organic controls on mercury stability and mobility in Amazonian soils.

4.1. Introduction

Mercury (Hg) is a highly toxic heavy metal with significant environmental and health impacts. It can be released into the environment from both natural and anthropogenic sources, with the latter being the primary contributor **(Yang et al., 2020)**. While geogenic sources contribute to Hg emissions, high concentrations in the Amazon are typically attributed to its use in artisanal and small-scale gold mining (ASGM) as an amalgam to extract gold (e.g., **Crespo-Lopez et al., 2021; Fritz et al., 2024; Nitschke et al., 2024**). In addition, these operations contribute directly to deforestation, as vegetation is cleared to enable mining activities. Deforestation exposes soil, increasing erosion rates and enhancing the transport of both anthropogenic and geogenic Hg into water bodies, surrounding soils, and atmosphere **(Siqueira et al., 2018; Fisher et al., 2023)**. Regardless of its origin, Hg has the potential to impact various environmental matrices, including soils, sediments, and water bodies, as well as wildlife (both plants and animals) and human health **(Espiritu et al., 2022; Gyamfi et al., 2021; Wilman et al., 2023; Pisconte et al., 2024)**.

Within this scenario, the international community adopted the Minamata Convention on Mercury, aiming to control the supply and trade of Hg, limit its use, and reduce its release into the environment **(UNEP, 2013)**. Even before ratifying the Convention in 2017, Brazil had already implemented national regulations to restrict and monitor mercury use, such as Decree No. 97,507/1989 **(Brazil, 1989a)** and Decree No. 97,634/1989 **(Brazil, 1989b)**. Following the Convention, additional measures were introduced to support the country's commitments, including Normative Instruction No. 08/2015 **(IBAMA, 2015)** and Ordinance No. 175/2021 **(MMA, 2021)**. However, despite these regulations, the ongoing irregular and illegal ASGM activities continue to threaten both ecosystem integrity and human health in the Brazilian Amazon. This persistence is tied to its historical and cultural roots, as ASGM developed independently from industrial mining, became the dominant mode of gold extraction **(de Theije, 2020)**, and is now a central part of Brazil's social reality—frequently discussed in environmental and political debates due to its informal and often illegal character **(Araujo et al., 2025)**.

Several studies have documented Hg contamination associated with ASGM in the Brazilian Amazon, particularly in sediments and soils (e.g., **Windmöller et al., 1996**; **Gonçalves et al., 2000; Egler et al., 2006; Teixeira et al., 2021; Jacques et al., 2023; Soares et al., 2024**). These studies have demonstrated that Hg concentrations often exceed the soil prevention level of 500 ng g^{-1}, established by the Brazilian National Environmental Council **(CONAMA, 2009)** to safeguard soil functionality and water quality. Furthermore, diverse studies have shown that (geo)environmental factors such as soil composition and vegetation cover influence the transport and fate of mercury in these systems **(**e.g., **Zhang et al., 2015; Debure et al., 2020; Diringer et al., 2020; Gómez-Armesto et al., 2020; Licht, 2020; Rodrigues et al., 2022; Lima et al., 2023; Liu et al., 2023; Qin et al., 2023; Sonke et al., 2023; Feinberg et al., 2024; McLagan et al., 2024; Soares et al., 2024)**.

While these findings have contributed to a broad understanding of ASGM-related Hg pollution, significant questions remain regarding the persistence of contamination in abandoned sites and the role of soil properties in Hg retention.

Although numerous studies have examined mercury contamination in ASGM areas within the Brazilian Amazon (e.g., **Teixeira et al., 2021; Jacques et al., 2023; Quintarelli et al., 2024**), few have focused specifically on sites that have been deactivated for decades, limiting our understanding of contamination persistence and spatial variability in former ASGM sites. In particular, the role of substrate characteristics, such as particle size distribution, in mercury retention remains poorly understood in these contexts. Addressing this gap is essential to inform risk assessment and guide remediation strategies in post-mining landscapes. Within this scenario, this study aims to evaluate the extent and persistence of mercury contamination in soils across three different ASGM sites in the Tapajós region, Brazilian Amazon: (I) active, (II) recently deactivated, and (III) deactivated for approximately 30 years. Specifically, we quantified total mercury (THg) concentrations in surface soils across the different ASGM contexts, assessed contamination and ecological risk indices (*i.e.*, I_{geo}, CF, and Er) **(Müller, 1979; Hakanson, 1980)**, and explored the influence of the proportion of fine particles on THg retention in the ASGM deactivated for approximately 30 years. We hypothesized that sites deactivated for longer periods would exhibit lower THg concentrations, influenced both by the time since mining activities ended and by the soil's capacity to retain mercury. By comparing active and inactive sites, we seek to better understand both the ongoing impacts of ASGM and the long-term environmental legacy of Hg use.

4.2. Materials and methods

4.2.1. Study area

The present study was conducted in April 2024, in the surroundings of Jardim do Ouro district (6°15'17.58"S, 55°46'8.90"W), located within the municipality of Itaituba in Pará State (Figure 25). Itaituba is considered the largest municipality in terms of ASGM extension (710 km²) in Brazil (**Neto et al., 2024**), being infamously known by its intense illegal ASGM activities **(Queiroz et al., 2022)**.

The region is characterized by tropical rainforest vegetation and lies within the Amazon biome. The climate is classified as warm and humid, with averages above 18 ºC in all months of the year and from one to three months of drought **(IBGE, 2002)**. Specifically, between 1991 and 2020, the annual average temperature in the municipality of Itaituba was 27.6 ºC **(INMET, 2022)**. During this period, Itaituba recorded an average of 8 days per year with precipitation exceeding 50 mm/day (all occurring between November and May), and 225 days per year with precipitation below 1 mm/day (primarily between July and October) **(INMET, 2022)**. Additionally, in 2024, when this study was conducted, the minimum and maximum temperatures were registered in August (22.49 ºC) and September (36.34 ºC), respectively **(INMET, n.d.)**. Days with precipitation above 50 mm/day occurred between November and May, while precipitation was typically below 10 mm/day from June to September **(INMET, n.d.)**.

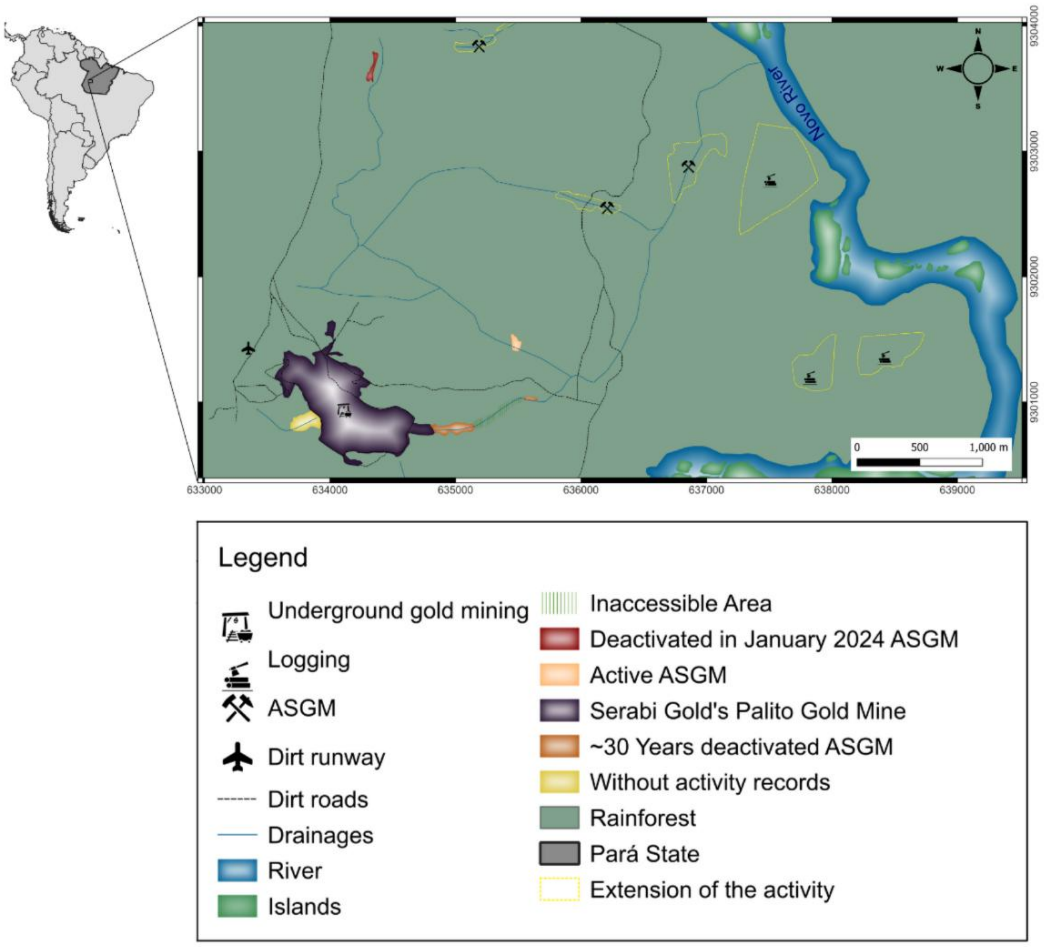


Figure 25: Location map of the study area, generated using WGS84/UTM Zone 21S, EPSG: 32721, with units in meters.

4.2.2. Soil sampling

A total of 73 soil samples (~300 g, 0—10 cm deep) were collected in April 2024 from three ASGM sites: (I) a site deactivated for approximately 30 years (n = 37); (II) a site deactivated in January 2024 (n = 15); and (III) an active site (n = 15). Additionally, six samples were collected from an area with no recorded ASGM activity to serve as background controls.

Samples were collected using an acrylic trowel, which was thoroughly cleaned between each sampling to prevent cross-contamination. Subsequently, the samples were stored in stand-up pouches.

4.2.3. Sample preparation and analysis

Aliquots of approximately 150 g of the soil samples were homogenized, frozen, and then lyophilized. After lyophilization, the samples were ground manually using an agate mortar.

The mass fraction of Hg in soil samples was determined by atomic absorption spectrometry. Measurements were performed at the LAGEOQ Laboratory of the Institute of Geosciences, State University of Campinas (UNICAMP), using a Mercury Analyzer (Ohio Lumex RA-915M/PYRO-915), previously calibrated with varying mass portions of the certified reference material NIST SRM 2709 (San Joaquin Soil). The estimated detection limit of the method is 1.0 ng g^{-1}, with values near this threshold showing low precision. The estimated measurement repeatability, based on duplicate results, was 2.3%.

The ASGM deactivated for approximately 30 years was selected for particle-size separation to investigate the potential relationship between grain size and total mercury (THg) concentrations, given the wide variability in THg levels observed at this site. Samples were dry-sieved using a sieve tower, and sieves were cleaned with an ultrasonic bath after each sample treatment to avoid cross-contamination. To estimate the proportion of fine particles (<105 µm), each sample was weighed prior to sieving, and the fine fraction (<105 µm) was weighed separately after sieving.

4.2.4. Data analysis

Statistical analyses were performed in R (*v4.3.1*; **R Core Team, 2023**) to assess differences in log-transformed THg concentrations among the three study areas (plus the reference one) using ANOVA, followed by Tukey-Kramer post hoc tests to account for unequal

sample sizes with *multcomp* package **(Hothorn et al., 2008)**. Assumptions of normality were verified via Shapiro-Wilk tests.

Hierarchical cluster analysis (HCA) was applied to log-transformed THg concentrations to identify concentration-based groupings within each study area. For each area independently, the optimal number of clusters (k) was determined using the silhouette width method. After clustering, the minimum log-transformed THg value for each cluster was identified and slightly adjusted (−0.05) to define threshold boundaries between clusters. These values were then back-transformed to the original scale (ng g^{-1}) to determine the concentration limits distinguishing groups. The resulting limits were used to draw vertical dashed lines in the cluster plot, enabling visual comparison of intra- and inter-area patterns.

The relationship between THg and fine particle content (<105 μm) was evaluated using linear regression.

4.2.5. Geostatistical analysis

Due to the insufficient spatial density and structural arrangement of the sampling points, the use of kriging was not considered appropriate for this study. Instead, the inverse distance weighting (IDW) was adopted as a more suitable interpolation technique, given its flexibility in handling sparse and unevenly distributed datasets. Spatial distribution of THg in the studied areas was then assessed through IDW interpolation using *gstat* (*v2.1.1*; **Pebesma, 2004; Gräler et al., 2016**) and *raster* (*v3.6-26*; **Hijmans, 2023**) packages, and maps were refined in QGIS (*v3.32.3*; **QGIS Development Team, 2023**).

For the active ASGM dataset, an IDP of 2.5 was applied to ensure a balance between capturing local variations and representing broader spatial patterns. In the first portion of the ~30 years deactivated ASGM dataset (*i.e.*, southwestern part in Figure 27A), an IDP of 3 was

selected to reduce the influence of extreme values and to produce a smoother interpolation surface. In contrast, the second portion of this dataset, characterized by a smaller number of samples and high variability, was interpolated using an IDP of 1.75, which allowed for greater emphasis on local differences. For the recently deactivated ASGM dataset, an IDP of 1.8 was chosen to highlight short-distance variations while still preserving overall spatial continuity.

4.2.6. Contamination and ecological risk indices

To calculate the contamination and ecological risk indices, we assumed 178.25 ng g^{-1} as the THg background (*i.e.*, the median of the samples collected within the forest—an area without records of ASGM activities). This value was chosen due to the absence of natural background data for the region and reflects the least-impacted conditions observed in the study area. Additionally, it is consistent with other soil background THg concentrations previously reported in the Brazilian Amazon (e.g., **Fadini & Jardim, 2001; Lima et al., 2022; Sahoo et al., 2023**).

The choice of the median, rather than the arithmetic mean, as the background estimator is supported by the observed asymmetry (*i.e.*, positively skewed) in the distribution of THg concentrations in forest soils **(Supplementary Figure 1)**. This positive skewness is a common feature in geochemical datasets influenced by natural heterogeneity or diffuse contamination sources **(Licht, 2020)**. In such cases, the median provides a more robust and unbiased estimate, as it is less sensitive to high-end values that can disproportionately affect the mean. This approach follows the recommendations of **Licht (2020)**, who emphasizes that in skewed distributions, the use of the median is statistically more appropriate than the mean for defining geochemical background levels.

Although some degree of contamination may still be present, this approach provides a consistent local reference for the calculation of contamination and ecological risk indices. All index calculations were performed using routines implemented in R software.

4.2.6.1. Geoaccumulation index (I_{geo})

The geoaccumulation index (I_{geo}) was used to assess the degree of Hg contamination in the samples. It was calculated according to **Equation 1** proposed by **Müller (1979)**.

$$I_{geo} = \log_2\left(\frac{C_n}{1.5 \cdot B_n}\right) \quad (1)$$

Where C_n is the THg concentration in the sample, 1.5 is the factor compensating the background content due to lithogenic effects, and B_n is the THg geochemical background. The I_{geo} is classified as follows: $I_{geo} \leq 0$ (uncontaminated), $0 < I_{geo} \leq 1$ (uncontaminated to moderately contaminated), $1 < I_{geo} \leq 2$ (moderately contaminated), $2 < I_{geo} \leq 3$ (moderately to heavily contaminated), $3 < I_{geo} \leq 4$ (heavily contaminated), $4 < I_{geo} \leq 5$ (heavily to extremely contaminated), $5 < I_{geo} \leq 6$ (extremely contaminated).

4.2.6.2. Contamination factor (CF) and ecological risk index (Er)

The contamination factor (CF) is calculated as the ratio between the concentration of a given metal in the sample and its respective background value **(Equation 2)**. It reflects the degree to which metal concentrations are elevated relative to natural baseline levels. CF is also a component of the potential ecological risk index (Er), as proposed by **Hakanson (1980)**,

which is determined by multiplying the CF by the toxic-response factor (Tr) of the element (e.g., 40 for Hg) **(Equation 3)**.

$$CF = \frac{C_{sample}}{C_{background}} \quad (2)$$

$$Er = CF \cdot Tr \quad (3)$$

Similarly to the I_{geo}, but without accounting for geochemical background variability, the CF is used to classify the contamination of soils and sediments as follows: $CF < 1$ (low), $1 \leq CF < 3$ (moderate), $3 \leq CF < 6$ (considerable), and $CF > 6$ (very high) **(Hakanson, 1980; Dantas et al., 2025)**. On the other hand, the potential ecological risks (Er) are classified as low ($Er < 40$), moderate ($40 \leq Er < 80$), considerable ($80 \leq Er < 160$), high ($160 \leq Er < 320$), and very high ($Er \geq 320$) **(Hakanson, 1980; Ferreira et al., 2022; Dantas et al., 2025)**.

4.3. Results

4.3.1. Total mercury (THg)

The THg concentrations were notably higher in the site deactivated for approximately 30 years compared to the other studied sites (Figure 26).

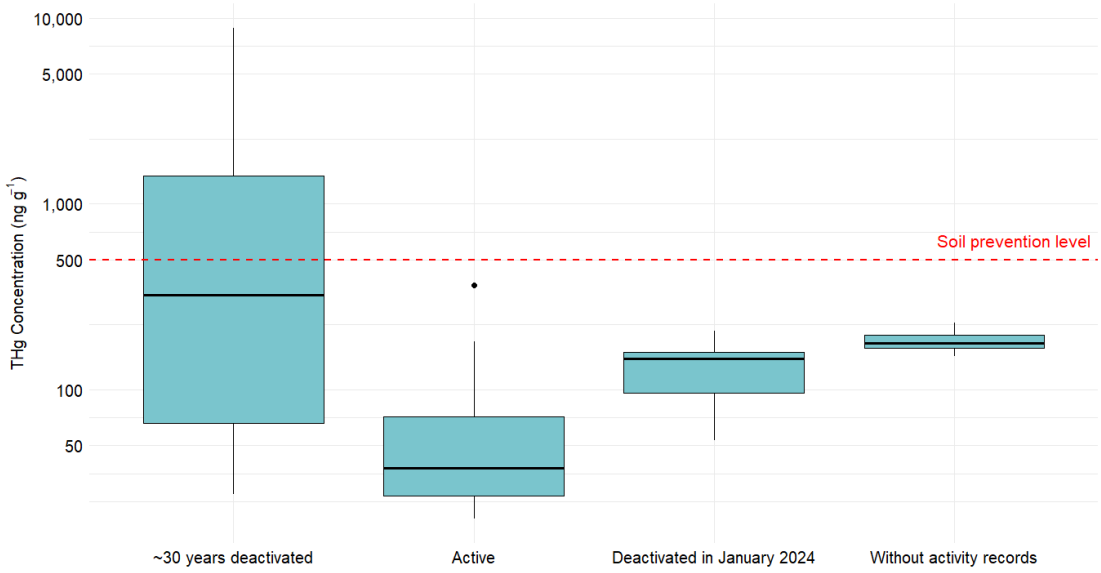
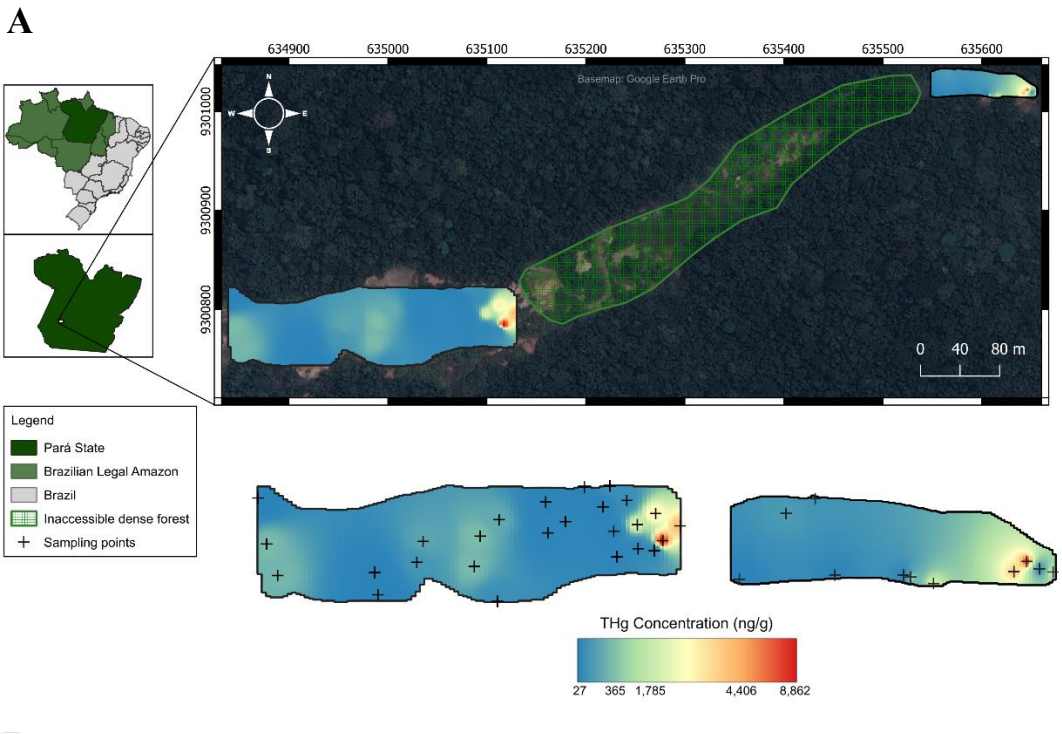


Figure 26: Boxplot of total mercury (THg) concentrations in soil from four sites with distinct ASGM activity histories (ng g-1, log scale). The red dashed line represents the soil prevention level established by CONAMA (2009).

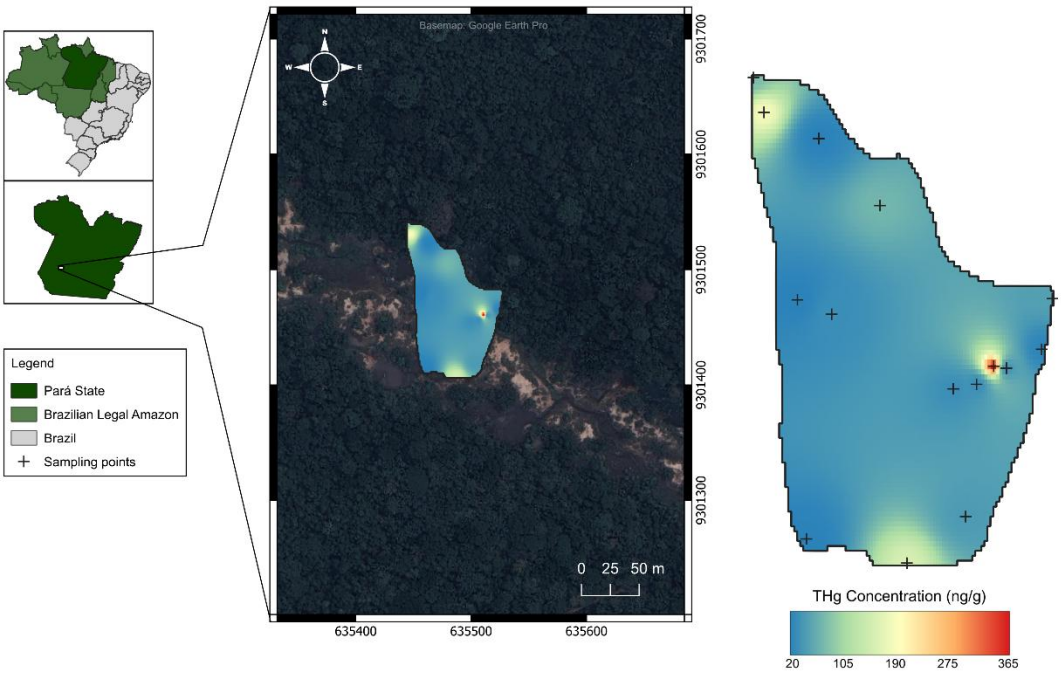
In the ASGM area deactivated for approximately 30 years, THg concentrations ranged from 27 to 8,862 ng g^{-1}, with a mean of 1,246 ng g^{-1}, a median of 324 ng g^{-1}, and a standard deviation (SD) of 1,971 ng g^{-1}. In contrast, the active ASGM site exhibited concentrations between 20 and 365 ng g^{-1}, with a mean of 77 ng g^{-1}, a median of 38 ng g^{-1}, and a SD of 93 ng g^{-1}. A narrower range was observed in the site deactivated in January 2024, with values from 54 to 207 ng g^{-1}, a mean of 134 ng g^{-1}, a median of 147 ng g^{-1}, and a SD of 44 ng g^{-1}. The reference area, with no recorded ASGM activity, showed the lowest variability, with concentrations ranging from 152 to 228 ng g^{-1}, a mean of 184 ng g^{-1}, a median of 178 ng g^{-1}, and a SD of 28 ng g^{-1}. All THg concentrations are reported in Appendix 2.

Spatial interpolation using the inverse distance weighted (IDW) method was applied to the log-transformed THg concentration data to visualize the concentration patterns for each

study area: (A) ASGM deactivated for approximately 30 years, (B) active ASGM, (C) site deactivated in January 2024 (Figure 27).



B


Basemap: Google Earth Pro
N
W
E
S
Legend
Pará State
Brazilian Legal Amazon
Brazil
Sampling points
0 25 50 m
635400
635500
635600
9301700
9301600
9301500
9301400
9301300
THg Concentration (ng/g)
20
105
190
275
365

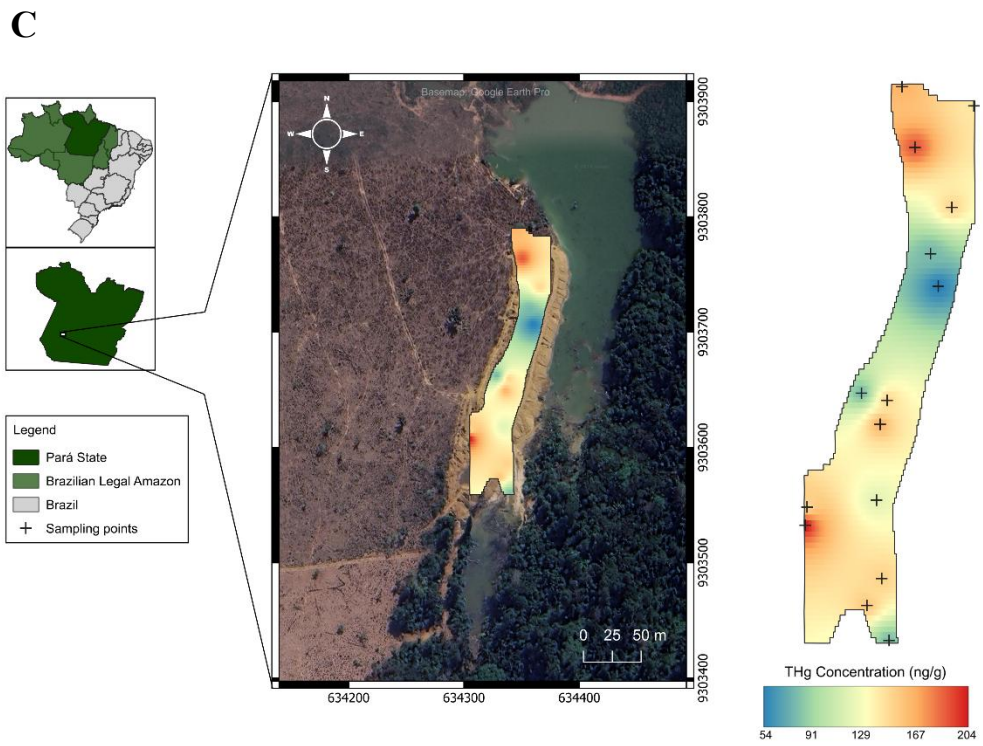


Figure 27: IDW-interpolated maps showing the spatial distribution of log-transformed THg concentrations in (A) site deactivated for approximately 30 years, (B) active site, and (C) site deactivated in January 2024. Maps were generated using WGS84/UTM Zone 21S, EPSG: 32721, with units in meters.

4.3.1.1. Association between THg concentrations and fine material content

An overall positive relationship between the percentage of fine material and THg concentration was observed in samples from the approximately 30 years deactivated ASGM (Figure 28). The percentage of <105 µm for each sample from the ~30 years deactivated ASGM is provided in Appendix 3. The R^2 of 0.73 indicates that 73% of the variability in the log-transformed THg concentration is explained by the percentage of fine material with particles smaller than 105 µm. Additionally, the slope coefficient of 0.0613 suggests that for each percentage point increase in the fine material content, the THg concentration increases by approximately 15%.

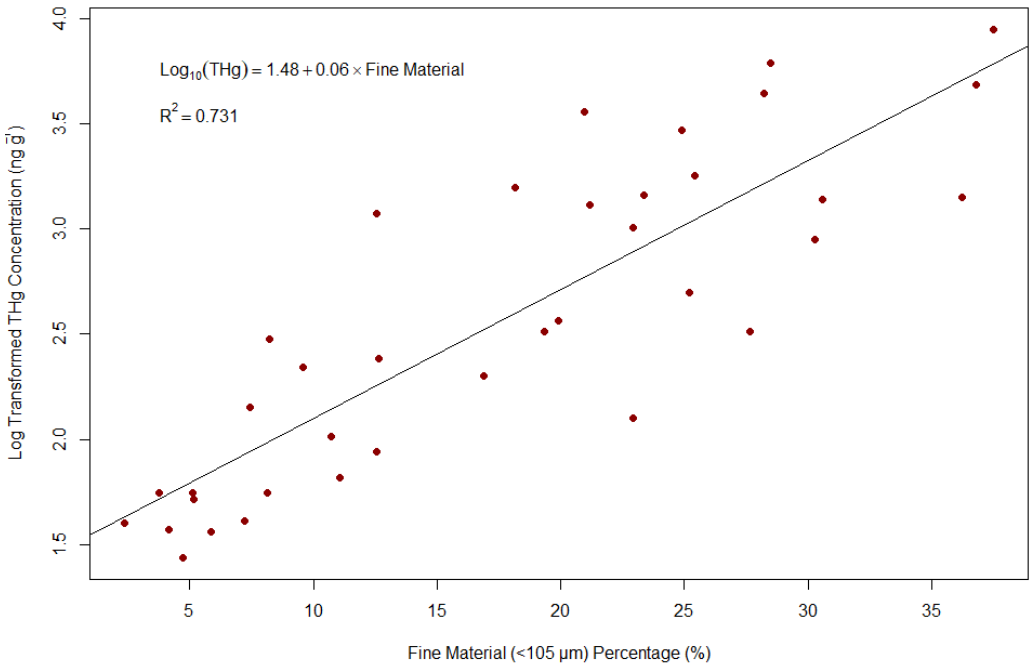


Figure 28: Relationship between fine material content (<105 µm) and log-transformed THg concentrations in the approximately 30 years deactivated ASGM. The linear trendline represents the fitted regression model.

4.3.2. Exploratory and comparative analyses of THg in the different ASGM areas

The Coefficient of Variation (CV) of the studied sites was: 158.24% in the ASGM deactivated for approximately 30 years, 121.45% in the active ASGM, 33.12% in the ASGM deactivated in January 2024, and 14.97% in the area without ASGM activity records. A significant difference in THg concentrations between the different areas was observed through the ANOVA (p = 0.00006), indicating that at least one of the areas has a mean THg concentration that is significantly different from the others. The W statistic obtained through the Shapiro-Wilk test was relatively close to 1 (W = 0.97), suggesting that the residuals are close to a normal distribution. In support of this, the Q-Q plot shows that the residuals closely follow the theoretical normal line. In addition, the p-value of 0.14 is greater than the common

significance level of 0.05, indicating that the residuals follow a normal distribution and confirming that the assumptions for the ANOVA are properly met. The difference indicated by the ANOVA was then confirmed through the Tukey-Kramer test, between the approximately 30 years deactivated and the active sites ($p = 2.58 \times 10^{-5}$).

As presented in Figure 29, four distinct clusters were identified for samples from the site deactivated for approximately 30 years. In contrast, only two clusters were identified in each of the other studied areas.

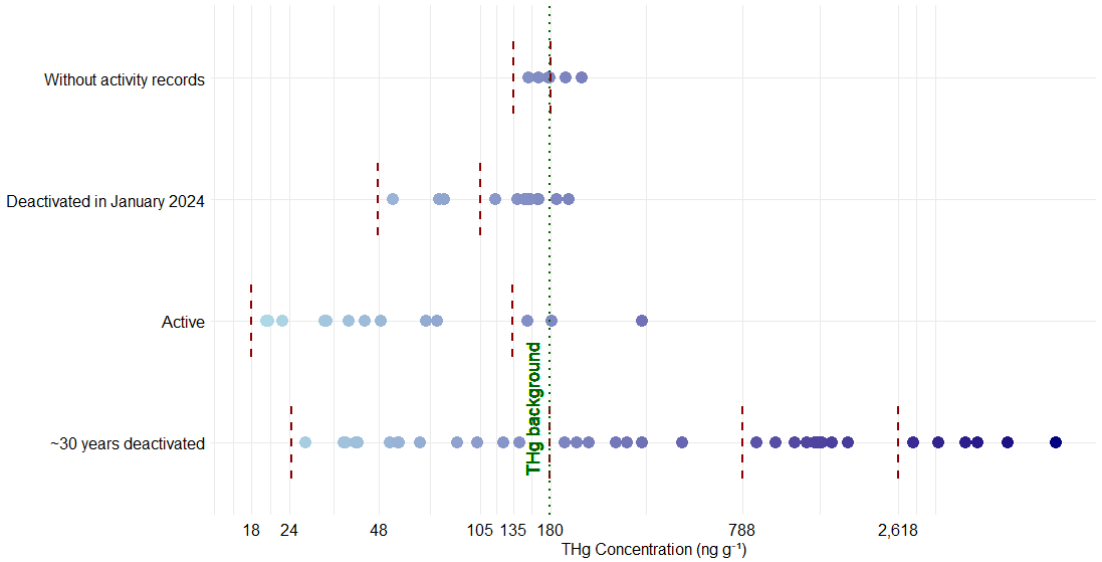


Figure 29: Hierarchical clustering of soil samples based on log-transformed THg concentrations. Vertical red dashed lines indicate cluster boundaries, while the green dotted line represents the THg background assumed in this study.

Concentration thresholds were identified at 24, 180, 788, and 2,618 ng g^{-1} for samples from the site deactivated for approximately 30 years. For the active ASGM area, limits were found at 18 and 135 ng g^{-1}, while samples from the site deactivated in January 2024 presented thresholds at 48 and 105 ng g^{-1}. In the area with no documented ASGM activity, thresholds occurred at 105 and 180 ng g^{-1}.

4.3.3. Geoaccumulation index (I_{geo})

Consistently with the results from the hierarchical cluster analysis, the I_{geo} also indicate that the site deactivated for approximately 30 years is the most contaminated. The active site contains one sample classified as moderately contaminated, while all samples from the recently deactivated site are uncontaminated (Figure 30).

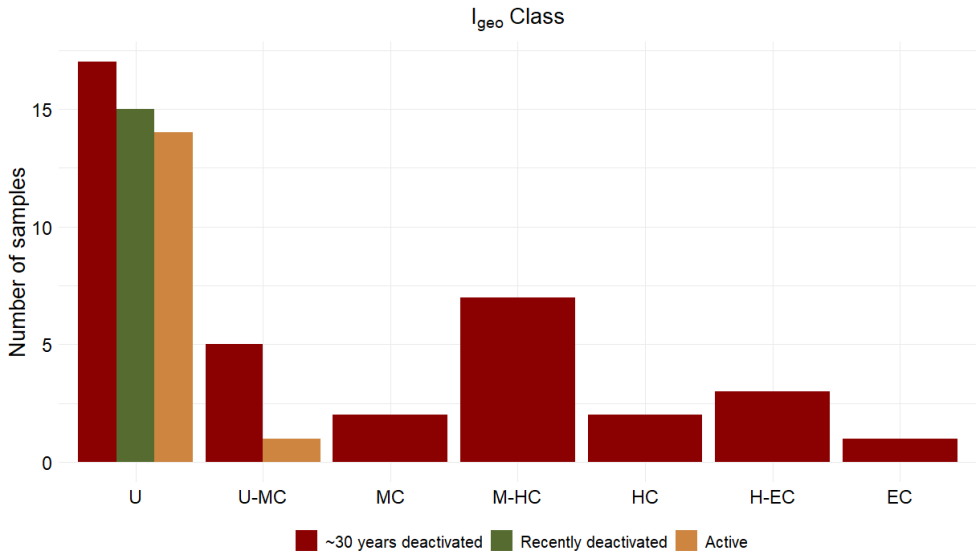


Figure 30: Distribution of Igeo classes by area. Igeo class abbreviations: U (Uncontaminated); U–MC (Uncontaminated to moderately contaminated); MC (Moderately contaminated); M–HC (Moderately to heavily contaminated); HC (Heavily contaminated); H–EC (Heavily to extremely contaminated); EC (Extremely contaminated).

4.3.4. Contamination factor (CF) and ecological risk index (Er)

Contamination factor (CF) and potential ecological risk (Er) indices were calculated to assess the intensity of mercury contamination and its potential ecological impact across the three study areas. Table 6 summarizes the range of CF and Er values observed for each site, alongside the proportion of samples exceeding the moderate ecological risk ($Er > 40$).

Table 6. Contamination factor (CF) and ecological risk index (Er) across study sites.

Site	n	CF (min—max)	Er (min—max)	n (%) of samples with $Er > 40$
~30 years deactivated	37	0.15—49.71	6.14—1988.56	23 (62.16)
Active	15	0.11—2.05	4.53—81.81	2 (13.33)
Recently deactivated	15	0.30—1.16	12—46.40	2 (13.33)

The area deactivated for ~30 years exhibited the highest values for both indices, with CF ranging from 0.15 to 49.71 and Er from 6.14 to 1988.56. Furthermore, the Er of 8 samples from the ~30 years deactivated site were classified as very high ecological risk (*i.e.*, $Er \geq 320$; **Hakanson, 1980**). In contrast, active and recently deactivated sites showed lower CF and Er values and a smaller percentage of high-risk samples. All I_{geo}, CF, and Er results are reported in Appendix 4.

4.4. Discussion

Our findings show heterogeneous THg distribution related to ASGM history. The highest contamination occurred at a site deactivated for over 30 years, with concentrations ranging from 27 to 8,862 ng g^{-1} (median = 324 ng g^{-1}) and four distinct populations identified by HCA, spanning low to high contamination levels. THg concentrations in this site were strongly correlated with the proportion of fine particles ($R^2 = 0.73$), highlighting the influence of particle size in Hg retention. In contrast, the recently deactivated site (January 2024) and the area without ASGM activity showed mean concentrations of 134 ± 44 ng g^{-1} and 184 ± 28 ng g^{-1}, respectively—both close to background levels (178 ng g^{-1})—with HCA separating samples into low and slightly elevated groups. The active ASGM site exhibited the lowest mean concentration (77 ± 93 ng g^{-1}), characterized mainly by background or mildly affected soils,

but with localized hotspots exceeding 135 ng g^{-1}, including one directly beneath the sluice box. Overall, the data suggest that legacy contamination, short-term operations, ongoing soil disturbance, and site-specific geoenvironmental factors—particularly fine particle content—are influenced by both legacy and current Hg-use practices.

The mean ± SD THg concentrations observed in both the area without activity records (184 ± 28 ng g^{-1}) and the ASGM site deactivated in January 2024 (134 ± 44 ng g^{-1}) were consistent with background THg values previously reported in the literature for the Brazilian Amazon, such as 149 ± 13 ng g^{-1} in Pará soils **(Lima et al., 2022)**, 117 ± 70 in soils from Itacaiúnas River **(Sahoo et al., 2023)**, and 172 ng g^{-1} in soils from the Rio Negro Basin **(Fadini & Jardim, 2001)**. Within this scenario, the predominant background-level THg concentrations observed in the site deactivated in January 2024 may be attributed to its short operating period (*i.e.*, a few months). Although most of the samples from this area showed concentrations similar to the assumed background (178 ng g^{-1}), two distinct groups were observed through the HCA: (I) samples with concentrations between 48 and 105 ng g^{-1}, and (II) samples exceeding 105 ng g^{-1} (Figure 29). The former may correspond to uncontaminated soils, whereas the latter might indicate slightly elevated THg levels relative to local background concentrations.

In contrast, the active ASGM site exhibited the lowest mean THg concentration (77 ± 93 ng g^{-1}), which aligns with findings by **Ramírez et al. (2021)**, who reported lower THg levels in impacted sites compared to a non-impacted reference forest. In a similar ASGM context, **Teixeira et al. (2021)** also reported low THg concentrations (*i.e.*, 100 ng g^{-1}). These reduced concentrations at the active site may indicate ongoing Hg remobilization driven by deforestation and the physical reworking of soils and sediments during ASGM activities, facilitating its transfer to surface and groundwater or promoting volatilization into the atmosphere **(Diringer et al., 2020; Sonke et al., 2023; Feinberg et al., 2024)**. Additionally,

the quartz-rich composition of the samples collected from this site may contribute to a lower Hg retention capacity.

Two distinct populations were identified by the HCA within the active ASGM: (I) samples with THg concentrations in the 18—135 ng g^{-1} range, which may represent the background or slightly impacted soils, and (II) samples with concentrations above 135 ng g^{-1}, potentially reflecting localized contamination or retention of mercury in specific microenvironments. Given that areas where gold amalgamation is practiced typically exhibit elevated Hg concentrations **(Alpers, 2017; Soe et al., 2022)**, the sample with the highest THg concentration (*i.e.*, outlier in Figure 26) identified at this site may be interpreted as a contamination hotspot (see Figure 27B), as it corresponds to a sample collected directly beneath the ASGM sluice box—precisely where mercury was used by artisanal miners to recover gold from sediments retained in the carpets.

On the other hand, although THg concentrations observed at the ASGM site deactivated for approximately 30 years (median of 324 ng g^{-1}, 27—8,862 ng g^{-1} range) were not as elevated as those reported in some other ASGM-impacted areas (e.g., **Teixeira et al., 2018**; **Gyamfi et al., 2021**), they were still substantially higher and more variable than those found in the other studied sites. This is supported by the results of the HCA, which distinguished this site from the others based on THg concentrations (Figure 29), as well as by the I_{geo} and CF assessments, which identified it as the only studied site with clearly contaminated samples (Figure 30) and samples classified as considerably contaminated (Table 6), respectively. The HCA enabled the identification of four distinct populations within this site, with concentration thresholds at 24, 180, 788, and 2,618 ng g^{-1} (Figure 29). These thresholds align closely with the CF classification proposed by **Hakanson (1980)**, based on the assumed background concentration of 178.25 ng g^{-1}. Specifically, they approximate the transition boundaries between low ($CF \approx 0.13$), moderate ($CF \approx 1.01$), considerable ($CF \approx 4.42$), and high ($CF \approx 14.69$) contamination levels

(Supplementary Table 1). This correspondence supports the interpretation that the clusters derived from HCA represent environmentally meaningful distinctions in contamination intensity. Furthermore, the Er indicated that 62% of the samples from this site exceeded the threshold for moderate ecological risk (Table 6), and it was the only site with samples classified as high and very high risk **(**see **Supplementary materials)**, reinforcing the concern regarding long-term environmental impacts.

However, although the Er results suggest potential ecological risk, it is important to highlight that mercury toxicity strongly depends on its chemical speciation **(Frossard et al., 2018)**. Therefore, in such cases, it would be more appropriate to base the indices on the concentrations of the most critical mercury species **(Ferreira et al., 2022)**, such as the organic compounds **(Azar et al., 2021; Cardoso et al., 2023)**. Nonetheless, although chemical speciation was not conducted in this study, the results based on THg concentrations remain valid for a preliminary assessment of contamination and ecological risk. The use of THg is still widely adopted as an initial indicator of potential environmental concern (e.g., **Gyamfi et al., 2021; Dantas et al., 2025**). Therefore, despite this limitation, the results from CF and Er indices—particularly in the site deactivated for ~30 years—provide robust evidence of ongoing contamination and underscore the need for more detailed investigations.

Moreover, as shown in Figure 28, THg concentrations in this area were positively associated with the proportion of fine particles (R^2 = 0.73), consistent with the results by **Quintarelli et al. (2024)** that also found a positive correlation between THg concentrations and the proportion of silt and clay fractions. Therefore, our results emphasize the influence of geoenvironmental factors on Hg retention capacity, such as the content of clay minerals **(Egler et al., 2006; Cesar et al., 2011; Zhu & Zhong, 2015; Licht, 2020; Lima et al., 2023; McLagan et al., 2024)**. Geoenvironmental factors that influence the soil's capacity to retain Hg, such as mineralogical composition **(Debure et al., 2020; Gómez-Armesto et al., 2020)**,

proportion of fine particles **(Egler et al., 2006; Cesar et al., 2011; Zhu & Zhong, 2015; Licht, 2020; Lima et al., 2023; McLagan et al., 2024)**, oxides content **(Zhang et al., 2015; Debure et al., 2020; Qin et al., 2023)**, and soil organic content **(Rodrigues et al., 2022; Liu et al., 2023; Soares et al., 2024)** may also help to explain the difference in THg concentrations between the ASGM site deactivated for approximately 30 years and the active ASGM.

This difference likely also reflects changes resulting from the implementation of legislation to control Hg use in Brazil —e.g. the Decree No. 97,507/1989 **(Brazil, 1989a)**, the Decree No. 97,634/1989 **(Brazil, 1989b)**, the Normative Instruction No. 08/2015 **(IBAMA, 2015)**, and the Ordinance No. 175/2021 **(MMA, 2021)**. These regulatory efforts are aligned with Brazil's commitments under the Minamata Convention on Mercury **(Brazil, 2018)**, which aims to protect human health and the environment from anthropogenic emissions and releases of mercury.

However, the persistence of elevated THg concentrations and evidence of ongoing contamination in some areas, as demonstrated by our data, suggest that significant challenges remain to the effective implementation and enforcement of these measures. This situation is further complicated by the informal and often illegal nature of ASGM activities in Brazil, which severely limits regulatory oversight and control. Estimates indicate that illegal gold production may range from 10% up to eight times the volume of legal ASGM output, leading to uncontrolled mercury use, insufficient emission control practices, and greater environmental and health risks **(Castilhos and Domingos, 2024)**. Actually, Brazil has been reported as one of the countries with the highest consumption of mercury, much of it uncontrolled, in the gold production sector, as specified by the Global Mercury Assessment 2018 (UNEP, 2019; Keane et al., 2023).As such, complementary actions (*i.e.*, sector formalization, improved environmental monitoring, and engagement with mining communities) are necessary to support the effectiveness of existing mercury control policies.

4.5. Conclusion

Our results demonstrate that mercury contamination persists in soils from ASGM areas even decades after mining activity has ceased. The site deactivated for over 30 years still show elevated THg concentrations and ecological risk levels above regulatory thresholds, indicating a long-term legacy of contamination. Specifically, THg concentrations in this ASGM site ranged from 27 to 8,862 ng g^{-1} (median = 324 ng g^{-1}). Moreover, the proportion of fine particles explained 73% of the variation in log-transformed THg concentrations, highlighting a log-linear relationship between particle size and THg retention**.** Therefore, our data emphasise the importance of considering substrate characteristics when assessing contamination levels and potential environmental risk.

By comparing active, recently deactivated, and long-inactive sites, this study provides new insight into the persistence and behaviour of mercury in post-ASGM landscapes. In both the recently deactivated and the active ASGM sites, THg concentrations did not significantly exceed the regional background level of 178 ng g^{-1}, except at activity hotspots (e.g., near the sluice box in the active ASGM site).

It is important to note that some aspects are still not fully understood. Although four contamination populations were identified in the ~30 years deactivated site using HCA, the specific role of mineralogy and other soil matrix properties in Hg retention remains unclear. Future studies should investigate the soil matrix in more detail, to assess mineralogy, oxide content, and organic matter composition, which may further influence mercury retention and mobility, especially in ASGM areas inactive for decades.

These insights are relevant for environmental monitoring, risk management, and the design of more effective remediation strategies in the Brazilian Amazon, aiming to support Brazil's commitments with the Minamata Convention on Mercury.

APPENDIX 2: Total mercury (THg) concentrations.

Sample ID	Duplicate 1 (ng/g)	Duplicate 2 (ng/g)	Mean (ng/g)	SD
MTBP-01	4,848.00	4,841.00	4,844.50	4.949747468
MTBP-02	6,157.00	6,015.00	6,086.00	100.4091629
MTBP-03	9,085.00	8,638.00	8,861.50	316.0767312
MTBP-04	202.80	198.90	200.85	2.757716447
MTBP-05	141.90	142.10	142.00	0.141421356
MTBP-06	3,526.00	3,630.00	3,578.00	73.53910524
MTBP-07	304.20	293.20	298.70	7.778174593
MTBP-08	361.00	369.90	365.45	6.293250353
MTBP-09	100.80	104.20	102.50	2.404163056
MTBP-10	56.00	55.70	55.85	0.212132034
MTBP-11	53.70	50.50	52.10	2.2627417
MTBP-12	35.90	37.20	36.55	0.919238816
MTBP-13	118.40	132.20	125.30	9.75807358
MTBP-14	88.60	86.40	87.50	1.555634919
MTBP-15	63.80	67.90	65.85	2.899137803
MTBP-17	1,027.00	1,007.00	1,017.00	14.14213562
MTBP-18	1,469.00	1,436.00	1,452.50	23.33452378
MTBP-19	1,389.00	1,363.00	1,376.00	18.38477631
MTBP-20	320.30	327.30	323.80	4.949747468
MTBP-21	850.10	918.70	884.40	48.50752519
MTBP-22	460.50	532.70	496.60	51.0531096
MTBP-23	55.00	55.90	55.45	0.636396103
MTBP-24	41.70	40.10	40.90	1.13137085
MTBP-25	1,300.00	1,304.00	1,302.00	2.828427125
MTBP-26	1,428.00	1,390.00	1,409.00	26.87005769
MTBP-27	37.30	36.80	37.05	0.353553391
MTBP-28	26.50	28.20	27.35	1.202081528
MTBP-29	220.20	221.10	220.65	0.636396103
MTBP-30	325.40	325.00	325.20	0.282842712
MTBP-31	54.30	56.80	55.55	1.767766953
MTBP-32	1,179.00	1,192.00	1,185.50	9.192388155
MTBP-33	40.40	40.00	40.20	0.282842712
MTBP-34	1,780.00	1,789.00	1,784.50	6.363961031
MTBP-35	2,943.00	2,931.00	2,937.00	8.485281374
MTBP-36	242.50	242.20	242.35	0.212132034
MTBP-37	4,315.00	4,497.00	4,406.00	128.6934342
MTBP-38	1,623.00	1,530.00	1,576.50	65.76093065
		Reference materials		
SRM2711	5,904.00			
GONV-1	889.90	943.10		
GXR-2	3,339.00	3,295.00		
GXR-2	3,443.00			
SRM2711	6,329.00			
MTBVP-01	230.20	226.40	228.30	2.687005769
MTBVP-02	150.70	153.00	151.85	1.626345597
MTBVP-03	201.70	203.80	202.75	1.48492424
MTBVP-04	179.20	175.70	177.45	2.474873734
MTBVP-05	206.20	151.90	179.05	38.39589822
MTBVP-06	166.40	162.60	164.50	2.687005769

MTPS-01	20.00	20.40	20.20	0.28
MTPS-02	31.70	31.50	31.60	0.14
MTPS-03	69.30	68.70	69.00	0.42
MTPS-04	74.00	75.90	74.95	1.34
MTPS-05	175.60	188.30	181.95	8.98
MTPS-06	21.40	19.60	20.50	1.27
MTPS-07	49.60	47.70	48.65	1.34
MTPS-08	22.50	23.20	22.85	0.49
MTPS-09	20.40	20.00	20.20	0.28
MTPS-10	144.50	157.30	150.90	9.05
MTPS-11	43.10	43.20	43.15	0.07
MTPS-12	31.90	31.40	31.65	0.35
MTPS-13	364.30	364.80	364.55	0.35
MTPS-14	43.20	32.60	37.90	7.50
MTPS-15	35.90	28.40	32.15	5.30
MTNC-01	189.70	186.80	188.25	2.05
MTNC-02	160.40	166.40	163.40	4.24
MTNC-03	143.60	136.10	139.85	5.30
MTNC-04	137.10	156.90	147.00	14.00
MTNC-05	76.50	76.50	76.50	0.00
MTNC-06	52.90	54.10	53.50	0.85
MTNC-07	155.50	140.10	147.80	10.89
MTNC-08	77.00	76.20	76.60	0.57
MTNC-09	164.60	164.40	164.50	0.14
MTNC-10	119.10	116.10	117.60	2.12
MTNC-11	151.90	147.70	149.80	2.97
MTNC-12	76.70	81.50	79.10	3.39
MTNC-13	152.50	156.30	154.40	2.69
MTNC-14	146.00	147.70	146.85	1.20
MTNC-15	209.00	204.50	206.75	3.18

APPENDIX 3: Percentage of fine particles (< 105 µm) for the ~30 years deactivated ASGM.

Sample ID	THg Concentration (ng/g)	Log_THg_Concentration	<105 (%)
MTBP-01	4,844.50	3.68524896	36.79
MTBP-02	6,086.00	3.784331948	28.49
MTBP-03	8,861.50	3.947507242	37.50
MTBP-04	200.85	2.302871836	16.88
MTBP-05	142.00	2.152288344	7.42
MTBP-06	3,578.00	3.553640336	20.94
MTBP-07	298.70	2.475235223	8.23
MTBP-08	365.45	2.562827966	19.92
MTBP-09	102.50	2.010723865	10.74
MTBP-10	55.85	1.747023177	8.12
MTBP-11	52.10	1.716837723	5.15
MTBP-12	36.55	1.562887381	5.85
MTBP-13	125.30	2.097951071	22.94
MTBP-14	87.50	1.942008053	12.58
MTBP-15	65.85	1.818555779	11.08
MTBP-17	1,017.00	3.007320953	22.93
MTBP-18	1,452.50	3.162116141	23.35
MTBP-19	1,376.00	3.138618434	30.59
MTBP-20	323.80	2.510276844	27.67
MTBP-21	884.40	2.946648734	30.27
MTBP-22	496.60	2.696006715	25.20
MTBP-23	55.45	1.74390155	3.77
MTBP-24	40.90	1.611723308	7.20
MTBP-25	1,302.00	3.114610984	21.19
MTBP-26	1,409.00	3.148910993	36.22
MTBP-27	37.05	1.568788212	4.15
MTBP-28	27.35	1.436957331	4.72
MTBP-29	220.65	2.343703932	9.59
MTBP-30	325.20	2.512150537	19.35
MTBP-31	55.55	1.744684063	5.14
MTBP-32	1,185.50	3.073901558	12.55
MTBP-33	40.20	1.604226053	2.38
MTBP-34	1,784.50	3.251516552	25.42
MTBP-35	2,937.00	3.467903947	24.90
MTBP-36	242.35	2.384443024	12.64
MTBP-37	4,406.00	3.644044493	28.21
MTBP-38	1,576.50	3.197693975	18.14

APPENDIX 4: Data — Contamination factor, ecological risk index, and geoaccumulation index.

Sample ID	THg Concentration (ng/g)	CF	ER	Igeo
MTBP-01	4844.5	27.17812	1087.125	4.179411
MTBP-02	6086	34.14306	1365.722	4.508558
MTBP-03	8861.5	49.71388	1988.555	5.050614
MTBP-04	200.85	1.126788	45.07153	-0.41275
MTBP-05	142	0.796634	31.86536	-0.91297
MTBP-06	3578	20.07293	802.9173	3.742217
MTBP-07	298.7	1.675736	67.02945	0.159833
MTBP-08	365.45	2.05021	82.00842	0.450809
MTBP-09	102.5	0.575035	23.0014	-1.38324
MTBP-10	55.85	0.313324	12.53296	-2.25924
MTBP-11	52.1	0.292286	11.69144	-2.35951
MTBP-12	36.55	0.205049	8.201964	-2.87092
MTBP-13	125.3	0.702945	28.11781	-1.09348
MTBP-14	87.5	0.490884	19.63534	-1.61151
MTBP-15	65.85	0.369425	14.777	-2.02161
MTBP-17	1017	5.70547	228.2188	1.927383
MTBP-18	1452.5	8.148668	325.9467	2.441602
MTBP-19	1376	7.719495	308.7798	2.363544
MTBP-20	323.8	1.81655	72.66199	0.276238
MTBP-21	884.4	4.961571	198.4628	1.725834
MTBP-22	496.6	2.785975	111.439	0.89322
MTBP-23	55.45	0.31108	12.4432	-2.26961
MTBP-24	40.9	0.229453	9.178121	-2.70869
MTBP-25	1302	7.304348	292.1739	2.283793
MTBP-26	1409	7.904628	316.1851	2.397735
MTBP-27	37.05	0.207854	8.314165	-2.85132
MTBP-28	27.35	0.153436	6.137447	-3.28925
MTBP-29	220.65	1.237868	49.51473	-0.2771
MTBP-30	325.2	1.824404	72.97616	0.282463
MTBP-31	55.55	0.311641	12.46564	-2.26701
MTBP-32	1185.5	6.650771	266.0309	2.148559
MTBP-33	40.2	0.225526	9.021038	-2.7336
MTBP-34	1784.5	10.01122	400.4488	2.738583
MTBP-35	2937	16.47686	659.0743	3.457407
MTBP-36	242.35	1.359607	54.38429	-0.14177
MTBP-37	4406	24.71809	988.7237	4.042533
MTBP-38	1576.5	8.84432	353.7728	2.559789
MTPS-01	20.2	0.113324	4.532959	-3.72644
MTPS-02	31.6	0.177279	7.091164	-3.08087
MTPS-03	69	0.387097	15.48387	-1.9542
MTPS-04	74.95	0.420477	16.81907	-1.83486
MTPS-05	181.95	1.020757	40.83029	-0.55532
MTPS-06	20.5	0.115007	4.600281	-3.70517
MTPS-07	48.65	0.272931	10.91725	-2.45835
MTPS-08	22.85	0.128191	5.12763	-3.5486
MTPS-09	20.2	0.113324	4.532959	-3.72644
MTPS-10	150.9	0.846564	33.86255	-0.82527
MTPS-11	43.15	0.242076	9.683029	-2.63143
MTPS-12	31.65	0.17756	7.102384	-3.07859
MTPS-13	364.55	2.045161	81.80645	0.447252
MTPS-14	37.9	0.212623	8.504909	-2.81859
MTPS-15	32.15	0.180365	7.214586	-3.05597
MTNC-01	188.25	1.056101	42.24404	-0.50621
MTNC-02	163.4	0.91669	36.6676	-0.71046
MTNC-03	139.85	0.784572	31.38289	-0.93498

MTNC-04	147	0.824684	32.98738	-0.86305
MTNC-05	76.5	0.429173	17.1669	-1.80533
MTNC-06	53.5	0.30014	12.00561	-2.32125
MTNC-07	147.8	0.829173	33.1669	-0.85522
MTNC-08	76.6	0.429734	17.18934	-1.80345
MTNC-09	164.5	0.922861	36.91445	-0.70078
MTNC-10	117.6	0.659748	26.3899	-1.18498
MTNC-11	149.8	0.840393	33.61571	-0.83583
MTNC-12	79.1	0.443759	17.75035	-1.75711
MTNC-13	154.4	0.866199	34.64797	-0.79219
MTNC-14	146.85	0.823843	32.95372	-0.86452
MTNC-15	206.75	1.159888	46.39551	-0.37098

References

Alpers, C. N. (2017). Arsenic and mercury contamination related to historical gold mining in the Sierra Nevada, California. *Geochemistry: Exploration, Environment, Analysis*, *17*(2), 92-100. https://doi.org/10.1144/geochem2016-018

Araujo, C. H. X., Ullah, I., & Tomi, G. D. (2025). Challenges in artisanal small-scale gold mining: perspectives and transformations to sustainability along BR-163 in Brazil. *Journal of Sustainable Mining*, *24*(2), 333-345. https://doi.org/10.46873/2300-3960.1458.

Azar, J., Yousef, M. H., El-Fawal, H. A., & Abdelnaser, A. (2021). Mercury and Alzheimer's disease: a look at the links and evidence. *Metabolic Brain Disease*, *36*(3), 361-374. https://doi.org/10.1007/s11011-020-00649-5.

Brazil. (1989a). Decree No. 97,507 of 13 February 1989. Retrieved August 6, 2025, from https://www.planalto.gov.br/ccivil_03/decreto/1980-1989/D97507.htm.

Brazil. (1989b). Decree No. 97,634 of 10 April 1989. Retrieved August 6, 2025, from https://www.planalto.gov.br/ccivil_03/decreto/1980-1989/d97634.htm.

Brazil. (2018). Decree No. 9,470 of 14 August 2018. Retrieved August 6, 2025, from https://www.planalto.gov.br/ccivil_03/_ato2015-2018/2018/Decreto/D9470.htm

Cardoso, P. G., Morais, H., Crespo, D., Tavares, D., Pereira, E., & Pardal, M. Â. (2023). Seasonal characterization of mercury contamination along the Portuguese coast: human health and environmental risk assessment. *Environmental Science and Pollution Research*, *30*(45), 101121-101132. https://doi.org/10.1007/s11356-023-29495-5.

Castilhos, Z. C., & Domingos, L. M. B. (2024). A picture of artisanal and small-scale gold mining (ASGM) in Brazil and its mercury emissions and releases. *Environmental Geochemistry and Health*, *46*(3), 101. https://doi.org/10.1007/s10653-024-01881-z.

Cesar, R., Egler, S., Polivanov, H., Castilhos, Z., & Rodrigues, A. P. (2011). Mercury, copper and zinc contamination in soils and fluvial sediments from an abandoned gold mining area in southern Minas Gerais State, Brazil. *Environmental Earth Sciences*, *64*, 211-222. https://doi.org/10.1007/s12665-010-0840-8.

CONAMA. (2009). Resolution No. 420 of 28 December 2009. Diário Oficial da União.

Crespo-Lopez, M. E., Augusto-Oliveira, M., Lopes-Araújo, A., Santos-Sacramento, L., Takeda, P. Y., de Matos Macchi, B., Nascimento, J. L. M., Maia, C. S. F., Lima, R. R., & Arrifano, G. P. (2021). Mercury: What can we learn from the Amazon?. *Environment International*, *146*, 106223. https://doi.org/10.1016/j.envint.2020.106223.

Dantas, S. V., Felix, C. S., Cunha, F. A., de Andrade, J. B., & Ferreira, S. L. (2025). Risk Assessment of Mercury in Soil, Water, and Sediments Collected in a Region Impacted by Gold Mining. *ACS omega*, *10*(8), 8152-8159. https://doi.org/10.1021/acsomega.4c09617.

de Theije, M. (2020). Brazil: forever informal. In *Global Gold Production Touching Ground: Expansion, Informalization, and Technological Innovation* (pp. 117-134). Cham: Springer International Publishing. https://doi.org/10.1007/978-3-030-38486-9_6.

Debure, M., Grangeon, S., Robinet, J. C., Madé, B., Fernández, A. M., & Lerouge, C. (2020). Influence of soil redox state on mercury sorption and reduction capacity. *Science of The Total Environment*, *707*, 136069. https://doi.org/10.1016/j.scitotenv.2019.136069.

Diringer, S. E., Berky, A. J., Marani, M., Ortiz, E. J., Karatum, O., Plata, D. L., Pan, W. K., & Hsu-Kim, H. (2019). Deforestation due to artisanal and small-scale gold mining exacerbates soil and mercury mobilization in Madre de Dios, Peru. *Environmental science & technology*, *54*(1), 286-296. https://doi.org/10.1021/acs.est.9b06620.

Egler, S. G., Rodrigues-Filho, S., Villas-Bôas, R. C., & Beinhoff, C. (2006). Evaluation of mercury pollution in cultivated and wild plants from two small communities of the Tapajós gold mining reserve, Pará State, Brazil. *Science of the total environment*, *368*(1), 424-433. https://doi.org/10.1016/j.scitotenv.2005.09.037.

Espiritu, E. Q., Claveria, R. J. R., & Bernadas, P. J. C. (2022). Assessment of surface water quality and mercury levels from Artisanal and small-scale gold mining (ASGM) along Acupan River, Benguet,

Philippines. *Environmental Geochemistry and Health*, *44*(10), 3655-3676. https://doi.org/10.1007/s10653-021-01137-0.

Fadini, P. S., & Jardim, W. F. (2001). Is the Negro River Basin (Amazon) impacted by naturally occurring mercury?. *Science of the Total Environment*, *275*(1-3), 71-82. https://doi.org/10.1016/S0048-9697(00)00855-X.

Feinberg, A., Jiskra, M., Borrelli, P., Biswakarma, J., & Selin, N. E. (2024). Deforestation as an anthropogenic driver of mercury pollution. *Environmental Science & Technology*, *58*(7), 3246-3257. https://doi.org/10.1021/acs.est.3c07851.

Ferreira, S. L., da Silva Junior, J. B., dos Santos, I. F., de Oliveira, O. M., Cerda, V., & Queiroz, A. F. (2022). Use of pollution indices and ecological risk in the assessment of contamination from chemical elements in soils and sediments–Practical aspects. *Trends in Environmental Analytical Chemistry*, *35*, e00169. https://doi.org/10.1016/j.teac.2022.e00169.

Fisher, J. A., Schneider, L., Fostier, A. H., Guerrero, S., Guimarães, J. R. D., Labuschagne, C., Leaner, J. J., Martin, L. G., Mason, R. P., Somerset, V., & Walters, C. (2023). A synthesis of mercury research in the Southern Hemisphere, part 2: Anthropogenic perturbations. *Ambio*, *52*(5), 918-937. https://doi.org/10.1007/s13280-023-01840-5.

Fritz, B., Peregovich, B., da Silva Tenório, L., da Silva Alves, A. C., & Schmidt, M. (2024). Mercury and CO2 emissions from artisanal gold mining in Brazilian Amazon rainforest. *Nature Sustainability*, *7*(1), 15-22. https://doi.org/10.1038/s41893-023-01242-1.

Frossard, A., Donhauser, J., Mestrot, A., Gygax, S., Bååth, E., & Frey, B. (2018). Long-and short-term effects of mercury pollution on the soil microbiome. *Soil Biology and Biochemistry*, *120*, 191-199. https://doi.org/10.1016/j.soilbio.2018.01.028.

Gómez-Armesto, A., Martínez-Cortizas, A., Ferro-Vázquez, C., Méndez-López, M., Arias-Estévez, M., & Nóvoa-Muñoz, J. C. (2020). Modelling Hg mobility in podzols: Role of soil components and environmental implications. *Environmental Pollution*, *260*, 114040. https://doi.org/10.1016/j.envpol.2020.114040.

Gonçalves, C., Fávaro, D. I. T., Melfi, A. J., De Oliveira, S. M. B., Vasconcellos, M. B. A., Fostier, A. H., Guimarães, J. R. D., Boulet, R., & Forti, M. C. (2000). Evaluation of mercury levels in sediment and soil samples from Vila Nova river basin, in Amapa State, Brazil, using radiochemical neutron activation analysis. *Journal of Radioanalytical and Nuclear Chemistry*, *243*(3), 789-796. https://doi.org/10.1023/A:1010611528825.

Gyamfi, O., Sørensen, P. B., Darko, G., Ansah, E., Vorkamp, K., & Bak, J. L. (2021). Contamination, exposure and risk assessment of mercury in the soils of an artisanal gold mining community in Ghana. *Chemosphere*, *267*, 128910. https://doi.org/10.1016/j.chemosphere.2020.128910.

Gräler, B., Pebesma, E., & Heuvelink, G. (2016). Spatio-temporal interpolation using gstat. *The R Journal*, *8*(1), 204-218.

Hakanson, L. (1980). An ecological risk index for aquatic pollution control. A sedimentological approach. *Water research*, *14*(8), 975-1001. https://doi.org/10.1016/0043-1354(80)90143-8.

Hijmans, R. (2023). _raster: Geographic Data Analysis and Modeling_. R package version 3.6-26, https://CRAN.R-project.org/package=raster.

Hothorn, T., Bretz, F., & Westfall, P. (2008). Simultaneous inference in general parametric models. *Biometrical Journal: Journal of Mathematical Methods in Biosciences*, *50*(3), 346-363. https://doi.org/10.1002/bimj.200810425.

IBAMA (Brazilian Institute of Environment and Renewable Natural Resources). (2015). Normative Instruction No. 08 of 08 May 2015. Retrieved August 6, 2025, from https://www.ibama.gov.br/component/legislacao/?view=legislacao&legislacao=135696.

IBGE (Brazilian Institute of Geography and Statistics). (2002). *Climate map of Brazil* [Map]. Scale 1:5,000,000. Brazilian Institute of Geography and Statistics. Retrieved August 6, 2025, from https://www.ibge.gov.br/geociencias/cartas-e-mapas/informacoes-ambientais/15817-clima.html?edicao=15887&t=acesso-ao-produto

INMET (National Institute of Meteorology). (2022). *Normais climatológicas do Brasil: 1991–2020*. Retrieved August 6, 2025, from https://portal.inmet.gov.br/normais#

INMET (National Institute of Meteorology). (n.d.). *Gráfico anual da estação convencional Itaituba (A231)*. Retrieved August 6, 2025, from https://tempo.inmet.gov.br/GraficosAnuais/A231

Jacques, P. D., Viglio, E. P., & de Oliveira d'El Rei Pinto, D. (2023). Environmental Geochemical Analysis in the Yanomami Indigenous Land, Mucajaí River Basin, State of Roraima, Brazil. *Toxics*, *11*(10), 861. https://doi.org/10.3390/toxics11100861.

Keane, S., Bernaudat, L., Davis, K. J., Stylo, M., Mutemeri, N., Singo, P., Twala, P., Mutemeri, I., Nakafeero, A., & Etui, I. D. (2023). Mercury and artisanal and small-scale gold mining: Review of global use estimates and considerations for promoting mercury-free alternatives. *Ambio*, *52*(5), 833-852. https://doi.org/10.1007/s13280-023-01843-2.

Li, Z., Ma, Z., van der Kuijp, T. J., Yuan, Z., & Huang, L. (2014). A review of soil heavy metal pollution from mines in China: pollution and health risk assessment. *Science of the total environment*, *468*, 843-853. https://doi.org/10.1016/j.scitotenv.2013.08.090.

Licht, O. B. (2020). Geochemical background-what a complex meaning has such a simple expression!. *Geochimica Brasiliensis*, *34*(2), 161-175. https://doi.org/10.21715/GB2358-2812.2020342161.

Lima, F. R., Pereira, P., Vasques, I. C., Junior, E. C. S., Mancini, M., Oliveira, J. R., Prianti, M. T. A., Windmöller, C. C., Weindorf, D. C., Curi, N., Ribeiro, B. T., Richardson, J., Marques, J. J., & Guilherme, L. R. G. (2023). Predictive modeling of total Hg background concentration in soils of the Amazon Rainforest biome with support of proximal sensors and auxiliary variables. *Journal of South American Earth Sciences*, *129*, 104510. https://doi.org/10.1016/j.jsames.2023.104510.

Lima, F. R., Pereira, P., Junior, E. C. S., Vasquez, I. C. F., Oliveira, J. R., Windmöller, C., Inda, A. V., Weindorf, D. C., Curi, N., Ribeiro, B. T., Guilherme, L. R. G., & Marques, J. J. (2022). Geochemistry signatures of mercury in soils of the Amazon rainforest biome. *Environmental Research*, *215*, 114147. https://doi.org/10.1016/j.envres.2022.114147.

Liu, Y. R., Guo, L., Yang, Z., Xu, Z., Zhao, J., Wen, S. H., Delgado-Baquerizo, M., & Chen, L. (2023). Multidimensional drivers of mercury distribution in global surface soils: insights from a global standardized field survey. *Environmental Science & Technology*, *57*(33), 12442-12452. https://doi.org/10.1021/acs.est.3c04313.

McLagan, D. S., Esser, C., Schwab, L., Wiederhold, J. G., Richard, J. H., & Biester, H. (2024). Organic matters, but inorganic matters too: column examination of elevated mercury sorption on low organic matter aquifer material using concentrations and stable isotope ratios. *Soil*, *10*(1), 77-92. https://doi.org/10.5194/soil-10-77-2024.

MMA (Ministry of Environment). (2021). Ordinance No. 175 of 22 April 2021. Retrieved August 6, 2025, from https://www.in.gov.br/en/web/dou/-/portaria-mma-n-175-de-22-de-abril-de-2021-315696586.

Müller, G. (1979). Schwermetalle in den Sedimenten des Rheins-Veränderungen seit 1971.

Neto, L. C. F., Diniz, C. G., Maretto, R. V., Persello, C., Silva Pinheiro, M. L., Castro, M. C., Sadeck, L. W. R., Filho, A. F., Cansado, J., Souza, A. A. A., Feitosa, J. P., Santos, D. C., Adami, M., Souza-Filho, P. W. M., Stein, A., Biehl, A., & Klautau, A. (2024). Uncontrolled illegal mining and Garimpo in the Brazilian Amazon. *Nature communications*, *15*(1), 9847. https://doi.org/10.1038/s41467-024-54220-2.

Nitschke, N., Guédron, S., Tessier, E., Tisserand, D., Campillo, S., & Amouroux, D. (2024). Evaluation of the Hg Contamination from Gold Mining in French Guiana at the Watershed Scale Using Hg Isotopic Composition in River Sediments. *ACS ES&T Water*, *4*(8), 3443-3452. https://doi.org/10.1021/acsestwater.4c00270.

Pebesma, E. (2004). Multivariable geostatistics in S: the gstat package. *Computers & Geosciences*, *30*, 683-691. https://doi.org/10.1016/j.cageo.2004.03.012.

Pisconte, J. N., Vega, C. M., Sayers, C. J., Sevillano-Ríos, C. S., Pillaca, M., Quispe, E., Tejeda, V., Ascorra, C., Silman, M. R., Fernandez, L. E. (2024). Elevated mercury exposure in bird communities inhabiting Artisanal and Small-Scale Gold Mining landscapes of the southeastern Peruvian Amazon. *Ecotoxicology*, *33*(4), 472-483. https://doi.org/10.1007/s10646-024-02740-4.

QGIS Development Team. (2023). QGIS (*v3.32.3*). https://www.qgis.org.

Qin, A., Ran, S., He, T., Yin, D., & Xu, Y. (2023). The effects of different soil component couplings on the methylation and bioavailability of mercury in soil. *Toxics*, *11*(11), 942. https://doi.org/10.3390/toxics11110942.

Queiroz, J., Gasparinetti, P., Bakker, L. B., Lobo, F., & Nagel, G. (2022). Socioeconomic cost of dredge boat gold mining in the Tapajós basin, eastern Amazon. *Resources Policy*, *79*, 103102. https://doi.org/10.1016/j.resourpol.2022.103102.

Quintarelli, J. M., Garnier, J., de Souza, J. P. R., de Sousa Tonhá, M., Barral, U. M., Roig, H. L., Martinez, J. M., Santini, W., Puita, O., Seyler, P., Kutter, V., & Souza, J. R. (2024). Mercury in river samples with artisanal and small-scale gold mining influence: The case of the upper Madeira River Basin (Brazil/Bolivia). *Journal of South American Earth Sciences*, *145*, 105070. https://doi.org/10.1016/j.jsames.2024.105070.

R Core Team. (2023). R: A Language and Environment for Statistical Computing_. R Foundation for Statistical Computing, Vienna, Austria. https://www.R-project.org/.

Ramírez, M. G. V., Ruiz, C. M. V., Gomringer, R. C., Pillaca, M., Thomas, E., Stewart, P. M., Miranda, L. A. G., Dañobeytia, F. R., Barrantes, J. A. G., Gushiken, M. C., Bardales, J. V., Silman, M., Fernandez, L., Ascorra, C., & Torres, D. D. (2021). Mercury in soils impacted by alluvial gold mining in the Peruvian Amazon. *Journal of Environmental Management*, *288*, 112364. https://doi.org/10.1016/j.jenvman.2021.112364.

Rodrigues, Y. O. S., Dórea, J. G., Landim, P. M. B., Bernardi, J. V. E., Monteiro, L. C., Souza, J. P. R., Pinto, L. C. M., Fernandes, I. O., Souza, J. V. V., Sousa, A. R., Sousa, J. P., Maciel, B. L. O., Delvico, F. M. S., & Souza, J. R. (2022). Mercury spatiality and mobilization in roadside soils adjacent to a savannah ecological reserve. *Environmental Research*, *205*, 112513. https://doi.org/10.1016/j.envres.2021.112513.

Sahoo, P. K., Dall'Agnol, R., Salomão, G. N., Guimarães, J. T. F., Angelica, R. S., Ramos, S. J., Costa, M. F., & de Siqueira, J. O. (2023). Mercury in multimedia system of Itacaiúnas Basin, Brazilian Amazon: An integrated approach to understand its distribution, origin, and ecological risk. *Environmental Research*, *232*, 115107. https://doi.org/10.1016/j.envres.2022.115107.

Siqueira, G. W., Aprile, F., Irion, G., & Braga, E. S. (2018). Mercury in the Amazon basin: human influence or natural geological pattern?. *Journal of South American Earth Sciences*, *86*, 193-199. https://doi.org/10.1016/j.jsames.2018.06.017.

Soares, M. B., Rodrigues, R. R., Péres, L. O., Cerri, C. E. P., & Alleoni, L. R. F. (2024). Impact of climatic seasons on the dynamics of carbon, nitrogen and mercury in soils of Brazilian biomes affected by gold mining. *Science of the Total Environment*, *954*, 176279. https://doi.org/10.1016/j.scitotenv.2024.176279.

Soe, P. S., Kyaw, W. T., Arizono, K., Ishibashi, Y., & Agusa, T. (2022). Mercury pollution from artisanal and small-scale gold mining in Myanmar and other southeast asian countries. *International Journal of Environmental Research and Public Health*, *19*(10), 6290. https://doi.org/10.3390/ijerph19106290.

Sonke, J. E., Angot, H., Zhang, Y., Poulain, A., Björn, E., & Schartup, A. (2023). Global change effects on biogeochemical mercury cycling. *Ambio*, *52*(5), 853-876. https://doi.org/10.1007/s13280-023-01855-y.

Teixeira, R. A., Fernandes, A. R., Ferreira, J. R., Vasconcelos, S. S., & Braz, A. M. S. (2018). Contamination and soil biological properties in the Serra Pelada Mine-Amazonia, Brazil. *Revista Brasileira de Ciência do Solo*, *42*, e0160354. https://doi.org/10.1590/18069657rbcs20160354.

Teixeira, R. A., da Silveira Pereira, W. V., de Souza, E. S., Ramos, S. J., Dias, Y. N., de Lima, M. W., Neto, H. F. S., Oliveira, E. S., & Fernandes, A. R. (2021). Artisanal gold mining in the eastern Amazon: Environmental and human health risks of mercury from different mining methods. *Chemosphere*, *284*, 131220. https://doi.org/10.1016/j.chemosphere.2021.131220.

UNEP (United Nations Environment Programme). (2013). *Minamata Convention on Mercury*. United Nations Environment Programme. https://treaties.un.org/doc/Treaties/2013/10/20131010%2011-16%20AM/CTC-XXVII-17.pdf.

UNEP (United Nations Environment Programme). (2019). *Global mercury assessment 2018*. UNEP Chemicals and Health Branch. https://www.unep.org/resources/publication/global-mercury-assessment-2018.

Wilman, B., Saniewska, D., Pyta, H., Wysiecki, D., & Bełdowska, M. (2023). Mercury fractionation-problems in method application. *Marine Pollution Bulletin*, *187*, 114560. https://doi.org/10.1016/j.marpolbul.2022.114560.

Windmöller, C. C., Wilken, R. D., & Jardim, W. D. F. (1996). Mercury speciation in contaminated soils by thermal release analysis. *Water, air, and soil pollution*, *89*(3), 399-416. https://doi.org/10.1007/BF00171644.

Yang, L., Zhang, Y., Wang, F., Luo, Z., Guo, S., & Strähle, U. (2020). Toxicity of mercury: Molecular evidence. *Chemosphere*, *245*, 125586. https://doi.org/10.1016/j.chemosphere.2019.125586

Zhang, H., Li, Y., Luo, Y., & Christie, P. (2015). Anthropogenic mercury sequestration in different soil types on the southeast coast of China. *Journal of Soils and Sediments*, *15*, 962-971. https://doi.org/10.1007/s11368-015-1062-1.

Zhu, D., & Zhong, H. (2015). Potential bioavailability of mercury in humus-coated clay minerals. *Journal of Environmental Sciences*, *36*, 48-55. https://doi.org/10.1016/j.jes.2015.02.011.

5. Physicochemical, mineralogical and thermal characterization of the soils

Artisanal and small-scale gold mining (ASGM) is recognized as one of the major anthropogenic sources of mercury (Hg) to the environment **(Yang et al., 2020; Cheng et al., 2023)**, particularly in tropical regions such as the Amazon Basin, where extensive and often unregulated (and/or illegal) ASGM activities have resulted in long-term contamination of soils and sediments **(Lourenço et al., 2025)**. In these systems, soils act not only as sinks but also as dynamic reservoirs of Hg, capable of releasing or retaining the element depending on physicochemical conditions and environmental disturbance (e.g., **Fostier et al., 2000; Lechler et al., 2000; Sahoo et al., 2020; Wang et al., 2021**).

The retention, speciation and mobility of Hg in soils are controlled by a complex interplay between mineralogical composition, surface chemistry and soil organic matter (SOM). In particular, interactions with organic functional groups have been shown to strongly control Hg complexation and stabilization through highly humified ligands **(Schuster, 1991; Cui et al., 2022)**, while iron and manganese (oxyhydr)oxides and clay minerals provide additional reactive surfaces for Hg retention in tropical soils **(Waychunas et al., 2005; Debure et al., 2020; Zhang et al., 2023; Vaňková et al., 2024)**.

Beyond bulk soil properties, small-scale heterogeneity plays a critical role in controlling Hg behavior **(**e.g., **Waychunas et al., 2005; Debure et al., 2020)**. Variations in texture, aggregation, surface functional groups and moisture distribution can generate microenvironments with contrasting geochemical conditions, particularly in physically disturbed soils **(Blouin et al., 2005; Guedron et al., 2009)**. Soil moisture, often expressed through water holding capacity (WHC), has been identified as a key factor influencing redox

dynamics and Hg partitioning, with implications for Hg mobility and potential bioavailability **(Zhao et al., 2022; Miele et al., 2023; Kondo et al., 2024)**.

In ASGM-affected environments, physical disturbance caused by soil reworking, sediment displacement and removal of organic-rich surface horizons further amplifies soil heterogeneity. These processes can modify pH, mineral surface exposure and organic matter stability **(Blouin et al., 2005; Li et al., 2023)**, while seasonal climatic variability in tropical regions introduces strong temporal fluctuations in soil moisture **(Spanner et al., 2022; Soares et al., 2024)**. Transitions between dry and rainy periods have been shown to affect soil organic matter stocks and stability in ASGM-impacted soils, with cascading effects on biogeochemical functioning and contaminant behavior **(Becerra-Lira et al., 2024; Soares et al., 2024)**.

Despite growing evidence of the importance of mineral–organic interactions and moisture-driven processes in controlling Hg dynamics **(**e.g., **Zhao et al., 2022; Wu et al., 2023; Li et al., 2025)**, few studies have integrated mineralogical, spectroscopic and thermal approaches to interpret soil heterogeneity in ASGM-affected tropical environments. In particular, there remains a need for process-based frameworks capable of linking physical disturbance, surface chemistry and organic matter stability to the observed spatial variability of Hg in soils.

In this context, the present section aims to propose an integrated physicochemical and mineralogical framework to interpret soil heterogeneity and the processes potentially controlling mercury retention and mobility in the studied ASGM sites. All 73 soil samples were characterized using qualitative X-ray diffraction (XRD), Attenuated Total Reflectance Fourier-Transformed Infrared (ATR-FTIR) spectroscopy, and simultaneous thermal analysis (STA), especifically thermogravimetric and differential scanning calorimetry (TG/DSC), combined with measurements of pH and water holding capacity (WHC) of representative samples. By integrating mineralogical composition, surface functional groups, thermal behavior, and

moisture-related properties with THg data presented in Section 4, this section provides a process-based interpretation of how physical disturbance and soil reworking associated with ASGM may generate heterogeneous microenvironments that influence mercury partitioning and stability in tropical soils.

5.1. Methodology

Aliquots of 10 g from all 73 lyophilized and ground bulk samples (described in Section 4.2.3) were separated, properly stored in zip-lock bags within a paper box, and transported to the Laboratory of Mineralogy and Petrography at the University of Sannio (Benevento, Italy).

5.1.1. Mineralogical composition

For mineralogical characterization, X-ray diffraction (XRD) analysis was also employed. Soil samples were manually ground using an agate mortar prior to analysis. XRD measurements were performed with a Panalytical AERIS diffractometer (CuKα radiation, 40 kV, 40 mA), operating over a 2θ scanning range of 3–80°, using an RTMS detector with a step size of 0.017° and a counting time of 60 s per step. Mineral phases were identified by the Panalytical Highscore Plus 3.0e software and PDF-2/ICSD mineral databases.

5.1.2. Attenuated Total Reflectance Fourier-Transformed Infrared (ATR-FTIR) characterization of soil functional groups

Fourier transform infrared (FTIR) analyses were conducted on powdered samples using the Attenuated Total Reflectance (ATR) technique with a BRUKER Alpha FTIR spectrometer

fitted with a diamond crystal. Spectra were collected in the mid-infrared region (4000–400 cm^{-1}) at a spectral resolution of 4 cm^{-1}, averaging 64 scans per measurement. Data acquisition and spectral processing were carried out using Opus 7.8.44 software.

5.1.3. Thermal behavior of soils assessed by Simultaneous Thermal Analysis (STA)

The powdered soils were characterized using simultaneous thermal analysis, specifically thermogravimetric analysis (TG) coupled with differential scanning calorimetry (DSC). Measurements were carried out with a NETZSCH STA 449 F3 Jupiter thermal analyzer using alumina crucibles (sample masses ca. 60 mg). The samples were subjected to dynamic heating conditions, with a heating rate of 10 °C/min over a temperature range of 40–1250 °C, under an ultrapure air atmosphere. Data processing was performed using Proteus 6.1.0 software.

5.1.4. Soil physicochemical properties: pH and water holding capacity (WHC)

Representative soil samples were selected from each site category to provide contextual information on physicochemical properties while keeping laboratory analyses feasible. Although the number of samples per site differs (n = 28 for ~30 years deactivated, n = 5 for deactivated in January 2024, n = 4 for active, and n = 3 for the site without ASGM records), the selection aimed to cover the main observed variability in each category, including differences in texture, mineral composition, and visible organic matter. This subset is therefore

considered representative of the soils from each ASGM context and suitable for the interpretation of mineralogical, spectroscopic, and thermal analyses.

Soil pH was measured in aqueous suspension following laboratory procedures, using a soil-to-distilled water ratio of 1:5 (w/v). The suspensions were mechanically agitated and allowed to equilibrate before pH measurement using a PC 62 DHS calibrated pH meter, with calibration verified using standard buffer solutions (pH 4.0 and 7.0) between measurement sessions.

Water holding capacity (WHC) was determined gravimetrically. After saturation with distilled water, soil samples were allowed to drain freely under gravity to remove excess water. The samples were then weighed to obtain the wet mass, oven-dried at 110 °C for 48 h, and weighed again to determine the dry mass. WHC was calculated as the mass of water retained after free drainage relative to the dry mass of the soil and expressed as a percentage (Equation 4).

$$WHC\ (\%) = \frac{W_{wet} - W_{dry}}{W_{dry}} \times 100 \quad (4)$$

Where:

W_{wet} = soil mass after saturation and free drainage (g).

W_{dry} = oven-dried soil (g).

5.2. Results

5.2.1. Mineralogical composition

Qualitative X-ray diffraction (XRD) patterns indicate a broadly similar mineralogical composition across all studied sites (Table 7). All X-ray diffraction patterns are presented in Appendix 5.

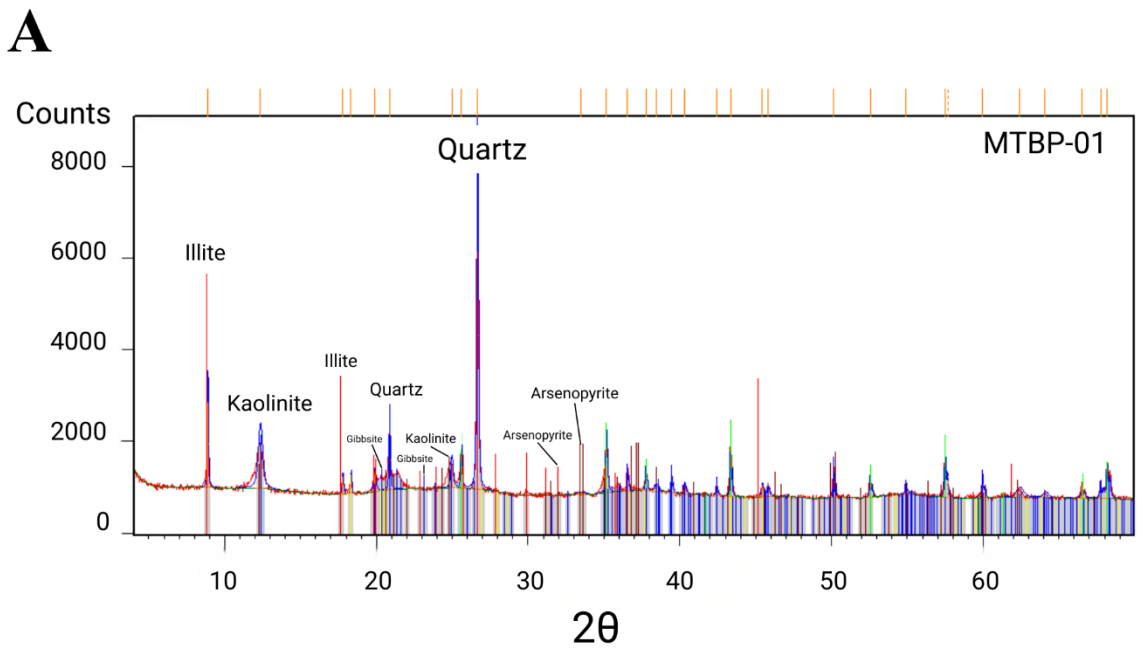
Table 7. Occurrence frequency (n) of mineral groups identified by qualitative XRD in soils across the studied sites.

	Studied sites			
Mineral group	**~30 years deactivated (MTBP, *n* = 37)**	**Deactivated in January 2024 (MTNC, *n* = 15)**	**Active (MTPS, *n* = 15)**	**Without ASGM records (MTBVP, *n* = 6)**
Quartz	37	15	15	6
Kaolinite-group	37	15	15	6
Gibbsite	16	8	1	3
Mica-type	16	0	1	1
Smectite	1	0	3	0
Fe/Mn (oxyhydr)oxides	5	2	0	1
Feldspars	4	0	3	0
Arsenopyrite*	3	10	0	0

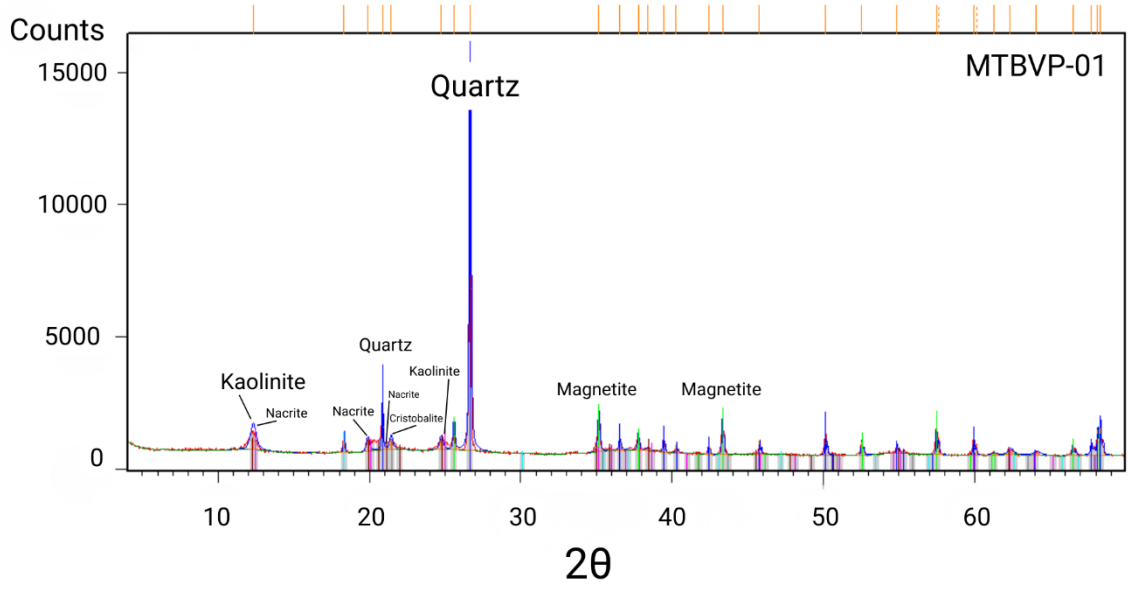
*Tentative identification.

Quartz is present in all analyzed soil samples, as residual crystallin e phase (Figure 31). Clay mineral assemblages are dominated by kaolinite-group minerals, consistently detected across all studied sites. Minor occurrences of mica-type phyllosilicates (illite and muscovite) and smectite were also observed in selected samples. However, the possibility of mixed-layered

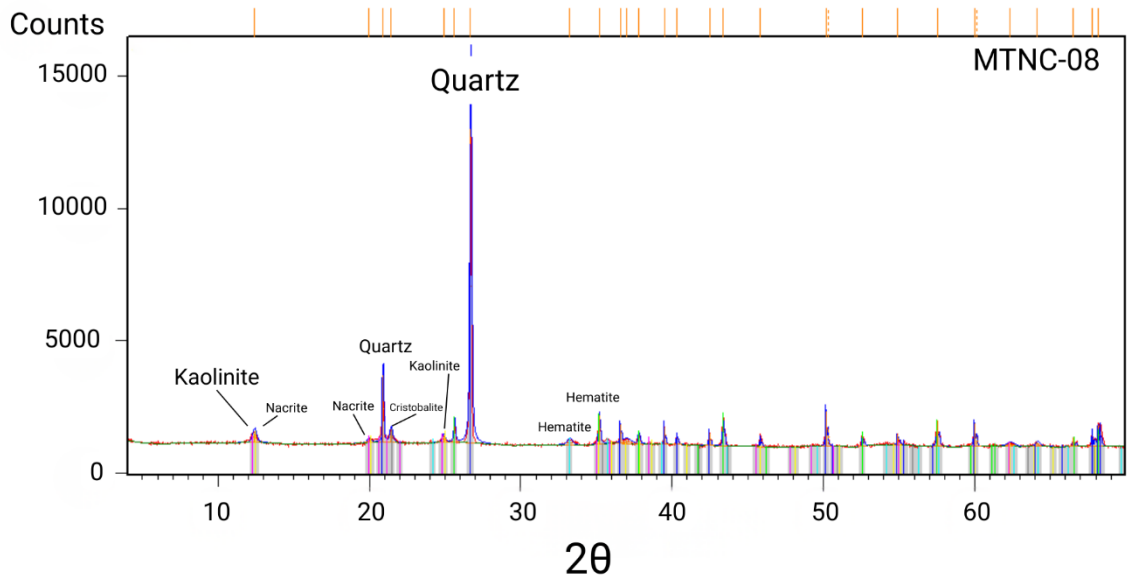
structures (not separated by XRD analysis) cannot be excluded, as interstratified sequences of illite and muscovite may occur in these soils. Aluminum hydroxides, particularly gibbsite, were frequently observed, especially in soils from the long-term and recently deactivated sites, as well as in samples from the control area. On the other hand, K-feldspars were detected sporadically (*i.e.*, some samples from the ~30 years deactivated and from the active ASGM sites). Iron and manganese (oxyhydr)oxides, including goethite, hematite, magnetite and birnessite, were identified in a subset of samples, although their detection was qualitative and limited by low crystallinity and potential peak overlap.



B


Counts
15000
10000
5000
0
MTBVP-01
Quartz
Kaolinite
Nacrite
Nacrite
Quartz
Nacrite
Cristobalite
Kaolinite
Magnetite
Magnetite
10
20
30
40
50
60
2θ

C


Counts
15000
10000
5000
0
MTNC-08
Quartz
Kaolinite
Nacrite
Nacrite
Quartz
Cristobalite
Kaolinite
Hematite
Hematite
10
20
30
40
50
60
2θ

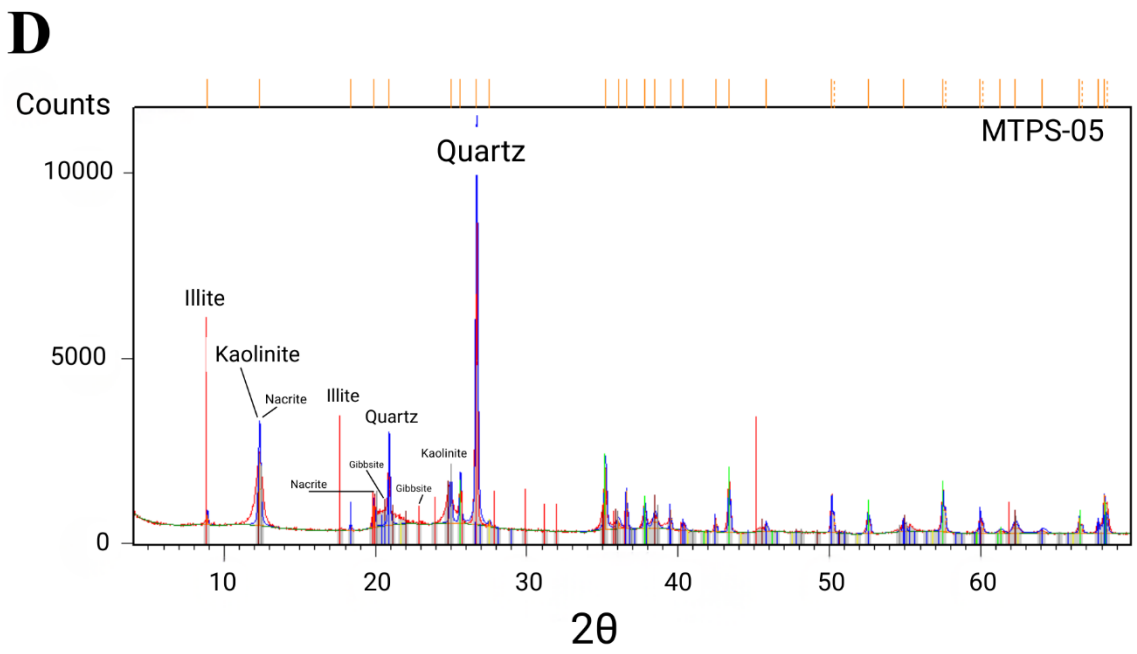


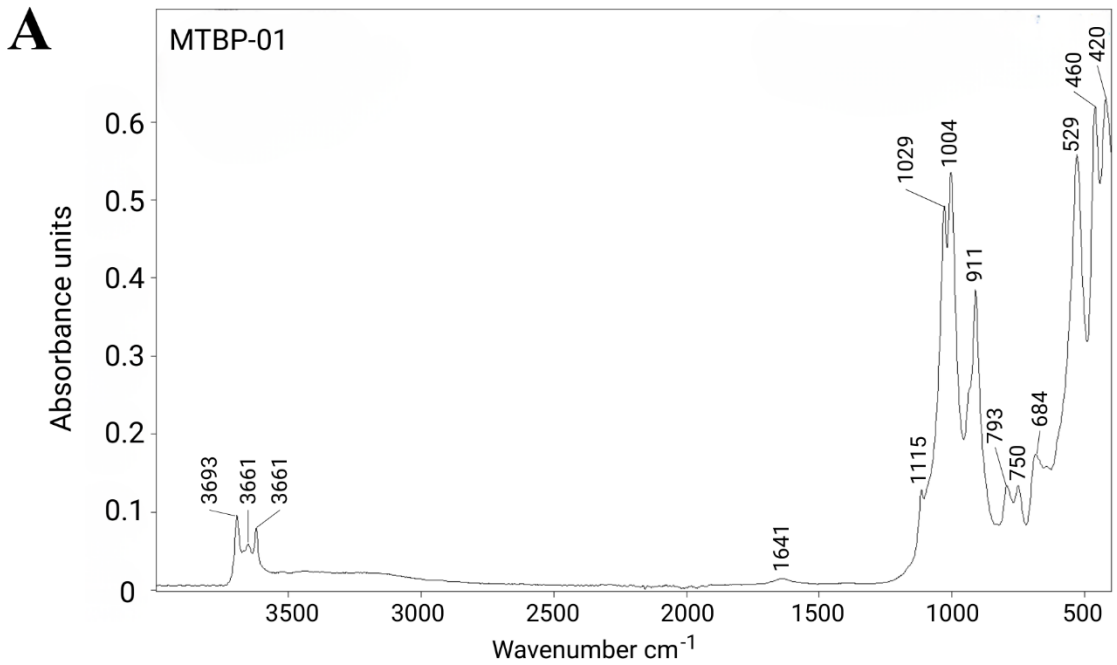
Figure 31: XRD diffractograms of the studied sites' representative samples. (A) MTBP-01, ~30 years deactivated ASGM, (B) MTBVP-01, without ASGM records, (C) MTNC-08, ASGM deactivated in January 2024, and (D) MTPS-05, active ASGM.

Minor reflections tentatively compatible with chalcogenide minerals. These minerals included arsenopyrite (FeAsS), that was more consistently detected in samples from the ASGM area deactivated in January 2024 (n = 10) and in 3 samples from the ~30 years deactivated ASGM. Given their low intensity and the complexity of soil mineral matrices, these identifications should be regarded as indicative rather than definitive.

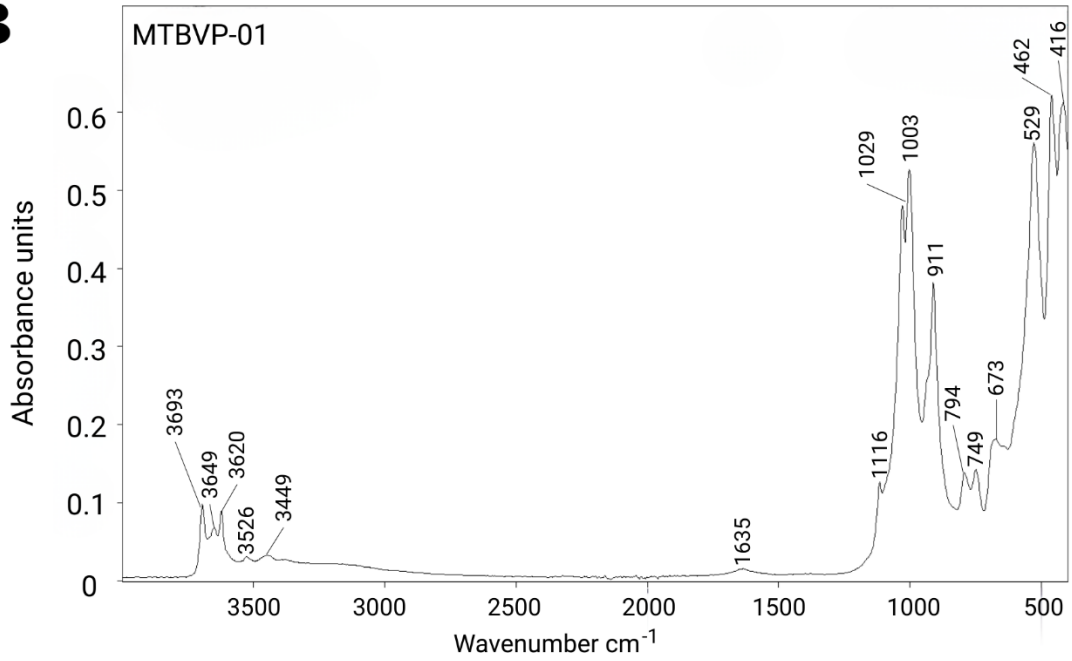
Overall, no mineralogical phases were uniquely associated with any specific studied ASGM site. While the soils share a common mineralogical background dominated by quartz and kaolinite, variations in accessory minerals were irregular and did not follow a consistent temporal pattern.

5.2.2. Attenuated Total Reflectance Fourier-Transformed Infrared (ATR-FTIR) characterization of soil functional groups

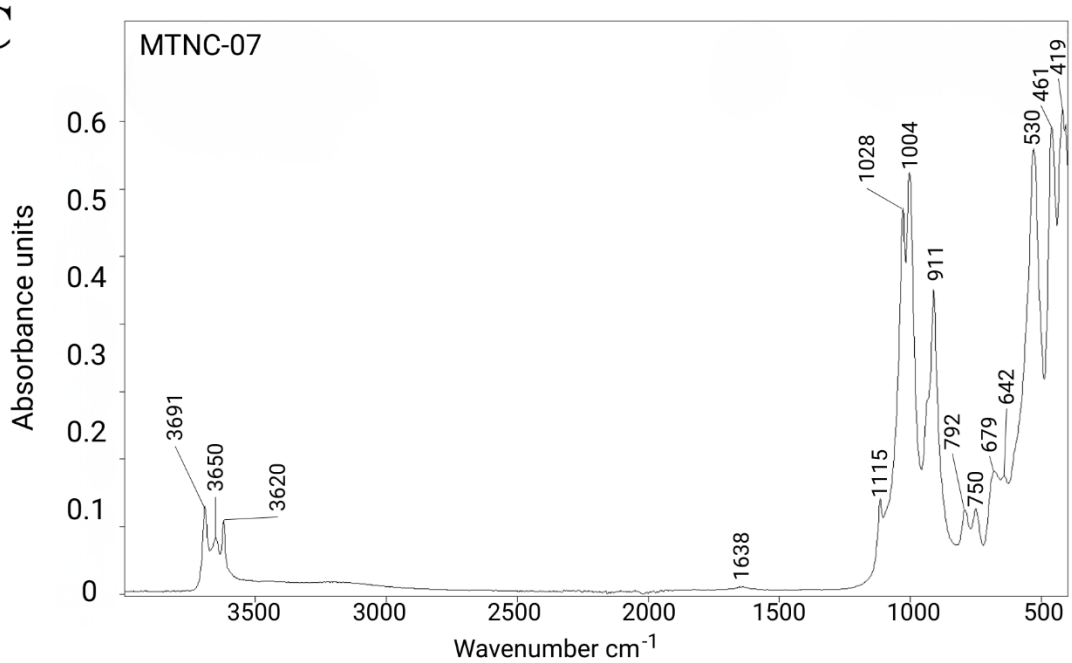
The spectra obtained through ATR-FTIR analysis of all soil samples were mostly represented by mineral-related absorption bands, reflecting the predominantly mineral nature of the studied soils. The most prominent features across all areas were sharp bands in the 3700–3600 cm^{-1} region, typically centered at ~3695, ~3650 and ~3620 cm^{-1}. These bands were consistently observed in samples from all studied sites, indicating the widespread presence of kaolinite-group minerals (Figure 32). In addition, features (*i.e.*, ~3621, ~3526 and ~3449 cm^{-1}) usually associated with gibbsite were consistently observed in samples from the area without ASGM records (Figure 32B).



B


MTBVP-01
Absorbance units
0
0.1
0.2
0.3
0.4
0.5
0.6
3693
3649
3620
3526
3449
1635
1116
1029
1003
911
794
749
673
529
462
416
3500
3000
2500
2000
1500
1000
500
Wavenumber cm-1

C


MTNC-07
Absorbance units
0
0.1
0.2
0.3
0.4
0.5
0.6
3691
3650
3620
1638
1115
1028
1004
911
792
750
679
642
530
461
419
3500
3000
2500
2000
1500
1000
500
Wavenumber cm-1

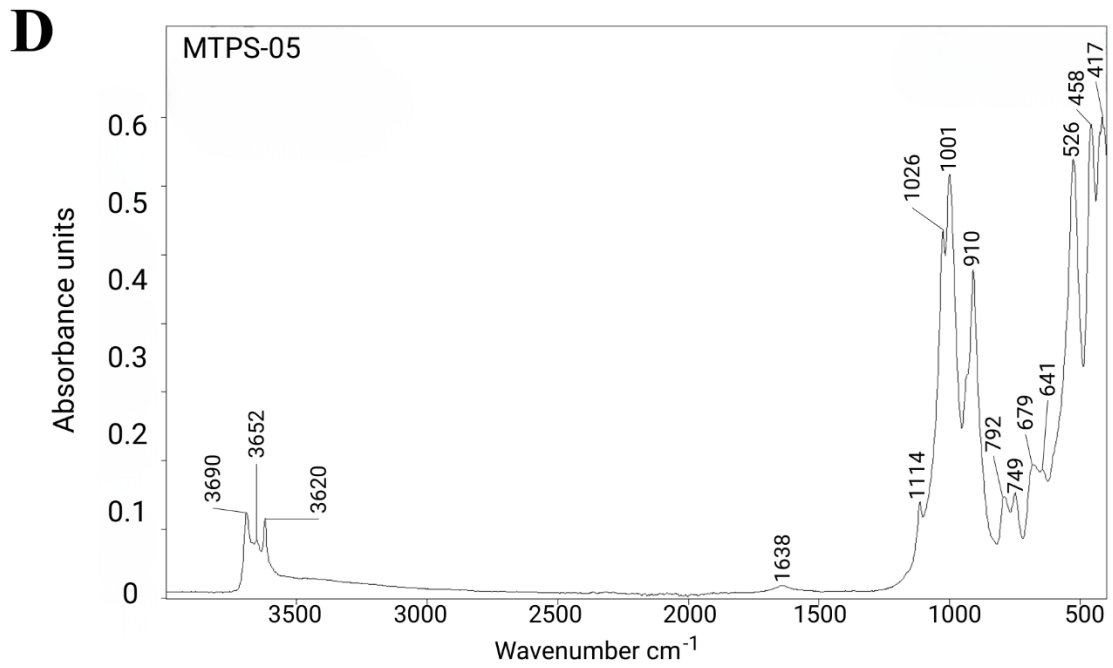


Figure 32: ATR-FTIR spectra of one representative sample from each area: (A) MTBP-01, (B) MTBVP-01, (C) MTNC-07, and (D) MTPS-05.

Additional mineral-related absorptions were observed in the 1200–1000 cm^{-1} region, with recurrent bands near ~1165–1115 and ~1035–1000 cm^{-1}, corresponding to Si–O vibrations of silicate minerals. A diagnostic band around ~913–910 cm^{-1}, attributed to Al–OH bending vibrations, was also detected in several samples, further supporting the dominance of kaolinite-type clay minerals. Bands below 800 cm^{-1}, including features near ~795–777 and ~695–690 cm^{-1}, were consistently present and are characteristic of quartz and other silicate phases. However, the doublet ~795–777 cm^{-1}, typically diagnostic for quarts, is not present in all samples.

Despite the overall similarity in mineralogical signatures, qualitative differences among the ASGM sites were observed in spectral regions commonly associated with soil organic matter (SOM). Absorptions in the 1750–1600 cm^{-1} range, typically centered between ~1650 and ~1620 cm^{-1}, were detected in most samples from recently and long-term deactivated

ASGM areas. These bands were also observed in soils from the control area, although with less variability, and were less consistently present in samples from the active ASGM site.

Overall, the ATR-FTIR results indicate a consistent mineralogical framework across all study areas, with subtle qualitative differences in organic-associated spectral features observed among sites with different disturbance histories.

5.2.3. Thermal behavior of soils assessed by Simultaneous Thermal Analysis (STA)

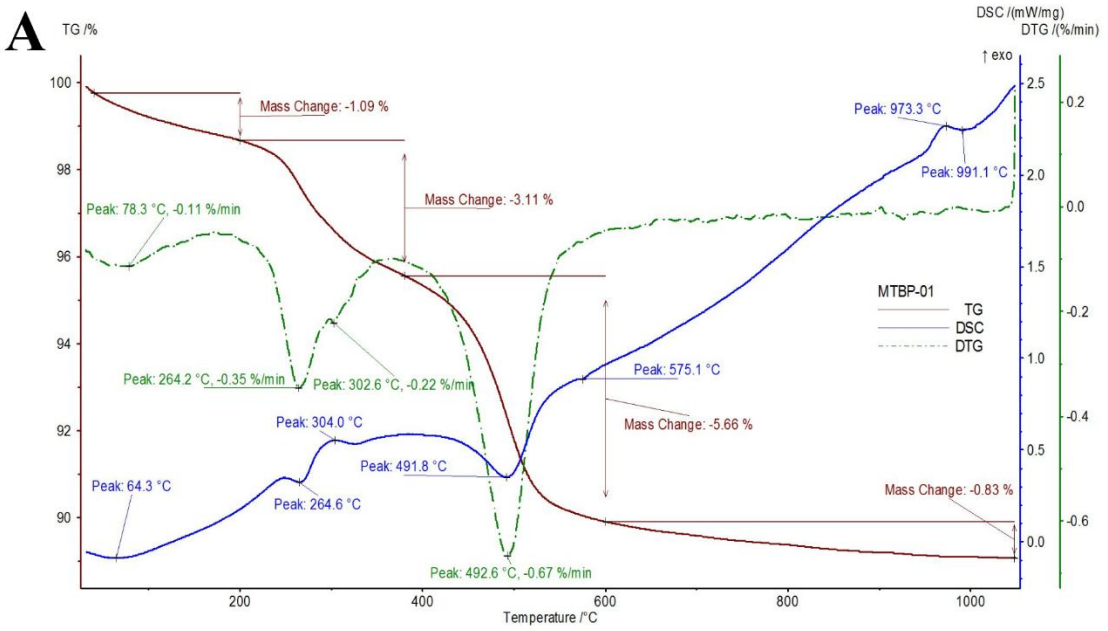
According to DTG curves, four main temperature ranges were defined for the examined samples (<200 °C, 200–380 °C, 380–600 °C and >600 °C; **Mercurio et al., 2022**). In the temperature range below 200 °C, all samples had minor mass losses, typically lower than 1.3%, with DTG peaks generally occurring between approximately 70 and 150 °C (Figure 33). This thermal range is generally attributable to dehydration processed due to the loss of hygroscopic water and, subordinately, interlayer H_2O of clay minerals (e.g., smectite and mixed layers).

Between 200 and 380 °C, mass losses were more variable, ranging from less than 1% to values exceeding 5% in some samples. DTG peaks in this interval were commonly observed between ~250 and 320 °C and were occasionally associated with endothermic or weakly exothermic DSC signals. In addition, in this interval, a noticeable variability within each site was observed, whereas the position of the main DTG peaks remained relatively consistent. These weight losses are generally due to dehydroxylation of (oxyhydr)oxides such as gibbsite and goethite.

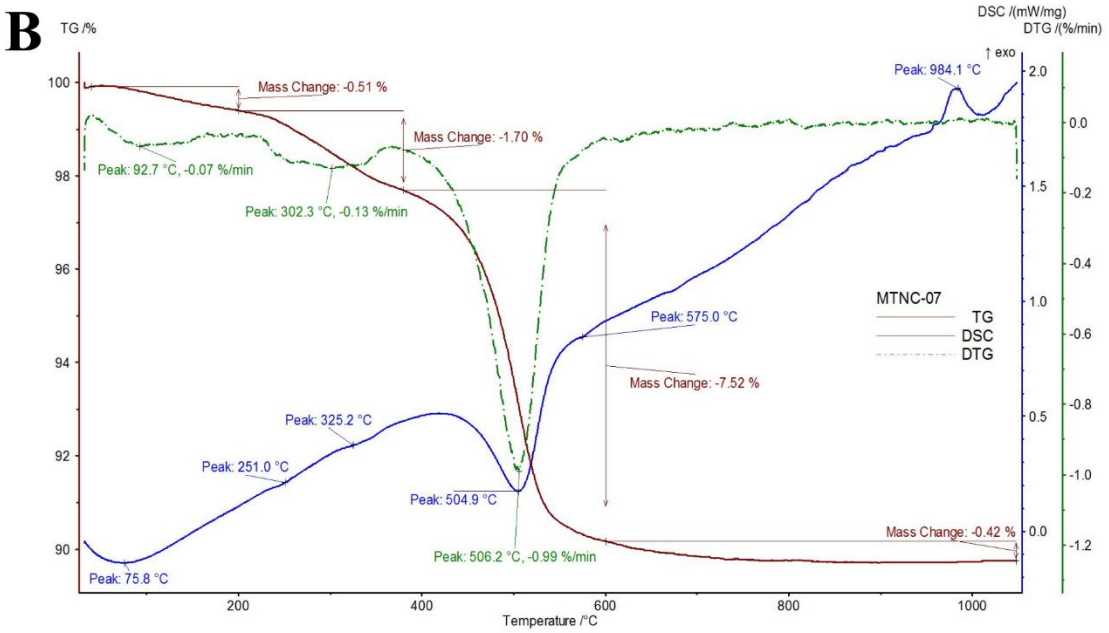
The most prominent mass loss for all samples occurred between 380 and 600 °C, with ΔW values typically ranging from approximately 1% to more than 9%. DTG peaks in this interval

were consistently centered between ~480 and 510 °C and were accompanied by clear endothermic DSC events. The main thermal event in this temperature interval exhibited limited variability in peak temperature across all sites. It is generally due to dehydroxylation of kaolinite mineral group leading to the formation of metakaolin and similar phases. The weak endothermic peaks at ca. 574°C indicate the polymorphic transition of alpha- to beta quartz.

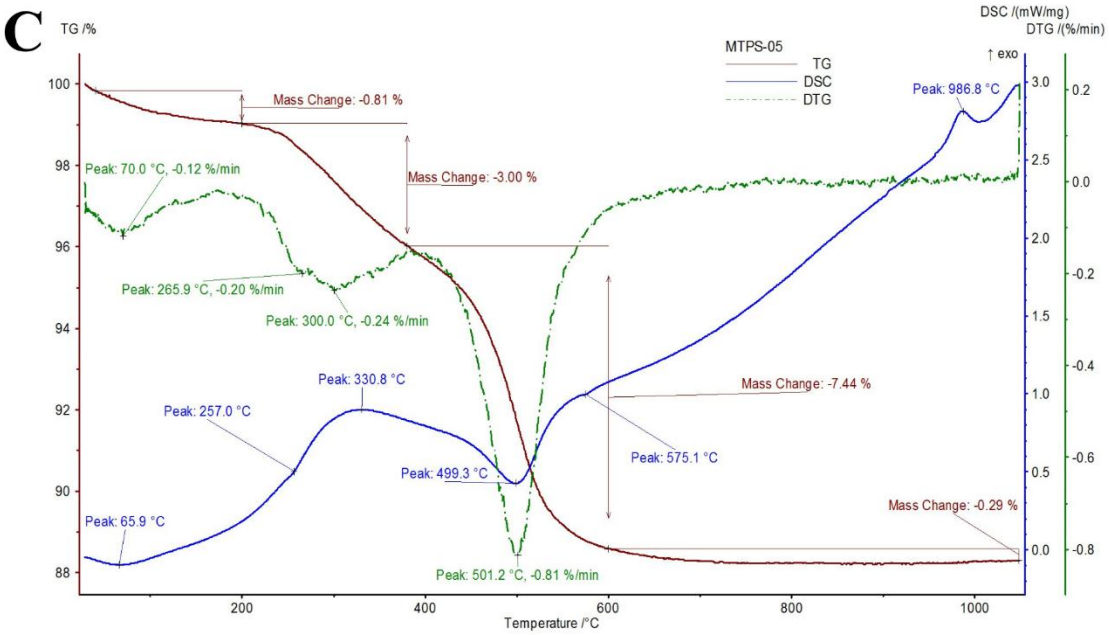
Above 600 °C, only minor additional mass losses were observed, generally below 1% and due to a residual dehydroxylation of phyllosilicates and/or release of halogens, with broad DSC exo-endothermic events typically occurring between ~950 and 1000 °C, that could suggest both the transformation of metakaolin in mullite and/or structural reorganization of other minor clay minerals. The TG/DSC curves for all samples are provided in Appendix 6.



B


TG /%
DSC /(mW/mg)
DTG /(%/min)
↑ exo
MTNC-07
TG
DSC
DTG
Mass Change: -0.51 %
Mass Change: -1.70 %
Mass Change: -7.52 %
Mass Change: -0.42 %
Peak: 92.7 °C, -0.07 %/min
Peak: 302.3 °C, -0.13 %/min
Peak: 984.1 °C
Peak: 575.0 °C
Peak: 325.2 °C
Peak: 251.0 °C
Peak: 504.9 °C
Peak: 506.2 °C, -0.99 %/min
Peak: 75.8 °C
Temperature /°C

C


TG /%
DSC /(mW/mg)
DTG /(%/min)
↑ exo
MTPS-05
TG
DSC
DTG
Mass Change: -0.81 %
Mass Change: -3.00 %
Mass Change: -7.44 %
Mass Change: -0.29 %
Peak: 70.0 °C, -0.12 %/min
Peak: 265.9 °C, -0.20 %/min
Peak: 300.0 °C, -0.24 %/min
Peak: 986.8 °C
Peak: 330.8 °C
Peak: 257.0 °C
Peak: 499.3 °C
Peak: 575.1 °C
Peak: 65.9 °C
Peak: 501.2 °C, -0.81 %/min
Temperature /°C

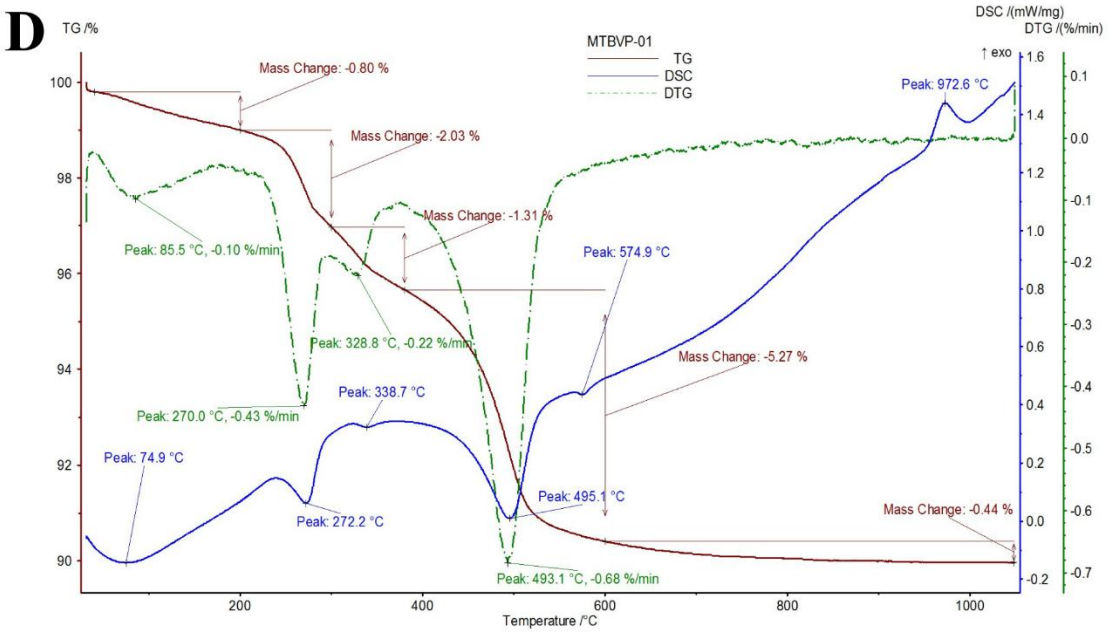


Figure 33: Representative TG, DTG and DSC curves of selected soil samples from the different studied sites: (A) ~30 years deactivated site (MTBP-01); (B) site deactivated in January 2024 (MTNC-07); (C) active ASGM site (MTPS-05); and (D) site without ASGM records (MTBVP-01).

5.2.4. Soil physicochemical properties: pH and water holding capacity (WHC)

Soil pH and water holding capacity (WHC) were determined for a subset of samples across the studied sites and are presented to provide physicochemical context for the interpretation of mineralogical, spectroscopic and thermal data (Figure 34). Detailed pH and WHC (%) data for the selected samples can be found in Appendix 7.

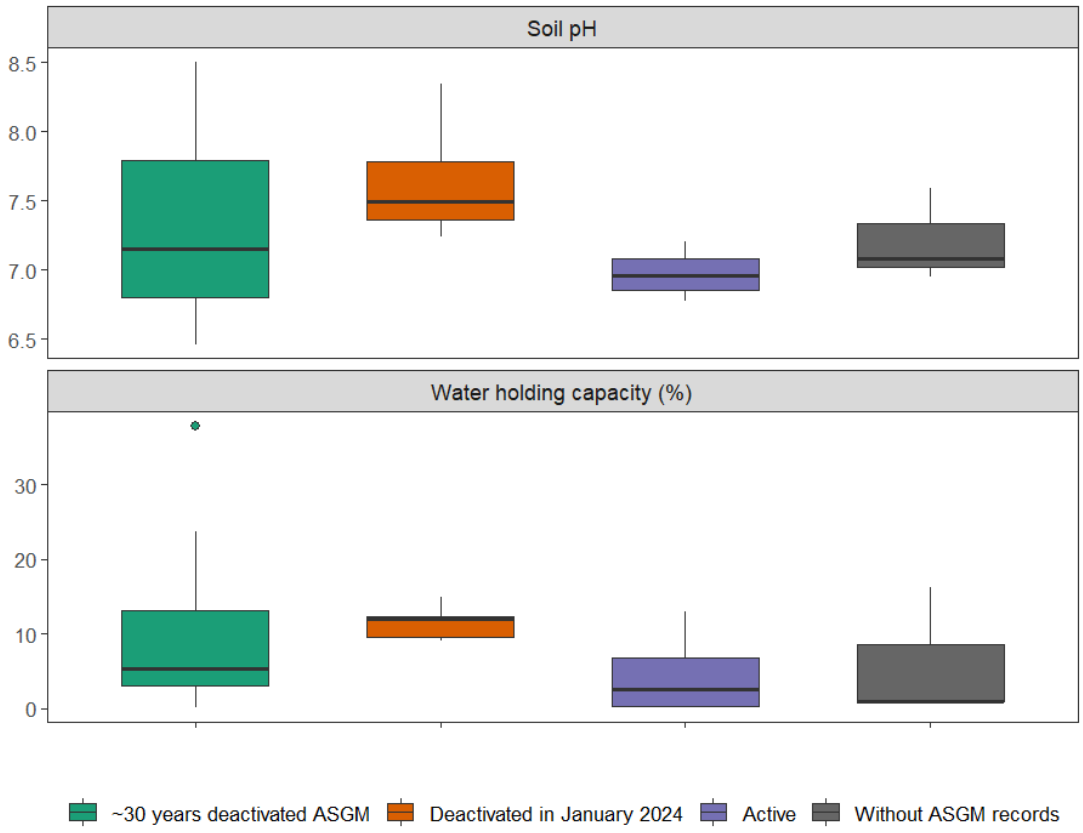


Figure 34: Distribution of soil pH and water holding capacity (%) across the studied sites. Boxplots summarize the median, interquartile range and overall variability for each parameter, with colors indicating site classification. Only samples for which pH and WHC were measured are included.

The ~30 years deactivated ASGM area exhibited a relatively broad pH range (6.46–8.50) with a median of 7.15 and an interquartile range (Q1–Q3) of 6.80–7.79. The site deactivated in January 2024 showed slightly higher values, with a median pH of 7.49 (Q1–Q3: 7.36–7.78) and a narrower range (7.24–8.34). The active ASGM site displayed the lowest median pH (6.96) and the smallest variability (6.85–7.08), while the area without recorded ASGM activity had intermediate values (median 7.08; Q1–Q3: 7.02–7.34).

In contrast, WHC values had a much broader range, varying from less than 1% to values exceeding 35% on a dry weight basis. Within individual sites, noticeable WHC variability was observed, indicating differences in texture, aggregation and/or organic matter content at the sample scale.

Although pH and WHC were not measured for all collected samples, the observed variability in these parameters provides important contextual information for assessing differences in thermal behavior and potential mercury retention mechanisms among the studied soils.

5.2.5. Integrated analysis of total mercury concentrations and behavior based on soil physicochemical, mineralogical and thermal properties

Understanding the factors that control mercury retention and mobility in ASGM-affected soils requires integrating total mercury concentrations with the physicochemical and mineralogical characteristics of the solid phase. In tropical environments, such as the Brazilian Amazon, where intense weathering promotes the formation of secondary minerals, soil constituents such as clays, organic matter, and metal (oxyhydr)oxides play a central role in regulating mercury behavior.

In this context, this section is dedicated to provide an integrated analysis of the data presented in Section 4 and Section 5, in order to explore the physicochemical and mineralogical controls on mercury retention and potential mobility in the studied ASGM-affected sites.

5.2.5.1. Fe–Mn (oxyhydr)oxides as potential sinks for total mercury in ASGM-affected soils

Iron and manganese (oxyhydr)oxides are widely recognized as highly reactive soil constituents in tropical environments, where intense weathering favors their formation and accumulation. In this sense, analyses were conducted to evaluate whether the presence of Fe–Mn (oxyhydr)oxides detected by XRD was associated with systematic differences in THg

concentrations within each studied ASGM context. This distinction is critical, as the objective is to assess the within-area influence of mineralogical components on mercury retention, minimizing confounding effects related to ASGM history, disturbance intensity, or spatial heterogeneity among sites. To achieve this objective, the THg concentration data (Section 4) was combined with the presence or absence of Fe–Mn (oxyhydr)oxides in the samples identified by qualitative XRD (Section 5) (Table 8).

Table 8. Total mercury (THg) concentrations in soils from ASGM sites at different ASGM stages, highlighting samples with identified Fe–Mn (oxyhydr)oxides.

ASGM site (*n*)	**Median THg (min–max) (ng g^{-1})**	**Presence of Fe–Mn (oxyhydr)oxides**	**THg (ng g^{-1})**
~30 years deactivated (37)	324 (27–8,862)	MTBP-04	201
		MTBP-05	142
		MTBP-10	56
		MTBP-24	41
		MTBP-33	40
Deactivated in January 2024 (15)	147 (54–207)	MTNC-03	140
		MTNC-08	77
Active (15)	38 (20–365)	-	-
Without activity records (6)	178 (152–228)	MTBVP-01	228

THg concentrations were log-transformed (log_{10}) prior to analysis to reduce heteroscedasticity. All statistical analyses were performed in R version 4.4.2 **(R Core Team, 2024)**, using the packages *robustbase* **(Maechler et al., 2025)** and *dplyr* **(Wickham et al., 2023)**. In this case, a robust linear regression model (MM-estimators) was selected to reduce sensitivity to outliers, and results were considered statistically significant when $p < 0.05$. The global model included Fe–Mn (oxyhydr)oxide presence, site, and their interaction, allowing the effect of (oxyhydr)oxides on THg to vary among areas. The global robust regression model

indicates that THg concentrations may be associated with both area and the presence of Fe–Mn (oxyhydr)oxides, with statistically significant interaction terms for two of the four areas, demonstrating that the direction and magnitude of this association vary according to ASGM context (Table 9).

Table 9. Effect of Fe–Mn oxyhydroxide presence on log-transformed THg concentrations by area (robust regression).

ASGM site	**Direction of effect**	**Regression coefficient* (log_{10} THg)**	***p*-value**	**Interpretation**
~30 years deactivated	Negative	-0.79	0.0003	THg is substantially lower in samples with Fe–Mn (oxyhydr)oxides
Deactivated in January 2024	Weak negative	-0.14	0.28	No statistically detectable difference
Without activity records	Positive	0.12	0.0039	THg is higher in samples with oxyhydroxides

**Regression coefficients represent the estimated difference in log_{10}-transformed THg concentrations between samples with and without Fe–Mn (oxyhydr)oxides within each area.*

The results presented in Table Y indicate that the association between Fe–Mn (oxyhydr)oxides and THg is strongly context-dependent. In the ~30 years deactivated site, the statistically lower THg concentrations observed in samples containing (oxyhydr)oxides suggest that, under this site conditions, these phases are not associated with enhanced mercury accumulation at the bulk-soil scale. On the other hand, in soils without recorded ASGM activity, the positive association between Fe–Mn (oxyhydr)oxide presence and THg point out to a scenario in which these mineral phases may contribute to mercury retention. The absence of a significant relationship in the ASGM site deactivated in January 2024 indicates that, shortly after mining cessation, the presence of Fe–Mn (oxyhydr)oxides alone does not represent an important factor controlling THg retention in soils.

Therefore, at the scale considered here, the results point to statistically contrasting associations between THg and Fe–Mn (oxyhydr)oxides among ASGM contexts, suggesting that the role of these phases in THg distribution is subject to site-specific environmental conditions and disturbance histories rather than reflecting a uniform control across the study area.

The interpretation of these results must be framed within the scope and resolution of the available data. The presence of Fe–Mn (oxyhydr)oxides was treated as a binary variable based on qualitative mineralogical identification, which does not capture variations in abundance, mineralogy, crystallinity, or surface reactivity. The analysis is further restricted to bulk THg concentrations and does not address Hg speciation, binding strength, or the stability of Hg–mineral associations.

Despite these constraints, the analytical strategy is appropriate for evaluating first order, within-area associations between THg and mineralogical attributes. The use of robust regression minimizes the influence of extreme values without requiring strict distributional assumptions. Importantly, the results are interpreted as area-specific statistical associations rather than as evidence of a single controlling mechanism, providing a defensible framework for integrating these findings with complementary physicochemical and mineralogical evidence discussed in subsequent sections.

5.2.5.2. Statistical analysis of thermogravimetric mass loss (ΔW, %) across ASGM sites

To evaluate differences in thermal stability and composition among ASGM site categories, mass loss distributions across defined temperature intervals were quantified for all 73 soil samples using thermogravimetric analysis (TG). Boxplots of mass loss (ΔW, %) illustrate the variation in each temperature interval among sites (Figure 35).

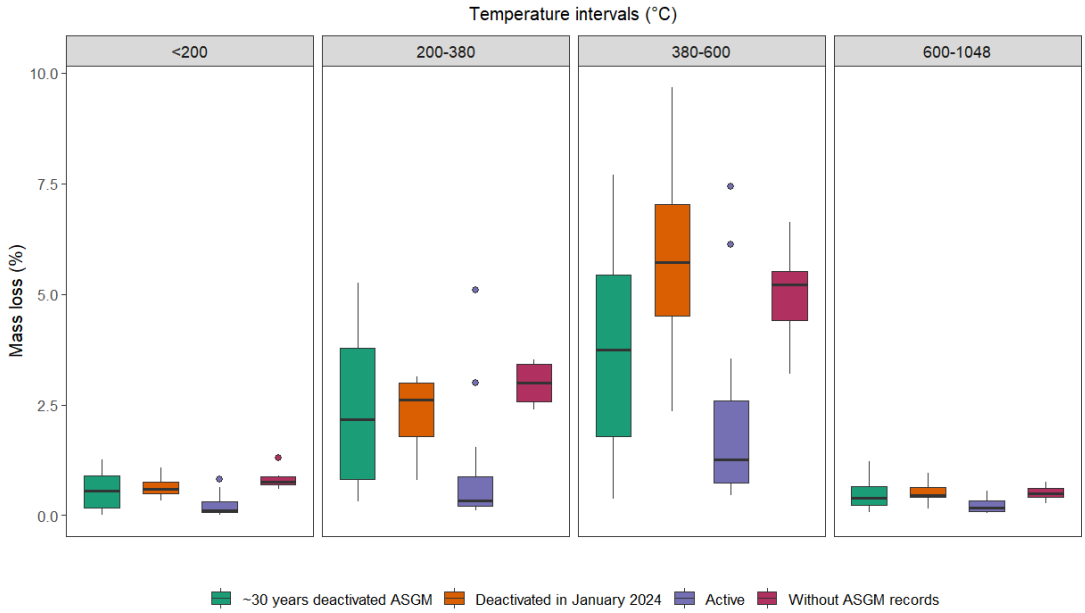


Figure 35: Boxplots of mass loss (ΔW, %) for each temperature interval derived from TG analysis, grouped by studied site. Boxes represent the interquartile range, the central line indicates the median, and whiskers extend to 1.5 times the interquartile range.

Below 200 °C, median mass losses are consistently low across all sites and show narrow interquartile ranges. In the 200–380 °C interval, a wider dispersion of ΔW values is observed, while in the 380–600 °C interval the highest median mass losses and the largest interquartile ranges occur across all sites, highlighting this temperature range as the dominant contributor to total mass loss. In contrast, above 600 °C, mass losses remain minor and exhibit limited variability among sites. Summary statistics for ΔW distributions are provided in Table 10.

Table 10. Summary statistics of mass loss (ΔW, %) for each temperature interval and site.

Studied site	Temp. interval (°C)	Median	IQR	Min—Max
~30 years deactivated (MTBP, *n* = 37)	<200	0.55	0.73	0.01–1.25
	200—380	2.17	2.97	0.32—5.26
	380—600	3.75	3.66	0.37—7.69
	600—1048	0.40	0.41	0.07—1.22
Deactivated in January 2024 (MTNC, *n* = 15)	<200	0.59	0.27	0.33—1.07
	200—380	2.62	1.22	0.79—3.14
	380—600	5.71	2.54	2.34—9.68

	600—1048	0.45	0.22	0.15—0.95
Active (MTPS, *n* = 15)	<200	0.10	0.24	0.01—0.81
	200—380	0.33	0.68	0.10—5.10
	380—600	1.25	1.85	0.46—7.44
	600—1048	0.18	0.25	0.04—0.56
Without ASGM records (MTBVP, *n* = 6)	<200	0.77	0.18	0.60—1.29
	200—380	2.99	0.85	2.38—3.52
	380—600	5.22	1.10	3.20—6.62
	600—1048	0.49	0.22	0.28—0.75

Non-parametric Kruskal–Wallis tests indicated statistically significant differences in mass loss distributions among sites for all evaluated temperature intervals (<200, 200–380, 380–600 and 600–1048 °C; $p < 0.01$), supporting the variability observed in the boxplot analysis. The strongest statistical differences among sites were observed in the 380–600 °C interval ($p = 0.00015$), which also corresponds to the dominant mass loss event in all samples.

To further investigate pairwise differences among sites within each temperature interval, a post-hoc Dunn test with Bonferroni adjustment was applied. The Dunn test identified specific site pairs with statistically significant differences in mass loss (Table 11).

Table 11. Pairwise comparisons of mass loss (%) among sites for each temperature interval using Dunn's test with Bonferroni adjustment.

Temp. interval (ºC)	**Comparison**	**Z**	***p*-adjusted**
<200	~30 years deactivated ASGM - Active	2.996	0.016
<200	Active - Deactivated in January 2024	-3.344	0.005
<200	Active - Without ASGM records	-3.466	0.003
200—380	~30 years deactivated ASGM - Active	3.530	0.002
200—380	Active - Deactivated in January 2024	-3.236	0.007
200—380	Active - Without ASGM records	-3.280	0.006
380—600	~30 years deactivated ASGM - Deactivated in January 2024	-2.932	0.020

380—600	Active - Deactivated in January 2024	-4.303	0.0001
600—1048	~30 years deactivated ASGM - Active	3.252	0.007
600—1048	Active - Deactivated in January 2024	-3.482	0.003
600—1048	Active - Without ASGM records	-2.720	0.039

In the < 200 ºC, 200—380 ºC, and 600—1048 ºC intervals, the active ASGM site statistically differs of all other sites, presenting less mass loss in these intervals. On the other hand, in the interval with higher mass losses for all sites (380—600 ºC interval), the ASGM site deactivate in January 2024 statistically differs from all sites with activity records (*i.e.*, ~30 years deactivated and active ASGM sites).

A PERMANOVA applied to the mass losses across all temperature intervals indicated significant differences in integrated thermogravimetric mass loss profiles among sites (p = 0.0002). Site category explained 25.3% of the total variability in mass loss (R^2 = 0.253), and the relatively high F value (F = 7.79) indicates strong separation among group centroids in the multivariate space, suggesting that these differences are not subtle. This multivariate separation is visually supported by the principal component analysis (PCA; Figure 36). The first principal component (PC1), which explains 80.5% of the total variance, reflects overall differences in the magnitude of thermogravimetric mass loss among sites. This separation is further supported by the distances between group centroids, which ranged from 1.04 (ASGM deactivated in January 2024 vs. without ASGM records) to 3.99 (ASGM deactivated in January 2024 vs. active sites), indicating considerable differences in integrated thermogravimetric profiles.

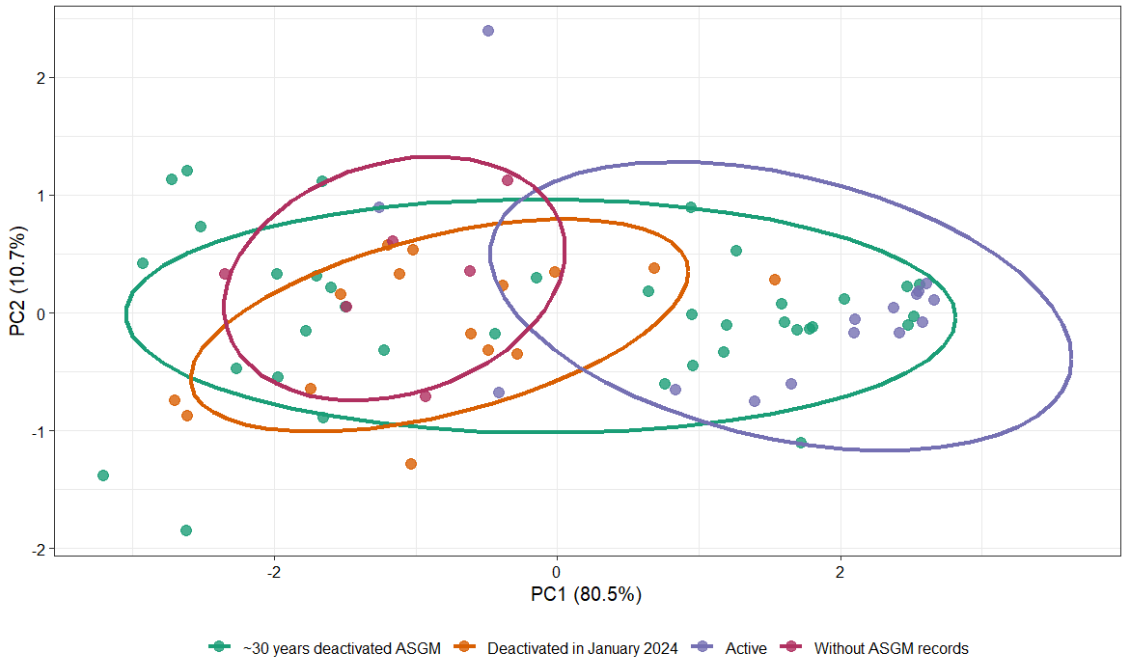


Figure 36: Principal component analysis (PCA) of thermogravimetric mass loss profiles across all temperature intervals. PC1 accounted for 80.5% of the total variance and represents the overall magnitude of mass loss, while PC2 accounted for 10.7% of the variance and contrasts mass losses occurring in the 200–380 °C interval with those occurring above 600 °C. Points represent individual samples and ellipses indicate the 68% confidence region for each site category.

However, PERMDISP results indicated statistically significant differences in multivariate dispersion among sites (p = 0.0466). The moderate F value (F = 2.68) suggests that some groups exhibit greater within-site heterogeneity than others. These differences in multivariate dispersion are illustrated by the violin plots of distances to group centroids (Figure 37). Distances to group centroids indicate higher heterogeneity in the ~30 years deactivated ASGM site (mean = 2.44 ± 1.09; median = 2.40), intermediate variability in the recently deactivated (mean = 1.71 ± 1.15; median = 1.47) and active sites (mean = 1.67 ± 2.17; median = 0.72), and the most homogeneous profiles in areas without ASGM records (mean = 1.08 ± 0.63; median = 0.94). Although differences in dispersion were detected, the pronounced separation among centroids indicates that site-related differences in thermogravimetric profiles are not solely driven by within-site variability.

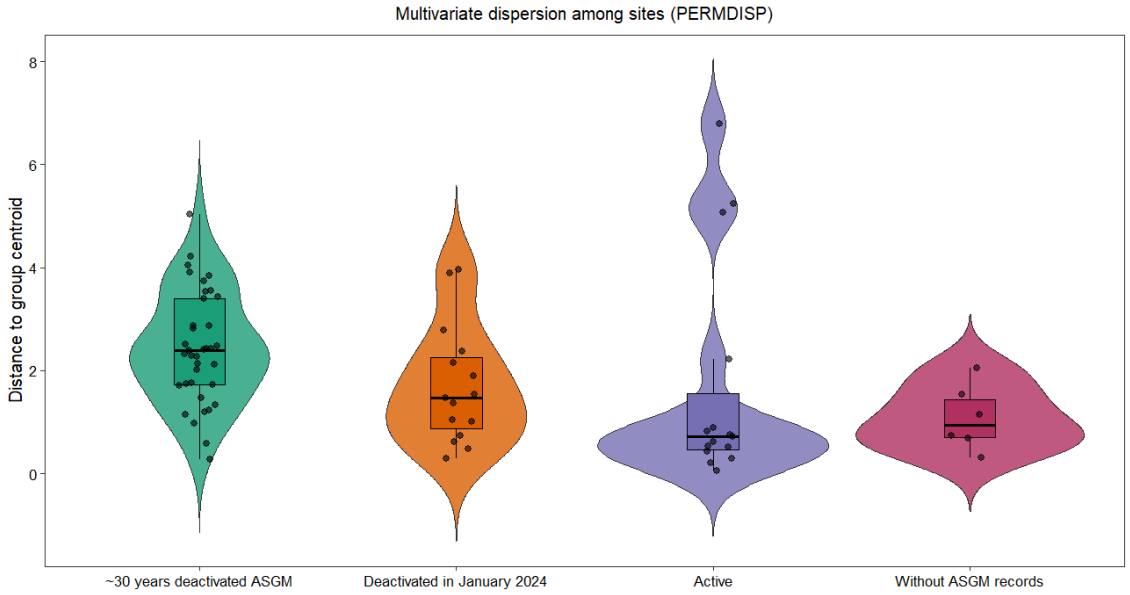


Figure 37: Violin plots of distances to group centroids obtained from the PERMDISP analysis, showing differences in multivariate dispersion among site categories. Violin width represents the density of distances, and boxplots summarize median and interquartile range. Larger distances indicate greater heterogeneity in thermogravimetric mass loss profiles within sites.

Spearman rank correlations were calculated between THg concentrations and mass loss (ΔW) for each site across specific temperature intervals to assess whether higher mercury content is associated with greater thermal degradation. ΔW is reported as the signed percentage mass change relative to the initial mass; negative values indicate mass loss. The results are summarized in Table 12.

Table 12. Spearman correlation between mass loss (ΔW, %) and THg concentrations (ng g-1) by ASGM context.

ASGM site	**Temperature interval (°C)**	**Spearman's ρ**	***p*-value**
~30 years deactivated	< 200	-0.809	1.42e-09***
	200–380	-0.867	3.93e-12***
	380–600	-0.803	1.44e-07***
	600–1048	-0.757	5.96e-08***
Deactivated in January 2024	< 200	-0.561	0.032*

	200–380	-0.677	0.0055**
Active	< 200	-0.671	0.0062**
	200–380	-0.642	0.0099**
	380–600	-0.685	0.0048**

*The asterisks denote the level of statistical significance of the Spearman correlation as follows: *** highly significant ($p < 0.001$), ** moderately significant ($0.001 \leq p < 0.01$), * significant ($0.01 \leq p < 0.05$).*

The correlations indicated a consistent negative association between THg concentrations and mass loss (ΔW) across most temperature intervals, particularly in the ~30 years deactivated ASGM site, where all intervals showed strong and highly significant correlations (ρ = -0.757 to -0.867, $p < 0.001$). Both the ASGM deactivated in January 2024 and the active ASGM sites also displayed moderate to strong negative correlations in specific lower temperature intervals (<200 °C and 200–380 °C). Because ΔW values are negative (mass loss), these results indicate that samples with higher mercury concentrations tend to exhibit more negative ΔW values (*i.e.*, greater mass loss), especially in the ~30 years deactivated ASGM site.

To further evaluate whether thermogravimetric mass loss patterns are associated with THg concentrations, multiple linear regression models were fitted using $\log_{10}$THg as the response variable and the thermogravimetric mass losses (ΔW, %) in each temperature interval as predictors. Three nested models (*i.e.*, models in which the simpler model is a reduced version of the more complex model, obtained by removing additional terms) were constructed.

In Model 1, $\log_{10}$THg was regressed only against the TG-derived mass losses in the four temperature intervals (<200 °C, 200–380 °C, 380–600 °C, and 600–1048 °C). This model showed strong explanatory power (R^2 = 0.652; adjusted R^2 = 0.631; $p < 0.001$), indicating that the thermogravimetric profile alone captures a substantial fraction of THg variability across the dataset. Within this model, the 200–380 °C interval ($p < 0.001$) and the 600–1048 °C

interval ($p < 0.001$) were significant predictors of $\log_{10}$THg, whereas mass losses below 200 °C and in the dominant 380–600 °C interval were not statistically significant. These results suggest that the variability in THg is not simply linked to the magnitude of the main decomposition event (380–600 °C), but rather to more specific thermal fractions.

In Model 2, site category was added as a categorical predictor while maintaining the same TG intervals. This model substantially improved goodness of fit ($R^2 = 0.766$; adjusted $R^2 = 0.740$; $p < 0.001$), demonstrating that site context explains additional THg variability beyond TG mass losses alone. After controlling for the thermogravimetric intervals, all site categories showed significantly lower $\log_{10}$THg relative to the reference site (~30 years deactivated ASGM). Importantly, the 200–380 °C interval remained statistically significant ($p = 0.005$) and the 600–1048 °C interval also remained significant ($p = 0.018$), suggesting that these TG-derived fractions are systematically associated with THg enrichment even after accounting for site category.

Regression coefficients for Models 1 and 2 are provided in Table 13, where: the Estimate (β) corresponds to the estimated regression coefficient, representing the expected change in $\log_{10}$(THg) associated with a one-unit increase in the predictor (holding all other variables constant); the SE is the standard error; the *t* value is the ratio between the coefficient and its standard error (β/SE), and it indicates how strongly the predictor differs from zero relative to its uncertainty; and the *p*-value is used to assess statistical significance.

Table 13. Multiple linear regression models linking log10(THg) to thermogravimetric mass loss (ΔW, %) and ASGM site context.

Model 1 (TG only)				
Predictor	**Estimate (β)**	**SE**	***t***	***p***
Intercept	1.422	0.100	14.146	< 0.001

ΔW <200 °C (%)	0.084	0.329	0.254	0.800
ΔW 200–380 °C (%)	-0.311	0.074	-4.207	< 0.001
ΔW 380–600 °C (%)	0.044	0.035	1.273	0.207
ΔW 600–1048 °C (%)	-0.950	0.266	-3.574	< 0.001

Model fit: $R^2 = 0.652$; adjusted $R^2 = 0.631$; residual SE = 0.399; df = 68

Model 2 (TG + Site)

Predictor	**Estimate (β)**	**SE**	***t***	***p***
Intercept	1.631	0.102	15.957	< 0.001
Active	-0.339	0.114	-2.974	0.004
Deactivated in January 2024	-0.596	0.124	-4.823	< 0.001
Without ASGM records	-0.555	0.157	-3.539	< 0.001
ΔW <200 °C (%)	-0.169	0.291	-0.579	0.564
ΔW 200–380 °C (%)	-0.192	0.066	-2.906	0.005
ΔW 380–600 °C (%)	-0.037	0.034	-1.099	0.276
ΔW 600–1048 °C (%)	-0.565	0.234	-2.420	0.018

Model fit: $R^2 = 0.765$; adjusted $R^2 = 0.740$; residual SE = 0.335; df = 65

Finally, Model 3 included interaction terms between site category and the TG intervals (Site vs. ΔW) to test whether the relationship between $\log_{10}$THg and thermogravimetric mass losses differs among sites. The comparison between Model 2 and Model 3 did not show clear improvement in model performance ($p = 0.076$), providing limited evidence that the slopes linking TG intervals to $\log_{10}$THg vary by site. Therefore, Model 2 was chosen as the main explanatory model due to its robust explanatory power. Model comparisons are shown in Table 14, where in the ANOVA section: Residual df is the residual degrees of freedom, RSS is the residual sum of squares, Δdf is the number of additional parameters between models, ΔRSS is the reduction in RSS, F tests whether the added terms significantly improve model fit, and *p* is the corresponding significance level; and in the AIC section: df is the number of estimated

parameters and AIC is the Akaike Information Criterion (lower values indicate better-supported models).

Table 14. Nested model and AIC-based comparisons among multiple linear regression models for log10THg.

Nested model comparison						
Model comparison	**Residual df**	**RSS**	**Δdf**	**ΔRSS**	**F**	***p***
Model 1 (TG only)	68	10.8143	-	-	-	-
Model 2 (TG + Site)	65	7.2801	3	3.5341	12.027	4.06e−06
Model 3 (TG + Site + interactions)	53	5.1912	12	2.0889	1.777	0.076
AIC-based model selection						
Model	**df**			**AIC**		
Model 1 (TG only)	6			79.7646		
Model 2 (TG + Site)	9			56.8773		
Model 3 (TG + Site + interactions)	21			56.1897		

The overall predictive performance of the selected model is illustrated by the observed vs. predicted relationship (Figure 38), showing that the model captures a substantial fraction of the variability in $\log_{10}$(THg) across sites.

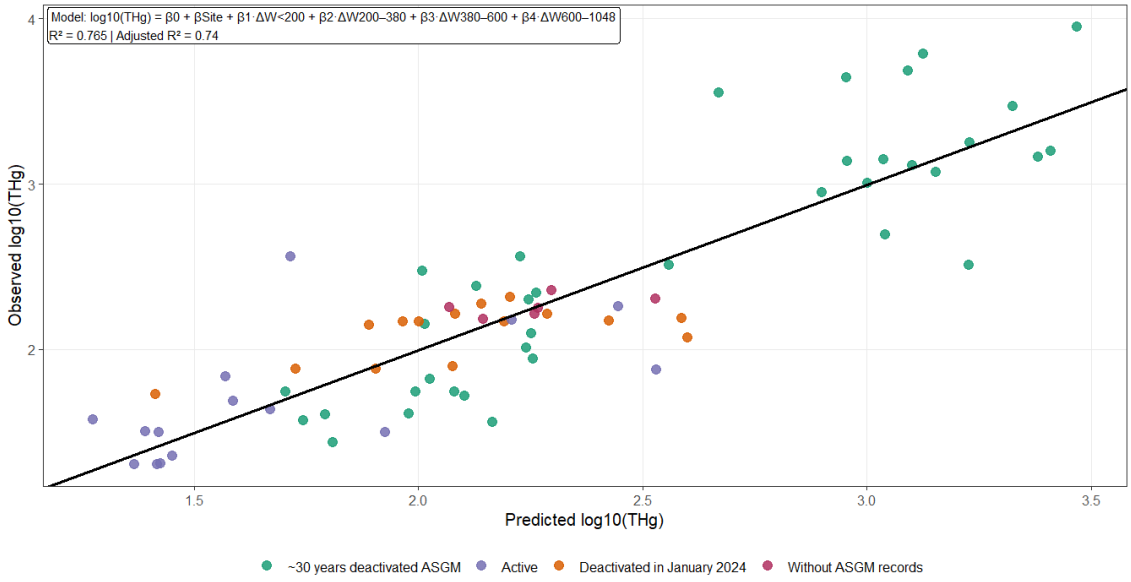


Figure 38: Observed versus predicted log10THg values obtained from the final multiple linear regression model (Model 2: TG + Site). Points represent individual soil samples and are colored by site category. The solid 1:1 line indicates perfect agreement between observed and predicted values; deviations from this line reflect model residuals.

Therefore, these regression results complement the correlation analysis and reinforce that THg variability is not driven exclusively by total thermogravimetric mass loss. Instead, the statistical signal is primarily associated with mass losses occurring in the 200–380 °C and 600–1048 °C intervals.

5.2.5.3. Influence of soil water holding capacity (WHC) and pH on THg concentrations in ASGM-affected soils

Water holding capacity (WHC) is a soil physical property and is commonly associated with sorption capacity, and fine particle content. In this context, this subsection evaluates whether systematic associations exist between WHC and THg concentrations within each ASGM context, focusing on within-area relationships.

Given the non-normal distribution of THg and the presence of extreme values, THg concentrations were $\log_{10}$-transformed and non-parametric (Spearman) and robust statistical approaches were applied. Statistical significance was assessed at $p < 0.05$. Spearman rank correlation analyses were first conducted to explore associations between WHC and $\log_{10}$THg concentrations within each ASGM context (Table 15).

Table 15. Spearman correlation between water holding capacity (WHC) and log10-transformed total mercury (THg) concentrations by ASGM context.

ASGM site (*n*)	**Spearman's ρ**	***p*-value**
~30 years deactivated (28)	0.54	0.0036
Deactivated in January 2024 (5)	-0.20	0.78
Active (4)	0.40	0.75
Without activity records (3)	0.50	1.00

A statistically significant positive correlation between WHC and THg was observed only in the site deactivated for approximately 30 years ($\rho = 0.54$, $p = 0.0036$). No statistically significant correlations were identified in the other sites. In these contexts, the low number of samples with available WHC data limits statistical power, and the observed correlation coefficients should therefore be interpreted as descriptive rather than inferential. These results suggest that any systematic relationship between soil water retention and bulk THg concentrations is not consistent across ASGM contexts.

In the ~30 years deactivated site, this relationship was further evaluated using robust linear regression (Figure 39).

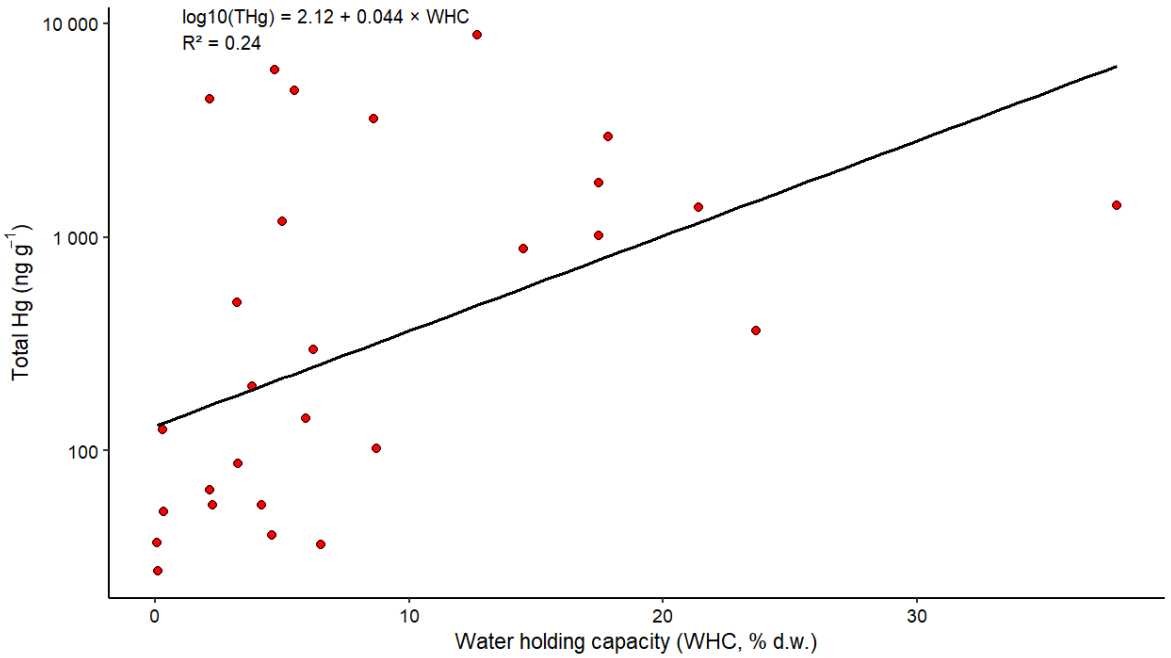


Figure 39: Relationship between WHC and THg concentrations in soils from the ~30 years deactivated ASGM site. Points represent individual samples. The solid line corresponds to the robust linear regression fitted using log_{10}-transformed THg concentrations. The y-axis is displayed on a logarithmic scale using original THg units (ng g^{-1}) to facilitate interpretation.

The model, fitted using an MM-estimator, indicated that increases in WHC were associated with higher log-transformed THg values (slope = 0.044, $p = 0.014$) in the ~30 years deactivated ASGM site. In addition, the model explained approximately 24% of the variability in log_{10}THg concentrations ($R^2 = 0.24$). The intercept (log_{10}THg ≈ 2.12) corresponds to baseline THg concentrations at low WHC values. These results indicate an association between enhanced water retention capacity and higher mercury concentrations in soils from the long-term deactivated studied area, although additional factors likely control a substantial fraction of the observed variability.

Spearman rank correlation analyses were also performed to evaluate the association between soil pH and log_{10}THg concentrations in the four studied areas, and no statistically significant association was identified. Due to the lack of correlation between both WHC and pH with THg in the other study areas, the relationships among THg concentrations and key soil

properties were explored through a Spearman rank correlation matrix exclusively for samples from the ~30 years deactivated ASGM site. The analysis included THg concentrations, WHC, soil pH, and the proportion of particles (<105 µm) (Figure 40).

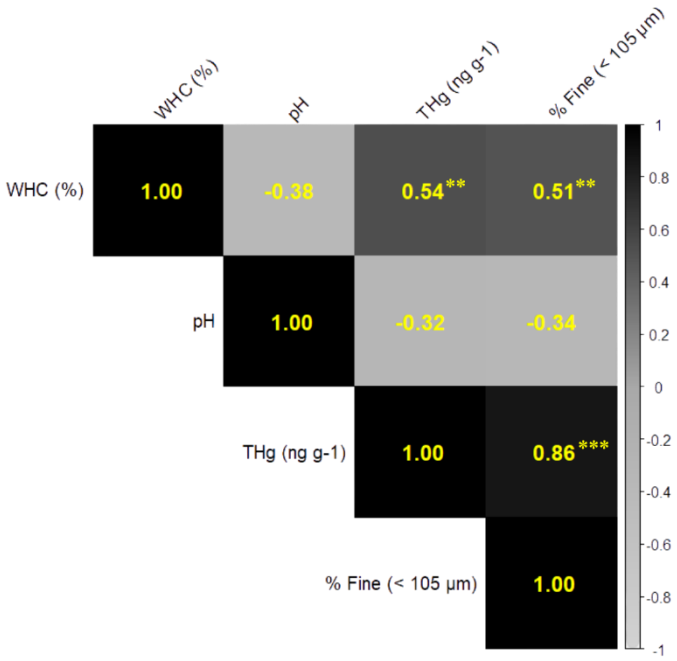


*Figure 40: Spearman correlation matrix among total mercury concentrations (THg), water holding capacity (WHC), soil pH, and fine particle content (<105 µm) for the ~30 years deactivated ASGM site. Numeric labels represent Spearman's correlation coefficients (ρ). Statistical significance is indicated by asterisks (**p < 0.01; ***p < 0.001).*

Significant positive associations were identified among WHC, fine fraction content (< 105 µm), and THg concentrations. WHC was positively correlated with the fine fraction ($\rho = 0.51$, $p = 0.006$) and with THg concentrations ($\rho = 0.54$, $p = 0.003$). In addition, THg showed a strong positive correlation with the fine fraction ($\rho = 0.86$, $p < 0.001$). These results indicate that soils with higher proportions of fine particles tend to retain more water and exhibit higher THg concentrations.

5.3. Discussion

Qualitative XRD results indicate that soils from all studied sites share a broadly similar mineralogical framework, dominated by the presence of quartz and kaolinite-group minerals in all samples from all studied areas (Table 7). In accordance, ATR-FTIR spectra from all sites were dominated by mineral-related absorption bands (Figure 32), consistently with the known sensitivity of ATR-FTIR to silicate matrices and soil water relative to organic functional groups **(Volkov et al., 2021)**. The constant presence of sharp OH-stretching bands in the 3700–3600 cm^{-1} region and strong Si–O absorptions between 1200 and 955 cm^{-1} (Figure 32) confirms the widespread occurrence of kaolinite-group minerals and quartz across the studied soils **(Langer & Flörke, 1974; Awadh & Yaseen, 2019; Tiwari et al., 2020; Al-Amin et al., 2025)**. This mineral assemblage is characteristic of highly weathered tropical soils, particularly Amazonian soils **(**e.g., **Aquino, 2013; Souza et al., 2018; Rocha et al., 2022)**, and reflects the influence of the parent material (*i.e.*, Palito Granite). Under prolonged tropical weathering, such lithological and alteration features favor the extensive leaching of mobile elements and the residual concentration of quartz together with the formation of kaolinite-group minerals.

Despite this overall similarity, accessory mineral phases such as gibbsite, as well as mineral phases indicating more immature soils such as mica-type phyllosilicates, smectites and sporadically occurring feldspars, were detected in selected samples (Table 7), consistent with results previously reported by **Aquino (2013)** and **Souza et al. (2018)** in studies conducted within the same region of the present work. In addition, iron and manganese (oxyhydr)oxides were identified in a subset of samples, although their detection was limited by low crystallinity and potential peak overlap. This limitation highlights the restricted sensitivity of bulk XRD for detecting amorphous, nanocrystalline and surface-associated mineral phases that, despite often occurring in minor amounts, exert a strong influence on soil surface reactivity and trace metal

interactions due to their high specific surface area and abundance of reactive sites **(Waychunas et al., 2005)**.

Experimental studies further demonstrate that Fe-bearing mineral assemblages may control not only the affinity of soils for mercury, but also the dominant retention mechanisms, including adsorption and redox-mediated transformations **(Debure et al., 2020)**. In tropical soils affected by ASGM, the role of Fe oxides in Hg retention may be further modulated by physical disturbance and redox conditions. **Guedron et al. (2009)** showed that in Amazonian soils impacted by historical ASGM activities in French Guiana, Hg is variably associated with Fe oxides, clay minerals and organic matter, while mechanical disturbance favors the presence of elemental Hg and disrupts soil structure.

To evaluate whether these Fe–Mn (oxyhydr)oxides actually influence mercury retention in the studied soils, qualitative XRD data was combined with THg concentrations measured in each sample. The obtained results (Table 8 and Table 9) indicate that the association between Fe–Mn (oxyhydr)oxides and THg is actually context-dependent. In the ~30 years deactivated site, samples containing Fe–Mn (oxyhydr)oxides exhibited significantly lower THg concentrations (robust regression coefficient = -0.79, p = 0.0003), whereas in soils without recorded ASGM activity, the presence of these phases was associated with higher THg (coefficient = 0.12, p = 0.0039). These empirical observations support the conceptual role of Fe–Mn (oxyhydr)oxides in controlling Hg retention in the studied soils, while also highlighting that their influence is modulated by site-specific environmental conditions and disturbance history, rather than exerting a uniform effect across all areas. Other studies further illustrate the mechanisms behind this context-dependency. **Miller et al. (2015)** showed that Hg(0) beads interacting with Mn-oxides form highly soluble Hg coatings, enhancing Hg mobility, whereas **Debure et al. (2020)** demonstrated that the retention and transformation of Hg on Fe-bearing minerals depends on the redox state: under oxidizing conditions Hg is adsorbed, while reducing

conditions can promote Hg reduction and mobilization. These mechanisms suggest that oxide-bearing samples may represent a distinct soil fraction or microenvironment in which THg is less concentrated, potentially due to co-variation with texture, organic matter distribution, and redox history. On the other hand, in the area without ASGM records, where soils were historically less disturbed and exposed, Fe–Mn (oxyhydr)oxides can retain Hg effectively, leading to higher THg in samples with these minerals.

In ATR-FTIR data, absorptions in ~1640 cm^{-1} that represent H–O–H bending mode of molecular water associated with hydroxylated clay minerals **(Volkov et al., 2021; Ayalew, 2023)**, were more consistently detected in soils from the ASGM deactivated in January 2024, in the ~30 years deactivated ASGM, as well as in the site without ASGM records (Figure 32). In contrast, these features were less systematically observed in samples from the active ASGM site, potentially reflecting the effects of ongoing physical disturbance of the soil associated with ASGM activities, including mechanical reworking and disruption of soil structure. Such disturbance has been shown to affect the distribution and composition of soil organic matter and to increase the spatial heterogeneity of THg concentrations and speciation in ASGM-impacted soils **(**e.g., **Guedron et al., 2009; Lourenço et al., 2025)**. The detection of aliphatic C–H stretching bands in the 2950–2850 cm^{-1} region in a single sample (MTPS-12, from the active ASGM) area suggests the presence of relatively labile, aliphatic-rich organic compounds that are sensitive to physical disturbance and typically associated with less humified soil organic matter **(Senesi et al., 1983; Song et al., 2023)**, indicative of the expected heterogeneous occurrence of organic matter previously reported in soil physical descriptions in Section 3.3, and the effects of ongoing mechanical reworking at the site.

Conversely, absorptions between ~3520 and ~3400 cm^{-1}, usually associated with hydrogen-bonded hydroxyl groups and adsorbed water, were exclusively detected in control soils and likely reflect the presence of gibbsite, given that its structural ν(OH) bands are reported in this

region **(Wang & Johnston, 2000)**. Although detected by XRD in all sites (Table 7), the presence of bands associated with gibbsite exclusively in the area without ASGM records likely reflect gibbsite's higher contribution to the bulk soil composition. It may indicate that this specific area reflects a relatively more weathered environment—*i.e.*, closer to the natural conditions expected for tropical soils (**Boeva et al., 2022; Gasparini et al., 2022; Junior et al., 2022**), compared to the other studied sites.

These observations point to differences in surface hydration and organic matter interactions that may influence sorption processes, even in soils with overall similar bulk mineralogy **(Schuttlefield et al., 2007; Parolo et al., 2017)**. In this sense, previous studies of tropical soils and sediments affected by ASGM reported that site-specific variations in surface-bound organic matter, mineral composition, and hydration influence mercury behavior, highlighting the importance of microscale chemical heterogeneity in controlling contaminant dynamics **(Moreno-Brush et al., 2019; Lázaro et al., 2025)**.

The distribution of mass loss values across temperature intervals is further illustrated in ΔW boxplots for each site (Figure 35), with summary statistics provided in Table 10. Below 200 °C, median mass losses were consistently low and exhibited narrow interquartile ranges across all sites, indicating similar moisture-related behavior. In contrast, wider dispersion of ΔW values was observed in the 200–380 °C interval, reflecting heterogeneity in labile organic matter (DSC exothermic peaks; Figure 33), and in low-temperature dehydroxylation processes (DSC endothermic peaks; Figure 33), consistent with contributions from hydroxylated phases such as gibbsite and/or goethite **(Peltre et al., 2013; Barreto et al., 2021)**. The 380–600 °C interval showed the highest median mass losses and the largest interquartile ranges across all sites, reinforcing its dominant contribution to total mass loss and highlighting variability in clay minerals (e.g., kaolinite) dehydroxylation processes (DSC endothermic peak between 490 and 505 ºC; Figure 33) **(Stone & Plante, 2015; Merino et al., 2023)**.

These site-level contrasts are not only visual but also statistically supported. Non-parametric Kruskal–Wallis tests indicated significant differences in ΔW distributions among sites for all temperature intervals (<200, 200–380, 380–600 and 600–1048 °C; $p < 0.01$), corroborating the variability shown in Figure 35. The strongest between-site differences were detected in the 380–600 °C interval ($p = 0.00015$), which corresponds to the dominant mass loss event in all samples, indicating that site-related differences are primarily expressed in the major soil fractions controlling thermal behavior, particularly kaolinite-group dehydroxylation and associated organo-mineral components, rather than being restricted to minor moisture- or labile-OM-related processes. Post-hoc Dunn tests with Bonferroni adjustment further identified the specific site pairs driving these differences (Table 11). In the <200 °C, 200–380 °C and 600–1048 °C intervals, the active ASGM site differed significantly from all other sites, consistently exhibiting lower mass losses (Table 11). In contrast, in the dominant 380–600 °C interval, the site deactivated in January 2024 differed significantly from the other ASGM sites with activity records (~30 years deactivated and active), suggesting a distinct thermal behavior shortly after cessation.

Together, these results suggest that ongoing ASGM activity is associated with systematically reduced mass losses in intervals linked to moisture, labile organic matter, and high-temperature stable fractions, consistent with physical disturbance, removal of fine particles, and depletion of reactive surface components. Conversely, the distinct behavior of the recently deactivated site in the dominant 380–600 °C interval indicates that shortly after cessation, soils may exhibit a transient mineral–organic configuration, particularly affecting kaolinite-dominated dehydroxylation processes.

Beyond interval-by-interval comparisons, multivariate analyses confirmed that the integrated thermogravimetric profiles differ among sites. PERMANOVA applied to ΔW values across all temperature intervals indicated significant between-site differences ($p = 0.0002$),

with site category explaining 25.3% of the total variability (R^2 = 0.253; F = 7.79). This separation is visually consistent with the PCA ordination (Figure 36), where PC1 (80.5% of the variance) primarily reflects differences in the overall magnitude of mass loss among sites. PERMDISP results also indicated statistically significant differences in multivariate dispersion among sites (p = 0.0466; F = 2.68), suggesting that within-site heterogeneity varies across site categories. Distances to group centroids (Figure 37) indicate higher heterogeneity in the ~30 years deactivated ASGM site (mean = 2.44 ± 1.09), intermediate variability in the recently deactivated and active sites, and the most homogeneous thermogravimetric profiles in soils from the area without ASGM records. Importantly, the pronounced centroid separation observed in PERMANOVA and PCA indicates that site-related differences are not solely driven by dispersion effects.

To evaluate whether these thermogravimetric patterns are linked to mercury enrichment, Spearman correlations were calculated between THg and ΔW within each site (Table 12). A consistent association was observed between THg and the magnitude of mass loss (ΔW), such that higher THg concentrations were linked to more negative ΔW values (*i.e.*, greater mass loss), particularly in the ~30 years deactivated ASGM site, where all temperature intervals showed strong and highly significant correlations (ρ = −0.757 to −0.867, $p < 0.001$). These results suggest that THg enrichment in the ~30 years deactivates ASGM is systematically associated with multiple thermal fractions, including moisture-related losses, organic matter decomposition, and mineral dehydroxylation processes. The active and recently deactivated sites also showed moderate-to-strong correlations, especially in the lower temperature intervals (<200 °C and 200–380 °C), indicating that under more disturbed conditions THg is more closely linked to labile and surface-associated soil fractions rather than to more thermally stable components.

Multiple linear regression models further indicate that THg variability is not explained simply by the magnitude of the dominant 380–600 °C event. A model including only thermogravimetric predictors explained 65.2% of the variance in $\log_{10}$THg (Model 1; R^2 = 0.652), with ΔW in the 200–380 °C and 600–1048 °C intervals emerging as significant predictors ($p < 0.001$). Adding site category substantially improved model performance (Model 2; R^2 = 0.765; Table 13), demonstrating that site context explains additional THg variability beyond TG-derived fractions alone. Interaction terms did not significantly improve model fit (Model 3 vs. Model 2; p = 0.076; Table 14), suggesting that the main TG–THg relationships are broadly consistent across sites. The observed vs. predicted relationship (Figure 38) confirms that the final model captures a substantial fraction of THg variability. Overall, these results reinforce that THg enrichment is statistically linked to specific thermogravimetric fractions (200–380 °C and >600 °C), rather than being controlled exclusively by total mass loss or by the main kaolinite dehydroxylation event.

Soil pH and water holding capacity distributions are presented in Figure 34 to provide physicochemical context for the interpretation of mineralogical, spectroscopic and thermal results. Measured pH values (medians for all sites varying between 6.96 and 7.49), with limited variability within individual sites, falls within a range known to influence surface charge development, organic matter solubility, and metal complexation reactions **(**e.g., **Schuster, 1991; Zhang et al., 2023)**. Tropical soils, particularly in the Amazon region, commonly exhibit acidic pH values due to intense weathering and high organic matter inputs **(**e.g., pH < 6; **Fernandes et al., 2018;** pH ~4.6–4.9; **Ferreira et al., 2021)**. More specifically, **Souza et al. (2018)** reported that most pH values (~70%) of soil samples from undisturbed areas in Pará State were between 3 and 4. In contrast, the pH range observed in the studied sites likely reflects the strong influence of mechanical disturbance associated with ASGM activities. Soil

reworking and sediment remobilization related to mining operations can remove organic-rich surface layers and expose less weathered subsurface materials (*i.e.*, naturally enriched in base cations, as reflected by the Palito Granite described in Section 4.1). This process may result in higher soil pH values, consistent with observations from other mechanically disturbed systems where the removal of organic surface layers and exposure of mineral soil led to increased soil pH **(Blouin et al., 2005)**.

In contrast, WHC values exhibited a much broader range (Figure 34). Noticeable variability within sites indicates differences in texture, aggregation and organic matter content at the sample scale **(Adamu & Aliyu, 2012; Bordoloi et al., 2018)**. Such variability in WHC may favor the development of microsites with contrasting moisture regimes, which can promote redox heterogeneity even within overall oxic soils **(Miele et al., 2023)**. This mechanism is relevant because localized decreases in oxygen diffusion and increases in microbial respiration can lower redox potential and modulate Hg partitioning and transformation through redox-sensitive pathways involving Fe/Mn cycling, dissolved organic carbon and microbial activity **(Zhao et al., 2022; Vaňková et al., 2024; Wang et al., 2024; Gustin & Stamenkovic, 2025)**. However, WHC data should be interpreted cautiously given the limited and unbalanced sample size across sites and the methodological sensitivity of WHC estimates to procedural factors. In ASGM-affected tropical soils, these moisture-driven microenvironments are further modulated by seasonal climatic variability, as transitions between dry and rainy periods have been shown to strongly affect soil organic matter stocks and stability in physically disturbed mining areas, thereby altering soil biogeochemical functioning **(Soares et al., 2024)**.

Spearman correlations between WHC and $\log_{10}$THg (Table 15) indicate that a statistically significant positive association was detected only in the ~30 years deactivated ASGM site (ρ = 0.54, p = 0.0036), whereas no significant relationships were identified in the other sites. However, these null results must be interpreted cautiously due to the very limited WHC dataset

in the active, deactivated in January 2024, and without ASGM records sites (n = 3–5), which strongly restricts statistical power and limits inference. Within the ~30 years deactivated ASGM site, robust linear regression further supports this relationship (Figure 39), showing that increasing WHC is associated with higher $\log_{10}$THg concentrations (slope = 0.044, p = 0.014), although WHC alone explains a moderate fraction of the variability (R^2 = 0.24). This indicates that WHC contributes to THg enrichment in this site, but additional factors (e.g., organic matter composition, mineral surface reactivity, and microscale redox variability) likely account for the remaining heterogeneity.

The correlation matrix constructed for this site (Figure 40) provides mechanistic support for the WHC–THg relationship by indicating that WHC is positively associated with the fine fraction (<105 μm) (ρ = 0.51, p = 0.006), and that THg is strongly correlated with fine particle content (ρ = 0.86, p < 0.001). Together, these results suggest that in the ~30 years deactivated ASGM site, higher THg concentrations preferentially occur in finer-textured soils that retain more water, consistent with the known affinity of mercury for fine particles due to their higher surface area and stronger organo-mineral sorption capacity (**Waychunas et al., 2005; Debure et al., 2020; Zhang et al., 2023; Vaňková et al., 2024**). In contrast, soil pH did not show statistically significant correlations with $\log_{10}$THg in any site, suggesting that pH is not a first-order control on bulk THg concentrations at the scale captured by this dataset.

Overall, the studied soils share a common mineralogical composition dominated by quartz and kaolinite-group minerals, consistent with highly weathered tropical environments. However, site-specific differences emerged in accessory phases, surface hydration features, and thermogravimetric behavior, indicating that ASGM disturbance history alters the mineral–organic configuration of the soils beyond what is captured by bulk XRD alone. The strongest between-site contrasts were expressed in the dominant 380–600 °C interval, and THg concentrations were consistently associated with specific thermogravimetric fractions rather

than with total mass loss alone, while site category remained an important predictor of THg variability. Within the ~30 years deactivated ASGM site, higher THg concentrations were preferentially linked to finer-textured soils with higher water retention, suggesting that fine particles and associated sorption surfaces provide a persistent control on THg enrichment long after mining cessation. In contrast, pH showed no systematic relationship with THg, reinforcing that physical disturbance, texture-driven heterogeneity, and mineral–organic interactions are likely the primary drivers of Hg retention patterns in these ASGM-affected soils.

5.4. Conclusion

The studied soils share a broadly similar mineralogical framework dominated by quartz and kaolinite-group minerals, consistent with highly weathered tropical soils developed on granitic parent material. However, accessory phases such as gibbsite, mica-type phyllosilicates, smectites and sporadically feldspars indicate that relevant differences persist at the sample scale, reflecting variations in weathering intensity, soil development, and disturbance history. In addition, the limited detectability of Fe–Mn (oxyhydr)oxides in bulk XRD reinforces that reactive phases controlling trace-metal behavior may occur in low crystallinity or minor amounts, and therefore require integrated interpretation with complementary datasets.

The association between Fe–Mn (oxyhydr)oxides and THg was not uniform across sites, indicating a context-dependent role of these phases in Hg retention. In the ~30 years deactivated ASGM site, samples containing Fe–Mn (oxyhydr)oxides exhibited lower THg, whereas in the area without ASGM records the presence of these phases was associated with higher THg. These contrasting patterns are consistent with the idea that Fe–Mn (oxyhydr)oxides can both retain Hg efficiently under stable conditions and, under disturbed or

redox-variable conditions, participate in Hg redistribution and transformation processes that weaken simple mineral–THg relationships.

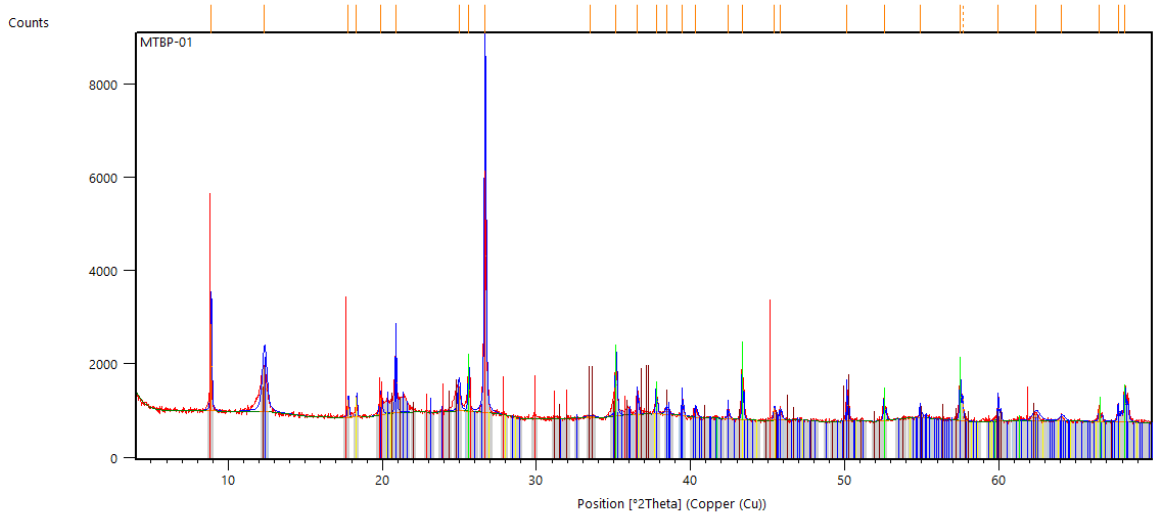
ATR-FTIR results further support subtle but meaningful differences in surface hydration and organic matter signals among sites. The more systematic detection of absorptions around ~1640 cm^{-1} in the deactivated and control sites suggests greater persistence of molecular water associated with hydroxylated clay minerals, whereas their less consistent occurrence in active ASGM soils is compatible with ongoing mechanical reworking and disruption of soil structure. In addition, the detection of aliphatic C–H stretching bands in only one active ASGM sample indicates a localized presence of relatively labile organic compounds, consistent with heterogeneous organic matter distribution under active disturbance. Conversely, OH-stretching absorptions between ~3520 and ~3400 cm^{-1} were exclusive to control soils and likely reflect a stronger contribution of gibbsite, suggesting that this area represents a more weathered and less disturbed environment within the studied landscape.

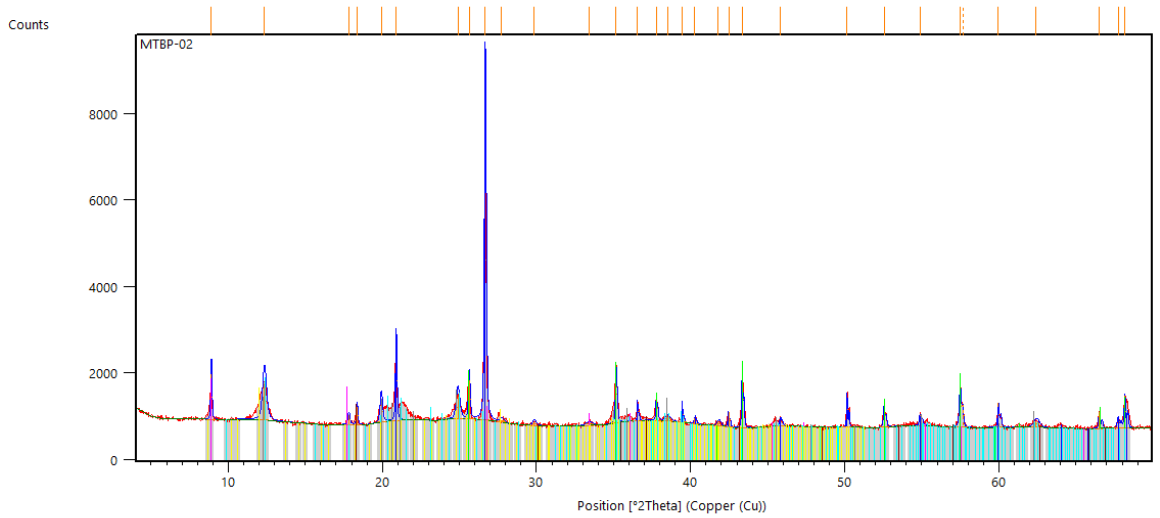
Thermogravimetric analyses showed that the dominant mass loss event across all samples occurs in the 380–600 °C interval, and that the strongest between-site differences are expressed in this temperature range. This indicates that site-related contrasts are primarily reflected in major soil fractions controlling thermal behavior, particularly kaolinite-group dehydroxylation and associated organo-mineral components, rather than being restricted to moisture-related or minor labile organic matter fractions. The active ASGM site consistently exhibited lower mass losses in several intervals, supporting the interpretation that ongoing disturbance reduces moisture-associated and reactive surface fractions. In contrast, the site deactivated in January 2024 differed from the other ASGM sites in the dominant 380–600 °C interval, suggesting that shortly after cessation soils may display a distinct mineral–organic configuration affecting the main dehydroxylation processes.

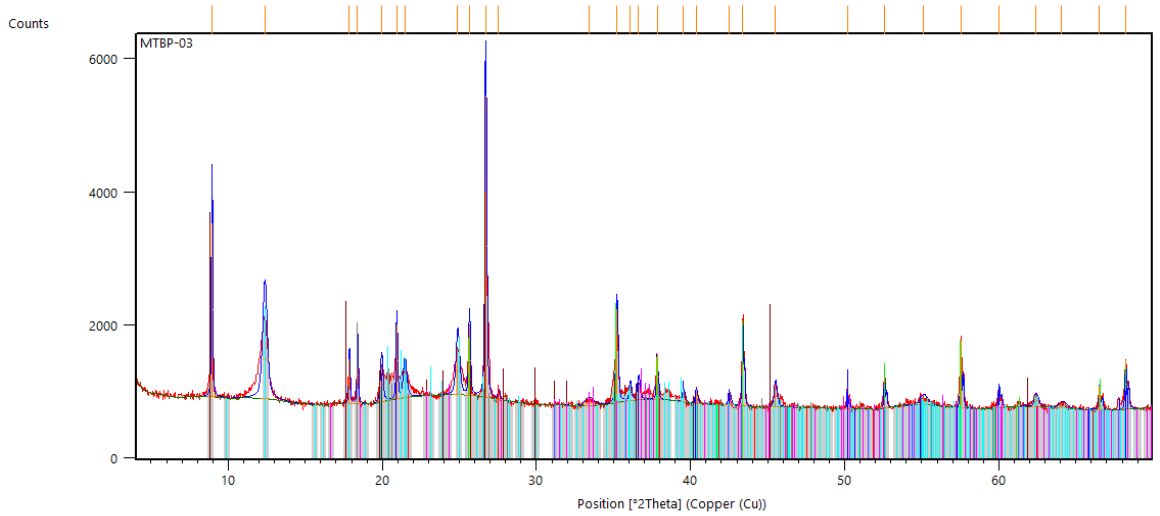
Across sites, THg concentrations were systematically associated with thermogravimetric fractions, particularly in the ~30 years deactivated ASGM site where strong correlations were observed across all temperature intervals. This indicates that Hg enrichment in long-term deactivated soils is linked to multiple soil components, including moisture-related losses, organic matter decomposition and mineral dehydroxylation processes. Regression models further indicate that THg variability is not controlled exclusively by the dominant 380–600 °C event, and that site category explains additional variance beyond TG-derived fractions alone, reinforcing the importance of environmental context and disturbance history.

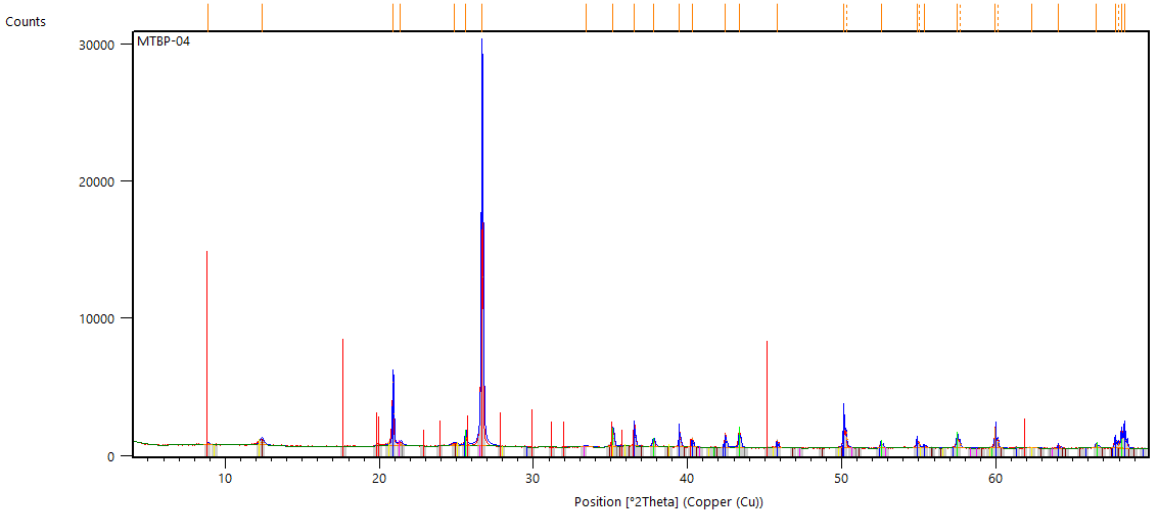
Finally, WHC results suggest that soil physical properties may contribute to within-site controls on THg distribution, but this relationship was not consistent across ASGM contexts. A significant positive association between WHC and THg was detected only in the ~30 years deactivated ASGM site, where WHC was also positively correlated with fine particle content and THg showed a strong affinity for the fine fraction. Together, these results indicate that in the long-term deactivated site, THg enrichment preferentially occurs in finer-textured soils with higher water retention capacity, consistent with increased sorption capacity and potentially greater micro-scale redox heterogeneity. In contrast, soil pH did not show significant correlations with THg, suggesting that pH is not a first-order control on bulk THg concentrations at the scale captured by this dataset.

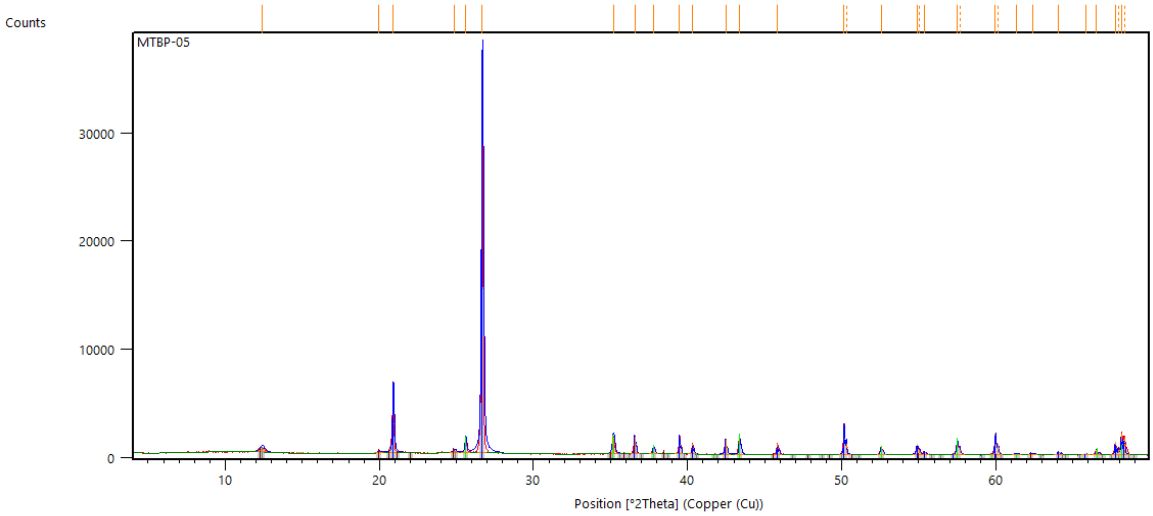
APPENDIX 5: X-ray diffraction patterns of all studied samples.

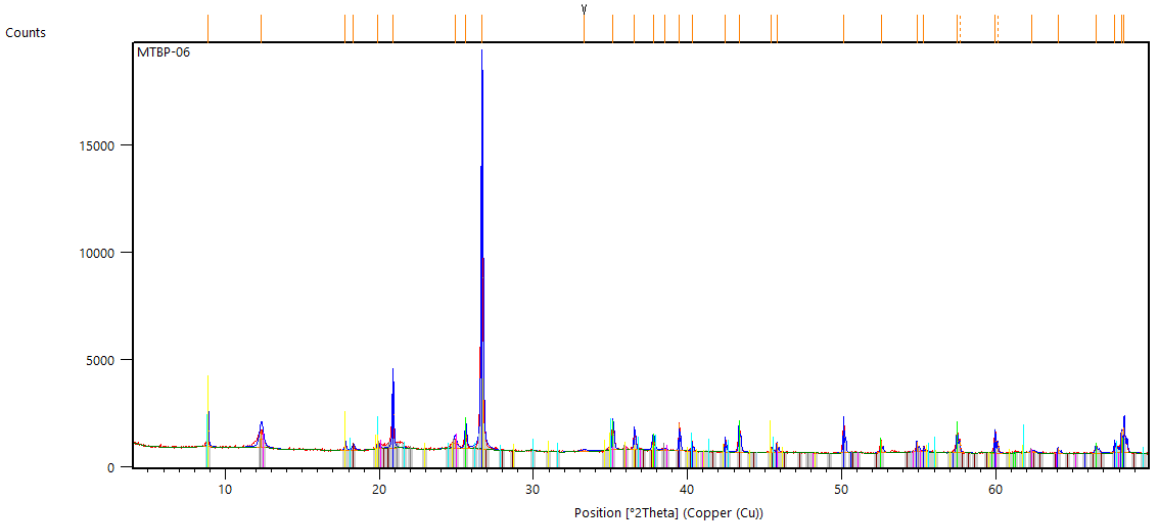


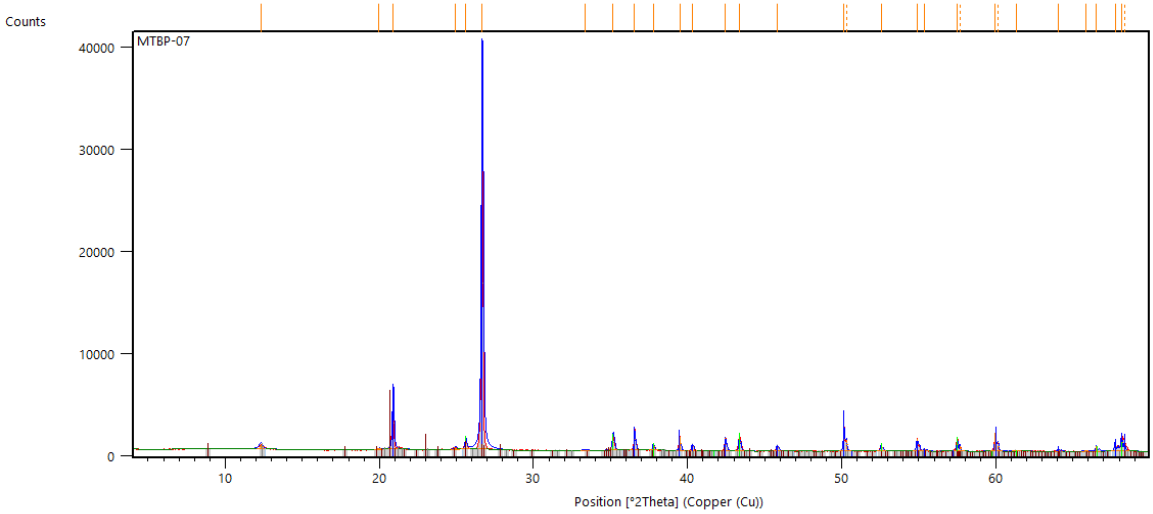


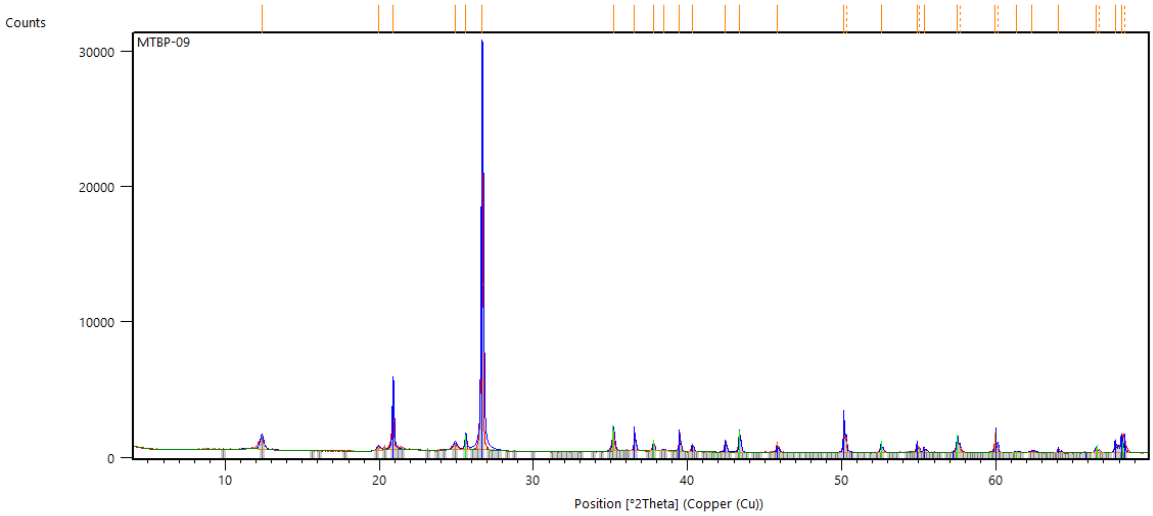


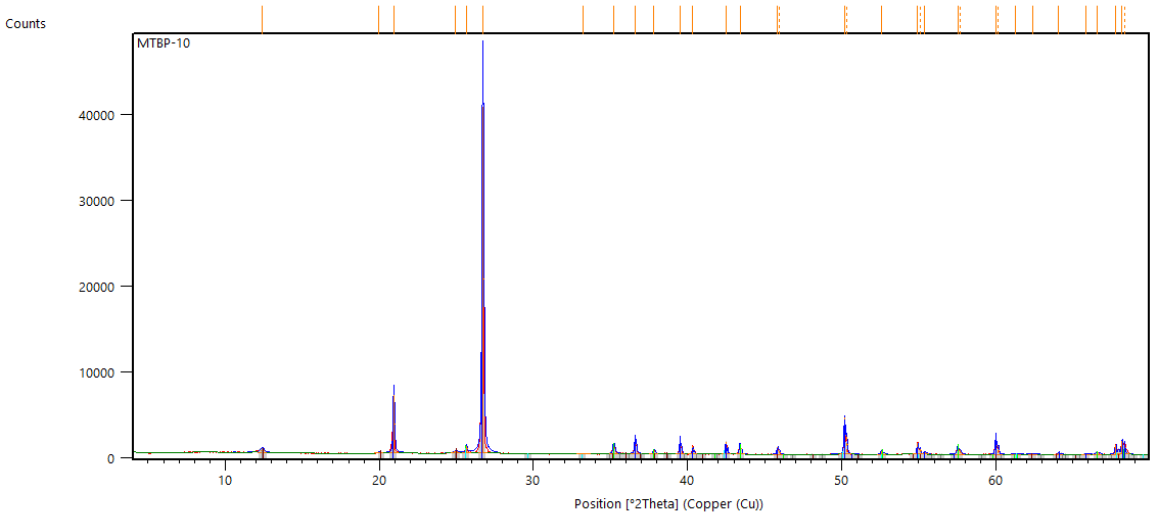

Counts
MTBP-04
30000
20000
10000
0
10
20
30
40
50
60
Position [°2Theta] (Copper (Cu))

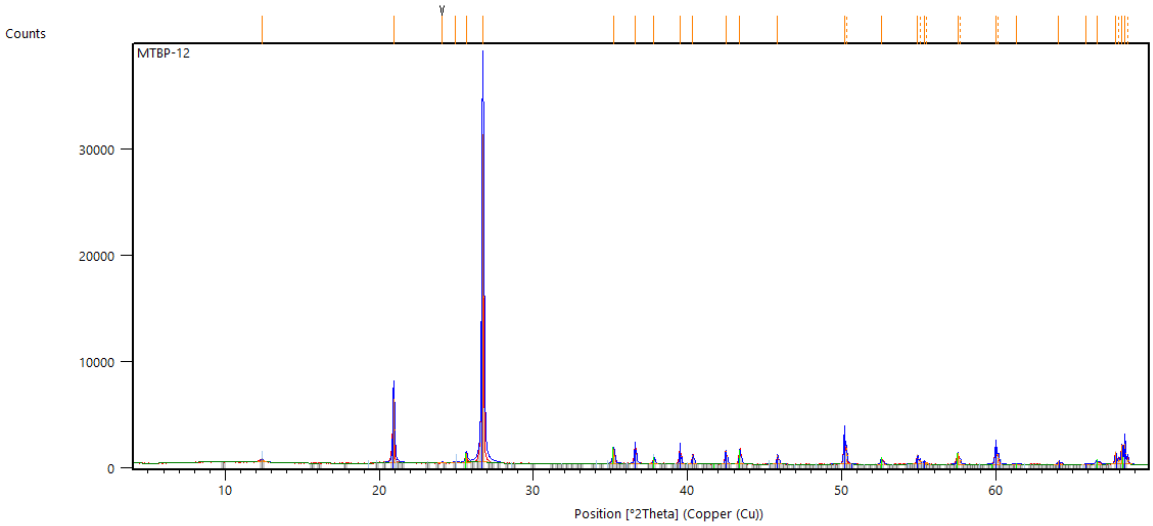

Counts
MTBP-05
30000
20000
10000
0
10
20
30
40
50
60
Position [°2Theta] (Copper (Cu))

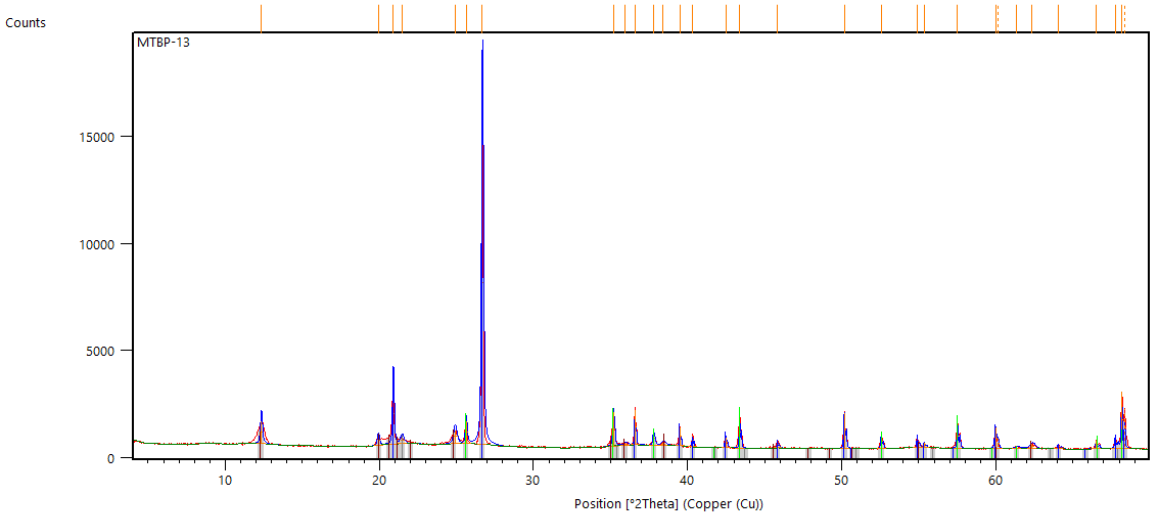

Counts
MTBP-06
15000
10000
5000
0
10
20
30
40
50
60
Position [°2Theta] (Copper (Cu))

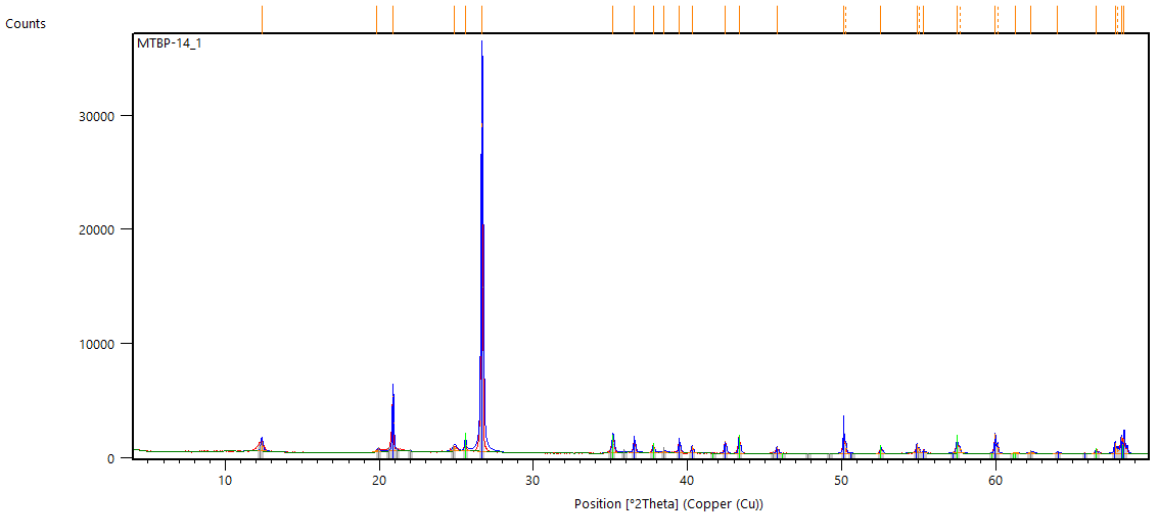

Counts
MTBP-07
40000
30000
20000
10000
0
10
20
30
40
50
60
Position [°2Theta] (Copper (Cu))

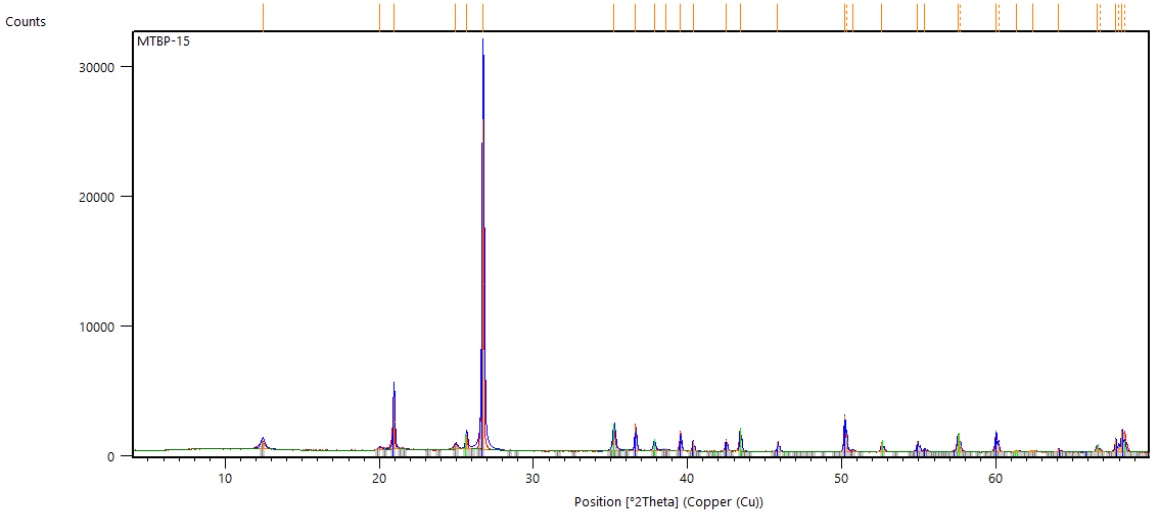

Counts
MTBP-09
30000
20000
10000
0
10
20
30
40
50
60
Position [°2Theta] (Copper (Cu))

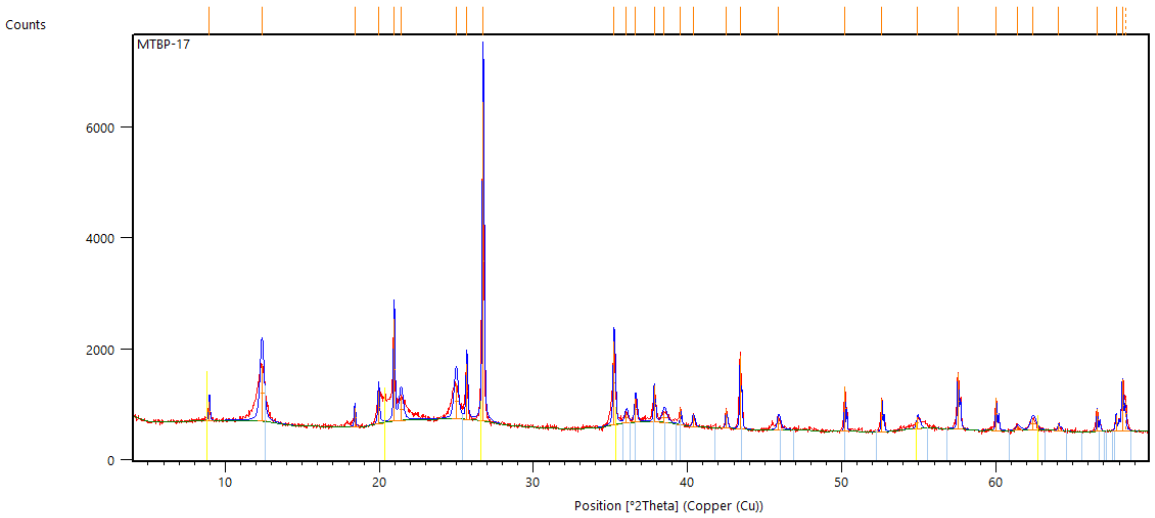

Counts
MTBP-10
40000
30000
20000
10000
0
10
20
30
40
50
60
Position [°2Theta] (Copper (Cu))

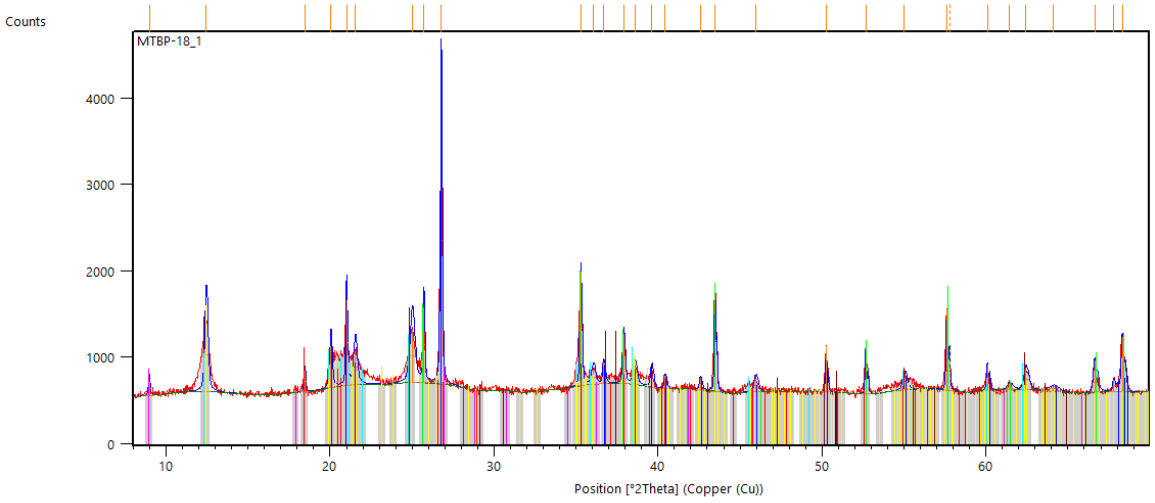

Counts
MTBP-12
30000
20000
10000
0
10
20
30
40
50
60
Position [°2Theta] (Copper (Cu))

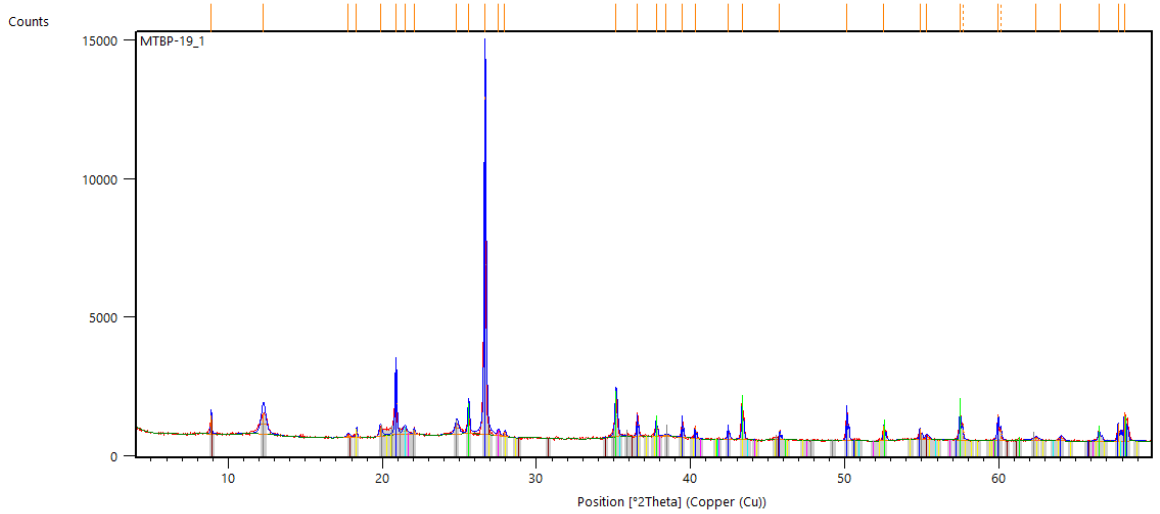

Counts
MTBP-13
15000
10000
5000
0
10
20
30
40
50
60
Position [°2Theta] (Copper (Cu))

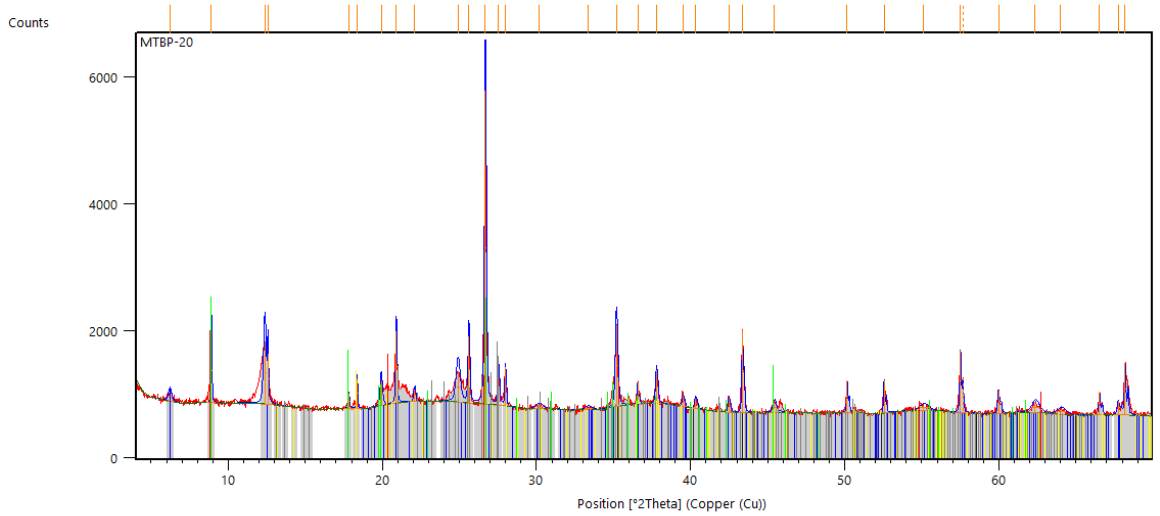

Counts
MTBP-14_1
30000
20000
10000
0
10
20
30
40
50
60
Position [°2Theta] (Copper (Cu))

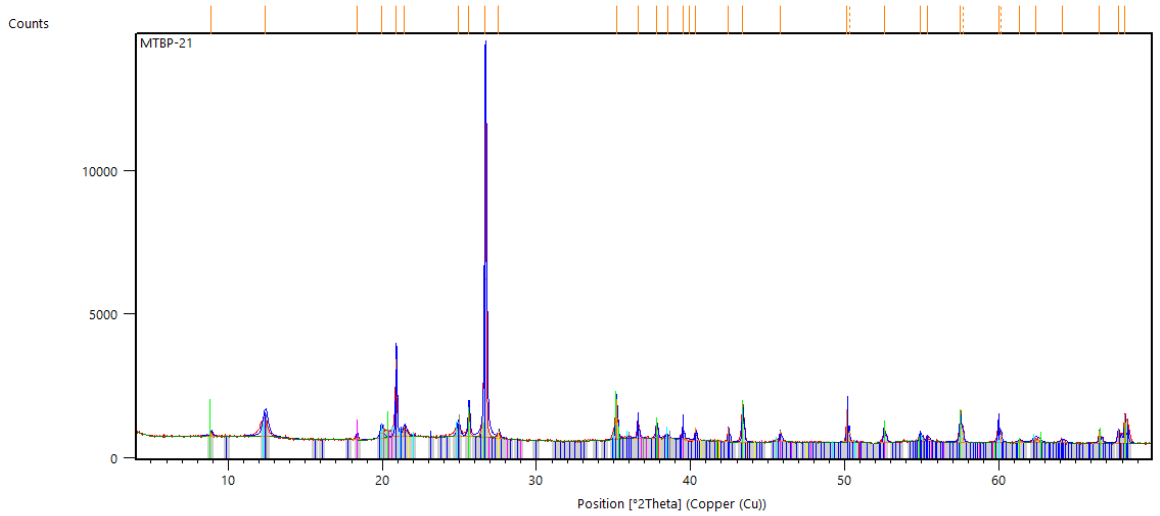

Counts
MTBP-15
30000
20000
10000
0
10
20
30
40
50
60
Position [°2Theta] (Copper (Cu))

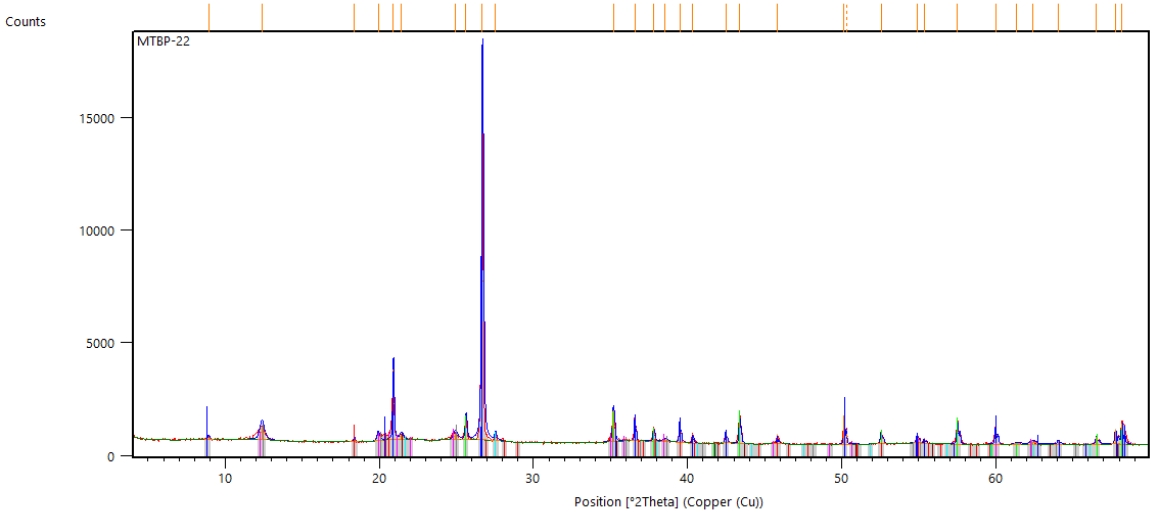

Counts
MTBP-17
6000
4000
2000
0
10
20
30
40
50
60
Position [°2Theta] (Copper (Cu))

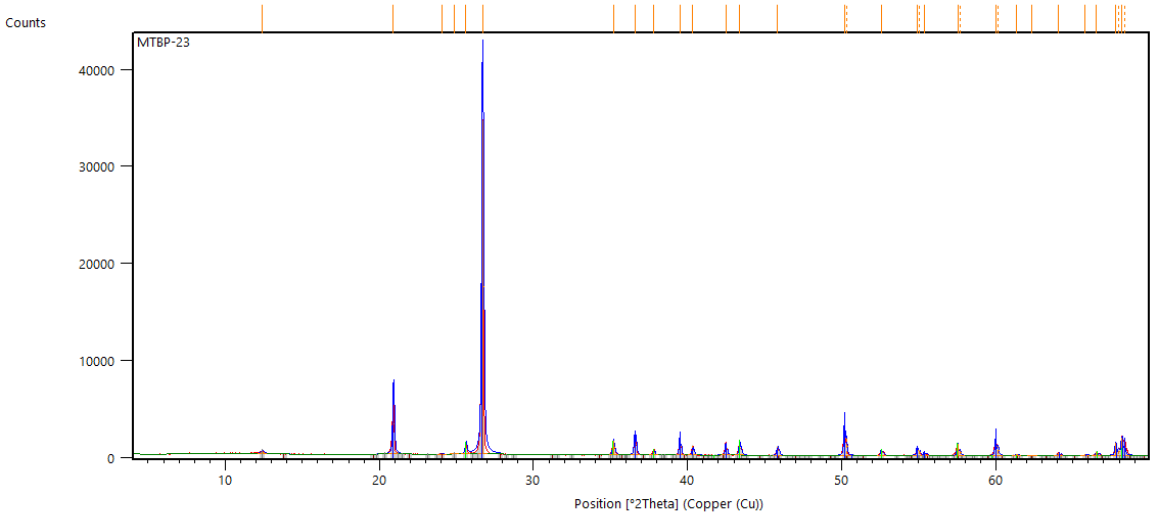

Counts
MTBP-18_1
4000
3000
2000
1000
0
10
20
30
40
50
60
Position [°2Theta] (Copper (Cu))

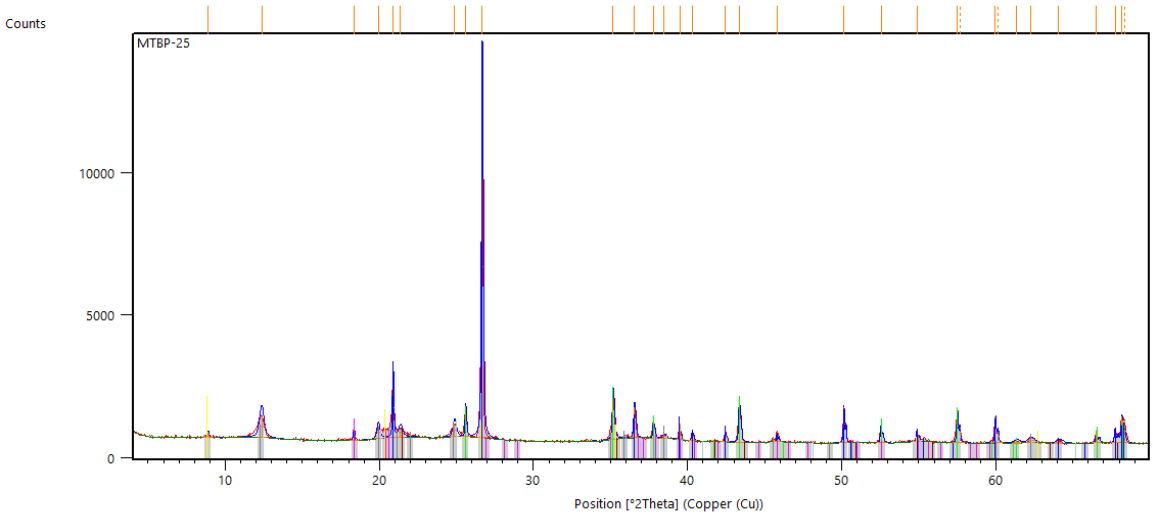

Counts
MTBP-19_1
15000
10000
5000
0
10
20
30
40
50
60
Position [°2Theta] (Copper (Cu))

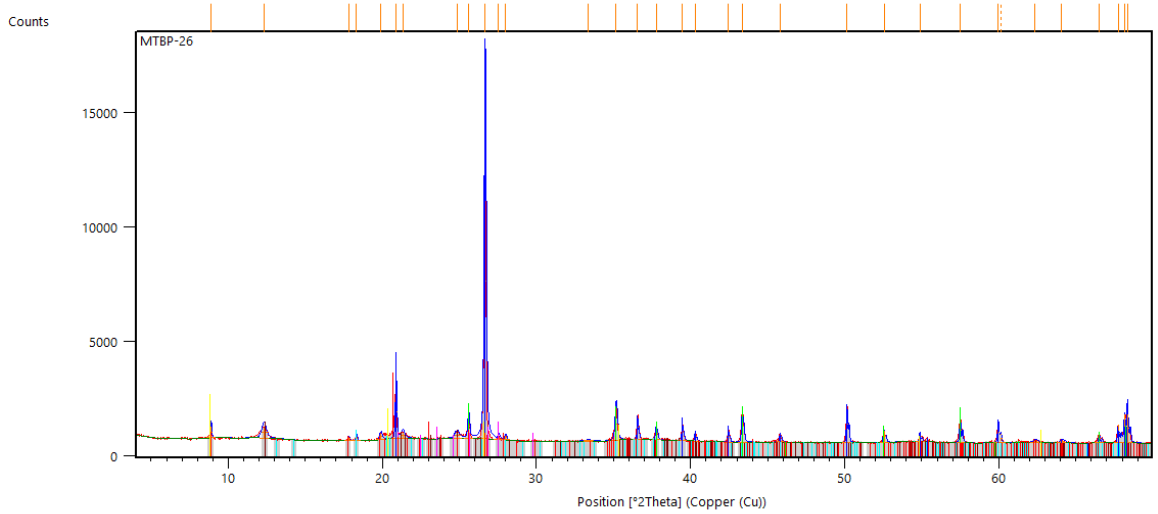

Counts
MTBP-20
6000
4000
2000
0
10
20
30
40
50
60
Position [°2Theta] (Copper (Cu))

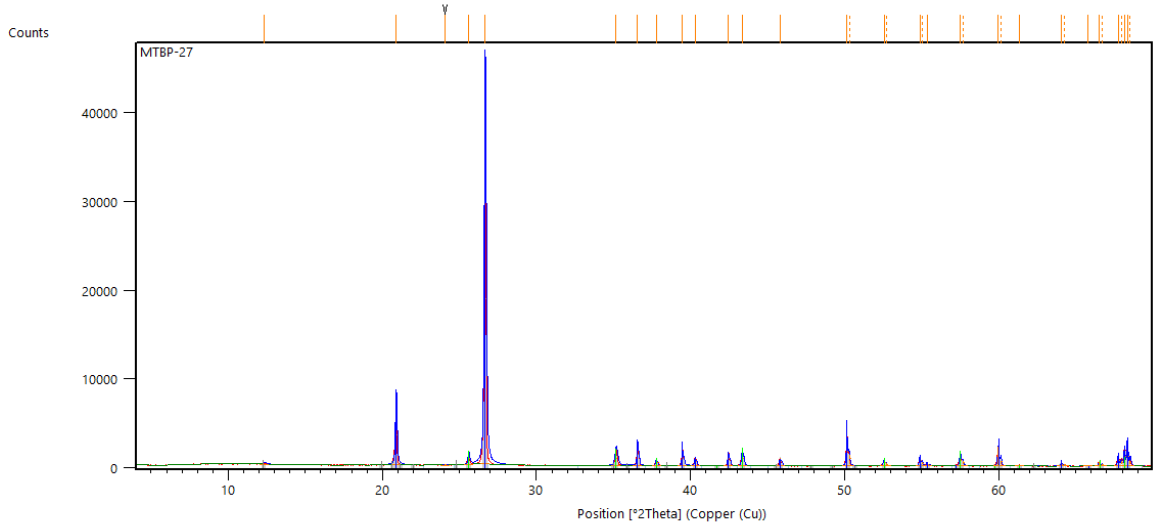

Counts
MTBP-21
10000
5000
0
10
20
30
40
50
60
Position [°2Theta] (Copper (Cu))

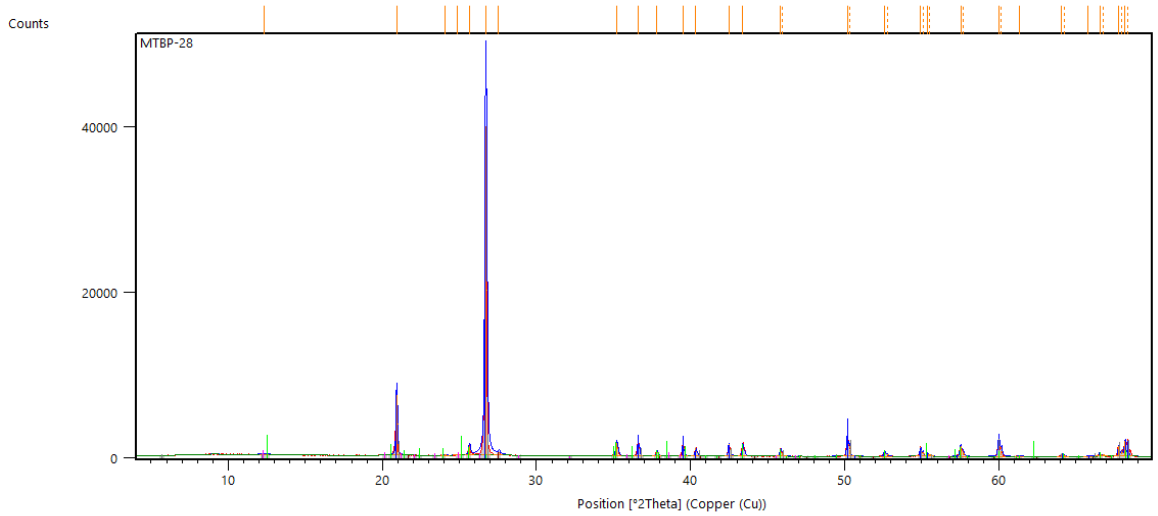

Counts
MTBP-22
15000
10000
5000
0
10
20
30
40
50
60
Position [°2Theta] (Copper (Cu))

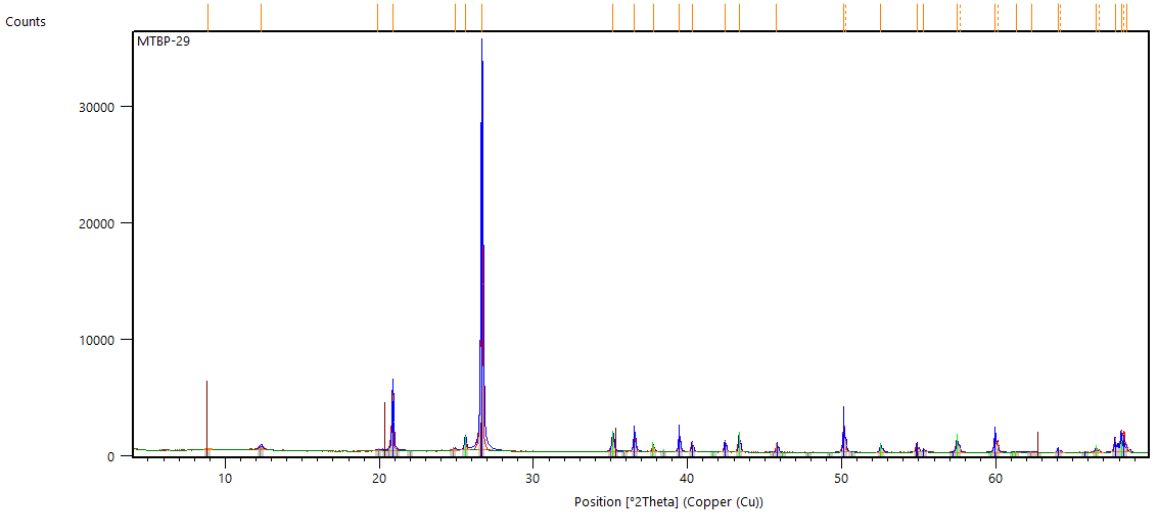

Counts
MTBP-23
40000
30000
20000
10000
0
10
20
30
40
50
60
Position [°2Theta] (Copper (Cu))

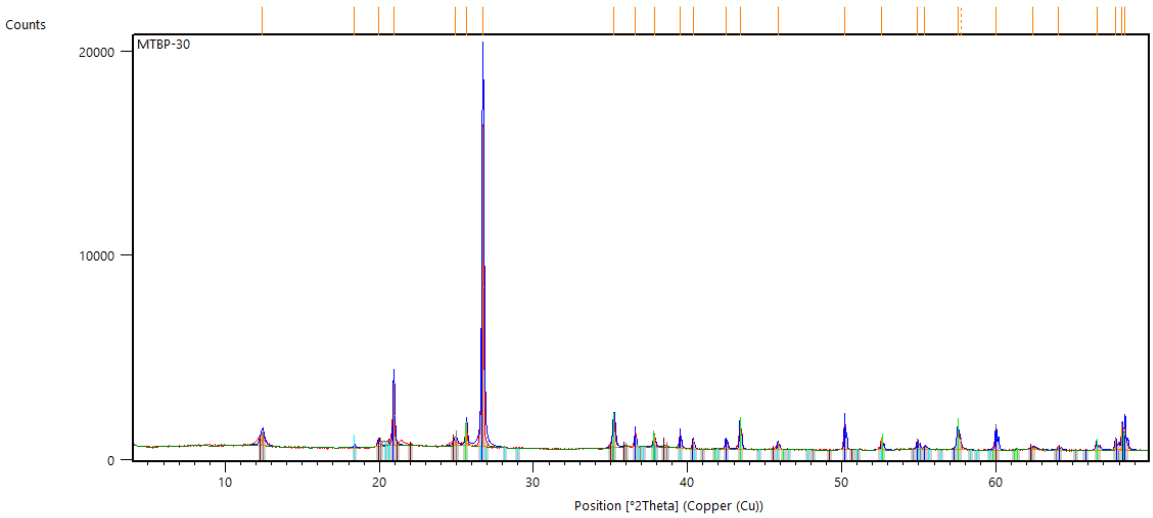

Counts
MTBP-25
10000
5000
0
10
20
30
40
50
60
Position [°2Theta] (Copper (Cu))

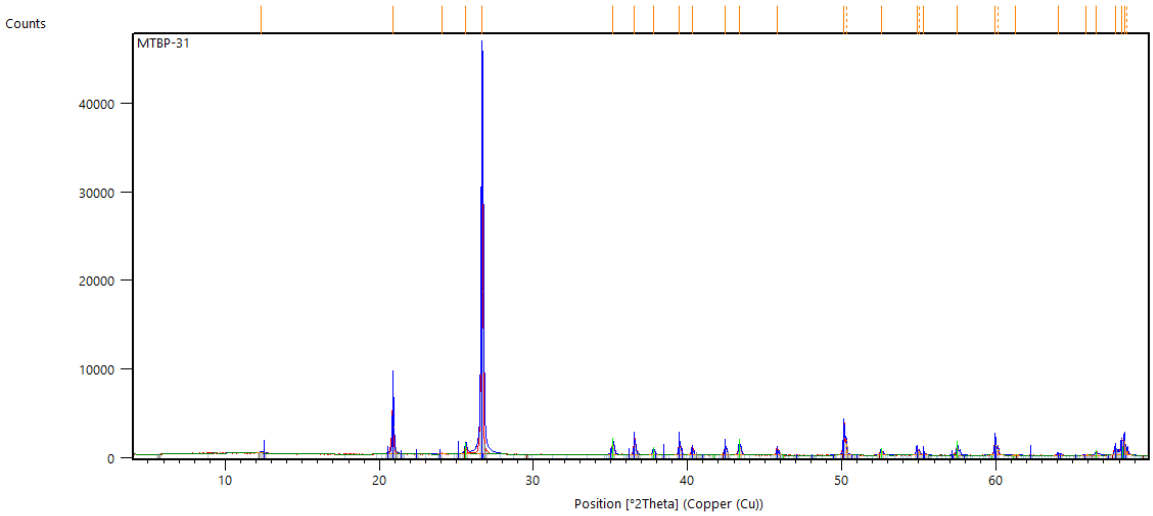

Counts
MTBP-26
15000
10000
5000
0
10
20
30
40
50
60
Position [°2Theta] (Copper (Cu))

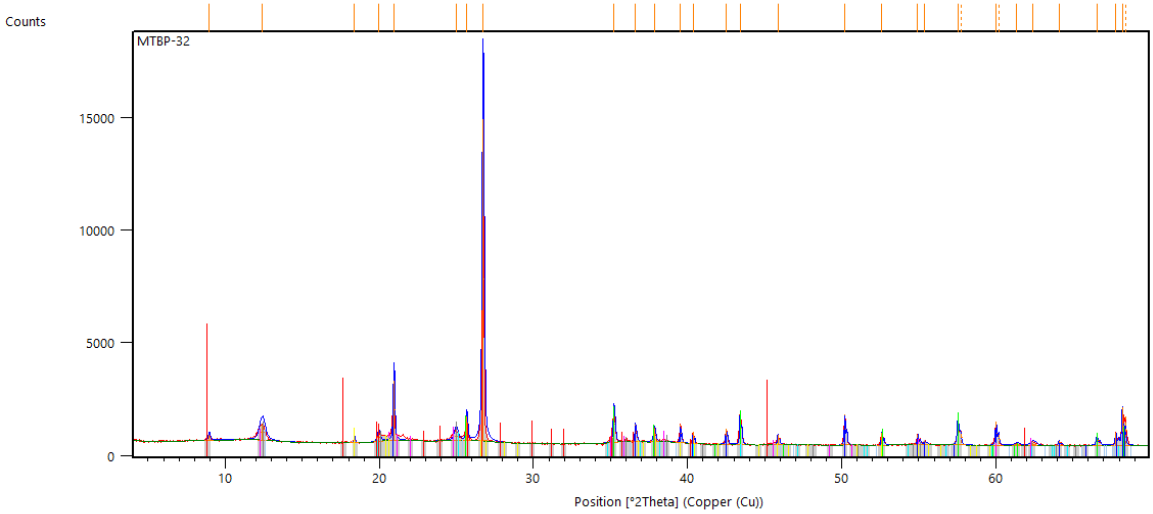

Counts
MTBP-27
40000
30000
20000
10000
0
10
20
30
40
50
60
Position [°2Theta] (Copper (Cu))

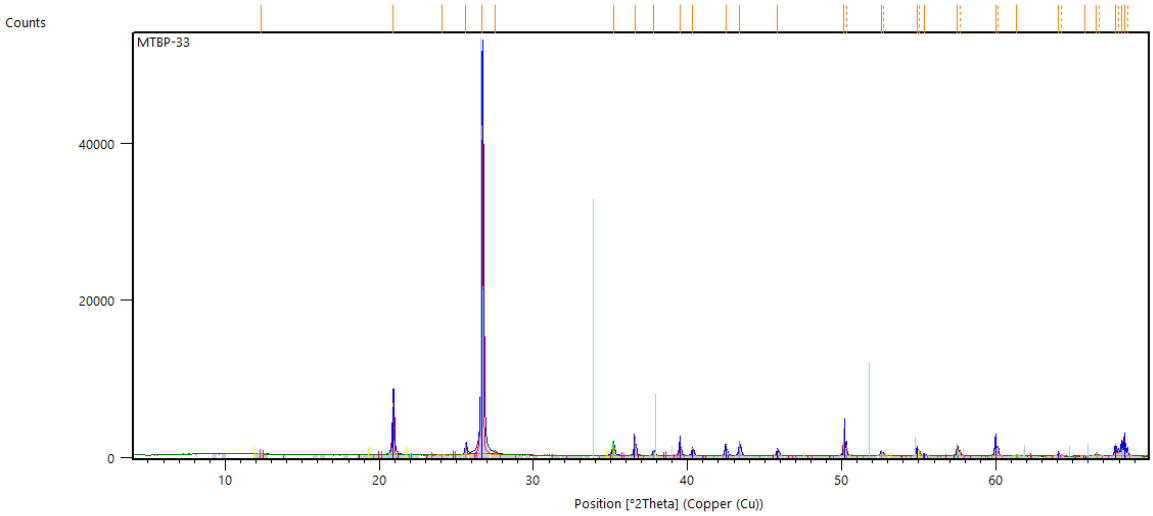

Counts
MTBP-28
40000
20000
0
10
20
30
40
50
60
Position [°2Theta] (Copper (Cu))

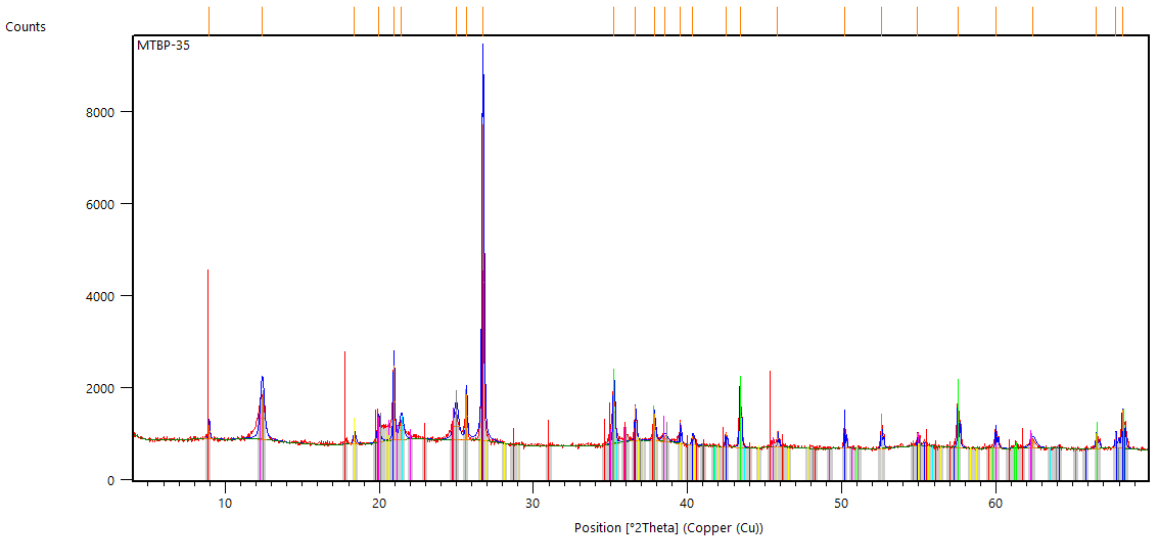

Counts
MTBP-29
30000
20000
10000
0
10
20
30
40
50
60
Position [°2Theta] (Copper (Cu))

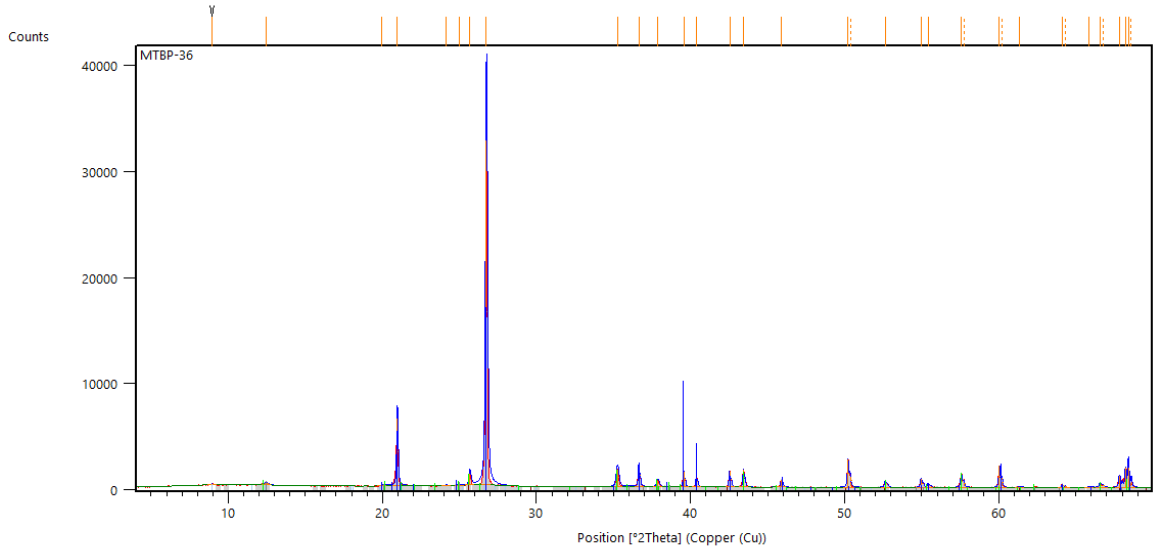

Counts
MTBP-30
20000
10000
0
10
20
30
40
50
60
Position [°2Theta] (Copper (Cu))

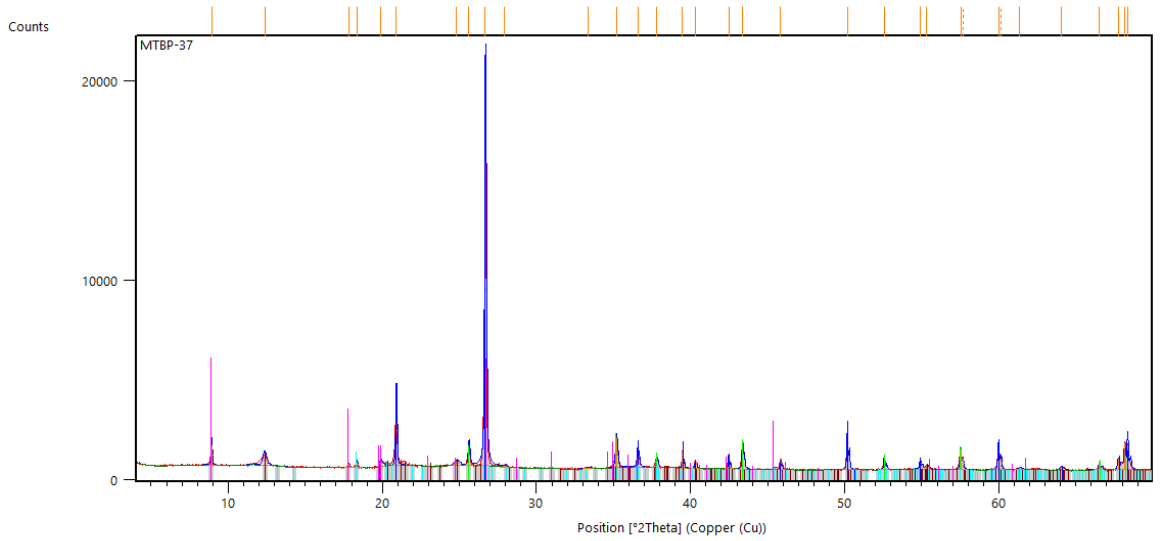

Counts
MTBP-31
40000
30000
20000
10000
0
10
20
30
40
50
60
Position [°2Theta] (Copper (Cu))

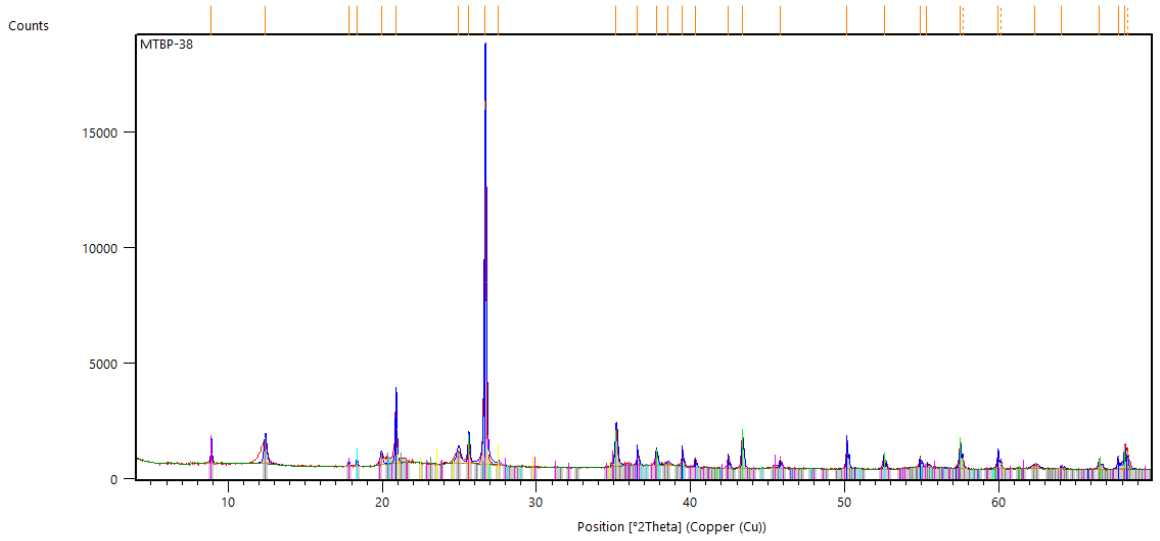

Counts
MTBP-32
15000
10000
5000
0
10
20
30
40
50
60
Position [°2Theta] (Copper (Cu))

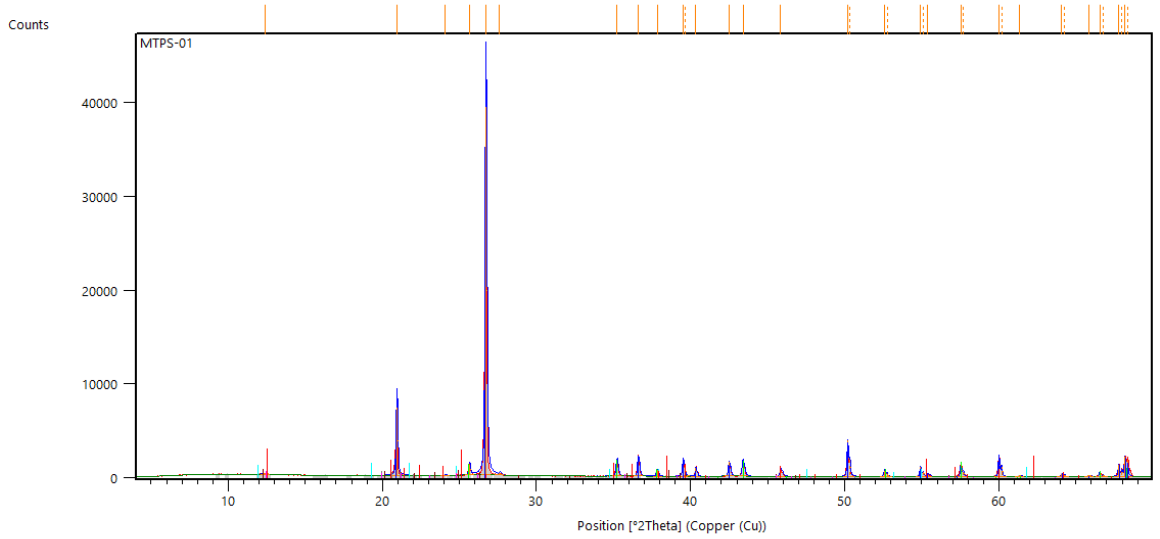

Counts
MTBP-33
40000
20000
0
10
20
30
40
50
60
Position [°2Theta] (Copper (Cu))

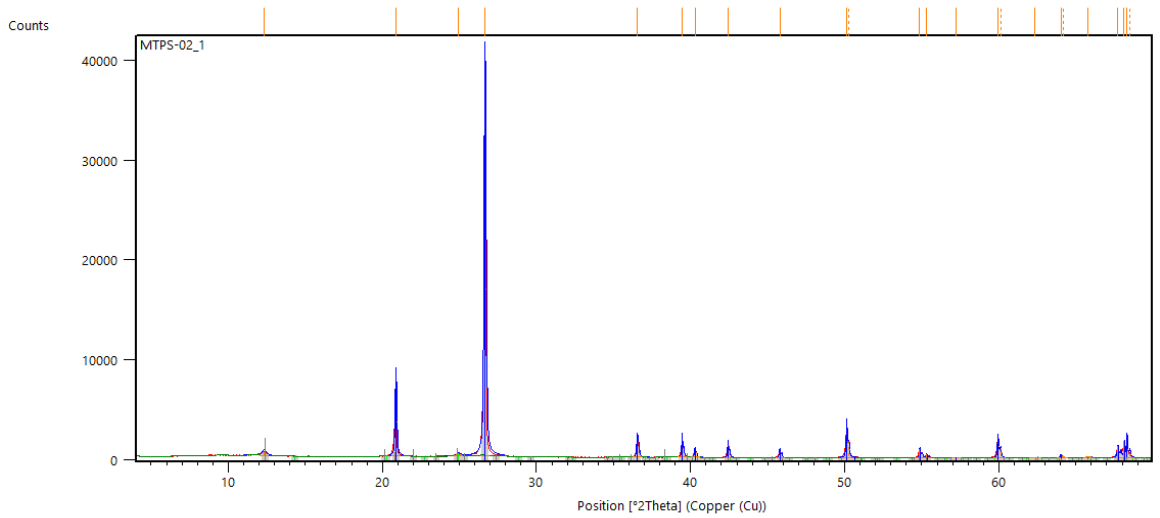

Counts
MTBP-35
8000
6000
4000
2000
0
10
20
30
40
50
60
Position [°2Theta] (Copper (Cu))

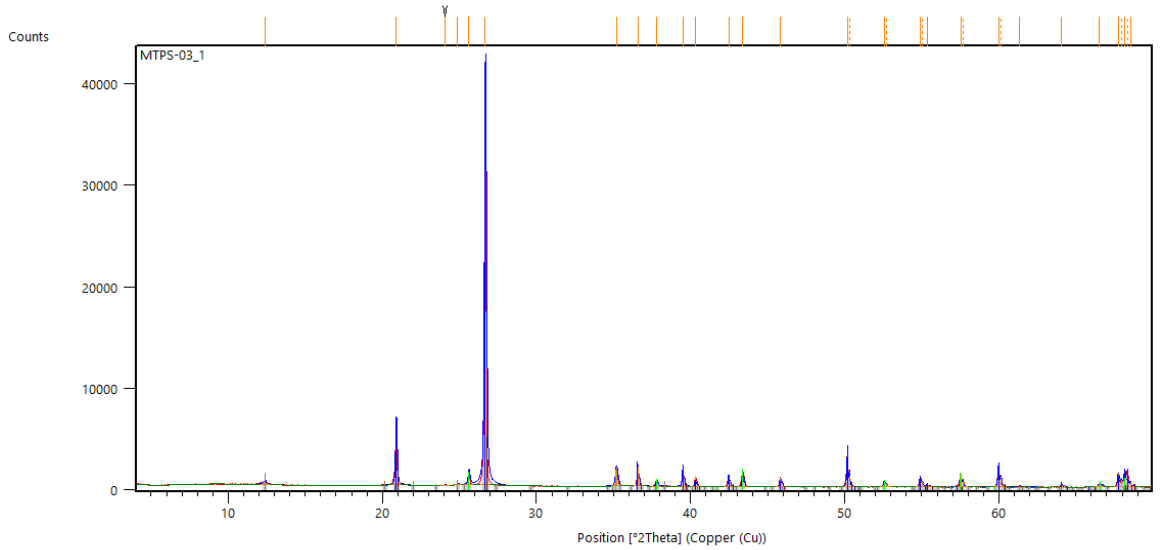

Counts
MTBP-36
40000
30000
20000
10000
0
10
20
30
40
50
60
Position [°2Theta] (Copper (Cu))

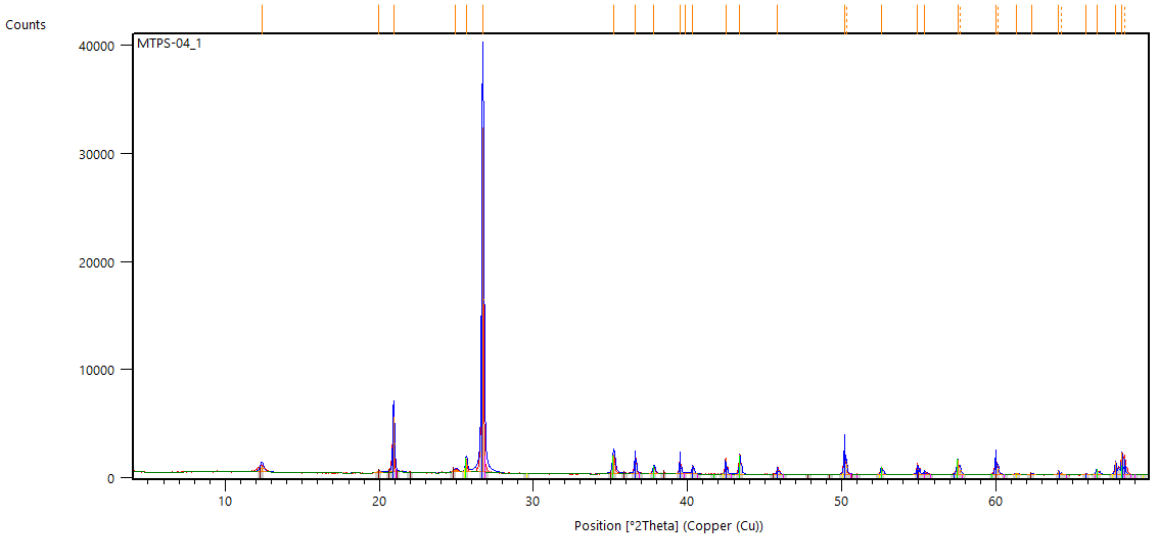

Counts
MTBP-37
20000
10000
0
10
20
30
40
50
60
Position [°2Theta] (Copper (Cu))

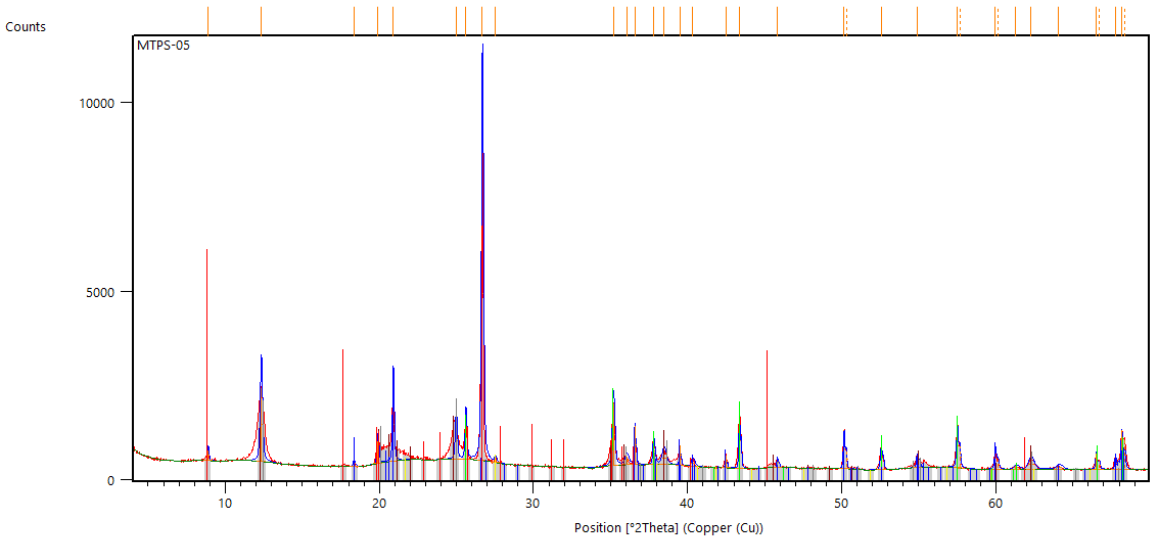

Counts
MTBP-38
15000
10000
5000
0
10
20
30
40
50
60
Position [°2Theta] (Copper (Cu))

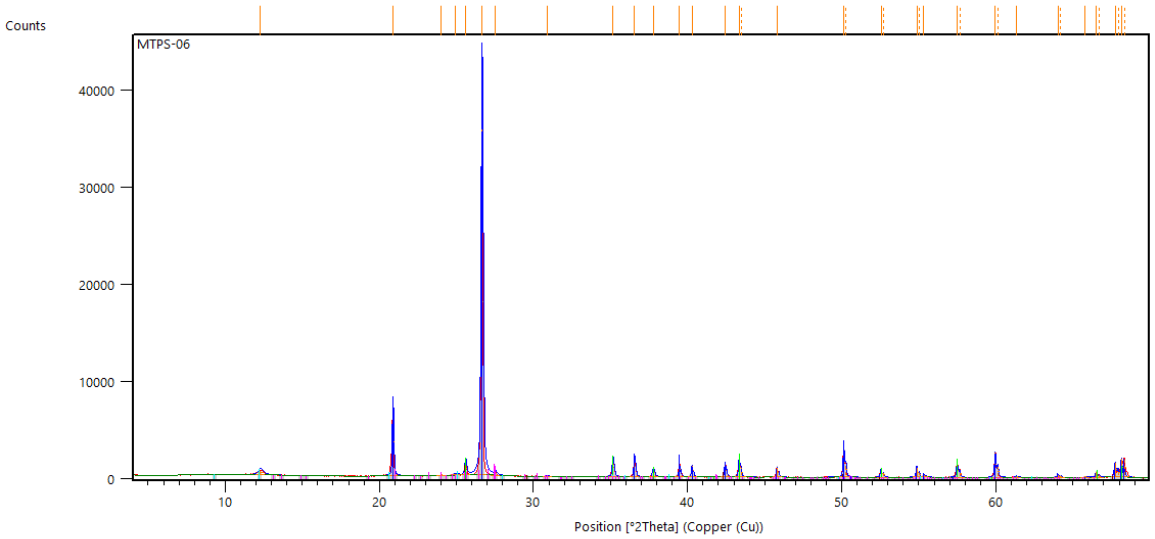

Counts
MTPS-01
40000
30000
20000
10000
0
10
20
30
40
50
60
Position [°2Theta] (Copper (Cu))

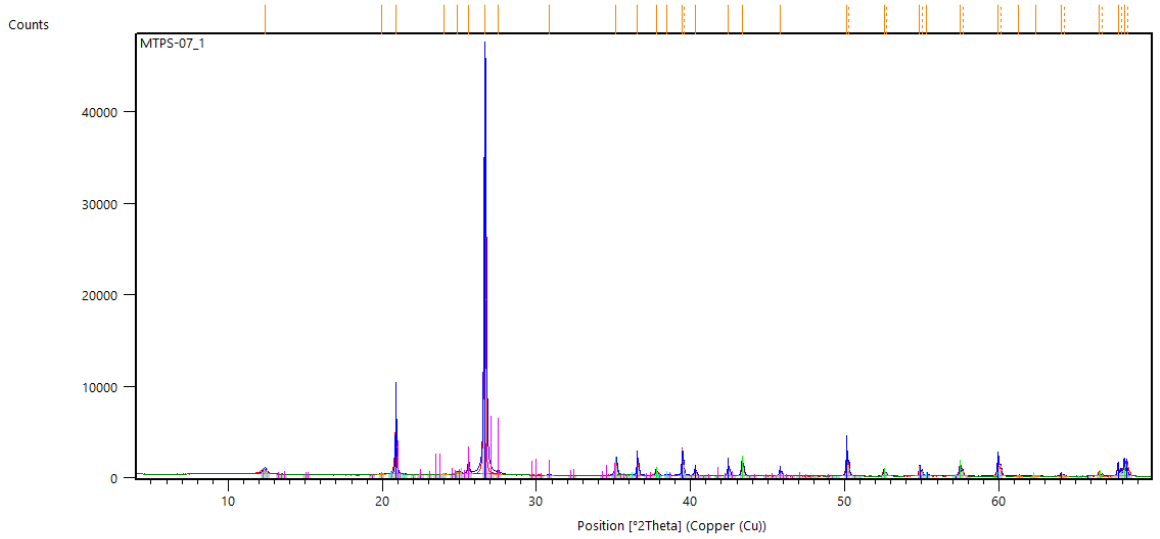

Counts
MTPS-02_1
40000
30000
20000
10000
0
10
20
30
40
50
60
Position [°2Theta] (Copper (Cu))

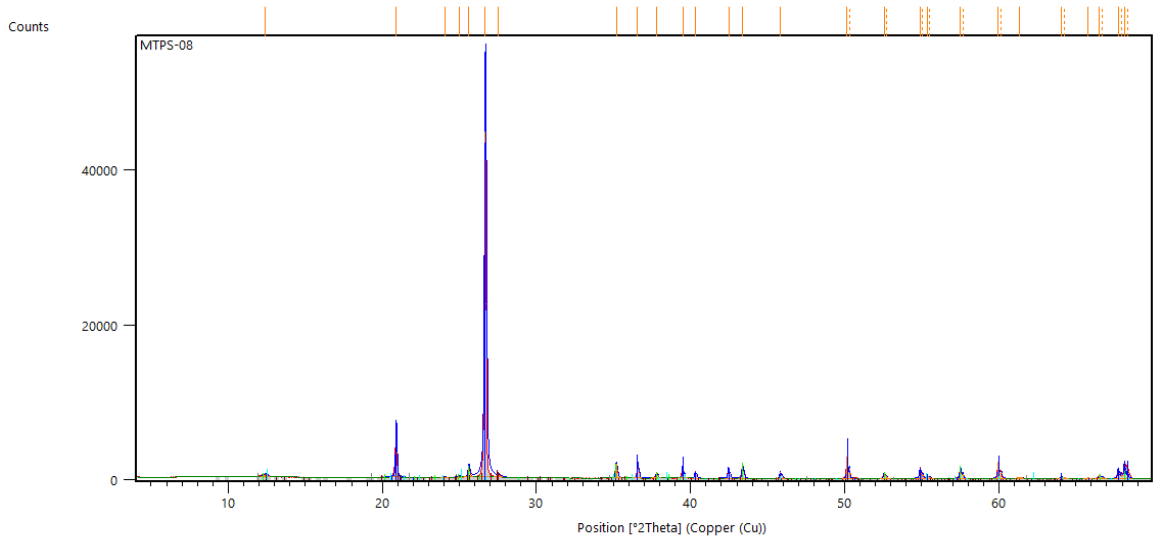

Counts
MTPS-03_1
40000
30000
20000
10000
0
10
20
30
40
50
60
Position [°2Theta] (Copper (Cu))

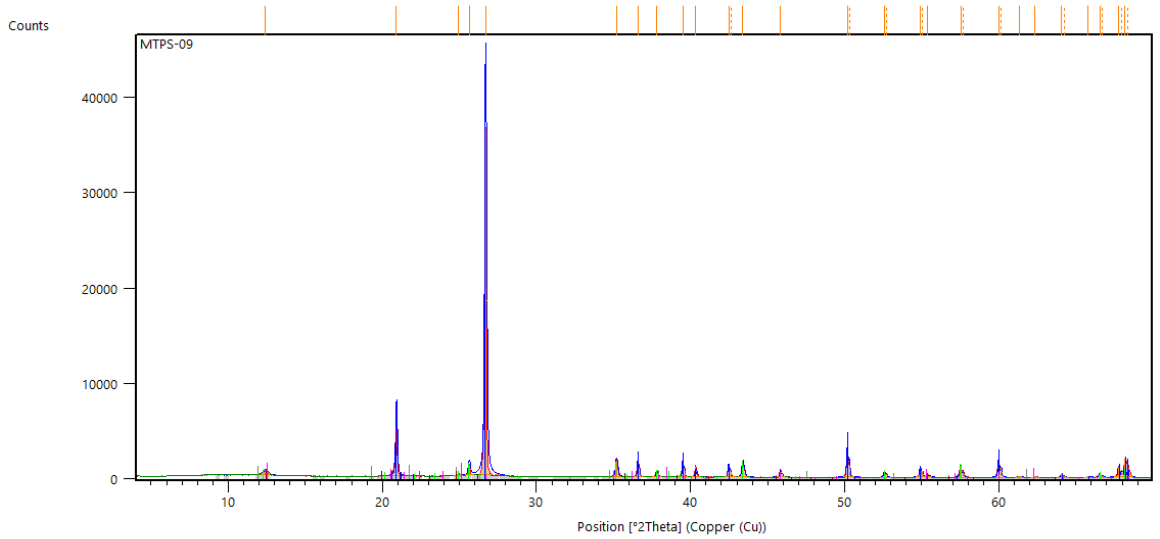

Counts
MTPS-04_1
40000
30000
20000
10000
0
10
20
30
40
50
60
Position [°2Theta] (Copper (Cu))

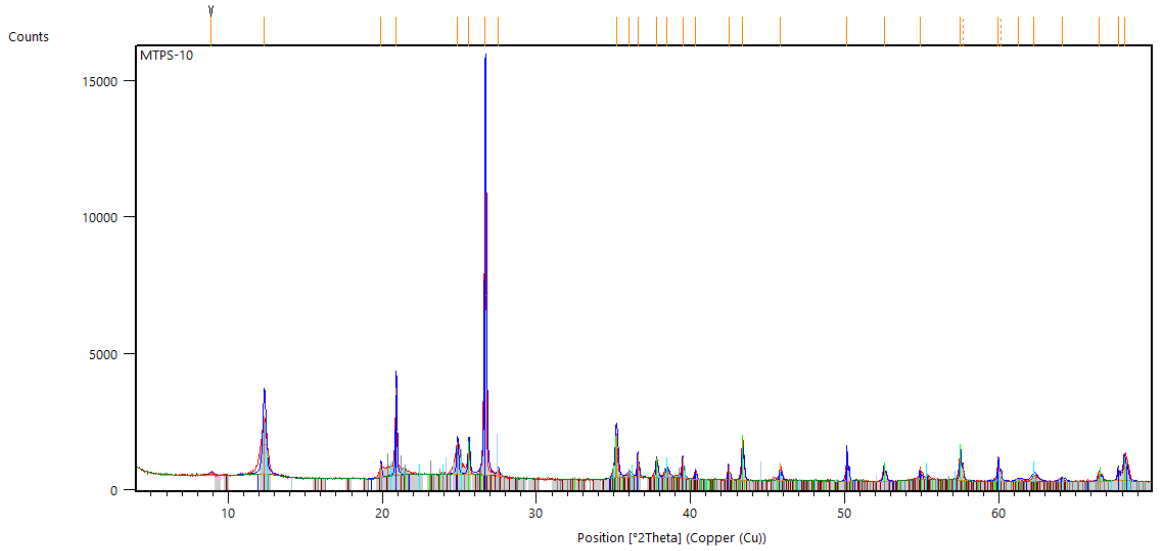

Counts
MTPS-05
10000
5000
0
10
20
30
40
50
60
Position [°2Theta] (Copper (Cu))

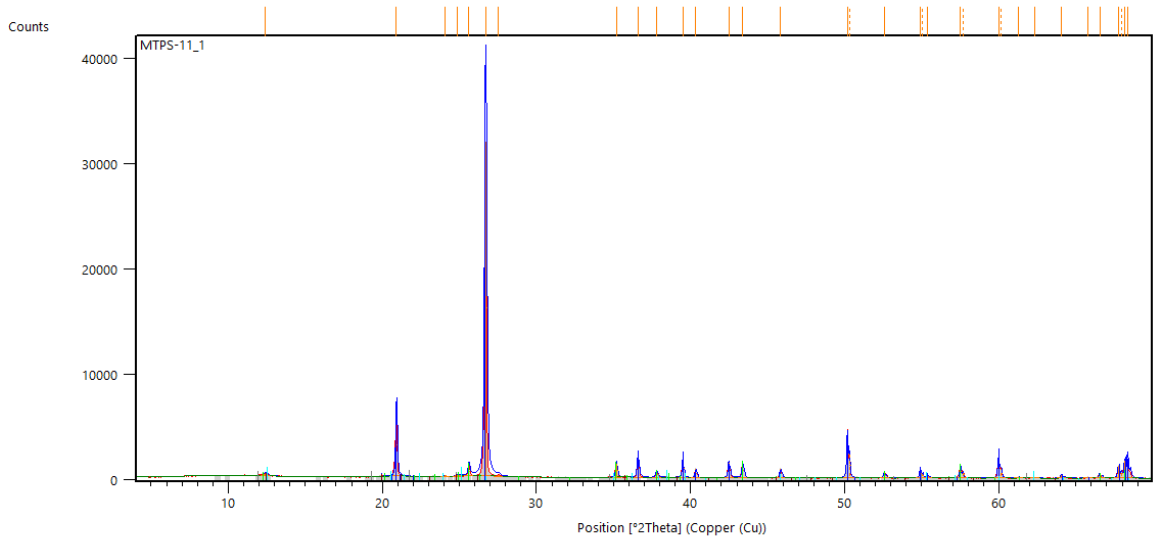

Counts
MTPS-06
40000
30000
20000
10000
0
10
20
30
40
50
60
Position [°2Theta] (Copper (Cu))

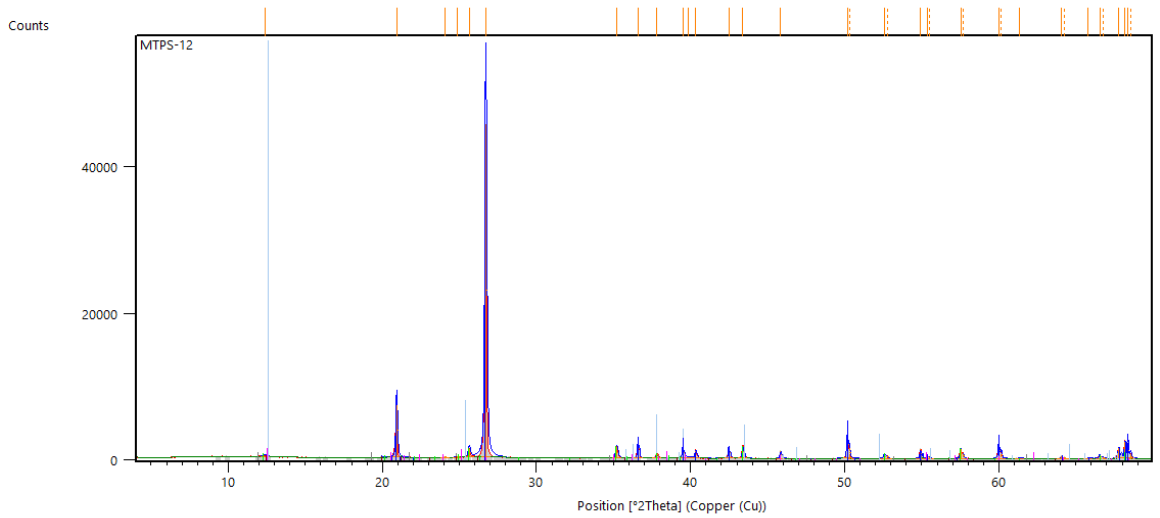

Counts
MTPS-07_1
40000
30000
20000
10000
0
10
20
30
40
50
60
Position [°2Theta] (Copper (Cu))

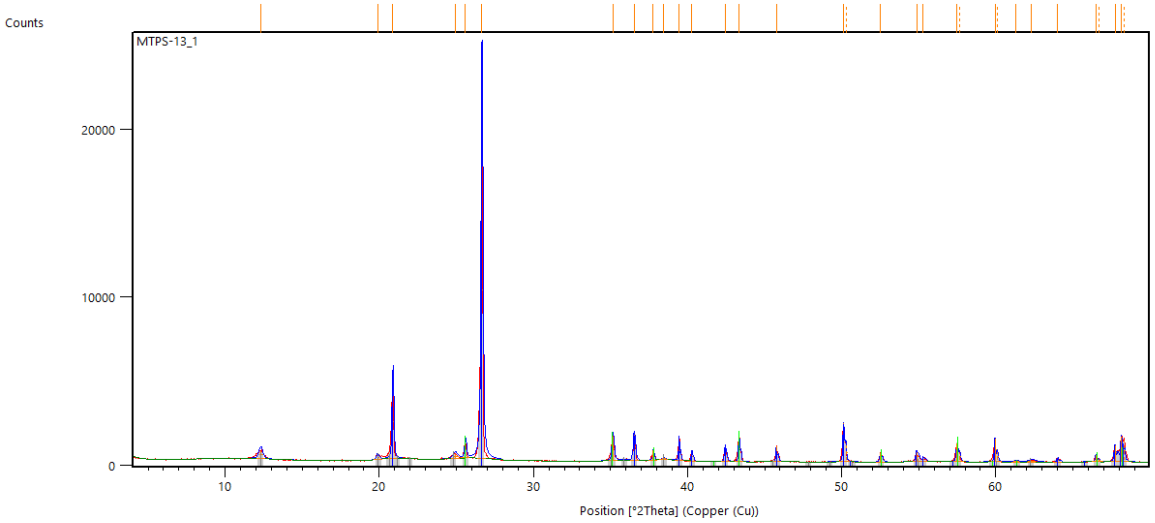

Counts
MTPS-08
40000
20000
0
10
20
30
40
50
60
Position [°2Theta] (Copper (Cu))

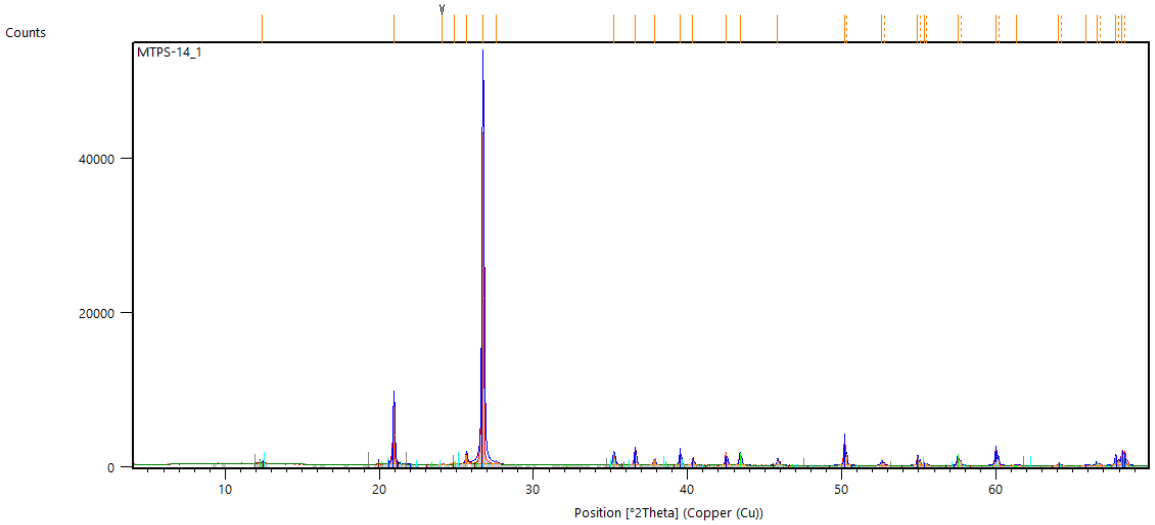

Counts
MTPS-09
40000
30000
20000
10000
0
10
20
30
40
50
60
Position [°2Theta] (Copper (Cu))

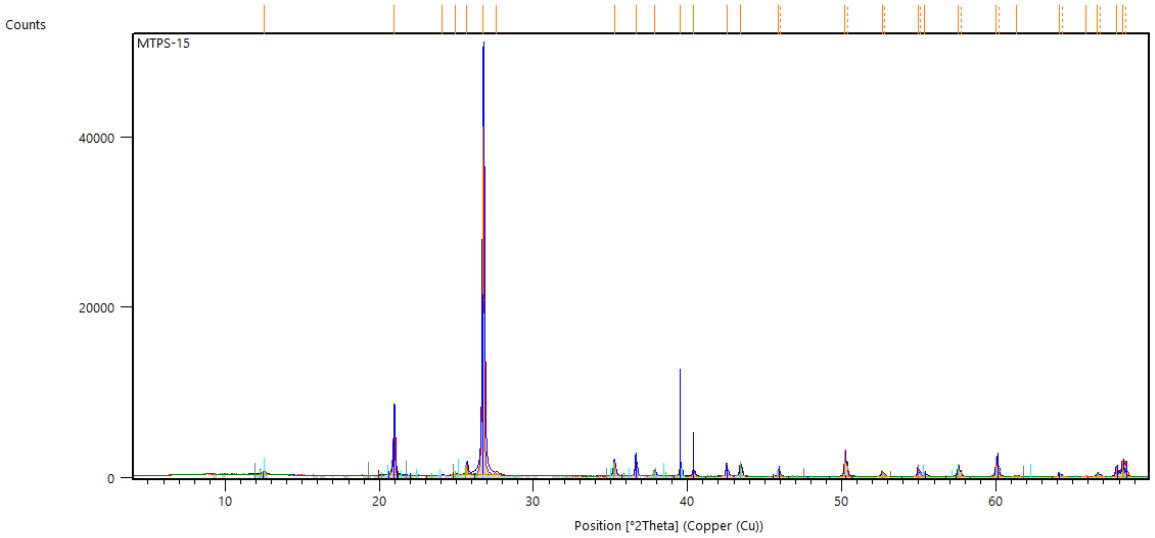

Counts
MTPS-10
15000
10000
5000
0
10
20
30
40
50
60
Position [°2Theta] (Copper (Cu))

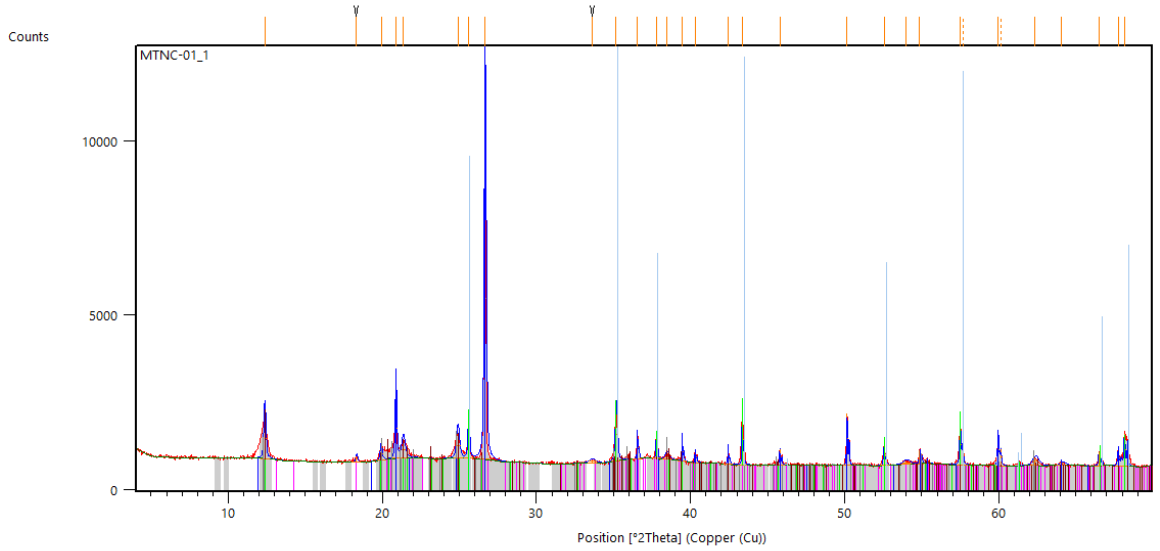

Counts
MTPS-11_1
40000
30000
20000
10000
0
10
20
30
40
50
60
Position [°2Theta] (Copper (Cu))

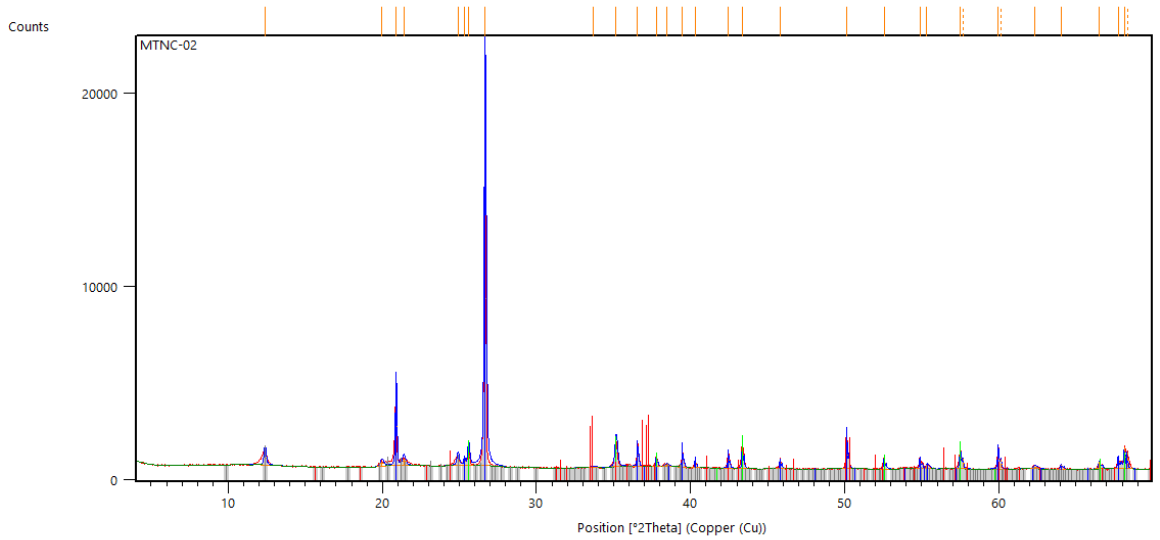

Counts
MTPS-12
40000
20000
0
10
20
30
40
50
60
Position [°2Theta] (Copper (Cu))

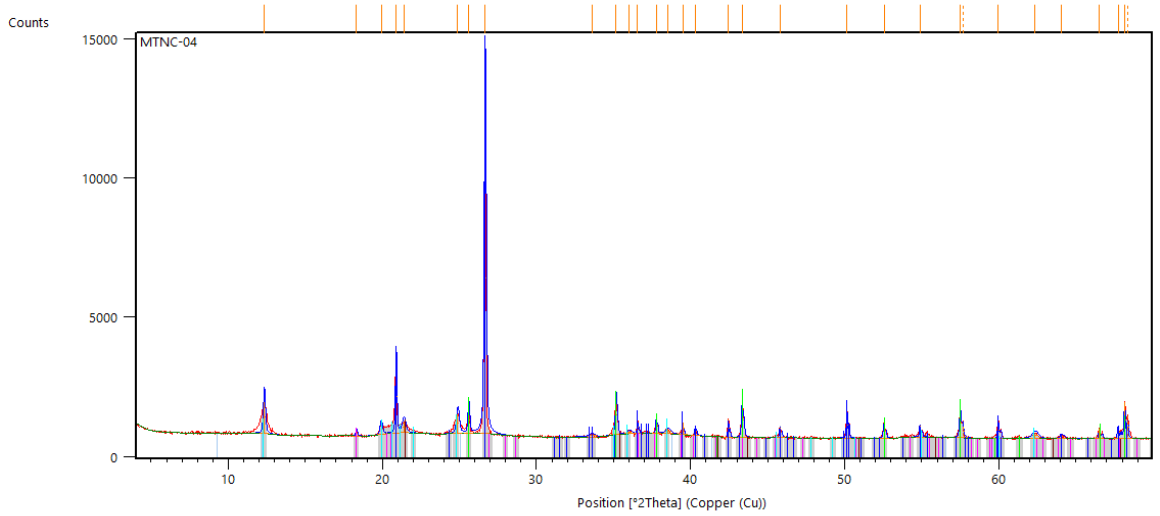

Counts
MTPS-13_1
20000
10000
0
10
20
30
40
50
60
Position [°2Theta] (Copper (Cu))

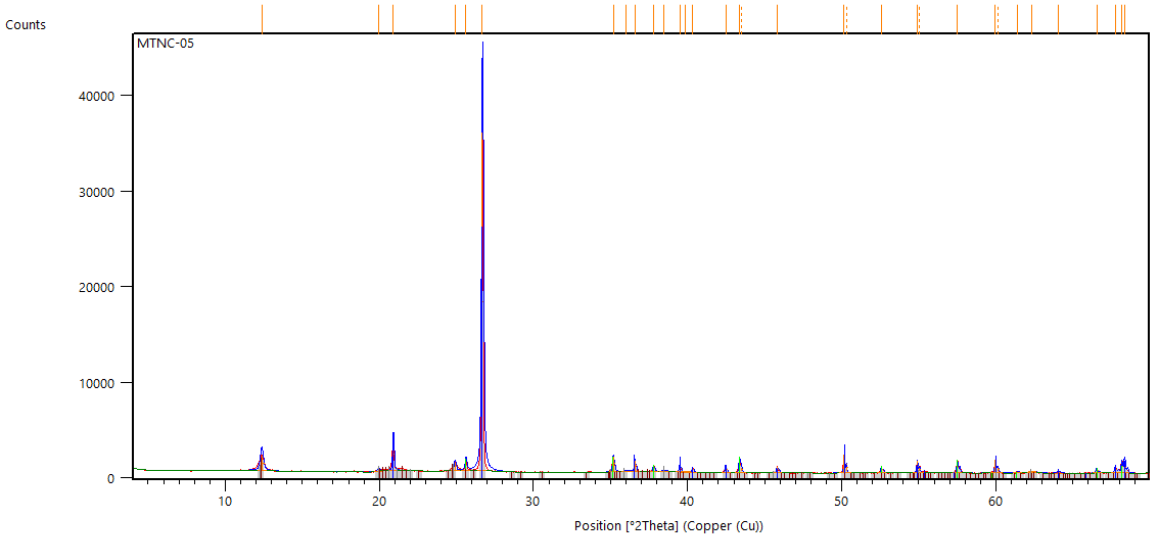

Counts
MTPS-14_1
40000
20000
0
10
20
30
40
50
60
Position [°2Theta] (Copper (Cu))

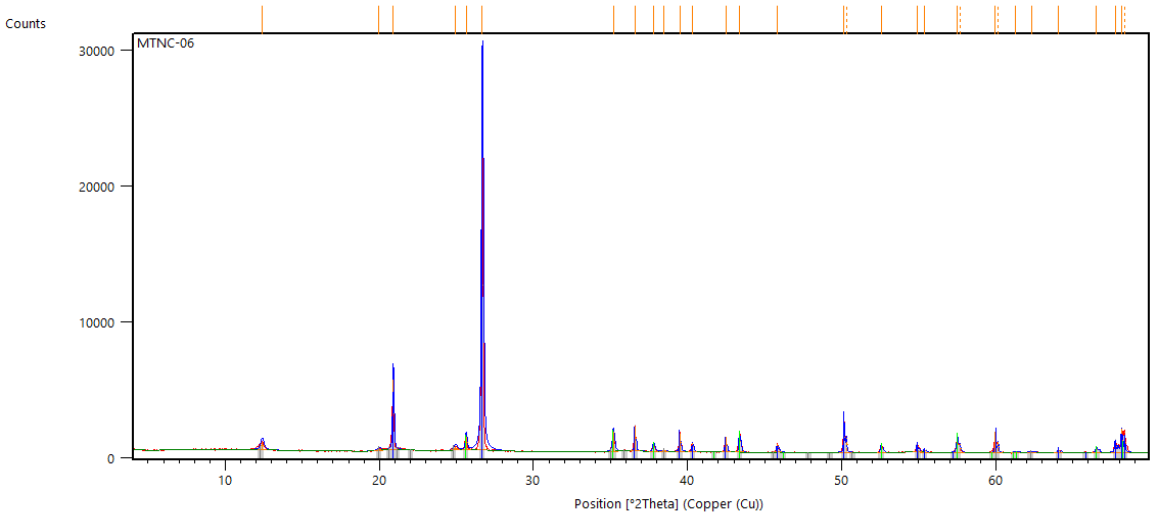

Counts
MTPS-15
40000
20000
0
10
20
30
40
50
60
Position [°2Theta] (Copper (Cu))

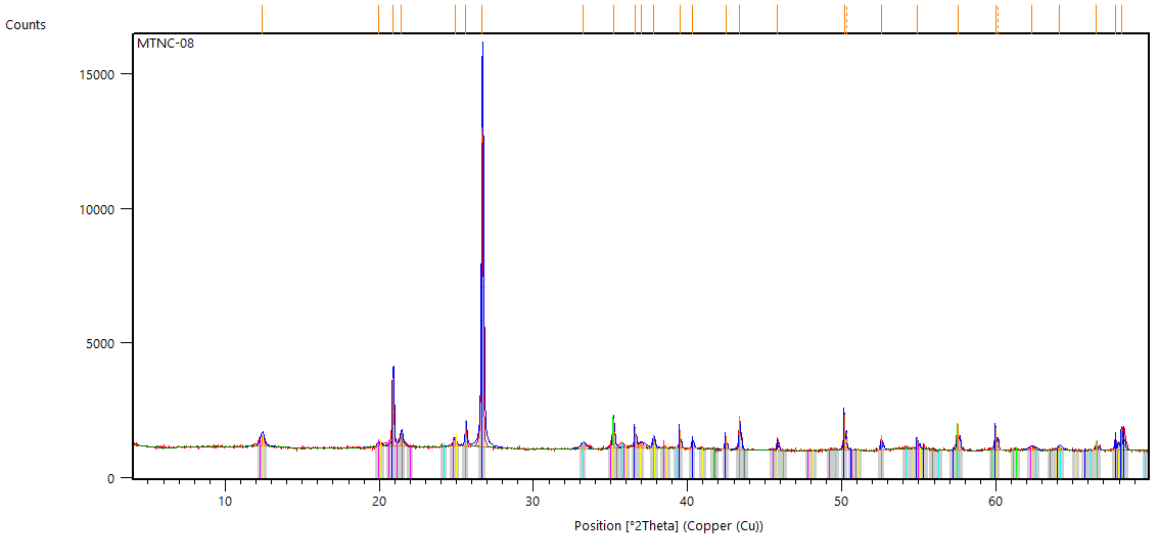

Counts
MTNC-01_1
10000
5000
0
10
20
30
40
50
60
Position [°2Theta] (Copper (Cu))

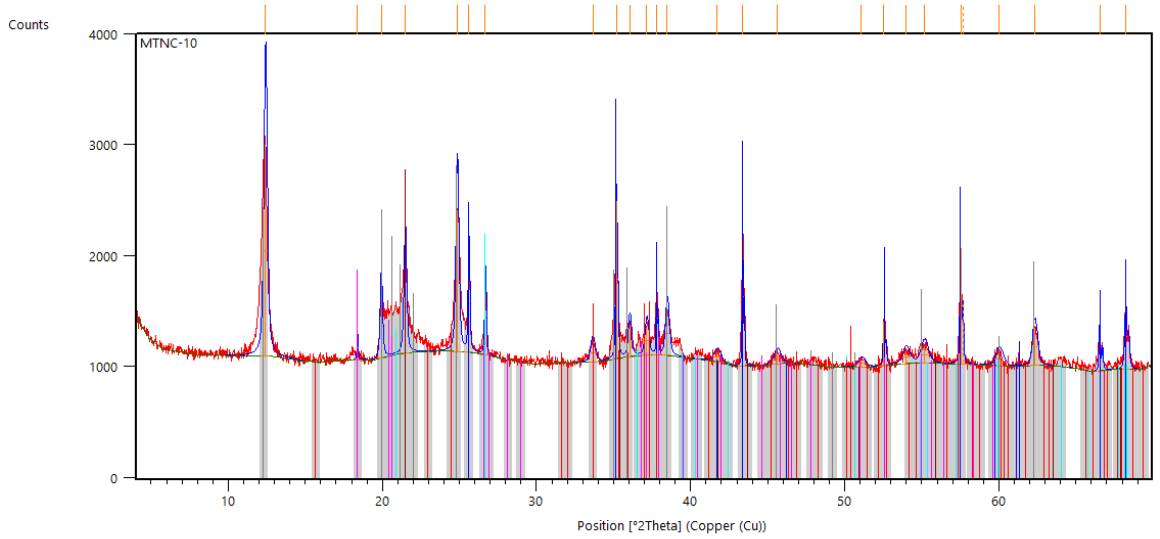

Counts
MTNC-02
20000
10000
0
10
20
30
40
50
60
Position [°2Theta] (Copper (Cu))

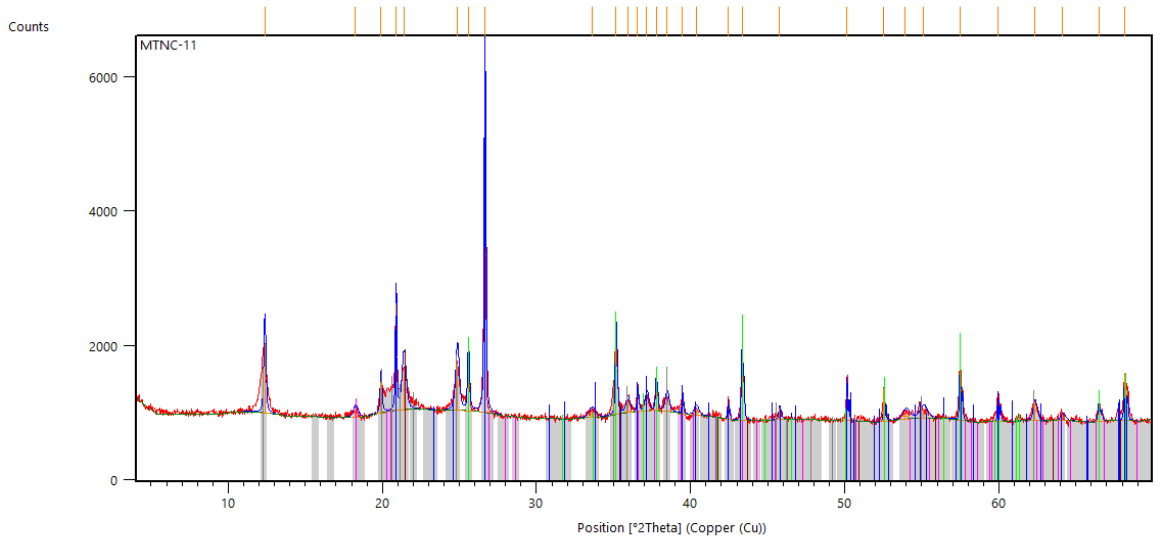

Counts
MTNC-04
15000
10000
5000
0
10
20
30
40
50
60
Position [°2Theta] (Copper (Cu))

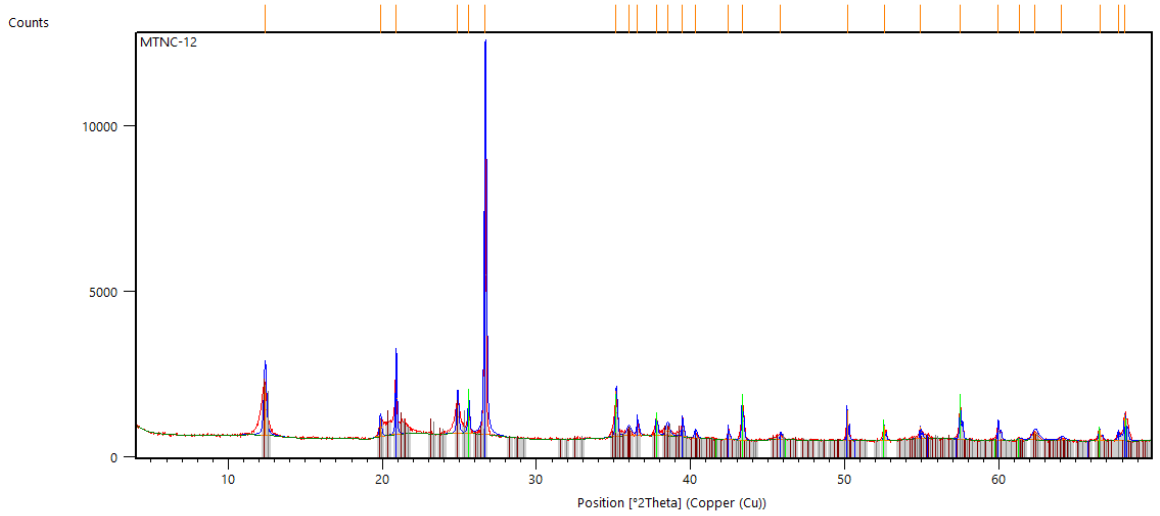

Counts
MTNC-05
40000
30000
20000
10000
0
10
20
30
40
50
60
Position [°2Theta] (Copper (Cu))

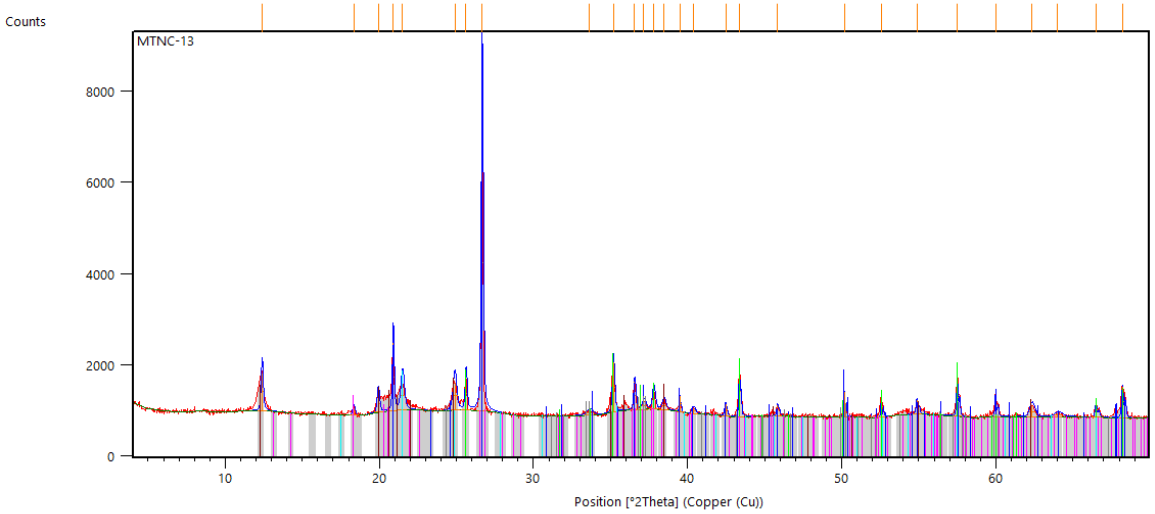

Counts
MTNC-06
30000
20000
10000
0
10
20
30
40
50
60
Position [°2Theta] (Copper (Cu))

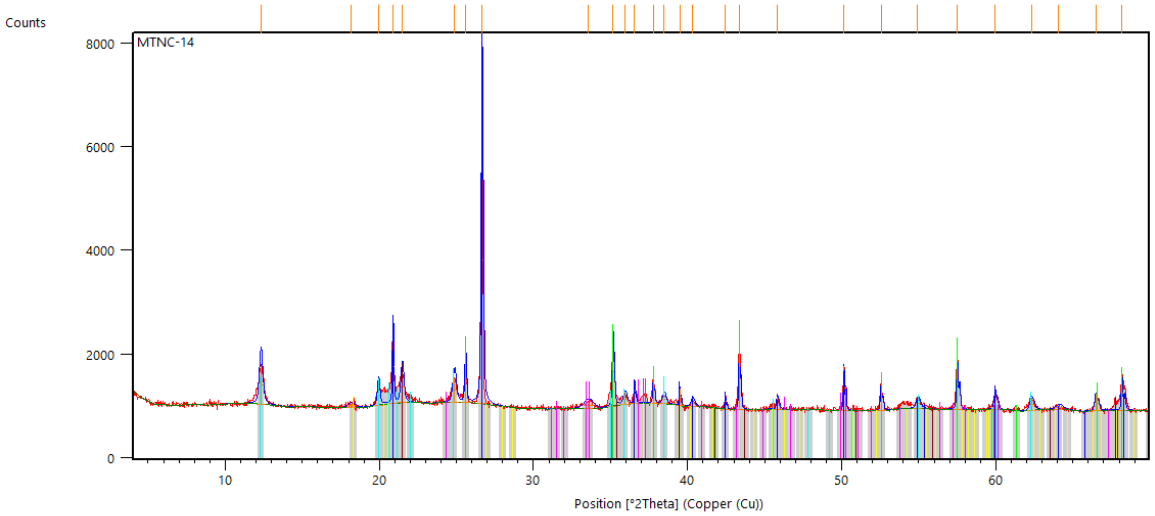

Counts
MTNC-08
15000
10000
5000
0
10
20
30
40
50
60
Position [°2Theta] (Copper (Cu))

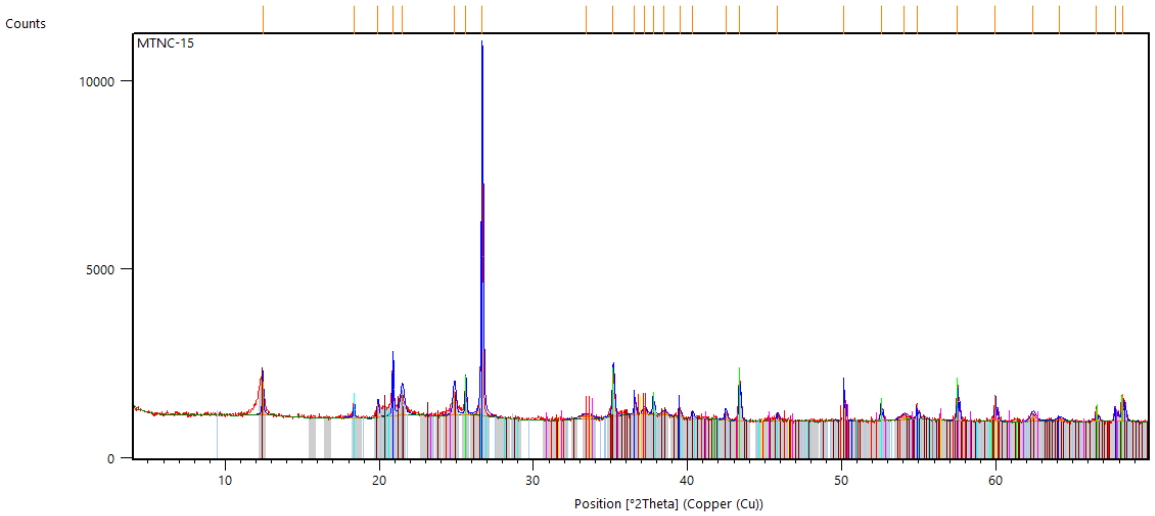

Counts
MTNC-10
4000
3000
2000
1000
0
10
20
30
40
50
60
Position [°2Theta] (Copper (Cu))

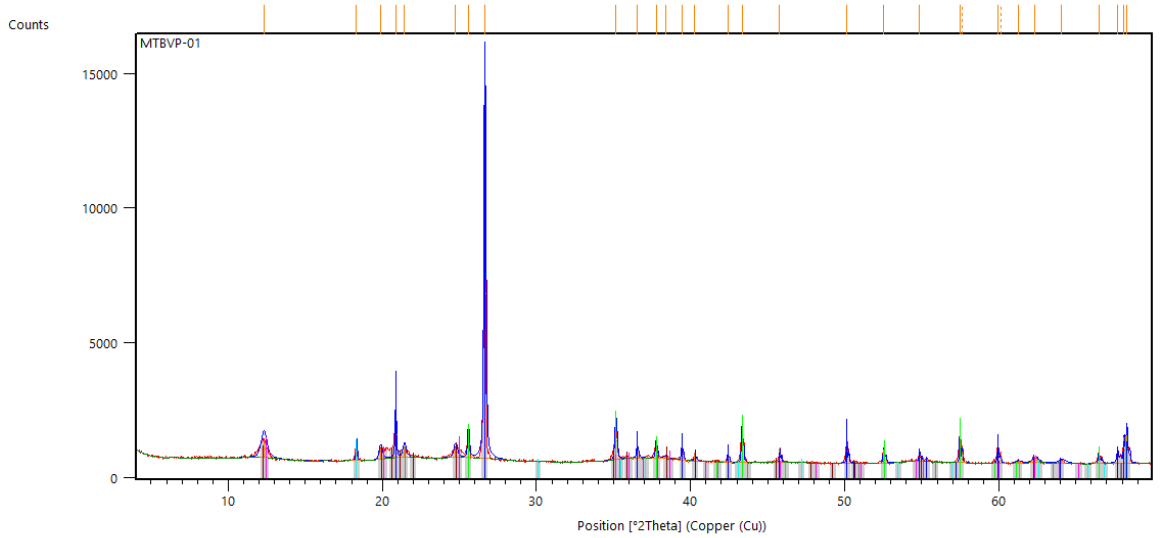

Counts
MTNC-11
6000
4000
2000
0
10
20
30
40
50
60
Position [°2Theta] (Copper (Cu))

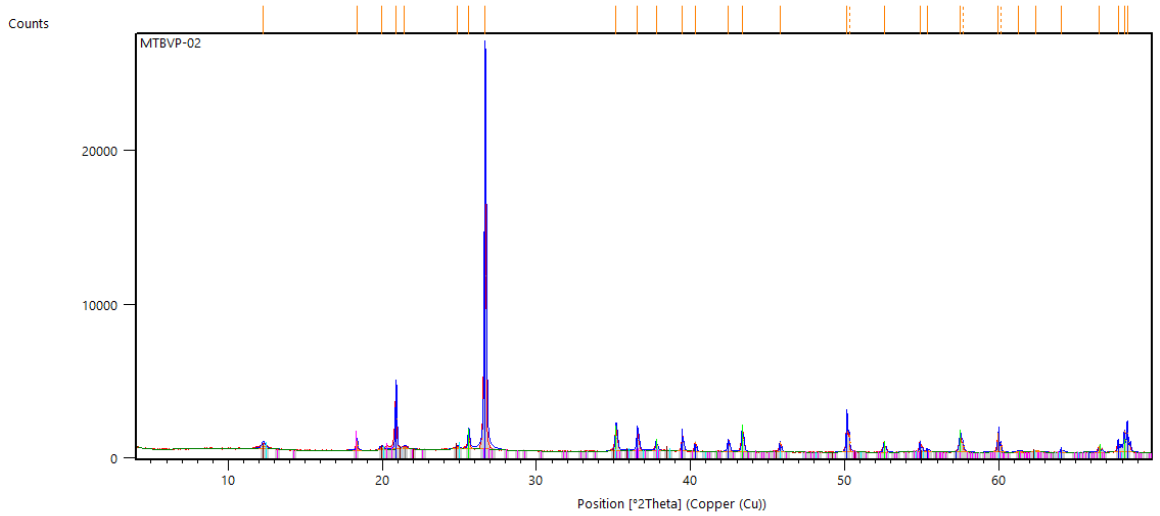

Counts
MTNC-12
10000
5000
0
10
20
30
40
50
60
Position [°2Theta] (Copper (Cu))

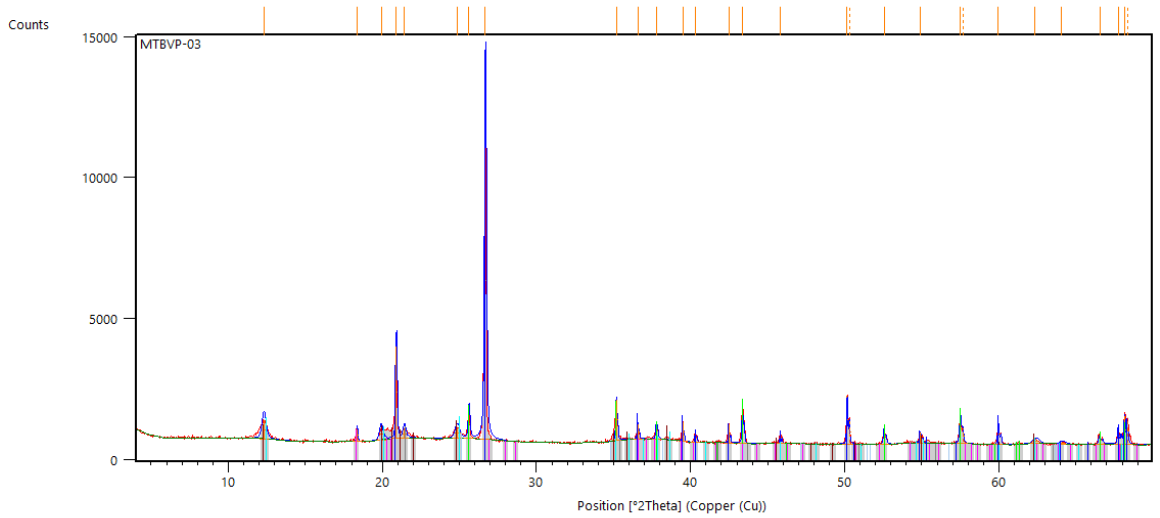

Counts
MTNC-13
8000
6000
4000
2000
0
10
20
30
40
50
60
Position [°2Theta] (Copper (Cu))

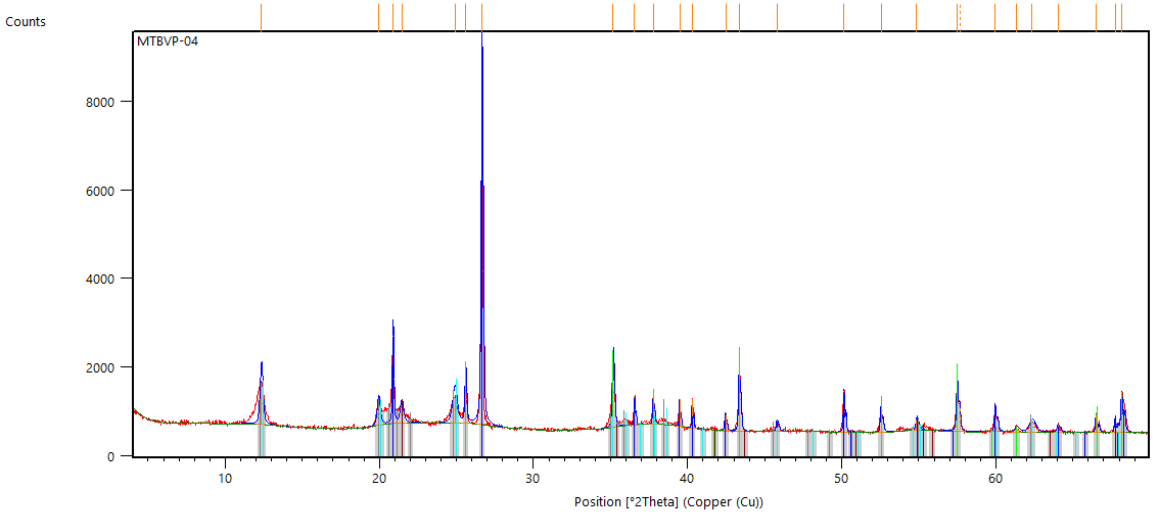

Counts
MTNC-14
8000
6000
4000
2000
0
10
20
30
40
50
60
Position [°2Theta] (Copper (Cu))

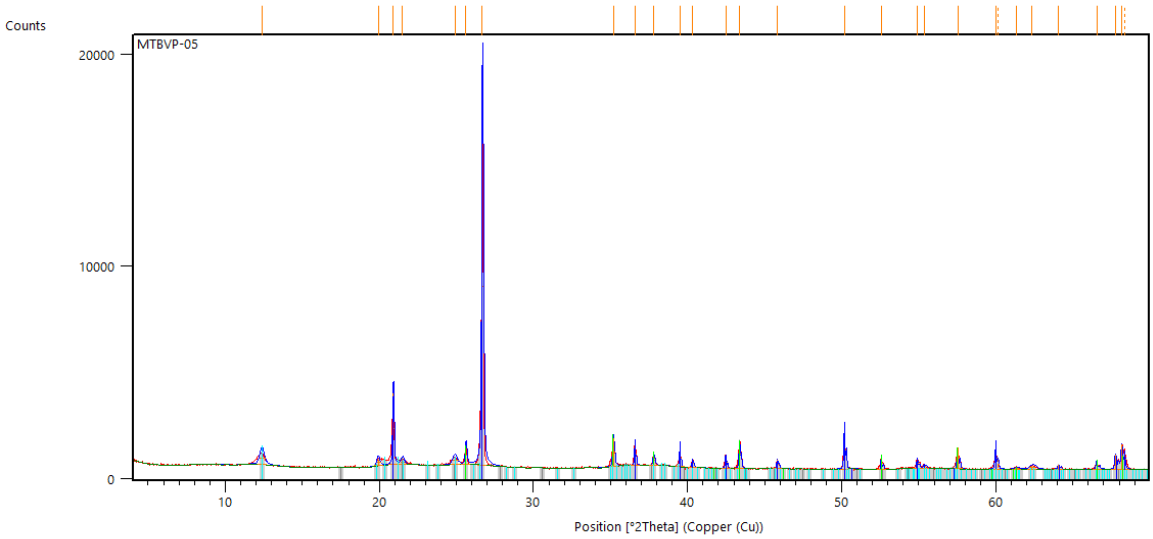

Counts
MTNC-15
10000
5000
0
10
20
30
40
50
60
Position [°2Theta] (Copper (Cu))

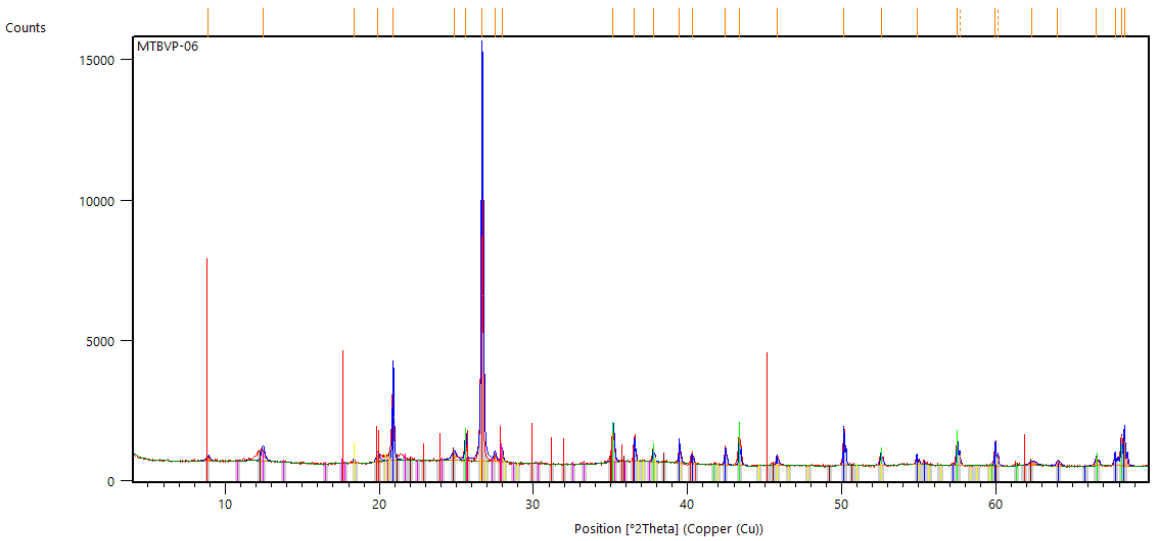

Counts
MTBVP-01
15000
10000
5000
0
10
20
30
40
50
60
Position [°2Theta] (Copper (Cu))


Counts
MTBVP-02
20000
10000
0
10
20
30
40
50
60
Position [°2Theta] (Copper (Cu))

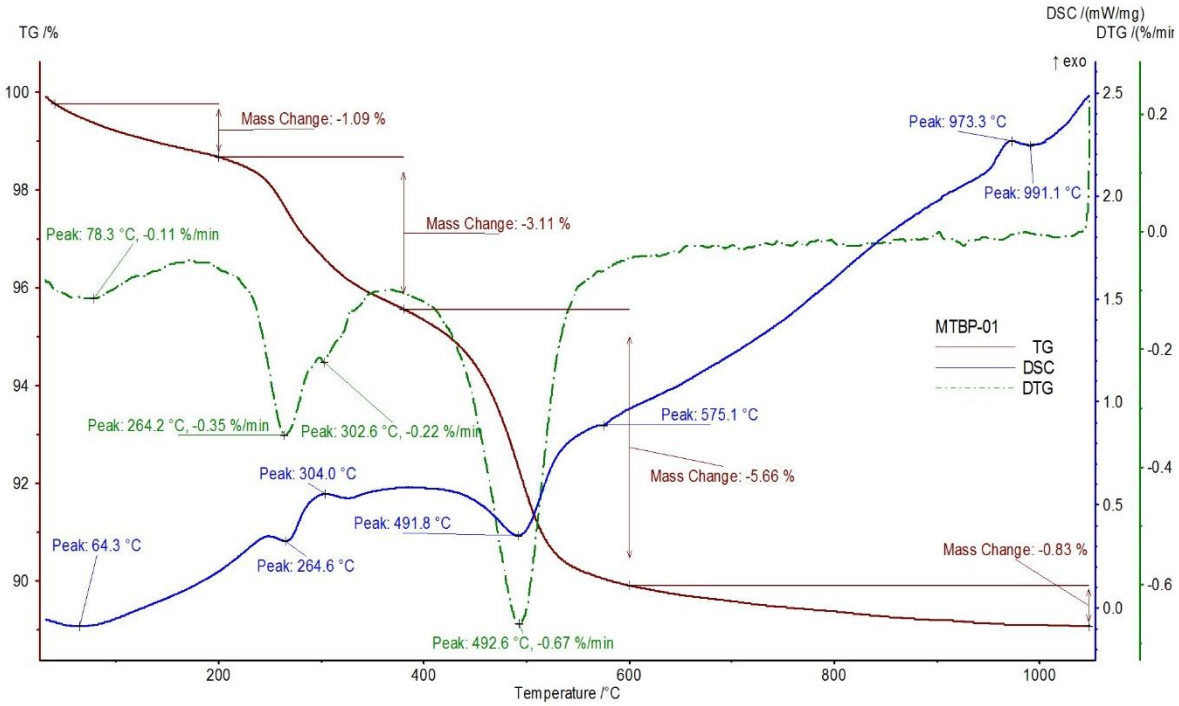

Counts
MTBVP-03
15000
10000
5000
0
10
20
30
40
50
60
Position [°2Theta] (Copper (Cu))

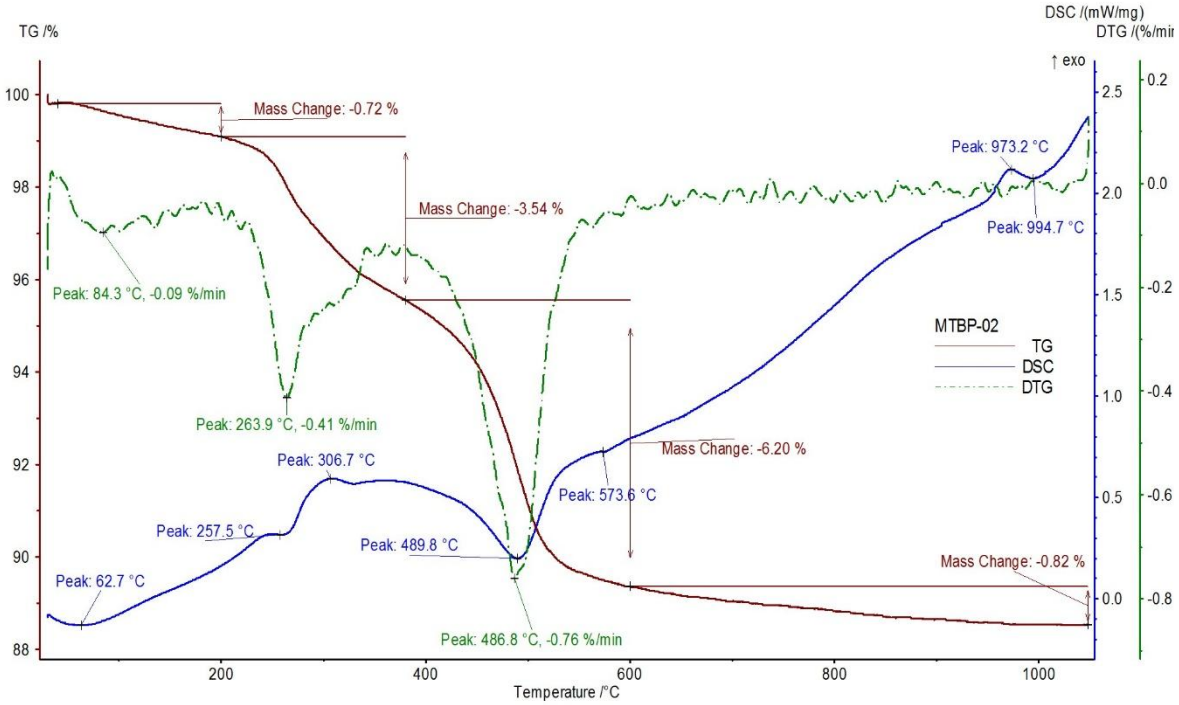

Counts
MTBVP-04
8000
6000
4000
2000
0
10
20
30
40
50
60
Position [°2Theta] (Copper (Cu))

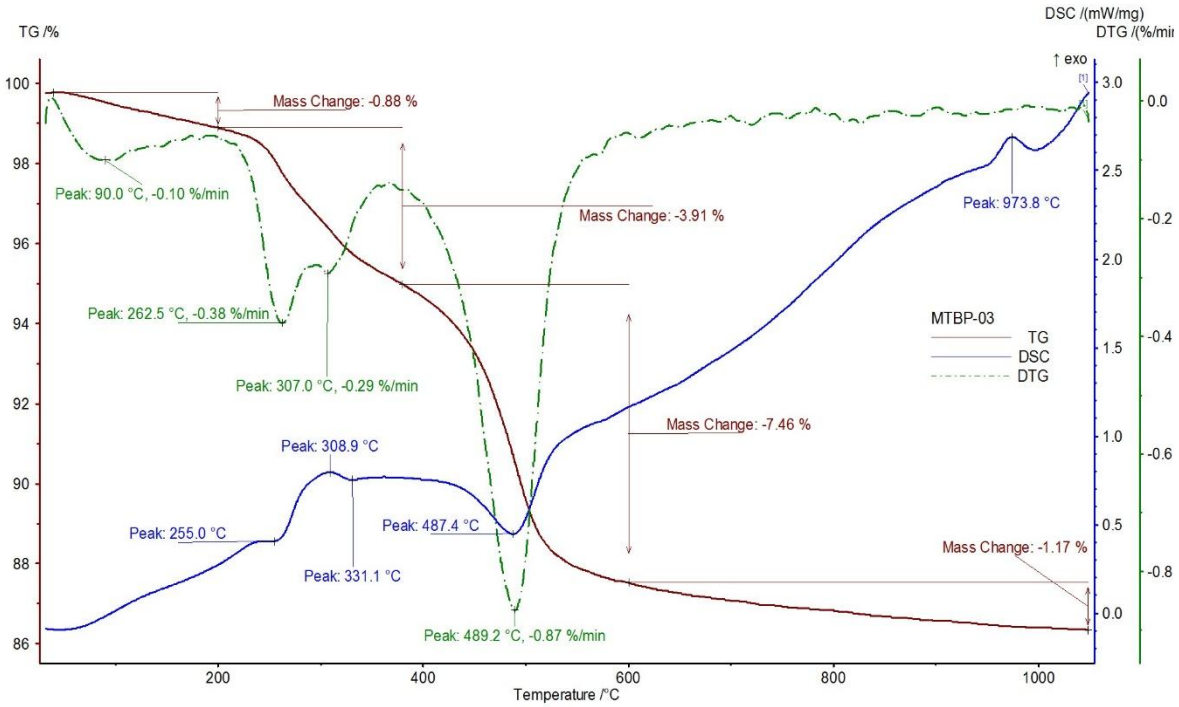

Counts
MTBVP-05
20000
10000
0
10
20
30
40
50
60
Position [°2Theta] (Copper (Cu))

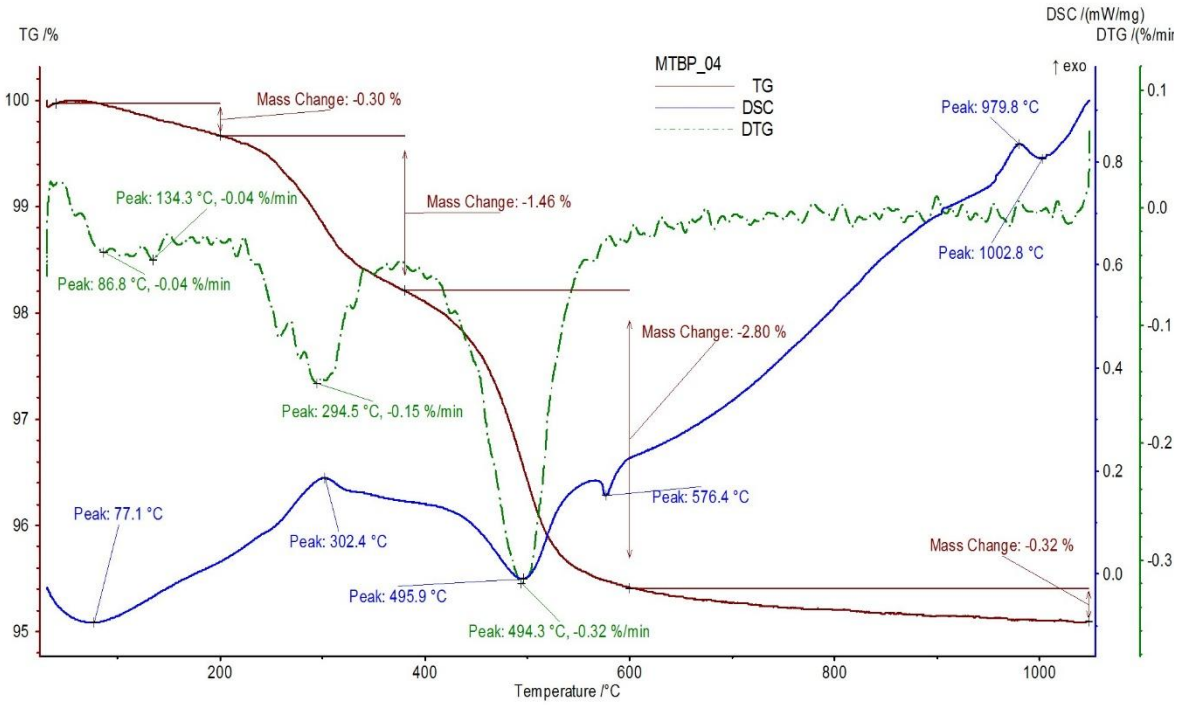

Counts
MTBVP-06
15000
10000
5000
0
10
20
30
40
50
60
Position [°2Theta] (Copper (Cu))

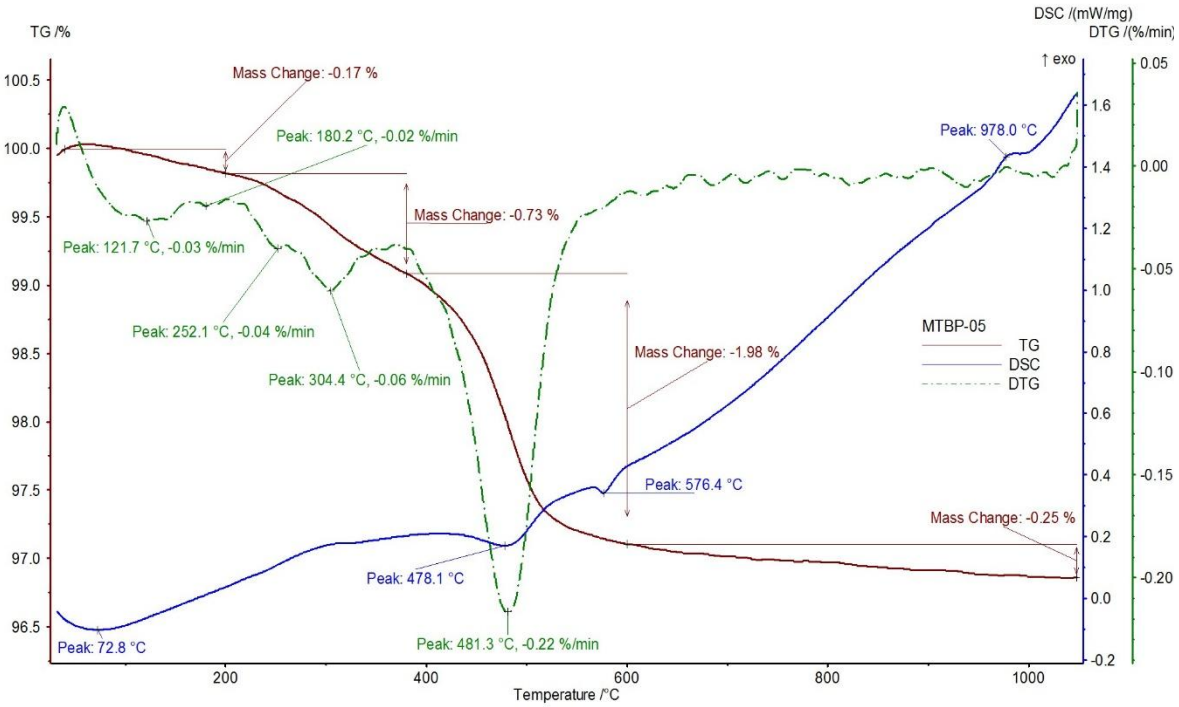
APPENDIX 6: TG/DSC curves of all samples.

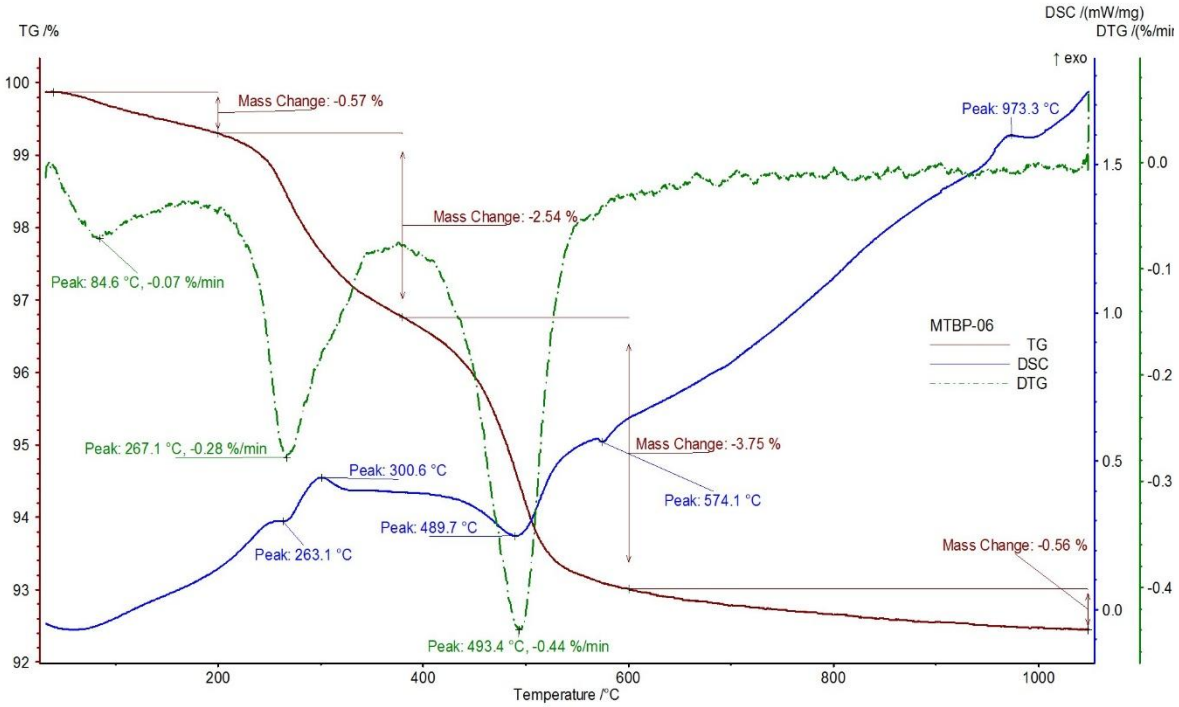


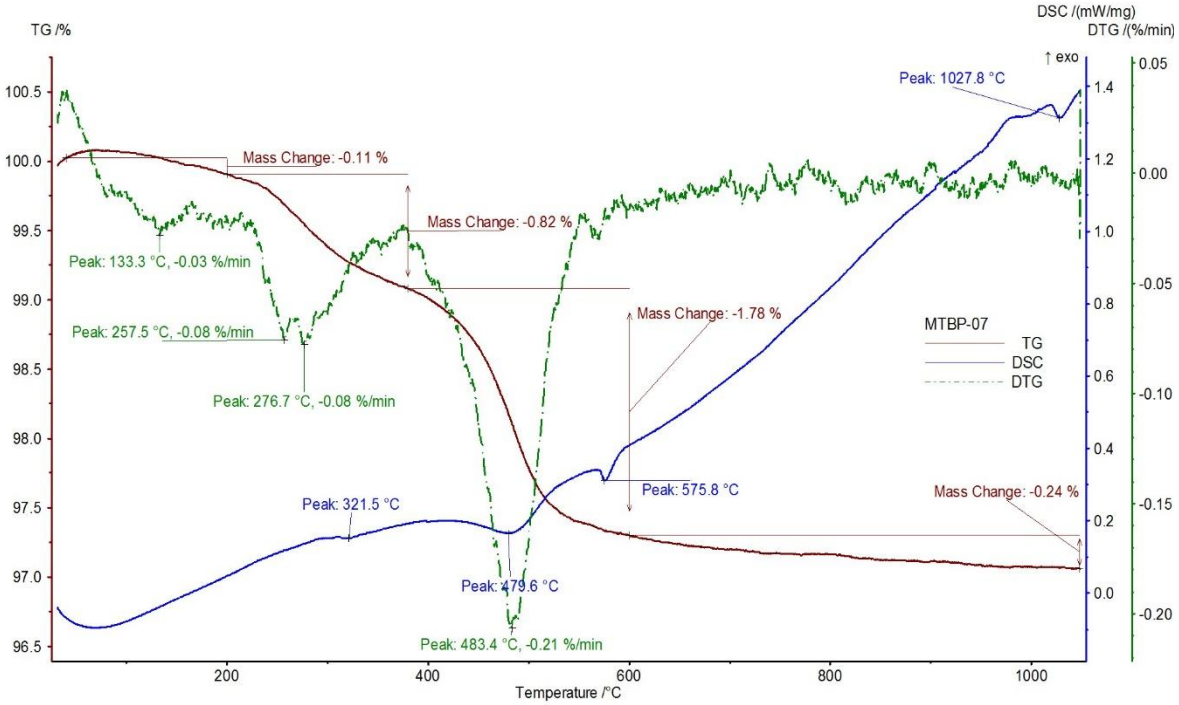


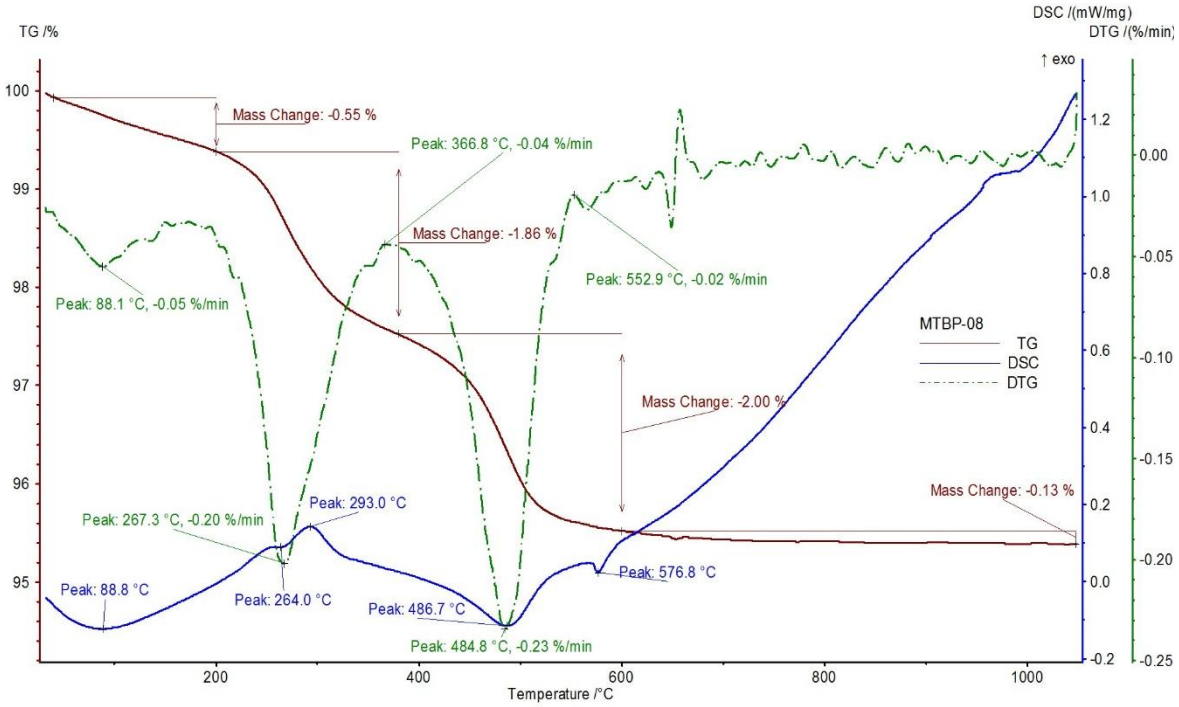

TG /%
DSC /(mW/mg)
DTG /(%/mi
↑ exo
MTBP-03
TG
DSC
DTG
Mass Change: -0.88 %
Mass Change: -3.91 %
Mass Change: -7.46 %
Mass Change: -1.17 %
Peak: 90.0 °C, -0.10 %/min
Peak: 262.5 °C, -0.38 %/min
Peak: 307.0 °C, -0.29 %/min
Peak: 308.9 °C
Peak: 255.0 °C
Peak: 331.1 °C
Peak: 487.4 °C
Peak: 489.2 °C, -0.87 %/min
Peak: 973.8 °C
Temperature /°C

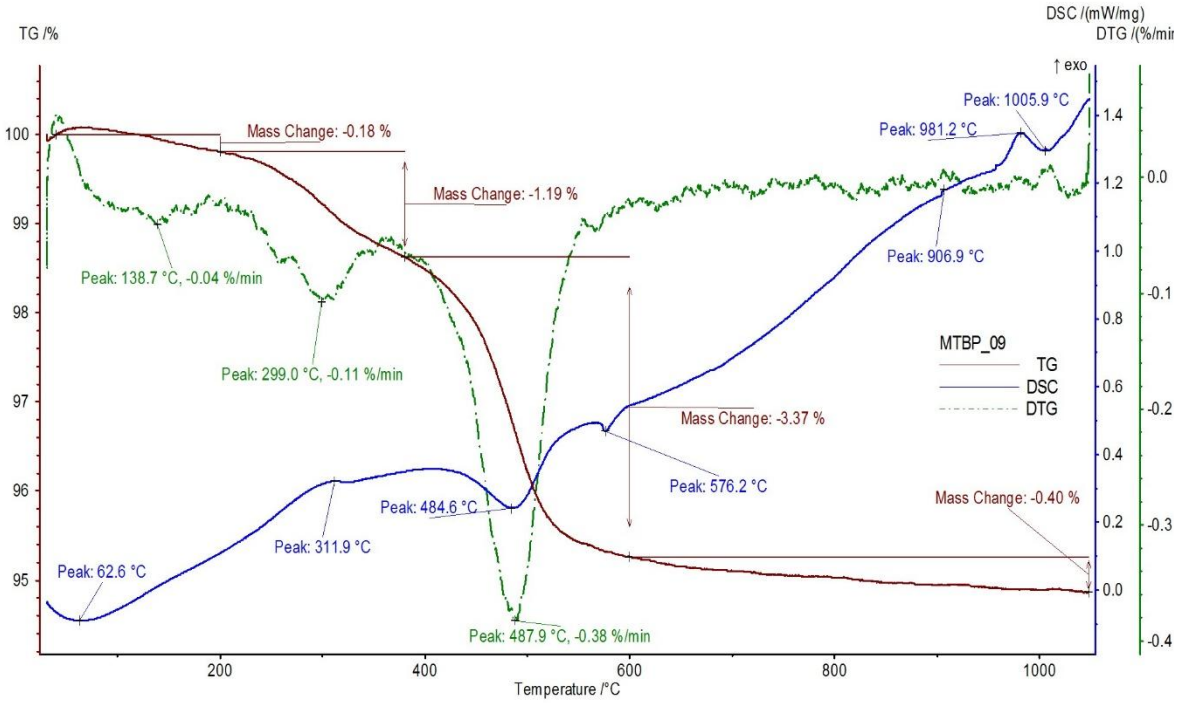

TG /%
DSC /(mW/mg)
DTG /(%/mi
↑ exo
MTBP_04
TG
DSC
DTG
Mass Change: -0.30 %
Mass Change: -1.46 %
Mass Change: -2.80 %
Mass Change: -0.32 %
Peak: 134.3 °C, -0.04 %/min
Peak: 86.8 °C, -0.04 %/min
Peak: 294.5 °C, -0.15 %/min
Peak: 77.1 °C
Peak: 302.4 °C
Peak: 495.9 °C
Peak: 494.3 °C, -0.32 %/min
Peak: 576.4 °C
Peak: 979.8 °C
Peak: 1002.8 °C
Temperature /°C

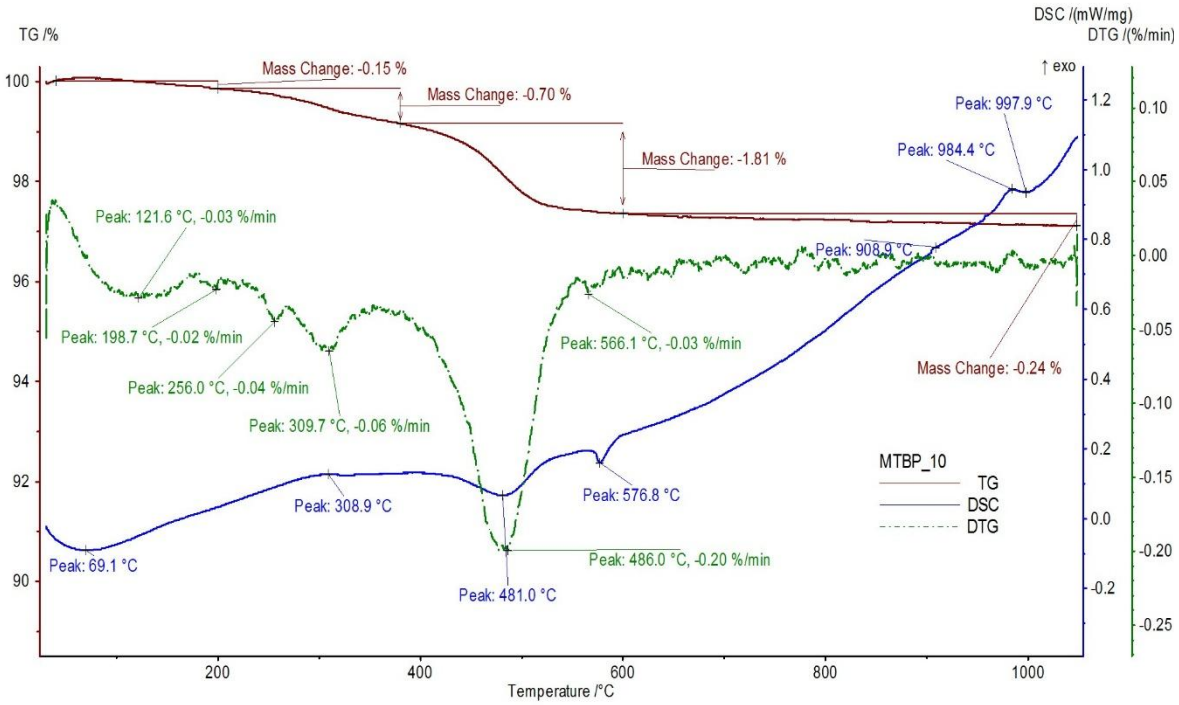

TG /%
DSC /(mW/mg)
DTG /(%/min)
↑ exo
Mass Change: -0.17 %
Peak: 180.2 °C, -0.02 %/min
Peak: 978.0 °C
Mass Change: -0.73 %
Peak: 121.7 °C, -0.03 %/min
Peak: 252.1 °C, -0.04 %/min
Mass Change: -1.98 %
Peak: 304.4 °C, -0.06 %/min
MTBP-05
TG
DSC
DTG
Peak: 576.4 °C
Mass Change: -0.25 %
Peak: 478.1 °C
Peak: 72.8 °C
Peak: 481.3 °C, -0.22 %/min
Temperature /°C

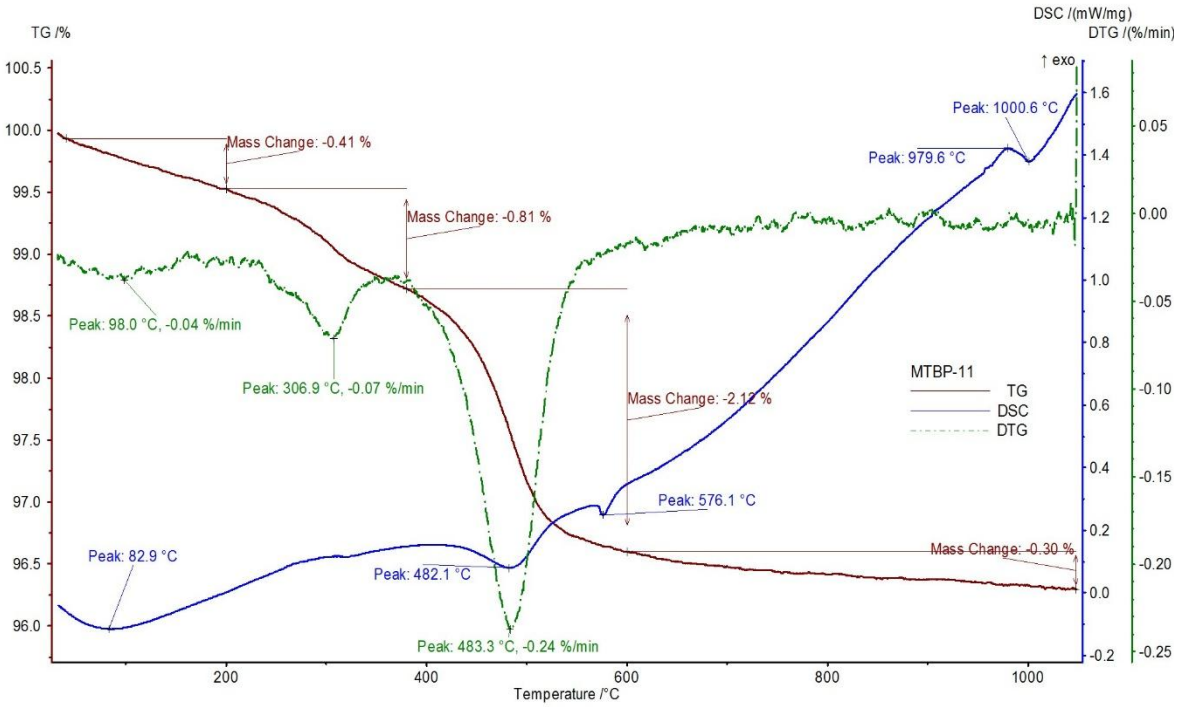

TG /%
DSC /(mW/mg)
DTG /(%/mi
↑ exo
Mass Change: -0.57 %
Peak: 973.3 °C
Mass Change: -2.54 %
Peak: 84.6 °C, -0.07 %/min
MTBP-06
TG
DSC
DTG
Peak: 267.1 °C, -0.28 %/min
Mass Change: -3.75 %
Peak: 300.6 °C
Peak: 574.1 °C
Peak: 489.7 °C
Peak: 263.1 °C
Mass Change: -0.56 %
Peak: 493.4 °C, -0.44 %/min
Temperature /°C

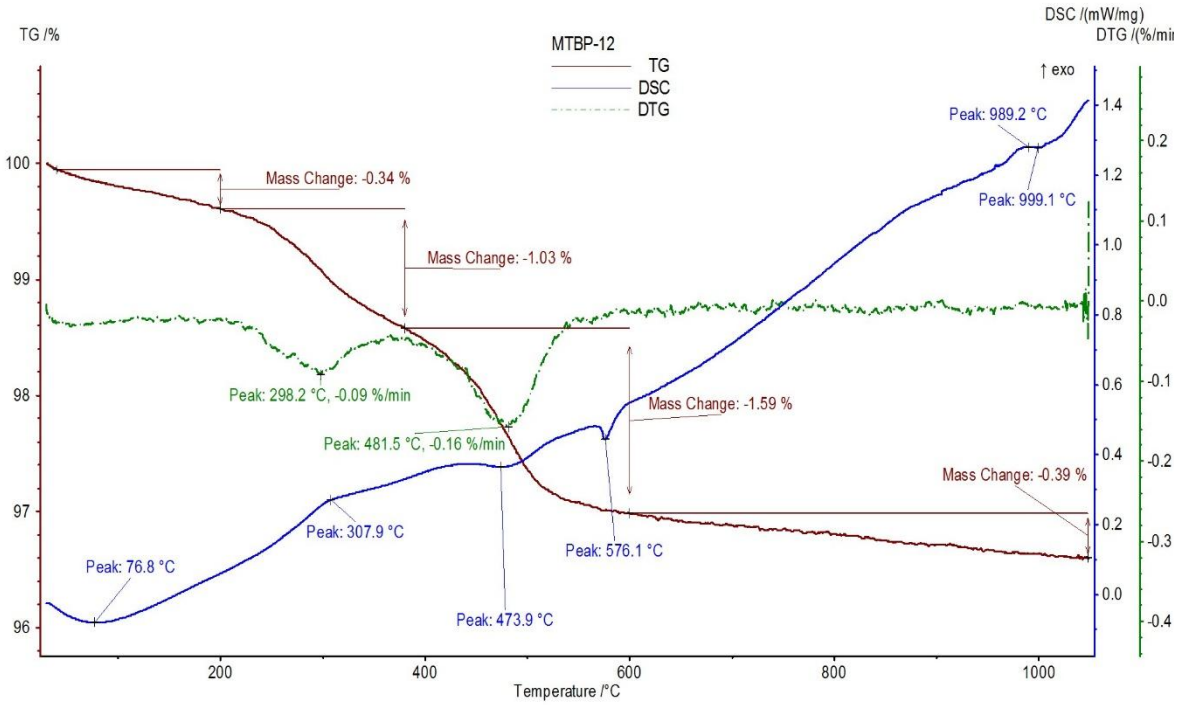

TG /%
DSC /(mW/mg)
DTG /(%/min)
↑ exo
Peak: 1027.8 °C
Mass Change: -0.11 %
Mass Change: -0.82 %
Peak: 133.3 °C, -0.03 %/min
Peak: 257.5 °C, -0.08 %/min
Mass Change: -1.78 %
Peak: 276.7 °C, -0.08 %/min
MTBP-07
TG
DSC
DTG
Peak: 321.5 °C
Peak: 575.8 °C
Mass Change: -0.24 %
Peak: 479.6 °C
Peak: 483.4 °C, -0.21 %/min
Temperature /°C

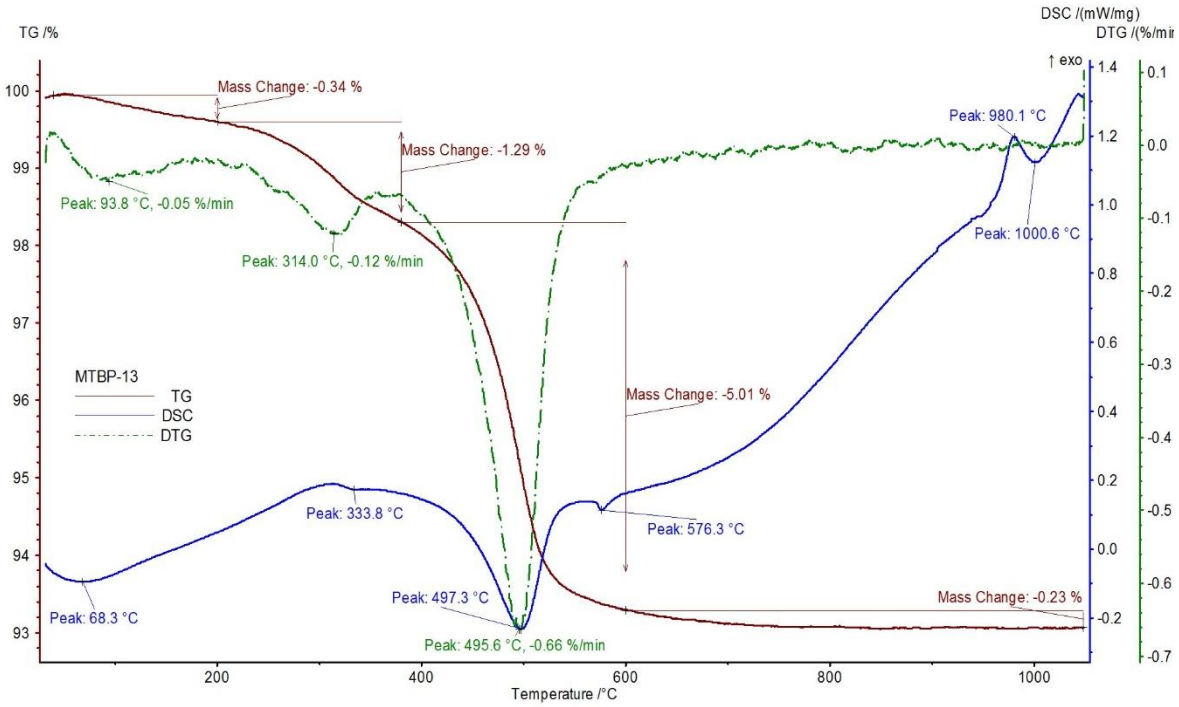

TG /%
DSC /(mW/mg)
DTG /(%/min)
↑ exo
Mass Change: -0.55 %
Peak: 366.8 °C, -0.04 %/min
Mass Change: -1.86 %
Peak: 552.9 °C, -0.02 %/min
Peak: 88.1 °C, -0.05 %/min
MTBP-08
TG
DSC
DTG
Mass Change: -2.00 %
Mass Change: -0.13 %
Peak: 267.3 °C, -0.20 %/min
Peak: 293.0 °C
Peak: 576.8 °C
Peak: 88.8 °C
Peak: 264.0 °C
Peak: 486.7 °C
Peak: 484.8 °C, -0.23 %/min
Temperature /°C

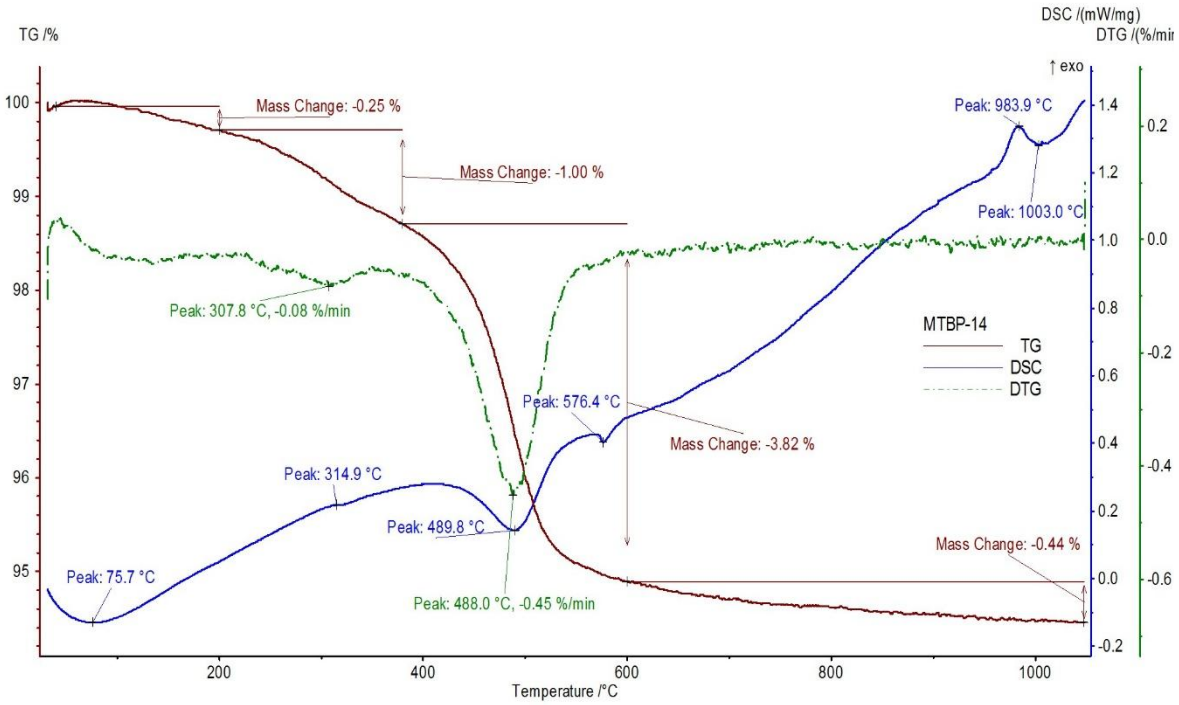

TG /%
DSC /(mW/mg)
DTG /(%/mi
↑ exo
Mass Change: -0.18 %
Mass Change: -1.19 %
Mass Change: -3.37 %
Mass Change: -0.40 %
Peak: 1005.9 °C
Peak: 981.2 °C
Peak: 906.9 °C
Peak: 138.7 °C, -0.04 %/min
Peak: 299.0 °C, -0.11 %/min
Peak: 576.2 °C
Peak: 484.6 °C
Peak: 311.9 °C
Peak: 62.6 °C
Peak: 487.9 °C, -0.38 %/min
MTBP_09
TG
DSC
DTG
Temperature /°C

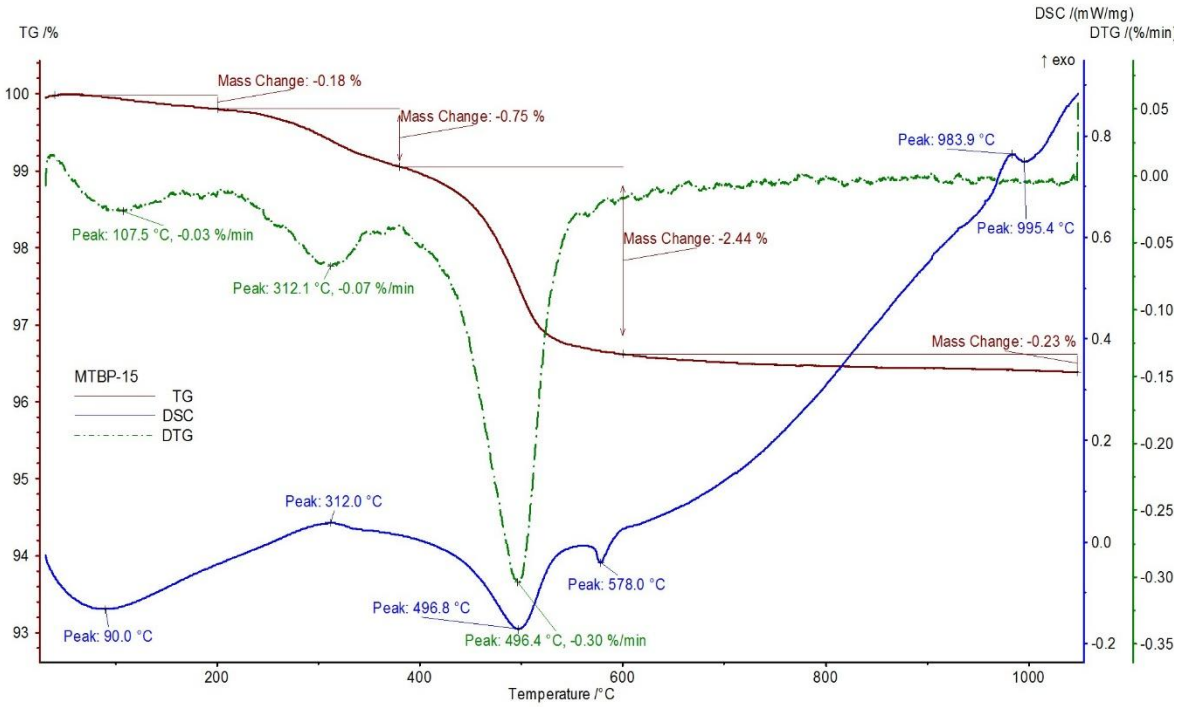

TG /%
DSC /(mW/mg)
DTG /(%/min)
↑ exo
Mass Change: -0.15 %
Mass Change: -0.70 %
Mass Change: -1.81 %
Mass Change: -0.24 %
Peak: 997.9 °C
Peak: 984.4 °C
Peak: 908.9 °C
Peak: 121.6 °C, -0.03 %/min
Peak: 198.7 °C, -0.02 %/min
Peak: 256.0 °C, -0.04 %/min
Peak: 309.7 °C, -0.06 %/min
Peak: 566.1 °C, -0.03 %/min
Peak: 308.9 °C
Peak: 576.8 °C
Peak: 69.1 °C
Peak: 486.0 °C, -0.20 %/min
Peak: 481.0 °C
MTBP_10
TG
DSC
DTG
Temperature /°C

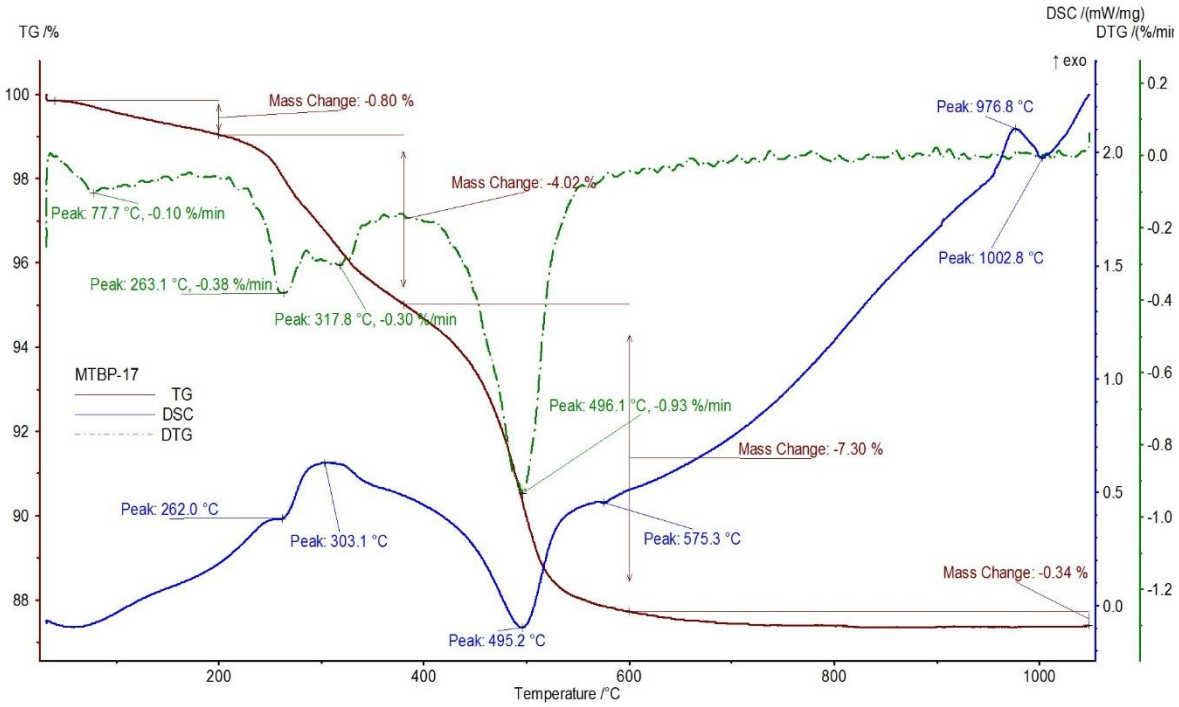

TG /%
DSC /(mW/mg)
DTG /(%/min)
↑ exo
Mass Change: -0.41 %
Mass Change: -0.81 %
Mass Change: -2.12 %
Mass Change: -0.30 %
Peak: 1000.6 °C
Peak: 979.6 °C
Peak: 98.0 °C, -0.04 %/min
Peak: 306.9 °C, -0.07 %/min
Peak: 576.1 °C
Peak: 82.9 °C
Peak: 482.1 °C
Peak: 483.3 °C, -0.24 %/min
MTBP-11
TG
DSC
DTG
Temperature /°C

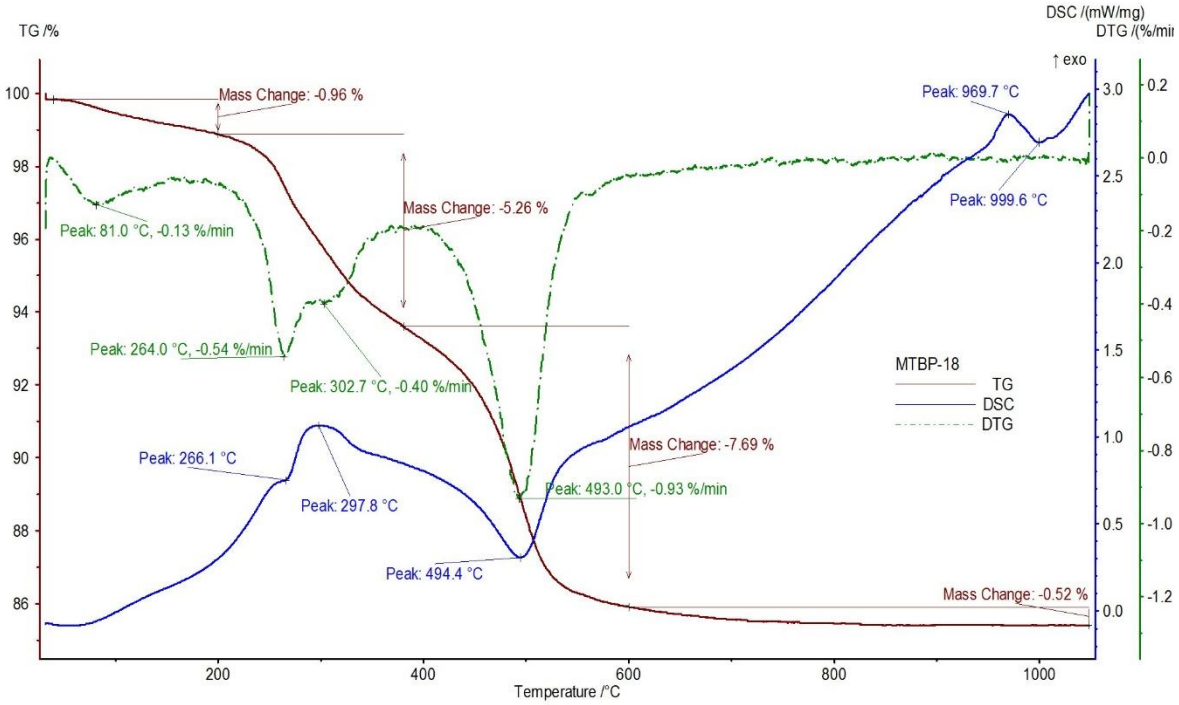

TG /%
DSC /(mW/mg)
DTG /(%/mi
MTBP-12
TG
DSC
DTG
↑ exo
Mass Change: -0.34 %
Mass Change: -1.03 %
Mass Change: -1.59 %
Mass Change: -0.39 %
Peak: 989.2 °C
Peak: 999.1 °C
Peak: 298.2 °C, -0.09 %/min
Peak: 481.5 °C, -0.16 %/min
Peak: 307.9 °C
Peak: 576.1 °C
Peak: 76.8 °C
Peak: 473.9 °C
Temperature /°C

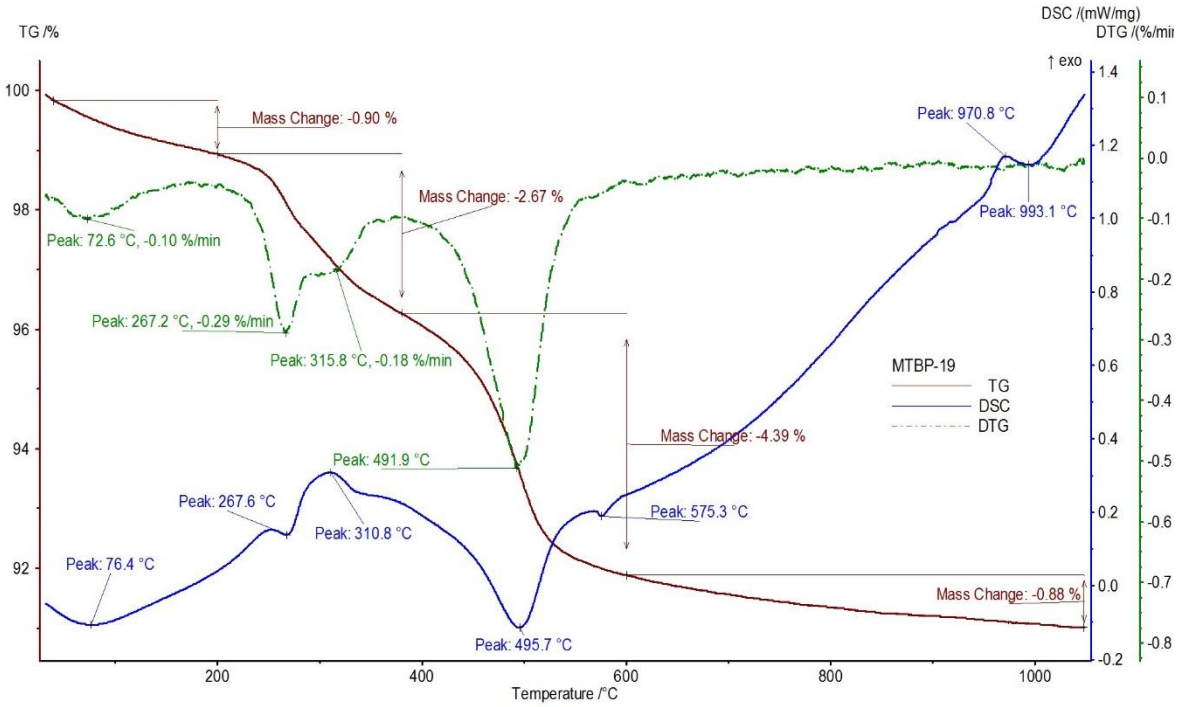

TG /%
DSC /(mW/mg)
DTG /(%/mi
↑ exo
Mass Change: -0.34 %
Mass Change: -1.29 %
Peak: 980.1 °C
Peak: 93.8 °C, -0.05 %/min
Peak: 1000.6 °C
Peak: 314.0 °C, -0.12 %/min
MTBP-13
TG
DSC
DTG
Mass Change: -5.01 %
Peak: 333.8 °C
Peak: 576.3 °C
Peak: 497.3 °C
Mass Change: -0.23 %
Peak: 68.3 °C
Peak: 495.6 °C, -0.66 %/min
Temperature /°C

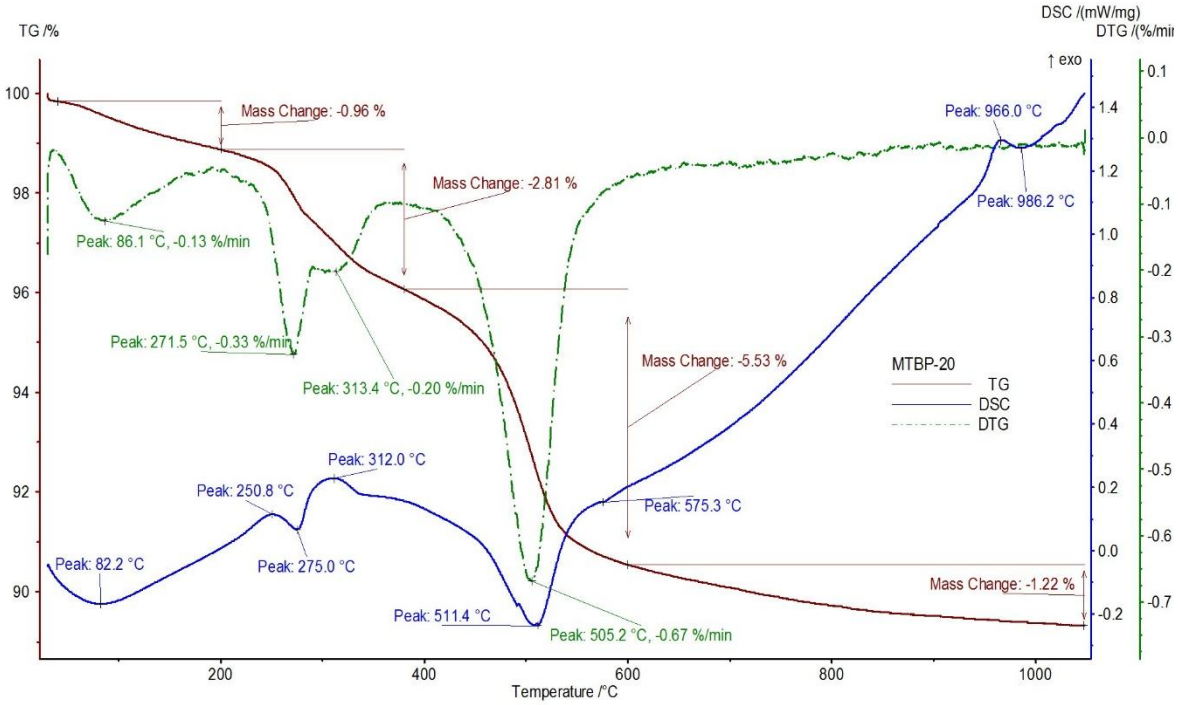

TG /%
DSC /(mW/mg)
DTG /(%/mi
↑ exo
Mass Change: -0.25 %
Peak: 983.9 °C
Mass Change: -1.00 %
Peak: 1003.0 °C
Peak: 307.8 °C, -0.08 %/min
MTBP-14
TG
DSC
DTG
Peak: 576.4 °C
Mass Change: -3.82 %
Peak: 314.9 °C
Peak: 489.8 °C
Mass Change: -0.44 %
Peak: 75.7 °C
Peak: 488.0 °C, -0.45 %/min
Temperature /°C

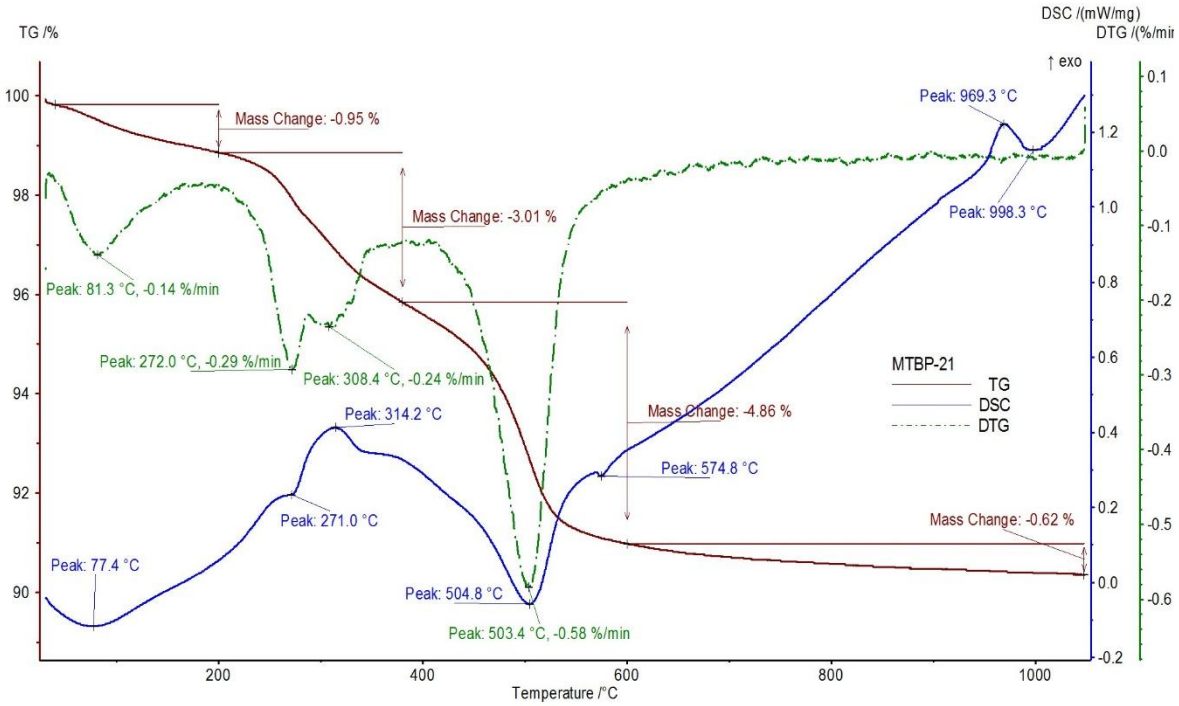

TG /%
DSC /(mW/mg)
DTG /(%/min)
↑ exo
Mass Change: -0.18 %
Mass Change: -0.75 %
Peak: 983.9 °C
Peak: 107.5 °C, -0.03 %/min
Peak: 995.4 °C
Mass Change: -2.44 %
Peak: 312.1 °C, -0.07 %/min
Mass Change: -0.23 %
MTBP-15
TG
DSC
DTG
Peak: 312.0 °C
Peak: 578.0 °C
Peak: 496.8 °C
Peak: 90.0 °C
Peak: 496.4 °C, -0.30 %/min
Temperature /°C

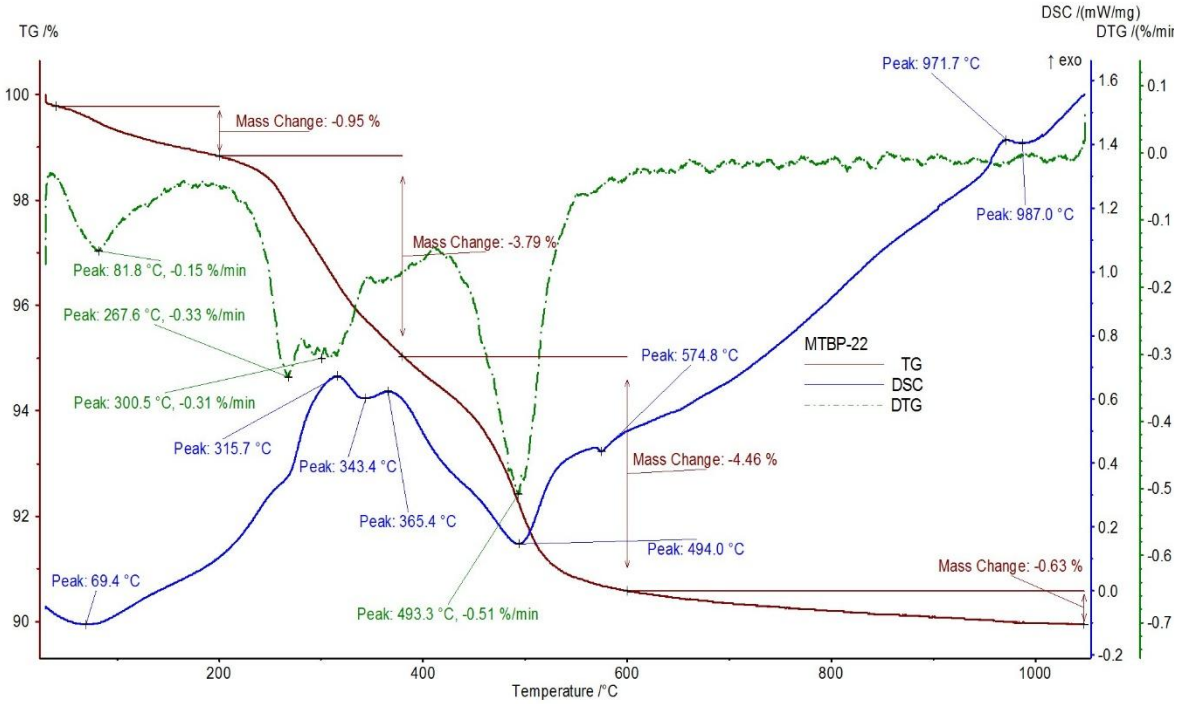

TG /%
DSC /(mW/mg)
DTG /(%/min)
↑ exo
Mass Change: -0.80 %
Peak: 976.8 °C
Mass Change: -4.02 %
Peak: 77.7 °C, -0.10 %/min
Peak: 1002.8 °C
Peak: 263.1 °C, -0.38 %/min
Peak: 317.8 °C, -0.30 %/min
MTBP-17
TG
DSC
DTG
Peak: 496.1 °C, -0.93 %/min
Mass Change: -7.30 %
Peak: 262.0 °C
Peak: 303.1 °C
Peak: 575.3 °C
Mass Change: -0.34 %
Peak: 495.2 °C
Temperature /°C

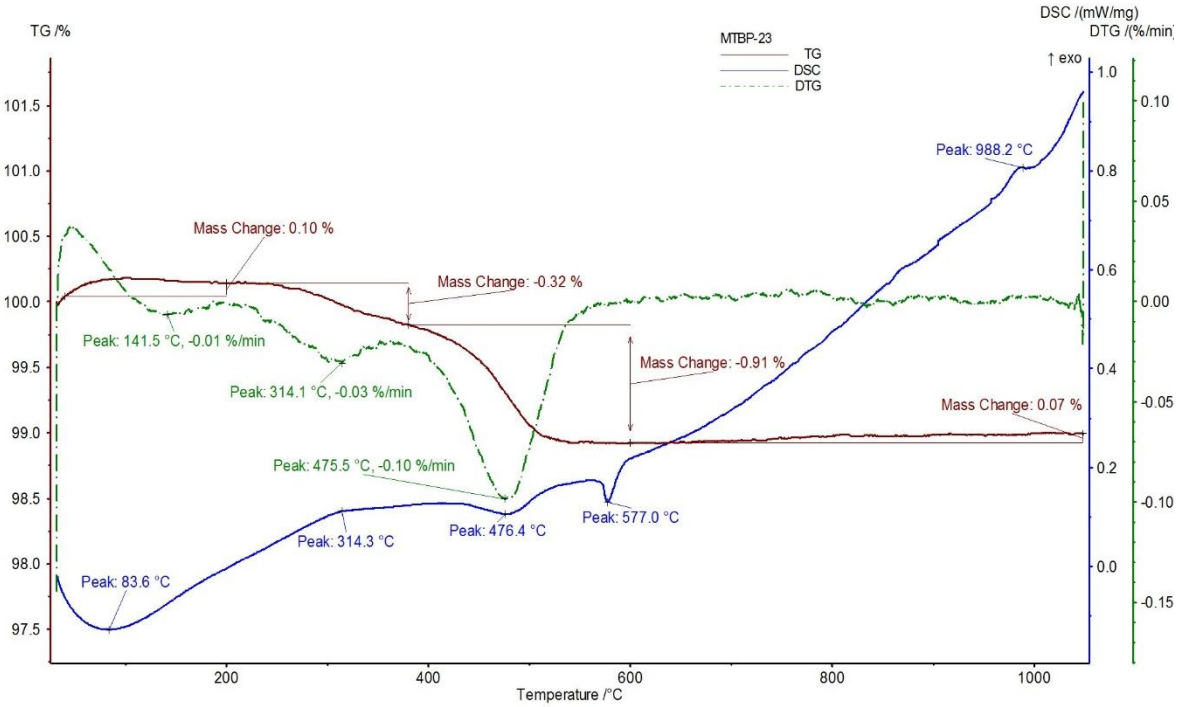

TG /%
DSC /(mW/mg)
DTG /(%/mi
↑ exo
Mass Change: -0.96 %
Peak: 969.7 °C
Peak: 999.6 °C
Peak: 81.0 °C, -0.13 %/min
Mass Change: -5.26 %
Peak: 264.0 °C, -0.54 %/min
Peak: 302.7 °C, -0.40 %/min
MTBP-18
TG
DSC
DTG
Mass Change: -7.69 %
Peak: 266.1 °C
Peak: 297.8 °C
Peak: 493.0 °C, -0.93 %/min
Peak: 494.4 °C
Mass Change: -0.52 %
Temperature /°C

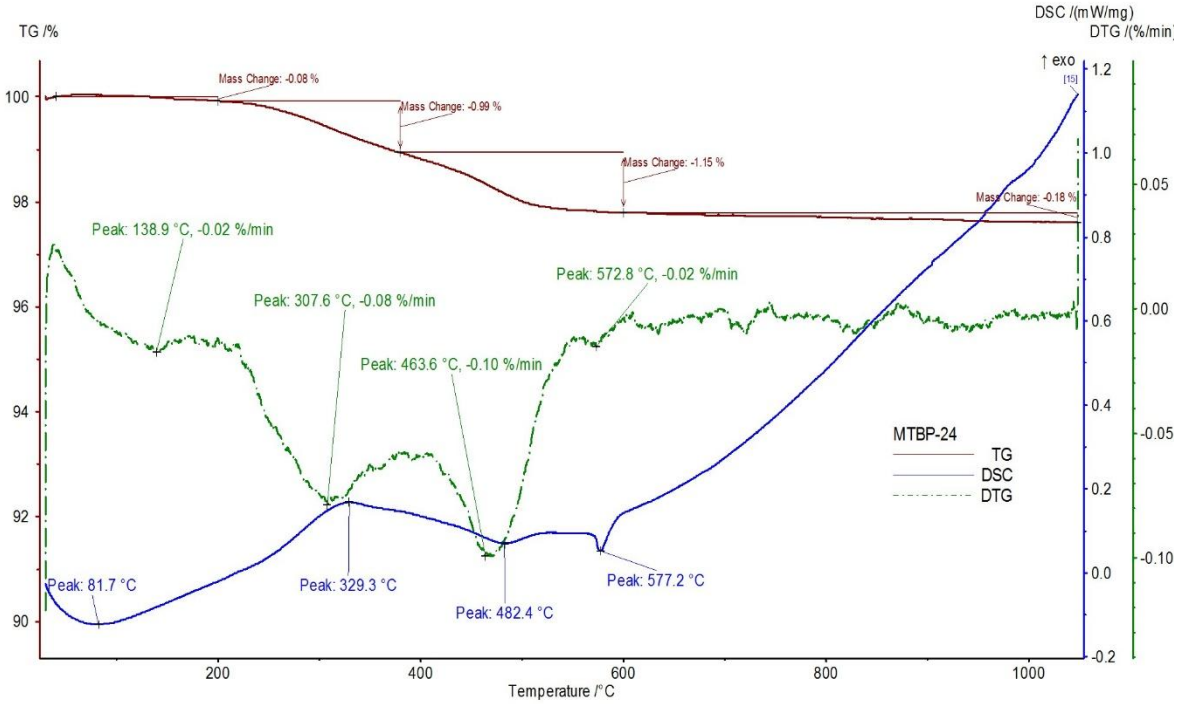

TG /%
DSC /(mW/mg)
DTG /(%/mi
↑ exo
Mass Change: -0.90 %
Peak: 970.8 °C
Peak: 993.1 °C
Mass Change: -2.67 %
Peak: 72.6 °C, -0.10 %/min
Peak: 267.2 °C, -0.29 %/min
Peak: 315.8 °C, -0.18 %/min
MTBP-19
TG
DSC
DTG
Mass Change: -4.39 %
Peak: 491.9 °C
Peak: 267.6 °C
Peak: 310.8 °C
Peak: 575.3 °C
Peak: 76.4 °C
Mass Change: -0.88 %
Peak: 495.7 °C
Temperature /°C

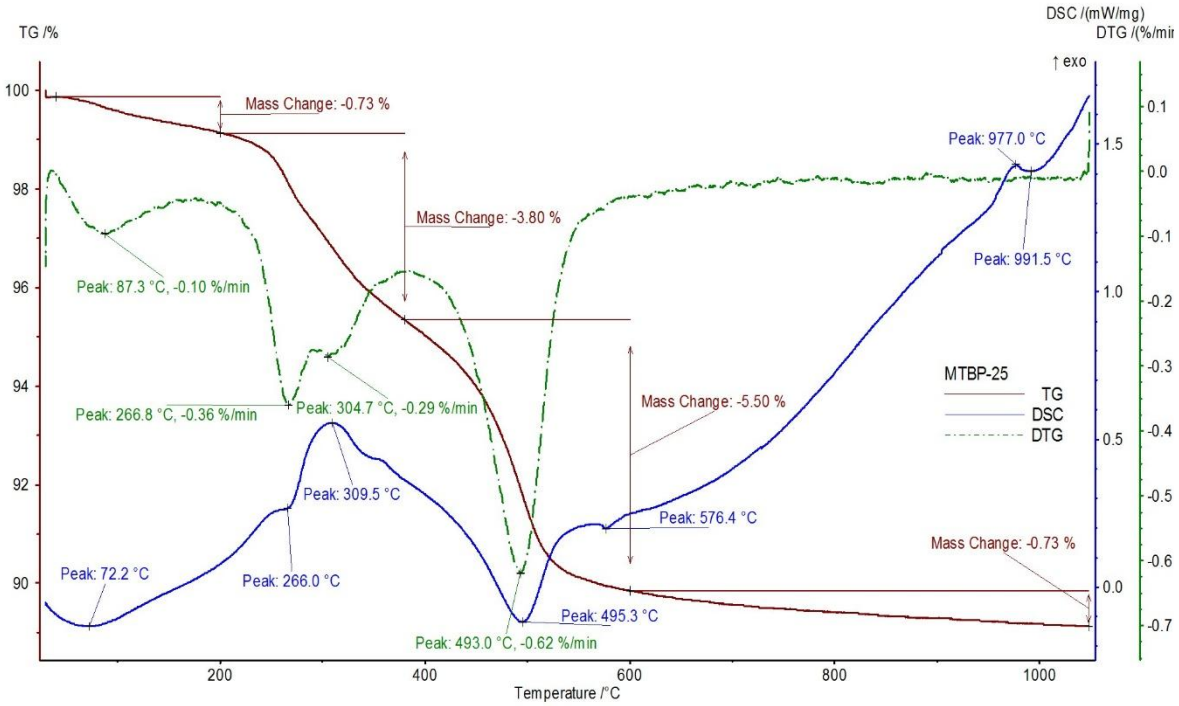

TG /%
DSC /(mW/mg)
DTG /(%/mi
↑ exo
Mass Change: -0.96 %
Mass Change: -2.81 %
Mass Change: -5.53 %
Mass Change: -1.22 %
Peak: 966.0 °C
Peak: 986.2 °C
Peak: 86.1 °C, -0.13 %/min
Peak: 271.5 °C, -0.33 %/min
Peak: 313.4 °C, -0.20 %/min
Peak: 312.0 °C
Peak: 250.8 °C
Peak: 82.2 °C
Peak: 275.0 °C
Peak: 575.3 °C
Peak: 511.4 °C
Peak: 505.2 °C, -0.67 %/min
MTBP-20
TG
DSC
DTG
Temperature /°C

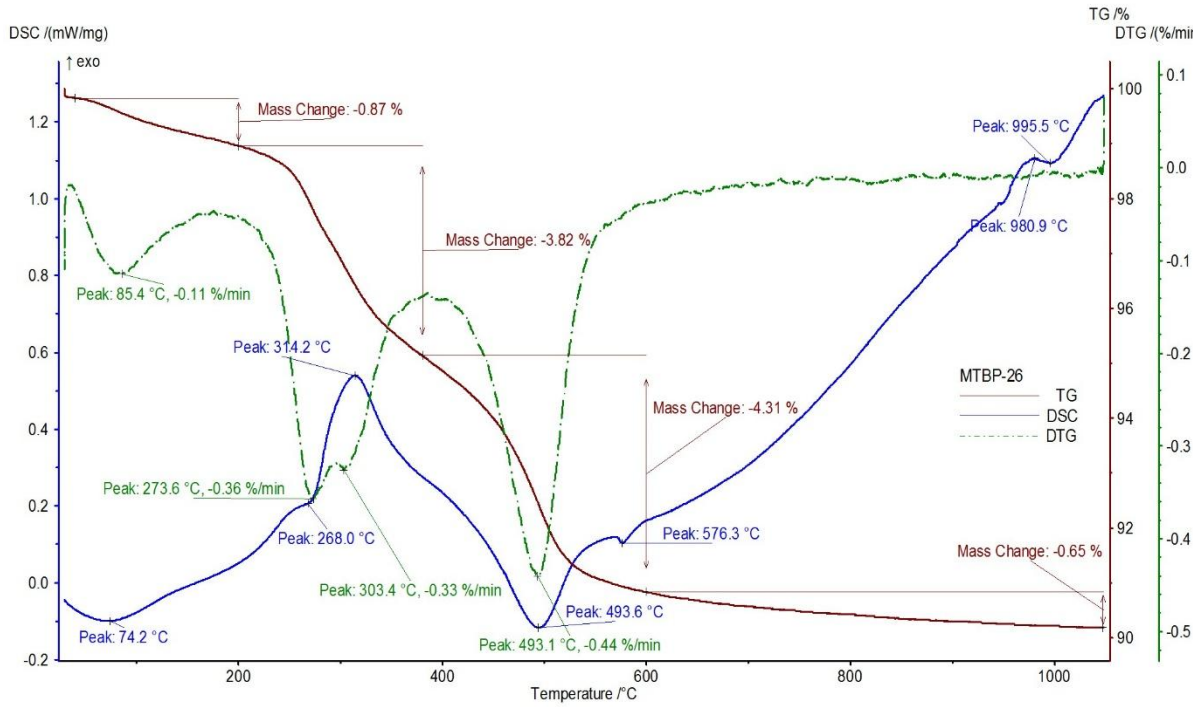

TG /%
DSC /(mW/mg)
DTG /(%/mi
↑ exo
Mass Change: -0.95 %
Mass Change: -3.01 %
Mass Change: -4.86 %
Mass Change: -0.62 %
Peak: 969.3 °C
Peak: 998.3 °C
Peak: 81.3 °C, -0.14 %/min
Peak: 272.0 °C, -0.29 %/min
Peak: 308.4 °C, -0.24 %/min
Peak: 314.2 °C
Peak: 271.0 °C
Peak: 77.4 °C
Peak: 574.8 °C
Peak: 504.8 °C
Peak: 503.4 °C, -0.58 %/min
MTBP-21
TG
DSC
DTG
Temperature /°C

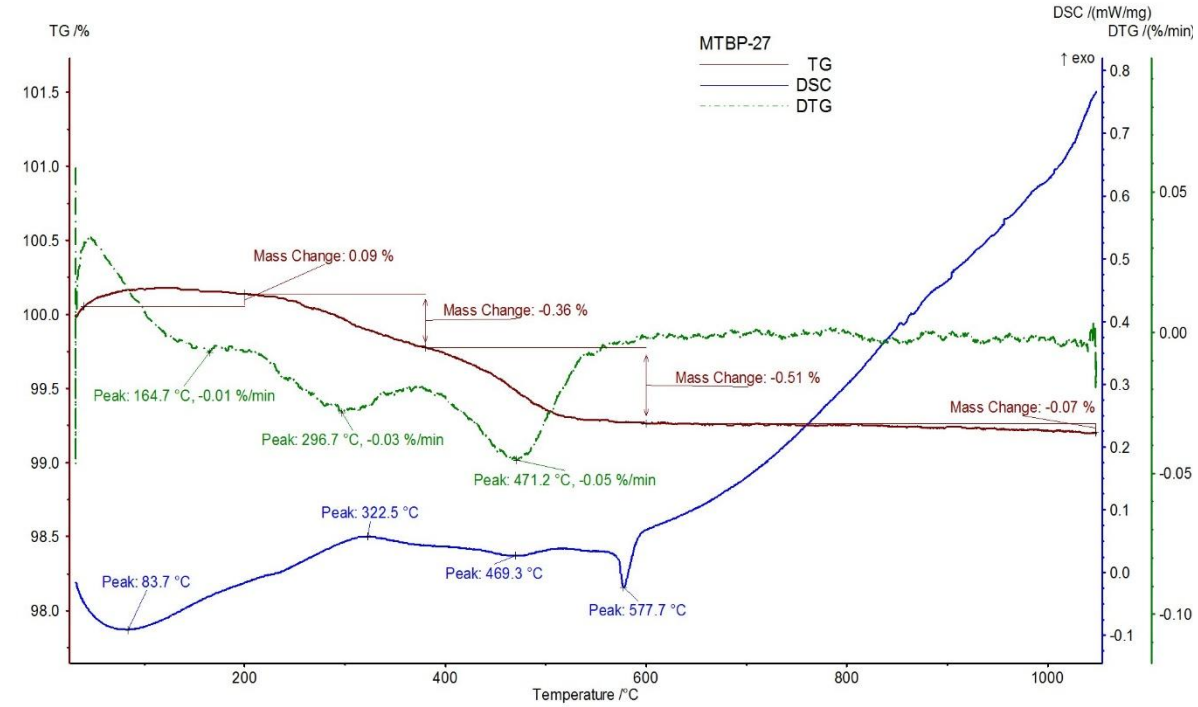

TG /%
DSC /(mW/mg)
DTG /(%/mi
↑ exo
MTBP-22
TG
DSC
DTG
Mass Change: -0.95 %
Mass Change: -3.79 %
Mass Change: -4.46 %
Mass Change: -0.63 %
Peak: 971.7 °C
Peak: 987.0 °C
Peak: 81.8 °C, -0.15 %/min
Peak: 267.6 °C, -0.33 %/min
Peak: 300.5 °C, -0.31 %/min
Peak: 574.8 °C
Peak: 315.7 °C
Peak: 343.4 °C
Peak: 365.4 °C
Peak: 494.0 °C
Peak: 69.4 °C
Peak: 493.3 °C, -0.51 %/min
Temperature /°C

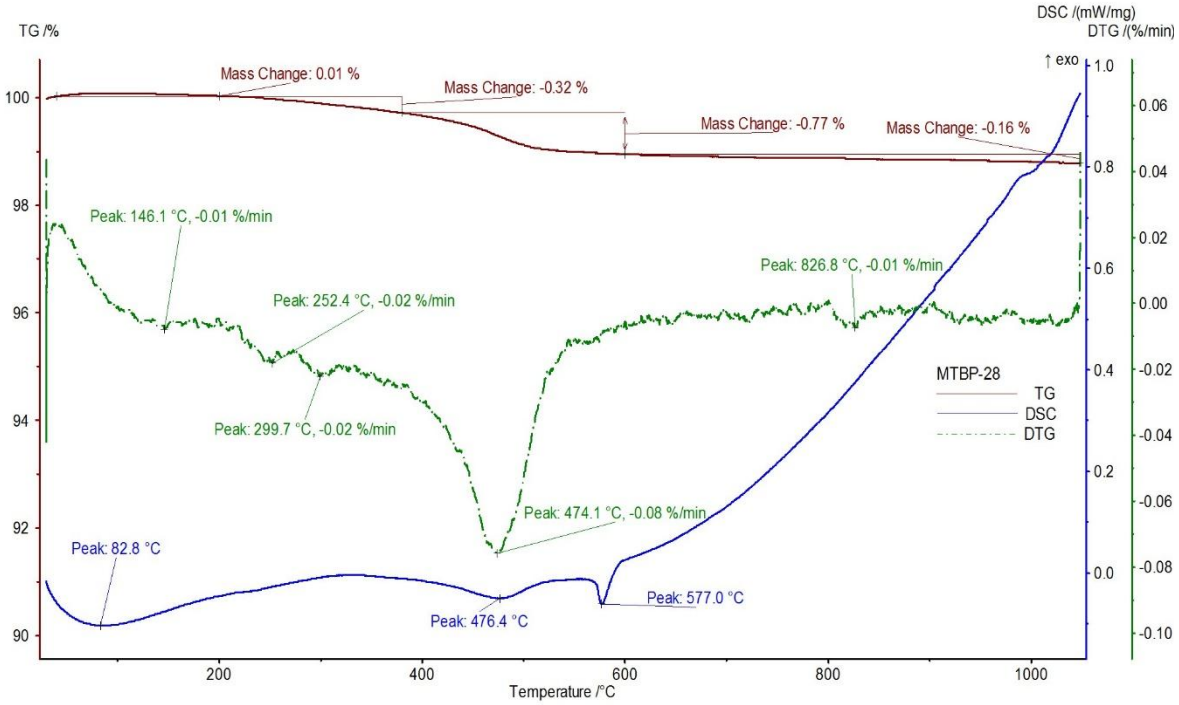

TG /%
DSC /(mW/mg)
DTG /(%/min
↑ exo
MTBP-23
TG
DSC
DTG
Mass Change: 0.10 %
Mass Change: -0.32 %
Mass Change: -0.91 %
Mass Change: 0.07 %
Peak: 988.2 °C
Peak: 141.5 °C, -0.01 %/min
Peak: 314.1 °C, -0.03 %/min
Peak: 475.5 °C, -0.10 %/min
Peak: 314.3 °C
Peak: 476.4 °C
Peak: 577.0 °C
Peak: 83.6 °C
Temperature /°C

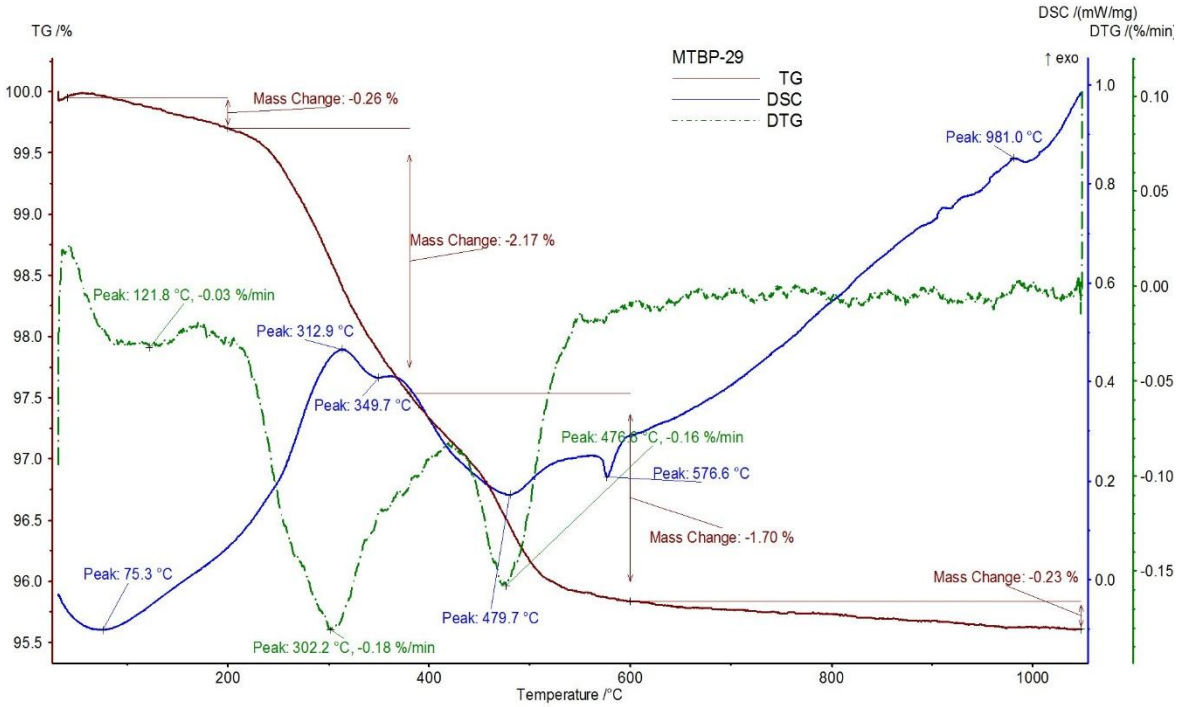

TG /%
DSC /(mW/mg)
DTG /(%/min)
↑ exo
Mass Change: -0.08 %
Mass Change: -0.99 %
Mass Change: -1.15 %
Mass Change: -0.18 %
Peak: 138.9 °C, -0.02 %/min
Peak: 307.6 °C, -0.08 %/min
Peak: 463.6 °C, -0.10 %/min
Peak: 572.8 °C, -0.02 %/min
Peak: 81.7 °C
Peak: 329.3 °C
Peak: 482.4 °C
Peak: 577.2 °C
MTBP-24
TG
DSC
DTG
Temperature /°C

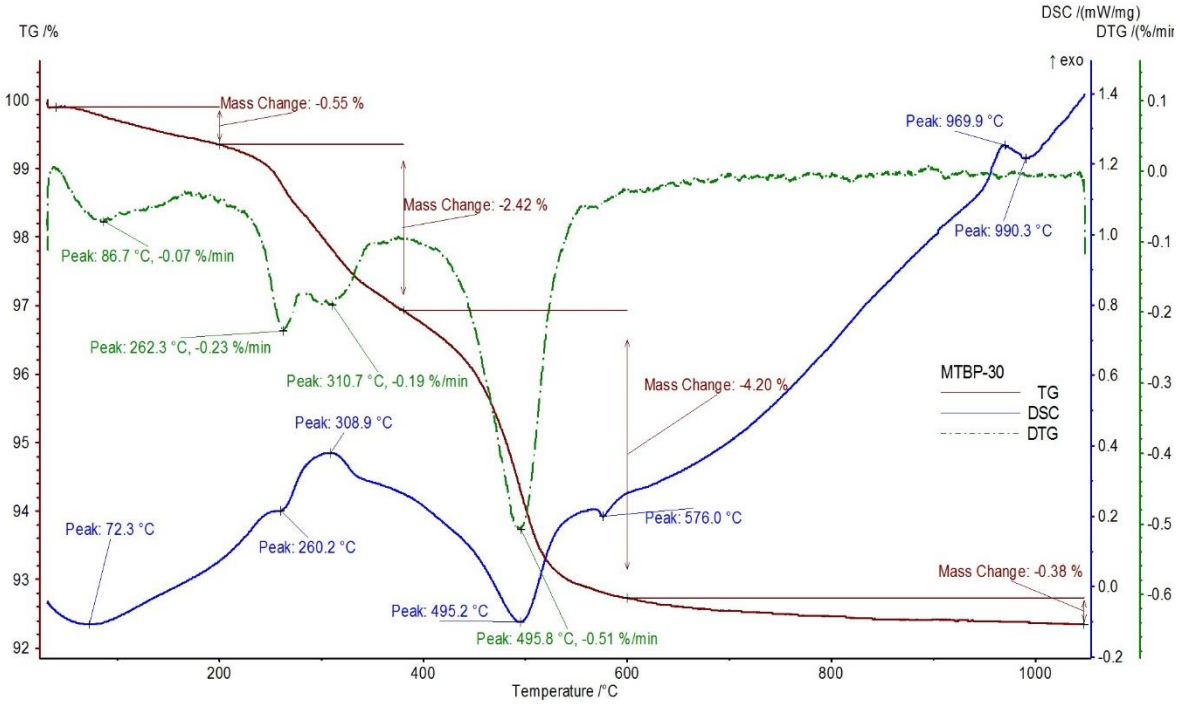

TG /%
DSC /(mW/mg)
DTG /(%/min)
↑ exo
Mass Change: -0.73 %
Mass Change: -3.80 %
Mass Change: -5.50 %
Mass Change: -0.73 %
Peak: 87.3 °C, -0.10 %/min
Peak: 266.8 °C, -0.36 %/min
Peak: 304.7 °C, -0.29 %/min
Peak: 977.0 °C
Peak: 991.5 °C
Peak: 309.5 °C
Peak: 576.4 °C
Peak: 72.2 °C
Peak: 266.0 °C
Peak: 495.3 °C
Peak: 493.0 °C, -0.62 %/min
MTBP-25
TG
DSC
DTG
Temperature /°C

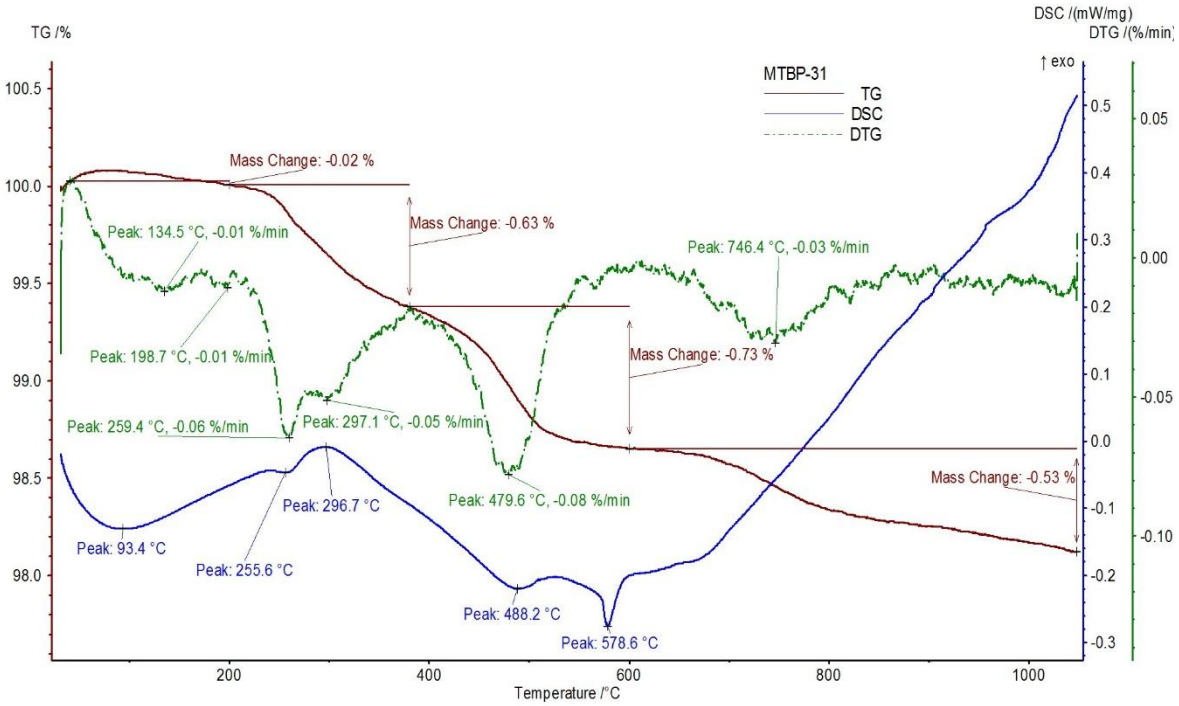

DSC /(mW/mg)
↑ exo
TG /%
DTG /(%/mi
Mass Change: -0.87 %
Mass Change: -3.82 %
Mass Change: -4.31 %
Mass Change: -0.65 %
Peak: 995.5 °C
Peak: 980.9 °C
Peak: 85.4 °C, -0.11 %/min
Peak: 314.2 °C
Peak: 273.6 °C, -0.36 %/min
Peak: 268.0 °C
Peak: 303.4 °C, -0.33 %/min
Peak: 576.3 °C
Peak: 493.6 °C
Peak: 74.2 °C
Peak: 493.1 °C, -0.44 %/min
MTBP-26
TG
DSC
DTG
Temperature /°C

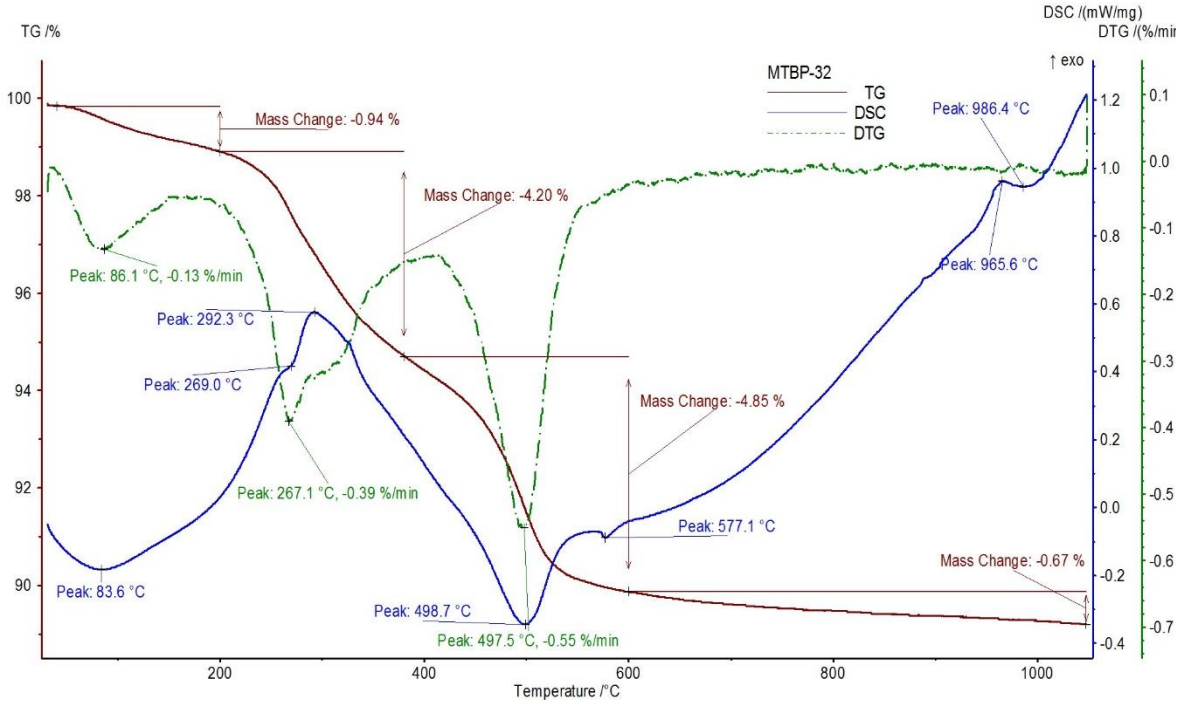

TG /%
DSC /(mW/mg)
DTG /(%/min)
↑ exo
MTBP-27
TG
DSC
DTG
Mass Change: 0.09 %
Mass Change: -0.36 %
Mass Change: -0.51 %
Mass Change: -0.07 %
Peak: 164.7 °C, -0.01 %/min
Peak: 296.7 °C, -0.03 %/min
Peak: 471.2 °C, -0.05 %/min
Peak: 322.5 °C
Peak: 83.7 °C
Peak: 469.3 °C
Peak: 577.7 °C
Temperature /°C

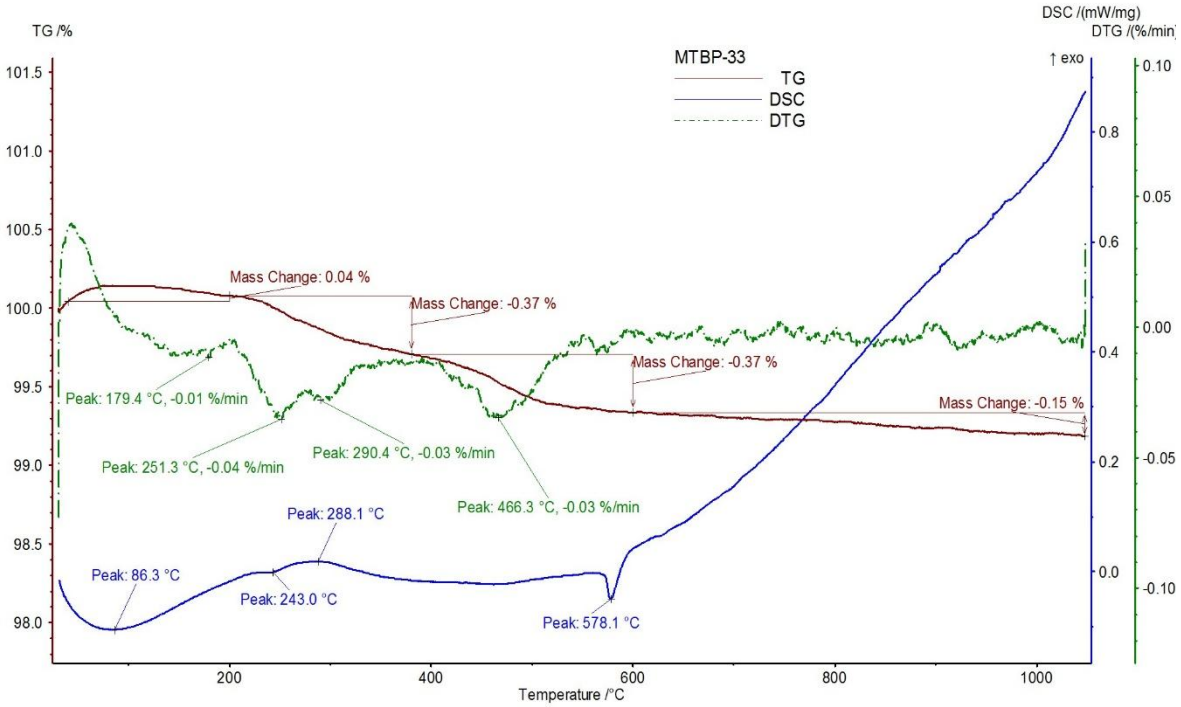

TG /%
DSC /(mW/mg)
DTG /(%/min)
↑ exo
Mass Change: 0.01 %
Mass Change: -0.32 %
Mass Change: -0.77 %
Mass Change: -0.16 %
Peak: 146.1 °C, -0.01 %/min
Peak: 252.4 °C, -0.02 %/min
Peak: 299.7 °C, -0.02 %/min
Peak: 826.8 °C, -0.01 %/min
Peak: 474.1 °C, -0.08 %/min
Peak: 82.8 °C
Peak: 476.4 °C
Peak: 577.0 °C
MTBP-28
TG
DSC
DTG
Temperature /°C

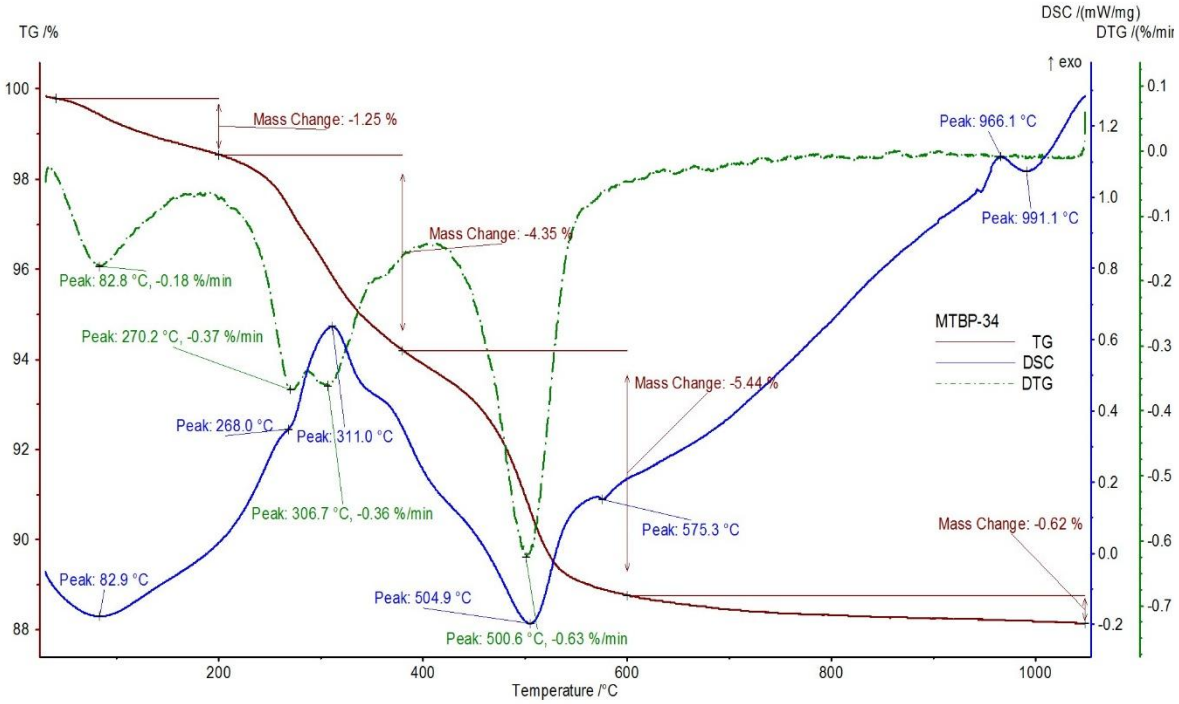

TG /%
DSC /(mW/mg)
DTG /(%/min)
MTBP-29
TG
DSC
DTG
↑ exo
Mass Change: -0.26 %
Mass Change: -2.17 %
Mass Change: -1.70 %
Mass Change: -0.23 %
Peak: 121.8 °C, -0.03 %/min
Peak: 312.9 °C
Peak: 349.7 °C
Peak: 476.8 °C, -0.16 %/min
Peak: 576.6 °C
Peak: 981.0 °C
Peak: 75.3 °C
Peak: 479.7 °C
Peak: 302.2 °C, -0.18 %/min
Temperature /°C

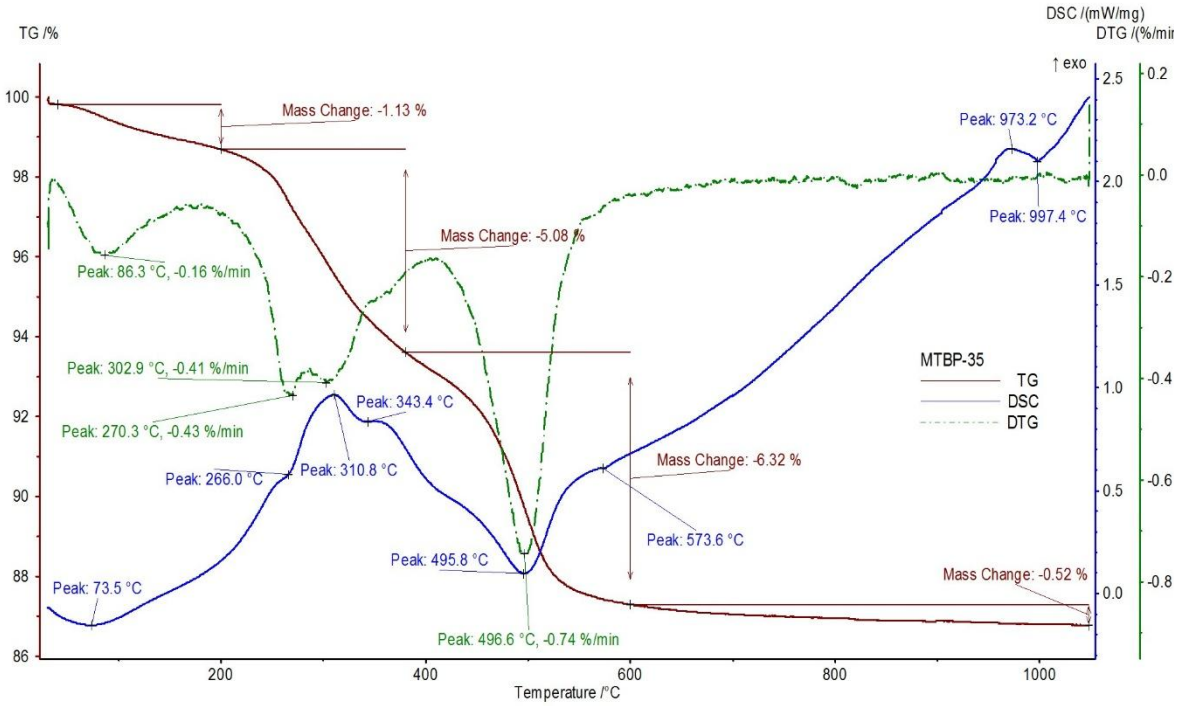

TG /%
DSC /(mW/mg)
DTG /(%/mi
↑ exo
MTBP-30
TG
DSC
DTG
Mass Change: -0.55 %
Mass Change: -2.42 %
Mass Change: -4.20 %
Mass Change: -0.38 %
Peak: 969.9 °C
Peak: 990.3 °C
Peak: 86.7 °C, -0.07 %/min
Peak: 262.3 °C, -0.23 %/min
Peak: 310.7 °C, -0.19 %/min
Peak: 308.9 °C
Peak: 72.3 °C
Peak: 260.2 °C
Peak: 576.0 °C
Peak: 495.2 °C
Peak: 495.8 °C, -0.51 %/min
Temperature /°C

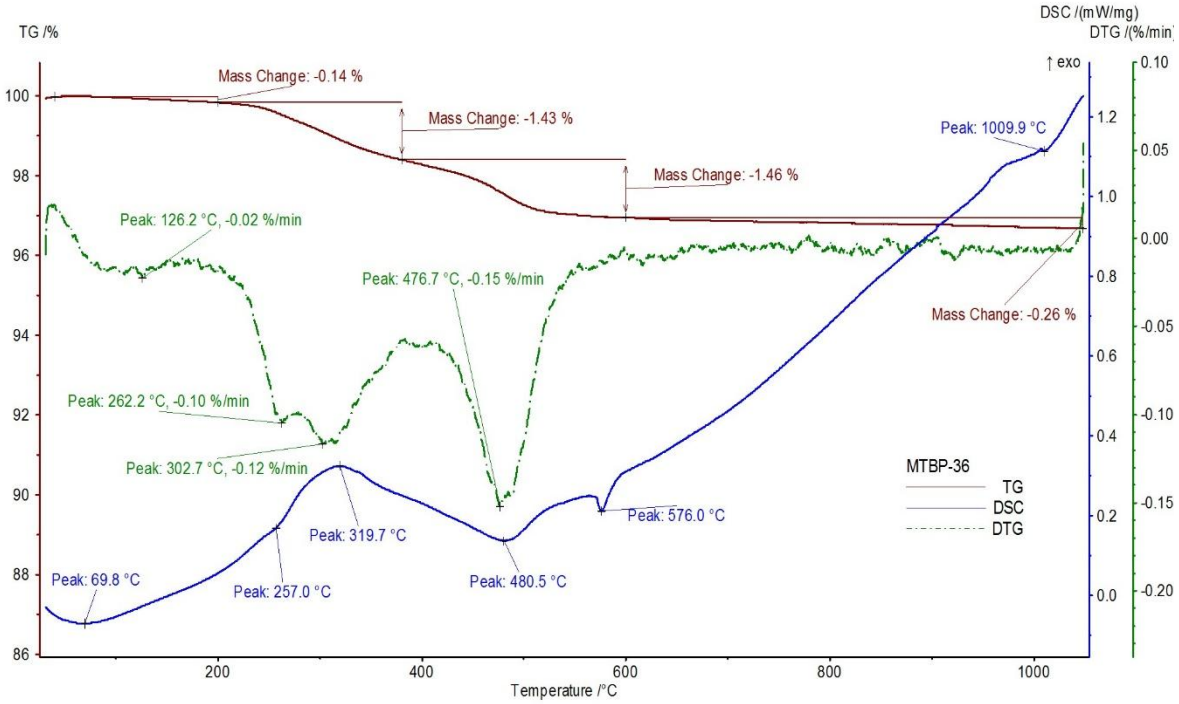

TG /%
DSC /(mW/mg)
DTG /(%/min)
↑ exo
MTBP-31
TG
DSC
DTG
Mass Change: -0.02 %
Mass Change: -0.63 %
Mass Change: -0.73 %
Mass Change: -0.53 %
Peak: 134.5 °C, -0.01 %/min
Peak: 198.7 °C, -0.01 %/min
Peak: 259.4 °C, -0.06 %/min
Peak: 297.1 °C, -0.05 %/min
Peak: 746.4 °C, -0.03 %/min
Peak: 479.6 °C, -0.08 %/min
Peak: 93.4 °C
Peak: 255.6 °C
Peak: 296.7 °C
Peak: 488.2 °C
Peak: 578.6 °C
Temperature /°C

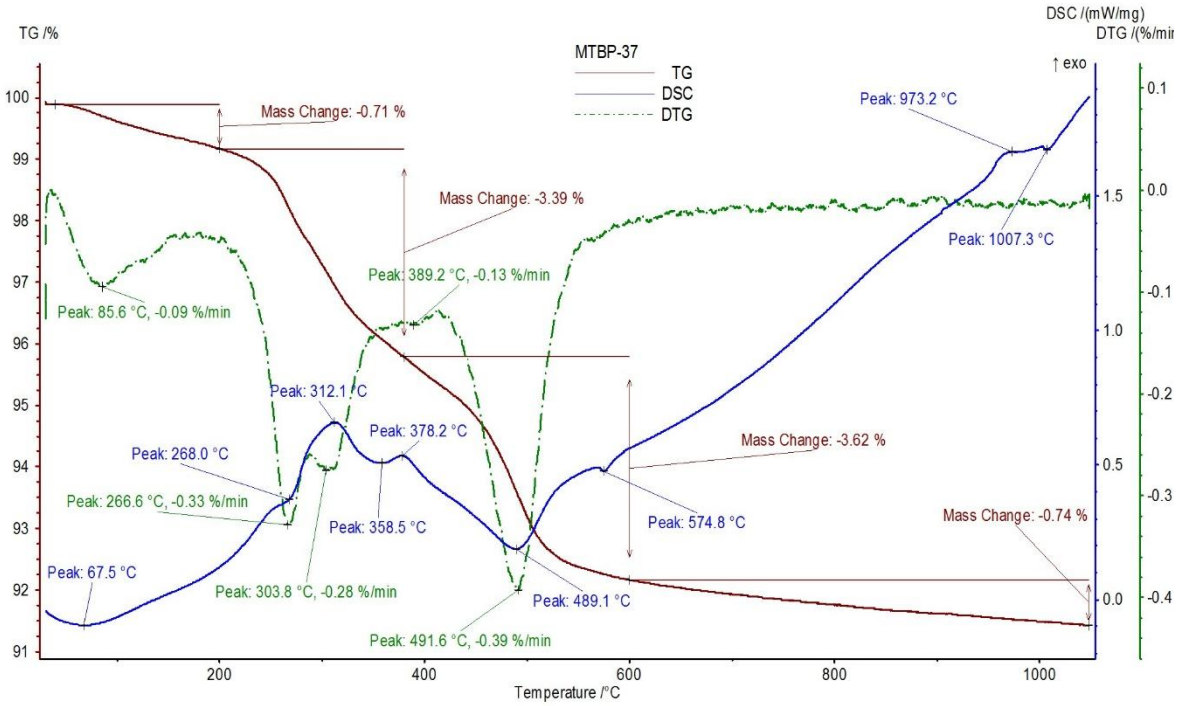

TG /%
DSC /(mW/mg)
DTG /(%/mi
↑ exo
MTBP-32
TG
DSC
DTG
Mass Change: -0.94 %
Mass Change: -4.20 %
Mass Change: -4.85 %
Mass Change: -0.67 %
Peak: 86.1 °C, -0.13 %/min
Peak: 292.3 °C
Peak: 269.0 °C
Peak: 267.1 °C, -0.39 %/min
Peak: 83.6 °C
Peak: 498.7 °C
Peak: 497.5 °C, -0.55 %/min
Peak: 577.1 °C
Peak: 986.4 °C
Peak: 965.6 °C
Temperature /°C

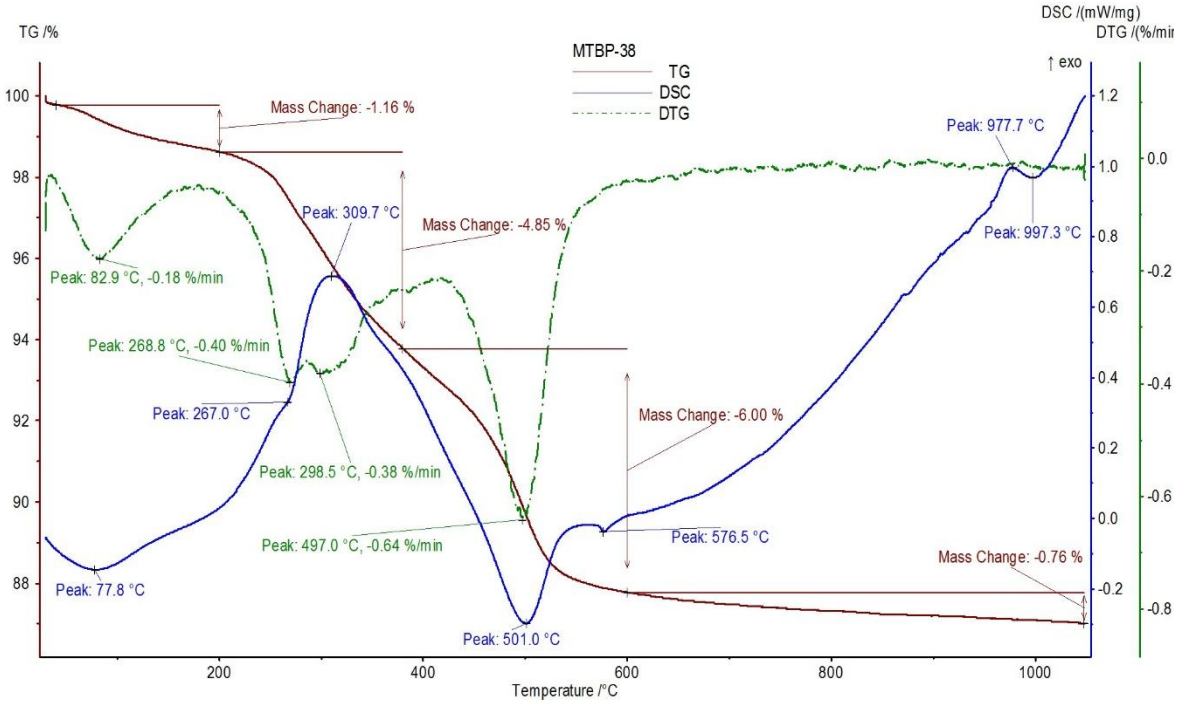

TG /%
DSC /(mW/mg)
DTG /(%/min
↑ exo
MTBP-33
TG
DSC
DTG
Mass Change: 0.04 %
Mass Change: -0.37 %
Mass Change: -0.37 %
Mass Change: -0.15 %
Peak: 179.4 °C, -0.01 %/min
Peak: 251.3 °C, -0.04 %/min
Peak: 290.4 °C, -0.03 %/min
Peak: 466.3 °C, -0.03 %/min
Peak: 288.1 °C
Peak: 86.3 °C
Peak: 243.0 °C
Peak: 578.1 °C
Temperature /°C

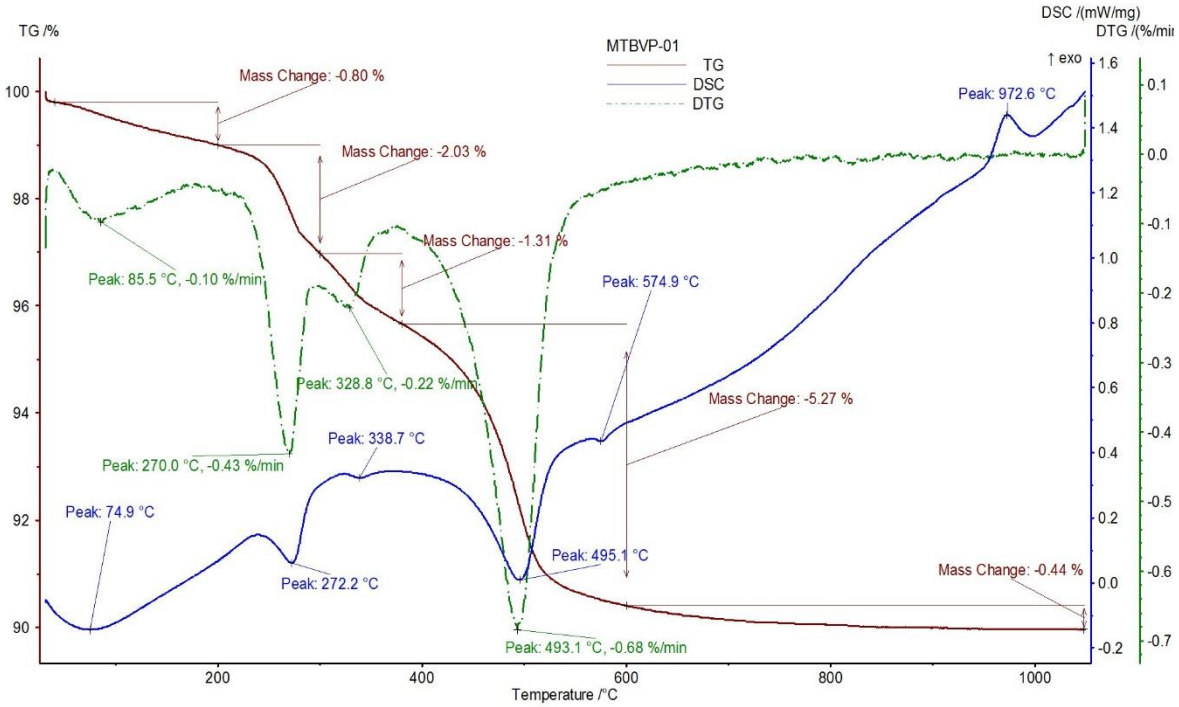

TG /%
DSC /(mW/mg)
DTG /(%/mir
↑ exo
Mass Change: -1.25 %
Mass Change: -4.35 %
Mass Change: -5.44 %
Mass Change: -0.62 %
Peak: 966.1 °C
Peak: 991.1 °C
Peak: 82.8 °C, -0.18 %/min
Peak: 270.2 °C, -0.37 %/min
Peak: 268.0 °C
Peak: 311.0 °C
Peak: 306.7 °C, -0.36 %/min
Peak: 575.3 °C
Peak: 82.9 °C
Peak: 504.9 °C
Peak: 500.6 °C, -0.63 %/min
MTBP-34
TG
DSC
DTG
Temperature /°C

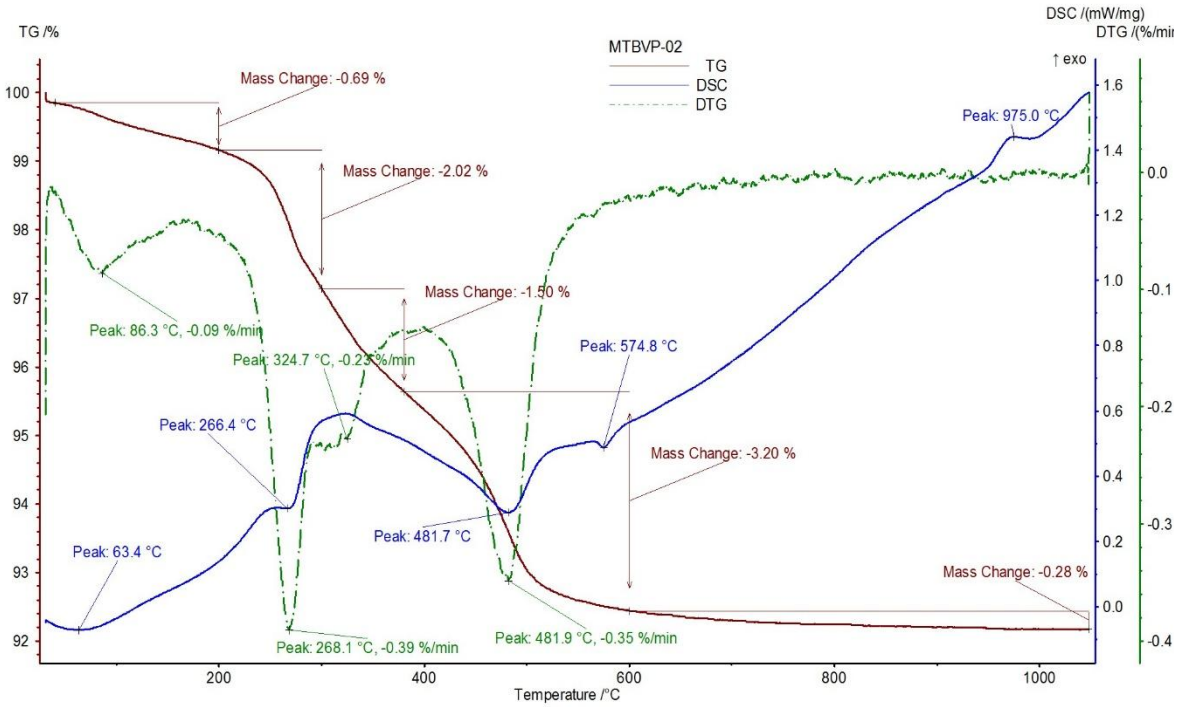

TG /%
DSC /(mW/mg)
DTG /(%/mir
↑ exo
Mass Change: -1.13 %
Mass Change: -5.08 %
Mass Change: -6.32 %
Mass Change: -0.52 %
Peak: 973.2 °C
Peak: 997.4 °C
Peak: 86.3 °C, -0.16 %/min
Peak: 302.9 °C, -0.41 %/min
Peak: 343.4 °C
Peak: 270.3 °C, -0.43 %/min
Peak: 266.0 °C
Peak: 310.8 °C
Peak: 573.6 °C
Peak: 495.8 °C
Peak: 73.5 °C
Peak: 496.6 °C, -0.74 %/min
MTBP-35
TG
DSC
DTG
Temperature /°C

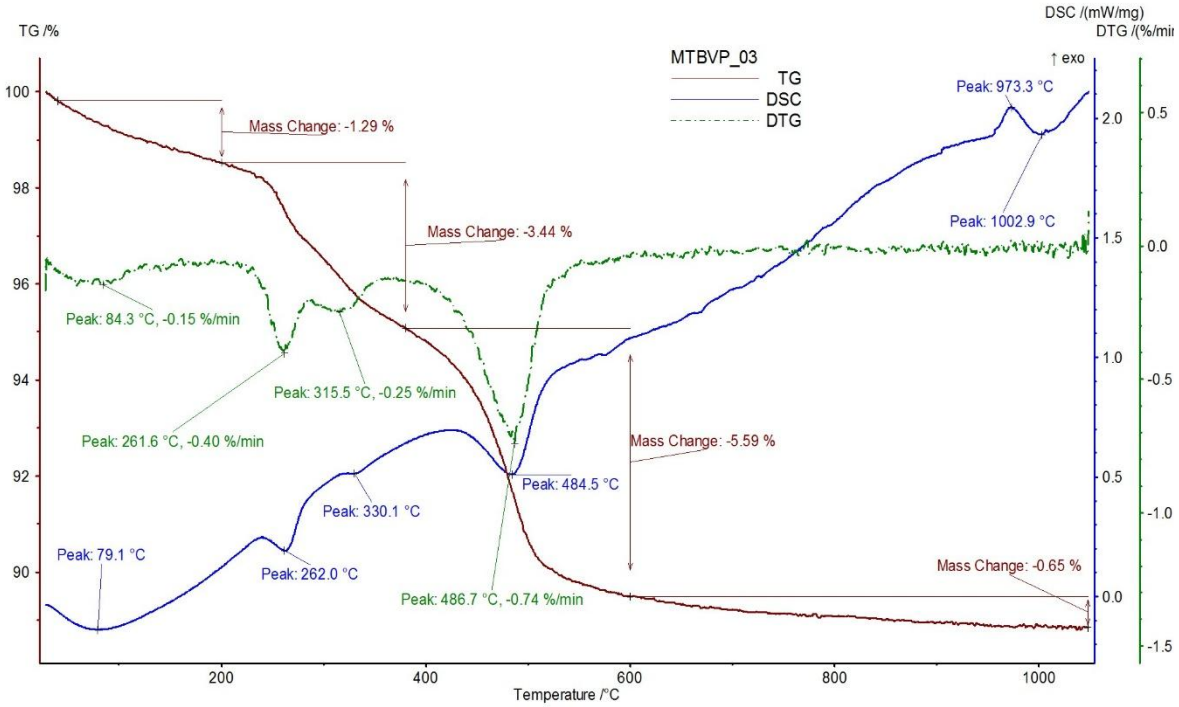

TG /%
DSC /(mW/mg)
DTG /(%/min)
↑ exo
Mass Change: -0.14 %
Mass Change: -1.43 %
Mass Change: -1.46 %
Peak: 1009.9 °C
Peak: 126.2 °C, -0.02 %/min
Peak: 476.7 °C, -0.15 %/min
Mass Change: -0.26 %
Peak: 262.2 °C, -0.10 %/min
Peak: 302.7 °C, -0.12 %/min
Peak: 319.7 °C
Peak: 576.0 °C
Peak: 69.8 °C
Peak: 257.0 °C
Peak: 480.5 °C
MTBP-36
TG
DSC
DTG
Temperature /°C

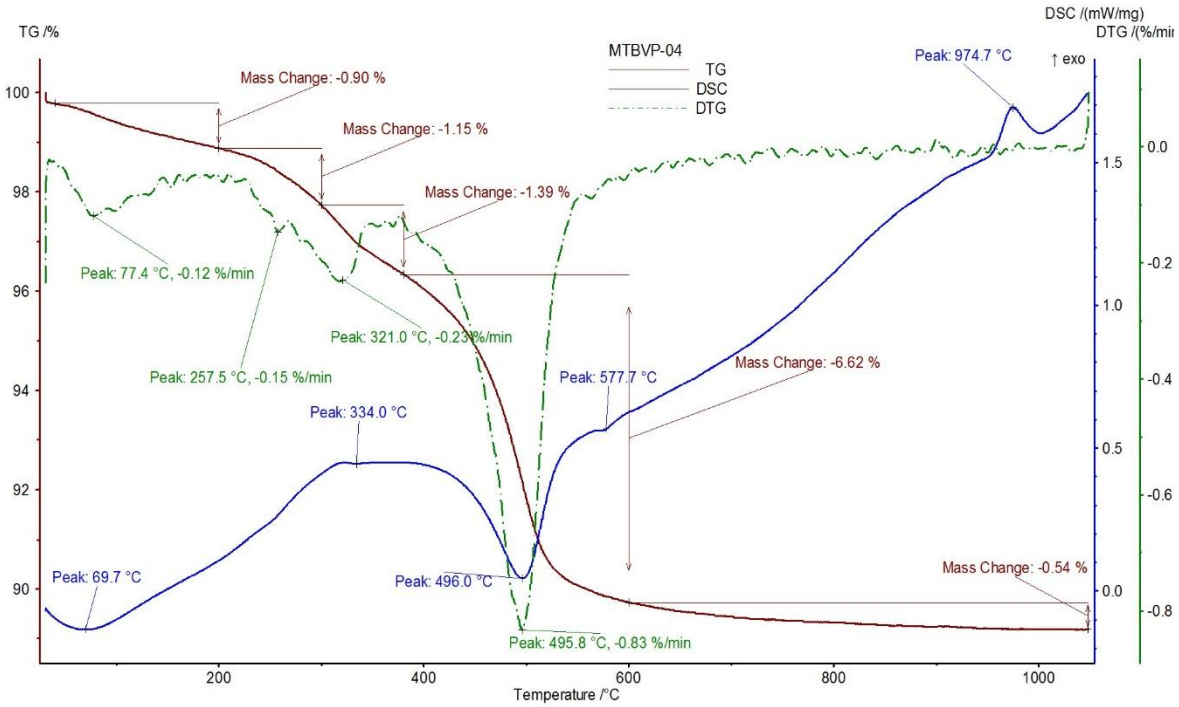

TG /%
DSC /(mW/mg)
DTG /(%/min)
MTBP-37
TG
DSC
DTG
↑ exo
Mass Change: -0.71 %
Mass Change: -3.39 %
Peak: 973.2 °C
Peak: 1007.3 °C
Peak: 389.2 °C, -0.13 %/min
Peak: 85.6 °C, -0.09 %/min
Peak: 312.1 °C
Peak: 378.2 °C
Peak: 268.0 °C
Mass Change: -3.62 %
Peak: 266.6 °C, -0.33 %/min
Peak: 358.5 °C
Peak: 574.8 °C
Mass Change: -0.74 %
Peak: 67.5 °C
Peak: 303.8 °C, -0.28 %/min
Peak: 489.1 °C
Peak: 491.6 °C, -0.39 %/min
Temperature /°C

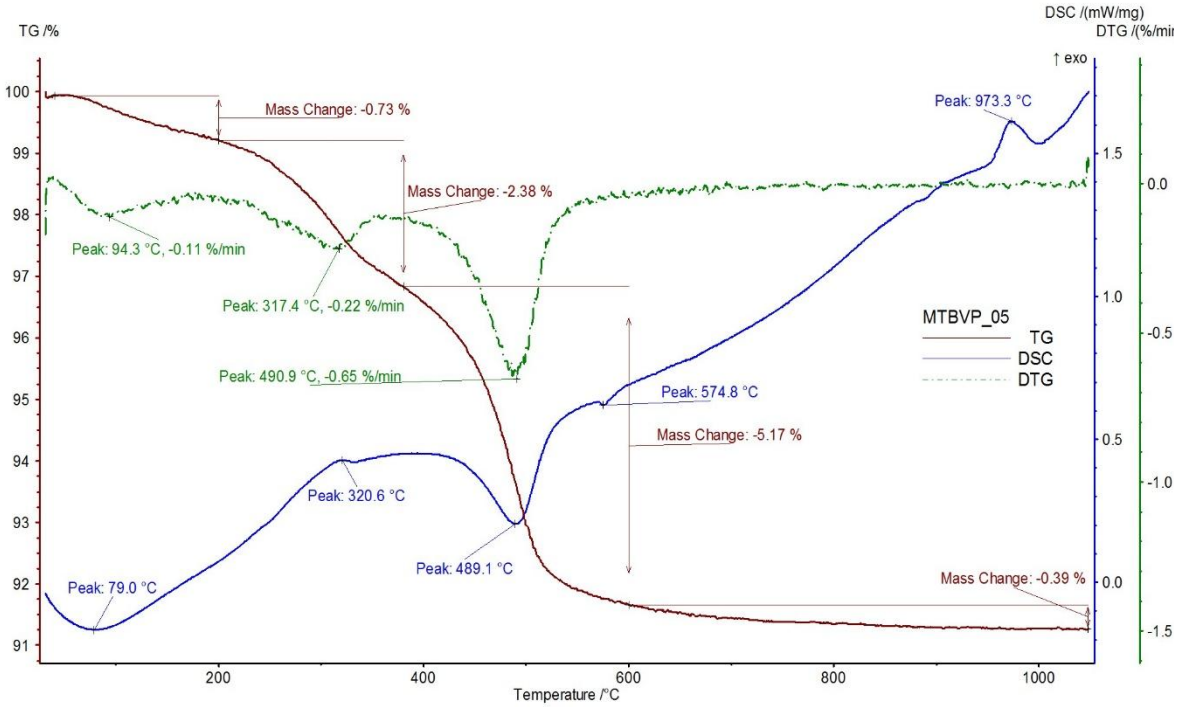

MTBP-38
TG
DSC
DTG
TG /%
DSC /(mW/mg)
DTG /(%/mi
↑ exo
Mass Change: -1.16 %
Peak: 309.7 °C
Mass Change: -4.85 %
Peak: 977.7 °C
Peak: 997.3 °C
Peak: 82.9 °C, -0.18 %/min
Peak: 268.8 °C, -0.40 %/min
Peak: 267.0 °C
Peak: 298.5 °C, -0.38 %/min
Mass Change: -6.00 %
Peak: 497.0 °C, -0.64 %/min
Peak: 576.5 °C
Mass Change: -0.76 %
Peak: 77.8 °C
Peak: 501.0 °C
Temperature /°C

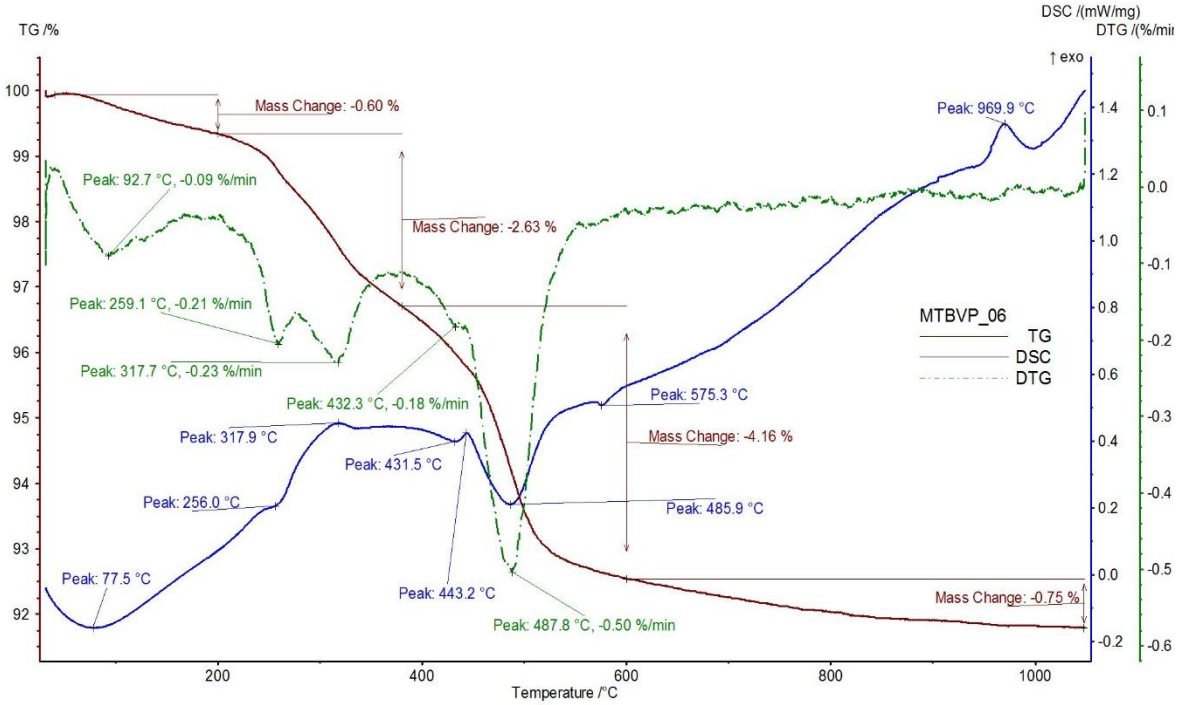

MTBVP-01
TG
DSC
DTG
TG /%
DSC /(mW/mg)
DTG /(%/mi
↑ exo
Mass Change: -0.80 %
Mass Change: -2.03 %
Peak: 972.6 °C
Mass Change: -1.31 %
Peak: 85.5 °C, -0.10 %/min
Peak: 574.9 °C
Peak: 328.8 °C, -0.22 %/min
Mass Change: -5.27 %
Peak: 338.7 °C
Peak: 270.0 °C, -0.43 %/min
Peak: 74.9 °C
Peak: 495.1 °C
Peak: 272.2 °C
Mass Change: -0.44 %
Peak: 493.1 °C, -0.68 %/min
Temperature /°C

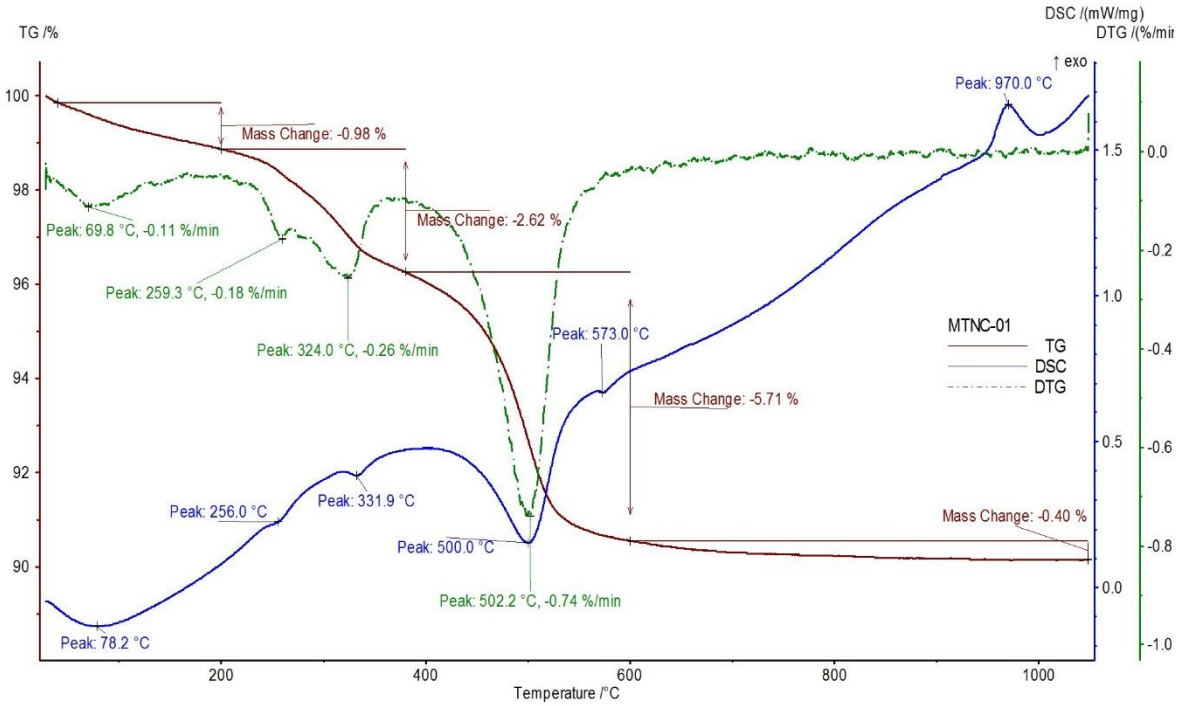

TG /%
DSC /(mW/mg)
DTG /(%/mi
MTBVP-02
TG
DSC
DTG
↑ exo
Mass Change: -0.69 %
Mass Change: -2.02 %
Mass Change: -1.50 %
Mass Change: -3.20 %
Mass Change: -0.28 %
Peak: 975.0 °C
Peak: 574.8 °C
Peak: 481.7 °C
Peak: 266.4 °C
Peak: 63.4 °C
Peak: 86.3 °C, -0.09 %/min
Peak: 324.7 °C, -0.23 %/min
Peak: 268.1 °C, -0.39 %/min
Peak: 481.9 °C, -0.35 %/min
Temperature /°C

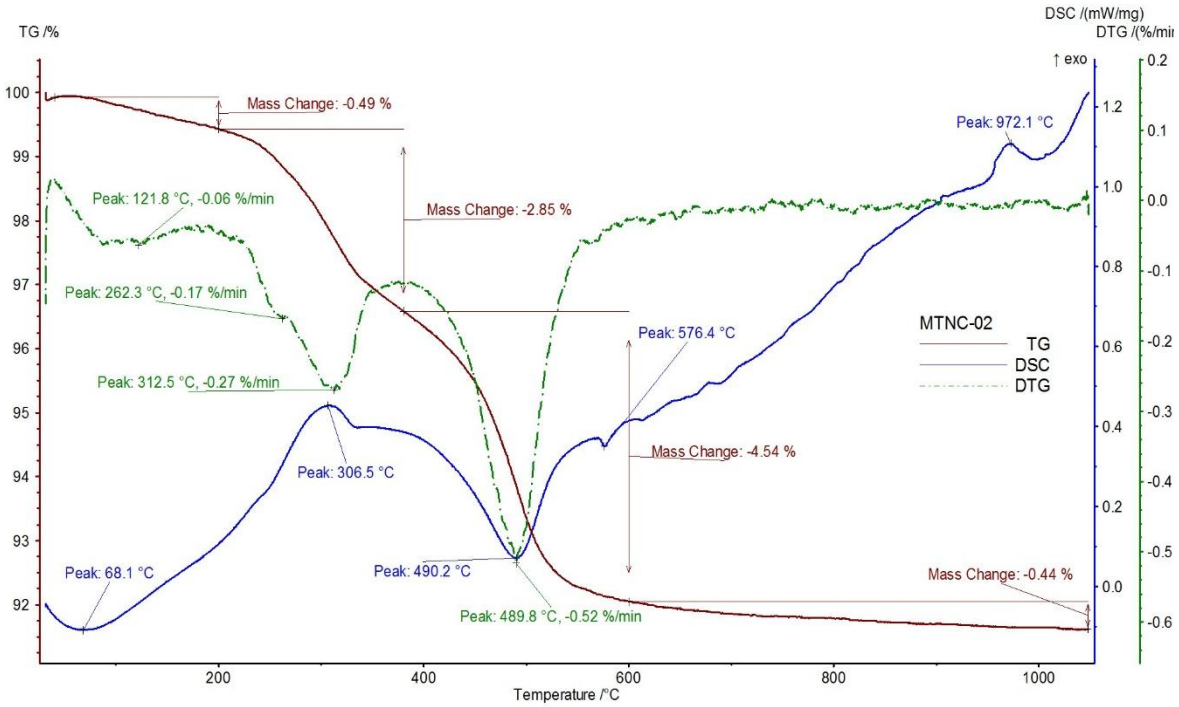

TG /%
DSC /(mW/mg)
DTG /(%/mi
MTBVP_03
TG
DSC
DTG
↑ exo
Mass Change: -1.29 %
Mass Change: -3.44 %
Mass Change: -5.59 %
Mass Change: -0.65 %
Peak: 973.3 °C
Peak: 1002.9 °C
Peak: 484.5 °C
Peak: 330.1 °C
Peak: 262.0 °C
Peak: 79.1 °C
Peak: 84.3 °C, -0.15 %/min
Peak: 315.5 °C, -0.25 %/min
Peak: 261.6 °C, -0.40 %/min
Peak: 486.7 °C, -0.74 %/min
Temperature /°C

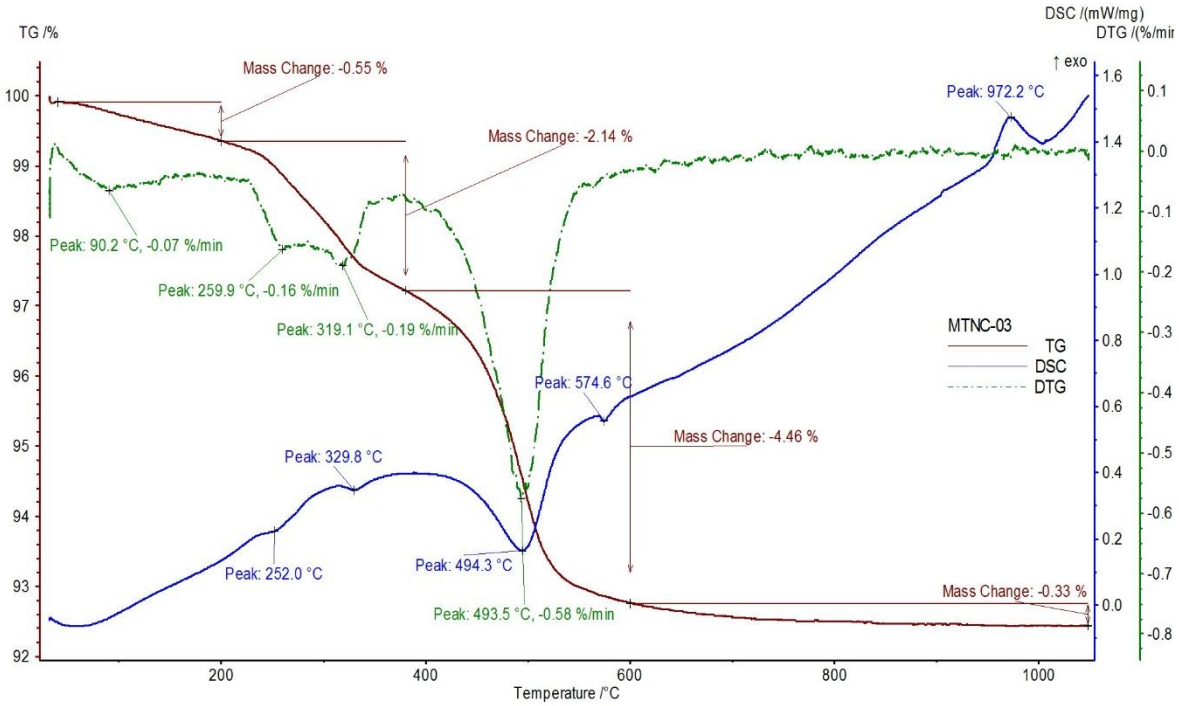

TG /%
DSC /(mW/mg)
DTG /(%/mi
MTBVP-04
TG
DSC
DTG
↑ exo
Mass Change: -0.90 %
Mass Change: -1.15 %
Mass Change: -1.39 %
Peak: 974.7 °C
Peak: 77.4 °C, -0.12 %/min
Peak: 321.0 °C, -0.23 %/min
Peak: 257.5 °C, -0.15 %/min
Peak: 577.7 °C
Mass Change: -6.62 %
Peak: 334.0 °C
Peak: 69.7 °C
Peak: 496.0 °C
Mass Change: -0.54 %
Peak: 495.8 °C, -0.83 %/min
Temperature /°C

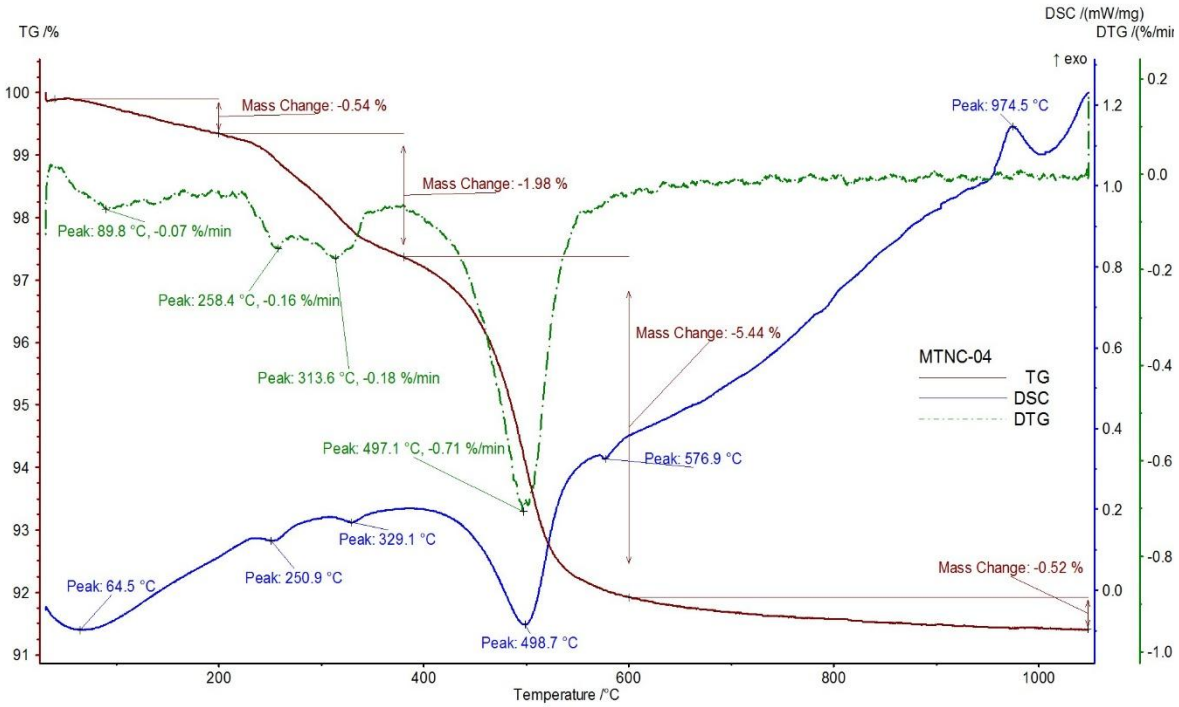

TG /%
DSC /(mW/mg)
DTG /(%/mi
↑ exo
Mass Change: -0.73 %
Peak: 973.3 °C
Mass Change: -2.38 %
Peak: 94.3 °C, -0.11 %/min
Peak: 317.4 °C, -0.22 %/min
MTBVP_05
TG
DSC
DTG
Peak: 490.9 °C, -0.65 %/min
Peak: 574.8 °C
Mass Change: -5.17 %
Peak: 320.6 °C
Peak: 489.1 °C
Peak: 79.0 °C
Mass Change: -0.39 %
Temperature /°C

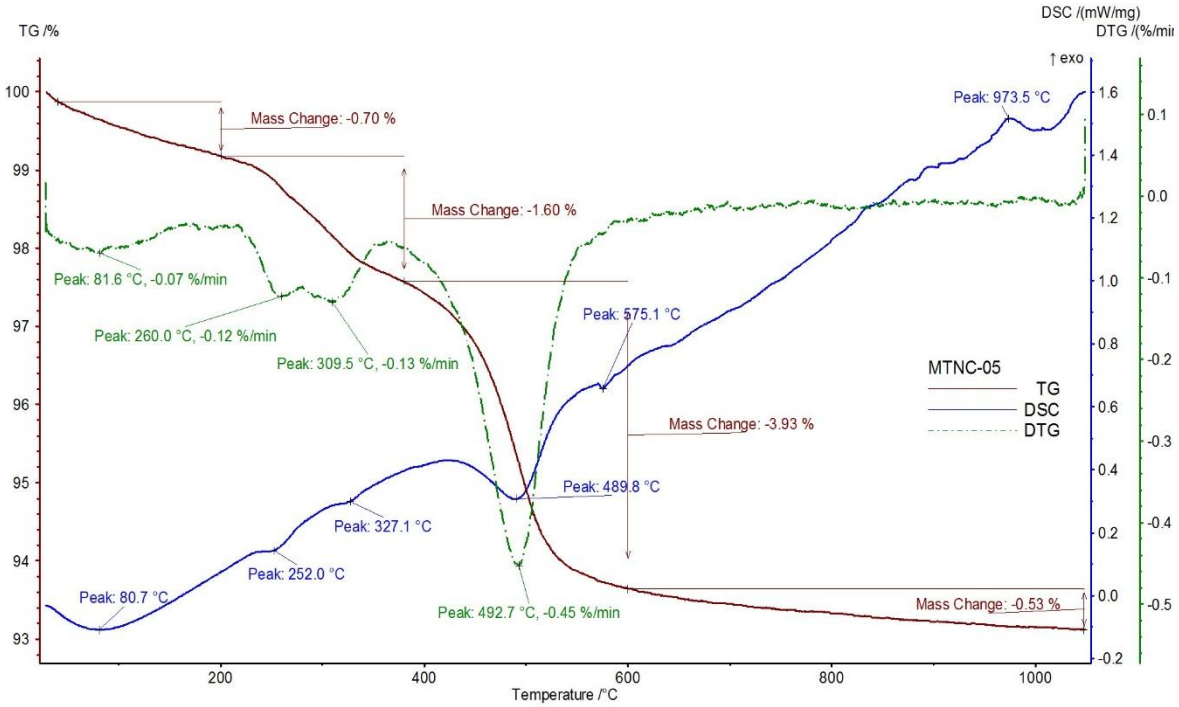

TG /%
DSC /(mW/mg)
DTG /(%/mi
↑ exo
Mass Change: -0.60 %
Peak: 92.7 °C, -0.09 %/min
Mass Change: -2.63 %
Peak: 259.1 °C, -0.21 %/min
Peak: 317.7 °C, -0.23 %/min
Peak: 432.3 °C, -0.18 %/min
Peak: 317.9 °C
Peak: 431.5 °C
Peak: 256.0 °C
Peak: 77.5 °C
Peak: 443.2 °C
Peak: 487.8 °C, -0.50 %/min
Peak: 969.9 °C
Peak: 575.3 °C
Mass Change: -4.16 %
Peak: 485.9 °C
Mass Change: -0.75 %
MTBVP_06
TG
DSC
DTG
Temperature /°C

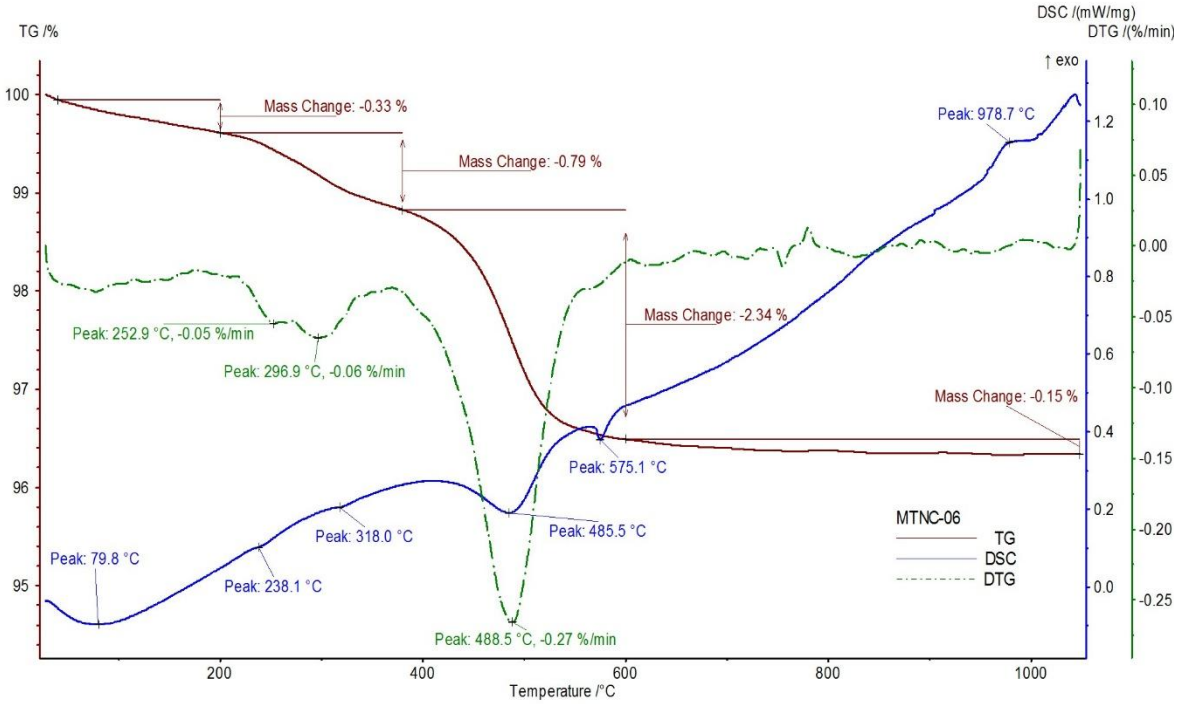

TG /%
DSC /(mW/mg)
DTG /(%/mi
↑ exo
Peak: 970.0 °C
Mass Change: -0.98 %
Peak: 69.8 °C, -0.11 %/min
Mass Change: -2.62 %
Peak: 259.3 °C, -0.18 %/min
Peak: 324.0 °C, -0.26 %/min
Peak: 573.0 °C
Mass Change: -5.71 %
Peak: 256.0 °C
Peak: 331.9 °C
Peak: 500.0 °C
Peak: 502.2 °C, -0.74 %/min
Peak: 78.2 °C
Mass Change: -0.40 %
MTNC-01
TG
DSC
DTG
Temperature /°C

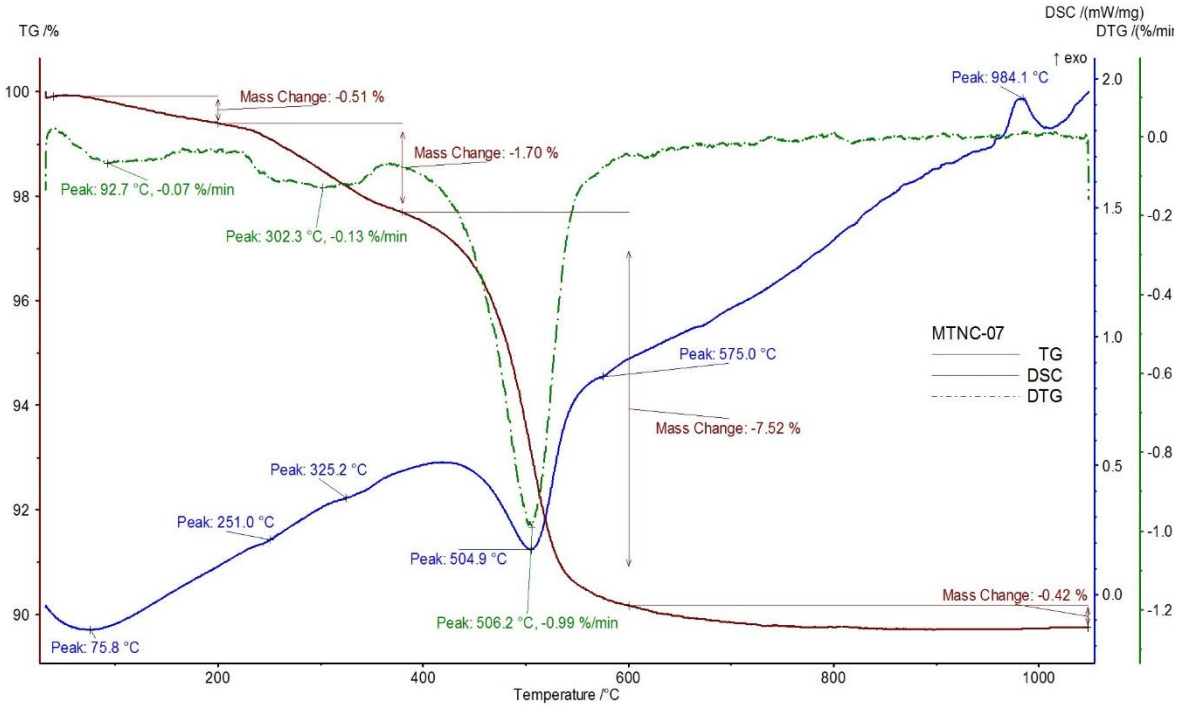

TG /%
DSC /(mW/mg)
DTG /(%/mi
↑ exo
Mass Change: -0.49 %
Peak: 121.8 °C, -0.06 %/min
Peak: 262.3 °C, -0.17 %/min
Peak: 312.5 °C, -0.27 %/min
Peak: 306.5 °C
Peak: 68.1 °C
Mass Change: -2.85 %
Peak: 490.2 °C
Peak: 489.8 °C, -0.52 %/min
Peak: 576.4 °C
Mass Change: -4.54 %
Peak: 972.1 °C
Mass Change: -0.44 %
MTNC-02
TG
DSC
DTG
Temperature /°C

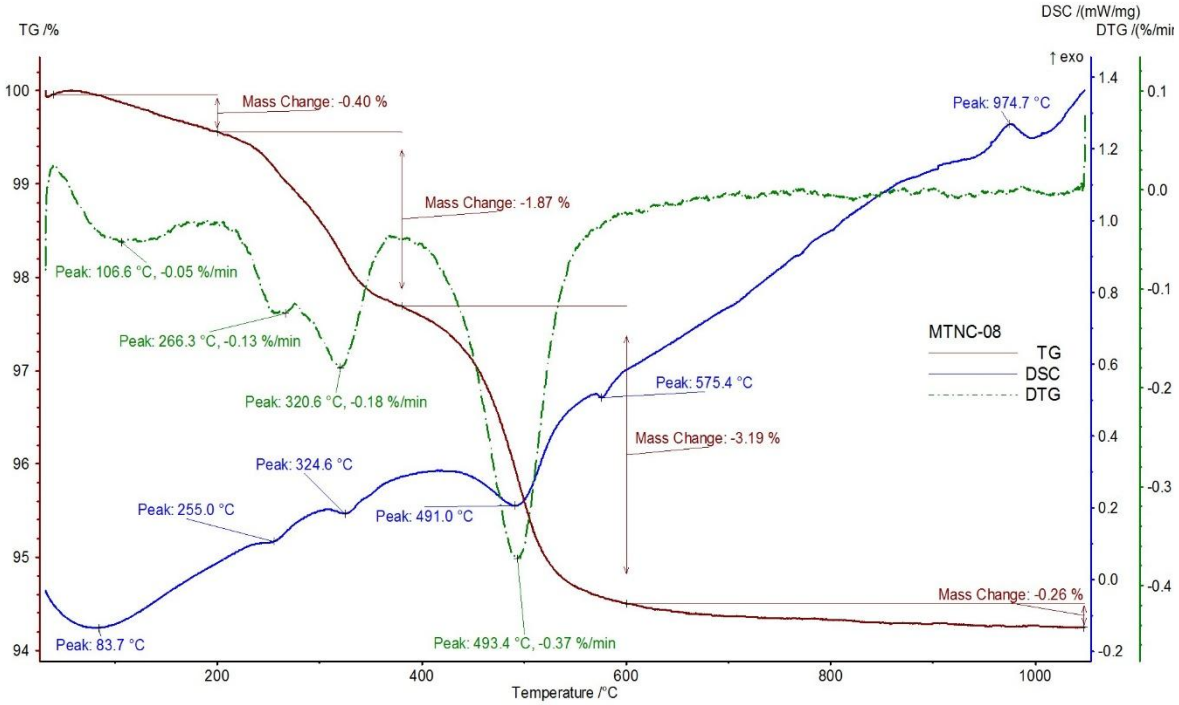

TG /%
DSC /(mW/mg)
DTG /(%/mi
↑ exo
Mass Change: -0.55 %
Peak: 90.2 °C, -0.07 %/min
Peak: 259.9 °C, -0.16 %/min
Peak: 319.1 °C, -0.19 %/min
Peak: 329.8 °C
Peak: 252.0 °C
Mass Change: -2.14 %
Peak: 494.3 °C
Peak: 493.5 °C, -0.58 %/min
Peak: 574.6 °C
Mass Change: -4.46 %
Peak: 972.2 °C
Mass Change: -0.33 %
MTNC-03
TG
DSC
DTG
Temperature /°C

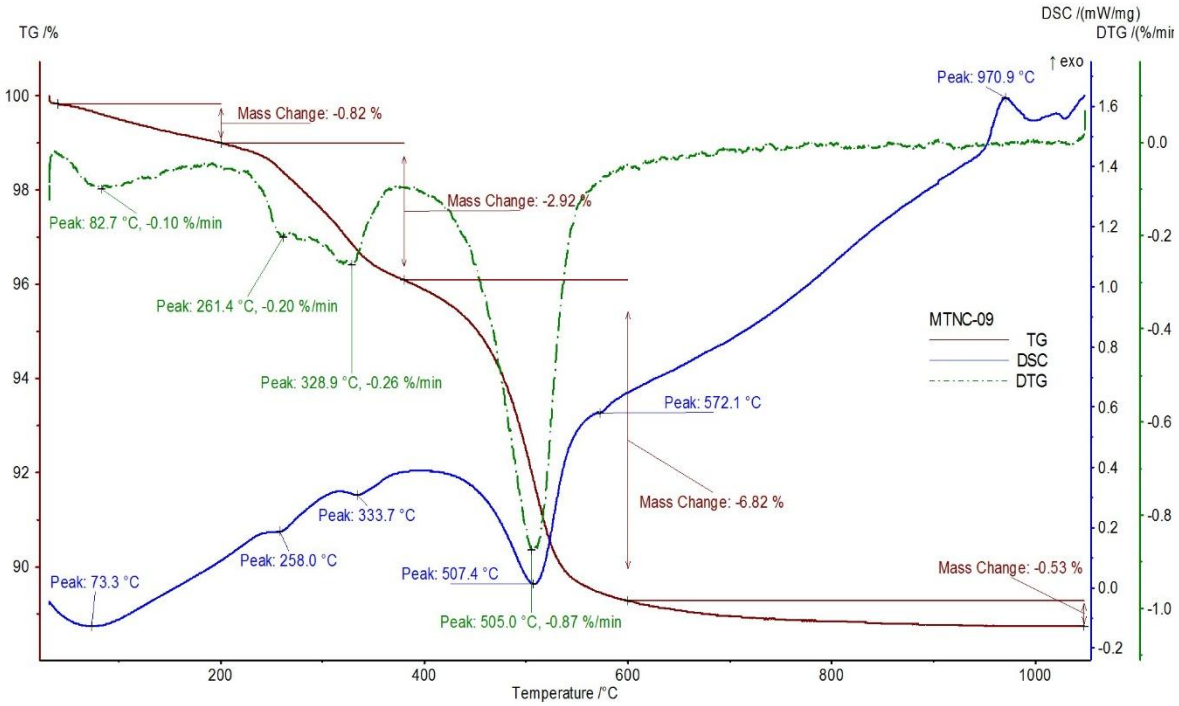

TG /%
DSC /(mW/mg)
DTG /(%/mi
↑ exo
Mass Change: -0.54 %
Mass Change: -1.98 %
Mass Change: -5.44 %
Mass Change: -0.52 %
Peak: 974.5 °C
Peak: 89.8 °C, -0.07 %/min
Peak: 258.4 °C, -0.16 %/min
Peak: 313.6 °C, -0.18 %/min
Peak: 497.1 °C, -0.71 %/min
Peak: 576.9 °C
Peak: 329.1 °C
Peak: 64.5 °C
Peak: 250.9 °C
Peak: 498.7 °C
MTNC-04
TG
DSC
DTG
Temperature /°C

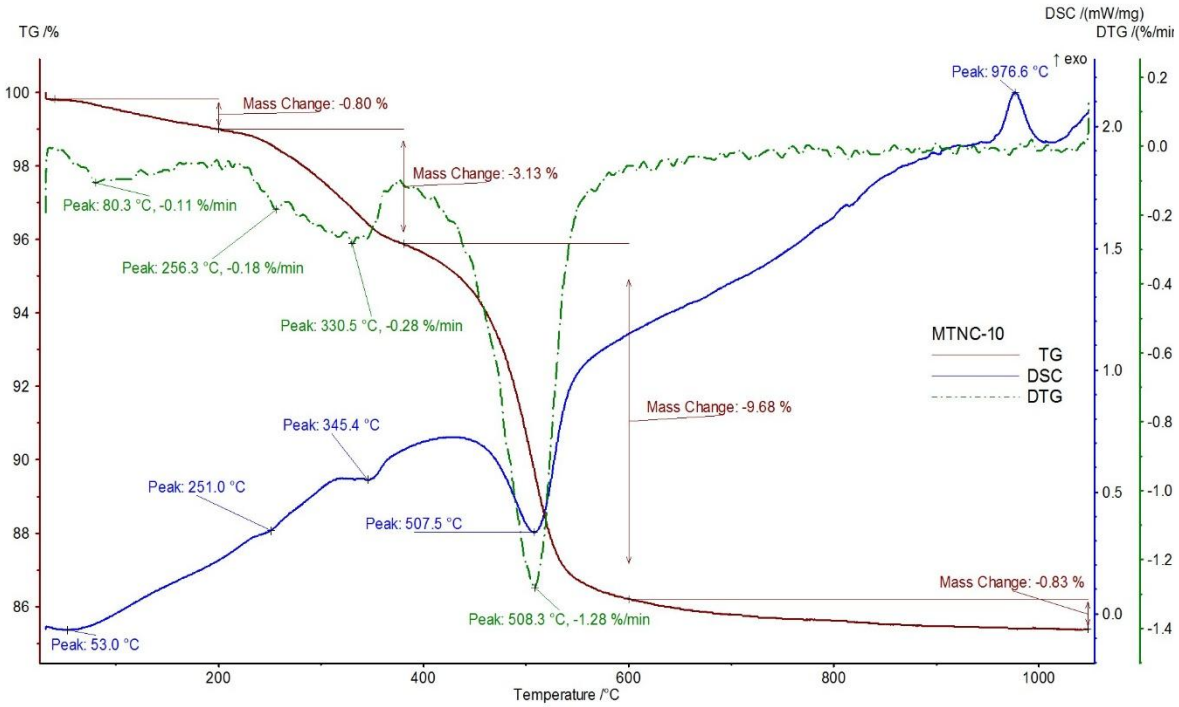

TG /%
DSC /(mW/mg)
DTG /(%/mi
↑ exo
Mass Change: -0.70 %
Mass Change: -1.60 %
Mass Change: -3.93 %
Mass Change: -0.53 %
Peak: 973.5 °C
Peak: 81.6 °C, -0.07 %/min
Peak: 260.0 °C, -0.12 %/min
Peak: 309.5 °C, -0.13 %/min
Peak: 575.1 °C
Peak: 489.8 °C
Peak: 327.1 °C
Peak: 252.0 °C
Peak: 80.7 °C
Peak: 492.7 °C, -0.45 %/min
MTNC-05
TG
DSC
DTG
Temperature /°C

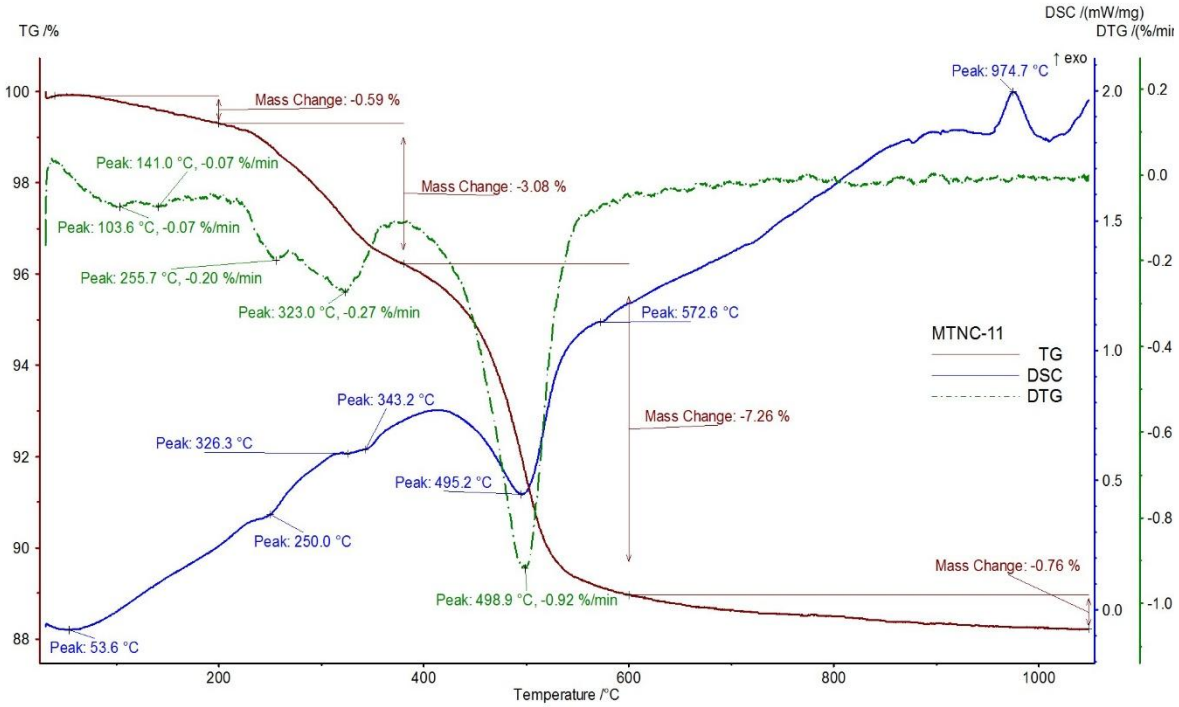

TG /%
DSC /(mW/mg)
DTG /(%/min)
↑ exo
Mass Change: -0.33 %
Mass Change: -0.79 %
Mass Change: -2.34 %
Mass Change: -0.15 %
Peak: 978.7 °C
Peak: 252.9 °C, -0.05 %/min
Peak: 296.9 °C, -0.06 %/min
Peak: 575.1 °C
Peak: 485.5 °C
Peak: 318.0 °C
Peak: 79.8 °C
Peak: 238.1 °C
Peak: 488.5 °C, -0.27 %/min
MTNC-06
TG
DSC
DTG
Temperature /°C

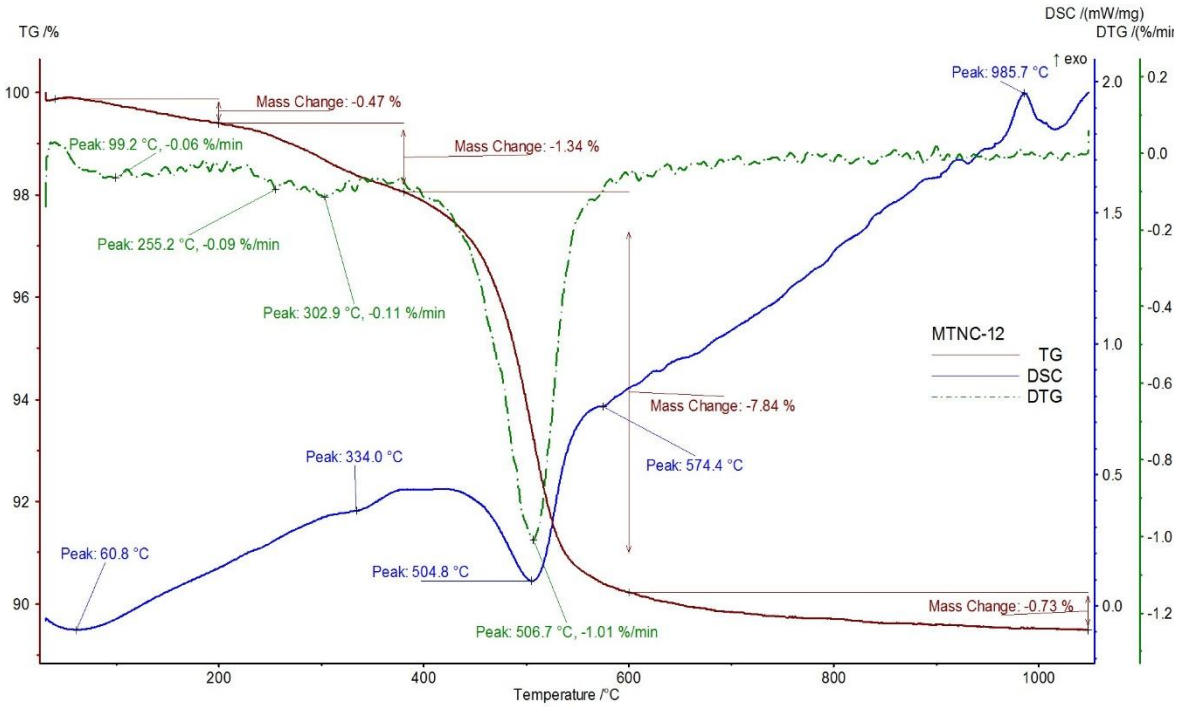

TG /%
DSC /(mW/mg)
DTG /(%/mi
↑ exo
Mass Change: -0.51 %
Mass Change: -1.70 %
Mass Change: -7.52 %
Mass Change: -0.42 %
Peak: 984.1 °C
Peak: 92.7 °C, -0.07 %/min
Peak: 302.3 °C, -0.13 %/min
Peak: 575.0 °C
Peak: 325.2 °C
Peak: 251.0 °C
Peak: 504.9 °C
Peak: 506.2 °C, -0.99 %/min
Peak: 75.8 °C
MTNC-07
TG
DSC
DTG
Temperature /°C

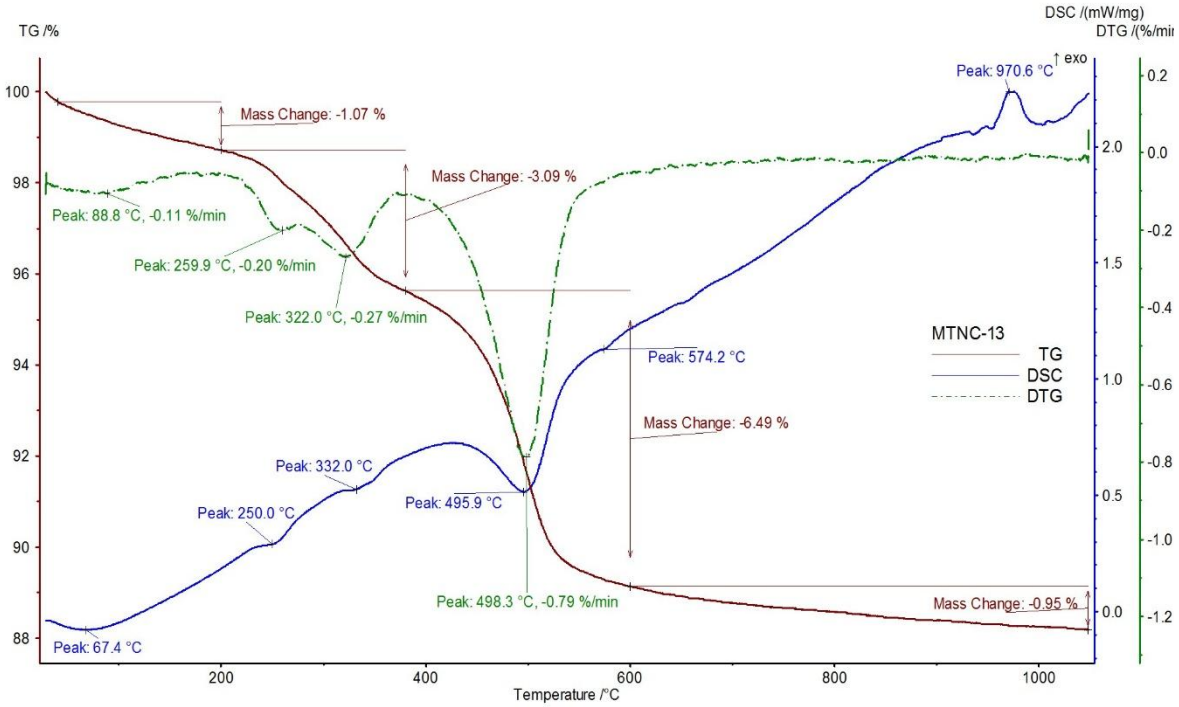

TG /%
DSC /(mW/mg)
DTG /(%/mi
↑ exo
Mass Change: -0.40 %
Mass Change: -1.87 %
Peak: 974.7 °C
Peak: 106.6 °C, -0.05 %/min
Peak: 266.3 °C, -0.13 %/min
Peak: 320.6 °C, -0.18 %/min
Peak: 575.4 °C
Mass Change: -3.19 %
Peak: 324.6 °C
Peak: 255.0 °C
Peak: 491.0 °C
Mass Change: -0.26 %
Peak: 83.7 °C
Peak: 493.4 °C, -0.37 %/min
MTNC-08
TG
DSC
DTG
Temperature /°C

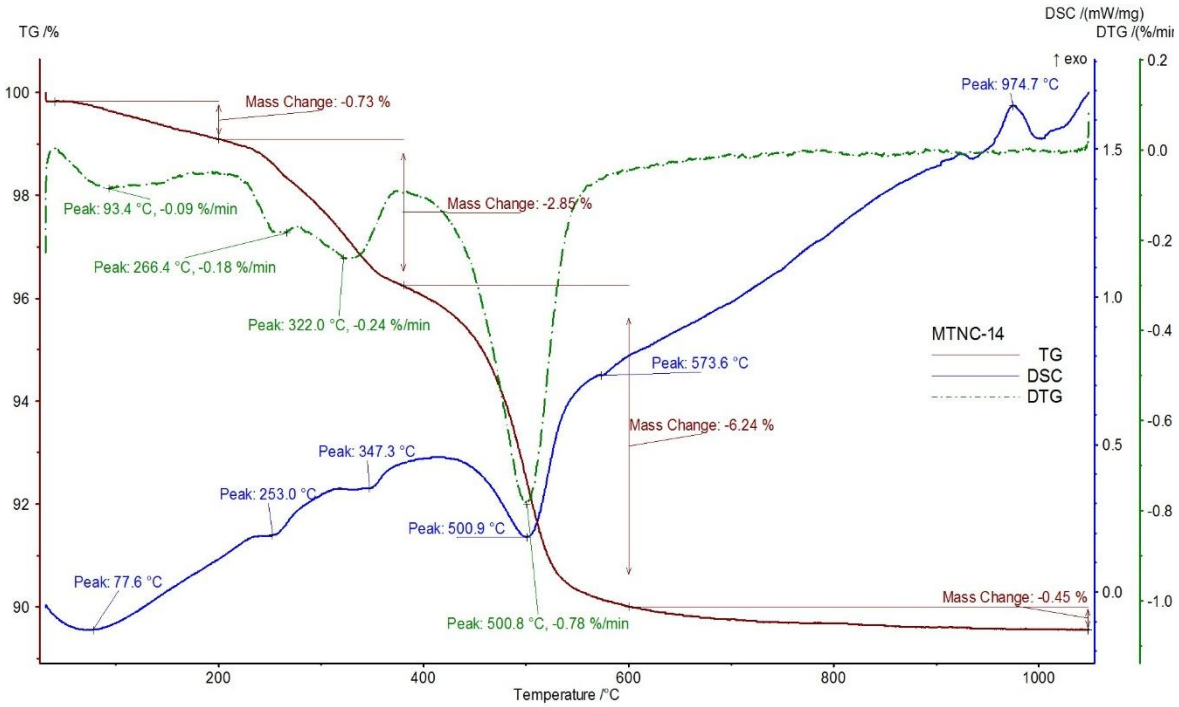

TG /%
DSC /(mW/mg)
DTG /(%/mi
↑ exo
Peak: 970.9 °C
Mass Change: -0.82 %
Mass Change: -2.92 %
Peak: 82.7 °C, -0.10 %/min
Peak: 261.4 °C, -0.20 %/min
Peak: 328.9 °C, -0.26 %/min
Peak: 572.1 °C
Mass Change: -6.82 %
Peak: 333.7 °C
Peak: 258.0 °C
Peak: 507.4 °C
Peak: 73.3 °C
Mass Change: -0.53 %
Peak: 505.0 °C, -0.87 %/min
MTNC-09
TG
DSC
DTG
Temperature /°C

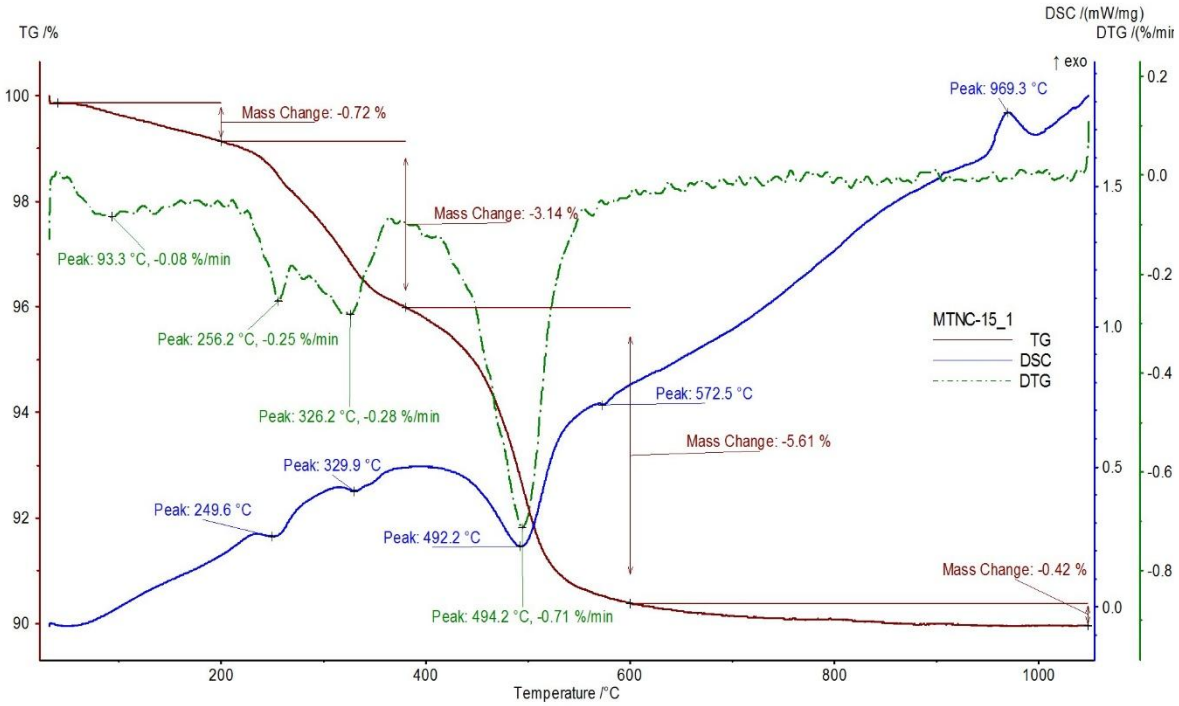

TG /%
DSC /(mW/mg)
DTG /(%/mi
↑ exo
Peak: 976.6 °C
Mass Change: -0.80 %
Mass Change: -3.13 %
Peak: 80.3 °C, -0.11 %/min
Peak: 256.3 °C, -0.18 %/min
Peak: 330.5 °C, -0.28 %/min
MTNC-10
TG
DSC
DTG
Mass Change: -9.68 %
Peak: 345.4 °C
Peak: 251.0 °C
Peak: 507.5 °C
Mass Change: -0.83 %
Peak: 508.3 °C, -1.28 %/min
Peak: 53.0 °C
Temperature /°C

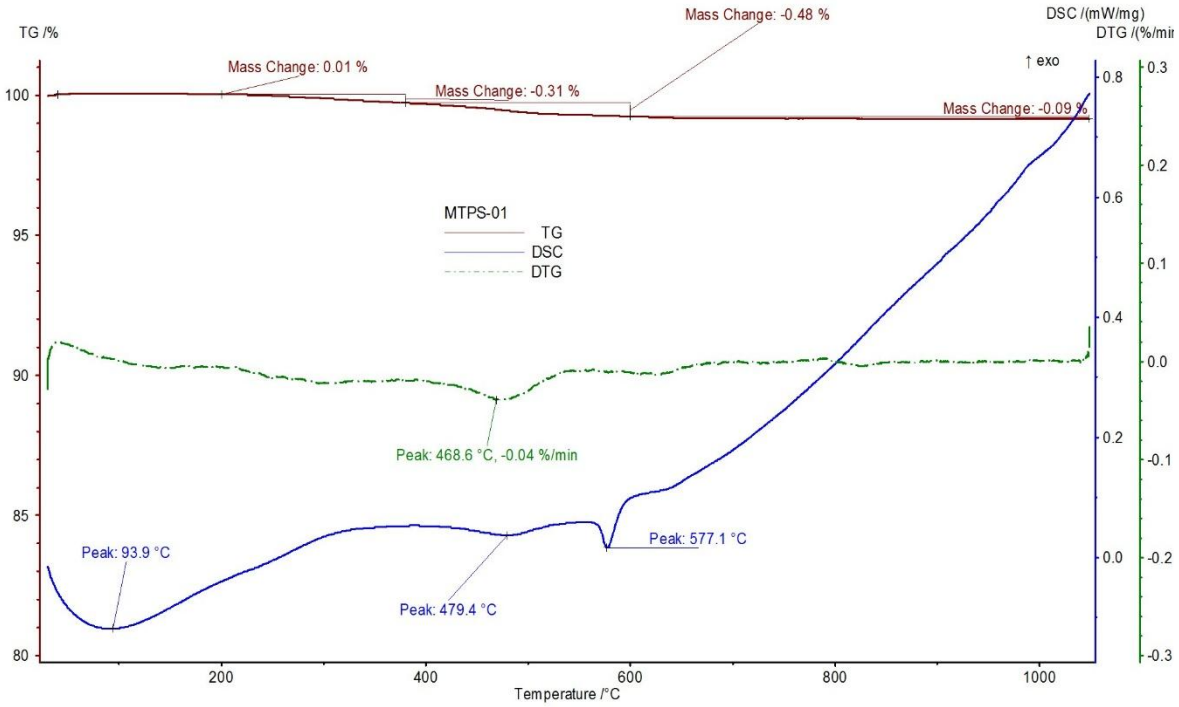

TG /%
DSC /(mW/mg)
DTG /(%/mi
↑ exo
Peak: 974.7 °C
Mass Change: -0.59 %
Peak: 141.0 °C, -0.07 %/min
Mass Change: -3.08 %
Peak: 103.6 °C, -0.07 %/min
Peak: 255.7 °C, -0.20 %/min
Peak: 323.0 °C, -0.27 %/min
Peak: 572.6 °C
MTNC-11
TG
DSC
DTG
Peak: 343.2 °C
Mass Change: -7.26 %
Peak: 326.3 °C
Peak: 495.2 °C
Peak: 250.0 °C
Mass Change: -0.76 %
Peak: 498.9 °C, -0.92 %/min
Peak: 53.6 °C
Temperature /°C

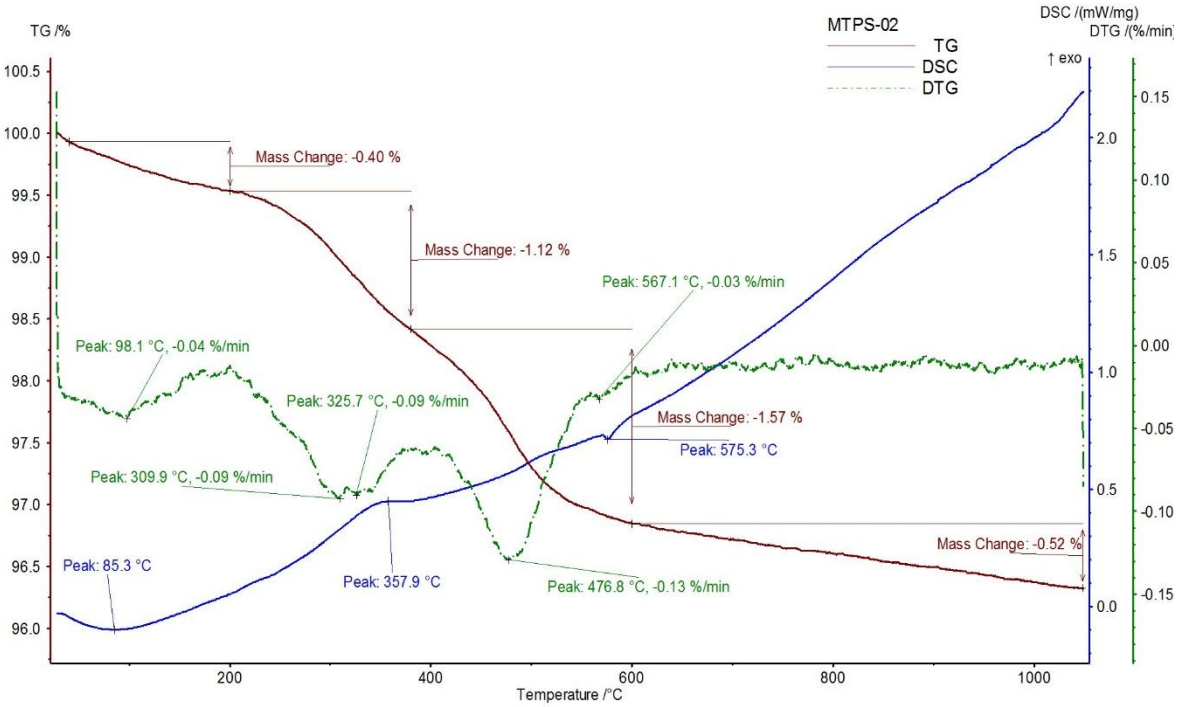

TG /%
DSC /(mW/mg)
DTG /(%/mi
↑ exo
Peak: 985.7 °C
Mass Change: -0.47 %
Peak: 99.2 °C, -0.06 %/min
Mass Change: -1.34 %
Peak: 255.2 °C, -0.09 %/min
Peak: 302.9 °C, -0.11 %/min
MTNC-12
TG
DSC
DTG
Mass Change: -7.84 %
Peak: 574.4 °C
Peak: 334.0 °C
Peak: 60.8 °C
Peak: 504.8 °C
Mass Change: -0.73 %
Peak: 506.7 °C, -1.01 %/min
Temperature /°C

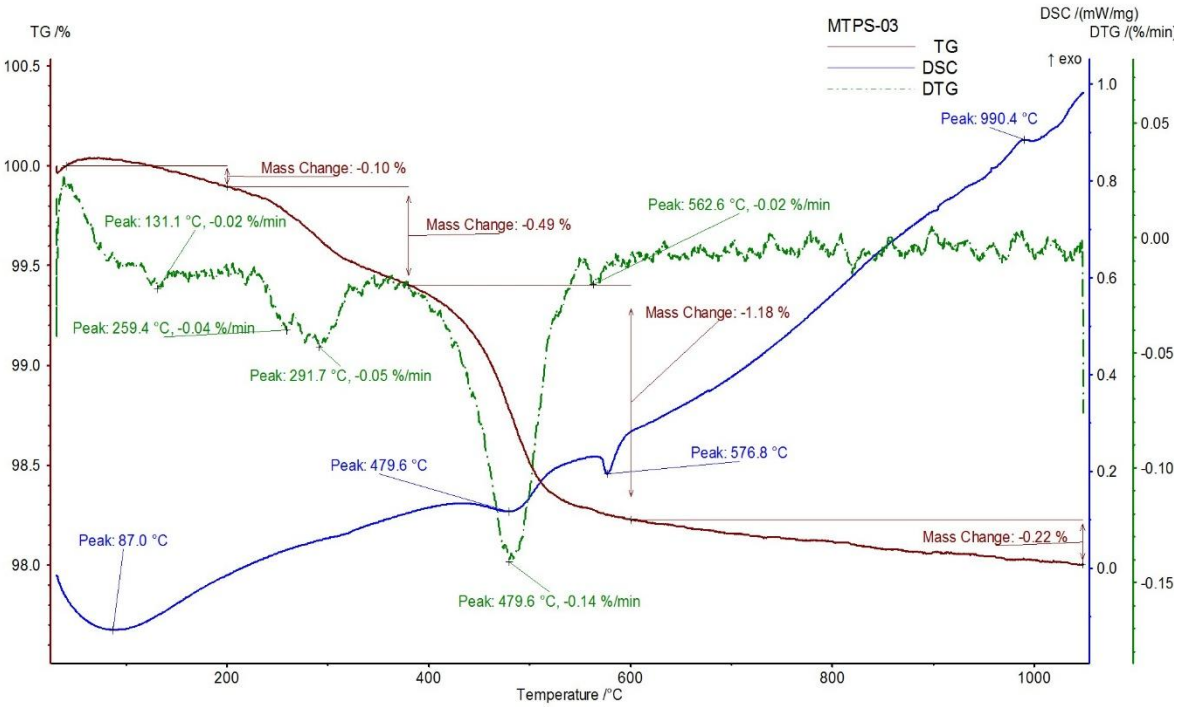

TG /%
DSC /(mW/mg)
DTG /(%/mi
↑ exo
Peak: 970.6 °C
Mass Change: -1.07 %
Mass Change: -3.09 %
Peak: 88.8 °C, -0.11 %/min
Peak: 259.9 °C, -0.20 %/min
Peak: 322.0 °C, -0.27 %/min
MTNC-13
TG
DSC
DTG
Peak: 574.2 °C
Mass Change: -6.49 %
Peak: 332.0 °C
Peak: 250.0 °C
Peak: 495.9 °C
Peak: 498.3 °C, -0.79 %/min
Mass Change: -0.95 %
Peak: 67.4 °C
Temperature /°C

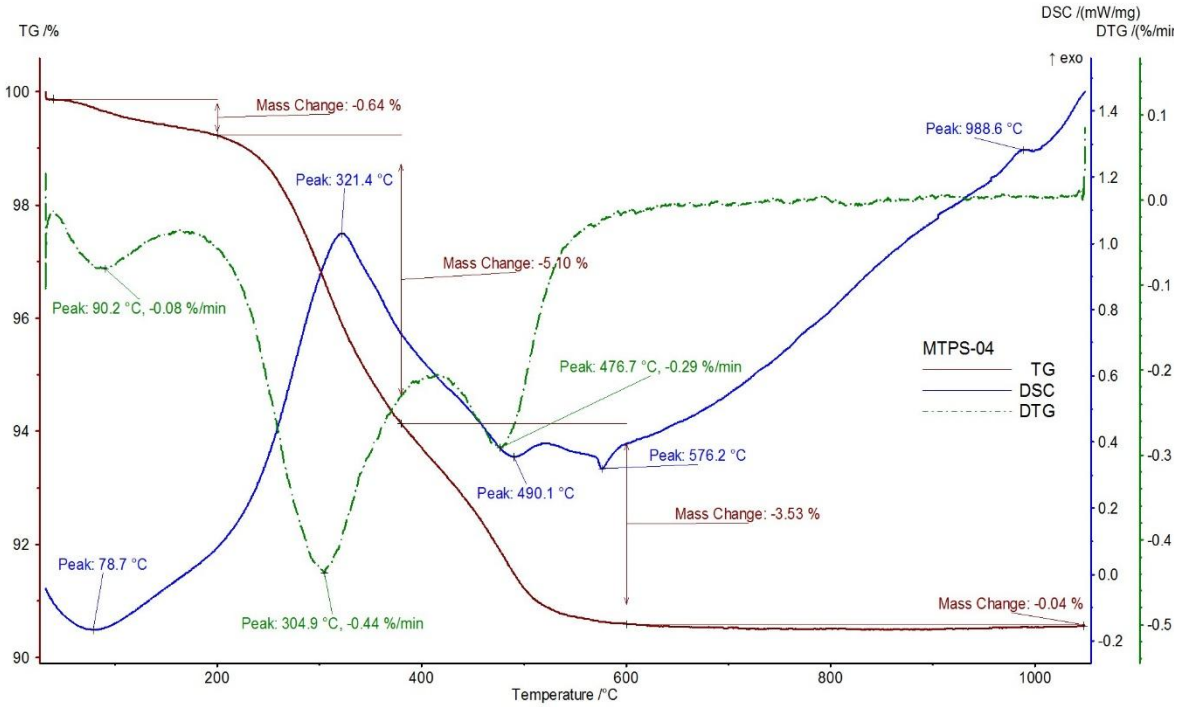

TG /%
DSC /(mW/mg)
DTG /(%/mi
↑ exo
Mass Change: -0.73 %
Peak: 974.7 °C
Peak: 93.4 °C, -0.09 %/min
Mass Change: -2.85 %
Peak: 266.4 °C, -0.18 %/min
Peak: 322.0 °C, -0.24 %/min
MTNC-14
TG
DSC
DTG
Peak: 573.6 °C
Mass Change: -6.24 %
Peak: 347.3 °C
Peak: 253.0 °C
Peak: 500.9 °C
Peak: 77.6 °C
Mass Change: -0.45 %
Peak: 500.8 °C, -0.78 %/min
Temperature /°C

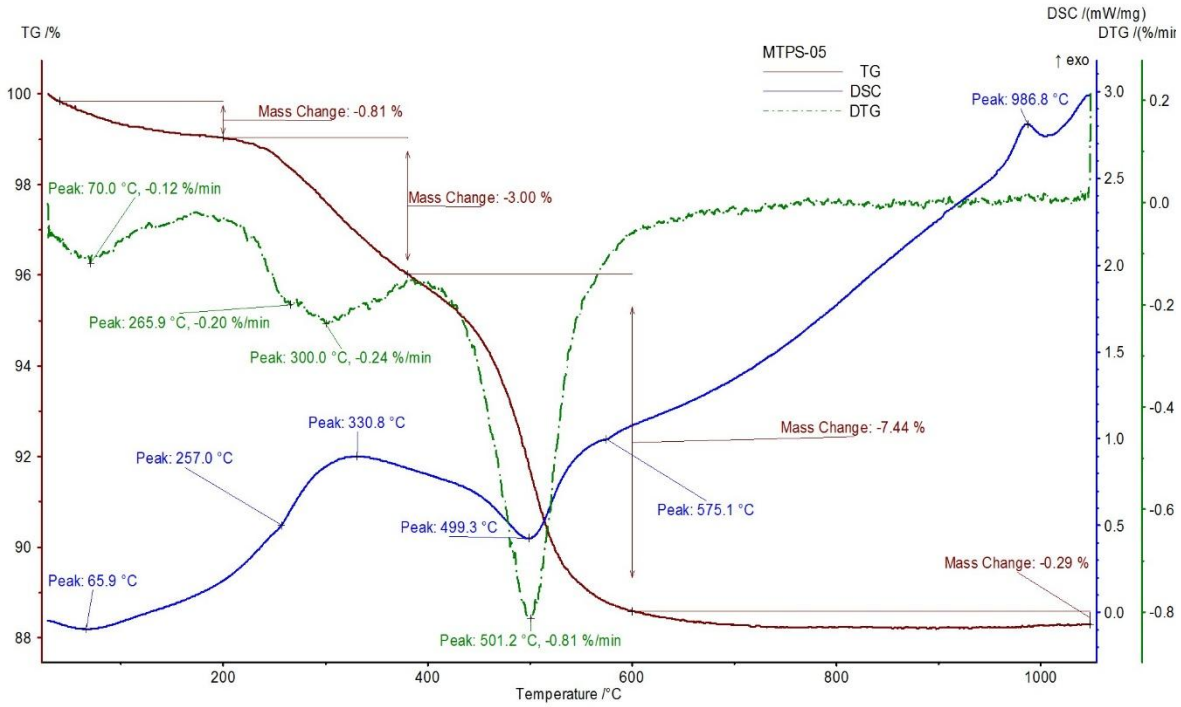

TG /%
DSC /(mW/mg)
DTG /(%/mi
↑ exo
Mass Change: -0.72 %
Peak: 969.3 °C
Mass Change: -3.14 %
Peak: 93.3 °C, -0.08 %/min
Peak: 256.2 °C, -0.25 %/min
MTNC-15_1
TG
DSC
DTG
Peak: 572.5 °C
Peak: 326.2 °C, -0.28 %/min
Mass Change: -5.61 %
Peak: 329.9 °C
Peak: 249.6 °C
Peak: 492.2 °C
Mass Change: -0.42 %
Peak: 494.2 °C, -0.71 %/min
Temperature /°C

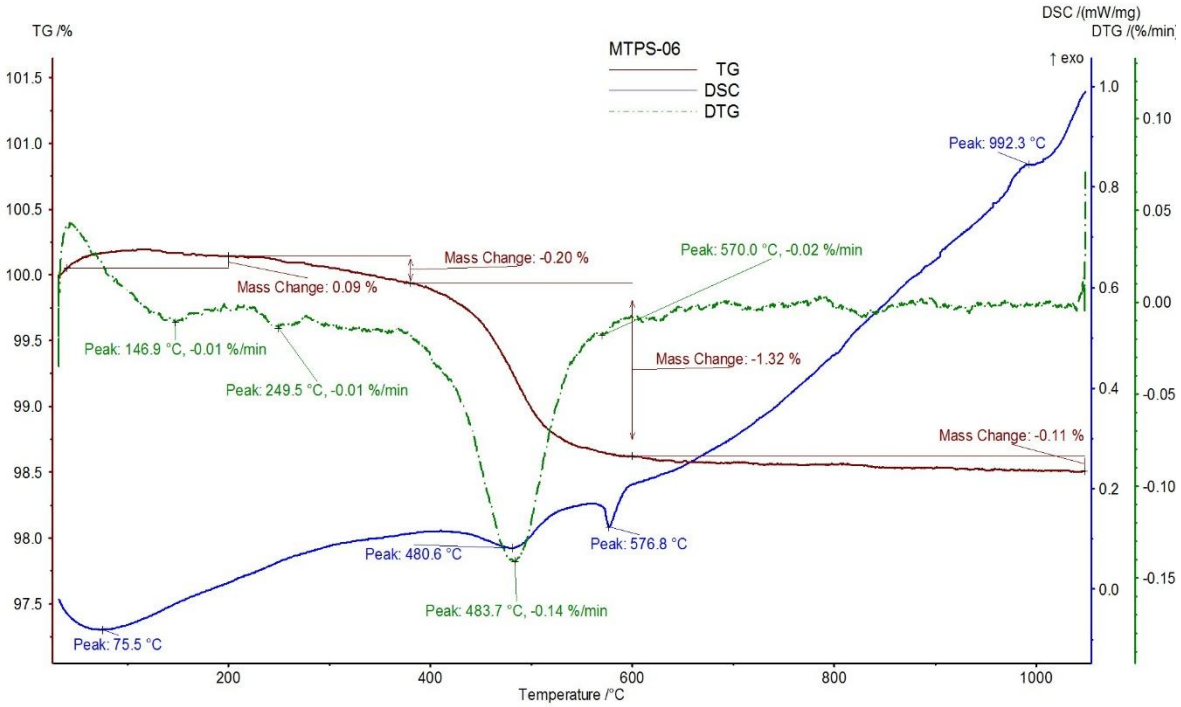

TG /%
DSC /(mW/mg)
DTG /(%/mi
↑ exo
Mass Change: 0.01 %
Mass Change: -0.31 %
Mass Change: -0.48 %
Mass Change: -0.09 %
MTPS-01
TG
DSC
DTG
Peak: 468.6 °C, -0.04 %/min
Peak: 93.9 °C
Peak: 479.4 °C
Peak: 577.1 °C
Temperature /°C

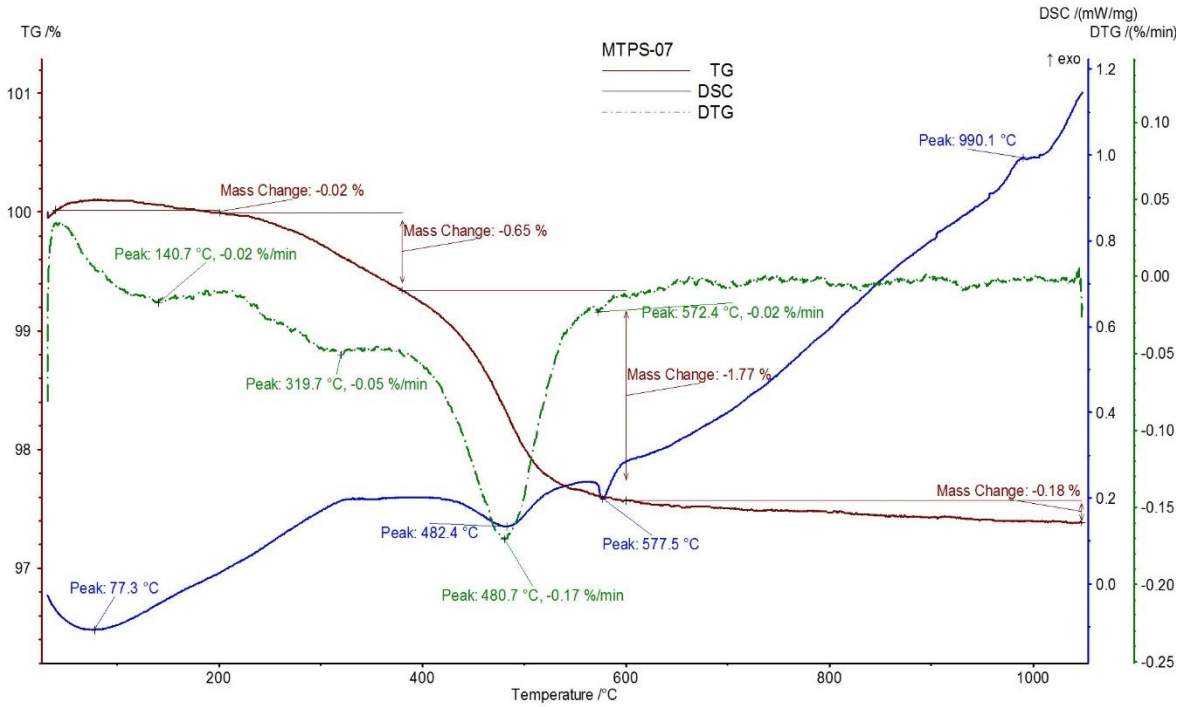

TG /%
DSC /(mW/mg)
DTG /(%/min
MTPS-02
TG
DSC
DTG
↑ exo
Mass Change: -0.40 %
Mass Change: -1.12 %
Mass Change: -1.57 %
Mass Change: -0.52 %
Peak: 98.1 °C, -0.04 %/min
Peak: 325.7 °C, -0.09 %/min
Peak: 309.9 °C, -0.09 %/min
Peak: 567.1 °C, -0.03 %/min
Peak: 575.3 °C
Peak: 85.3 °C
Peak: 357.9 °C
Peak: 476.8 °C, -0.13 %/min
Temperature /°C

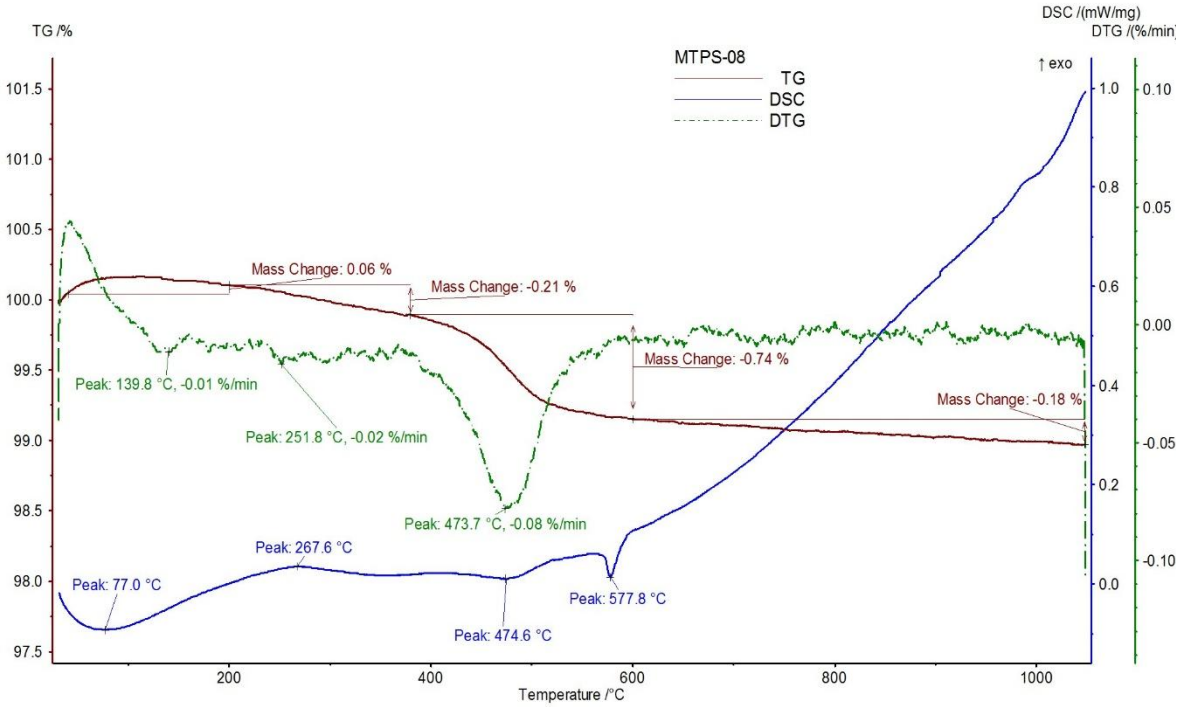

MTPS-03
TG
DSC
DTG
TG /%
DSC /(mW/mg)
DTG /(%/min)
↑ exo
Mass Change: -0.10 %
Mass Change: -0.49 %
Mass Change: -1.18 %
Mass Change: -0.22 %
Peak: 131.1 °C, -0.02 %/min
Peak: 259.4 °C, -0.04 %/min
Peak: 291.7 °C, -0.05 %/min
Peak: 562.6 °C, -0.02 %/min
Peak: 479.6 °C, -0.14 %/min
Peak: 990.4 °C
Peak: 576.8 °C
Peak: 479.6 °C
Peak: 87.0 °C
Temperature /°C

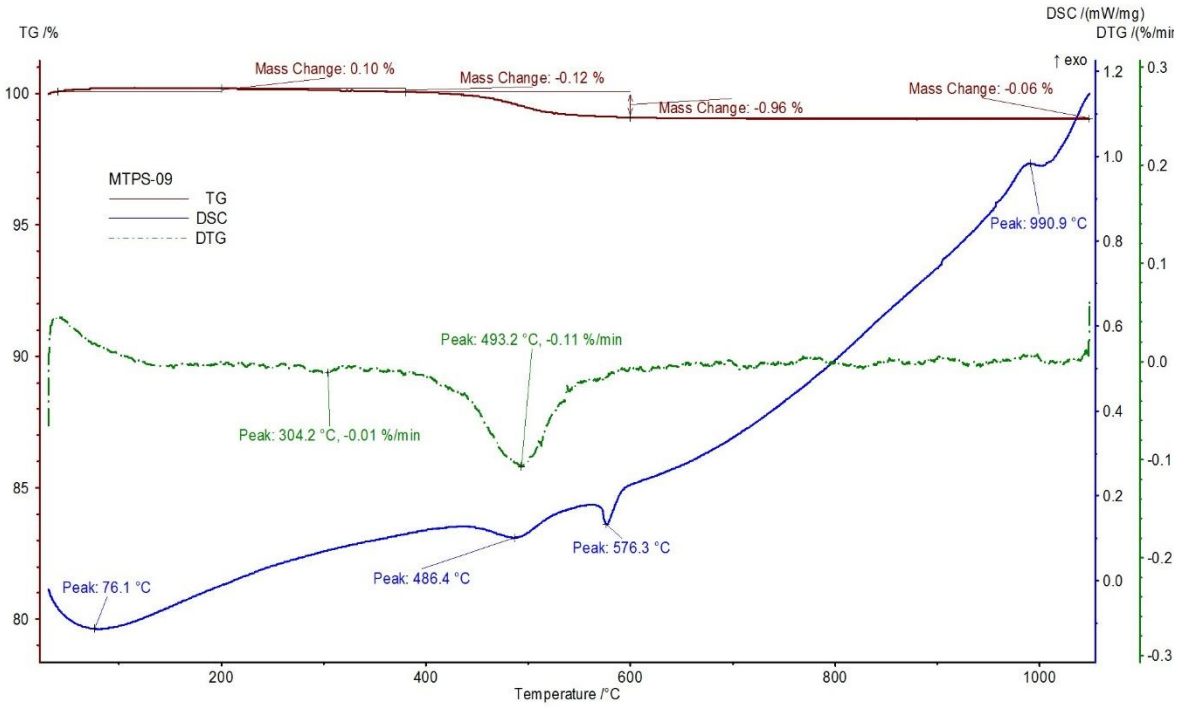

MTPS-04
TG
DSC
DTG
TG /%
DSC /(mW/mg)
↑ exo
Mass Change: -0.64 %
Mass Change: -5.10 %
Mass Change: -3.53 %
Mass Change: -0.04 %
Peak: 90.2 °C, -0.08 %/min
Peak: 321.4 °C
Peak: 476.7 °C, -0.29 %/min
Peak: 304.9 °C, -0.44 %/min
Peak: 988.6 °C
Peak: 576.2 °C
Peak: 490.1 °C
Peak: 78.7 °C
Temperature /°C

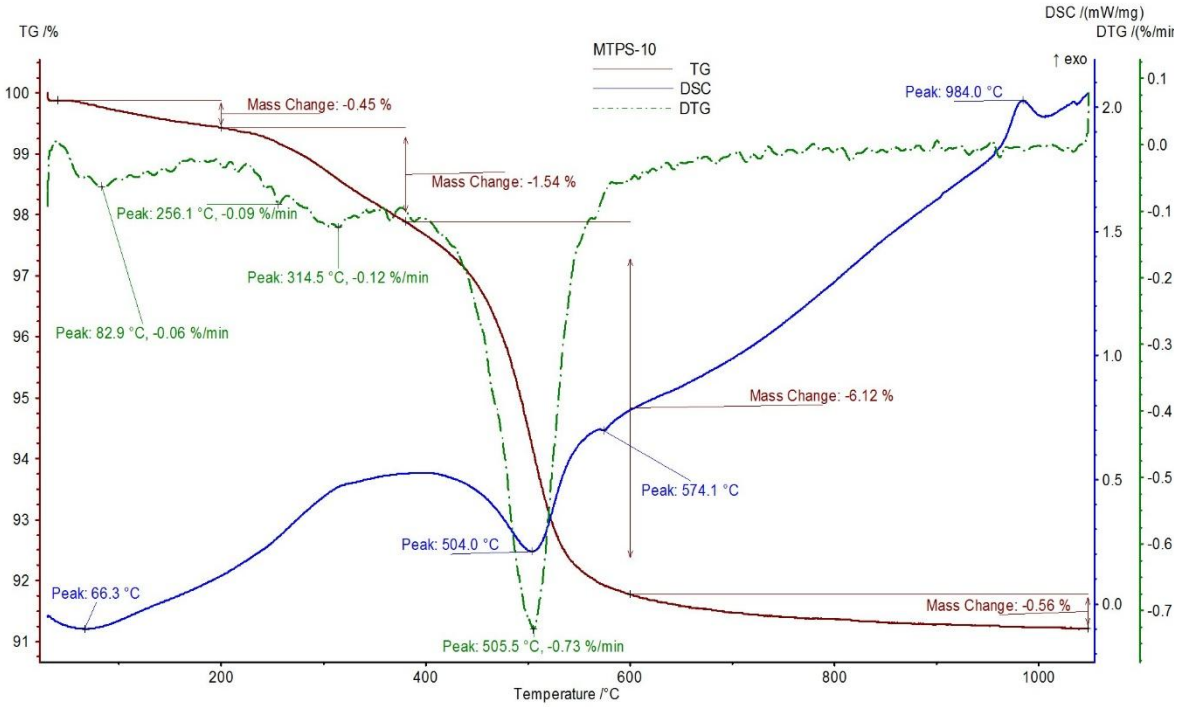

TG /%
DSC /(mW/mg)
DTG /(%/mi
MTPS-05
TG
DSC
DTG
↑ exo
Mass Change: -0.81 %
Mass Change: -3.00 %
Mass Change: -7.44 %
Mass Change: -0.29 %
Peak: 70.0 °C, -0.12 %/min
Peak: 265.9 °C, -0.20 %/min
Peak: 300.0 °C, -0.24 %/min
Peak: 330.8 °C
Peak: 257.0 °C
Peak: 499.3 °C
Peak: 575.1 °C
Peak: 986.8 °C
Peak: 65.9 °C
Peak: 501.2 °C, -0.81 %/min
Temperature /°C

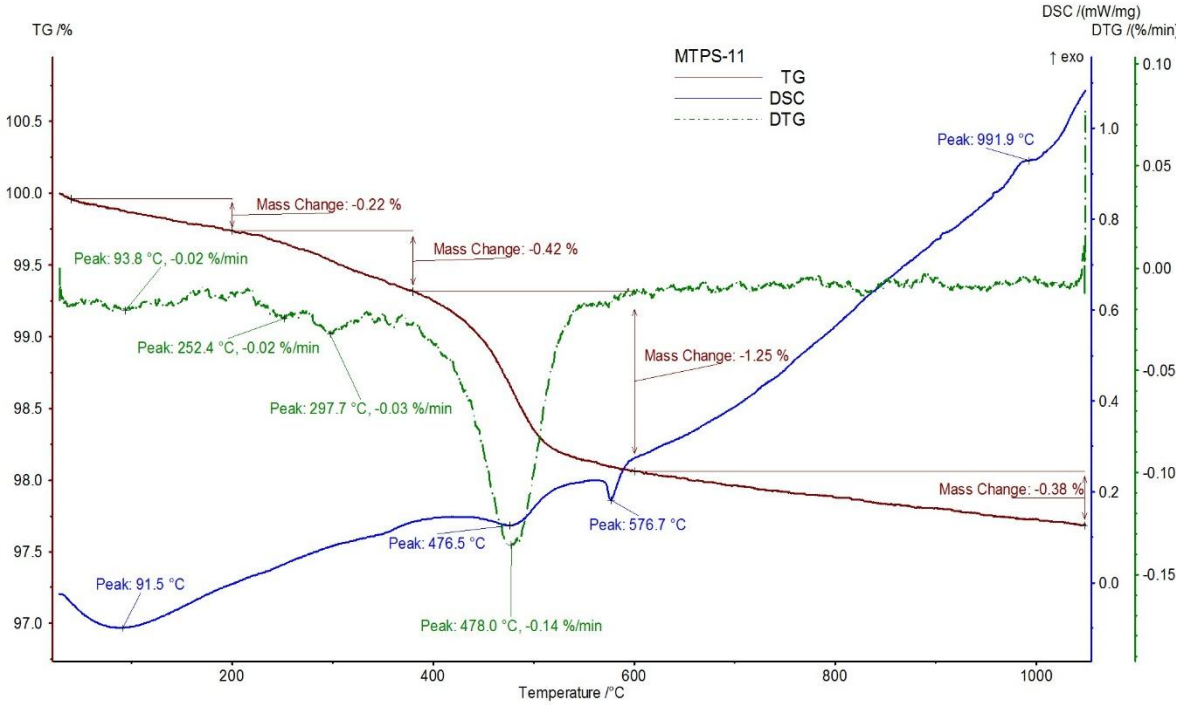

TG /%
DSC /(mW/mg)
DTG /(%/min
MTPS-06
TG
DSC
DTG
↑ exo
Mass Change: -0.20 %
Mass Change: 0.09 %
Mass Change: -1.32 %
Mass Change: -0.11 %
Peak: 146.9 °C, -0.01 %/min
Peak: 249.5 °C, -0.01 %/min
Peak: 570.0 °C, -0.02 %/min
Peak: 992.3 °C
Peak: 480.6 °C
Peak: 576.8 °C
Peak: 483.7 °C, -0.14 %/min
Peak: 75.5 °C
Temperature /°C

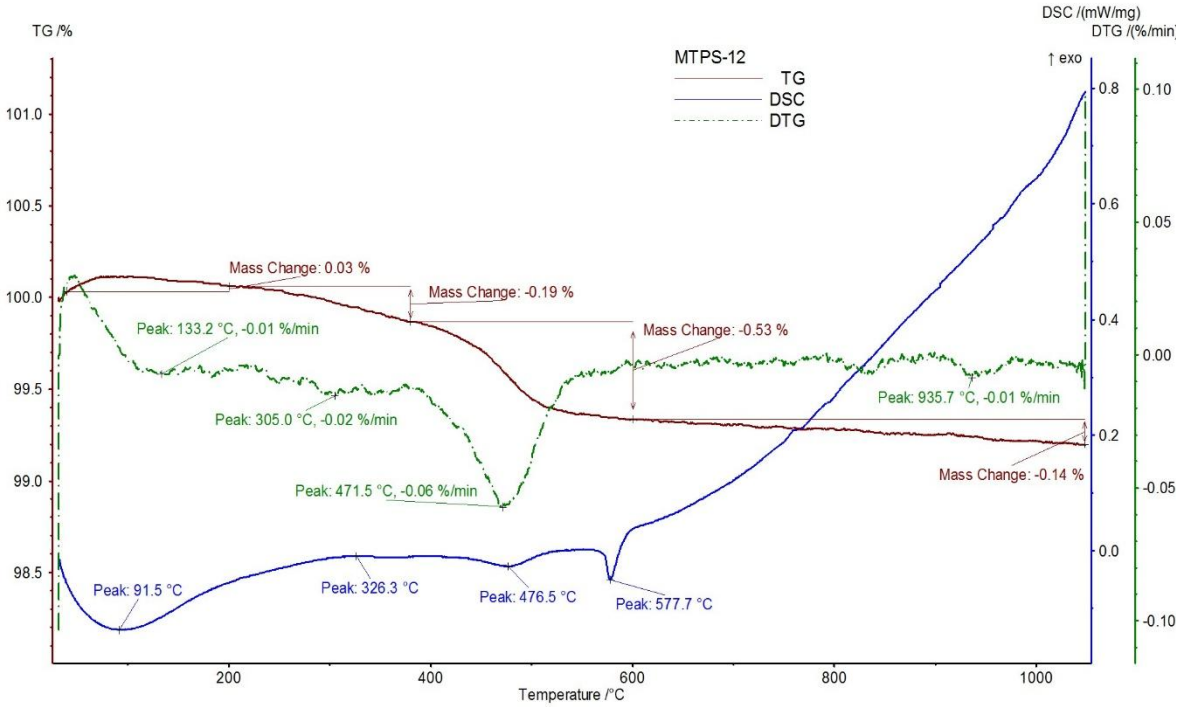

TG /%
DSC /(mW/mg)
DTG /(%/min)
MTPS-07
TG
DSC
DTG
↑ exo
Mass Change: -0.02 %
Mass Change: -0.65 %
Peak: 140.7 °C, -0.02 %/min
Peak: 572.4 °C, -0.02 %/min
Peak: 319.7 °C, -0.05 %/min
Mass Change: -1.77 %
Peak: 990.1 °C
Mass Change: -0.18 %
Peak: 482.4 °C
Peak: 577.5 °C
Peak: 77.3 °C
Peak: 480.7 °C, -0.17 %/min
Temperature /°C

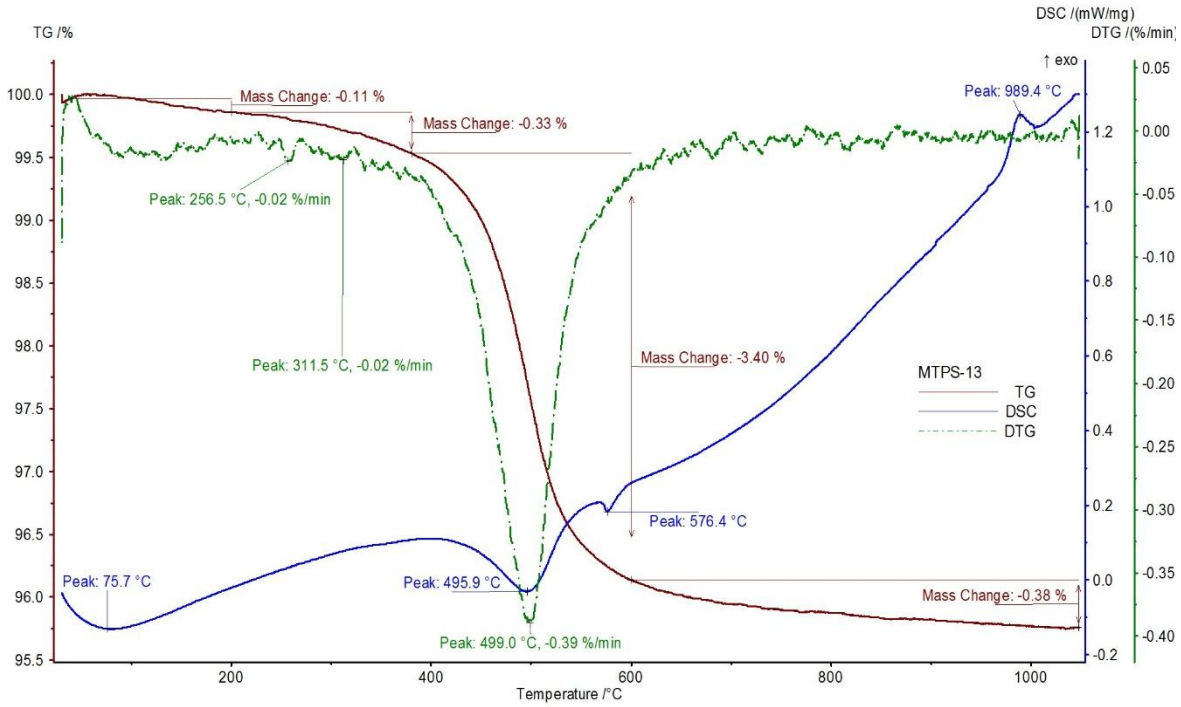

TG /%
DSC /(mW/mg)
DTG /(%/min)
MTPS-08
TG
DSC
DTG
↑ exo
Mass Change: 0.06 %
Mass Change: -0.21 %
Peak: 139.8 °C, -0.01 %/min
Mass Change: -0.74 %
Mass Change: -0.18 %
Peak: 251.8 °C, -0.02 %/min
Peak: 473.7 °C, -0.08 %/min
Peak: 267.6 °C
Peak: 77.0 °C
Peak: 577.8 °C
Peak: 474.6 °C
Temperature /°C

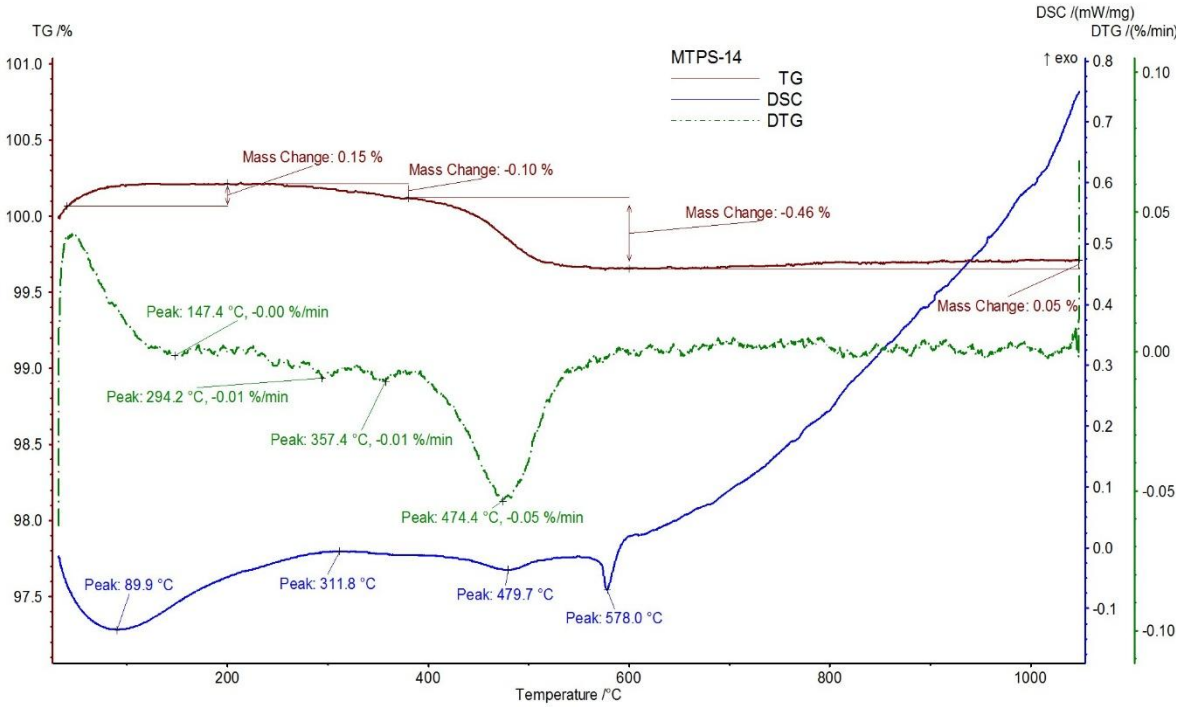

TG /%
DSC /(mW/mg)
DTG /(%/mi
↑ exo
MTPS-09
TG
DSC
DTG
Mass Change: 0.10 %
Mass Change: -0.12 %
Mass Change: -0.96 %
Mass Change: -0.06 %
Peak: 990.9 °C
Peak: 493.2 °C, -0.11 %/min
Peak: 304.2 °C, -0.01 %/min
Peak: 576.3 °C
Peak: 486.4 °C
Peak: 76.1 °C
Temperature /°C

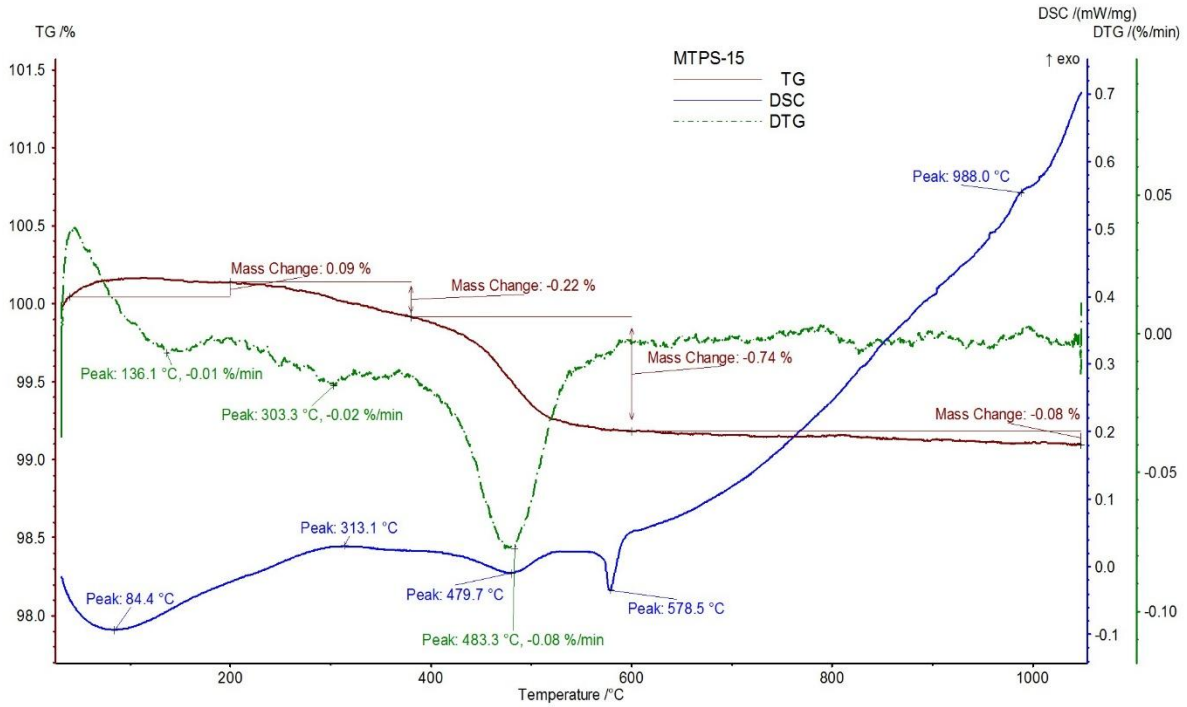

TG /%
DSC /(mW/mg)
DTG /(%/mi
↑ exo
MTPS-10
TG
DSC
DTG
Mass Change: -0.45 %
Mass Change: -1.54 %
Mass Change: -6.12 %
Mass Change: -0.56 %
Peak: 984.0 °C
Peak: 256.1 °C, -0.09 %/min
Peak: 314.5 °C, -0.12 %/min
Peak: 82.9 °C, -0.06 %/min
Peak: 574.1 °C
Peak: 504.0 °C
Peak: 66.3 °C
Peak: 505.5 °C, -0.73 %/min
Temperature /°C


TG /%
DSC /(mW/mg)
DTG /(%/min)
MTPS-11
TG
DSC
DTG
↑ exo
Mass Change: -0.22 %
Mass Change: -0.42 %
Mass Change: -1.25 %
Mass Change: -0.38 %
Peak: 93.8 °C, -0.02 %/min
Peak: 252.4 °C, -0.02 %/min
Peak: 297.7 °C, -0.03 %/min
Peak: 991.9 °C
Peak: 576.7 °C
Peak: 476.5 °C
Peak: 91.5 °C
Peak: 478.0 °C, -0.14 %/min
Temperature /°C


TG /%
DSC /(mW/mg)
DTG /(%/min)
MTPS-12
TG
DSC
DTG
↑ exo
Mass Change: 0.03 %
Mass Change: -0.19 %
Mass Change: -0.53 %
Mass Change: -0.14 %
Peak: 133.2 °C, -0.01 %/min
Peak: 305.0 °C, -0.02 %/min
Peak: 471.5 °C, -0.06 %/min
Peak: 935.7 °C, -0.01 %/min
Peak: 91.5 °C
Peak: 326.3 °C
Peak: 476.5 °C
Peak: 577.7 °C
Temperature /°C


TG /%
DSC /(mW/mg)
DTG /(%/min)
↑ exo
Mass Change: -0.11 %
Mass Change: -0.33 %
Peak: 989.4 °C
Peak: 256.5 °C, -0.02 %/min
Peak: 311.5 °C, -0.02 %/min
Mass Change: -3.40 %
MTPS-13
TG
DSC
DTG
Peak: 576.4 °C
Peak: 75.7 °C
Peak: 495.9 °C
Mass Change: -0.38 %
Peak: 499.0 °C, -0.39 %/min
Temperature /°C


TG /%
DSC /(mW/mg)
DTG /(%/min)
MTPS-14
TG
DSC
DTG
↑ exo
Mass Change: 0.15 %
Mass Change: -0.10 %
Mass Change: -0.46 %
Mass Change: 0.05 %
Peak: 147.4 °C, -0.00 %/min
Peak: 294.2 °C, -0.01 %/min
Peak: 357.4 °C, -0.01 %/min
Peak: 474.4 °C, -0.05 %/min
Peak: 89.9 °C
Peak: 311.8 °C
Peak: 479.7 °C
Peak: 578.0 °C
Temperature /°C


TG /%
DSC /(mW/mg)
DTG /(%/min)
MTPS-15
TG
DSC
DTG
↑ exo
Mass Change: 0.09 %
Mass Change: -0.22 %
Mass Change: -0.74 %
Mass Change: -0.08 %
Peak: 136.1 °C, -0.01 %/min
Peak: 303.3 °C, -0.02 %/min
Peak: 988.0 °C
Peak: 313.1 °C
Peak: 84.4 °C
Peak: 479.7 °C
Peak: 578.5 °C
Peak: 483.3 °C, -0.08 %/min
Temperature /°C

APPENDIX 7: pH and WHC (%) data.

Sample ID	pH	WHC (% d.w.)
MTBP-01	7.43	5.464546215
MTBP-02	6.94	4.694494678
MTBP-03	6.46	12.69313287
MTBP-04	8.35	3.796928328
MTBP-05	8.5	5.939287286
MTBP-06	8.32	8.582746479
MTBP-07	7.45	6.220095694
MTBP-08	6.7	23.67109542
MTBP-09	7.74	8.723021583
MTBP-10	7.72	4.177433247
MTBP-11	7.01	0.305077835
MTBP-12	7.93	6.536474357
MTBP-13	7.04	0.300149207
MTBP-14	8.4	3.258145363
MTBP-15	7.97	2.140077821
MTBP-17	6.66	17.48514851
MTBP-18	-	-
MTBP-19	6.94	21.38625248
MTBP-20	-	-
MTBP-21	7.38	14.48382126
MTBP-22	6.72	3.206725082
MTBP-23	7.11	2.242424242
MTBP-24	-	-
MTBP-25	-	-
MTBP-26	6.73	37.87567215
MTBP-27	7.95	0.051078734
MTBP-28	7.01	0.102285692
MTBP-29	-	-
MTBP-30	-	-
MTBP-31	-	-
MTBP-32	7.19	4.985961581
MTBP-33	6.59	4.577933024
MTBP-34	6.82	17.47404844
MTBP-35	6.6	17.85234899
MTBP-36	-	-
MTBP-37	7.54	2.140199202
MTBP-38	-	-
MTPS-01	6.88	0.147222496
MTPS-02	-	-
MTPS-03	-	-
MTPS-04	-	-
MTPS-05	7.2	13.01879822
MTPS-06	-	-
MTPS-07	6.77	4.659919981
MTPS-08	-	-
MTPS-09	-	-
MTPS-10	-	-
MTPS-11	-	-
MTPS-12	-	-
MTPS-13	7.04	0.300149207
MTPS-14	-	-
MTPS-15	-	-
MTNC-01	-	-
MTNC-02	-	-
MTNC-03	-	-
MTNC-04	-	-
MTNC-05	-	-

MTNC-06	8.34	12.27401835
MTNC-07	-	-
MTNC-08	-	-
MTNC-09	7.36	12.04488701
MTNC-10	7.78	14.82697099
MTNC-11	-	-
MTNC-12	7.24	9.084144201
MTNC-13	-	-
MTNC-14	-	-
MTNC-15	7.49	9.478070036
MTBVP-01	6.95	16.14104545
MTBVP-02	7.08	0.9217059
MTBVP-03	-	-
MTBVP-04	7.59	0.835310869

References

Adamu, G. K., & Aliyu, A. K., 2012. Determination of the influence of texture and organic matter on soil water holding capacity in and around Tomas Irrigation Scheme, Dambatta Local Government Kano State. Research Journal of Environmental and Earth Sciences, 4(12), 1038-1044.

Al-Amin, K., Kawsar, M., Mamun, M. T. R. B., & Hossain, M. S., 2025. Fourier transform infrared spectroscopic technique for analysis of inorganic materials: a review. Nanoscale Advances, 7(21), 6677-6702. https://doi.org/10.1039/D5NA00522A

Aquino, L. B. M. D., 2013. Geologia e geocronologia do Granito Palito e de sua mineralização, depósito aurífero do Palito, Província Aurífera do Tapajós, Itaituba-PA. Available at: https://bdm.ufpa.br/server/api/core/bitstreams/b468d540-ffcf-45ca-9352-62a02410e390/content

Awadh, S. M., & Yaseen, Z. M., 2019. Investigation of silica polymorphs stratified in siliceous geode using FTIR and XRD methods. Materials Chemistry and Physics, 228, 45-50. https://doi.org/10.1016/j.matchemphys.2019.02.048

Ayalew, A. A., 2023. Physiochemical characterization of Ethiopian mined kaolin clay through beneficiation process. Advances in Materials Science and Engineering, 2023(1), 9104807. https://doi.org/10.1155/2023/9104807

Barreto, M. S. C., Ramlogan, M., Oliveira, D. M. S., Verburg, E. E. J., Elzinga, E. J., Rouff, A. A., Jemo, M., & Alleoni, L. R. F., 2021. Thermal stability of soil organic carbon after long-term manure application across land uses and tillage systems in an oxisol. Catena, 200, 105164. https://doi.org/10.1016/j.catena.2021.105164

Becerra-Lira, E., Rodriguez-Achata, L., Ushñahua, A. M., Gomringer, R. C., Thomas, E., Garate-Quispe, J., Vargas, L. H., Herbay, P. R. N., Miranda, L. A. G., Umpiérrez, E., Barrantes, J. A. G., Pillaca, M., Auca, E. C., Valdeiglesias, J. P., Russo, R., Torres, D. C., & Ramírez, M. G. V. 2024. Spatio-temporal trends of mercury levels in alluvial gold mining spoils areas monitored between rainy and dry seasons in the Peruvian Amazon. Environmental Research, 245, 118073. https://doi.org/10.1016/j.envres.2023.118073

Blouin, V. M., Schmidt, M. G., Bulmer, C. E., & Krzic, M., 2005. Mechanical disturbance impacts on soil properties and lodgepole pine growth in British Columbia's central interior. Canadian Journal of Soil Science, 85(5), 681-691. https://doi.org/10.4141/S04-077

Boeva, N. M., Makarova, M. A., Shipilova, E. S., Slukin, A. D., Soboleva, S. V., Zhegallo, E. A., Zaitseva, L. V., & Bortnikov, N. S., 2022. Gibbsite and Boehmite in Weathering Crusts of Different Ages Affected by Lateritization: Location and Formation. Dokl. Earth Sc. 504, 353–361. https://doi.org/10.1134/S1028334X22060046

Bordoloi, R., Das, B., Yam, G., Pandey, P. K., & Tripathi, O. P., 2019. Modeling of water holding capacity using readily available soil characteristics. Agricultural Research, 8(3), 347-355. https://doi.org/10.1007/s40003-018-0376-9

Cheng, Y., Watari, T., Seccatore, J., Nakajima, K., Nansai, K., & Takaoka, M., 2023. A review of gold production, mercury consumption, and emission in artisanal and small-scale gold mining (ASGM). Resources Policy, 81, 103370. https://doi.org/10.1016/j.resourpol.2023.103370

Cui, H., Zhao, Y., Zhao, L., & Wei, Z., 2022. Characterization of mercury binding to different molecular weight fractions of dissolved organic matter. Journal of Hazardous Materials, 431, 128593. https://doi.org/10.1016/j.jhazmat.2022.128593

Debure, M., Grangeon, S., Robinet, J. C., Madé, B., Fernández, A. M., & Lerouge, C., 2020. Influence of soil redox state on mercury sorption and reduction capacity. Science of The Total Environment, 707, 136069. https://doi.org/10.1016/j.scitotenv.2019.136069

Fernandes, A. R., de Souza, E. S., de Souza Braz, A. M., Birani, S. M., & Alleoni, L. R. F., 2018. Quality reference values and background concentrations of potentially toxic elements in soils from the Eastern Amazon, Brazil. Journal of Geochemical Exploration, 190, 453-463. https://doi.org/10.1016/j.gexplo.2018.04.012

Ferreira, M. S., Fontes, M. P. F., Bellato, C. R., Neto, J. O. M., Lima, H. N., & Fendorf, S., 2021. Geochemical signatures and natural background values of rare earth elements in soils of Brazilian Amazon. Environmental Pollution, 277, 116743. https://doi.org/10.1016/j.envpol.2021.116743

Fostier, A. H., Forti, M. C., Guimaraes, J. R. D., Melfi, A. J., Boulet, R., Santo, C. E., & Krug, F. J., 2000. Mercury fluxes in a natural forested Amazonian catchment (Serra do Navio, Amapa State, Brazil). Science of the Total Environment, 260(1-3), 201-211. https://doi.org/10.1016/S0048-9697(00)00564-7

Gasparini, A. S., Fontes, M. P. F., Pacheco, A. A., & Ker, J. C., 2022. Gibbsite crystallinity and morphology in ferralsols and bauxites. Minerals, 12(11), 1441. https://doi.org/10.3390/min12111441

Guedron, S., Grangeon, S., Lanson, B., & Grimaldi, M., 2009. Mercury speciation in a tropical soil association; Consequence of gold mining on Hg distribution in French Guiana. Geoderma, 153(3-4), 331-346. https://doi.org/10.1016/j.geoderma.2009.08.017

Gustin, M. S., & Stamenkovic, J., 2005. Effect of watering and soil moisture on mercury emissions from soils. Biogeochemistry, 76(2), 215-232. https://doi.org/10.1007/s10533-005-4566-8

Junior, E. C. S., Wadt, L. H. O., da Silva, K. E., de Lima, R. M. B., Batista, K. D., Guedes, M. C., Junior, R. C. O., Reis, A. R., Lopes, G., Broadley, M. R., Young, S. D., & Guilherme, L. R. G., 2022. Geochemistry of selenium, barium, and iodine in representative soils of the Brazilian Amazon rainforest. Science of the Total Environment, 828, 154426. https://doi.org/10.1016/j.scitotenv.2022.154426

Kondo, M., Korre, A., Komai, T., & Watanabe, N., 2024. Multi-layered physical factors govern mercury release from soil: Implications for predicting the environmental fate of mercury. Journal of Environmental Management, 352, 120024. https://www.sciencedirect.com/science/article/pii/S0301479724000100

Langer, K., & Flörke, O.W., 1974. Near infrared absorption spectra (4000-9000 CM-1) of opals and the vole of "water" in these SiO2.NH2O minerals.

Lázaro, W. L., Oliveira, E. S., Santos, F. L. D., Oliveira, E. D., Poleto, C., & Ignácio, Á. R. A., 2025. Mapping total mercury in rivers of Mato Grosso: baselines and contamination hotspots by biome. Revista Ambiente & Água, 20, e3119. https://doi.org/10.4136/ambi-agua.3119

Lechler, P. J., Miller, J. R., Lacerda, L. D. D., Vinson, D., Bonzongo, J. C., Lyons, W. B., & Warwick, J. J., 2000. Elevated mercury concentrations in soils, sediments, water, and fish of the Madeira River basin, Brazilian

Amazon: a function of natural enrichments?. Science of the Total Environment, 260(1-3), 87-96. https://doi.org/10.1016/S0048-9697(00)00543-X

Li, Q., Wang, L., Fu, Y., Lin, D., Hou, M., Li, X., Hu, D., & Wang, Z., 2023. Transformation of soil organic matter subjected to environmental disturbance and preservation of organic matter bound to soil minerals: a review. Journal of Soils and Sediments, 23(3), 1485-1500. https://doi.org/10.1007/s11368-022-03381-y

Li, X., Schindler, M., Zhou, J., Samaradiwakara, S., & Wu, L., 2025. Interaction between metal (loid) s and soil mineral-organic matter associations. Critical Reviews in Environmental Science and Technology, 55(9), 624-647. https://doi.org/10.1080/10643389.2024.2434328

Lourenço, M. S. T. A., Debruyne, D., Di Maggio, R. M., Germinario, C., Grifa, C., Izzo, F., Langella, A., de Paula, L. S., Salvador, F. A. S., & Mercurio, M., 2025. Mercury contamination in Brazil related to (historical) artisanal and small-scale gold mining activity: a narrative review with quantitative synthesis. Environmental Geochemistry and Health, 48(1), 45. https://doi.org/10.1007/s10653-025-02929-4

Maechler, M., Rousseeuw, P., Croux, C., Todorov, V., Ruckstuhl, A., Salibian-Barrera, M., Verbeke, T., Koller, M., Conceição, E. L. T., & Palma, M. A., 2025. robustbase: Basic Robust Statistics R package version 0.99-6. URL http://CRAN.R-project.org/package=robustbase

Mercurio, M., Izzo, F., Langella, A., & Sarkar, B., 2022. Simultaneous Thermal Analysis (STA): A Powerful Tool for Forensic Investigation of Geomaterials. In Mineralogical Analysis Applied to Forensics: A Guidance on Mineralogical Techniques and Their Application to the Forensic Field (pp. 193-224). Cham: Springer International Publishing. https://doi.org/10.1007/978-3-031-08834-6_7

Merino, A., Omil, B., Pineiro, V., Barros, N., Souza-Alonso, P., & Campo, J., 2023. Soil C dynamics after deforestation and subsequent conversion of arable cropland to grassland in humid temperate areas. Science of The Total Environment, 901, 165793. https://doi.org/10.1016/j.scitotenv.2023.165793

Miele, F., Benettin, P., Wang, S., Retti, I., Asadollahi, M., Frutschi, M., Mohanty, B., Bernier-Latmani, R., & Rinaldo, A., 2023. Spatially explicit linkages between redox potential cycles and soil moisture fluctuations. Water Resources Research, 59(3), e2022WR032328. https://doi.org/10.1029/2022WR032328

Miller, C. L., Watson, D. B., Lester, B. P., Howe, J. Y., Phillips, D. H., He, F., Liang, L., & Pierce, E. M., 2015. Formation of soluble mercury oxide coatings: transformation of elemental mercury in soils. Environmental Science & Technology, 49(20), 12105-12111. doi: 10.1021/acs.est.5b00263

Moreno-Brush, M., McLagan, D. S., & Biester, H., 2019. Fate of mercury from artisanal and small-scale gold mining in tropical rivers: Hydrological and biogeochemical controls. A critical review. Critical Reviews in Environmental Science and Technology, 50(5), 437-475. https://doi.org/10.1080/10643389.2019.1629793

Parolo, M. E., Savini, M. C., & Loewy, R. M., 2017. Characterization of soil organic matter by FT-IR spectroscopy and its relationship with chlorpyrifos sorption. Journal of environmental management, 196, 316-322. https://doi.org/10.1016/j.jenvman.2017.03.018

Peltre, C., Fernández, J. M., Craine, J. M., & Plante, A. F., 2013. Relationships between biological and thermal indices of soil organic matter stability differ with soil organic carbon level. Soil Science Society of America Journal, 77(6), 2020-2028. https://doi.org/10.2136/sssaj2013.02.0081

Rocha, D. R., Barber, X., Jordán-Vidal, M. M., Urbano, A., Melquiades, F. L., Thomaz, E. L., & Mataix-Solera, J., 2022. Multivariate analysis with XRD data as a fingerprinting technique to study burned soils. Minerals, 12(11), 1402. https://doi.org/10.3390/min12111402

Sahoo, P. K., Dall'Agnol, R., Salomão, G. N., Junior, J. S. F., Silva, M. S., Souza Filho, P. W. M., Costa, M. L., Angélica, R. S., Filho, C. A. M., Costa, M. F., Guilherme, L. R. G., & Siqueira, J. O., 2020. Regional-scale mapping for determining geochemical background values in soils of the Itacaiúnas River Basin, Brazil: The use of compositional data analysis (CoDA). Geoderma, 376, 114504. https://doi.org/10.1016/j.geoderma.2020.114504

Schuster, E., 1991. The behavior of mercury in the soil with special emphasis on complexation and adsorption processes-a review of the literature. Water Air & Soil Pollution, 56(1), 667-680. https://doi.org/10.1007/BF00342308

Schuttlefield, J. D., Cox, D., & Grassian, V. H., 2007. An investigation of water uptake on clays minerals using ATR-FTIR spectroscopy coupled with quartz crystal microbalance measurements. Journal of Geophysical Research: Atmospheres, 112(D21). https://doi.org/10.1029/2007JD008973

Senesi, N., Testini, C., & Polemio, M., 1983. Chemical and spectroscopic characterization of soil organic matter fractions isolated by sequential extraction procedure. Journal of Soil Science, 34(4), 801-813. https://doi.org/10.1111/j.1365-2389.1983.tb01073.x

Soares, M. B., Rodrigues, R. R., Péres, L. O., Cerri, C. E. P., & Alleoni, L. R. F., 2024. Impact of climatic seasons on the dynamics of carbon, nitrogen and mercury in soils of Brazilian biomes affected by gold mining. Science of the Total Environment, 954, 176279. https://doi.org/10.1016/j.scitotenv.2024.176279

Song, G., Simpson, A. J., & Hayes, M. H., 2023. Compositional changes in the humin fraction resulting from the long-term cultivation of an Irish grassland soil: Evidence from FTIR and multi-NMR spectroscopies. Science of the Total Environment, 880, 163280. https://doi.org/10.1016/j.scitotenv.2023.163280

Souza, E. S. D., Fernandes, A. R., De Souza Braz, A. M., Oliveira, F. J. D., Alleoni, L. R. F., & Campos, M. C. C., 2018. Physical, chemical, and mineralogical attributes of a representative group of soils from the eastern Amazon region in Brazil. Soil, 4(3), 195-212. https://doi.org/10.5194/soil-4-195-2018

Spanner, G. C., Gimenez, B. O., Wright, C. L., Menezes, V. S., Newman, B. D., Collins, A. D., Jardine, K. J., Negrón-Juárez, R., Lima, A. J. N., Rodrigues, J. R., Chambers, J. Q., Higuchi, N., & Warren, J. M., 2022. Dry season transpiration and soil water dynamics in the Central Amazon. Frontiers in plant science, 13, 825097. https://doi.org/10.3389/fpls.2022.825097

Stone, M. M., & Plante, A. F., 2015. Relating the biological stability of soil organic matter to energy availability in deep tropical soil profiles. Soil Biology and Biochemistry, 89, 162-171. https://doi.org/10.1016/j.soilbio.2015.07.008

Tiwari, N., Satyam, N., & Shukla, S. K., 2020. An experimental study on micro-structural and geotechnical characteristics of expansive clay mixed with EPS granules. Soils and Foundations, 60(3), 705-713. https://doi.org/10.1016/j.sandf.2020.03.012

Vaňková, M., Vieira, A. M. D., Ettler, V., Vaněk, A., Trubač, J., Penížek, V., & Mihaljevič, M., 2024. Tracing anthropogenic mercury in soils from Fe–Hg mining/smelting area: Isotopic and speciation insights. Chemosphere, 357, 142038. https://doi.org/10.1016/j.chemosphere.2024.142038

Volkov, D. S., Rogova, O. B., & Proskurnin, M. A., 2021. Organic matter and mineral composition of silicate soils: FTIR comparison study by photoacoustic, diffuse reflectance, and attenuated total reflection modalities. Agronomy, 11(9), 1879. https://doi.org/10.3390/agronomy11091879

Wang, S. L., & Johnston, C. T., 2000. Assignment of the structural OH stretching bands of gibbsite. American Mineralogist, 85(5-6), 739-744. https://doi.org/10.2138/am-2000-5-612

Wang, X., Yuan, W., Lin, C. J., & Feng, X., 2022. Mercury cycling and isotopic fractionation in global forests. Critical Reviews in Environmental Science and Technology, 52(21), 3763-3786. https://doi.org/10.1080/10643389.2021.1961505

Wang, J., Rinklebe, J., & Feng, X., 2024. Redox Transformation of Mercury in Soils. In Methylmercury Accumulation in Rice (pp. 126-140). CRC Press.

Waychunas, G. A., Kim, C. S., & Banfield, J. F., 2005. Nanoparticulate iron oxide minerals in soils and sediments: unique properties and contaminant scavenging mechanisms. Journal of nanoparticle research, 7(4), 409-433. https://doi.org/10.1007/s11051-005-6931-x

Wickham, H., François, R., Henry, L., Müller, K., Vaughan, D., 2023. _dplyr: A Grammar of Data Manipulation_. R package version 1.1.4, <https://CRAN.R-project.org/package=dplyr>.

Wu, J., Xie, W., Tan, J., & Liu, L., 2023. Understanding the sources of mercury release from coal: A combined experimental and molecular simulation study. Journal of Hazardous Materials, 460, 132429. https://doi.org/10.1016/j.jhazmat.2023.132429

Yang, L., Zhang, Y., Wang, F., Luo, Z., Guo, S., & Strähle, U., 2020. Toxicity of mercury: Molecular evidence. Chemosphere, 245, 125586. https://doi.org/10.1016/j.chemosphere.2019.125586

Zhang, Y., Wang, X., Yang, Y., Huang, Y., Li, X., Hu, S., Liu, K., Pang, Y., & Li, F., 2023. Retention and transformation of exogenous Hg in acidic paddy soil under alternating anoxic and oxic conditions: Kinetic and mechanistic insights. Environmental Pollution, 323, 121335. https://doi.org/10.1016/j.envpol.2023.121335

Zhao, S., Terada, A., Nakamura, K., Nakashima, M., Komai, T., Riya, S., Hosomi, M., & Hou, H., 2022. Significance of soil moisture on temperature dependence of Hg emission. Journal of Environmental Management, 305, 114308. https://doi.org/10.1016/j.jenvman.2021.114308

6. General conclusions

This thesis investigated the persistence, geochemical controls, and environmental implications of mercury (Hg) associated with artisanal and small-scale gold mining (ASGM) in Brazil, with a particular focus on Amazonian contexts. The systematic review (Section 2) confirmed that Hg contamination linked to *garimpos* is widespread and persistent across the country, especially in the Amazon, with impacts documented across multiple environmental and biological matrices. The review also reinforced that the main exposure pathways include occupational inhalation of elemental Hg vapor and dietary intake of methylmercury through fish consumption in riverine and Indigenous communities. However, the consolidated evidence shows that elevated Hg levels in many regions cannot be attributed solely to ASGM. Naturally enriched soils, long-term atmospheric deposition, and dynamic processes such as erosion and sediment transport contribute substantially to Hg distribution. Human disturbances such as ASGM, deforestation, and damming, can further mobilize legacy or geogenic Hg, sustaining methylation potential and ecological risk. In the absence of regionally defined geochemical baselines, there is a clear risk of misattribution, which may distort both policy responses and public health advisories.

Building on these gaps, the empirical chapters of this thesis evaluated soils from sites with contrasting ASGM histories (active, deactivated in January 2024, deactivated for ~30 years, and a control site without ASGM records). Section 4 demonstrated that Hg contamination in soils can persist for decades after mining activity has ceased. The ~30 years deactivated ASGM site still exhibited elevated THg concentrations (27 to 8,862 ng g^{-1}; median = 324 ng g^{-1}) and ecological risk levels above regulatory thresholds, indicating a long-term contamination legacy. In contrast, the active and recently deactivated sites generally displayed THg concentrations near the regional background value (178 ng g^{-1}), with exceedances largely restricted to

localized hotspots directly associated with ASGM operations (e.g., near the sluice box in the active site). These results indicate that current activity does not necessarily translate into higher median THg in soils at the site scale, whereas long-term deactivated areas can remain environmentally relevant sources of Hg exposure and risk.

Chapter 4 further showed that Hg retention in the long-term deactivated site is strongly controlled by substrate properties. Fine particle content explained 73% of the variability in $\log_{10}$-transformed THg, highlighting a robust log-linear relationship between particle size and Hg retention. This finding reinforces that contamination assessment and risk interpretation in ASGM landscapes must incorporate soil physical properties, particularly in highly heterogeneous tropical settings.

The final section expanded the mechanistic interpretation of Hg behavior through an integrated approach combining XRD, ATR-FTIR, TG-DSC, pH, and WHC. The studied soils share a broadly similar mineralogical framework dominated by quartz and kaolinite-group minerals, consistent with highly weathered tropical soils developed on granitic parent material. Nevertheless, accessory phases such as gibbsite, mica-type phyllosilicates, smectites, and sporadically occurring feldspars indicate that meaningful differences persist at the sample scale, reflecting variability in weathering intensity, soil development, and disturbance history. In addition, the limited detectability of Fe–Mn (oxyhydr)oxides in bulk XRD highlights that reactive phases controlling trace-metal behavior may occur as low-crystallinity or minor components, requiring interpretation in combination with complementary datasets.

The association between Fe–Mn (oxyhydr)oxides and THg was not uniform across sites, indicating a context-dependent role of these phases in Hg retention. In the ~30 years deactivated ASGM site, samples containing Fe–Mn (oxyhydr)oxides exhibited significantly lower THg, whereas in the control area the presence of these phases was associated with higher

THg. These contrasting patterns are consistent with the idea that oxides can both retain Hg efficiently under relatively stable conditions and, under disturbed or redox-variable conditions, participate in Hg redistribution and transformation processes that weaken simple mineral–THg relationships.

ATR-FTIR results also supported subtle but consistent differences in surface hydration and organic matter signals among sites. The more systematic detection of absorptions around ~1640 cm^{-1} in the deactivated and control sites suggests greater persistence of molecular water associated with hydroxylated clay minerals, whereas their less consistent occurrence in active ASGM soils is compatible with ongoing mechanical reworking and disruption of soil structure. The detection of aliphatic C–H stretching bands (2950–2850 cm^{-1}) in only one active ASGM sample suggests localized occurrence of relatively labile organic compounds, consistent with heterogeneous organic matter distribution under active disturbance. Conversely, OH-stretching absorptions between ~3520 and ~3400 cm^{-1} were exclusive to control soils and likely reflect a stronger contribution of gibbsite, suggesting that this area represents a more weathered and less disturbed environment within the studied landscape.

Thermogravimetric analyses showed that the dominant mass loss event across all samples occurs in the 380–600 °C interval, and that the strongest between-site differences are expressed in this temperature range. This indicates that site-related contrasts are primarily reflected in major soil fractions controlling thermal behavior, particularly kaolinite-group dehydroxylation and associated organo-mineral components, rather than being restricted to moisture-related or minor labile organic matter fractions. The active ASGM site consistently exhibited lower mass losses across several intervals, supporting the interpretation that ongoing disturbance reduces moisture-associated and reactive surface fractions. In contrast, the site deactivated in January 2024 differed from the other ASGM sites in the dominant 380–600 °C interval, suggesting that

shortly after cessation soils may display a distinct mineral–organic configuration affecting the main dehydroxylation processes.

Across sites, THg concentrations were systematically associated with thermogravimetric fractions, particularly in the ~30 years deactivated ASGM site where strong correlations were observed across all temperature intervals. This indicates that Hg enrichment in long-term deactivated soils is linked to multiple soil components, including moisture-related losses, organic matter decomposition, and mineral dehydroxylation processes. Regression models further showed that THg variability is not controlled exclusively by the dominant 380–600 °C event, and that site category explains additional variance beyond TG-derived fractions alone, reinforcing the importance of environmental context and disturbance history.

Finally, WHC results suggest that soil physical properties contribute to within-site controls on THg distribution, although this relationship was not consistent across ASGM contexts. A significant positive association between WHC and THg was detected only in the ~30 years deactivated ASGM site, where WHC was also positively correlated with fine particle content and THg showed a strong affinity for the <105 μm fraction. Together, these results indicate that in the long-term deactivated site, THg enrichment preferentially occurs in finer-textured soils with higher water retention capacity, consistent with increased sorption capacity and potentially greater micro-scale redox heterogeneity. In contrast, soil pH did not show significant correlations with THg in any site, suggesting that pH is not a first-order control on bulk THg concentrations at the scale captured by this dataset.

Overall, this thesis demonstrates that Hg risk in ASGM landscapes is not determined solely by the presence of active mining, but by the interaction between contamination legacy, soil texture, physical properties, reactive mineral phases, and disturbance history. These findings reinforce the need for integrated approaches to source attribution and risk assessment, aligned

with a One Health perspective, and support recommendations for long-term monitoring, development of regional geochemical baselines to support regionalized pertinent legislation on Hg concentrations in the soil, and incorporation of soil matrix properties into management and remediation strategies.

Main contributions of this thesis

This thesis provides empirical evidence that Hg risk in ASGM landscapes is not necessarily highest where mining is currently active, but can remain environmentally relevant for decades after cessation, depending on soil properties and disturbance history. By using a regional control area as a geogenic baseline, the study also reinforces the importance of avoiding misattribution, particularly in Amazonian contexts, where naturally enriched substrates and legacy pools can contribute substantially to measured THg. At the site scale, the results demonstrate that particle-size distribution might be used a predictor of THg retention, with fine fractions explaining most of the within-site variability in the long-term deactivated area. The integrated interpretation of XRD, ATR-FTIR and TG/DSC data further shows that mineralogical controls on Hg retention are likely context-dependent, particularly regarding Fe–Mn (oxyhydr)oxides, and that thermogravimetric fractions provide a useful proxy for identifying soil components systematically associated with THg. Finally, the WHC results indicate that soil physical properties can contribute to Hg enrichment in specific contexts, especially where fine particles and water retention co-vary, highlighting the relevance of micro-scale heterogeneity in post-ASGM soils.